



HAL
open science

Wooden materials assembly : effect of oxygen on fire development and on gas and aerosol emissions

Adèle Lamande

► **To cite this version:**

Adèle Lamande. Wooden materials assembly : effect of oxygen on fire development and on gas and aerosol emissions. Other. Centrale Lille Institut, 2023. English. NNT : 2023CLIL0034 . tel-04593677

HAL Id: tel-04593677

<https://theses.hal.science/tel-04593677v1>

Submitted on 30 May 2024

HAL is a multi-disciplinary open access archive for the deposit and dissemination of scientific research documents, whether they are published or not. The documents may come from teaching and research institutions in France or abroad, or from public or private research centers.

L'archive ouverte pluridisciplinaire **HAL**, est destinée au dépôt et à la diffusion de documents scientifiques de niveau recherche, publiés ou non, émanant des établissements d'enseignement et de recherche français ou étrangers, des laboratoires publics ou privés.

CENTRALE LILLE

THESE

Présentée en vue d'obtenir le grade de

DOCTEUR

En

Spécialité : Molécules et Matière Condensée

Par

Adèle Lamandé

DOCTORAT DELIVRE PAR CENTRALE LILLE

Wooden materials assembly: effect of oxygen on fire development and on gas and aerosol emissions

-

Assemblage de matériaux bois : effet de l'oxygène sur le développement de l'incendie et sur l'émission de gaz et d'aérosols

Soutenue le 17 novembre 2023 devant le jury d'examen :

Président	Guillaume Legros, Prof., Université d'Orléans
Rapporteur	Anna A. Stec, Prof., University of Central Lancashire
Rapporteur	Anne Elise Steen-Hansen, Prof., Norwegian University of Science and Technology
Co-directeur	Serge Bourbigot, Prof., Centrale Lille
Co-encadrante	Véronique Marchetti, Dr., CSTB
Directrice de thèse	Gaëlle Fontaine, Prof., Centrale Lille

Thèse préparée dans le Laboratoire CSTB et UMET
Ecole Doctorale SMRE 104

CENTRALE LILLE

THESE

Présentée en vue d'obtenir le grade de

DOCTEUR

En

Spécialité : Molécules et Matière Condensée

Par

Adèle Lamandé

DOCTORAT DELIVRE PAR CENTRALE LILLE

Wooden materials assembly: effect of oxygen on fire development and on gas and aerosol emissions

-

Assemblage de matériaux bois : effet de l'oxygène sur le développement de l'incendie et sur l'émission de gaz et d'aérosols

Soutenue le 17 novembre 2023 devant le jury d'examen :

Président	Guillaume Legros, Prof., Université d'Orléans
Rapporteur	Anna A. Stec, Prof., University of Central Lancashire
Rapporteur	Anne Elise Steen-Hansen, Prof., Norwegian University of Science and Technology
Co-directeur	Serge Bourbigot, Prof., Centrale Lille
Co-encadrante	Véronique Marchetti, Dr., CSTB
Directrice de thèse	Gaëlle Fontaine, Prof., Centrale Lille

Thèse préparée dans le Laboratoire CSTB et UMET
Ecole Doctorale SMRE 104

Acknowledgements

Je tiens tout d'abord à remercier mes directeurs de thèse, Gaëlle Fontaine et Serge Bourbigot, pour avoir dirigé cette thèse et pour m'avoir solidement accompagné durant ces trois ans. Vous avez toujours été disponibles, compréhensifs et de bons conseils pour mener ce projet. Travailler avec vous a toujours été un réel plaisir et j'espère réitérer notre collaboration sur d'autres projets. Je ne peux aussi que remercier mon encadrante au CSTB, Véronique Marchetti, pour s'être impliquée et m'avoir guidée tout au long de ma thèse. Je te serai toujours reconnaissante pour ton soutien, autant sur le point de vue professionnel que personnel.

Toute ma gratitude va aussi à Valérie Gourvès, Philippe Leblond et ElMehdi Koutaiba pour leur accueil au sein de la Division RISC du CSTB, et plus particulièrement au sein du pôle Feu. Je vous remercie pour la confiance que vous m'avez accordée en m'offrant l'opportunité de rejoindre le pôle Feu à l'issue de ma thèse.

Je remercie vivement Anna A. Stec et Anne Elise Steen-Hansen qui ont accepté d'être rapportrices de cette thèse. Merci aussi à Guillaume Legros et Paul-Antoine Santoni pour le temps qu'ils ont accordé à l'examen de mes travaux.

Un grand merci à toutes les équipes du CSTB qui m'ont épaulé durant ma thèse. En premier lieu Sébastien Ritoux pour son prêt de l'ELPI et Céline Le Dreff pour son partage de connaissances sur l'ELPI. Je remercie aussi l'équipe de la DIMI, particulièrement Philippe, Amir et Sylvain, qui s'est toujours adaptée à mes (nombreux) problèmes techniques. Un éternel merci à toute l'équipe EEF pour son accueil et sa bonne humeur quotidienne. Vous avez égayé mes 3 ans de thèse ! Plus particulièrement, Valentin qui m'a partagé son expérience et aidé sur le cône calorimètre, Sébastien qui m'a résolu un nombre infini de problèmes techniques et aidé sur les essais à échelle intermédiaire (et promis je me mets à la muscu !), Frédéric qui a subi tant de fois mes plaintes sans rechigner et Dominique et Brahim pour leur aide sur les conceptions de bancs d'essais. Je remercie aussi toute l'équipe de RISC pour leur soutien et leur bienveillance. Particulièrement, un grand merci à Mara pour avoir géré toute la logistique de ma soutenance. Un merci aussi à l'équipe SMP, votre bonne humeur a toujours été au rendez-vous. Et enfin... merci à Renato et Benoit-Louis, mes fidèles comparses de pause-café, blaguounettes et navette (BLAR 4 ever) ! Et bien-sûr merci à toute l'équipe afterwork (elle se reconnaîtra !!!), vous m'avez changé les idées un nombre incalculable de fois (et fait boire beaucoup trop de bière !!). Enfin je remercie Margaux, ma

collègue, mon amie, ma jumelle qui a toujours été à mon écoute, dans les bons mais surtout dans les mauvais moments. Ces trois ans auraient été bien plus difficiles sans toi.

Je remercie aussi toute l'équipe ISP de Lille, particulièrement Johan, Anaïs et Pierre pour avoir toujours été disponibles pour m'aider et me former. Un merci aussi à tous les doctorants pour leur accueil chaleureux lors de mes visites.

Enfin, merci à mes fidèles amis, Marine, Romane, Clémence (MARC <3), Virgil, Alice et Fanny, vous êtes mes piliers et je vous en serai éternellement reconnaissante. Je remercie évidemment ma famille, Moka, Laura, Flo, maman, papa et mes grands-parents. Cette année aura été particulièrement éprouvante mais vous avez toujours été présents. Un dernier merci pour ma mamie, pour tout ce que tu m'as apporté et transmis durant toutes ces années. J'espère que tu es fière de moi de là où tu es.

Table of contents

ACKNOWLEDGEMENTS	5
TABLE OF CONTENTS	7
LIST OF TABLES	11
LIST OF FIGURES	12
INTRODUCTION	21
CHAPTER 1: STATE OF THE ART	25
1. FIRE HAZARDS	26
1.1. FIRE GENERATION	27
1.2. FIRE SMOKE	28
1.2.1. <i>Effluents</i>	28
1.2.2. <i>Aerosols</i>	30
1.3. FIRE STAGES AND ASSOCIATED RISKS	33
1.3.1. <i>Non-flaming fires</i>	35
1.3.2. <i>Well-ventilated flaming fires</i>	35
1.3.3. <i>Under-Ventilated fires</i>	36
1.3.4. <i>Post-flashover fires</i>	36
2. SCALING EFFECT	37
2.1. TEST SCALES	37
2.1.1. <i>Matter scale</i>	38
2.1.2. <i>Material scale</i>	39
2.2. MULTI-SCALING APPROACH	40
3. WOOD	41
3.1. PROPERTIES	41
3.1.1. <i>Chemical properties</i>	41
3.1.2. <i>Physical properties</i>	43
3.2. REACTION-TO-FIRE	44
3.2.1. <i>Pyrolysis</i>	45
3.2.2. <i>Thermo-oxidative pyrolysis</i>	49
3.2.3. <i>Ignition</i>	49
3.2.4. <i>Flaming</i>	50
3.2.5. <i>Smoldering</i>	50
3.3. WOOD PROPERTIES INFLUENCING ITS BURNING BEHAVIOR	51
3.4. EFFECT OF OXYGEN	55
3.4.1. <i>Matter scale tests</i>	55
3.4.2. <i>Bench-scale test</i>	57
4. CONCLUSIONS	59
CHAPTER 2: MATERIAL AND METHODS	60
1. MATERIALS	61

1.1.	CROSS-LAMINATED TIMBER (CLT)	61
1.2.	WOOD FIBER (WF)	61
2.	SMOKE ANALYSIS	62
2.1.	GAS ANALYSIS	62
2.2.	AEROSOL ANALYSIS	63
3.	MATTER SCALE STUDY	66
3.1.	PYROLYSIS-GAS CHROMATOGRAPHY MASS SPECTROSCOPY	66
3.2.	THERMOGRAVIMETRIC ANALYSIS-FOURIER TRANSFORMED INFRARED SPECTROSCOPY	66
4.	MATERIAL-SCALE	67
4.1.	STATE-OF-THE-ART	67
4.1.1.	<i>Overview of the main techniques</i>	67
4.1.2.	<i>Controlled-Atmosphere Cone Calorimeter (CACC)</i>	71
4.2.	DESIGN OF THE CACC/FTIR/ELPI BENCH	80
4.2.1.	<i>Design of the apparatus</i>	80
4.2.2.	<i>Equipment for smoke analysis</i>	83
4.3.	EXPERIMENTAL PROCEDURE	86
4.3.1.	<i>Sample preparation</i>	86
4.3.2.	<i>Testing conditions</i>	86
4.4.	MEASURED AND CALCULATED DATA IN THE CACC/FTIR/ELPI BENCH	87
4.4.1.	<i>Heat Release Rate calculation</i>	87
4.4.2.	<i>Gas yield calculation</i>	90
4.5.	TESTING ON PMMA	92
5.	INTERMEDIATE SCALE	95
5.1.	THEORETICAL BACKGROUND	95
5.2.	DESIGN OF THE ENCLOSURE	97
5.2.1.	<i>Design</i>	97
5.2.2.	<i>Equipment for smoke analysis</i>	98
5.3.	SAMPLE PREPARATION	98
5.4.	MEASURED AND CALCULATED DATA IN THE ENCLOSURE	98
5.5.	HEAT FLUX ANALYSIS	100
6.	CONCLUSION	102
CHAPTER 3: MATTER SCALE ANALYSIS		104
1.	CHARACTERIZATION OF CROSS-LAMINATED TIMBER THERMAL BEHAVIOR	104
1.1.	CHARACTERIZATION OF CROSS-LAMINATED TIMBER BY THERMOGRAVIMETRIC ANALYSIS COUPLED TO FOURIER TRANSFORM INFRARED SPECTROSCOPY	104
1.1.1.	<i>Inert atmosphere</i>	105
1.1.2.	<i>Oxidative atmosphere</i>	108
1.1.3.	<i>Comparison between inert and oxidative atmospheres</i>	111
1.2.	CHARACTERIZATION OF CROSS LAMINATED TIMBER BY PYROLYSIS-GAS CHROMATOGRAPHY MASS SPECTROSCOPY	113
2.	CHARACTERIZATION OF WOOD FIBER THERMAL BEHAVIOR	116
2.1.	CHARACTERIZATION OF WOOD FIBER BY THERMOGRAVIMETRIC ANALYSIS COUPLED TO FOURIER TRANSFORM INFRARED SPECTROSCOPY	116
2.1.1.	<i>Inert atmosphere</i>	116

2.1.2.	<i>Oxidative atmosphere</i>	119
2.1.3.	<i>Comparison between inert and oxidative atmospheres</i>	122
2.2.	CHARACTERIZATION OF WOOD FIBER BY PYROLYSIS-GAS CHROMATOGRAPHY MASS SPECTROSCOPY	124
CONCLUSION		126
CHAPTER 4: FIRE BEHAVIOR, GAS AND AEROSOL EMISSIONS OF AN ASSEMBLY OF CROSS-LAMINATED TIMBER/WOOD FIBER WITH A CONTROLLED-ATMOSPHERE CONE CALORIMETER COUPLED TO A FOURIER TRANSFORMED INFRARED SPECTROSCOPY AND AN ELECTRICAL LOW PRESSURE IMPACTOR		
1. EFFECT OF OXYGEN AND HEAT FLUX ON THE FIRE BEHAVIOR, GAS AND AEROSOL PRODUCTION OF CROSS-LAMINATED TIMBER		
128		
1.1.	EFFECT OF OXYGEN ON CROSS-LAMINATED TIMBER AT 50 kW/M ²	129
1.1.1.	<i>Mass loss and heat release of Cross-Laminated Timber at 50 kW/m²</i>	129
1.1.2.	<i>Gas production of Cross-Laminated Timber at 50 kW/m²</i>	133
1.1.3.	<i>Aerosol production of Cross-Laminated Timber at 50 kW/m²</i>	137
1.2.	EFFECT OF OXYGEN ON CROSS-LAMINATED TIMBER AT 20 kW/M ²	138
1.2.1.	<i>Mass loss and heat release of Cross-Laminated Timber at 20 kW/m²</i>	138
1.2.2.	<i>Gas production of Cross-Laminated Timber at 20 kW/m²</i>	141
1.2.3.	<i>Aerosol production of Cross-Laminated Timber at 20 kW/m²</i>	142
1.3.	COMPARATIVE EFFECT OF OXYGEN AND HEAT FLUX OF CROSS-LAMINATED TIMBER.....	143
1.4.	CONCLUSION	147
2. EFFECT OF OXYGEN AND HEAT FLUX ON THE FIRE BEHAVIOR, GAS AND AEROSOL PRODUCTION OF WOOD FIBER		
148		
2.1.	EFFECT OF OXYGEN ON WOOD FIBER AT 50 kW/M ²	148
2.1.1.	<i>Mass loss and heat release of wood fiber at 50 kW/m²</i>	148
2.1.2.	<i>Gas production of wood fiber at 50 kW/m²</i>	151
2.1.3.	<i>Aerosol production of wood fiber at 50 kW/m²</i>	153
2.2.	EFFECT OF OXYGEN ON WOOD FIBER AT 20 kW/M ²	155
2.2.1.	<i>Mass loss and heat release of wood fiber at 20 kW/m²</i>	155
2.2.2.	<i>Gas production of wood fiber at 20 kW/m²</i>	157
2.2.3.	<i>Aerosol production of wood fiber at 20 kW/m²</i>	159
2.3.	COMPARATIVE EFFECT OF OXYGEN AND HEAT FLUX OF WOOD FIBER	160
2.4.	CONCLUSION	164
3. EFFECT OF OXYGEN ON THE FIRE BEHAVIOR, GAS AND AEROSOL PRODUCTION OF AN ASSEMBLY OF CROSS-LAMINATED TIMBER AND WOOD FIBER		
164		
3.1.	EFFECT OF THE ASSEMBLY AND THE OXYGEN LEVEL AT 50 kW/M ²	165
3.1.1.	<i>Fire behavior, gas production and aerosol production of the Cross-Laminated Timber/Wood Fiber assembly</i> 165	
3.1.2.	<i>Effect of oxygen level on the CLT/WF assembly fire behavior, gas and aerosol production at 50 kW/m²</i> 172	
3.2.	EFFECT OF THE ASSEMBLY AND THE OXYGEN LEVEL AT 20 kW/M ²	176
3.2.1.	<i>Fire behavior of the assembly, gas production and aerosol production of the Cross-Laminated Timber/Wood Fiber assembly at 20 kW/m²</i>	176
3.2.2.	<i>Effect of oxygen level on the CLT/WF assembly fire behavior, gas and aerosol production at 20 kW/m²</i> 184	
3.3.	COMPARATIVE EFFECT OF OXYGEN AND HEAT FLUX	187
3.4.	CONCLUSION	192

4. CONCLUSION193

**CHAPTER 5: FIRE BEHAVIOR, GAS AND AEROSOL EMISSIONS OF AN ASSEMBLY OF CROSS-LAMINATED
TIMBER/WOOD FIBER WITH AN INTERMEDIATE SCALE ENCLOSURE COUPLED TO A FOURIER TRANSFORMED
INFRARED SPECTROSCOPY AND AN ELECTRICAL LOW PRESSURE IMPACTOR194**

1. FIRE BEHAVIOR, GAS AND AEROSOL PRODUCTION OF THE CROSS-LAMINATED TIMBER/WOOD FIBER ASSEMBLY AT 40 kW 194

2. FIRE BEHAVIOR, GAS AND AEROSOL PRODUCTION OF THE CROSS-LAMINATED TIMBER/WOOD FIBER ASSEMBLY AT 90 kW 197

3. CONCLUSION..... 200

CONCLUSION.....202

PERSPECTIVES202

BIBLIOGRAPHY206

APPENDIX.....215

APPENDIX 1..... 215

APPENDIX 2..... 218

APPENDIX 3..... 220

APPENDIX 4..... 220

APPENDIX 5..... 222

APPENDIX 6..... 222

APPENDIX 7..... 228

APPENDIX 8..... 229

APPENDIX 9..... 232

APPENDIX 10..... 237

APPENDIX 11..... 240

APPENDIX 12..... 247

APPENDIX 13..... 250

APPENDIX 14..... 256

APPENDIX 15..... 260

APPENDIX 16..... 265

APPENDIX 17..... 268

APPENDIX 18..... 270

APPENDIX 19..... 275

APPENDIX 20..... 278

APPENDIX 21..... 279

List of Tables

TABLE 1: MAIN FIRE EFFLUENTS, MODIFIED FROM [4]	29
TABLE 2: CHARACTERISTICS OF FIRE STAGES [11]	34
TABLE 3: INFLUENCE OF PROPERTIES AND FACTORS ON THE CHARRING RATE OF WOOD	55
TABLE 4: CLT PROPERTIES GIVEN BY THE MANUFACTURER.....	61
TABLE 5: WOOD FIBER PROPERTIES GIVEN BY THE MANUFACTURER.....	62
TABLE 6: GAS PARAMETERS OF THE QUANTIFICATION METHOD	84
TABLE 7: RANGE OF MEASUREMENT FOR EACH PLATE OF THE ELPI	85
TABLE 8: TRANSFER TIMES ACCORDING TO THE DATA MEASURED.....	87
TABLE 9: TGA PARAMETERS OF CLT UNDER NITROGEN ATMOSPHERE	105
TABLE 10: TGA PARAMETERS OF CLT UNDER DIFFERENT OXYGEN CONCENTRATIONS	109
TABLE 11: IDENTIFICATION OF THE MAIN DECOMPOSITION PRODUCTS OF CLT	115
TABLE 12: TGA PARAMETERS OF WF UNDER NITROGEN.....	117
TABLE 13: TGA PARAMETERS OF WF UNDER DIFFERENT OXYGEN CONCENTRATIONS.....	120
TABLE 14: IDENTIFICATION OF THE MAIN DECOMPOSITION PRODUCTS OF WF.....	125
TABLE 15: INFLUENCE OF OXYGEN ON THE FIRE PARAMETERS OF CLT AT 50 kW/M ²	131
TABLE 16: ORGANIC COMPOUNDS DETECTED IN FTIR ANALYSIS AND THEIR POSSIBLE WAY OF FORMATION.....	134
TABLE 17: INFLUENCE OF OXYGEN ON THE FIRE PARAMETERS OF CLT AT 20kW/M ²	140
TABLE 18: INFLUENCE OF OXYGEN ON THE FIRE PARAMETERS OF WF AT 50 kW/M ²	150
TABLE 19: INFLUENCE OF OXYGEN ON THE FIRE PARAMETERS OF WF AT 20 kW/M ²	156
TABLE 20: FIRE PARAMETERS OF CLT/WF AT 50 kW/M ²	166
TABLE 21: FIRE PARAMETERS OF CLT/WF AT 20 kW/M ²	177

List of Figures

FIGURE 1: CONVENTIONAL TESTS ACCORDING TO MATERIAL SIZE	23
FIGURE 2: IDEALIZED FIRE GROWTH CURVE AND TYPICAL TEMPERATURES FROM [4]	28
FIGURE 3: SOOT PARTICLES FORMATION AND EVOLUTION IN A FLAME [8].....	31
FIGURE 4: UNDER-VENTILATED FIRE IN ENCLOSED COMPARTMENT, MODIFIED FROM [4]	36
FIGURE 5: CELLULOSE	42
FIGURE 6: A. D-XYLOSE UNIT, B. D-MANNOSE UNIT	42
FIGURE 7: POSSIBLE LIGNIN MOLECULE.....	43
FIGURE 8: CHEMICAL AND PHYSICAL PROCESSES WITHIN A BURNING TIMBER, MODIFIED FROM [25]	45
FIGURE 9: HEMICELLULOSE PYROLYSIS: MAIN REACTIONS OCCURRING AND EVOLUTION OF THE CHEMICAL STRUCTURES OF THE RINGS THROUGHOUT THE TEMPERATURE INCREASE FROM [26]	46
FIGURE 10: CELLULOSE PYROLYSIS: MAIN REACTIONS OCCURRING AND EVOLUTION OF THE CHEMICAL STRUCTURES OF THE RINGS THROUGHOUT THE TEMPERATURE INCREASE, FROM [26]	47
FIGURE 11: LIGNIN PYROLYSIS: MAIN REACTIONS OCCURRING AND EVOLUTION OF THE CHEMICAL STRUCTURES OF THE RINGS THROUGHOUT THE TEMPERATURE INCREASE, FROM [26]	48
FIGURE 12: TGA STUDY UNDER NITROGEN OF WOOD AND ITS COMPONENTS [40].....	49
FIGURE 13: GRAIN DIRECTIONS [46]	52
FIGURE 14: TGA CURVE OF PINUS SYLVESTRIS UNDER DIFFERENT OXYGEN CONCENTRATION [16].....	56
FIGURE 15: INFLUENCE OF OXYGEN AND HEAT FLUX ON THE IGNITION THRESHOLDS FOR TIMBER [55].....	58
FIGURE 16: DIAGRAM OF SCANNING MOBILITY PARTICLE SIZER [58]	64
FIGURE 17: CASCADE IMPACTOR [60].....	65
FIGURE 18: STRANDS OF SPRUCE TAKEN FROM CLT (LEFT) AND LOOSE FIBERS TAKEN FROM WOOD FIBER BOARD (RIGHT).....	67
FIGURE 19: THE CONE CALORIMETER [65]	68
FIGURE 20: SMOKE DENSITY CHAMBER [4].....	69
FIGURE 21: STEADY-STATE TUBULAR FURNACE [69]	70
FIGURE 22: FIRE PROPAGATION APPARATUS [4].....	70
FIGURE 23: CACC DESIGN FROM BABRAUSKAS AND MULHOLLAND [71] [72].....	72
FIGURE 24: CACC DESIGN FROM PETRELLA AND CHRISTY [73] [74].....	72
FIGURE 25: CACC DESIGN FROM LEONARD] [76]	73
FIGURE 26: CACC BASIC DESIGN FROM [79] [80].....	74
FIGURE 27: CACC DESIGN WITH A CHIMNEY FROM [83].....	75
FIGURE 28: GAS SAMPLING SYSTEM ON THE CONE CALORIMETER FROM [85].....	76
FIGURE 29: SAMPLING SYSTEM USED BY MARQUIS AND GUILLAUME [87]	77
FIGURE 30: SAMPLING SYSTEM OF CHATENET [23]	78

FIGURE 31: SAMPLING SYSTEM FROM MUSTAFA [10].....	79
FIGURE 32: CACC DESIGN FROM ISO 5660-5 [88].....	80
FIGURE 33: DIAGRAM OF THE HOMEMADE CACC	81
FIGURE 34: A. DESIGNED METALLIC CHIMNEY FOR RAW SAMPLING; B. TOP VIEW OF FTIR PROBES.....	82
FIGURE 35: SAMPLE CONFIGURATION A. WOOD FIBER, B. CLT, C. CLT/WF.....	86
FIGURE 36: EFFECT OF OXYGEN LEVEL ON THE HRR OF PMMA AT 50 kW/M ²	93
FIGURE 37: EFFECT OF OXYGEN ON THE CO ₂ PRODUCTION RATE OF PMMA AT 50 kW/M ²	93
FIGURE 38: EFFECT OF OXYGEN ON THE CO PRODUCTION RATE OF PMMA AT 50 kW/M ²	94
FIGURE 39: EFFECT OF OXYGEN CONCENTRATION ON THE PMMA BEHAVIOR IN THE GAS PHASE. (A) AVERAGE HRR (B) AVERAGE GENERATION RATE OF CO ₂ AND (C) AVERAGE GENERATION RATE OF CO [84]	95
FIGURE 40: SINGLE BURNING ITEM (SBI) TEST	96
FIGURE 41: EXPERIMENTAL DEVICE OF LAFDAL, A. PHOTO OF THE ENCLOSURE, B. 3D MODEL	97
FIGURE 42: DESIGN OF THE LARGE SCALE TESTING ENCLOSURE	98
FIGURE 43: POSITIONS OF THE FLUXMETERS ON THE SILICATE CALCIUM BOARD	101
FIGURE 44: MAPPING OF THE HEAT FLUX PERCEIVED BY A SILICATE CALCIUM PANEL AT 40 KW. A. REPLICA 1 B. REPLICA 2.....	101
FIGURE 45: MAPPING OF THE HEAT FLUX PERCEIVED BY A SILICATE CALCIUM PANEL AT 90 KW. A. REPLICA 1 B. REPLICA 2.....	102
FIGURE 46: TGA-FTIR UNDER N ₂ AT 10°C/MIN. A. TG CURVE B. DTG CURVE (BLACK) AND CHEMIGRAM (BLUE)	105
FIGURE 47: FTIR SPECTRA OF CLT UNDER NITROGEN AT 220, 330, 370, 470, 575 AND 700°C	106
FIGURE 48: SUPERPOSITION OF THE FTIR SPECTRA OF CLT UNDER NITROGEN AT 330°C (PURPLE) AND 370°C (RED) ALONG WITH SPECTRA OF FORMIC ACID.....	108
FIGURE 49: TGA CURVES OF CLT UNDER N ₂ AND DIFFERENT OXYGEN CONCENTRATIONS AT 10°C/MIN. A. TG CURVES B. DTG CURVES C. CHEMIGRAMS	109
FIGURE 50: FTIR SPECTRA OF CLT AT 21 VOL-% O ₂ AT 150, 320, 333, 390 AND 443°C.....	110
FIGURE 51: SUPERPOSITION OF THE FTIR SPECTRA OF CLT AT 21 VOL-% O ₂ AT 333°C ALONG WITH SPECTRA OF FORMIC ACID.....	111
FIGURE 52: GASES RELEASED DURING THE DECOMPOSITION OF CLT UNDER OXIDATIVE (RED) AND INERT (BLUE) ATMOSPHERE AS A FUNCTION OF TEMPERATURE	112
FIGURE 53: CLT CHROMATOGRAM A. FULL SIZE B. ZOOM FROM 97 TO 137 MIN.....	114
FIGURE 54: TGA-FTIR OF WF UNDER N ₂ AT 10°C/MIN. A. TG CURVE B. DTG CURVE (BLACK) AND CHEMIGRAM (BLUE)	117
FIGURE 55: FTIR SPECTRA OF WF UNDER NITROGEN AT 220, 316, 367, AND 490°C.....	117
FIGURE 56: SUPERPOSITION OF THE FTIR SPECTRA OF WF AT 316°C (RED) AND AT 367°C (PURPLE).....	119
FIGURE 57: TGA-FTIR OF WF UNDER N ₂ AND DIFFERENT OXYGEN LEVELS AT 10°C/MIN. A. TG CURVES B. DTG CURVES C. CHEMIGRAMS	120
FIGURE 58: FTIR SPECTRA OF WF AT 21% O ₂ AT 150, 340, 400, AND 480°C	121
FIGURE 59: SUPERPOSITION OF THE FTIR SPECTRA OF WF AT 340°C	122

FIGURE 60: GASES RELEASED DURING THE DECOMPOSITION OF WF UNDER OXIDATIVE (RED) AND INERT (BLUE) ATMOSPHERE AS A FUNCTION OF TEMPERATURE	123
FIGURE 61: WF CHROMATOGRAM A. FULL SIZE B. ZOOM FROM 97 TO 137 MIN	124
FIGURE 62: EFFECT OF OXYGEN CONCENTRATION ON CLT AT 50 kW/M ² : A. MLR; B. MASS LOSS	130
FIGURE 63: EFFECT OF OXYGEN CONCENTRATION ON CLT AT 50 kW/M ² ON THE HRR	131
FIGURE 64: SLICED CLT AFTER 32 MIN OF TEST AT 50 kW/M ² AT A. 21 VOL-% O ₂ , B. 18 VOL-% O ₂ , C. 15 VOL-% O ₂ AND D. 10 VOL-% O ₂	133
FIGURE 65: INFLUENCE OF THE OXYGEN LEVEL ON THE GASEOUS EMISSIONS OF CLT AT 50 kW/M ² : A. CH ₂ O, B. CO ₂ ; C. CO AND D. CH ₄	136
FIGURE 66: DISTRIBUTION SIZE OF AEROSOLS OF CLT AT 50 kW/M ² AT: A. TI, B. 1500s	138
FIGURE 67: EFFECT OF OXYGEN CONCENTRATION ON CLT AT 20 kW/M ² : A. MASS LOSS; B. MLR	139
FIGURE 68: EFFECT OF OXYGEN CONCENTRATION ON THE HRR OF CLT AT 20kW/M ²	139
FIGURE 69: SLICED CLT AFTER 32 MIN OF TEST AT 20 kW/M ² AT A. 21 VOL-% O ₂ , B. 18 VOL-% O ₂ , C. 15 VOL-% O ₂ AND D. 10 VOL-% O ₂	140
FIGURE 70: INFLUENCE OF THE OXYGEN LEVEL THE GASEOUS EMISSIONS OF CLT AT 20 kW/M ² : A. CH ₂ O; B. CO; C.CH ₄ AND D. CO ₂ . (X IS FOR FLAMEOUT)	142
FIGURE 71: DISTRIBUTION SIZE OF AEROSOLS OF CLT AT 20 kW/M ² AT: A. TI, B. 1500s	143
FIGURE 72: EFFECT OF OXYGEN AND HEAT FLUX ON THE MAXIMUM MLR OF CLT.....	144
FIGURE 73: TOTAL YIELDS OF CO ₂ , CO, CH ₂ O AND CH ₄ OF CLT AS A FUNCTION OF OXYGEN LEVEL AND HEAT FLUX.....	145
FIGURE 74: FLAMING AND NON-FLAMING DECOMPOSITION OF CLT.....	146
FIGURE 75: CLASSIFICATION OF FIRE BEHAVIOR OF CLT ACCORDING TO OXYGEN LEVEL AND HEAT FLUX	147
FIGURE 76: EFFECT OF OXYGEN CONCENTRATION ON WF AT 50 kW/M ² : A. MLR, B. MASS LOSS.....	149
FIGURE 77: EFFECT OF OXYGEN CONCENTRATION ON THE HRR OF WF AT 50 kW/M ²	149
FIGURE 78: INFLUENCE OF THE OXYGEN LEVEL THE GASEOUS EMISSIONS OF WF AT 50 kW/M ² : A. CO ₂ ; B. CO; C. CH ₂ O; D. CH ₄ ; AND E. C ₂ H ₄	153
FIGURE 79: DISTRIBUTION SIZE OF AEROSOLS OF WF AT 50 kW/M ² AT: A. TI, B. 800s.....	154
FIGURE 80: EFFECT OF OXYGEN CONCENTRATION ON WF AT 20 kW/M ² : A. MASS LOSS; B. MLR	156
FIGURE 81: EFFECT OF OXYGEN CONCENTRATION ON THE HRR OF WF AT 20 kW/M ² , X IS FOR FLAMEOUT.....	156
FIGURE 82: INFLUENCE OF THE OXYGEN LEVEL THE GASEOUS EMISSIONS OF WF AT 20 kW/M ² : A. CO ₂ ; B. CO; C. CH ₂ O AND D. CH ₄ ..	158
FIGURE 83: DISTRIBUTION SIZE OF AEROSOLS OF WF AT 20 kW/M ² AT: A. TI, B. 800s	159
FIGURE 84: EFFECT OF OXYGEN AND HEAT FLUX ON THE MAXIMUM MLR OF WF	161
FIGURE 85: TOTAL YIELD OF CO ₂ , CO, CH ₂ O AND CH ₄ OF WF AS A FUNCTION OF OXYGEN LEVEL AND HEAT FLUX	162
FIGURE 86: FLAMING AND NON-FLAMING DECOMPOSITION OF WF	163
FIGURE 87: CLASSIFICATION OF FIRE BEHAVIOR OF WF ACCORDING TO OXYGEN LEVEL AND HEAT FLUX	164

FIGURE 88: EFFECT OF THE COMBINATION ON THE HRR AT 50 kW/M ² AT A. 21 VOL-% O ₂ , B. 18 VOL-% O ₂ , C. 15 VOL-% O ₂ AND D. 10 VOL-% O ₂ , X IS FOR FLAMEOUT	167
FIGURE 89: GAS PRODUCTION OF THE CLT/WF COMBINATION, HALF SAMPLES AND ENTIRE SAMPLES OF CLT AND WF AT 21 VOL-% O ₂ . A. CH ₂ O, B.CO ₂ , C. CO, D. CH ₄	169
FIGURE 90: GAS PRODUCTION OF THE CLT/WF COMBINATION, HALF SAMPLES AND ENTIRE SAMPLES OF CLT AND WF AT 10 VOL-% O ₂ . A. CH ₂ O, B.CO ₂ , C. CO, D. CH ₄	170
FIGURE 91: DISTRIBUTION SIZE OF AEROSOLS AT 50 kW/M ² : A. 21 VOL-% O ₂ , B. 18 VOL-% O ₂ , C. 15 VOL-% O ₂ AND D. 10 VOL-% O ₂	171
FIGURE 92: EFFECT OF OXYGEN ON THE HRR OF THE CLT/WF ASSEMBLY AT 50 kW/M ² , X IS FOR FLAMEOUT.....	173
FIGURE 93: INFLUENCE OF THE OXYGEN LEVEL THE GASEOUS EMISSIONS OF THE CLT/WF ASSEMBLY AT 50 kW/M ² : A. CO ₂ ; B. CO; C. CH ₂ O D.CH ₄ ; AND E. C ₂ H ₄ , X IS FOR FLAMEOUT	175
FIGURE 94: DISTRIBUTION SIZE OF AEROSOLS OF THE CLT/WF ASSEMBLY AT 50 kW/M ² AT: A. TI OR THE BEGINNING OF THE THERMAL EXPOSURE	176
FIGURE 95: EFFECT OF THE COMBINATION ON THE HRR AT 20 kW/M ² AT A. 21 VOL-% O ₂ , B. 18 VOL-% O ₂ , C. 15 VOL-% O ₂ AND D. 10 VOL-% O ₂ , X IS FOR FLAMEOUT.....	178
FIGURE 96: GAS PRODUCTION OF THE CLT/WF COMBINATION, HALF SAMPLES AND ENTIRE SAMPLES OF CLT AND WF AT 20 kW/M ² AND 21 VOL-% O ₂ . A. CH ₂ O, B.CO ₂ , C. CO, D. CH ₄	180
FIGURE 97: GAS PRODUCTION OF THE CLT/WF COMBINATION, HALF SAMPLES AND ENTIRE SAMPLES OF CLT AND WF AT 20 kW/M ² AND 18 VOL-% O ₂ . A. CH ₂ O, B.CO ₂ , C. CO, D. CH ₄	181
FIGURE 98: GAS PRODUCTION OF THE CLT/WF COMBINATION, HALF SAMPLES AND ENTIRE SAMPLES OF CLT AND WF AT 20 kW/M ² AND 10 VOL-% O ₂ . A. CH ₂ O, B.CO ₂ , C. CO, D. CH ₄	182
FIGURE 99: DISTRIBUTION SIZE OF AEROSOLS OF WF AT 20 kW/M ² AT TI: A. 21 VOL-% O ₂ , B. 18 VOL-% O ₂ , C. 15 VOL-% O ₂ AND AT THE BEGINNING OF THERMAL EXPOSURE: D. 10 VOL-% O ₂	183
FIGURE 100: EFFECT OF OXYGEN OF CLT/WF ON HRR AT 20 kW/M ²	185
FIGURE 101: INFLUENCE OF THE OXYGEN LEVEL ON THE GASEOUS EMISSIONS OF CLT/WF ASSEMBLY AT 20 kW/M ² : A. CO ₂ ; B. CO; C. CH ₂ O D. C ₂ H ₄ O; AND E. CH ₄	186
FIGURE 102: EFFECT OF OXYGEN ON THE DISTRIBUTION SIZE OF AEROSOLS OF CLT/WF AT 20 kW/M ² AT TI OR THE BEGINNING OF THERMAL EXPOSURE	187
FIGURE 103: EFFECT OF OXYGEN LEVEL ON THE TIMES TO IGNITION OF THE CLT/WF ASSEMBLY AT 50 AND 20 kW/M ²	188
FIGURE 104: EFFECT OF OXYGEN ON THE THR _{600s} OF THE CLT/WF ASSEMBLY AT 50 AND 20 kW/M ²	189
FIGURE 105: EFFECT OF OXYGEN ON THE GASEOUS EMISSIONS OF THE CLT/WF ASSEMBLY AT 50 AND 20 kW/M ² FOR 600s OF TEST..	190
FIGURE 106: FLAMING AND NON-FLAMING DECOMPOSITION OF THE ASSEMBLY OF CLT/WF	191
FIGURE 107: CLASSIFICATION OF FIRE BEHAVIOR OF THE CLT/WF ASSEMBLY ACCORDING TO OXYGEN LEVEL AND HEAT FLUX.....	192
FIGURE 108: PHOTOS TAKEN AFTER 30 MIN OF TEST AT 40 kW. A. CLT, B. WF AND C. CLT/WF	195
FIGURE 109: OXYGEN CONSUMPTION OF CLT, WF AND CLT/WF AT 40 kW	195

FIGURE 110: GAS PRODUCTION OF CLT, WF AND CLT/WF AT 40 kW. A. CO ₂ , B. CO AND C. CH ₄	196
FIGURE 111: GLOBAL AEROSOL SIZE DISTRIBUTION OF CLT, WF AND CLT/WF AT 40 kW.....	197
FIGURE 112: PHOTOS TAKEN AFTER 30 MIN OF TEST AT 90 kW. A. CLT, B. WF AND C. CLT/WF.....	198
FIGURE 113: OXYGEN CONSUMPTION OF CLT, WF AND CLT/WF AT 90 kW.....	198
FIGURE 114: GAS PRODUCTION OF CLT, WF AND CLT/WF AT 90 kW. A. CO ₂ , B. CO AND C. CH ₄	199
FIGURE 115: GLOBAL AEROSOL SIZE DISTRIBUTION OF CLT, WF AND CLT/WF AT 90 kW.....	200
FIGURE 116: FIRE BEHAVIOR OF PMMA AT 50 kW/M ² AND 21 VOL-% O ₂ : A. HRR, B. CO ₂ PRODUCTION RATE AND C. CO PRODUCTION RATE.....	215
FIGURE 117: FIRE BEHAVIOR OF PMMA AT 50 kW/M ² AND 18 VOL-% O ₂ : A. HRR, B. CO ₂ PRODUCTION RATE AND C. CO PRODUCTION RATE.....	216
FIGURE 118: FIRE BEHAVIOR OF PMMA AT 50 kW/M ² AND 15 VOL-% O ₂ : A. HRR, B. CO ₂ PRODUCTION RATE AND C. CO PRODUCTION RATE.....	217
FIGURE 119: FIRE BEHAVIOR OF PMMA AT 50 kW/M ² AND 10 VOL-% O ₂ : A. HRR, B. CO ₂ PRODUCTION RATE AND C. CO PRODUCTION RATE.....	218
FIGURE 120: TGA-FTIR TEST OF CLT AT 21 VOL-% O ₂ : A. TG AND B. DTG.....	218
FIGURE 121: TGA-FTIR TEST OF CLT AT 18 VOL-% O ₂ : A. TG AND B. DTG.....	219
FIGURE 122: TGA-FTIR TEST OF CLT AT 15 VOL-% O ₂ : A. TG AND B. DTG.....	219
FIGURE 123: TGA-FTIR TEST OF CLT AT 10 VOL-% O ₂ : A. TG AND B. DTG.....	219
FIGURE 124: FTIR SPECTRA OF CLT UNDER N ₂ , 21, 18, 15 AND 10 VOL-% O ₂ AT THE FIRST PEAK OF DECOMPOSITION.....	220
FIGURE 125: TGA-FTIR TEST OF WF UNDER N ₂ : A. TG AND B. DTG.....	220
FIGURE 126: TGA-FTIR TEST OF WF AT 21 VOL-% O ₂ : A. TG AND B. DTG.....	221
FIGURE 127: TGA-FTIR TEST OF WF AT 18 VOL-% O ₂ : A. TG AND B. DTG.....	221
FIGURE 128: TGA-FTIR TEST OF WF AT 15 VOL-% O ₂ : A. TG AND B. DTG.....	221
FIGURE 129: FTIR SPECTRA OF WF UNDER N ₂ , 21, 18, 15 AND 10 VOL-% O ₂ AT THE FIRST PEAK OF DECOMPOSITION.....	222
FIGURE 130: FIRE BEHAVIOR OF CLT AT 50 kW/M ² AND 21 VOL-% O ₂ : A. MLR, B. MASS LOSS AND C. HHR.....	223
FIGURE 131: GAS PRODUCTION OF CLT AT 50 kW/M ² AND 21 VOL-% O ₂ : A. CO ₂ , B. CO, C. FORMALDEHYDE AND C. METHANE.....	223
FIGURE 132: AEROSOL SIZE DISTRIBUTION OF CLT AT 50 kW/M ² AND 21 VOL-% O ₂ : A. TI, B. 1500s.....	223
FIGURE 133: FIRE BEHAVIOR OF CLT AT 50 kW/M ² AND 18 VOL-% O ₂ : A. MLR, B. MASS LOSS AND C. HHR.....	224
FIGURE 134: GAS PRODUCTION OF CLT AT 50 kW/M ² AND 18 VOL-% O ₂ : A. CO ₂ , B. CO, C. FORMALDEHYDE AND C. METHANE.....	225
FIGURE 135: AEROSOL SIZE DISTRIBUTION OF CLT AT 50 kW/M ² AND 18 VOL-% O ₂ : A. TI, B. 1500s.....	225
FIGURE 136: FIRE BEHAVIOR OF CLT AT 50 kW/M ² AND 15 VOL-% O ₂ : A. MLR, B. MASS LOSS AND C. HHR.....	226
FIGURE 137: GAS PRODUCTION OF CLT AT 50 kW/M ² AND 15 VOL-% O ₂ : A. CO ₂ , B. CO, C. FORMALDEHYDE AND C. METHANE.....	226
FIGURE 138: AEROSOL SIZE DISTRIBUTION OF CLT AT 50 kW/M ² AND 15 VOL-% O ₂ : A. TI, B. 1500s.....	227
FIGURE 139: FIRE BEHAVIOR OF CLT AT 50 kW/M ² AND 10 VOL-% O ₂ : A. MLR, B. MASS LOSS AND C. HHR.....	227

FIGURE 140: GAS PRODUCTION OF CLT AT 50 kW/M ² AND 10 VOL-% O ₂ : A. CO ₂ , B. CO, C. FORMALDEHYDE, D. METHANE AND E. ETHENE	228
FIGURE 141: AEROSOL SIZE DISTRIBUTION OF CLT AT 50 kW/M ² AND 10 VOL-% O ₂ : A. 25s, B. 1500s.....	228
FIGURE 142: A. TEMPERATURE RISE AND HRR OF CLT AT 50 kW/M ² AND 21 VOL-% O ₂ AND B. LOCATION OF THERMOCOUPLES.....	229
FIGURE 143: FTIR SPECTRA OF CLT AT 50 kW/M ² AT 21, 18, 15 AND 10 VOL-% O ₂ AT THE START OF THERMAL EXPOSURE.....	229
FIGURE 144: ZOOM ON THE FTIR SPECTRA OF CLT AT 50 kW/M ² , 21 VOL-% O ₂ AT THE START OF THERMAL EXPOSURE (RED) ALONG WITH SPECTRA OF FORMALDEHYDE (PURPLE), METHANOL (PINK) AND FORMIC ACID (GREEN) BETWEEN 1150 AND 750 CM ⁻¹ (A) AND BETWEEN 3300 AND 2500 CM ⁻¹ (B).....	230
FIGURE 145: ZOOM ON THE FTIR SPECTRA OF CLT AT 50 kW/M ² , 10 VOL-% O ₂ AT THE START OF THERMAL EXPOSURE (RED) ALONG WITH SPECTRA OF FORMALDEHYDE (PURPLE), METHANOL (PINK), FORMIC ACID (GREEN), METHANE (BLUE) AND ETHENE (ORANGE) BETWEEN 1900 AND 900 CM ⁻¹ (A) AND BETWEEN 3200 AND 2000 CM ⁻¹ (B).....	231
FIGURE 146: FTIR SPECTRA OF CLT AT 50 kW/M ² AT 21, 18, 15 AND 10 VOL-% O ₂ AT IGNITION.....	231
FIGURE 147: FTIR SPECTRA OF CLT AT 50 kW/M ² AT 21, 18, 15 AND 10 VOL-% O ₂ AT 20 MIN OF TEST	232
FIGURE 148: FIRE BEHAVIOR OF CLT AT 20 kW/M ² AND 21 VOL-% O ₂ : A. MLR, B. MASS LOSS AND C. HHR	233
FIGURE 149: GAS PRODUCTION OF CLT AT 20 kW/M ² AND 21 VOL-% O ₂ : A. CO ₂ , B. CO, C. FORMALDEHYDE, C. METHANE	233
FIGURE 150: AEROSOL SIZE DISTRIBUTION OF CLT AT 20 kW/M ² AND 21 VOL-% O ₂ : A. TI, B. 1500s.....	234
FIGURE 151: FIRE BEHAVIOR OF CLT AT 20 kW/M ² AND 18 VOL-% O ₂ : A. MLR, B. MASS LOSS AND C. HHR.....	234
FIGURE 152: GAS PRODUCTION OF CLT AT 20 kW/M ² AND 18 VOL-% O ₂ : A. CO ₂ , B. CO, C. FORMALDEHYDE, C. METHANE	235
FIGURE 153: AEROSOL SIZE DISTRIBUTION OF CLT AT 20 kW/M ² AND 18 VOL-% O ₂ : A. TI, B. 1500s.....	235
FIGURE 154: FIRE BEHAVIOR OF CLT AT 20 kW/M ² AND 15 VOL-% O ₂ : A. MASS LOSS AND B. HHR	236
FIGURE 155: GAS PRODUCTION OF CLT AT 20 kW/M ² AND 15 VOL-% O ₂ : A. CO ₂ , B. CO, C. FORMALDEHYDE, C. METHANE	236
FIGURE 156: FIRE BEHAVIOR OF CLT AT 20 kW/M ² AND 10 VOL-% O ₂ : A. MASS LOSS AND B. HHR	237
FIGURE 157: GAS PRODUCTION OF CLT AT 20 kW/M ² AND 10 VOL-% O ₂ : A. CO ₂ , B. CO, C. FORMALDEHYDE, C. METHANE	237
FIGURE 158: FTIR SPECTRA OF CLT AT 20 kW/M ² AT 21, 18, 15 AND 10 VOL-% O ₂ AT THE START OF THERMAL EXPOSURE.....	238
FIGURE 159: ZOOM ON THE FTIR SPECTRA OF CLT AT 20 kW/M ² , 21 VOL-% O ₂ AT THE START OF THERMAL EXPOSURE (RED) ALONG WITH SPECTRA OF FORMALDEHYDE (PURPLE), METHANOL (PINK) AND FORMIC ACID (GREEN) BETWEEN 1500 AND 900 CM ⁻¹ (A) AND BETWEEN 3500 AND 2000 CM ⁻¹ (B).....	239
FIGURE 160: ZOOM ON THE FTIR SPECTRA OF CLT AT 20 kW/M ² , 10 VOL-% O ₂ AT THE START OF THERMAL EXPOSURE (RED) ALONG WITH SPECTRA OF FORMALDEHYDE (PURPLE), METHANOL (PINK) AND FORMIC ACID (GREEN) BETWEEN 2000 AND 900 CM ⁻¹ (A) AND BETWEEN 3500 AND 2000 CM ⁻¹ (B).....	239
FIGURE 161: FTIR SPECTRA OF CLT AT 20 kW/M ² AT 21, 18, 15 AND 10 VOL-% O ₂ AT IGNITION.....	240
FIGURE 162: FTIR SPECTRA OF CLT AT 20 kW/M ² AT 21, 18, 15 AND 10 VOL-% O ₂ AT 20 MIN	240
FIGURE 163: FIRE BEHAVIOR OF WF AT 50 kW/M ² AND 21 VOL-% O ₂ : A. MLR, B. MASS LOSS AND C. HHR	241
FIGURE 164: GAS PRODUCTION OF WF AT 50 kW/M ² AND 21 VOL-% O ₂ : A. CO ₂ , B. CO, C. FORMALDEHYDE, C. METHANE.....	242
FIGURE 165: AEROSOL SIZE DISTRIBUTION OF WF AT 50 kW/M ² AND 21 VOL-% O ₂ : A. TI, B. 800s	242

FIGURE 166: FIRE BEHAVIOR OF WF AT 50 kW/M ² AND 18 VOL-% O ₂ : A. MLR, B. MASS LOSS AND C. HHR	243
FIGURE 167: GAS PRODUCTION OF WF AT 50 kW/M ² AND 18 VOL-% O ₂ : A. CO ₂ , B. CO, C. FORMALDEHYDE, C. METHANE.....	243
FIGURE 168: AEROSOL SIZE DISTRIBUTION OF WF AT 50 kW/M ² AND 21 VOL-% O ₂ : A. TI, B. 800s	244
FIGURE 169: FIRE BEHAVIOR OF WF AT 50 kW/M ² AND 15 VOL-% O ₂ : A. MLR, B. MASS LOSS AND C. HHR	244
FIGURE 170: GAS PRODUCTION OF WF AT 50 kW/M ² AND 15 VOL-% O ₂ : A. CO ₂ , B. CO, C. FORMALDEHYDE, C. METHANE.....	245
FIGURE 171: AEROSOL SIZE DISTRIBUTION OF WF AT 50 kW/M ² AND 15 VOL-% O ₂ : A. TI, B. 800s	245
FIGURE 172: FIRE BEHAVIOR OF WF AT 50 kW/M ² AND 10 VOL-% O ₂ : A. MLR, B. MASS LOSS AND C. HHR	246
FIGURE 173: GAS PRODUCTION OF WF AT 50 kW/M ² AND 15 VOL-% O ₂ : A. CO ₂ , B. CO, C. FORMALDEHYDE, C. METHANE, D. ETHENE	247
FIGURE 174: FTIR SPECTRA OF WF AT 50 kW/M ² AT 21, 18, 15 AND 10 VOL-% O ₂ AT THE START OF THERMAL EXPOSURE	247
FIGURE 175: ZOOM ON THE FTIR SPECTRA OF WF AT 50 kW/M ² , 21 VOL-% O ₂ AT THE START OF THERMAL EXPOSURE (RED) ALONG WITH SPECTRA OF FORMALDEHYDE (PURPLE), METHANOL (PINK) AND FORMIC ACID (GREEN) BETWEEN 2000 AND 900 CM ⁻¹ (A) AND BETWEEN 3500 AND 2000 CM ⁻¹ (B).....	248
FIGURE 176: ZOOM ON THE FTIR SPECTRA OF WF AT 50 kW/M ² , 10 VOL-% O ₂ AT THE START OF THERMAL EXPOSURE (RED) ALONG WITH SPECTRA OF FORMALDEHYDE (PURPLE), METHANOL (PINK), FORMIC ACID (GREEN), METHANE (BLUE) AND ETHENE (ORANGE) BETWEEN 2000 AND 850 CM ⁻¹ (A) AND BETWEEN 3200 AND 2000 CM ⁻¹ (B)	249
FIGURE 177: FTIR SPECTRA OF WF AT 50 kW/M ² AT 21, 18, 15 AND 10 VOL-% O ₂ AT IGNITION	249
FIGURE 178: FTIR SPECTRA OF WF AT 50 kW/M ² AT 21, 18, 15 AND 10 VOL-% O ₂ AT 20 MIN	250
FIGURE 179: FIRE BEHAVIOR OF WF AT 20 kW/M ² AND 21 VOL-% O ₂ : A. MLR, B. MASS LOSS AND C. HHR	250
FIGURE 180: GAS PRODUCTION OF WF AT 20 kW/M ² AND 21 VOL-% O ₂ : A. CO ₂ , B. CO, C. FORMALDEHYDE, C. METHANE.....	251
FIGURE 181: AEROSOL SIZE DISTRIBUTION OF WF AT 20 kW/M ² AND 21 VOL-% O ₂ : A. TI, B. 800s	251
FIGURE 182: FIRE BEHAVIOR OF WF AT 20 kW/M ² AND 18 VOL-% O ₂ : A. MLR, B. MASS LOSS AND C. HHR	252
FIGURE 183: GAS PRODUCTION OF WF AT 20 kW/M ² AND 18 VOL-% O ₂ : A. CO ₂ , B. CO, C. FORMALDEHYDE, C. METHANE.....	253
FIGURE 184: AEROSOL SIZE DISTRIBUTION OF WF AT 20 kW/M ² AND 18 VOL-% O ₂ : A. TI, B. 800s	253
FIGURE 185: FIRE BEHAVIOR OF WF AT 20 kW/M ² AND 15 VOL-% O ₂ : A. MLR, B. MASS LOSS AND C. HHR	254
FIGURE 186: GAS PRODUCTION OF WF AT 20 kW/M ² AND 15 VOL-% O ₂ : A. CO ₂ , B. CO, C. FORMALDEHYDE, C. METHANE.....	254
FIGURE 187: AEROSOL SIZE DISTRIBUTION OF WF AT 20 kW/M ² AND 15 VOL-% O ₂ : A. TI, B. 800s	255
FIGURE 188: FIRE BEHAVIOR OF WF AT 20 kW/M ² AND 10 VOL-% O ₂ : A. MLR, B. MASS LOSS AND C. HHR	255
FIGURE 189: GAS PRODUCTION OF WF AT 20 kW/M ² AND 10 VOL-% O ₂ : A. CO ₂ , B. CO, C. FORMALDEHYDE, C. METHANE.....	256
FIGURE 190: AEROSOL SIZE DISTRIBUTION OF WF AT 20 kW/M ² AND 10 VOL-% O ₂ : A. TI, B. 800s	256
FIGURE 191: FTIR SPECTRA OF WF AT 20 kW/M ² AT 21, 18, 15 AND 10 VOL-% O ₂ AT THE START OF THERMAL EXPOSURE	257
FIGURE 192: ZOOM ON THE FTIR SPECTRA OF WF AT 20 kW/M ² , 21 VOL-% O ₂ AT THE START OF THERMAL EXPOSURE (RED) ALONG WITH SPECTRA OF FORMALDEHYDE (PURPLE), METHANOL (PINK) AND FORMIC ACID (GREEN) BETWEEN 2000 AND 900 CM ⁻¹ (A) AND BETWEEN 3200 AND 2000 CM ⁻¹ (B).....	258

FIGURE 193: ZOOM ON THE FTIR SPECTRA OF WF AT 20 kW/M ² , 10 VOL-% O ₂ AT THE START OF THERMAL EXPOSURE (RED) ALONG WITH SPECTRA OF FORMALDEHYDE (PURPLE), METHANOL (PINK) AND FORMIC ACID (GREEN) BETWEEN 1900 AND 1000 CM ⁻¹ (A) AND BETWEEN 3100 AND 2000 CM ⁻¹ (B).....	259
FIGURE 194: FTIR SPECTRA OF CLT AT 20 kW/M ² AT 21, 18, 15 AND 10 VOL-% O ₂ AT IGNITION.....	259
FIGURE 195: FTIR SPECTRA OF CLT AT 20 kW/M ² AT 21, 18, 15 AND 10 VOL-% O ₂ AT 20 MIN	260
FIGURE 196: HRR OF CLT/ WF AT 50 kW/M ² AND 21 VOL-% O ₂	260
FIGURE 197: GAS PRODUCTION OF CLT/WF AT 50 kW/M ² AND 21 VOL-% O ₂ : A. CO ₂ , B. CO, C. FORMALDEHYDE, C. METHANE	261
FIGURE 198: AEROSOL SIZE DISTRIBUTION OF CLT/WF AT 50 kW/M ² AND 21 VOL-% O ₂ AT TI	261
FIGURE 199: HRR OF CLT/ WF AT 50 kW/M ² AND 18 VOL-% O ₂	261
FIGURE 200: GAS PRODUCTION OF CLT/WF AT 50 kW/M ² AND 18 VOL-% O ₂ : A. CO ₂ , B. CO, C. FORMALDEHYDE, C. METHANE.....	262
FIGURE 201: AEROSOL SIZE DISTRIBUTION OF CLT/WF AT 50 kW/M ² AND 18 VOL-% O ₂ AT TI	262
FIGURE 202: HRR OF CLT/ WF AT 50 kW/M ² AND 15 VOL-% O ₂	263
FIGURE 203: GAS PRODUCTION OF CLT/WF AT 50 kW/M ² AND 15 VOL-% O ₂ : A. CO ₂ , B. CO, C. FORMALDEHYDE, C. METHANE	263
FIGURE 204: AEROSOL SIZE DISTRIBUTION OF CLT/WF AT 50 kW/M ² AND 15 VOL-% O ₂ AT TI	264
FIGURE 205: HRR OF CLT/ WF AT 50 kW/M ² AND 10 VOL-% O ₂	264
FIGURE 206: GAS PRODUCTION OF CLT/WF AT 50 kW/M ² AND 10 VOL-% O ₂ : A. CO ₂ , B. CO, C. FORMALDEHYDE, D. METHANE AND E. ETHENE	265
FIGURE 207: AEROSOL SIZE DISTRIBUTION OF CLT/WF AT 50 kW/M ² AND 10 VOL-% O ₂ AT 25s.....	265
FIGURE 208: FTIR SPECTRA OF CLT/WF AT 50 kW/M ² AT 21, 18, 15 AND 10 VOL-% O ₂ AT THE START OF THERMAL EXPOSURE	266
FIGURE 209: ZOOM ON THE FTIR SPECTRA OF CLT/WF AT 50 kW/M ² , 21 VOL-% O ₂ AT THE START OF THERMAL EXPOSURE (RED) ALONG WITH SPECTRA OF FORMALDEHYDE (PURPLE), METHANOL (PINK) AND FORMIC ACID (GREEN) BETWEEN 2000 AND 900 CM ⁻¹ (A) AND BETWEEN 3100 AND 2000 CM ⁻¹ (B).....	266
FIGURE 210: ZOOM ON THE FTIR SPECTRA OF CLT/WF AT 50 kW/M ² , 10 VOL-% O ₂ AT THE START OF THERMAL EXPOSURE (RED) ALONG WITH SPECTRA OF FORMALDEHYDE (PURPLE), METHANOL (PINK), FORMIC ACID (GREEN), METHANE (BLUE) AND ETHENE (ORANGE) BETWEEN 1900 AND 900 CM ⁻¹ (A) AND BETWEEN 3150 AND 2000 CM ⁻¹ (B)	267
FIGURE 211: FTIR SPECTRA OF CLT/WF AT 50 kW/M ² AT 21, 18, 15 AND 10 VOL-% O ₂ AT IGNITION	268
FIGURE 212: FTIR SPECTRA OF CLT/WF AT 50 kW/M ² AT 21, 18, 15 AND 10 VOL-% O ₂ AT 20 MIN.....	268
FIGURE 213: GAS PRODUCTION OF THE CLT/WF COMBINATION, HALF SAMPLES AND ENTIRE SAMPLES OF CLT AND WF AT 20 kW/M ² AND 18 VOL-% O ₂ . (A) CARBON DIOXIDE (B) CARBON MONOXIDE (C) FORMALDEHYDE (D) METHANE.....	269
FIGURE 214: GAS PRODUCTION OF THE CLT/WF COMBINATION, HALF SAMPLES AND ENTIRE SAMPLES OF CLT AND WF AT 20 kW/M ² AND 15 VOL-% O ₂ . (A) CARBON DIOXIDE (B) CARBON MONOXIDE (C) FORMALDEHYDE (D) METHANE	270
FIGURE 215: HRR OF CLT/ WF AT 20 kW/M ² AND 21 VOL-% O ₂	270
FIGURE 216: GAS PRODUCTION OF CLT/WF AT 20 kW/M ² AND 21 VOL-% O ₂ : A. CO ₂ , B. CO, C. FORMALDEHYDE, C. METHANE	271
FIGURE 217: AEROSOL SIZE DISTRIBUTION OF CLT/WF AT 20 kW/M ² AND 21 VOL-% O ₂ AT TI	271
FIGURE 218: HRR OF CLT/ WF AT 20 kW/M ² AND 18 VOL-% O ₂	271

FIGURE 219: GAS PRODUCTION OF CLT/WF AT 20 kW/M ² AND 18 VOL-% O ₂ : A. CO ₂ , B. CO, C. FORMALDEHYDE, C. METHANE	272
FIGURE 220: AEROSOL SIZE DISTRIBUTION OF CLT/WF AT 20 kW/M ² AND 18 VOL-% O ₂ AT TI	272
FIGURE 221: HRR OF CLT/ WF AT 20 kW/M ² AND 15 VOL-% O ₂	273
FIGURE 222: GAS PRODUCTION OF CLT/WF AT 20 kW/M ² AND 15 VOL-% O ₂ : A. CO ₂ , B. CO, C. FORMALDEHYDE, C. METHANE.....	273
FIGURE 223: AEROSOL SIZE DISTRIBUTION OF CLT/WF AT 20 kW/M ² AND 15 VOL-% O ₂ AT TI	274
FIGURE 224: GAS PRODUCTION OF CLT/WF AT 20 kW/M ² AND 10 VOL-% O ₂ : A. CO ₂ , B. CO, C. FORMALDEHYDE, C. METHANE.....	274
FIGURE 225: AEROSOL SIZE DISTRIBUTION OF CLT/WF AT 20 kW/M ² AND 10 VOL-% O ₂ AT 25s	275
FIGURE 226: FTIR SPECTRA OF CLT/WF AT 20 kW/M ² AT 21, 18, 15 AND 10 VOL-% O ₂ AT THE START OF THERMAL EXPOSURE	275
FIGURE 227: ZOOM ON THE FTIR SPECTRA OF CLT/WF AT 20 kW/M ² , 21 VOL-% O ₂ AT THE START OF THERMAL EXPOSURE (RED) ALONG WITH SPECTRA OF FORMALDEHYDE (PURPLE), METHANOL (PINK) AND FORMIC ACID (GREEN) BETWEEN 2000 AND 850 CM ⁻¹ (A) AND BETWEEN 3150 AND 2000 CM ⁻¹ (B).....	276
FIGURE 228: ZOOM ON THE FTIR SPECTRA OF CLT/WF AT 20 kW/M ² , 10 VOL-% O ₂ AT THE START OF THERMAL EXPOSURE (RED) ALONG WITH SPECTRA OF FORMALDEHYDE (PURPLE), METHANOL (PINK) AND FORMIC ACID (GREEN) BETWEEN 2000 AND 900 CM ⁻¹ (A) AND BETWEEN 3150 AND 2000 CM ⁻¹ (B).....	277
FIGURE 229: FTIR SPECTRA OF CLT/WF AT 20 kW/M ² AT 21, 18, 15 AND 10 VOL-% O ₂ AT IGNITION.....	278
FIGURE 230: FTIR SPECTRA OF CLT/WF AT 20 kW/M ² AT 21, 18, 15 AND 10 VOL-% O ₂ AT 20 MIN.....	278
FIGURE 231: GAS PRODUCTION OF THE CLT/WF COMBINATION, HALF SAMPLES AND ENTIRE SAMPLES OF CLT AND WF AT 20 kW/M ² AND 15 VOL-% O ₂ . (A) CARBON DIOXIDE (B) CARBON MONOXIDE (C) FORMALDEHYDE (D) METHANE	279
FIGURE 232: OXYGEN CONSUMPTION OF CLT AT 40 AND 90 kW	279
FIGURE 233: GAS PRODUCTION OF CLT AT 40 AND 90 kW. A. CO ₂ , B.CO, C. FORMALDEHYDE, D. METHANE	280
FIGURE 234: GLOBAL AEROSOL SIZE DISTRIBUTION OF CLT AT 40 AND 90 kW	280
FIGURE 235: OXYGEN CONSUMPTION OF WF AT 40 AND 90 kW	281
FIGURE 236: GAS PRODUCTION OF WF AT 40 AND 90 kW. A. CO ₂ , B.CO, C. FORMALDEHYDE, D. METHANE	281
FIGURE 237: GLOBAL AEROSOL SIZE DISTRIBUTION OF WF AT 40 AND 90 kW.....	282
FIGURE 238: OXYGEN CONSUMPTION OF CLT/WF AT 40 AND 90 kW	282
FIGURE 239: GAS PRODUCTION OF WF AT 40 AND 90 kW. A. CO ₂ , B.CO, C. FORMALDEHYDE, D. METHANE	283
FIGURE 240: GLOBAL AEROSOL SIZE DISTRIBUTION OF CLT/WF AT 40 AND 90 kW	283

Introduction

Regarding climate change, sustainable construction has become a major challenge in the building field these past years. Construction should aim to minimize environmental impact, conserve resources, and enhance the quality of life for current and future generations. Especially, developing energy efficient buildings with a low carbon footprint is crucial. To meet this challenge, the use of synthetic materials should be reduced. As a result, there is a growing trend toward using renewable and/or recycled construction materials, including for example plant-based wools, which are projected to comprise 13.16% of the global insulating wools market by 2030¹. More precisely, wood-based materials such as Cross-Laminated Timber (CLT) and wood fiber (WF) are of great interest in eco-friendly buildings. CLT is widely used because of its structural properties. With low weight and fast construction times, CLT challenges the use of traditional dense materials like steel and concrete. Furthermore, wood fiber is a serious competitor to traditional polymeric foams because of its excellent thermal and phonic insulation properties. Above all, these two renewable materials offer two significant advantages concerning climate change. Firstly, wood acts as a carbon sink, capable of absorbing carbon from the atmosphere and store it. Thereby, the carbon extracted from the atmosphere no longer contributes to global warming. Secondly, emissions from fossil fuels to produce energy and material are avoided by substitution with wood.

However, like many organic materials, CLT and WF are easily flammable and could increase the risk of fire. They also participate in smoke production, with the release of gases and aerosols, which are restrictive parameters to ensure the safe evacuation of a building. Indeed, during a building fire, most deaths are due to smoke release [1]. Smoke reduces visibility, causes impaired vision and respiratory problems due to irritating and asphyxiating gases. Consequently, this increases the time to escape and the probability of injuries or death [2]. To ensure safe evacuation, the standard ISO 13571 [3] subdivides the risks to people escaping a fire into the effects of heat, asphyxiant and irritant gases, and visual obscuration by smoke. Each component is assessed separately and untenability is defined when one of the components reaches a level that prevents escape. This underlines the need to assess the toxicity of materials to have a better understanding of phenomena occurring during a fire. This investigation should be done under different fire conditions to simulate various scenarios of fire development into a room. Indeed, the production and yield of gases and aerosols depend on the material composition but also the environmental conditions,

¹ Connaissance de la filière des matériaux biosourcés pour la construction en Pays de Loire – DREAL Pays de Loire janvier 2013 – p. 32 – source ALCIMED

including oxygen concentration and temperature. An under-ventilated or low oxygen level (vitiating) atmosphere increases the production of gases potentially dangerous. Indeed, the oxygen level quickly decreases until it no longer allows complete combustion. A dense, carbon monoxide (CO) rich smoke as well as other toxic gases and non-toxic gases are produced. A complete assessment of the thermal decomposition of materials with gaseous emissions and aerosols production is thus crucial for fire safety [2] [4] [5].

When studying the behavior, gas, and aerosol emissions of materials during a room fire, several considerations must be carefully addressed. Firstly, the effect of scale is a major parameter to consider. Indeed, phenomena observed at small-scale differ from those at real scale. The challenge is to determine which combustion scale is the closest to reality while still being feasible in the laboratory and affordable. Generally, in the building field, the reaction to fire of materials is assessed via a prescriptive approach with standardized tests, ranging from bench-scale tests to real scale (Figure 1). The most used tests are (i) the Single Burning Item (SBI) test, which typically involves meter-sized samples, and (ii) the Cone Calorimeter test, with samples of a few centimeters. Moreover, these tests often consider ignition time, heat release and smoke opacity as relevant parameters for assessing fire risks, omitting the gas and aerosol production. Besides, they are carried out in well-ventilated conditions, which are not the most critical conditions compared to under-ventilated or vitiating ones. As a result, and like the railway sector, European working groups are now addressing these concerns and actively working on establishing emission criteria for buildings.

A last point to address is the constructive system in which materials are integrated. Indeed, in a building, materials are not considered separately but as part of a constructive solution. For example, for a wall, it consists at the very least in a CLT frame and a wood fiber insulation. However, they can potentially interact when subjected to fire. These interactions may modify fire behaviors as well as gas and aerosol emissions. At present, this subject is not covered by standards or regulations, and there is little literature on it.

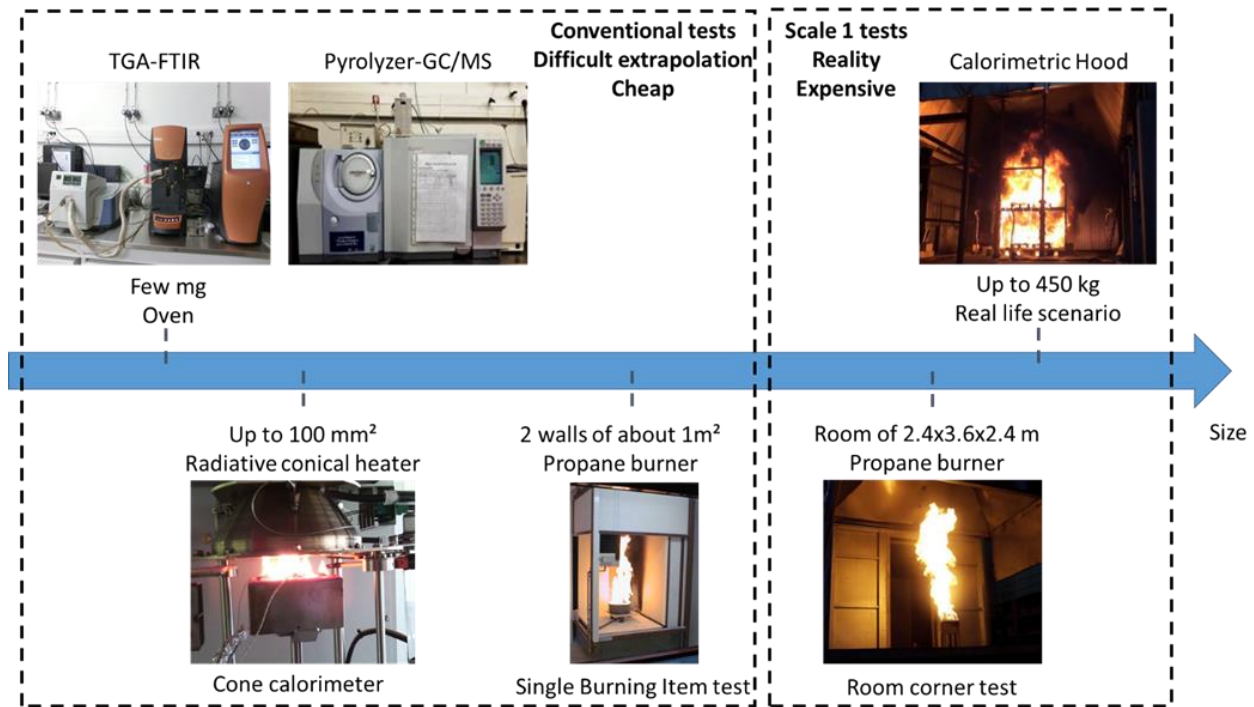


Figure 1: Conventional tests according to material size

In this context, oxygen depletion is considered to influence the fire behavior and gas and aerosol emissions of materials. Moreover, in a building system, the coexistence of diverse types of materials and their potential interactions in a fire scenario could generate different effects from those observed for the same materials taken individually. However, the assessment of these interactions regarding fire development has not been studied. It is therefore important to focus on these aspects to answer the following question: what is the impact of the fire scenario on the fire behavior of associated materials in a building system? This approach involves a detailed study of the influence of oxygen content and different levels of thermal attack on the nature of gas and aerosol emissions. Especially, the study deals with Cross-Laminated Timber, wood fiber and the assembly of both CLT and WF to explore their potential interactions during a fire.

The investigation aims to be conducted at different scales and under different fire scenarios, ranging from well-ventilated to vitiated fires. To do so, this PhD was conducted at the Centre Scientifique et Technique du Bâtiment (CSTB) in collaboration with the Unité des Matériaux et Transformations (UMET). Two homemade benches were adapted at CSTB.

This PhD work is organized into five chapters. The first chapter gives a theoretical background of fire hazards, including fire generation, smoke, and fire stages. The importance of test scales is then depicted

with information on matter and macro scale, as well as on the multi-scaling approach. Finally, a state-of-the-art review depicts wood properties and examines the impact of oxygen on the fire reaction of wood.

In the second chapter, the experimental methodologies employed in this research are depicted. First, a detailed technical description of the matter scale tests is provided. Then, to design an apparatus adapted to the problematic, a state-of-the-art review of the existing bench-scale devices is presented. Considering the gaps identified in the literature review, a homemade bench-scale apparatus, the Controlled-Atmosphere Cone Calorimeter (CACC) coupled to Fourier-Transform Infrared Spectroscopy (FTIR) and Electrical Low-Pressure Impactor (ELPI) was elaborated and is presented. This section explains its technical specifications, analytical equipment and calibration methods using a reference material. Finally, following a review of existing intermediate-scale benches, a homemade enclosure coupled to FTIR and ELPI was developed and is presented. The technical specifications, analytical equipment and calibrations are provided.

The third chapter is dedicated to results of the matter scale analyses. The thermal behavior of CLT is first assessed with the Thermogravimetric Analysis (TGA) coupled to FTIR and with the Pyrolysis-Gas Chromatography/Mass Spectroscopy (Py-GC/MS). Then, the same tests are conducted on wood fiber. These analyses provide valuable insights into the decomposition process and offer a comprehensive understanding on the gaseous emissions at molecular scale.

The fourth chapter focuses on the effect of vitiation on the fire development, gas, and aerosol emissions of CLT, WF and the combination of both at bench-scale with the CACC-FTIR-ELPI. To study various flaming scenarios, the oxygen varies from 21 to 10 vol-% O₂ while the heat flux is set at 50 and 20 kW/m².

The fifth chapter deals with the preliminary results obtained with the intermediate scale bench. It consists in an enclosure equipped with a propane burner, a FTIR and an ELPI. Meter size panels of CLT, WF and the combination of the two were submitted to flame powers of 90 and 40 kW. This section gives an overview of the fire behavior of a larger-scale structural wood/insulation assembly in a fire scenario incorporating a flame attack. Gas and aerosol production are analyzed and discussed in this configuration.

Finally, a conclusion to this PhD work and perspectives are given.

Chapter 1: State of the art

1. FIRE HAZARDS.....	26
1.1. FIRE GENERATION	27
1.2. FIRE SMOKE.....	28
1.2.1. Effluents.....	28
1.2.2. Aerosols.....	30
1.2.2.1. Formation.....	30
1.2.2.2. Morphology of aerosol.....	31
1.2.2.2.1. Equivalent electrical mobility diameter	31
1.2.2.2.2. Equivalent aerodynamic diameter	32
1.2.2.3. Particle size distribution	32
1.3. FIRE STAGES AND ASSOCIATED RISKS	33
1.3.1. Non-flaming fires	35
1.3.2. Well-ventilated flaming fires.....	35
1.3.3. Under-Ventilated fires.....	36
1.3.4. Post-flashover fires	36
2. SCALING EFFECT	37
2.1. TEST SCALES	37
2.1.1. Matter scale	38
2.1.1.1. Phenomena considered.....	38
2.1.1.2. Testing methods	38
2.1.2. Material scale	39
2.1.2.1. Phenomena considered.....	39
2.1.2.2. Testing method.....	40
2.1.2.2.1. Bench-scale	40
2.1.2.2.2. Intermediate and real-life scale	40
2.2. MULTI-SCALING APPROACH	40
3. WOOD	41
3.1. PROPERTIES.....	41
3.1.1. Chemical properties	41
3.1.1.1. Elementary composition.....	41
3.1.1.2. Chemical composition	42
3.1.2. Physical properties	43
3.1.2.1. Density.....	43
3.1.2.2. Moisture content.....	43
3.1.2.3. Heating value.....	44
3.2. REACTION-TO-FIRE.....	44
3.2.1. Pyrolysis	45
3.2.1.1. Dehydration reactions	45
3.2.1.2. Low temperature pyrolysis.....	46
3.2.1.3. High temperature pyrolysis	46
3.2.2. Thermo-oxidative pyrolysis	49
3.2.3. Ignition	49
3.2.4. Flaming	50
3.2.5. Smoldering	50

3.3.	WOOD PROPERTIES INFLUENCING ITS BURNING BEHAVIOR	51
3.3.1.1.	Material properties	51
3.3.1.2.	Sample properties	52
3.3.1.3.	Summary	55
3.4.	EFFECT OF OXYGEN	55
3.4.1.	<i>Matter scale tests</i>	55
3.4.2.	<i>Bench-scale test</i>	57
4.	CONCLUSIONS	59

As previously introduced, fire smoke is responsible for most of the deaths and injuries in a building fire [4]. Thus, it is essential to understand how smoke is generated, why it is dangerous and to what extent. The difficulty with this study is that the assessment of fire hazards is a complex multidisciplinary process, combining both fire conditions and fuel chemistry. It requires a well understanding of how a fire is generated, what stages it can go through and which ones are the most dangerous. In parallel, a good knowledge in smoke generation, from gases to aerosols formation, is also primordial to evaluate the smoke composition and its potential hazards. The objective is to get an overview of the risks associated to the smoke generated by a thermally decomposing material in different enclosure fire scenarios. Moreover, all these considerations must consider scale effects, which can greatly affect fire behaviors. Indeed, fire behaviors generally differ at small-scale from those at real scale, the challenge is to get as close as possible to reality. As discussed in the introduction of this thesis, due to the widespread use of wood materials in the building field, a special emphasis to the fire behavior of wood, from matter scale to macro-scale and according to fire conditions, is addressed here.

The first section of this chapter deals with the fire hazards in an enclosure, with a focus on fire and smoke generation. The second section depicts the effects of scale on the reaction to fire of materials, with a description of the relevant testing methods from matter to macro-scale. The third section focuses on wood materials, especially on their reaction to fire along with gas and aerosol emissions from matter scale to macro-scale.

1. Fire hazards

During a fire, the main obstacles to people escaping a building are heat, smoke visual obscuration and smoke toxicity. Smoke can be defined as a mixture of gases and aerosols, including suspended particles created by combustion and pyrolysis during a fire [6]. Its dangerousness depends on the fire conditions and the material composition.

1.1. Fire generation

Generally, a fire is referred as an uncontrolled combustion, which can take many forms. They all involve a chemical reaction between a fuel and oxidizing agent (oxygen in most cases) in a presence of a source of heat. According to combustion conditions, namely temperature and ventilation, fires can be characterized into different stages (ISO 19706). As an example, a simplified curve of an enclosure fire that goes through all possible stages is considered (Figure 2). It generally begins with a non-flaming induction period where the material starts to decompose under heating. Its temperature increases by heat transfer from the surface to the bulk. At a critical temperature, the chemical bonds of the material break, thus producing volatile species of low molecular weight. Some of these volatiles mix with the surrounding oxygen by diffusion into the layer close to the material surface [7]. This results in the formation of free radicals (hydrogen radical (H)[•] and hydroxide radical (OH)[•]) able to ignite spontaneously or in the presence of an external spark. This stage highly depends on the type of combustible, its geometrical arrangement, ventilation, and the source of ignition. Then, if ignition occurred, the decomposition switches to flaming combustion. The combustion of gases, resulting from the formation of (H)[•] and OH[•], increases the production of new combustible gases which sustain the fire. Generally, when the fire is small compared the enclosure size and the air supply is sufficient, the fire is considered well-ventilated. The fire produces hot smoke that fills the volume of the enclosure. The fire will grow rapidly until it reaches a quasi-steady state maintained by either the fuel (fuel controlled) or the air supply (under-ventilated flaming). Finally, it decays and self-extinguishes. According to the fire conditions, a fire can remain at one of these stages and be referred to as a particular type of fire: non-flaming, smoldering, well-ventilated, developed fuel controlled or developed ventilation controlled [4]. In all cases, a more or less large quantity of smoke will be produced.

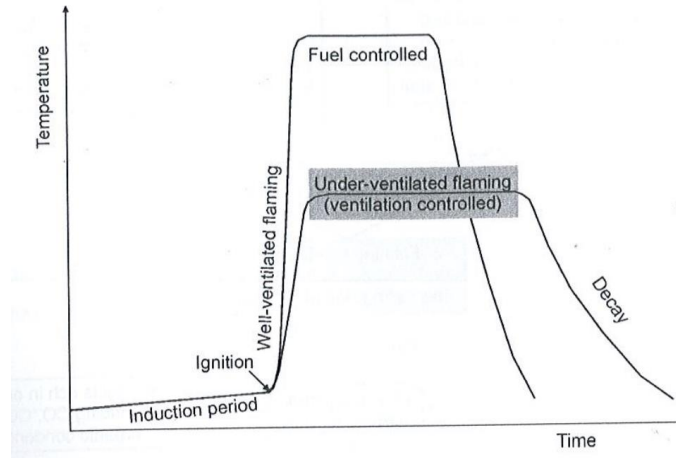


Figure 2: Idealized fire growth curve and typical temperatures from [4]

1.2. Fire smoke

When decomposing under thermal stress, the solid phase material generally produces dangerous smoke in the gas phase. It contains a mixture of aerosols and effluents resulting from complete and incomplete combustion [4]. Effluents and aerosols are described in the next sections.

1.2.1. Effluents

The composition of fire effluents strongly depends on the chemical composition of the thermally decomposing material [1][4] as well as on the fire conditions (described in the section 1.3). The composition of building materials is varied; thus, a complex chemical mixture of gases can be generated during a building fire. Fire effluents are composed of oxidized products (mainly carbon dioxide) and products resulting from potential incomplete combustion. These latter are composed of partially oxidized products (carbon monoxide and aldehydes), fuel decomposition products (aliphatic or aromatic hydrocarbons) and other relatively stable molecules (hydrogen halides and hydrogen cyanide).

From a toxicological perspective, these effluents can be divided into asphyxiants and irritants (Table 1). Asphyxiant gases, mainly carbon monoxide and hydrogen cyanide (HCN), prevent oxygen uptake by cells with loss of consciousness and ultimately death. Asphyxiation may also be aggravated by carbon dioxide (CO₂), which increases the inhalation of oxygen and toxic gases produced by the fire and by low oxygen concentration. Oxygen depletion can be lethal at a level lower than 6% but it is generally assumed that heat and other gases will be harmful before this threshold. Furthermore, irritant gases cause immediate incapacitation (eyes and upper respiratory tract) and longer-term damage in the lung. Their effects depend on the dose received and the exposure time. It includes hydrogen halides, nitrogen-based and sulfuric-

based gases and organo irritants (low molecular weight organics such as acetaldehyde, acrolein, formaldehyde, benzene, or phenol). It should be highlighted that most irritants have the tendency to penetrate deep into the lungs when attached to submicron-sized particles such as soot, causing pulmonary irritation [4].

Table 1: Main fire effluents, modified from [4]

Type of component	Name	Sources
Asphyxiant gases	Carbon monoxide (CO)	All fuels
	Hydrogen cyanide (HCN)	Nitrogen containing fuels, e.g., polyurethane (PU), Nylon, wool, silk
Irritant gases	Hydrogen fluoride (HF)	Fluorine containing fuels, e.g., polytetrafluoroethylene (PTFE)
	Hydrogen chloride (HCl)	Chlorine containing fuels, e.g., poly (vinyl chloride) (PVC)
	Hydrogen bromide (HBr)	Bromine containing fuels, e.g., Br-flame retarded material
	Nitrogen oxide (NO), nitrogen dioxide (NO ₂), other nitrogen oxides (NO _x)	Nitrogen containing fuels, e.g., Nylon
	Ammonia (NH ₃)	Nitrogen containing fuels, e.g., Nylon
	Sulfur dioxide (SO ₂)	Sulfur containing fuels, e.g., wool
	Organo irritant	Many fuels, e.g., cellulosic materials, polyethylene (PE), polypropylene (PP), acrylonitrile butadiene styrene (ABS)
Other components to monitor	Dioxygen (O ₂)	All fuels
	Carbon dioxide (CO ₂)	All fuels

Carbon dioxide and carbon monoxide are always found in the fire smoke produced by any material. A detailed composition of fire effluent of wood is given in the section 3.

1.2.2. Aerosols

In addition to gases, aerosols also present a problem in term of fire hazards. Indeed, they are sufficiently small to cause respiratory issues. Aerosols include both micro-droplets formed by organic vapor condensation and carbonaceous agglomerated structures. These latter are known as soot and consist in hundreds to thousands of nearly spherical primary particles [8]. Few investigations have been made regarding the size, distribution, and composition of particulates despite them being generated in large quantity during fires.

1.2.2.1. Formation

The formation of soot is a complex multi-stage process. Nonetheless, the mechanism can be simplified into five steps: nucleation, surface growth, coalescence, agglomeration and oxidation [8]. During the nucleation stage (Figure 3), primary particles with a diameter up to two nanometers, are produced in high quantity in the most reactive part of the flame. These particles, called nuclei, are formed through the condensation of products of oxidation or pyrolysis of the fuel. These products are unsaturated hydrocarbons such as acetylene and polycyclic aromatic hydrocarbons (PAH) and are key intermediate compounds in soot formation [8]. Then, during the surface growth step (Figure 3), nuclei grow by heterogeneous reactions between their surface and reactive gases such as acetylene, PAH, and benzene. This process, representing the main mass production phase, occurs until the particles reach a quasi-spherical shape with a diameter close to 10 nm. Then, two phenomena (Figure 3) of inter-particles collisions will impose the morphology of aggregates: coagulation and agglomeration. For “fresh” particles of about 10 nm, collisions can lead to coalescence. This corresponds to two particles merging due to high concentration and strong Brownian motion in the flame. For “older” particles of diameters superior to 10 nm, their internal structure is harder to reorganize so particles glue without merging, this corresponds to agglomeration. During these coagulation and agglomeration, where particles randomly collide to merge or glue, the complex morphology of soot and the particle size distribution establish [8]. Moreover, during coagulation and agglomeration, the total mass of aerosol does not evolve while the number of particles decreases. Finally, in the less reactive part of the flame where oxygen is more abundant, oxidation of particles (Figure 3) may occur. It corresponds to a partial combustion of aggregates by oxygen and hydroxyl radicals [8]. Oxygen induces internal oxidation leading to fracture and break-up of particles while hydroxyl radicals diffuse over the surface of particles tending to break down the aggregates and reduce their mass.

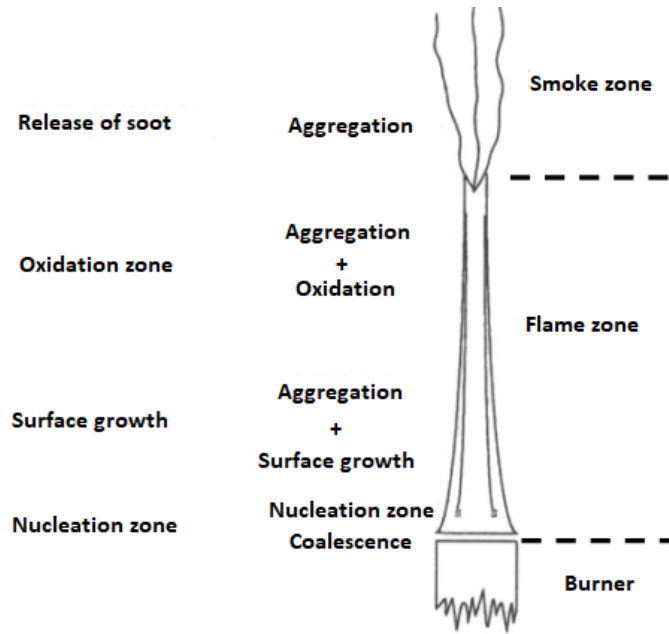


Figure 3: Soot particles formation and evolution in a flame [8]

1.2.2.2. Morphology of aerosol

The previous section highlighted how complex soot formation is. As a result, these aggregates display a wide range of sizes, shapes, and densities. Even though nuclei are spherical, when they agglomerate into aggregates, they cannot be considered as spherical particles too. As such, to best describe their morphology, different parameters need to be introduced. Based on the several behaviors of the particles under the influence of different forces, the diffusion, aerodynamic, electrical, and optical equivalent diameter are defined, each representing a measurable index of the particle. The parameters used to characterize the sizes are the aerodynamic diameter and the electric mobility diameter. Other additional diameters such as the volume equivalent diameter, gyration diameter, and aggregate diameter exist but this section focuses on the two main definitions. Further information can be found in reference [8].

1.2.2.2.1. Equivalent electrical mobility diameter

The electrical mobility diameter D_m corresponds to the diameter of a spherical particle with the same electrical mobility Z_p as the considered particle. The electrical mobility is equivalent to the velocity acquired by a particle of charge $N.e$ in an electric field E (Equation 1):

Equation 1:

$$Z_p = \frac{v_{TE}}{E} = NeB = \frac{NeC_c}{3\pi\mu D_m} D_m = \frac{C_c}{3\pi\mu B}$$

With:

v_{TE} : electrostatic terminal velocity

E: electric field

N: number of elementary charges on the particle

e: elementary charge (1.6×10^{-19} C)

μ : gas viscosity

B: dynamic mobility

C_c : Cunningham correction factor

1.2.2.2.2. Equivalent aerodynamic diameter

The aerodynamic diameter D_a (Equation 3) corresponds to the diameter of a spherical particle with a density of $\rho_0 = 1 \text{ g/cm}^3$ and with the same settling velocity as the considered particle. Generally, this diameter is determined with an impactor (see Chapter 2 section 2.2 p63). With such a device, particles are classified according to their relaxation time τ (Equation 2):

Equation 2:

$$\tau = m_p B$$

With:

m_p : mass of the particle

And:

Equation 3:

$$D_a = \sqrt{\frac{18\mu\tau}{\rho_0 C_c}}$$

With these two diameters defined, size distribution of aerosols can be determined with the appropriate device.

1.2.2.3. Particle size distribution

The size distribution of aerosol is a statistical representation of the total particle sizes contained in a sampled aerosol [9]. Fire aerosols are polydisperse and their diameter may range over two to three magnitudes. A graphical representation of the size distribution is generally done as a histogram with the discrete concentration contained in a size bar. Another way of representing the size distribution is by using

a frequency distribution or cumulative distribution curve. From a cumulative distribution, the fraction above or below a fixed size can be easily determined. Most aerosols with long tails at larger sizes have an asymmetrical shape of frequency distribution. In contrast to normal distribution, the mode, median and mean sizes are different, and the particle diameter distributions are in the hierarchy of smaller to larger values of the mode, median and mean. The mode is the recurrent size, the median is the size that cuts the distribution into two equal areas, and the mean is the average value. Because larger sizes have a skewed distribution consisting of a long tail, aerosol size distributions are most often represented by a log-normal distribution [10]. Very few data on the soot aggregates sampled outside the flame are available in the literature because of the difficulty of sampling in and out the flame. Nonetheless, it is admitted that both primary particles and aggregates diameters follow a log-normal distribution with a sub-micron distribution [8].

The composition and thus dangerousness of fire smoke can be various according to the studied material. However, the release of gases and aerosols is also strongly dependent on the fire conditions.

1.3. Fire stages and associated risks

The fire stages mentioned in the previous section are classified into a small set for which the decomposition conditions can be replicated in small or large-scale tests. It allows having a better understanding of the role they play in fire hazards and how a material decomposes in these conditions. The ISO 19706 [11] classifies these stages in terms of heat flux, temperature, oxygen concentration and CO₂/CO ratio (Table 2). The Table 2 describes each fire stage as a function of heat flux, temperature, oxygen and [CO]/[CO₂] ratio. A brief description is given for all stages in the next sections.

Table 2: Characteristics of fire stages [11]

Fire stage	Heat flux to fuel surface (kW/m ²)	Max. temperature (°C)		Oxygen (vol %)		[CO]/[CO ₂]
		Fuel surface	Upper layer	Entrained	Exhausted	
1. Non-flaming						
1a. Self-sustaining (smoldering)	n.a	450 to 800	25 to 85	20	20	0.1 to 1
1b. Oxidative pyrolysis from external radiation	-	300 to 600	^a	20	20	^b
1c. Anaerobic pyrolysis from external radiation	-	100 to 500	^a	0	0	^b
2. Well-ventilated flaming						
Well-ventilated flaming	0 to 60	350 to 650	50 to 500	~20	~20	<0,05
3. Under-ventilated flaming						
3a. Small, localized fire, generally in a poorly ventilated compartment	0 to 30	300 to 600	50 to 500	15 to 20	5 to 10	0.2 to 0.4
3b. Post flash-over	50 to 150	350 to 650	>600	<15	<5	0.1 to 0.4
^a The temperature in the upper layer of the fire room is most likely determined by the source of the externally applied radiation and room geometry. ^b There are few data; but for pyrolysis, this ratio is expected to vary widely depending on the material chemistry and the local ventilation and thermal conditions						

1.3.1. Non-flaming fires

Non-flaming thermal decomposition occurs when sufficient heat provokes the thermal breakdown of the material structure. The simplest pyrolysis (Stage 1c in Table 2) is endothermic and takes place in inert atmospheres. Materials decompose into a limited range of organic compounds, which have similar structure as the parent material. The most common form of thermal decomposition occurring in fires is exothermic oxidative pyrolysis (Stage 1b in Table 2). Reaction with oxygen occurs both at the surface of the material and in the gas phase at temperatures exceeding 300 °C. The thermo-oxidative mechanism is a free radical mechanism that is summarized by an initiation step, a propagation step, a ramification step and a termination step [12]. Oxidative pyrolysis is often the precursor to flaming combustion.

Char-forming materials, i.e., materials forming open porous carbon rich residue after endothermic and exothermic pyrolysis, may undergo additional exothermic oxidation in the solid phase [4]. With sufficient air, a glowing char is formed and constitutes smoldering decomposition (Stage 1a in Table 2). In this stage, mainly carbon dioxide and carbon monoxide are released from carbon oxidation.

Non-flaming decomposition and particularly smoldering of porous materials increases the yields of partially oxidized products such as carbon monoxide, volatile organic compounds, polyaromatic hydrocarbons and particulate matter. Although the yield of dangerous species is larger in non-flaming decomposition than in flaming fires [4], the rate of production is much lower. As a result, a non-flaming decomposition of long duration inside an enclosure can be lethal.

1.3.2. Well-ventilated flaming fires

In the initial stage, flaming fires (Stage 2 in Table 2) are always well-ventilated and will remain so if the fire is small in comparison with the size of the enclosure and the ventilation sufficient. The hot gases rising from the flame entrain air, which mixes with the fuel gases. This burning mixture produces heat, carbon dioxide, water, and small amounts of sooty smoke while the yields of partially oxidized products such as carbon monoxide remain low. In enclosure fires, fire effluents rise and form a layer under the ceiling, which gradually fills the enclosure from the top down. The heat from the smoke is radiated back to the fire, which accelerates the fire intensity and may lead to under-ventilated fires if the enclosure is filled with smoke.

This stage represents the least dangerous case as fires are generally small and do not generate enough effluents to cause harm, except in a very small enclosure. Both escape and extinguishment are often still possible.

1.3.3. Under-Ventilated fires

Under-ventilated fires (Stage 3a in Table 2) are common in building as they essentially consist in enclosed compartments with low ceilings, or a series of interconnected enclosures. As the fire grows, the ceiling is filled with hot smoke until part of the flames penetrate the upper layer of the smoke (Figure 4). The filling time depends on the rate of fire growth and the upper layer volume of the enclosure.

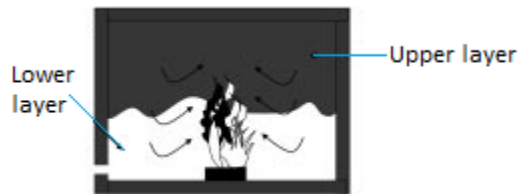


Figure 4: Under-ventilated fire in enclosed compartment, modified from [4]

As the upper layer goes down with fire growth, an increased part of the flames is burning in the upper layer, which gradually becomes depleted in oxygen. Moreover, the mass of fresh air entrained into the fire is reduced. As a result, the combustion becomes vitiated (i.e., oxygen concentration reduced) and incomplete. The yields of carbon dioxide decrease while those of carbon monoxide, volatile organic compounds and aerosols increase. The heat of combustion also decreases and when the upper layer reaches the base of the fire, this latter extinguishes. The oxygen concentration is typically between 12 and 15% at extinguishment [4].

The hazards from under-ventilated fires are mainly from incomplete combustion which give rise to high yields of asphyxiant gases and irritant smoke. The height of the upper layer is also critical to survivability and escape.

1.3.4. Post-flashover fires

With sufficient fuel and ventilation, the fire may reach flashover conditions (Stage 3b in Table 2). When the temperature of the hot layer of smoke is high enough to be reactive (between 500 and 600 °C), heat is radiated downwards to ignite all combustible materials in the enclosure, which causes a widespread growth of fire called flashover. The fire is then controlled by the air supply in the room (ventilation controlled) as there is more fuel than oxygen, which produces large amounts of hot and toxic fire effluents. If enough ventilation is available, the fire continues to burn until all the fuel is consumed [4].

To summarize, oxidative pyrolysis and smoldering can generate potentially toxic effluents. However, the rate of reaction and so the number of compounds generated is generally too small to affect occupants in

the immediate vicinity. Similarly, well-ventilated fires are generally small (sufficient air supply), and smoke is located above head, so extinguishment and escape are possible. However, fires that are under-ventilated or vitiated are much larger and produce greater volume of effluents, which make them of great interest regarding the assessment of fire hazards. Most real hazardous fires involve vitiated flaming combustion, either pre- or post- flashover. A risky scenario would be a relatively small fire in an enclosed building, which rapidly becomes under-ventilated and fills open areas with lethal fire effluents. Building occupants can be incapacitated and die during this stage. What could be worse would be occupants opening windows or doors, resulting in a rapid-fire growth and flashover [4].

To conclude this section, the hazards encountered in fires have been highlighted in terms of fire conditions and gases and aerosols production. Under-ventilated and vitiated fires are the most dangerous fires as the fire spread is fast and a great volume of effluents containing unburnt gases and submicronic aerosols is released. The oxygen level is an important parameter influencing the combustion and its effects will be discussed in the case of the burning of wood (see section 3.4 p. 55). However, to properly assess the behavior of a material in a fire scenario, the notion and effect of scale must be discussed.

2. Scaling effect

To fully assess the fire reaction of materials, phenomena occurring at both matter and macro-scale must be understood. Moreover, behaviors observed at bench-scale might differ from the ones observed at a larger scale or reality. It is thus essential to study the links between matter and material scale to follow a multi-scaling approach.

2.1. Test scales

The fire behavior of materials can be assessed either with conventional tests (bench-scale or intermediate scale tests) or with real-life situation tests (scale 1). Though real scale tests are highly recommended, they are expensive, and it is difficult to monitor variability between tests. Consequently, it is preferable to choose for conventional tests while trying to get as close as possible to the real fire behavior of the materials. Tests can be classified into the size of the tested material (Figure 1 p23). Each test has its characteristics (nature of the thermal attack, testing atmosphere) and provides data on fire behaviors such as time to ignition, decomposition temperature, mass loss rate or heat release rate [13].

2.1.1. Matter scale

2.1.1.1. *Phenomena considered*

The experimental evaluation of thermal behaviors at matter scale focuses on the three stages of heating, pyrolysis, and oxidative pyrolysis. This corresponds to the induction period described in 1.1 p27 and the stages 1b and 1c of Table 2 p34. The heating stage only depends on the intrinsic chemical and physical properties of the material. Indeed, as the sample is thermally thin, temperature gradient effects are neglected. Moreover, the pyrolysis and the oxidative pyrolysis describes the combustion chemical reaction.

Studying materials at a matter scale has a double purpose. First, it allows the thermal decomposition analysis of the material. It can also provide information on the estimation of pyrolysis parameters such as kinetic parameters and residual mass fraction for each identified reaction. Secondly, when combined to a gas analysis system, the nature of gases emitted during the decomposition can also be assessed.

2.1.1.2. *Testing methods*

With a very few quantities of material (μg), tests at matter scale such as Thermogravimetric Analysis (TGA), Pyrolysis-gas Chromatography Mass Spectroscopy (Py-GC/MS), Differential Scanning Calorimetry (DSC) and Pyrolysis Combustion Flow Calorimeter (PCFC) can provide first insight of the thermal decomposition and gas production of materials. This leads to test thermally thin materials with restricted heat and oxygen transfers inside the sample, which is not representative of real cases. However, as they are controlled by chemical kinetics, these tests allow a good control of experimental parameters such as the heating temperature and the working atmosphere.

Under TGA experiments, the sample is heated according to a temperature ramp or isothermal temperature. The weight loss of the sample is recorded versus time or temperature. This technique allows the determination of the thermal stability of materials and is widely used in the literature [14], [15], [16]. In addition to TGA, DSC experiments allow the determination of the heat capacity, the enthalpies of physical transitions and chemical reactions. It measures the differential heat flow necessary to maintain the sample and an inert reference at the same temperature when exposed to a temperature change. The rate of heat flux is proportional to its heat capacity. The DSC analysis provides this value by comparison with the rate of the heat flux within a reference of a well-known heat capacity.

Py-GC/MS is an identification method by mass spectroscopy. The sample is brought at its decomposition temperature in the pyrolyzer. The evolved gases are introduced inside the GC/MS part where they are separated according to their size and their interaction with the polarized GC column. They are introduced inside the MS according to their retention time. The MS spectrometer splits molecules into ionized fragments and, with comparison with a data base, the molecule can be identified.

Finally, the PCFC technique [17] was developed by Lyon and Walters. It measures the rate at which the heat of combustion of fuel gases is released by a sample during controlled pyrolysis in an inert gas stream. The fuel gases are mixed with an excess of oxygen and combusted in a separate chamber where the instantaneous heat of combustion of the flowing gas stream is measured by oxygen consumption calorimetry.

2.1.2. Material scale

2.1.2.1. *Phenomena considered*

At material scale, additional stages are considered in the experimental evaluation of the fire behavior. Indeed, ignition follows oxidative pyrolysis if the amount of oxygen and heat are sufficient. Then, exothermic reactions of combustion take place, which release combustion products (gases and aerosols) as described in the section 1.2 p28. As a difference with matter scale, the heating stage considers shapes factor such as thickness, which induces a thermal gradient as the heat diffusion is not instantaneous. At this scale, the diffusion of the gaseous compounds inside the material from the bulk to the surface are considered as well as the oxygen diffusion through the sample. Moreover, the ignition stages consider the flame radiative feedback to the fuel surface that will further decompose and yield combustible gases to the flame.

At material scale, it is first necessary to verify that the decomposition mechanisms are like the ones at matter scale. Bench-scale tests, such as cone calorimeter tests, allow for the quantification of energetic parameters such as ignition time and heat release of a material exposed to a radiative heater. It is also essential to acquire information on the chemistry of the decomposition processes. For instance, Fourier-Transform Infrared spectroscopy analysis enables the examination of volatiles released from the solid surface.

At the intermediate scale, the objective is to evaluate the fire behavior, especially the fire spread, of meter-size materials exposed to a burner flame. This flame is like the one it could be exposed to in real fire

situations. A qualitative and quantitative description of the propagation and development of fire on the tested material is made.

2.1.2.2. Testing method

2.1.2.2.1. Bench-scale

At material scale, with samples up to a surface of 100 mm², bench-scale tests such as Cone Calorimeter coupled to gas and aerosols on-line analysis, Smoke Density Chamber, Steady-state Tube Furnace, or Fire Propagation Apparatus can be carried out to study the fire reaction. Given the considerable challenges posed by the design of a bench-scale apparatus in this study, the Chapter 2 (section 4.1 p67) provides a comprehensive overview of the current state-of-the-art.

2.1.2.2.2. Intermediate and real-life scale

With samples of about the meter size, tests in enclosure or the Single Burning Item (SBI) test can be done to study fire propagation of a system. A detailed state-of-the-art is depicted in the Chapter 2 (section 5.1 p95) on intermediate scale tests. Finally, at real scale, room tests and real-life scenario tests are done to have an assessment of the “real” fire behavior. Further details can be found in the reference [13].

Nowadays, research turns to multi-scaling studies in order to predict at best the fire behavior of a material [18], [19], [20], [21]. The goal is to understand macroscopic fire behaviors from phenomenon observed at smaller scales. Furthermore, these experimental data can also be imputed in numerical studies and validate fire models. The exchange of data between these two domains will allow an optimization of fire safety.

2.2. Multi-scaling approach

As previously highlighted, scale is an important parameter that has an influence on the fire behavior, gas and aerosol production obtained from experiments. It is difficult to extrapolate laboratory results to phenomenon observed in real fires. Therefore, the multi-scaling approach allows for making parallels between the different scales. This method consists in using successively the results of experiments and simulations at small scales as input parameters for simulations at larger scales. The importance of the change of scale concerns all types of materials. Bustamante Valencia [18] studied the thermal decomposition of a polyether polyurethane foam at three scales. He is one of the first scientists to verify that the decomposition mechanism remains unchanged regardless of the scale studied. Marquis [19] also adopted a multi-scale approach to evaluate the fire behavior of a composite sandwich. Through this

methodology, he observed that each of these scales provides additional information on the fire behavior of the product used, to simulate the development of a full-scale fire. Many researchers developed a multi-scale approach (TGA tests and cone calorimeter) to better interpret the fire behavior of materials including plywood [22], PMMA [23], PVC [23] and Scotch pine [16]. Vincent [21] developed a bench-scaled called RAPACES that allows for studying the fire behavior of materials such as PMMA and plywood while modifying the size of the sample. She observed that geometrical factors play a major role on the ignition and on the combustion dynamics through structural phenomena.

To conclude, it is essential to conduct laboratory experiments at different scales to better explain the phenomenon occurring during the combustion of materials. This approach would be benefic for wood materials as they are increasingly used in the construction field.

3. Wood

Wood materials are key products to sustainable building. They are widespread in construction (structure, flooring, cladding, insulation, etc.) and in furniture. It is therefore essential to understand at best their response to thermal exposure, especially to fire. The chemical and physical properties of wood are key parameters to understand the thermal behavior of wood at all scales.

3.1. Properties

The chemical properties, including the elementary composition and the chemical composition of wood, are first described to have a first insight on its components. Then, the physical properties ranging from the density to the heating values are depicted.

3.1.1. Chemical properties

To better assess the wood thermal behavior, the elementary and chemical composition are first described. These parameters serve as key insights into the underlying factors shaping wood's properties.

3.1.1.1. *Elementary composition*

Wood is an anisotropic material mainly composed of carbon, oxygen, hydrogen, and nitrogen. The proportion of these elements vary according to the wood species but remains relatively steady across the different parts of the tree. For dry wood (2% of residual water), a chemical formula taking into account nitrogen is $C_6H_{8.4}O_{3.5}N_{0.1}$ [24]. It is generally presented without nitrogen as $C_6H_{8.6}O_4$ considering 50% of carbon, 6% of hydrogen and 44% of oxygen [24].

3.1.1.2. Chemical composition

The main components of wood are polymers (cellulose, hemicellulose and lignin), extracts (terpenes, resins, tannin, etc.) and ashes (oxides of calcium, potassium, sodium, magnesium) [24]. The distribution of these compounds varies according to the species, the tree line, and the essence but the major ones are the three polymers.

Cellulose is 40 to 50% of wood composition. It is a linear polymer mainly composed of D-glucose units ($C_6H_{12}O_6$) linked together by ether bonds (R-O-R') (Figure 5).

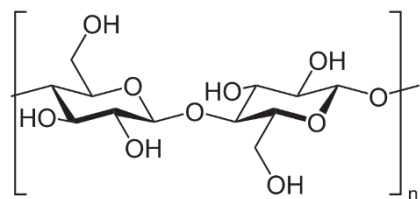


Figure 5: Cellulose

Hemicellulose is 30 to 50% of wood composition. It is a heterogeneous family of polysaccharides composed of branched polymers with D-xylose ($C_5H_{10}O_5$) (Figure 6a) and of a stereoisomer of glucose called D-mannose ($C_6H_{12}O_6$) (Figure 6b).

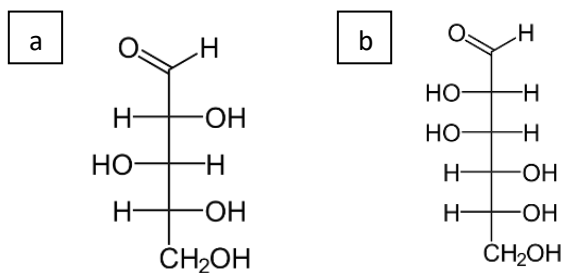


Figure 6: a. D-Xylose unit, b. D-Mannose unit

Lignin is 25 to 30% of wood composition. It is a complex three-dimensional network of monolignol polymers such as paracoumaryl alcohol, coniferyl alcohol and synapilic alcohol linked together with furan ring or ether bonds (Figure 7). Although large variability within the same species may be found in lignin composition, the basic unit is generally a phenylpropane unit. Lignin is also an agent for fixing cellulose fibers together.

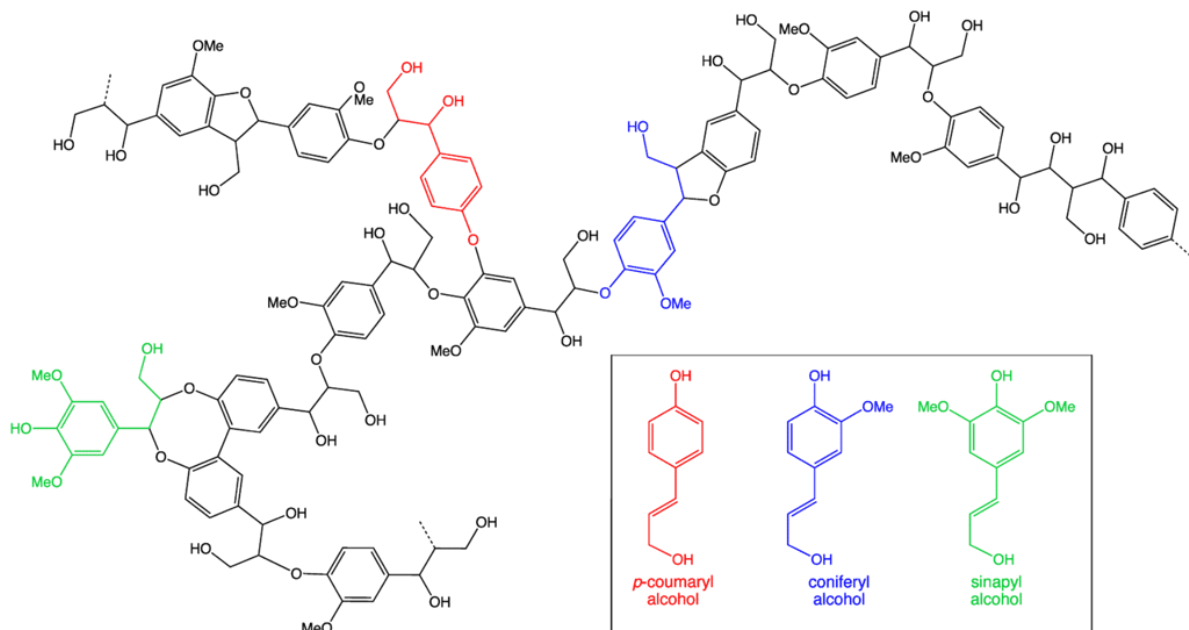


Figure 7: Possible lignin molecule

3.1.2. Physical properties

The physical properties, including density, moisture content and heating value are depicted in this section. Thanks to its structure made of conductive cells, known as tracheid, wood materials have unique physical properties.

3.1.2.1. Density

The cellular tissues of wood vary according to the essence, which leads to important differences in density. Indeed, the density of wood as a material construction can vary from 400 kg/m³ for fir to 700 kg/m³ for beech. Moreover, the heterogeneity of wood, and especially with nodes, can influence the density of a same species [24]. For example, the density of dry spruce² is comprised between 450 and 550 kg/m³.

3.1.2.2. Moisture content

Wood is very hygroscopic, that is it easily retains water by absorption. The quantity of retained water varies easily and quickly as it depends on the environment, and especially on temperature, pressure, and humidity. However, after a long drying period, the moisture content drops from 50 to 15%, corresponding to the humidity that takes part in its structure [25]. The moisture content can be defined according to its gross mass M or its dry mass M_0 . It is expressed according to the gross mass of the wood (Equation 4)

² <http://www.selection-vosges.com/fr/epicea.html>

Equation 4:

$$H = \frac{M - M_0}{M} * 100$$

3.1.2.3. Heating value

The lower heating value (or lower calorific value) of wood varies within essences but it is relatively low, from 15 to 20 MJ/kg. Anhydrous wood ignites around 275°C but the ignition time and temperature depend, for the same wood, on its moisture content, the size of wood particles and its specific gravity [25].

3.2. Reaction-to-fire

The fire behavior of wood is a complex chemical and physical process (Figure 8). Fives zones are considered when a sample of wood is burning: the wet zone, the dehydration zone, the pyrolysis zone, the char zone, and the gas zone. The two first correspond respectively to condensation and evaporation of water in the sample. The pyrolysis zone is ascribed to the area where cellulose, hemicellulose and lignin decompose into CO, CO₂, H₂O, pyrolysis gases, tar and char [26]. Wood tar consists of more than 400 organic chemicals with a wide range of matter weights (60–300 g/mol) and oxygenated volatile and nonvolatile components involving organic acids, alcohols, aldehydes, ketones, phenols, furans, benzenes, sugars, bitumen, and their derivatives [27]. The char zone corresponds to the black, porous and carbon rich residue formed from wood thermal decomposition. The last zone corresponds to the gas zone where water, pyrolysis gases, CO and CO₂ are released from the solid. The main steps of decomposition occurring in the areas previously described are detailed in the following.

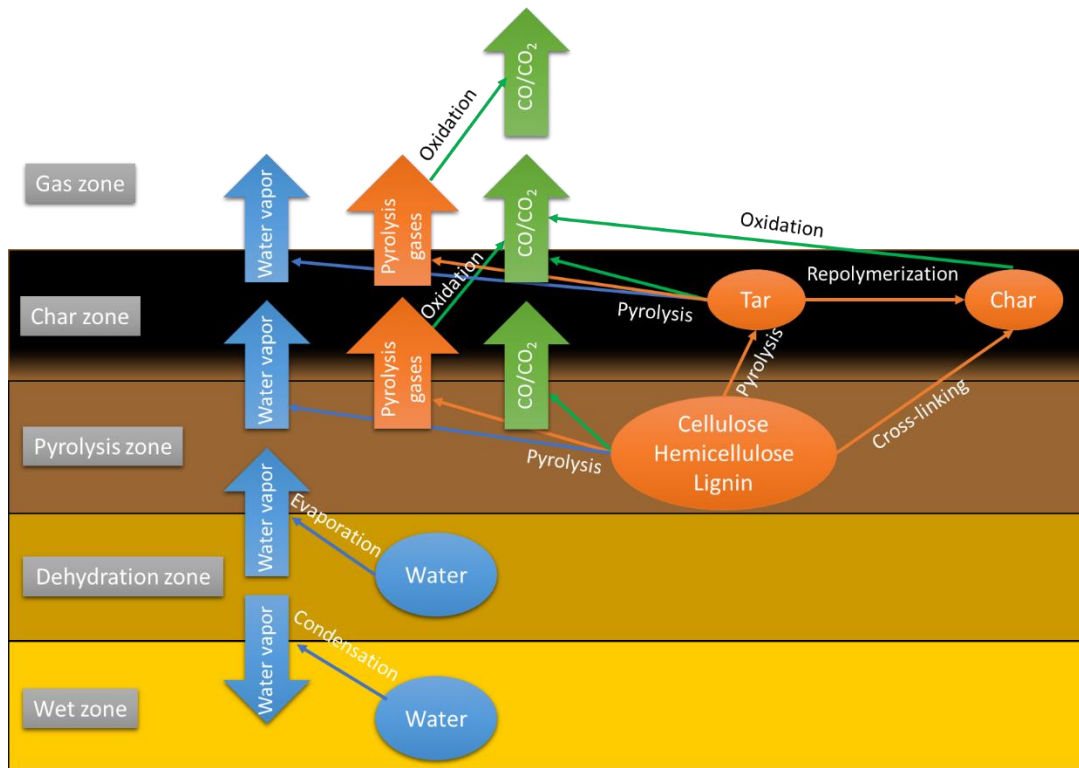


Figure 8: Chemical and physical processes within a burning timber, modified from [25]

3.2.1. Pyrolysis

When heated, cellulose, hemicellulose and lignin decompose and produce inert and combustible gases, liquid tars, a solid carbonaceous char and inorganic ash [28]. Wood typically undergoes three stages of pyrolysis because of its relatively low thermal conductivity and density and relatively high specific heat. First, it dehydrates and very slowly, pyrolysis takes place below 200 °C. Then, up to 300 °C, the onset of pyrolysis occurs. Finally, a rapid pyrolysis is observed above 300 °C.

3.2.1.1. Dehydration reactions

When subjected to thermal exposure, free water contained in wood starts to evaporate around 100 °C. It is possible that a part of the water migrates deeper into the sample [29], [30], [31] and re-condenses, which would increase the local moisture content [27] [29]. However, it is assumed that most of the water vapor leaves from the surface [29], [30], [31]. At low heat fluxes (27.7 kW/m² in the study), dehydration reactions and pyrolysis take place one after the other while at higher heat fluxes it happens simultaneously. When they happen at the same time, moisture slows down the temperature rise inside wood [33] due to the energy supplied being used for evaporation rather than for heating. It cools the pyrolysis zone through convective mass flow of water vapor [33]. Finally, bound water is released later.

3.2.1.2. Low temperature pyrolysis

Wood slowly starts to lose mass at temperature below 200 °C [28] while releasing mostly non-combustible volatiles such as carbon dioxide, formic acid and acetic acid [25] [27] [31]. When the temperature reaches 200 °C, discoloration appears [32] and slow charring begins. Virgin wood remains at a moderate temperature due to the high heat loss from the char layer [32]. The main pyrolysis reactions begin from 225 to 275 °C [30].

3.2.1.3. High temperature pyrolysis

During pyrolysis, wood behaves as a mixture of its three constituents: cellulose, hemicellulose, and lignin. Of these three, hemicellulose is the least thermally stable one. Its decomposition temperature is comprised over a wide range from 200 to 325 °C [34], [35], [36], [37]. This temperature range depends on the heating rate, species, density, and moisture content [27]. Hemicellulose decomposition (Figure 9) starts with the fragmentation of the polymer into methanol (CH₃OH), CO₂, formic acid (HCOOH) and acetic acid (CH₃COOH). This step is followed by the conversion in monomer units (xylose), which then decomposes into volatiles products such as furfural, CO, CO₂, hydroxyacetaldehyde (HAA), hydroxyacetone (HA) and acetic acid. From 500°C, the residue becomes increasingly more aromatic with the conversion the short substituents of the aromatic rings, such as -CH₃ into CH₄ or -OH into CO and H₂.

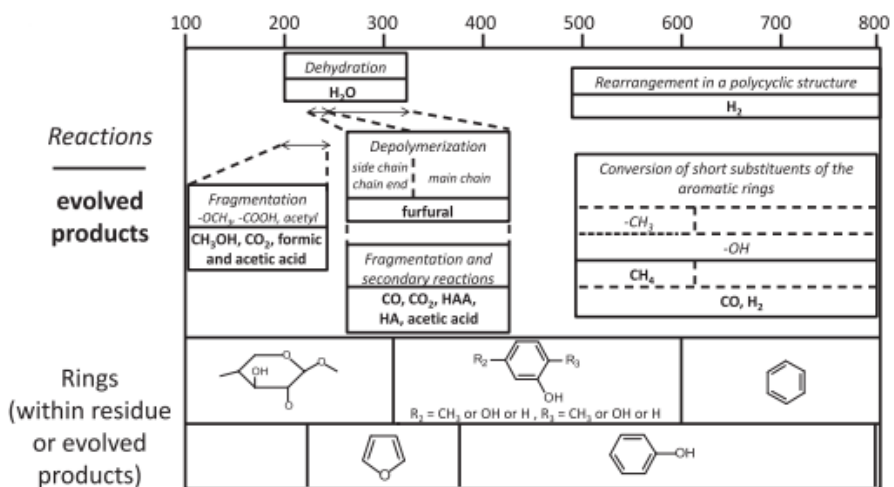


Figure 9: Hemicellulose pyrolysis: main reactions occurring and evolution of the chemical structures of the rings throughout the temperature increase from [26]

Then, cellulose starts to decompose around 240 to 400 °C. As for hemicellulose, this temperature range depends on the heating rate, species, density, and moisture content [27]. Cellulose decomposes through

two main processes. The first is by breaking a link in the carbon ring and cross-linking to produce char alongside carbon monoxide, carbon dioxide and water [38]. The second one (Figure 10) is by chain scission with depolymerization. In this step, cellulose decomposes into levoglucosan, 5-hydroxymethylfurfural (5-HMF) and furfural. The reaction of depolymerization also leads to the formation of unstable compounds, which may undergo fragmentation and produce CO, CO₂, HAA, HA and acetaldehyde (AA). As for hemicellulose, from 500°C, the residue becomes increasingly more aromatic with the conversion the short substituents of the aromatic rings, such as -CH₃ into CH₄ or -OH into CO and H₂.

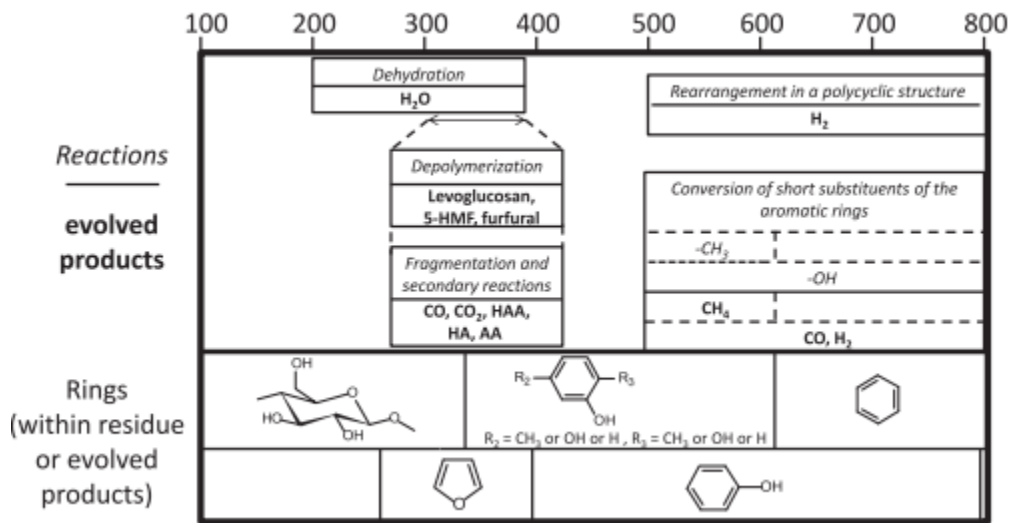


Figure 10: Cellulose pyrolysis: main reactions occurring and evolution of the chemical structures of the rings throughout the temperature increase, from [26]

Finally, lignin undergoes pyrolysis between 225 and 500 °C [34]. It produces aromatic compounds when decomposing and thus yields more char than cellulose and hemicellulose [28]. During this pyrolysis, no predominant products are observed. This reflects the complexity of lignin macromolecules where many aromatic rings are linked together by furan rings or ether bonds. The first steps in lignin decomposition (Figure 11) are the breaking of fragile ether bonds (C-O) into aromatic fragments (vanillin, syringaldehyde, phenol or cresol for example) and the rupture of C-C bonds into formaldehyde, CO₂, and CO. At higher temperature (around 300°C), the alkyl chains of lignin are converted into CO, CO₂, CH₄, acetic acid and acetaldehyde. Moreover, the aromatic compounds decompose as the temperature rises into CH₄ and methanol, which comes from the methoxy (-OCH₃) groups of the lignin and its aromatic derivatives.

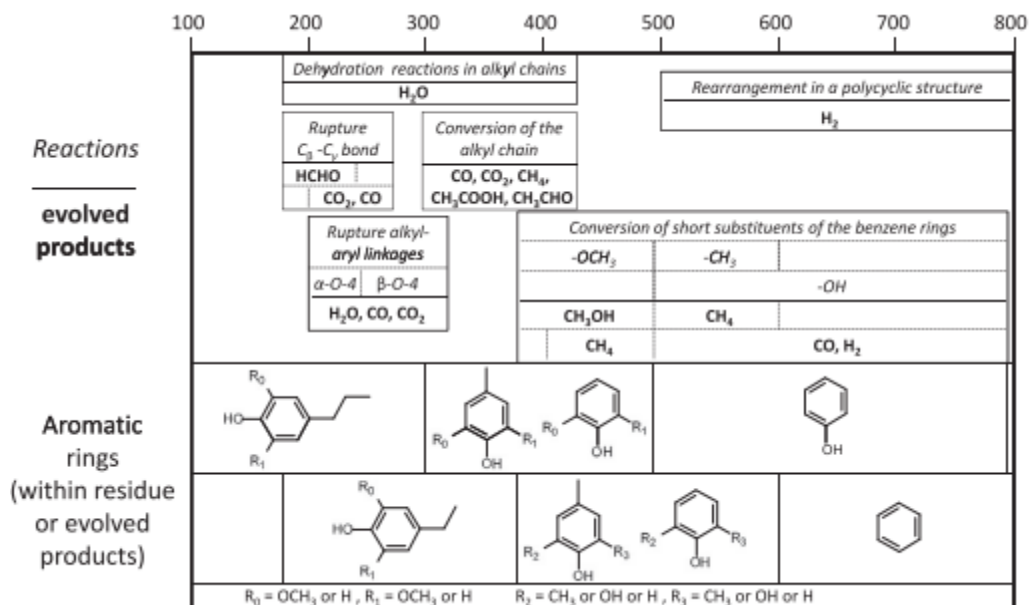


Figure 11: Lignin pyrolysis: main reactions occurring and evolution of the chemical structures of the rings throughout the temperature increase, from [26]

Between 300 and 500 °C, the pyrolysis rate increases rapidly [27] [31]. It leads to the release of flammable gases in the pyrolyzate. This fast pyrolysis results in a residual char, that is less easily volatilized than the virgin wood [39]. Overall, it is admitted that 300 °C represents the onset of rapid pyrolysis and char formation.

However, as cellulose, hemicellulose and lignin are linked together, it appears that the wood decomposition is more complex. An example of TGA for cottonwood under inert atmosphere is presented (Figure 12) [40]. The thermo-gravimetric analysis describes the mass loss rate of wood, acid lignin, milled wood lignin, xylan, and cellulose as a function of temperature increase. Each component undergoes decomposition within a specific temperature range, as previously mentioned. However, the decomposition curve of wood follows its unique path, featuring different temperature ranges. Specifically, the onset temperature falls between those of xylan, which decomposes first, and the temperatures of cellulose and lignin [40].

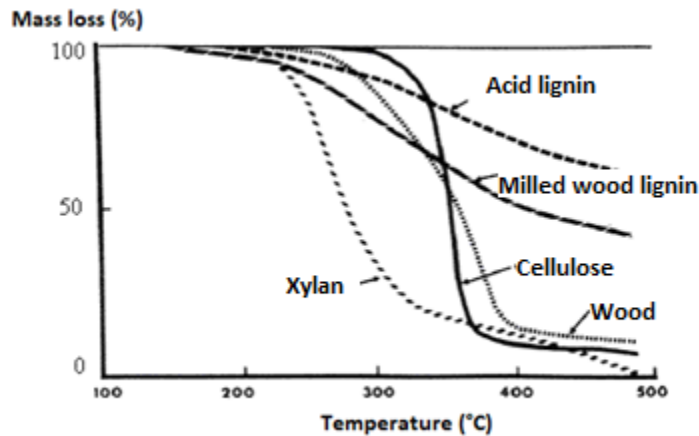


Figure 12: TGA study under nitrogen of wood and its components [40]

As a conclusion, the pyrolysis of wood can be separated several stages depending on the temperature [24] while the main gases released are CO, CO₂, CH₄ and H₂.

3.2.2. Thermo-oxidative pyrolysis

In oxygenated environments, Di Blasi et al. [7] show that air can enter and diffuse within the wood solid matrix. This is the source of heterogeneous oxidation reactions whose rate are slow as they are controlled by the rate of oxygen transported to the char. When the heat flow is important, a fast pyrolysis of the solid matrix occurs and leads to the formation of volatile products and char. The surface oxidation reactions are then non-existent, since the devolatilization rate is higher than the air diffusion rate. The thermal decomposition then takes place in an inert atmosphere and is thus like pyrolysis. Under these conditions, several authors note that the thermal decomposition, whether under air or inert atmosphere, does not present any difference [41]. For intermediate temperatures, the devolatilization rate is low enough for air to diffuse to the solid matrix. However, under intermediate temperatures, the air diffusion rate is not high enough to generate a flame [42]. Smoldering can then take place.

3.2.3. Ignition

Once pyrolysis has started, the products released by wood decomposition may ignite and undergo a rapid exothermic reaction of combustion in the presence of oxygen. Ignition can be piloted with a spark or unpiloted where volatiles must reach the necessary energy for ignition to happen. A critical heat flux, e.g. the lowest surface temperature for ignition to occur, is generally found between 10 to 13 kW/m² with piloted ignition while 25 to 33 kW/m² for unpiloted ignition [25]. Nonetheless, ignition varies with the experimental setup, sample orientation and ambient temperature while density, moisture content and

thickness influence the heat required for ignition. For example, moisture delays ignition as more heat is lost to evaporate water. Moreover, if ignition has not occurred by the time a char layer has formed, then a higher surface temperature will be needed to provide necessary heat flux to the virgin wood. Indeed, as char is a porous material, it has good insulation properties [25].

3.2.4. Flaming

After ignition, the oxidation of the pyrolysis gases in the gas phase generates flaming combustion, with cellulose being the main contributor as it produces more volatiles than char. This oxidation sustains the reaction of combustion, thus the rate of combustion is mainly determined by the rate of pyrolysis [30]. Most of the available oxygen is consumed in the flame, which leads to a combustion occurring in a locally vitiated environment. To keep the combustion flaming, a permanent exchange between the flame and the solid is required: part of the energy produced by the flame is transmitted by radiation and convection towards the surface of the fuel and thus maintains its gasification. The flame acts as a second source of heat and its size influenced the gaseous mass flux. The burning rate is considered steady after the initial strong flaming because of the good insulation properties of the char. Thus, flaming is intense in the beginning but weakens until deeper wood is decomposed [28] [31]. Indeed, the thickness of the char increases gradually and has a protective effect on virgin wood, which causes a decrease in the speed of the charring rate. Then, combustion of the char may begin to appear if the gas flow is no longer sufficient to prevent oxygen from diffusing to the virgin phase of the material. Finally, the flame extinguishes when its heat losses surpass the heat release. It results in a decrease below a critical threshold in the mass flux of flammable gases.

When flaming, wood mainly releases water, carbon dioxide and carbon monoxide. Hertzberg and al. [43] studied the reaction to fire of wood with a cone calorimeter coupled to an ELPI. ELPIs allow for the determination of particle size distribution. They observed that wood materials tend to oxidize all available substances and so minimize the number of particles in the smoke gas. The maximum in size distribution was located at 0.1-0.3 μm and the number size distribution had a maximum at the smallest detectable particle size with the instrument used, i.e. 30 nm [43].

3.2.5. Smoldering

Smoldering refers to the slow, low temperature, flameless burning of wood. According to the material involved and oxygen availability, temperatures can vary from 450 to 800°C (Table 2). At the surface of the char, air diffuses into its pores. Smoldering is characterized by the direction in which the combustion front

moves relative to the airflow and the peak fuel temperature. The peak temperature occurs where the oxygen is reacting most rapidly, generally below the external surface of the product. Thus, a thermal wave passes through wood. Typical peak temperatures are between 450 and 700 °C and the heat release rate per unit area of burning front in the range of 10 to 30 kW/m² [7]. As the oxygen level is null at the reaction zone (excess of fuel), much of the gases are not fully oxidized to carbon dioxide. The current understanding on wood smoldering is limited because of the complexity and coupling of transport and thermochemical processes inside char.

3.3. Wood properties influencing its burning behavior

The phenomena described above are strongly influenced by the material properties and the testing conditions. To properly assess the fire behavior of wood materials, it is essential to understand the elements that might affect it. In literature, this is characterized by the charring rate, which corresponds to the rate at which wood is converted into char; it is an important property in fire behaviors. The parameters relative to wood are first described while the external factors are described in a second part. Detailed information can be found in the review [25] and a particular attention on the effect of oxygen concentration is given in the section 3.4 p55.

3.3.1.1. *Material properties*

- Wood density

The charring rate is strongly dependent on the wood density [25] [31]. Indeed, decreased density, due to an increase in void volume, reduces the thermal conductivity and thus produces localized heating and heat accumulation. This results in increased flame spread rates. From radiant exposure tests and furnace tests [43] [44], it has been found that charring rates increased with decreasing density. Samples with higher densities will more slowly generate char due to the larger mass of material to be pyrolyzed, requiring more energy to fuel this endothermic process.

- Moisture content

Moisture content is acknowledge to delay pyrolysis [28], [31], [32], [33], [34], [45] due to a heat sink effect. The more water the wood contains, the greater the energy required to evaporate it and thus less energy available for pyrolysis.

- Permeability

Permeability affects charring rate [25] [31] due to grain direction. The fibers are predominantly oriented in the longitudinal direction of the trunk. Three main observation directions are defined: longitudinal (L), radial (R) and tangential (T) (Figure 13). These three directions constitute the wood's orthotropic axes. Permeability along (L) the grain is around four orders of magnitude higher than that across (R and T) the grain [28]. Increased permeability allows an increased flow of volatiles, which contributes to faster pyrolysis.

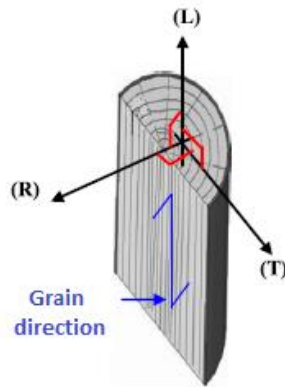


Figure 13: Grain directions [46]

- Type of species

In addition to affecting density, moisture content and permeability, species also affects the rate of pyrolysis. This is mainly due to the chemical composition [25] [31], especially lignin content, and wood anatomy (tracheid). No quantitative conclusions have been found in literature however, it can be noted that difference in species may influence charring rates. Friquin et al. [28] attribute this to lignin content, with higher lignin content giving higher char yields.

3.3.1.2. *Sample properties*

- Sample orientation

As the orientation of the surface of the sample in relation to the thermal attack influences fire dynamics and airflow, the pyrolysis is affected by it. In vertical orientations, buoyancy will drive convection upwards parallel to the sample [25]. Charring rates are thus expected to be greater for vertically oriented samples due to increased radiation from the flame. However, few authors investigate orientation thus no firm conclusions can be drawn.

- Sample size

In addition to orientation, the sample size influences the pyrolysis behavior. Increase in scale usually corresponds to lesser heat losses per unit volume of material, thus making the sample easier to ignite. Friquin et al. [28] highlight that the scale of samples affects the heat and mass transfer and thus pyrolysis. The researchers agree that the rate of pyrolysis with sample size.

- Grain direction

The grain direction (Figure 13) has an effect on pyrolysis because of the large increase in permeability parallel to the grain [28] due to the alignment of tracheid. Small changes in grain angle may result in large changes in moisture and oxygen movement, thus affecting the charring rate. Moreover, thermal conductivity is greater parallel to the grain than perpendicular to it [28]. It is thus expected that charring rate will be greater parallel to the grain than perpendicular.

- Delamination

Delamination is specific to wood materials made of glued lamella such as plywood and cross-laminated timber. It corresponds to the phenomenon through which the outer lamella detaches from the second lamella, thus exposing virgin wood to the fire. The presence of the char layer acts as protection for the unburnt wood beneath it [25] [29]. Consequently, the pyrolysis rate is initially high whilst no protective layer exists, before decreasing to a lower quasi steady value once a char layer has formed [25] [27] [28] [37]. This steady state char layer corresponds to a steady-state heat transfer into the underlying wood. Moreover, it is generally acknowledged that when the layer falls off, the pyrolysis rate increases due to the absence of a protective char layer. The thickness of the lamella is thus important to the fire behavior. If it is sufficiently thick, materials such as CLT are supposed to behave more like solid wood. Friquin et al. [28] underline that the protective quality of the char layer is attributed to several factors. Indeed, the char layer will typically be thinner than the original virgin wood if phenomena, including char oxidation, mechanical surface degradation and char contraction, occur.

- Heating scenario

The heating scenario is known to have a great influence on the pyrolysis rate [28] [30] [31] [37]. Indeed, the charring rate increases with increasing heat flux. As exposures are not consistent between works, it is hard to draw conclusions.

- Material combination

In real fire scenarios, different materials are burning and may physically or chemically interact, which may induce a modification of their fire behaviors. This applies to wood materials in the building field, which can be combined to polymeric materials (polyurethane (PU) or polystyrene (PS)) or cellulosic materials (wool or other wooden materials). This possible interaction between materials has rarely been studied in the field of reaction to fire.

At bench-scale, Mowrer and Williamson [47] introduced a superposition method to evaluate HRR for composite products. They successfully applied this technique to analyze the combustion of a stack of upholstered banquet chairs, achieving an accurate representation of the complex burning behavior. Moreover, stacked assemblies comprising fabric, cotton, and foam were examined to evaluate the fire behavior of furniture foam sofas and predict their burning rates. However, the additive method used initially proved inadequate in accurately describing the transient fire behavior of the assembly, due to thermal radiation from the burning surface [48]. This same method was applied to various materials such as poly(methyl methacrylate) (PMMA), poly(vinyl chloride) (PVC), polycarbonate (PC), and wood. In these cases, it was determined that a simple additive law through superposition was sufficient for estimating resultant HRR curves for horizontal assemblies [49] [50].

At higher scale, Vincent et al. [21] introduced a device called RAPACES, designed for studying the energetic influence of one material on another. PMMA, plywood and polypropylene (PP) were combined either by juxtaposition or by superposition. Particularly in juxtaposition, a detrimental effect of the highly flammable material, in this case, PMMA, on wood was observed. Simulating fire behaviors of material combinations using an additive law provides an accurate description of dynamic combustion. However, for superposed materials, the additive law is not suitable because one of the materials serves as a thermal shield for the other.

While there have been limited studies examining the impact of material combinations on burning rates, there is a scarcity of data regarding their effects on gas and aerosol production, which are key factors in assessing fire hazards. Furthermore, most of these studies have concentrated on superposed materials, with little attention given to materials in juxtaposition, a scenario encountered in building fires.

3.3.1.3. Summary

The effects of all the parameters described above on the wood charring rate are summarized in the Table 3. The effect of wood properties and external conditions on the charring rate are well understood. However, the effect of material combination remains to be investigated.

Table 3: Influence of properties and factors on the charring rate of wood

Parameter	Effect
Density	High density woods have a lower charring rate
Moisture content	High moisture content decreases the charring rate
Chemical composition	Increased lignin content gives higher char yield and lower pyrolysis rate
Grain orientation and permeability	The permeability of wood varies with the grain direction and is largest longitudinal to the grain. The charring rate is greater in the longitudinal direction
Scale effect	Thicker samples pyrolyze slower and large surfaces pyrolyze faster
Thermal exposure	The charring rate increases with increasing temperature while char yield decreases
Material combination	Too little data

As previously described in the fire hazards in section 1 p26, oxygen has a key role on the reaction to fire of wood and may dramatically affect it.

3.4. Effect of oxygen

In a fire, oxygen concentration in the environment changes, thus causing complex influence both on the pyrolysis, charring rates, and combustion reactions. Research on the effect of oxygen on the fire behavior are presented at different scales of testing.

3.4.1. Matter scale tests

Ohlemiller et al. [39] performed thermogravimetric analysis of wood in both nitrogen and oxygen. He observed that in nitrogen, water is released first and is followed by tars around 300 to 400 °C. Carbon monoxide, carbon dioxide and hydrocarbons follow more slowly at the same temperature. As tars pass through the char layer, they may undergo cracking to smaller hydrocarbons, or polymerization to char.

Since the hydrocarbon yield does not increase as rapidly as tar production falls, this suggests that some tars do repolymerize to char, possibly forming water in the process. In oxygen environments, it was found that char oxidize between 400 to 500 °C. The yield of carbon monoxide and carbon dioxide increases dramatically in oxygen, due to greater availability of oxygen to form these compounds through char oxidation.

Yang et al. [16] also carried out TGA-FTIR tests on *Pinus sylvestris* wood under nitrogen, but also with oxygen levels varying from 23 to 15 vol-% O₂. They observed that decomposition in oxygen is a two stages process whereas it is a one stage process in nitrogen (Figure 14). The first stage is ascribed to the release of volatiles while the second one is due to char oxidation with release of CO₂ and CO. They noted that the decomposition temperature at 5% weight loss is approximately the same under nitrogen or oxygen, i.e., 265°C. As the oxygen increases, the temperature at the maximum mass loss rates moves to lower values because of the thermal oxidation reaction. Higher oxygen content promotes earlier the generation of volatiles such as CO₂, H₂O, CH₄, CO and light tar fractions (acids, aldehydes, alcohols, ethers, alkane, and aromatic compounds). These volatiles are similar whatever the atmosphere at the maximum of mass loss rate. Moreover, they performed TGA coupled to mass spectroscopy. They observed that the atmosphere has no effect on the type of products, and all products reach their maximum at the maximum thermal decomposition temperature. The gases detected are H₂, CH₄, H₂O, CO, NO, CO₂, NO₂, formaldehyde, acetaldehyde, acetic acid, hydroxyacetone, benzene, 2-methylfuran, toluene, phenol, furfural, and xylose.

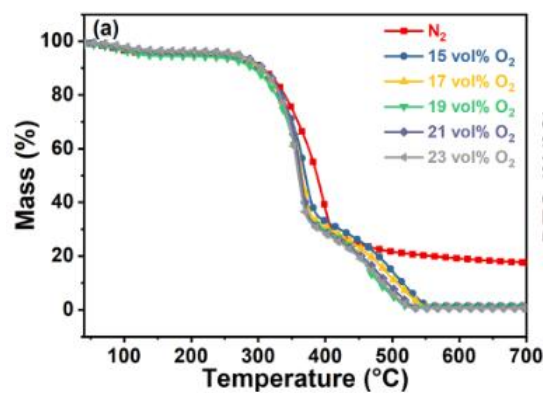


Figure 14: TGA curve of *Pinus sylvestris* under different oxygen concentration [16]

In steady-state tubular furnaces, Blomqvist et al. [51] studied the effect of under ventilation on wood board. They observed with a four stages cascade impactor that wood showed preferable predisposition towards the production of small-sized particles during flaming combustion. The difference in size was not significant between well-ventilated and under ventilated combustion. Under oxidative pyrolysis

conditions, a notably distinct particle size distribution was observed. The peak in particle mass was shifted to larger particle sizes and the production of smaller particles was restricted.

3.4.2. Bench-scale test

This section focuses now on samples of a few centimeters to meters in size. Especially at bench-scale, under radiative heating tests, Mikkola et al. [31] observed with the cone calorimeter that mass loss rates decrease approximately by 20 % when the oxygen concentration decreases from 21 to 10.5 vol-% O₂. With zero oxygen, mass loss rate is only 50 % of its value with a normal oxygen concentration. For Douglas fir, the results show a 35% decrease in the mass loss rate between 21 and 0 vol-% O₂. Ohlemiller et al. [39] tested white pine and red oak samples at oxygen levels of 0, 10.5 and 21 vol-% O₂ parallel to the grain. They noted that at 40 kW/m², mass flux was about twice that in nitrogen and at 25 kW/m², it was approximately four times. Moreover, oxygen concentration starts having effects on pyrolysis at surface temperatures around 350°C. Indeed, char forms more rapidly in oxygen-rich environments, which increases the local temperature rise and pyrolysis reactions. The pyrolysis zone thickness was 10 mm in nitrogen but 15 mm in air. The exothermic char oxidation process adds to the external heat flux, which increases the pyrolysis rates. Similarly, in furnace tests, Babrauskas et al. [52] found that at around 8% to 10 vol-% O₂, charring rates decreased by around 20% from ambient conditions, and by 33% at 4 vol-% O₂.

In cone calorimeter tests, Delichatsios [53] exposed regular and fire retarded plywood to 25, 35 and 50 kW/m² heat fluxes at oxygen concentrations of 21, 18 and 15 vol-% O₂. The fire retarded plywood had ignition times increasing very slightly with decreasing oxygen concentration and decreasing with increasing heat flux. The regular plywood samples showed little dependence on oxygen level.

In fire propagation apparatus tests, Cuevas et al. [54] studied the burning behavior of five ply Radiata Pine cross laminated timbers under varied oxygen concentrations at 50 kW/m². They observed that the ignition time is greatly affected by the oxygen level, with an increase by 30% and 58% when oxygen is reduced to 19 vol-% O₂ and 17 vol-% O₂ respectively. The oxygen availability directly affects the oxygen/fuel ratio above the solid surface, which enables sustained flaming combustion. Then, they observed that the behavior before reaching a steady state of burning, after the formation of the char layer, is similar for all oxygen levels. The time to reach this steady state has a weak dependence on oxygen level. Finally, they noted that the magnitude of mass loss rate in the steady state is dependent of the oxygen level. As oxygen decreases, the char oxidation reaction is directly affected with a slower propagation and thus an increase in char layer thickness. As the char layer thickness increases, so does the amount of heat retained by it.

The energy provided by both flame and char oxidation reactions also increases. This leads to a decrease in the heat reaching pyrolysis front, which directly affects the thermal decomposition rate of the sample. Similarly, Richter and al. [55] studied the influence of oxygen on fire behavior of particleboard at heat fluxes between 10 to 70 kW/m². They observed that heat flux has a considerable influence on the charring rate and the time to ignition. Moreover, they highlighted that oxygen controls the mode of burning with pyrolysis dominating below 4 vol-% O₂, smoldering between 4 vol-% O₂ and 15 vol-% O₂ and flaming above 15 vol-% O₂. By studying simultaneously, the effect of oxygen and heat flux, they noted a threshold (Figure 15) for ignition in smoldering and flaming. The limited minimum oxygen concentration required for ignition reduces with heat flux for both smoldering and flaming. They revealed a triple point for the ignition of wood at a heat flux of 22 kW/m² and an oxygen concentration of 17 vol-% O₂. At this point, slight changes in conditions can lead to either smoldering, flaming or pyrolysis.

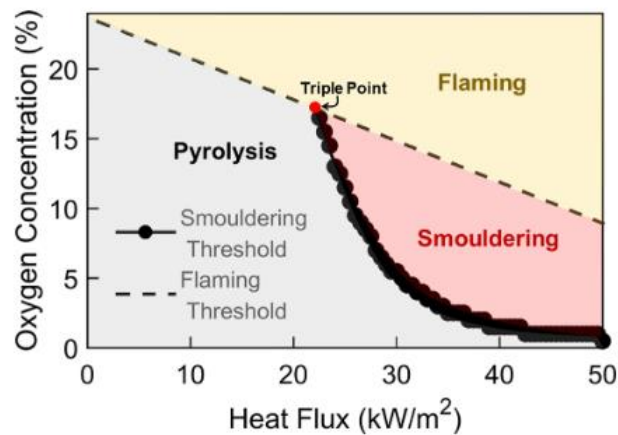


Figure 15: Influence of oxygen and heat flux on the ignition thresholds for timber [55]

At higher scale, Cedering's [45] tested timber stud walls with oxygen concentration set at 4, 7 and 10 vol-% O₂. It was observed that the charring rate increased with oxygen content – with averages of 0.65 mm/min at 4 vol-% O₂, 0.68 mm/min at 7 vol-% O₂ and 0.70 mm/min at 10 vol-% O₂.

In general, the decrease in oxygen leads to lower rates of char oxidation and pyrolysis. Oxygen has a strong influence on char oxidation but a weak one on pyrolysis front, as the char layer increases for low oxygen level. Low oxygen content also leads to a decrease in mass loss rates. Unfortunately, data on gas and aerosols production are too scarce to draw conclusions. This underlines the need to further assess the effect of oxygen of the fire behavior of wood and that with proper experimental devices.

4. Conclusions

The generalities on fire hazards in buildings have been reviewed, with a focus on fire generation and stages. As smoke inhalation is responsible for most deaths in a fire, a special attention has been drawn to fire smoke and the production of gases and aerosols. From these investigations, under-ventilated and vitiated fires revealed to be dangerous fire scenarios as the production of asphyxiant and irritant gases and submicronic aerosols is promoted.

When studying the fire behavior of a material, it is important to consider the effects of scale. Both behaviors at matter and material scale must be assessed to properly understand thermal decomposition. To do so, the relevant tests have been presented from the matter scale (TGA-FTIR, pyrolysis-GC/MS) to the material scale (Cone Calorimeter, SBI). Each test provides necessary and complementary data to understand the fire behavior of a material. The multiscale approach is one of the current approaches allowing to do the link between laboratory scales and real fire.

The previous findings have been applied to wood as it increasingly used in sustainable building. Because of its structure made of three polymers (cellulose, lignin, and hemicellulose), wood combustion revealed to be a complex process even more as wood is a charring material. Wood fire behavior consists of a few stages: heating, pyrolysis, oxidative pyrolysis, ignition, combustion and in certain cases smoldering. The wood properties and external factors that influences its combustion have been underlined however scarce data are available on the effect of material combination which may impact fire behaviors. Moreover, as vitiated fire scenarios were highlighted as dangerous conditions, the effect of oxygen on wood thermal decomposition was presented. It mainly affects the char oxidation and the burning process. Too little data are available on the gas and aerosol production. This underlines the need to further assess the wood fire behavior with a proper experimental device able to create vitiated conditions and to measure the gas and aerosol production. For this purpose, a new bench scale device was developed in the scope of these research and will be presented in the next chapter.

Chapter 2: Material and Methods

1. MATERIALS	61
1.1. CROSS-LAMINATED TIMBER (CLT)	61
1.2. WOOD FIBER (WF)	61
2. SMOKE ANALYSIS	62
2.1. GAS ANALYSIS	62
2.2. AEROSOL ANALYSIS	63
3. MATTER SCALE STUDY	66
3.1. PYROLYSIS-GAS CHROMATOGRAPHY MASS SPECTROSCOPY	66
3.2. THERMOGRAVIMETRIC ANALYSIS-FOURIER TRANSFORMED INFRARED SPECTROSCOPY	66
4. MATERIAL-SCALE	67
4.1. STATE-OF-THE-ART	67
4.1.1. <i>Overview of the main techniques</i>	67
4.1.1.1. Open test: the Cone Calorimeter	67
4.1.1.2. Closed chamber test: the Smoke Density Chamber (SDC)	69
4.1.1.3. Steady-state tube furnace test	69
4.1.1.4. Non-steady flow-through test: the Fire Propagation Apparatus (FPA)	70
4.1.2. <i>Controlled-Atmosphere Cone Calorimeter (CACC)</i>	71
4.1.2.1. Closed designs	71
4.1.2.2. Basic open-designs	73
4.1.2.3. Open designs with raw sampling method	75
4.1.2.4. ISO 5660-5: Heat release rate and smoke production rate under reduced oxygen atmospheres	79
4.2. DESIGN OF THE CACC/FTIR/ELPI BENCH	80
4.2.1. <i>Design of the apparatus</i>	80
4.2.2. <i>Equipment for smoke analysis</i>	83
4.2.2.1. Gases analysis using FTIR	83
4.2.2.2. Aerosol analysis using ELPI	85
4.3. EXPERIMENTAL PROCEDURE	86
4.3.1. <i>Sample preparation</i>	86
4.3.2. <i>Testing conditions</i>	86
4.4. MEASURED AND CALCULATED DATA IN THE CACC/FTIR/ELPI BENCH	87
4.4.1. <i>Heat Release Rate calculation</i>	87
4.4.2. <i>Gas yield calculation</i>	90
4.5. TESTING ON PMMA	92
5. INTERMEDIATE SCALE	95
5.1. THEORETICAL BACKGROUND	95
5.2. DESIGN OF THE ENCLOSURE	97
5.2.1. <i>Design</i>	97
5.2.2. <i>Equipment for smoke analysis</i>	98
5.3. SAMPLE PREPARATION	98
5.4. MEASURED AND CALCULATED DATA IN THE ENCLOSURE	98
5.5. HEAT FLUX ANALYSIS	100
6. CONCLUSION	102

This chapter is dedicated to the experimental methods to assess the fire behavior and the gas and aerosol production of wood materials at different scales. Two benches are designed at both bench-scale and intermediate scale with the implementation of smoke measurement.

The first section of this chapter details the material studied, namely Cross-Laminated Timber (CLT) and wood fiber (WF). In the second section, the description of the Thermogravimetric Analysis-Fourier Transformed Infrared spectroscopy (TGA-FTIR) and Pyrolysis-gas chromatography mass spectroscopy (Py-GC/MS) apparatuses used is made. In the third section, a state-of-the art is first made to describe the apparatuses used at material-scale to assess fire behaviors. Then, the full description of the designed Controlled Atmosphere Cone Calorimeter coupled to Fourier Infrared Spectroscopy and Electrical Low-Pressure Impactor (CACC/FTIR/ELPI) equipment is made, as well as the experimental procedure and the parameters associated. Finally, this bench is tested on a reference material (Poly(methyl methacrylate (PMMA))). In the last section, before presenting the enclosure designed, a brief theoretical background is done on the devices used to study fire reaction at intermediate scale. At last, an analysis of the heat flux perceived in the enclosure is made.

1. Materials

1.1. Cross-Laminated Timber (CLT)

The material used in this study is a commercial Cross-Laminated Timber (CLT) made from spruce. The panels used consist of three 20 mm thick lamellas glued perpendicular to each other. The glue used is polyurethane based and does not release formaldehyde according to EN 15425 [56]. The specimens are conditioned at 23 ± 2 °C and at a relative humidity of 50 ± 5 % until the mass is constant, in order to reach a moisture of wood close to 11% as described in the standard EN 13238 [57]. This CLT has a specific gravity of 500 kg/m^3 , a thermal conductivity of 0.12 W/m.K and a heat capacity of 1600 J/kg.K (Table 4).

Table 4: CLT properties given by the manufacturer

Specific gravity	500 kg/m ³
Thermal conductivity	0.12 W/m.K
Heat capacity	1600 J/kg.K

1.2. Wood fiber (WF)

The material used in this study is a commercial wood fiber board made from softwood and manufactured by dry process. The panels are 40 mm thick. The specimens are conditioned at 23 ± 2 °C and at a relative

humidity of 50±5 % until the mass is constant, in order to reach a moisture of wood close to 11% as described in the standard EN 13238 [57]. The Table 5 specifies the properties of the studied wood fiber. This WF is made of softwood at 95% and of additives at 5%. These additives include poly Methylene Diphenyl Diisocyanate (pMDI) adhesive (4-5%) and paraffin emulsion (<1%). This WF has a specific gravity of 110 kg/m³, a thermal conductivity of 0.038 W/m.K and a heat capacity of 2100 J/kg.K (Table 5).

Table 5: Wood fiber properties given by the manufacturer

Softwood fibers	95 ± 1 %
Additive	5 ± 1 %
Specific gravity	110 kg/m ³
Thermal conductivity	0.038 W/m.K
Heat capacity	2100 J/kg.K

2. Smoke analysis

Both smoke sampling and analysis are a complex process. Indeed, as explained in the Chapter 1 (section 1.2 p28), fire smoke contains a large number of chemical species and aerosols, which complicates the analysis while the sampling can be disturbed by the fire dynamic itself. Nonetheless, with appropriate sampling and measurement techniques [11], the assessment of phenomena taking place in the gas phase during thermal decomposition can be done.

2.1. Gas analysis

A widely used technique to investigate gases emissions from fire smoke is Fourier Transform Infrared spectroscopy (FTIR). It is a structural characterization technique relying on the interaction of electromagnetic waves between 0.8 and 100 μm (1400 – 10 cm⁻¹) and matter. Some molecules absorb infrared radiations, which frequency and degree of absorbance is dependent on the structure of the molecule. These absorptions are dependent on the resonant frequencies of the vibrational and/or rotational mode of their chemical bonds. Molecules pass from their ground state to an excited state. The electric field of the incident electromagnetic radiation interacts with the dipole moment of the chemical bond. To be active in infrared spectroscopy, chemical bonds must present a barycenter of negative charges different to the one of positive charges. Homonuclear diatomic molecules such as dioxygen or nitrogen share a non-polarized bond and thus cannot be active in infrared spectroscopy. As each molecule has a

specific structure, each molecule has a unique absorption of infrared spectrum. The limitations of this technique are the phenomena of overlapping and interference. Indeed, some molecules possess the same functional groups but are different. They will have a different spectrum, but they will share some absorption zones, which leads to overlapping of their absorbance areas. Moreover, it is possible that species have infrared activity in the exact same range as another species, which causes interference.

Another widespread technique is Gas Chromatography coupled to Mass Spectrometry (GC/MS). Gas chromatography separates the vaporized compounds while mass spectrometry elucidates the structure of these molecules by measuring their mass to charge ratio. This combination enables investigation of complex mixtures in trace amounts; however, it cannot follow the gas species released during the thermal decomposition process in real time. Indeed, the detection of volatiles by mass spectroscopy detector only occurs as the separated substances start leaving the gas chromatography column.

Finally, paramagnetic oxygen sensors are used to measure the dioxygen, carbon dioxide and carbon monoxide concentration. It uses the paramagnetic property of oxygen due to the unpaired electrons in its electronic structure that makes the magnetic dipole of dioxygen molecules shifts towards the external magnetic field direction \vec{H} . This results in the sample having a magnetization \vec{M} dependent on both the magnetic susceptibility χ_m and the external magnetic field. χ_m is a function of temperature, that is why the sample is cooled down to ambient temperature before being analyzed.

All these techniques are relevant and easy to implement on bench scale tests, thus they will be used for the experiments carry out in this work.

2.2. Aerosol analysis

The objectives in aerosol analysis are often to characterize the size distribution, number or mass concentration and the structure and/or morphology. Two approaches are considered when assessing aerosols from thermal decomposition: in situ, which involves the direct study of particles inside the flame and ex situ, which involves the study of the particles suspended in the smoke. In the scope of our study, only the second approach is considered.

As presented in the section Chapter 1 (section 1.2.2 p30), particle size analyzers rely on the principles of electric mobility and/or aerodynamic diameter. One of the currently used devices is the Scanning Mobility Particle Sizer (SMPS), it consists of an ionization system or charger, a Differential Mobility Analyzer (DMA) or Condensation Nucleus Counter (CNC) (Figure 16). A charge is imposed to the particles through the

ionization system, after which particles are classified in the DMA according to their electrostatic mobility and then counted in the CNC [58]. For instance, the use of SMPS has been reported in the investigation of particles emitted during the thermal decomposition of wood pellets used for domestic heating [59]. However, one of its drawbacks is its limiting determination of particle size distributions to within the sole range of submicron.

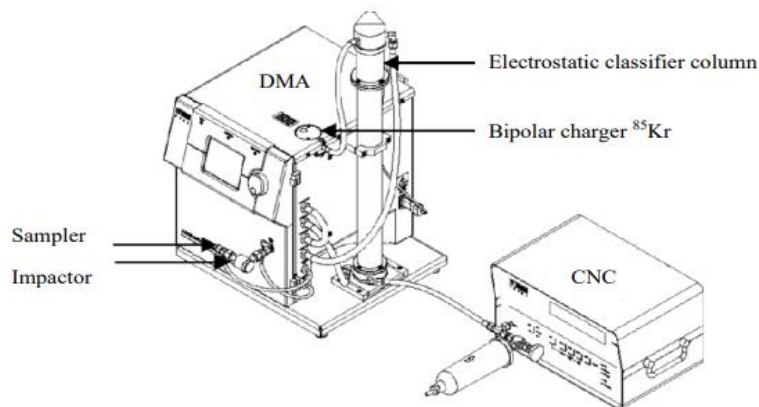


Figure 16: Diagram of Scanning Mobility Particle Sizer [58]

In addition to SMPS, cascade impactors are widely used as ex situ particle analyzers. It consists of a powered flow chamber containing several plates (Figure 17), each representing a stage of the impactor. These stages are assembled in order of decreasing size allowing separation of particles according to their size fractions: from large (20 μm) to small (0.5 μm). Particles are drawn from stage to stage with progressive smaller jets at each stage. The lighter the particle, the further it travels into the impactor. Once the entire sample has passed through the impactor, the particle quantities on each plate are collected to determine the dispersion rate of aerosols emitted from the material.

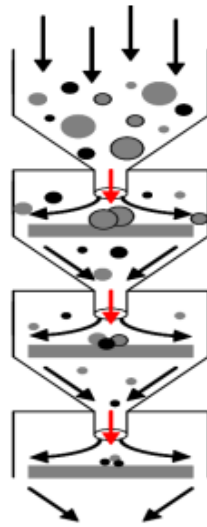


Figure 17: Cascade impactor [60]

One of the drawbacks of this device is that it does not provide the concentration in number of particles. Consequently, a relatively new instrument developed by Keskinen et al. [61] is increasingly used [61]. Indeed, Electrical Low-Pressure Impactor (ELPI) combines a variety of functionalities including particle charging, size classification according to the aerodynamic diameter and electrical detection. It is used at low pressure, meaning that the drag force is dependent on the Cunningham correction factor, which is itself dependent on the pressure. Thus, lowering the pressure allows lowering the diameter inferior limit [8]. In real time, the size distribution, and the concentration of particles from 6 nm to 10 μm can be measured. It is made of a cascade impactor, a unipolar diode charger and a multichannel electrometer. The instrument samples air inside the ELPI column with a vacuum pump. A flush pump is used to zero the electrometers by passing dried and filtered air through the instrument. The sample is first charged; the charged particles are then introduced into the cascade impactor. According to their terminal velocity and thus aerodynamic diameter, they are classified into 14 size fractions on the impactor. The multichannel electrometer measures simultaneously the charges carried by the collected particles from each stage. The measured current signals are then converted to the number concentration based on the response function of the charger. ELPI can also be used for sampling particles with the use of filters, to carry out chemical or morphological analysis with scanning electron microscopy for instance.

Compared to SMPS, ELPIs assemble in one device multiple capacities with the real time analysis and the concentration in number and mass of a wide range of aerosol sizes. This leads us to choose the ELPI as the suitable device to study aerosol emissions from fires.

3. Matter scale study

To study the wood thermal behavior, the techniques used in our study are TGA-FTIR and Py-GC/MS because they give relevant information of the decomposition stages along with simultaneous gas composition. It is a first insight on how wood could behave and what the fire smoke could contain at higher scale.

3.1. Pyrolysis-Gas Chromatography Mass Spectroscopy

The Py-GC/MS analysis is performed on a Shimadzu GC-MS QP2010 SE and a Frontier Lab PZ-20-20iD micro furnace pyrolyzer. The experiment is performed under inert conditions using helium. Sample mass is about 300 μ g. The sample is set in a stainless-steel cup and heated from 40 °C to 800°C with a 10°C/min heating ramp. Evolved gases are introduced into the GC/MS system and are separated using a fused silica capillary column of dimension 30x0.25 mm with a 10°C/min heating ramp starting once the pyrolyzer program is over. Each experiment is repeated 2 times.

3.2. Thermogravimetric Analysis-Fourier Transformed Infrared spectroscopy

TGA-FTIR experiments were performed on TA Instrument Discovery TGA coupled with a ThermoScientific Nicolet™ Istm10 spectrometer. Experiments were carried out using 250 μ L open alumina pans, which contained a sample of 10 ± 2 mg. The TGA balance flow was set to 15 mL/min. Tests were carried out under nitrogen and varied oxygen concentration of 21, 18, 15 and 10 vol-% O₂. Under nitrogen tests, the purge flow of nitrogen was set at 15 mL/min and samples underwent a 40°C isotherm for 120 minutes followed by a 10°C/min linear heating ramp from 40 °C to 800 °C. Under oxygen tests, samples underwent a 40 °C isotherm for 10 minutes followed by a 10 °C/min linear heating ramp from 40 °C to 800 °C.

During TGA experiments, gases are transferred to the FTIR cell continuously through a heated line set at 225 °C to avoid condensation. The spectra are recorded using the OMNIC software in a range of 450-4000 cm^{-1} . The number of scans is fixed at 8 and the resolution at 4 cm^{-1} . Each experiment is repeated 2 times.

The samples consisted in no glued strands taken from CLT and loose fiber taken from the wood fiber board (Figure 18).



Figure 18: Strands of spruce taken from CLT (left), and loose fibers taken from wood fiber board (right)

4. Material-scale

Material-scale testing involves larger samples in the range of grams to kilograms submitted to a constant and calibrated heat source, which leads the sample to behave representatively of a real fire. Mass and heat transfers as well as oxygen diffusion are not neglected at this scale. The condensed phase and the gas phase are not separated so the self-maintained phenomenon of combustion is represented. One of the objectives of this work is to study the vitiation effect on the fire behavior. Thus, a literature review has been completed to choose the more suitable device to study wood fire behavior in oxygen depleted environments.

4.1. State-of-the-art

4.1.1. Overview of the main techniques

To this day, there are many bench-scale devices available to carry out combustion experiments in different fire scenarios (including vitiated ones), but there is no international agreement on which one to use specifically to fire hazards in the building field. Each technique presents its advantages and drawbacks, the main challenges being to correlate with real scale as well as to simulate and control different fire scenarios defined by ISO 19706 [11]. Bench-scale tests can be classified between four general methods [4]:

- Open tests replicating well-ventilated fire conditions
- Closed chamber tests replicating under-ventilated fire conditions without any control of the oxygen concentration because it encloses the sample in a fixed volume of air
- Steady-state tube furnace tests replicating under-ventilated conditions
- Non-steady flow-through tests replicating under-ventilated fire conditions by controlling the oxygen concentration in the flow-through gas mixture and its volume flow rate

4.1.1.1. *Open test: the Cone Calorimeter*

To study the fire behavior of a material at bench-scale, the Cone Calorimeter is a reference and a widely used device in the literature. It is a relatively easy tool use, fast and not expensive technique to determine

flammability parameters and smoke composition. It is an open device (Figure 19) developed by V. Babrauskas and it is standardized in ISO 5660-1 [63]. It enables the determination of fire properties such as the Heat Release Rate (HRR), the Mass Loss Rate (MLR) and the Effective Heat of Combustion (EHC). The HRR is determined by measurement of the oxygen consumption derived from the oxygen concentration and the flow rate in the combustion product stream. Indeed, it is generally assumed that the net heat of combustion is proportional to the amount of oxygen required for combustion. According to Huggett [64], $13,1 \times 10^3$ kJ of heat is released per kilogram of oxygen consumed. Moreover, the device has been further improved to measure smoke production and gas production too. The dynamic smoke production rate is calculated from measurement of the attenuation of a laser light beam by the combustion product stream [64] [65].

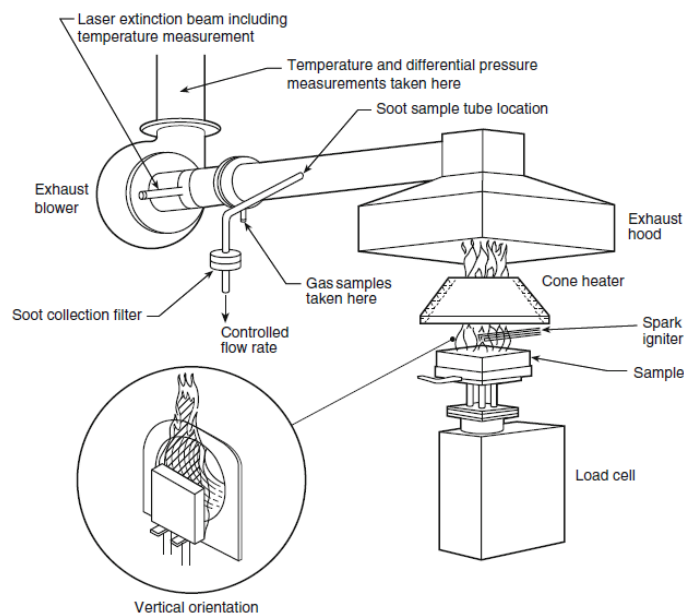


Figure 19: The Cone Calorimeter [65]

Following the standard, a 100 mm square and up to 50 mm thick horizontal specimen is exposed to a 5 kW radiant heat flux from a conical radiator pre-set to between 10 to 100 kW/m² mounted beneath a hood and duct. A spark ignition is used, and the specimen is mounted on a load cell to obtain the MLR during the test. Combustion products and dilution air are extracted through the hood and exhaust duct by a high-temperature fan. The initial flow rate can be adjusted between 10 and 32 L/s. The gas flow rate in the exhaust duct is calculated from the pressure drop across and temperature at a pre-calibrated orifice plate in the duct and the concentration in oxygen is measured with a paramagnetic analyzer [66].

One of the main disadvantages of the cone calorimeter for the study of effluents is that its fire model is generally well ventilated and corresponds to ISO stage 1b for non-flaming tests and to stage 2 for flaming tests (Table 2 p34). Moreover, the high dilution of fire gases in the hood and duct may lead to difficulties in detecting some effluent components. Also, fire gases go through the conical heater, in direct contact with its hottest surfaces, which may modify their composition.

4.1.1.2. Closed chamber test: the Smoke Density Chamber (SDC)

The Smoke Density Chamber (Figure 20) [67] allows the determination of smoke generated by solid materials mounted in the vertical orientation within a closed chamber. It measures the specific optical density of smoke generated by materials when a flat specimen, is exposed to a radiant heat source of 25 kW/m², in a closed chamber, with or without the use of a pilot flame. The sample, of 75 mm square and up to 25 mm thick, is decomposed inside the closed cabinet of 914x914x610 mm. A drawback of this method is that the gases in the chamber are not well mixed, thus the position of the gas sampling probe affects the results.

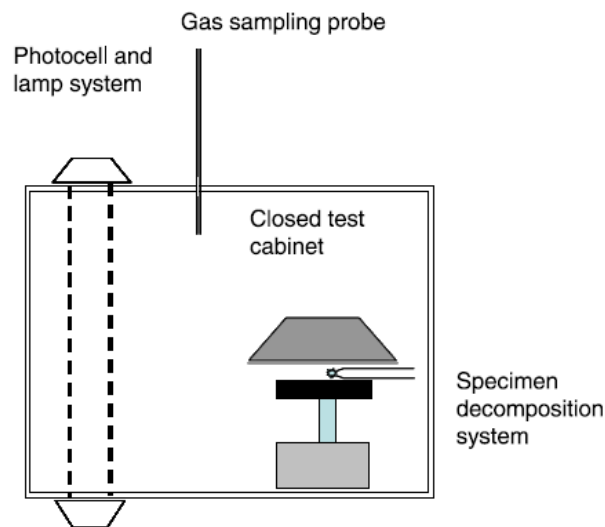


Figure 20: Smoke Density Chamber [4]

4.1.1.3. Steady-state tube furnace test

The Steady-State Turbular Furnace (SSTB) [68] (Figure 21) consist in feeding the sample into a furnace at fixed rate, under a fixed air supply, inside a narrow horizontal tube. It ensures adequate mixing of fuel and oxidant. The heat flux is continuously increased to sustain combustion even at low oxygen concentrations. However, achieving a continuous feeding is difficult at bench scale and the varying parameters of these test conditions make the comprehension of the phenomena involved in the material decomposition and

the production of effluents at different oxygen levels difficult. Moreover, the natural dynamic of the solid combustion is lost as the combustion is forced.

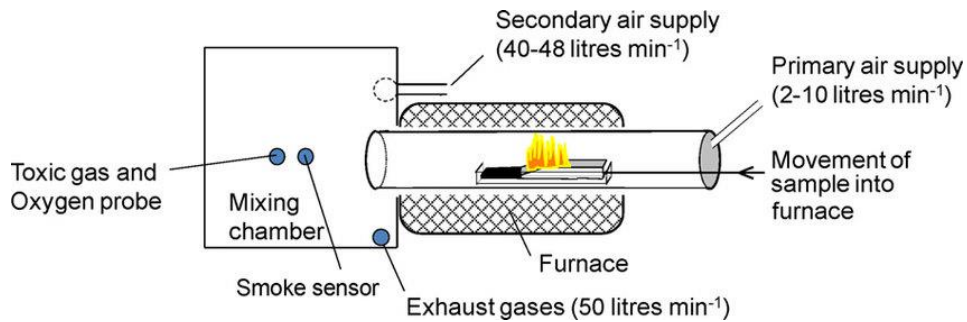


Figure 21: Steady-state tubular furnace [69]

4.1.1.4. Non-steady flow-through test: the Fire Propagation Apparatus (FPA)

A. Tewarson designed the Fire Propagation Apparatus (FPA) (Figure 22) in the mid-1970s and it is now standardized as ISO 12136 [70]. This method is like the one of the Cone Calorimeter, but the fire zone is contained within a 172 mm diameter vertical silica tube allowing better control of the fire atmosphere. Samples of 100 mm square and up to 25 mm thick are exposed to thermal radiation and a pilot flame. A mixture of oxygen and nitrogen is supplied at the bottom of the tube. A stainless steel exhaust duct is located above the tube and diluted air is entrained in the area between the tube and the exhaust system. One of the drawbacks of this device is the mixing of exhaust gases with the ambient air before analysis. They exhaust gases may continue to burn as it emerges from the chamber giving ultimately well-ventilated burning conditions.

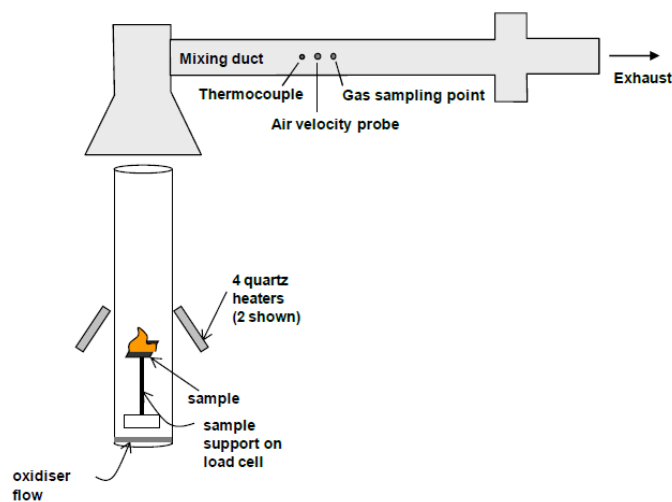


Figure 22: Fire Propagation Apparatus [4]

Another non-steady flow through test is the Controlled-Atmosphere Cone Calorimeter (CACC), which is derived from the Cone Calorimeter. A special focus is made on the CACC in the next section.

4.1.2. Controlled-Atmosphere Cone Calorimeter (CACC)

To overcome the free ventilation issue of the standard cone calorimeter, modified cone calorimeters have been developed during the last three decades. The principle of these modified designs mainly consists in the sample being in a controlled-atmosphere chamber where the oxygen level can be controlled as well as the ventilation. When the ventilation is controlled i.e., the amount of air at 21% of oxygen let in the system is under-ventilated whereas when the oxygen level is reduced the system is vitiated. As there was no international standard back then, each design differs between the laboratories. Werrel et al. [71] classified the designs into two categories: the open controlled-atmosphere cone calorimeters and the closed controlled-atmosphere cone calorimeters. The open controlled-atmosphere cone calorimeters have an open connection between the cone calorimeter exhaust hood and the controlled atmosphere chamber whereas the closed controlled-atmosphere cone calorimeters have a sealed connection between a controlled-atmosphere enclosure and the ductwork.

4.1.2.1. Closed designs

The closed designs were the first to be describe in the literature in the 90s. Babrauskas and Mulholland [71] [72], Petrella and Christy [73] [74], and Leonard [76] were the main scientists working on the subject and each reported a different CACC.

Firstly, Babrauskas and Mulholland [71] [72] developed a device (Figure 23) where the sample is inside a 50 cm cubic steel enclosure with Pyrex windows. It has four inlet gas pipes as well as baffles plates and a glass bed to have a homogeny gas distribution and dissipate vertical momentum. The load cell has been located below the bench-top because the temperature of some sample's area could be high and thus overheating the load cell. The device can provide heat fluxes to the specimen in the range of 0 to 100 kW/m² like the standard cone calorimeter. The exhaust system is the same than the standard cone.

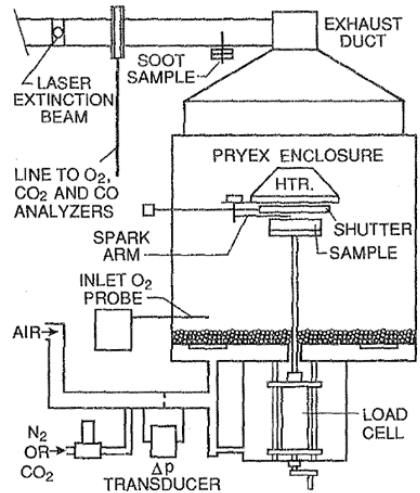


Figure 23: CACC design from Babrauskas and Mulholland [71] [72]

Petrella and Christy [73] [74] also developed a CACC with slight changes compared to the previous one (Figure 24). Indeed, it is still a 50 cm cubic steel enclosure, but the chamber is constructed from square double-walled stainless steel panels and, to minimize exposure of the sample to the radiant heat source, the sample holder and the load cell are on an electronically operated retractable mechanical arm. The sample is rotated away from the cone rather than shielded in place from the cone. The device can provide heat fluxes to the specimen in the range of 0 to 100 kW/m² like the standard cone calorimeter and the exhaust system is the same than the standard cone.

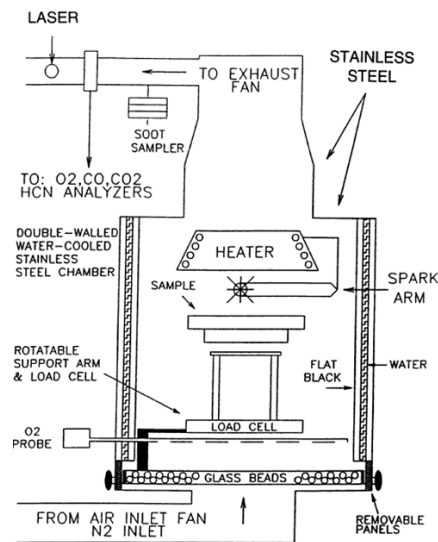


Figure 24: CACC design from Petrella and Christy [73] [74]

Finally, Leonard [76] developed another design (Figure 25). The main difference between the previous designs and this one is the delocalization of the fan to avoid leaks in the system. It has been set upstream

to create a blow-through system rather of a suck-through system. It still has four inlet pipes and a glass bed and deliver heat flux from 0 to 100 kW/m².

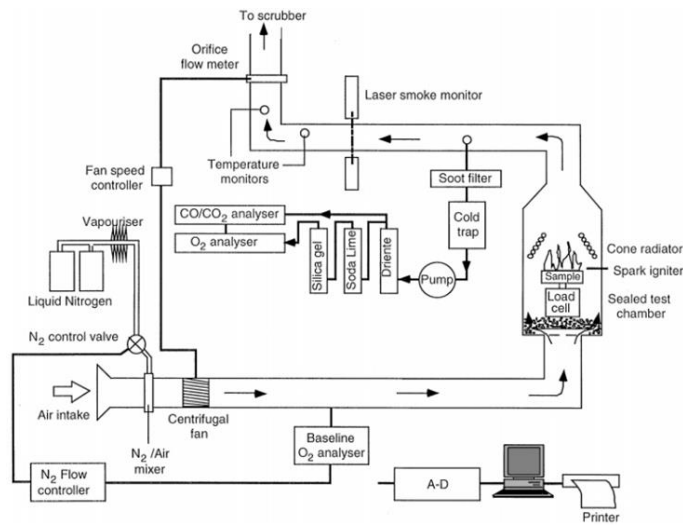


Figure 25: CACC design from Leonard] [76]

The main advantage of these designs is that no air from the lab enters the chamber, so the exhaust gases are not oxidized. However, these designs, by being closed, are exposed to risks of explosion (overpressure or auto-ignition of the sample) even if there are blow-out panels. Open-designs have been then preferentially developed to avoid these risks.

4.1.2.2. Basic open-designs

Concurrently, Mikkola [77] was the first in 1993 to introduce an open CACC which was then commercialized by Fire Testing Technology (FTT). Following his work, Hietaniemi [77] [78], Gomez and Janssens [79] [80], Werrel [71] and Marquis and Guillaume [19], [82], [83], [84] used setups similar to Mikkola's design.

The basic design of the device is the following (Figure 26) [79] [80]. The box, set under the standard exhaust duct, consists of a stainless-steel enclosure of 40x40x40 cm in dimensions with a door with observation window on the front. Inside the box there are still the standard shutter and the spark igniter. To limit radiation from the enclosure, a cooling rig is placed between furnace and topside of the box. Contrarily to the designs of the closed CACC, there are only two gas inlet ports at the bottom of the box. The sample is set on the standard load cell located in the box which must be water cooled to avoid damages. The enclosure is supplied with a mixture of air and nitrogen through the gas ports to create the combustion atmosphere having the desired oxygen concentration and the desired flow rate. The atmosphere is

adjusted by controlling of the volume flow rate of air and nitrogen, each with a rotameter and monitored by an additional oxygen analyzer that is linked to the enclosure. On top of the enclosure, the setup is in accordance with the common cone calorimeter configuration. It consists of an exhaust hood and an exhaust duct, a blower taking in the exhaust gases, an orifice plate with pressure ports for differential pressure measurement, and thermocouples that measure the exhaust gas temperature. A FTIR can be set on the line to analyze the composition of the effluent.

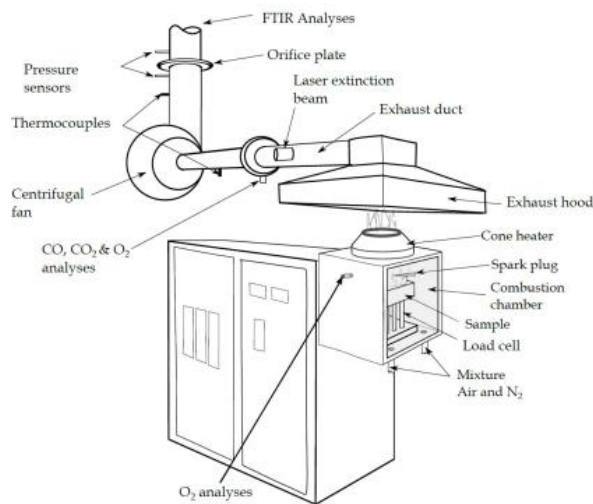


Figure 26: CACC basic design from [79] [80]

An issue has been underlined by Hietaniemi [77] [78] concerning the phenomenon of post-oxidation of gases at the output of the cone heater. Indeed, ambient air can backflow around the chimney and then effluents going out of the chamber can burn in ambient air and eventually lead to flames. For this reason, a chimney (Figure 27) was proposed by Hietaniemi on top of the cone heater to avoid the phenomenon previously explained. It was then adopted by other scientists, but they do not use the same dimension of chimney, its height can vary between 18 and 60 cm. The chimney can be made metallic or made of quartz to observe the possible oxidation of gases in the chimney. Marquis and Guillaume [83] studied the influence of the chimney on the combustion of polymethyl methacrylate (PMMA). They concluded that, due to the thermal and optical properties of the material used that can favor the heat exchange and thus the gas phase oxidation, the chimney has a significant effect on the physical and chemical processes occurring in the gas phase. Indeed, they observed small differences in Heat Release Rate (HRR) for PMMA at 50 kW/m² and 21% of oxygen with the metallic chimney yielding higher HRR than the quartz one. The

metallic chimney can have the effect of increasing the radiative heat by reflection while the quartz chimney by being transparent to IR allows the gas to cool before being mixed with air in the exhaust duct. The height of the chimney has also an influence on the behavior of the gas phase, it must be high enough to avoid or at least limit the oxidation of the gas at the outlet. They concluded that a 20 cm chimney proposed by Hietaniemi and Werrel is not enough as it yields results like those without a chimney, but a chimney of 60 cm is good enough.

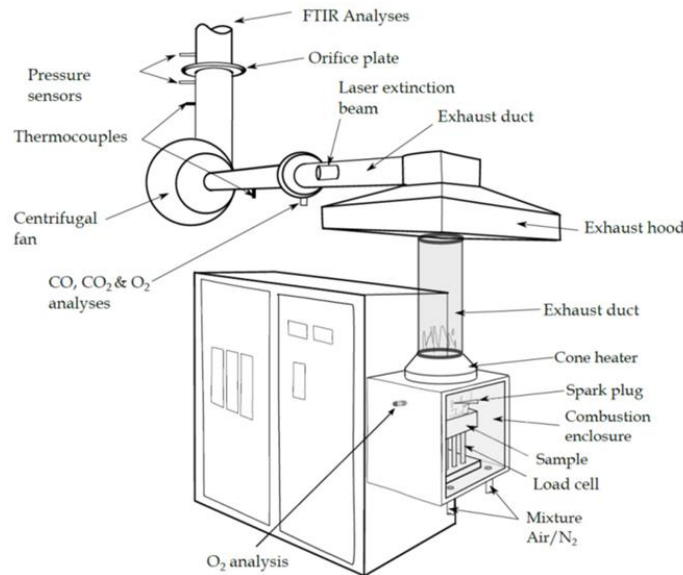


Figure 27: CACC design with a chimney from [83]

The main disadvantage of the design is, as explained above and yet limited by the chimney, the possible post-oxidation and dilution of gases at the output. Dilution of the gases can lead to errors when calculating the HRR with the oxygen consumption method. For this reason, few authors have been studying the raw sampling method.

4.1.2.3. Open designs with raw sampling method

The raw sampling method was recently developed to avoid the loss of effluents when assessing its composition. Indeed, the effluents can condensate while being transported and more importantly when diluted species are lost due to their low concentration (acrolein or formaldehyde for example). Dilution lowers the dew point of the sample so that the water vapor in the effluents does not condense when the sample is cooled by dilution [85]. The setup of the device is the same except that the sampling of the effluent is made in the chimney instead of in the exhaust duct. Different approaches have been developed on what probe must be used and where it must be to sample the effluents. Alarifi [85] used a 21 cm in height and 8 cm in diameter metallic chimney where he inserted a single point stainless steel tube. This

tube was then connected to a 190 °C heated line itself connected to a heated pump and sample filter system and then connected to a FTIR through another heated line. This is very important because it ensures that there are no losses of toxic species due to condensation. However, obtaining a mean gas sample from the chimney is problematic as Irshad [86] underlined in his work which used the same cone as Alarifi. He changed the probe for a four-hole sample probe, and then a 76 mm diameter 20 hole “X” probe at the bottom of the chimney. The last probe was better, but the major problem was the air entrained in the chimney. To solve this, he added a chimney exit backpressure grid plate with 90 % blockage; sensible gas analysis results were then achieved. Contrarily to standard cone tests, the oxygen is analyzed after FTIR measurements on the line. The airflow to the combustion chamber was measured using a variable air flow meter and varied from 6 to 28 L/min from compressed air supply. Moreover, he insulated the walls of the device to remove any heat losses. The final gas sampling system is shown on Figure 28.

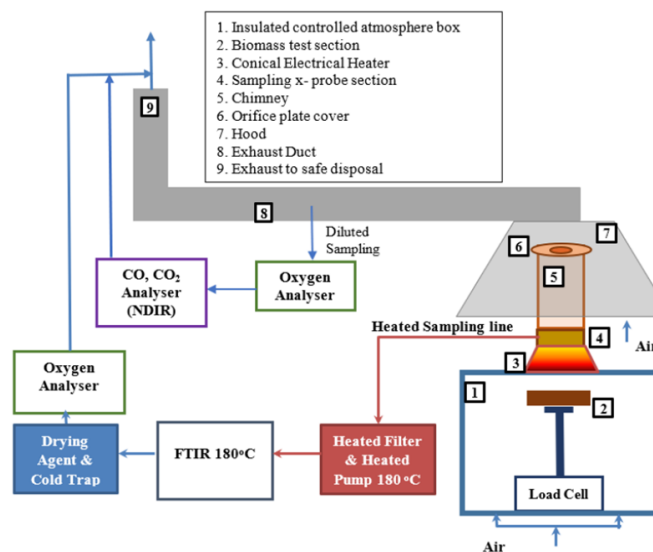


Figure 28: Gas sampling system on the cone calorimeter from [85]

Some authors also set the sampling probe at the top of the chimney. Marquis and Guillaume [87] used a ring probe (Figure 29) considering that the distance downstream was sufficient for adequate mixing. The holes of the ring probes were facing away the stream of effluent to avoid clogging of the probe due to the soot. A small number of holes is also used to provide a certain degree of smoothing regarding the duct flow turbulence. As above, the probe is linked to a FTIR via a heated line at 180 °C.

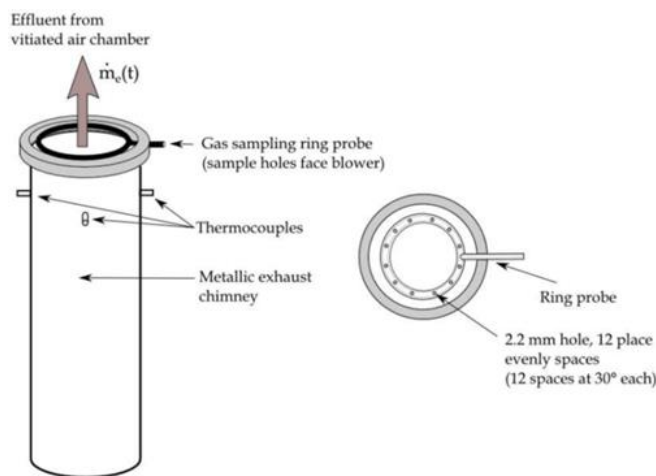
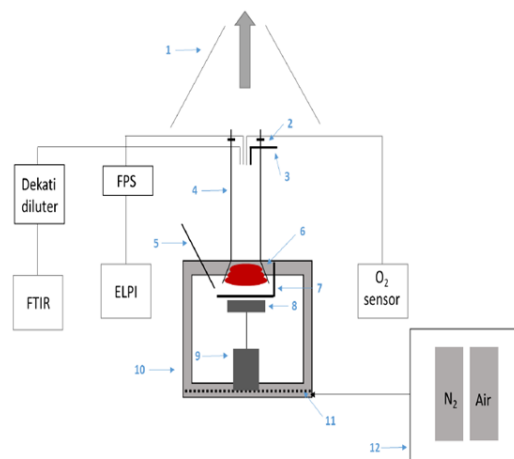


Figure 29: Sampling system used by Marquis and Guillaume [87]

Chatenet [23] also used sampling at the top of the chimney but the enclosure was slightly different. Indeed, the enclosure was a 60x60x60 cm steel with polycarbonate observation door box. The bigger dimensions than other setups previously shown ensured that the polycarbonate did not deteriorate. The metallic chimney was 60 cm high like in the basic design. It was added a zirconium oxygen controller to measure the oxygen level inside the enclosure, it has the advantage of measuring oxygen without using a reference gas and without drying the sample gas. What differs from other sampling is the addition of an Electrical Low-Pressure Impactor (ELPI) on the line (Figure 30). Moreover, being in confined configurations, the gas concentrations are above the maximum measurement range for FTIR quantification. Consequently, it was set a diluter upstream the FTIR. In the same way, a Fine Particle Sampler (FPS) was added to dilute the aerosol concentration.



Key

- | | |
|----------------------------|------------------------------------|
| 1. Air extraction | 7. Movable shutter |
| 2. Thermocouples | 8. Sample holder |
| 3. Flow velocity sensor | 9. Load cell |
| 4. Chimney | 10. Enclosure |
| 5. Zirconium oxygen sensor | 11. Sintered stainless-steel plate |
| 6. Heater | 12. Gas mixing board |

Figure 30: Sampling system of Chatenet [23]

Similarly, Mustafa [10] studied the aerosol concentration but a Particle Size Analyzer was added (Figure 31) which is a real time nanoparticle size spectrometer. The difference with Chatenet [23], beside the device used to analyze aerosols, is the point of sampling. Mustafa set it in the exhaust duct where the stream is diluted. It was concluded that the DMS analyzer was not suited for the study of combustion aerosols of wood because the range of size was more above 1000 nm, which is above the DMS range, and that an ELPI would be more suited [10]. The rest of the sampling line is the same as Irshad [86] as they are from the same research team.

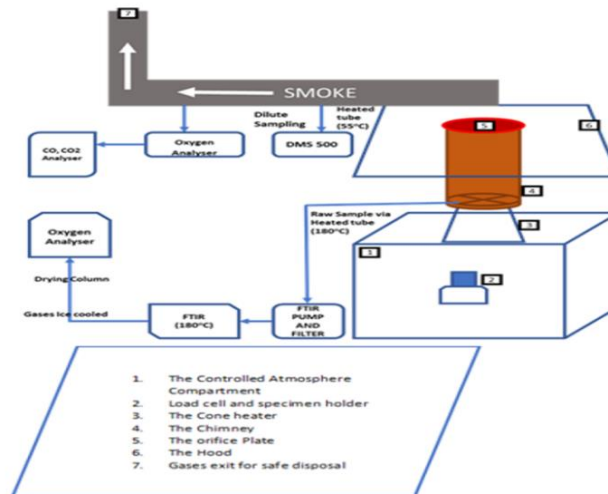


Figure 31: Sampling system from Mustafa [10]

This raw sampling method is very pertinent to precisely studying the composition of effluents as it avoids the loss of species with condensation. However, careful attention must be on obtaining a mean mixing when sampling and ensuring that surrounding air is not entrained in the chimney. The disadvantage of using a grid plate on top of the chimney might be the change of regime of the flow and the loss of soot on it.

4.1.2.4. ISO 5660-5: Heat release rate and smoke production rate under reduced oxygen atmospheres

Very recently an experimental standard was released, it is entitled “ISO 5660-5: Heat release rate (cone calorimeter method) and smoke production rate (dynamic measurement) under reduced oxygen atmospheres” [88]. It specifies how to use the cone calorimeter to do tests in controlled atmospheres. The standard specifies that the device can work under 1% to 20.95% of oxygen and deliver between 10 and 180 L/min of gas. The design (Figure 32) is very similar to the previous open designs (4.1.2.2 p73). The enclosure is a stainless-steel box of 37 x 30 x 30 cm in dimensions with a door and a window. It has a chimney above it of 60 cm long and of 11.5 cm in diameter, it can be made of metal or of quartz, the differences have been discussed in 4.1.2.2 p73. Its upper part must go inside the exhaust duct on 45 mm; the top diameter of the chimney can also be reduced to 50 mm instead of 115 mm to assure a sufficient velocity flow of the smoke in the duct. The flow and the oxygen are measured inside the box. The exhaust and analysis systems are the same as the standard cone calorimeter. The drawbacks of this device are the same as the open designs namely the possible post-oxidation and dilution of gases at the output.

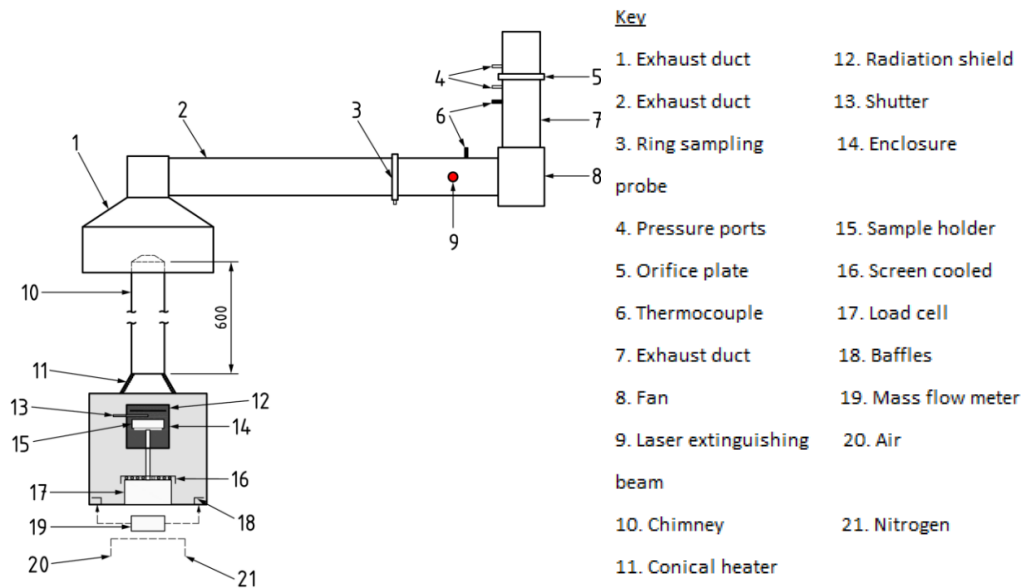


Figure 32: CACC design from ISO 5660-5 [88]

To conclude, many Controlled-Atmosphere Cone Calorimeter designs have been developed since the 90s. The one that stands out and in harmony with the standard, for reasons of safety and practicality, is the open design with a chimney of 60 cm in height. According to the purpose of the study, it is interesting to use the raw sampling method, especially when assessing the effluent composition with a FTIR. This however requires additional set-ups and attention. The review literature also highlighted the possibility of assessing the aerosol size distribution with devices such as cascade impactors. From these observations, a homemade CACC was designed to study the reaction to fire and the production of gases and aerosols in under-ventilated or vitiated atmospheres of materials, and especially wood materials.

4.2. Design of the CACC/FTIR/ELPI bench

4.2.1. Design of the apparatus

The apparatus is displayed on the Figure 33 and specific elements are detailed hereafter.

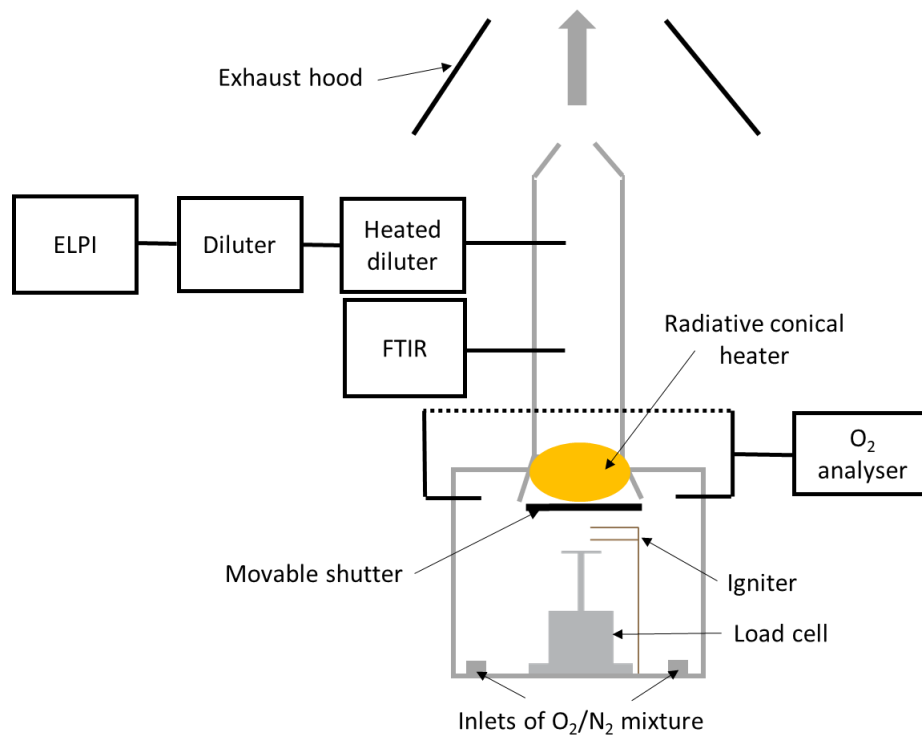


Figure 33: Diagram of the homemade CACC

Airtight enclosure:

The enclosure used is the one supplied by FTT. It is a stainless-steel enclosure of 37 x 30 x 30 cm in dimensions with a door including an observation window on the front. The inside walls are insulated with silicate calcium panels of 20 mm thick in order to avoid radiations and heat losses from the walls [86].

Cone calorimeter elements:

The conical radiative heater is fixed on the top of the enclosure and can be used from 0 to 100 kW/m². A two-pieces shutter made of stainless steel is put under the conical heater to protect the sample from the heat flux before the beginning of the test. A spark igniter, that provides a tension of 10 kV between its two electrodes, is set to be above the surface of the sample. The sample is put in FTT's samples holder, which consists of a refractory firebrick in which the aluminum wrapped sample is set. A frame retainer is positioned over the sample and covers the board of the sample to control the exposed surface. The sample lies on the FTT's load cell, which has a sample capacity of over 500g and an accuracy of 0.01g. Moreover, to avoid excessive heating and radiation of the system, a cooling ring is set between the cone heater and the top of the enclosure as well as a cooling hood on the load cell and a cooling serpentine around the load cell's rod.

On top of the enclosure, the setup is in accordance with the common cone calorimeter configuration. It consists of an exhaust hood and an exhaust duct, a blower taking in the exhaust gases, an orifice plate with pressure ports for differential pressure measurement, and thermocouples that measure the exhaust gas temperature.

Supply and distribution system of the gases:

Two gas inlet ports are located on each bottom side of the enclosure. The composition of the atmosphere is adjusted by control of the volume flow rate of air and nitrogen with a rotameter for each. The premixed mixture of air and nitrogen passes then through the inlet ports. The inlet gas flow rate can be varied between 20 L/min and 200 L/min.

Designed chimney:

A new stainless steel chimney (Figure 34a) was designed to insert a sampling probe for the FTIR and another one for the ELPI. The chimney is 60 cm long and of 11.5 cm in diameter with its top diameter reduced to 5 cm to assure a sufficient velocity flow of the smoke in the duct. The FTIR sampling probe (Figure 34b) is located near the outlet of the cone and is composed of two flute probes of four holes each to have a homogenous mixture. The holes face away the stream of effluent. The ELPI measurement consists in a single point probe that ensures isokinetic sampling.

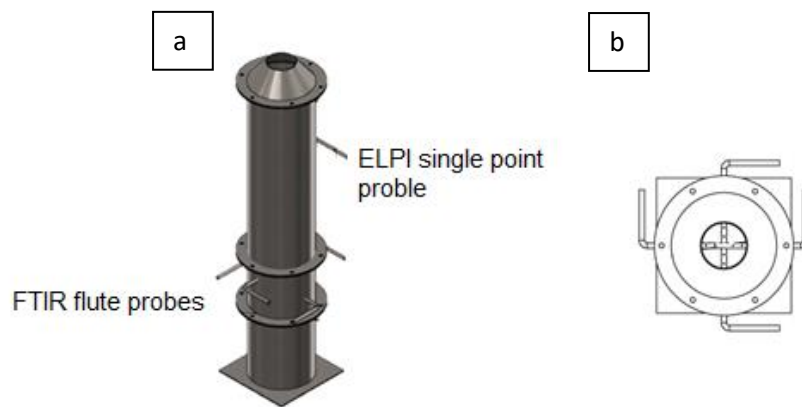


Figure 34: a. designed metallic chimney for raw sampling; b. top view of FTIR probes

4.2.2. Equipment for smoke analysis

In the chimney, smoke is continuously sampled continuously via two probes: the multi-holes probes linked to the FTIR, and the single point probe linked to the ELPI.

4.2.2.1. *Gases analysis using FTIR*

The device used is an Antaris IGS FTIR spectrometer equipped with a nitrogen Mercury Cadmium Telluride (MCT) detector cooled with liquid nitrogen, a 0.2L volume gas cell with a 2m optical path length. In the chimney, the gases are sampled at 10 L/min through a PTFE line to a FTIR cell. The FTIR gas cell as well as the PTFE gas transport line are heated at 180°C to avoid condensation. At the end, gases are cooled down, dried, filtered and then eliminated by a membrane pump. The gas cell was kept at a constant pressure of 650 Torr with a pressure gauge with regulating valve. Each scan was taken at 1.76s and 0.5 cm⁻¹ as spectral resolution. The background is made with 20 scans to get rid of the influence of the environment (ambient air or internal materials of the spectrometer) on the gas spectra. The background is made before each test. Each gas is calibrated using the Classical Least Square (CLS) algorithm in the OMNIC software. It consists in defining characteristic absorption areas and peaks of each gas. The wavenumber ranges selected to calibrate each gas are described in the first column of the Table 6. These wavenumbers have been selected by considering all the unavoidable interferences between substances (second column of the Table 6) and overlapping areas [62]. The maximum measurement range is reported in the third column of the Table 6.

Table 6: Gas parameters of the quantification method

Gas	Wavenumber range (cm ⁻¹)	Interferences	Maximum measurement range (ppm)
CO ₂ (carbon dioxide)	67.-687 758-796	H ₂ O, HCN	250 000
CO (carbon monoxide)	203-2022 2098-2100 2111-2113 2119-2121 21277-2179	H ₂ O	2000
H ₂ O (water)	857-867	-	25
CH ₂ O (formaldehyde)	2657-2784	HBr, HCl, C ₃ H ₄ O, CH ₄	100
C ₃ H ₄ O (acrolein)	2690-2880	NO ₂ , HCl, H ₂ O	150
C ₂ H ₄ O (acetaldehyde)	2700-2680	H ₂ O, HCl, HF, CH ₂ O, C ₃ H ₄ O	150
CH ₄ (methane)	3205-3150	H ₂ O, SO ₂ , HCl, CH ₂ O, CH ₃ H ₄ O	10 000
C ₂ H ₄ (ethene)	867-1070	NH ₃ , C ₃ H ₄ O, CH ₂ O, HCl, HBr, H ₂ O, NO ₂ , CO ₂	200
C ₃ H ₆ (propene)	2963-2943	H ₂ O, CH ₄ , C ₂ H ₄	200
HCl (hydrogen chloride)	2940-2965	H ₂ O, SO ₂ HBr, CH ₄	750
HBr (hydrogen bromide)	2470-2640	CO, H ₂ O, HCl, SO ₂	750
HF (hydrogen fluoride)	4108-4200	H ₂ O, CO, HBr	750
HCN (hydrogen cyanide)	3248-3249 32613263 3267-3270 3286-3288 3329-3332 3350-3354 3358-3359	H ₂ O,	250
NO (nitric oxide)	1814-1817 1849-1858	H ₂ O, CO ₂	500
NO ₂ (nitrogen dioxide)	1584-1589 1597-1600	H ₂ O, NH ₃	500
NH ₃ (ammonia)	903-954	H ₂ O, C ₃ H ₄ O, CH ₂ O, CO	1000
SO ₂ (sulfur dioxide)	1336-1333 1354-1354 1382-1386 1376-1377	H ₂ O, CH ₄ , HCN	1000

4.2.2.2. Aerosol analysis using ELPI

The apparatus used is the ELPI from Dekati with 13 stages. The charger delivers a 5 kV +/- 0.5 kV voltage and a 1µA current. The aerosols are classified (Table 7) into size of 0.007 to 10 µm according to their aerodynamic diameter. The sampling is made via the single point probe, which is heated at 160 °C thanks to a heated wire to avoid effects of humidity. A vacuum pump is set to regulate isokinetic flow at a rate of 10 L/min. The measured current values are converted to give several particles by cm³ using transfer functions provided by manufacturers.

Table 7: Range of measurement for each plate of the ELPI

Stage	Particle diameter D50% (µm)
1	0.0070
2	0.0290
3	0.0570
4	0.1010
5	0.1650
6	0.2550
7	0.3930
8	0.6370
9	0.9900
10	1.6100
11	2.4600
12	3.9700
13	10.1500

Before entering the ELPI, the sample is diluted with two Dekati DI-1000 diluters. The operating principle of the diluter is based on ejection dilution. Purified pressurized dilution air flows at high speed around an ejector nozzle and causes a pressure drop which draws the sample into the diluter through the nozzle. The raw sample is instantaneously diluted as it mixes with the dilution airflow always providing a homogeneous and stable sample. The first one is heated at 200°C to avoid loss in aerosol concentration while the second one prevents nucleation of the aerosols. The diluters are set in series to provide a ratio of dilution of 83.

4.3. Experimental procedure

4.3.1. Sample preparation

Samples are tested in the horizontal orientation. The sample holder is used with a frame to better control the exposed surface of the sample. A 64 kg/m^3 ceramic fiber insulation pad is put on the backside of the sample as specified in the ISO 5660-1 standard [63]. For the tests carried out on single specimens, the samples are $100 \times 100 \times 40 \text{ mm}$ (Figure 35a and Figure 35b) and wrapped in alumina. More precisely, the “CLT” samples consist in 2 lamellas of 20 mm each perpendicularly glued together. Each sample was carefully chosen with as few defects as possible (knots and resin bags). Moreover, for the combination tests, half samples of $100 \times 50 \times 40 \text{ mm}$, each wrapped in alumina, are juxtaposed in the sample holder (Figure 35c). To separate them and better control the boundary conditions, a ceramic fiber is set between the two half samples. Tests were also carried out by replacing one of the half samples by a $100 \times 50 \times 40$ ceramic fiber blanket.

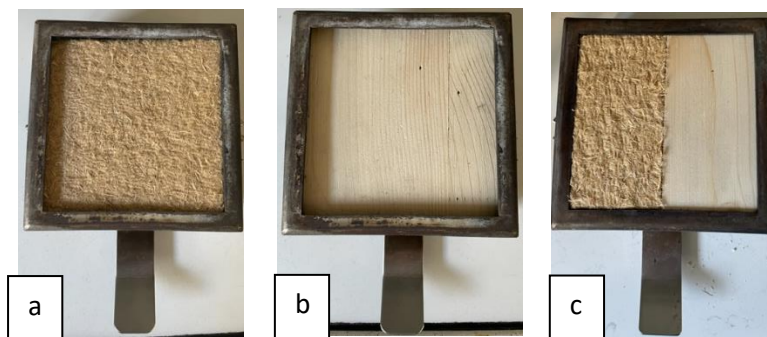


Figure 35: Sample configuration a. Wood fiber, b. CLT, c. CLT/WF

4.3.2. Testing conditions

The volumetric flow rate of extraction through the exhaust duct of the calorimeter is set at $24 \pm 2 \text{ L/s}$ at $23 \text{ }^\circ\text{C}$. The inlet volume flow rate is set at $150 \pm 5 \text{ L/min}$ at $23 \text{ }^\circ\text{C}$. Tests are carried out at 20 and 50 kW/m^2 and at 21, 18, 15 and 10% of oxygen respectively. All tests are performed at least three times and the curve presented represents a single specimen that fits the best the mean curve. The studied parameters are considered repeatable when it falls within two times the standard deviation. Moreover, the combustion is considered incomplete when the CO/CO_2 ratio is superior to 0.05 [4].

The transfer times and sampling intervals are gathered in Table 8 according to the data measured and the method used. The gas and aerosol production and the HRR measurements have a 10s transfer time while the mass measurement is instantaneous. The sampling interval is made each second for the mass, HRR

and aerosol measurements whereas it is of 1.76s for the gas production. The time to ignition and the time to extinction are visual measurements and therefore instantaneous. Overall, all transfer times are below 10s to ensure a fast sampling.

Table 8: Transfer times according to the data measured

Data	Measurement method	Transfer time (s)	Sampling interval (s)
Time to ignition and time to extinction	Observation	≈0	-
Mass	Load cell	≈0	1
HRR	Paramagnetic oxygen sensor	≈10	1
Gases	FTIR	≈10	1.76
Aerosols	ELPI	≈10	1

4.4. Measured and calculated data in the CACC/FTIR/ELPI bench

The fire parameters that can be measured in the CACC are the same as the ones measured in the standard cone calorimeter: Heat Release Rate (HRR), Mass Loss Rate (MLR) and smoke density. From FTIR analysis, the gas production and yield are obtained while from ELPI analysis the aerosol size distribution is collected.

4.4.1. Heat Release Rate calculation

The HRR is determined with the oxygen consumption method. Oxygen calorimetry is based on Thornton's work [89], which states that the net heat released from a fire is nearly proportional to the oxygen consumed for the complete combustion of most organic liquids and gases. Huggett [64] then showed that this proportionality is also applicable to organic solids. He found the average value of the net heat release to be 13.1 kJ per gram of oxygen consumed with an accuracy of +/- 5% for most fuels and complete combustion. He expressed (Equation 5) the HRR measurement as:

Equation 5:

$$\dot{q} = E(\dot{m}_{O_2}^0 - \dot{m}_{O_2})$$

With \dot{q} the heat release rate

E the average value of the net heat release rate per unit mass of oxygen consumed

$\dot{m}_{O_2}^0$ mass flow rate of oxygen in the incoming air

\dot{m}_{O_2} mass flow rate of oxygen in the exhaust gases

When the composition and heat of combustion of the material are known, a more accurate value can be calculated with the theoretical stoichiometric combustion equation. After ignition, the combustion products are collected in the exhaust hood and removed through the duct in which the flow rate and composition of the gases is measured to determine how much oxygen has been used for combustion. The HRR can therefore be calculated using the relationship between the oxygen consumed and the energy released. For the standard cone calorimeter, the calculation is based on Janssens' work [90] who published a set of equations to calculate the HRR based on Huggett's proportionality of the oxygen consumption. The equations (Equation 6 and Equation 7) consider incomplete combustion by the generation of carbon monoxide and according to the Hess Law:

Equation 6:

$$\dot{q} = [E\Phi - (E_{CO} - E) \frac{1 - \Phi X_{CO}^A}{2 X_{O_2}^A}] \frac{\dot{m}_e}{1 + \Phi(\alpha - 1)} \frac{M_{O_2}}{M_a} (1 - X_{H_2O}^0) X_{O_2}^A$$

With Φ the depletion factor as:

Equation 7:

$$\Phi = \frac{X_{O_2}^{A^0} (1 - X_{CO_2}^A - X_{CO}^A) - X_{O_2}^A (1 - X_{O_2}^{A^0})}{(1 - X_{O_2}^A - X_{CO_2}^A - X_{CO}^A) X_{O_2}^{A^0}}$$

With E_{CO} the net heat release per unit mass of oxygen for CO

X_{CO}^A the measured mole fraction of carbon monoxide in the exhaust gases

$X_{O_2}^A$ the measured mole fraction of oxygen in the exhaust gases

\dot{m}_e the mass flow rate in the exhaust duct

α the chemical expansion factor

M_{O_2}, M_a the molecular weight of O_2 and air

$X_{H_2O}^0$ the mole fraction of water vapor in the incoming air

$X_{O_2}^A$ the measured mole fraction of oxygen in the incoming air

$X_{CO_2}^A$ the measured mole fraction of carbon dioxide in the exhaust gases

However, it is not adapted to the CACC because of the space between the enclosure and the hood. Indeed, the exhaust gases are diluted by excess air drawn from the laboratory surroundings. The heat-induced changes in the dilution ratio affect the measurement of the oxygen and the calculation of the heat release rate. As a result, Werrel et al. [71] showed that the error increases at a significant order of magnitude ($\approx 30\%$) when the oxygen content in the enclosure is decreased below 18 vol-%. In regards to Janssens's approach [90], Werrel defined another formula to calculate the HRR, correcting the pre-experimental oxygen intake for each time step. Werrel et al. approach is summarized in Equation 8 to Equation 13.

Equation 8:

$$\dot{q}(t) = 1.10 * \Delta h_{O_2} * X_{O_2}^i * \dot{m}_e * \left[\frac{\Phi - 0.5 \left(\frac{\Delta h_{CO}}{\Delta h_{O_2}} - 1 \right) (1 - \Phi) \left(\frac{X_{CO}^A}{X_{O_2}^A} \right)}{(1 - \Phi) + \Phi (1 + (\beta - 1) X_{O_2}^{A0})} \right] (1 - X_{H_2O}^S \tilde{\gamma})$$

With Φ the depletion factor as:

Equation 9:

$$\Phi(t) = \frac{X_{O_2}^i (1 - X_{CO_2}^A - X_{CO}^A) - X_{O_2}^A (1 - X_{CO_2}^S \tilde{\gamma})}{X_{O_2}^i (1 - X_{O_2}^A - X_{CO_2}^A - X_{CO}^A)}$$

$X_{O_2}^i$ the intake mole fraction of oxygen as:

Equation 10:

$$X_{O_2}^i = X_{O_2}^{A0} \gamma - X_{O_2}^{AS} (\gamma - 1)$$

$X_{H_2O}^S$ the mole fraction of water in the diluting surrounding air as:

Equation 11:

$$X_{H_2O}^S(t) = \frac{RH}{100} \frac{P_s(T_a)}{P_a}$$

γ the thermal expansion factor as:

Equation 12:

$$\gamma(t) = \frac{\dot{m}_e^0}{\dot{m}_e}$$

$\tilde{\gamma}$ the dilution factor as:

Equation 13:

$$\tilde{\gamma}(t) = 1 - \frac{m_g^B}{\dot{m}_e}$$

And with Δh_{O_2} the net heat of combustion per unit mass of oxygen consumed (MJ/kg)

Δh_{CO} the net heat release per unit mass of O_2 consumed for the oxidation of CO into CO_2

β the stoichiometric dilution factor ($\beta \approx 1.5$)

$X_{O_2}^A$ the mole fraction of oxygen in the diluting surrounding air

RH the relative humidity (%)

$P_s(T_a)$ the saturation pressure of water vapor at T_a , P_a , T_a is the air temperature (K) and P_a the air pressure (Pa)

\dot{m}_e the mass flow rate in the exhaust duct during the test (kg/s)

\dot{m}_e^0 the mass flow rate in the exhaust duct prior to the test (kg/s)

m_g^B the mass flow rate of the incoming gas mixture to the enclosure (kg/s)

1.10 the ratio of molecular weights of oxygen and air

In this work, the HRR will be calculated with this equation.

4.4.2. Gas yield calculation

The gas yields are determined with FTIR results. Indeed, the total production yield of a gaseous species j, is defined as the ratio between the total mass of species j generated and the total mass of solid burnt (

Equation 14).

Equation 14:

$$Y_j = \int_{t=t_0}^{t_f} y_j(t) dt = \frac{G_j}{W}$$

With Y_j the total production yield of species j per unit of burnt mass (kg/kg)

$y_j(t)$ the yield of species j per unit of burnt mass (kg/kg) at time t

W the total mass of solid burnt (kg)

G_j the total mass of species j generated in gaseous form (kg)

t_0 the time (s) when the sample starts to be exposed to the heat flux

t_f the time (s) at which the production of species j stops

The total mass of solid burnt is (Equation 15):

Equation 15

$$W = S \int_{t=t_0}^{t_f} \dot{m}''(t) dt$$

With $\dot{m}''(t)$ the mass loss rate of the sample (kg/m²/s) at time t

S the surface (m²) of the sample

The total mass of gaseous species j generated by the sample is (Equation 16):

Equation 16

$$G_j = S \int_{t=t_0}^{t_f} \dot{g}_j''(t) dt$$

With $\dot{g}_j''(t)$ the mass flow rate of the gaseous product j at time t (kg/m²/s)

The generation rate of the gaseous species j is (Equation 16):

$$\dot{g}_j''(t) = \frac{X_j * \dot{V}}{S} * \frac{M_j}{V_{m,j}}$$

With \dot{V} the volumetric flow rate of the gaseous product j in the exhaust line (m³/s)

M_j the molar mass of species j (kg/mol)

X_j the volumetric fraction of species j

$V_{m,j}$ the molar volume of species j (m^3/mol)

4.5. Testing on PMMA

To verify the accuracy of our device, experiments at different oxygen levels were made with PMMA, whose fire behavior has been greatly studied [21] [82] [83]. The PMMA used is from Fire Testing Technology and it is 18 mm thick. Experiments were carried out at 50 kW/m^2 and 21, 15, 12.5 and 10 vol-% O_2 to compare with the work of Marquis et al. [84]. The volume flow of air at the inlet of the combustion enclosure was adjusted to $160 \pm 5 \text{ L/min}$ at $23 \text{ }^\circ\text{C}$ and the sampling was made in exhaust duct as in [84]. The Appendix 1 p215 gathers the duplicate curves of each oxygen level tested while the curves below only present the curve that fitted the best the mean one. The standard deviation was 7% at 21 vol-% O_2 , 4% at 15 vol-% O_2 , 14% at 12.5 vol-% O_2 and 98% at 11 vol-% O_2 but is not shown in the figures for clarity.

From the HRR curves (Figure 36), it is observed that the oxygen level influences the gas phase behavior. Indeed, under 12.5 vol-% O_2 , flaming combustion does not occur at the surface of PMMA. Especially, it was visually observed that a 12.5 vol-% O_2 the samples struggled to ignite, and that the flaming combustion takes place in the chimney. Marquis et al. explained that the mixture of gas and oxidant is close to the lean flammability limit (LFL), and because of the turbulent mixing conditions, the LFL of the Air/Fuel/ N_2 mixture is achieved in the chimney, leading to premixed combustion. At 21 vol-% O_2 , the HRR and the generation rate of CO_2 (Figure 37) are the highest while it decreases with oxygen depletion. When the oxygen level is equal to 10 vol-%, the quantity of available oxidant seems to be lower than the limiting oxygen concentration and flaming cannot be sustained. As a result, the HRR and CO_2 generation rate are significantly reduced. For the CO production rate (Figure 38), at 21 and 15 vol-% O_2 , the peak is recorded at the highest heat release rate. This suggests that the mixture is below stoichiometry and that there is not enough oxygen and radicals to oxidize fuel gases into CO_2 [91] [92]. Similarly, at 12.5 vol-% O_2 and 10 vol-% of O_2 , the oxidation reactions of the gases to CO seem to be promoted rather than the generation of CO_2 . It suggests that the available amount of O_2 entering the enclosure is insufficient to oxidize CO to CO_2 , leading to incomplete combustion and vitiation of the atmosphere.

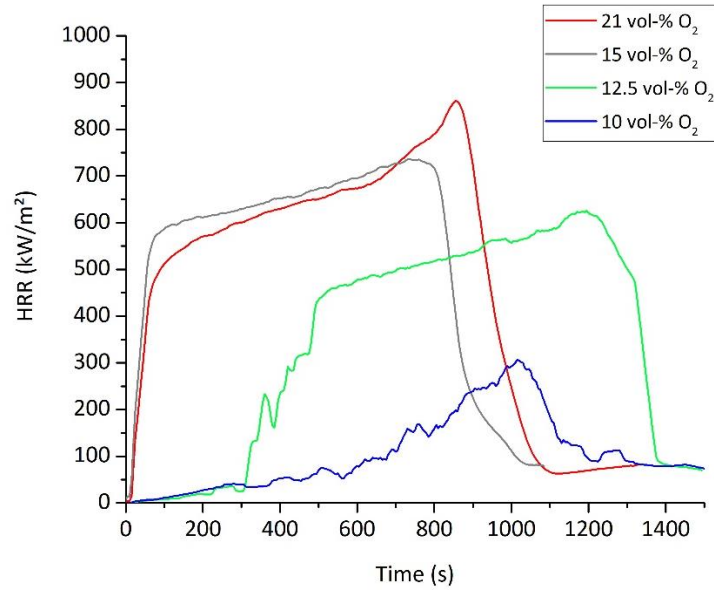


Figure 36: Effect of oxygen level on the HRR of PMMA at 50 kW/m²

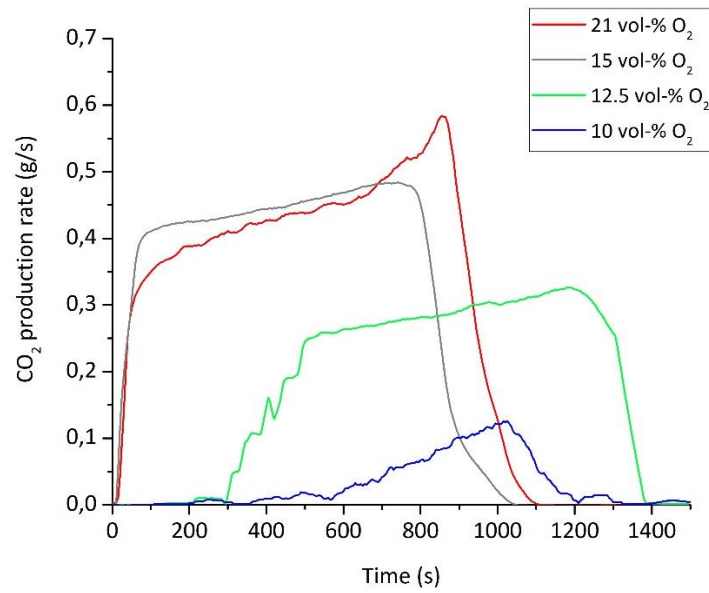


Figure 37: Effect of oxygen on the CO₂ production rate of PMMA at 50 kW/m²

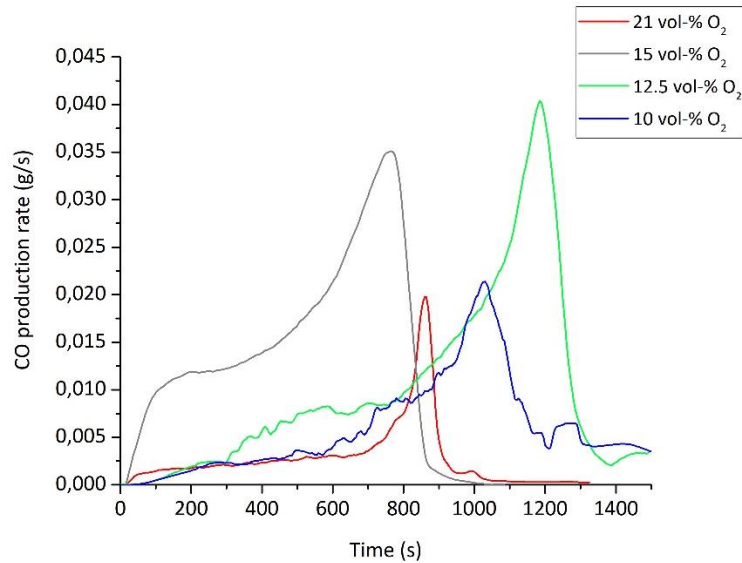


Figure 38: Effect of oxygen on the CO production rate of PMMA at 50 kW/m²

These observations agree with the work of Marquis et al. (Figure 39). Indeed, they highlighted that the oxygen concentration affects the burning behavior of PMMA with a transition below 12.5 vol-% O₂ from a diffusion flame at the PMMA sample to a premixed flame inside the chimney, while at 10 vol-% O₂ the decomposition occurs without flame. They underlined that this behavior does not occur in absence of chimney and thus depends upon CACC design. From their results, it can be seen that the same shape of HRR curves (Figure 39a), CO₂ production rate curves (Figure 39b) and CO production rate curves (Figure 39c) are obtained. However, the peak values of these latter are lower in our CACC bench with a decrease of 26%, 17%, 16% and 57% in HRR at 21, 16, 12.5 and 10 vol-% O₂ respectively. This can be due to the insulated walls of our bench that reduce the heat radiation towards the sample. Moreover, the PMMA used are different in composition, which can induce changes in the HRR and thus CO and CO₂ production rates.

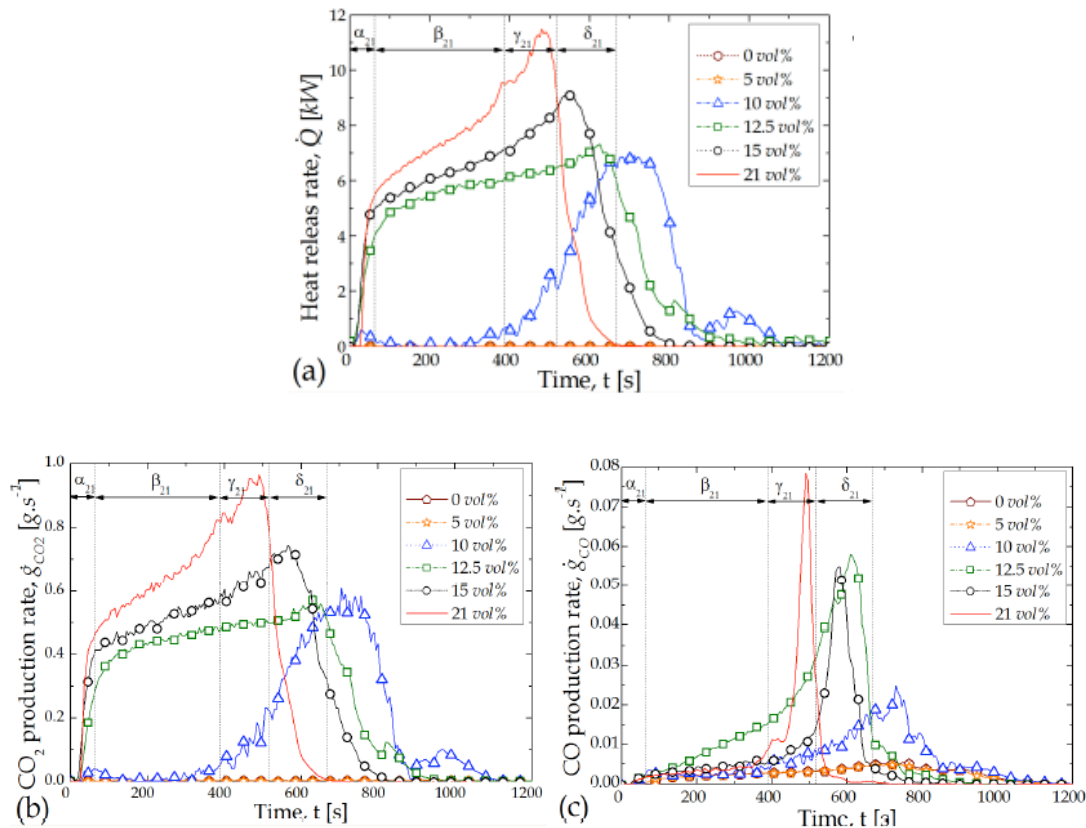


Figure 39: Effect of oxygen concentration on the PMMA behavior in the gas phase. (a) average HRR (b) average generation rate of CO_2 and (c) average generation rate of CO [84]

To conclude, a homemade CACC has been developed and presents the same δ_{21} phenomena and as other studies on the PMMA reaction-to-fire. However, as the sampling was made in the exhaust duct, gas measurement in the chimney could not be compared with their results.

As explained in the Chapter 1 (section 2 p37) one of the challenges of this study is to correlate data between different scales. Thus, a larger scale bench has been designed to link the data obtained in the CACC with data at a higher scale. Moreover, at this scale the effects of dripping and flame spread are considered.

5. Intermediate scale

5.1. Theoretical background

At intermediate scale, one of the widely used apparatus in the building field is the standardized Single Burning Item (Figure 40) [93]. It assesses the fire response of a material system in a corner configuration (Figure 40). The sample consists of two parts: one of $0.5 \times 1.5 \text{ m}^2$ and the second of $1.0 \times 1.5 \text{ m}^2$. It is exposed

to a 30 kW gas flame ignition. The measurement of fire growth, HRR, smoke production rate (SPR) and O₂ and CO₂ production are the main results obtained with this test. One of the drawbacks of this test is that the gas production apart from O₂ and CO₂ is not assessed, as well as the aerosol production. Moreover, the corner configuration induces some changes on the flame spread that are out scope for our study.

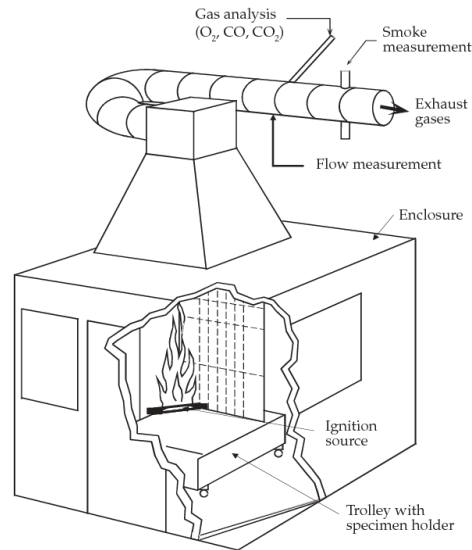


Figure 40: Single Burning Item (SBI) test

Recently, Lafdal [94] carried out tests in a cubic compartment (Figure 41) of intermediate size of 1.4 m of side with an opening in the form of a door of 0.8 m width and variable height from 0 to 1.4 m to study the impact of the type of burner on the fire regime. The walls were made of cellular concrete, with a thickness of 20 cm. The burner considered during these tests was a square burner of 0.17m side positioned in the middle of the compartment and supplied with propane. Oxygen, carbon monoxide and carbon dioxide concentrations were measured with two analyzers, one placed at the burner and the second in the upper part of the enclosure.

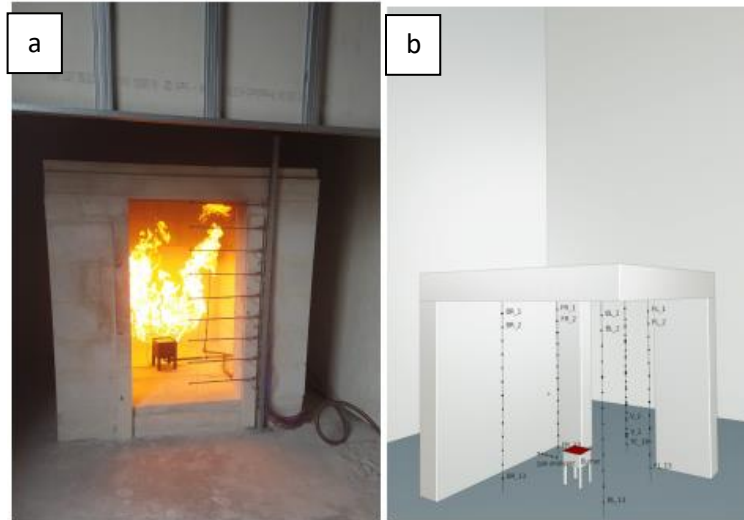


Figure 41: Experimental device of Lafdal, a. Photo of the enclosure, b. 3D model

From these two tests, it would be interesting to design a compartment where a material panel is exposed to the flame of a burner. This allows to free itself from the corner effects of the SBI while FTIR and ELPI could be implemented through the enclosure walls.

5.2. Design of the enclosure

5.2.1. Design

A compartment () was designed to assess the fire reaction of materials at the system scale. It consists of a 1500mm x 1500mm x 2200mm fire compartment with an exhaust hood above it. The exhaust hood is linked to an exhaust duct as in the SBI test design [93]. The walls are 20 mm thick calcium silicate boards. The front panel has a 500 mm opening and an observation door of 400x400 mm is fitted. In the middle of the compartment, a square propane burner of 17 mm side is set. The gas flow is monitored by a mass flow meter, which allows controlling the power. The sample surface is up to 1200 x 1500 mm².

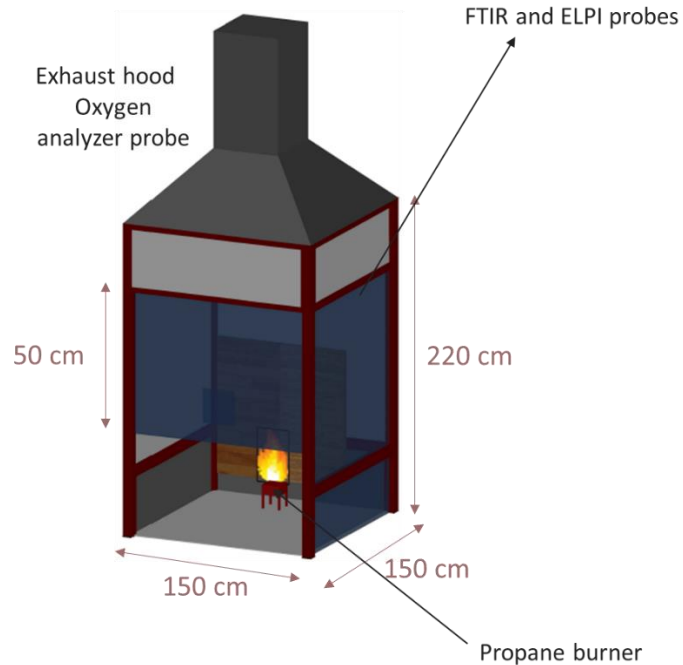


Figure 42: Design of the large scale testing enclosure

5.2.2. Equipment for smoke analysis

As for the CACC experiments, the FTIR and the ELPI are used to measure the gas production and the aerosol production respectively. For the FTIR analysis, a stainless steel pipe with 2mm holes shaped in a semicircle is set on top of the wall of the enclosure. It is linked to a 10m PTFE heated line at 180 °C that goes to the FTIR cell. For the ELPI sampling, a U-shape single point probe is used to provide isokinetic collection. As for CACC experiments, the sample is then diluted twice (ratio of 83) thanks to Dekati diluters. In the exhaust duct, oxygen measurement is made with a paramagnetic oxygen analyzer.

5.3. Sample preparation

Samples are tested in the vertical orientation and set on a metallic frame in front of the burner. A calcium silicate board is put on the backside of the sample. For the tests carried out on CLT, the samples are 1200x1500x60 mm. Each sample was carefully chosen with as few defects as possible (knots and resin bags). For the wood fiber board, the samples are 1200x1500x40 mm and backed with a 20 mm calcium silicate board. Moreover, for the combination tests, half samples of 600x1500 mm were juxtaposed on the

metallic frame. To separate them and better control the boundary conditions, a ceramic fiber is set between the two half samples.

5.4. Measured and calculated data in the enclosure

The fire parameters assessed in this experiment are the HRR, the gas production and the aerosol production. These latter are calculated as described in the section 4.4 p87 whereas the calculation of HRR is described below.

The HRR is determined in accordance with the ISO 13823 [93]. It is determined by oxygen consumption and represents the total heat release that is the heat produced by the material but also by the burner. It corresponds to Equation 17 along with Equation 18, Equation 19 and Equation 20:

Equation 17:

$$\dot{q}_{total} = E\dot{V}_{298}X_{O_2}^a \left(\frac{\Phi}{\Phi(\alpha - 1) + 1} \right)$$

With Φ the depletion factor as:

Equation 18:

$$\Phi(t) = \frac{X_{O_2}^{A^0}(1 - X_{CO_2}^A) - X_{O_2}^A(1 - X_{CO_2}^{A^0})}{X_{O_2}^{A^0}(1 - X_{O_2}^A - X_{CO_2}^A)}$$

And $X_{O_2}^a$ the ambient mole fraction of oxygen as:

Equation 19:

$$X_{O_2}^a = X_{O_2}^{A^0} \left[1 - \frac{RH}{100p} \exp \left(23,2 - \frac{3816}{T_a - 46} \right) \right]$$

And \dot{V}_{298} (m³/s) the volume flow rate in the exhaust duct at atmospheric pressure and ambient temperature:

Equation 20:

$$\dot{V}_{298} = \left(\frac{Ak_t}{k_p} \right) * \frac{1}{\rho_{298}} * \left(2 * \frac{\Delta p T_0 \rho_0}{T_S} \right)^{\frac{1}{2}} = 22.4 \left(\frac{Ak_t}{k_p} \right) \left(2 * \frac{\Delta p}{T_S} \right)^{\frac{1}{2}}$$

With T_S the gas temperature in the exhaust duct (K)

T_0 the ambient temperature (K)

Δp the pressure difference (Pa)

ρ_0 the air density at 273, 15 K and atmospheric pressure (kg/m^3)

A the cross-sectional area of the exhaust duct (m^2)

k_t the ratio of the average mass flow per unit area to mass flow per unit area in the centre of the exhaust duct

k_p the Reynolds number correction

Finally, the HRR contribution of the material corresponds to Equation 21:

Equation 21:

$$HRR_{material} = HRR_{total} - HRR_{burner}$$

5.5. Heat flux analysis

To link the HRR data obtained with the CACC to the HRR data measured in the enclosure, the heat flux perceived by a material from the burner should be close to the one perceived by the radiative heater of the CACC. Hence an incombustible material, here calcium silicate, was exposed to two different powers to map the perceived heat flux. The calcium silicate board is 1200x1500x20 mm in dimensions and is pierced of 30 mm holes at 40 different positions (Figure 43) to insert cooled fluxmeters (Gardon type). For each power and measuring points, the flow is recorded for 5 minutes. When the burner is switched on, it takes about 30 seconds to reach a constant value of the desired power. Consequently, the average of the flow value and its standard deviation are calculated only for the remaining 270s. The tested powers are 40 and 90 kW to obtain a perceived heat flux of 20 and 50 kW/m^2 respectively. Each test was made twice to ensure the repeatability of the experiment.

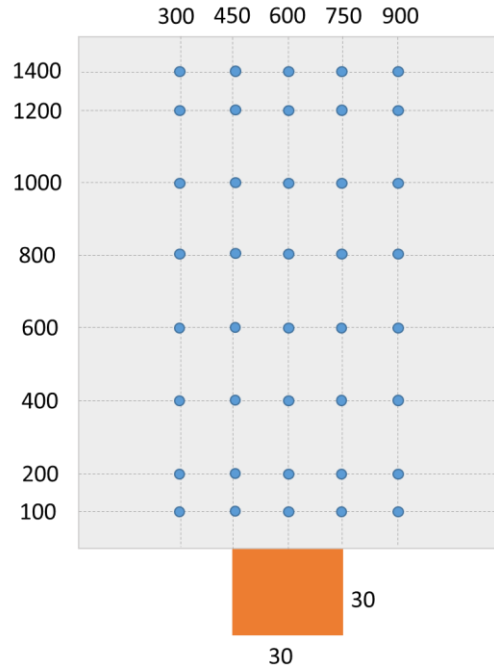


Figure 43: Positions of the fluxmeters on the silicate calcium board

At 40 kW, the mean measured flux (Figure 44a and Figure 44b) is at least of 18 kW/m² over a width of 200 mm and a length of 1000 with a mean maximum value above the burner of 28 ± 3 kW/m². At 90 kW, the mean measured flux (Figure 45a and Figure 45b) is at least of 34 kW/m² over a width of 200 mm and a length of 1300 with a mean maximum value above the burner of 53 ± 3 kW/m². For each power and replica, the total perceived heat fluxes are in the same range considering the standard deviations.

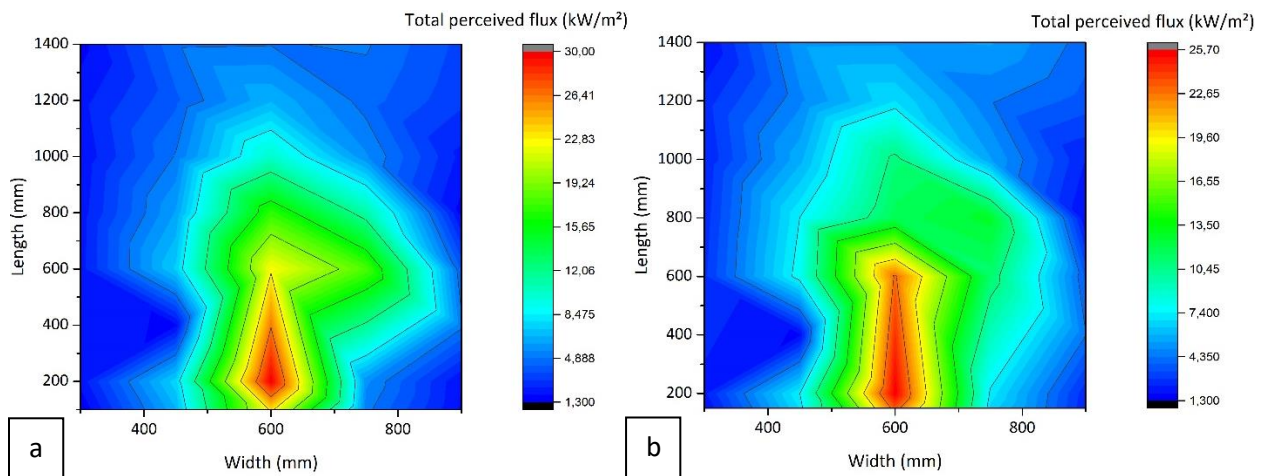


Figure 44: Mapping of the heat flux perceived by a silicate calcium panel at 40 kW. a. Replica 1 b. Replica 2

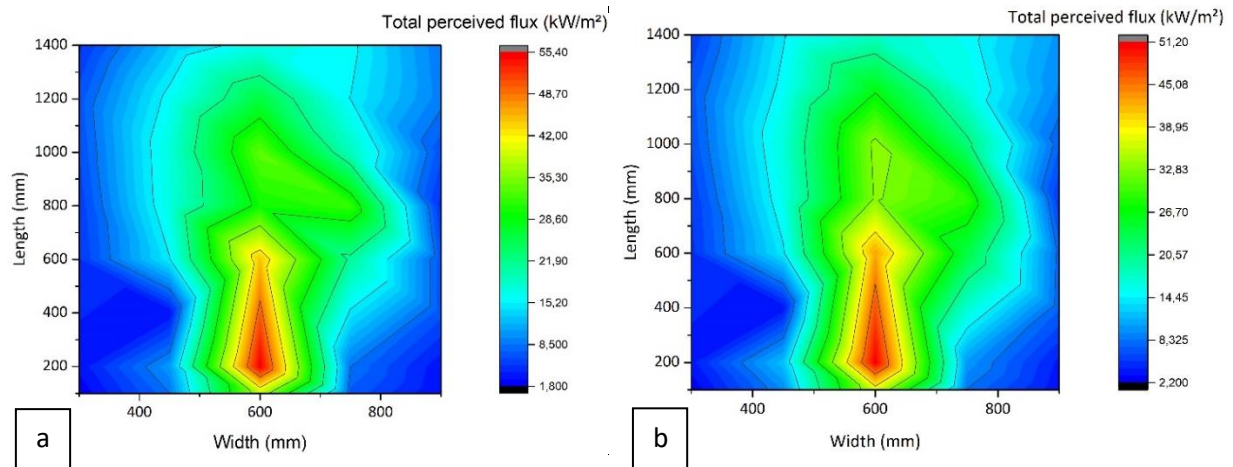


Figure 45: Mapping of the heat flux perceived by a silicate calcium panel at 90 kW. a. Replica 1 b. Replica 2

To conclude, the mapping of the perceived heat flux from a propane burner by an incombustible material has been realized at 40 and 90 kW. It has been verified that in the closest areas to the flame of the burner received at least a flux of 20 and 50 kW/m², which allows for linking the data to the ones of the CACC.

6. Conclusion

First, a brief literature review of the available experimental methods to assess the reaction to fire and the gas and aerosol production of Cross-Laminated Timber and wood fiber at three different scales has been realized. This review enabled to choose suitable devices to carry out the experimental investigation.

At matter scale, the thermal decomposition of the wooden materials is studied with Py-GC/MS and with TGA/FTIR. Both techniques complement each other on the thermal decomposition process and the gas production along.

At material scale, a homemade CACC combined to a FTIR and an ELPI allow the study of the reaction to fire, the gas production and aerosol size distribution both in well-ventilated conditions and in vitiated environments. The accuracy of the CACC was compared with results of literature on PMMA material.

At system intermediate scale, an open enclosure with a propane burner was designed and implemented with FTIR and ELPI measurements. Fire spread, gas production and aerosol size distribution can be assessed. The mapping of the perceived heat flux at 40 and 90 kW was performed and allowed to verify that an incombustible material received respectively 20 and 50 kW/m².

Finally, apart from matter scale, all experiments will be realized first on a single material, CLT or WF, and then on the combination of the two.

Chapter 3: Matter scale analysis

1. CHARACTERIZATION OF CROSS-LAMINATED TIMBER THERMAL BEHAVIOR	104
1.1. CHARACTERIZATION OF CROSS-LAMINATED TIMBER BY THERMOGRAVIMETRIC ANALYSIS COUPLED TO FOURIER TRANSFORM INFRARED SPECTROSCOPY	104
1.1.1. <i>Inert atmosphere</i>	105
1.1.2. <i>Oxidative atmosphere</i>	108
1.1.3. <i>Comparison between inert and oxidative atmospheres</i>	111
1.2. CHARACTERIZATION OF CROSS LAMINATED TIMBER BY PYROLYSIS-GAS CHROMATOGRAPHY MASS SPECTROSCOPY	113
2. CHARACTERIZATION OF WOOD FIBER THERMAL BEHAVIOR	116
2.1. CHARACTERIZATION OF WOOD FIBER BY THERMOGRAVIMETRIC ANALYSIS COUPLED TO FOURIER TRANSFORM INFRARED SPECTROSCOPY	116
2.1.1. <i>Inert atmosphere</i>	116
2.1.2. <i>Oxidative atmosphere</i>	119
2.1.3. <i>Comparison between inert and oxidative atmospheres</i>	122
2.2. CHARACTERIZATION OF WOOD FIBER BY PYROLYSIS-GAS CHROMATOGRAPHY MASS SPECTROSCOPY	124
CONCLUSION	126

This chapter deals with the analysis of the thermal decomposition of Cross-Laminated Timber and Wood-Fiber at matter scale. This study allows for having a first insight on the thermal behavior and on the gas production of these materials under both inert and oxidative atmospheres. Indeed, experiments consist in Thermogravimetric analysis coupled to Fourier-Transform Infrared spectroscopy (TGA-FTIR) and Pyrolysis-Gas Chromatography Mass Spectroscopy (Py-GC/MS). TGA-FTIR is carried out under nitrogen but also in several oxygen concentrations to study the impact of the later. Py-GC/MS allows for having further details on the chemical composition of the gases released during pyrolysis.

The thermal behavior of CLT is first described with TGA-FTIR and Py-GC/MS analysis. Then, the same study is done on wood fiber.

1. Characterization of Cross-Laminated Timber thermal behavior

1.1. Characterization of Cross-Laminated Timber by Thermogravimetric Analysis coupled to Fourier Transform Infrared spectroscopy

TGA-FTIR experiments are performed on CLT samples. The studied conditions are 100% N₂, 21, 18, 15 and 10 vol-% O₂. The studied parameters are the initial decomposition temperature (T_{5wt%}) at 5 wt% weight loss, the burnout temperature (T_f) at the end set temperature, the maximum mass loss rate (DTG_{max}) and

the total weight loss of CLT (Table 9 and Table 10). The Appendix 2 p218 gathers the duplicate curves of each oxygen level tested while the curves below only present the curve that fitted the best the mean one.

1.1.1. Inert atmosphere

Under nitrogen, the thermal decomposition of CLT is an apparent one-stage process (Figure 46a) taking place between 220°C and 388°C with 76% of weight loss (Table 9). From the dTG curve (Figure 46b), a single peak, corresponding to the fastest mass loss, is observed around 370 °C at 12.5 %/min (Table 9). However, a break in slope in the dTG peak is noted around 330°C, which indicates potential additional reactions of decomposition. To further investigate the phenomena occurring during the thermal decomposition of CLT, the chemigram of the FTIR analysis is plotted along with the dTG (Figure 46b). From the chemigram, six temperatures of interest are noted, and each corresponding spectrum is plotted (Figure 47).

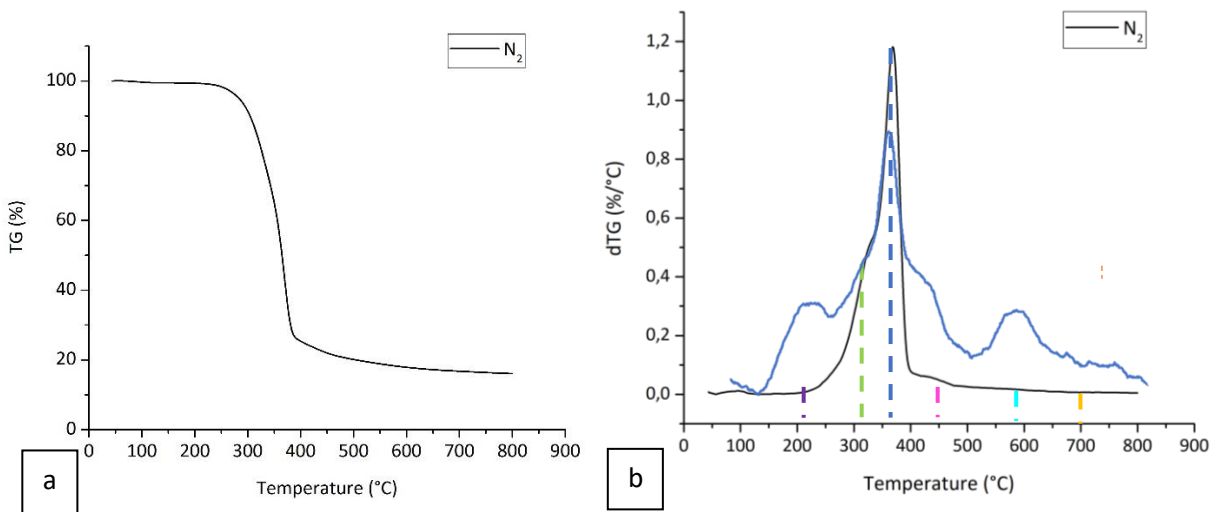


Figure 46: TGA-FTIR under N_2 at $10^\circ\text{C}/\text{min}$. a. TG curve b. dTG curve (black) and chemigram (blue)

Table 9: TGA parameters of CLT under nitrogen atmosphere

Atmosphere	$T_{5wt\%}$ (°C)	T_f (°C)	DTG_{max} (%/min)	Weight loss (%)
N_2	284	388	12.5	76

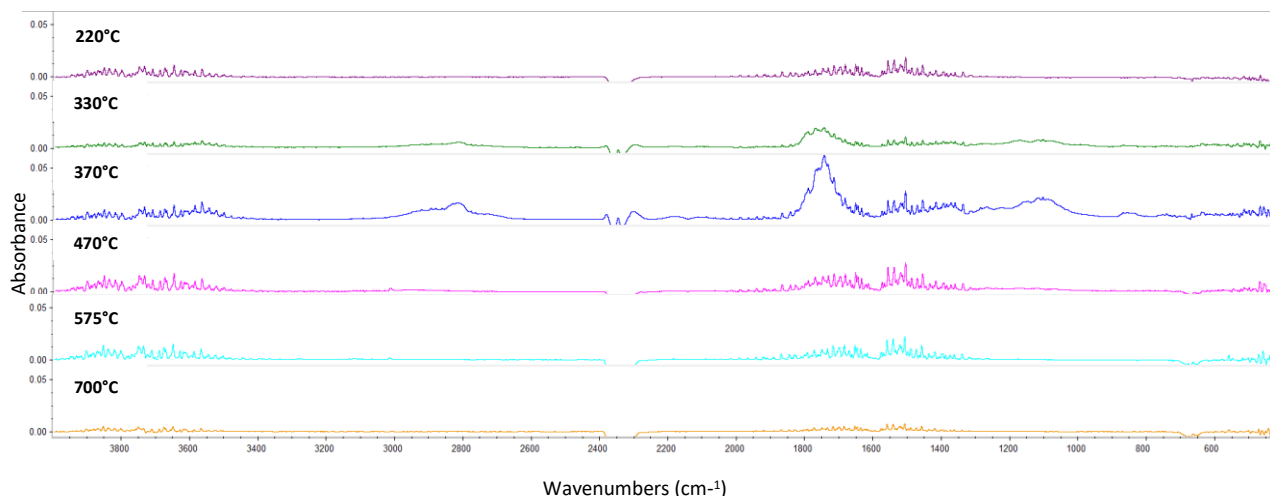
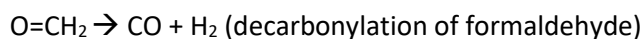


Figure 47: FTIR spectra of CLT under nitrogen at 220, 330, 370, 470, 575 and 700°C

Water devolatilization of CLT starts during the isothermal step at 40°C done before the experiment, with a loss of about 10% of its initial weight (not shown on the TG curve). On the chemigram (Figure 46b), a first increase is observed between 160 and 260°C with water release. Indeed, at 220°C (Figure 47) there is absorption in the range 4000-3500 cm⁻¹, which corresponds to the O-H stretching vibration. CLT is first transformed by breaking the bonds between constituent water and wood, which are part of the weakest bonds [40]. This step may correspond to the beginning of hemicellulose devolatilization [36], [95]. From 220°C to 370°C, as the decomposition rate rapidly increases, the release of volatiles increases too (Figure 46b) with additional absorption bands on FTIR spectra (Figure 48). This increase could be ascribed to cellulose and lignin devolatilization [96], [97]. As explained before, a break in slope of the dTG is observed around 330°C before reaching a peak at 370 °C. To better understand the phenomena occurring between these two steps, the FTIR spectra at 330 and 370°C are compared with reference gases^{3 4} (). For both spectra, there is a strong absorption in the range 4000-3500 cm⁻¹ due to the O-H stretching vibration related to H₂O but also phenols and alcohols. Characteristic absorptions in the range 2240-2050 cm⁻¹ reveal the presence of CO. CO mainly originates from the break of the C=O bond and of the ether bond. An example is given below with formaldehyde, itself released from fragmentation of hemicellulose and rupture of C-C bonds of lignin (see Figure 9 p46 and Figure 11 p48).



³NIST Chemistry WebBook - <https://webbook.nist.gov/chemistry/>

⁴Nicolet TGA Vapor Phase library

Between 3000 and 2700 cm^{-1} , the absorptions are attributed to C-H stretching vibrations. More precisely, the small peak at 3000 cm^{-1} is attributed to methane formation (). Methane mainly comes from the decomposition of methylene ($-\text{CH}_2-$), methyl ($-\text{CH}_3$) and methoxy ($-\text{OCH}_3$) functional groups of wood and particularly lignin (Figure 11 p48). Moreover, there is a strong absorption in the range 1850-1600 cm^{-1} , which corresponds to the C=O stretching of aldehydes, ketones, and acids. These compounds also greatly absorb in the range 1475-1000 cm^{-1} , which is characteristic of the C-C, C-O, and carbon chain skeletons. More precisely, the spectrum formic acid fits with peaks at 700, 1106, 1093, 1120 and 1790 cm^{-1} (). Some differences are observed in the area between 1150 cm^{-1} and 1200 cm^{-1} for spectra at 330°C and 370°C, which indicate successive reactions of decomposition taking place (). Indeed, at 330°C, the absorption is located around 1144-1203 with a peak at 1175 cm^{-1} while at 370 °C it is around 1137-1179 cm^{-1} with a peak at 1149 cm^{-1} . Precise identification of volatiles is challenging due to four overlapping chemical groups (alcohols, aldehydes, ketones, and carboxylic acids) in the same region. Finally, peaks in the range 900 to 700 cm^{-1} are characteristics of aromatic C-C stretching, which could indicate the presence of complex aromatic compounds released from lignin decomposition as cresol or guaiacol type compounds or from cellulose and hemicellulose decomposition as furan (see Figure 9 p46, Figure 10 p47 and Figure 11 p48).

After reaching a peak at 370°C, the dTG and the intensity of the gas production drop. At 400°C, a break in slope is observed in the dTG and in the chemigram, which may be ascribed to the end of cellulose and hemicellulose decomposition [95], [97]. The gas production slowly decreases up to 470°C where another break in slope is observed, which may correspond to the end of lignin volatilization [96]. It leads to a fastest decrease until a temperature of 540°C is reached (Figure 46b). A last peak is observed between 540 and 650°C. From the FTIR spectra (

), it only corresponds to H_2O and CH_4 release while the previous mentioned organics compounds have disappeared. At 700°C, no more gases are released.

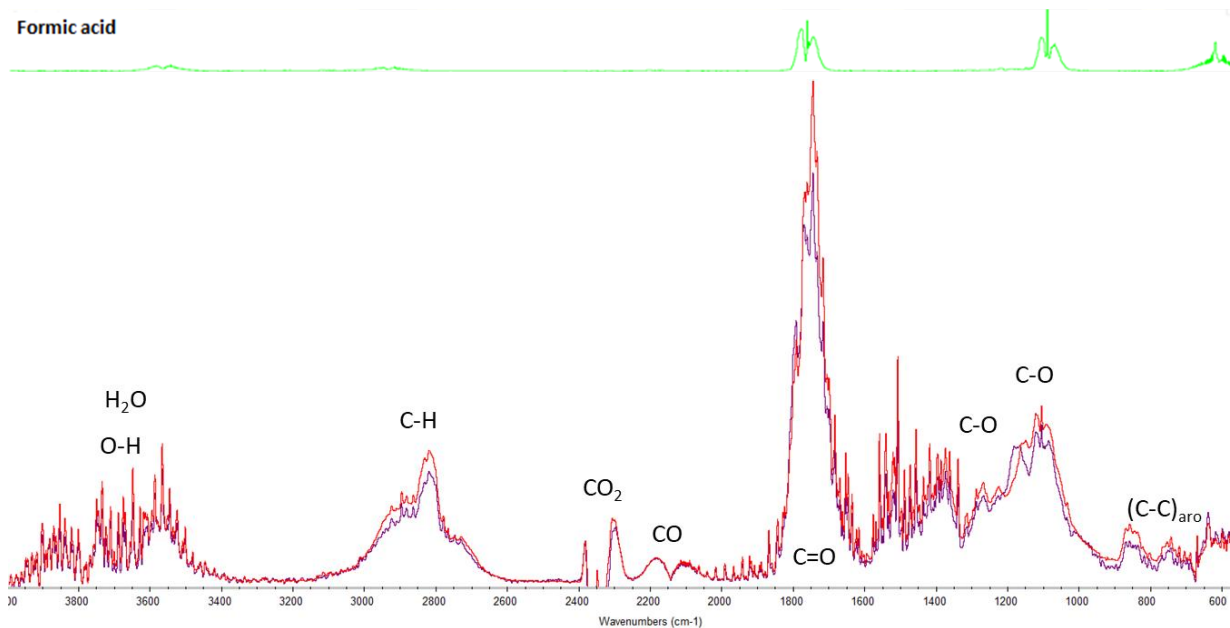


Figure 48: Superposition of the FTIR spectra of CLT under nitrogen at 330°C (purple) and 370°C (red) along with spectra of formic acid

1.1.2. Oxidative atmosphere

Under 21% of oxygen, the thermal decomposition of CLT is an apparent two-stage process (Figure 49a) taking place between 272 and 460°C with 90% of weight loss (Table 10). From the dTG curve (Figure 49b), two peaks are observed at 333 °C at 22.5 %/min and at 443°C at 28.8 %/min (Table 10). From the chemigram, four temperatures of interest (150, 333, 390 and 443°C) are revealed and each corresponding spectra is plotted (Figure 50).

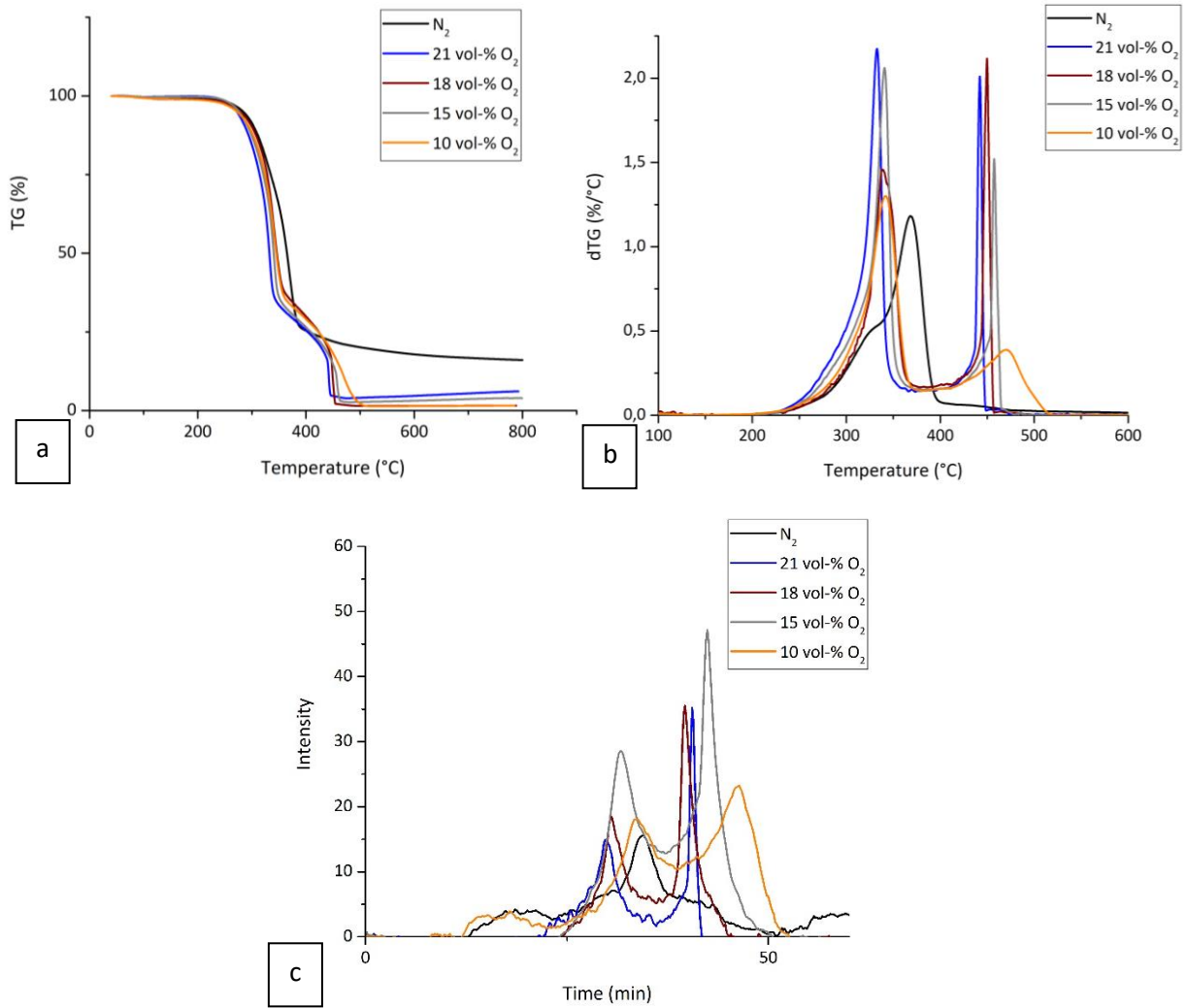


Figure 49: TGA curves of CLT under N₂ and different oxygen concentrations at 10°C/min. a. TG curves b. dTG curves c. chemigrams

Table 10: TGA parameters of CLT under different oxygen concentrations

Atmosphere	T _{5wt%} (°C)	T _f (°C)	DTG _{max} (%/min)	Weight loss (%)
N ₂	284	388	12.5	76
21 vol-% O ₂	272	445	22.5	90
18 vol-% O ₂	279	453	15.4	91
15 vol-% O ₂	269	455	20.9	91
10 vol-% O ₂	279	512	14.0	92

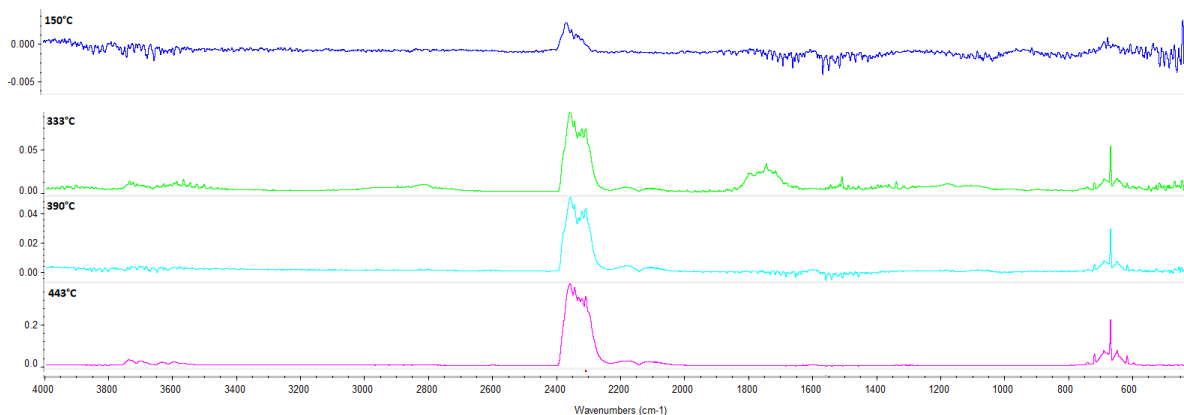


Figure 50: FTIR spectra of CLT at 21 vol-% O₂ at 150, 333, 390 and 443°C

Water devolatilization of CLT begins during the isothermal step at 40°C with a loss of about 10% of its initial weight (not shown on the TG curve). From ambient temperature to 200°C, water devolatilization is observed with a strong absorption in the range 4000-3500 cm⁻¹, which corresponds to the O-H stretching vibration (Figure 50). Then, from 200°C to 333°C, with an increasing decomposition rate, the release of volatiles increases (Figure 49b and Figure 49c) with additional absorption bands on FTIR spectra (Figure 50). On the FTIR spectrum at 333°C (), there is an absorption in the range 4000-3500 cm⁻¹ due to the O-H stretching vibration related to H₂O but also phenols and alcohols. Between 3000 and 2700 cm⁻¹, the absorptions are attributed to C-H stretching vibrations while those in the range 1850-1600 cm⁻¹ correspond to the C=O stretching of aldehydes, ketones, and acids (). More precisely, in the range 1475-1000 cm⁻¹, which is characteristic of the C-C, C-O and carbon chain skeletons, formic acid with a peak at 1106 cm⁻¹ (). Moreover, characteristic absorptions in the range 2400-2240 cm⁻¹ and 2240-2050 cm⁻¹ reveal the presence of respectively CO₂ and CO. In addition to decarboxylation reactions and carbonyl breakage, CO₂ is released from the reaction between the carbon of the residue and oxygen. CO also is produced from incomplete reaction between fixed carbon and oxygen, in addition to carbonyl and ether bond breakage [26]. The strong peak at 1508 cm⁻¹ is attributed to benzene ring skeletons in aromatic compounds of lignin [16].

After reaching a peak at 333°C, the dTG and the intensity of the gas production drop to reach a plateau between 352 and 415°C (Figure 49b and Figure 49c) due to the end of cellulose and hemicellulose devolatilization. During this period, only CO, CO₂ and small amounts of water are produced (Figure 50). Lignin finishes decomposing while the low rate of devolatilization allows for the oxygen to interact at the surface of wood. A heterogeneous mechanism of oxidation takes place in the char previously formed. Then, the dTG and the chemigram rapidly increase again to reach a peak at 443°C; this is characterized by a second decrease in the TG curve (Figure 49). From the FTIR spectra at 443°C (Figure 50), CO and CO₂ are detected with a great absorbance. This second step corresponds to the oxidation of the remaining

components. Then, both the chemigram and the dTG curve decrease (Figure 49b and Figure 49c) to reach a zero value to 460°C to 800°C.

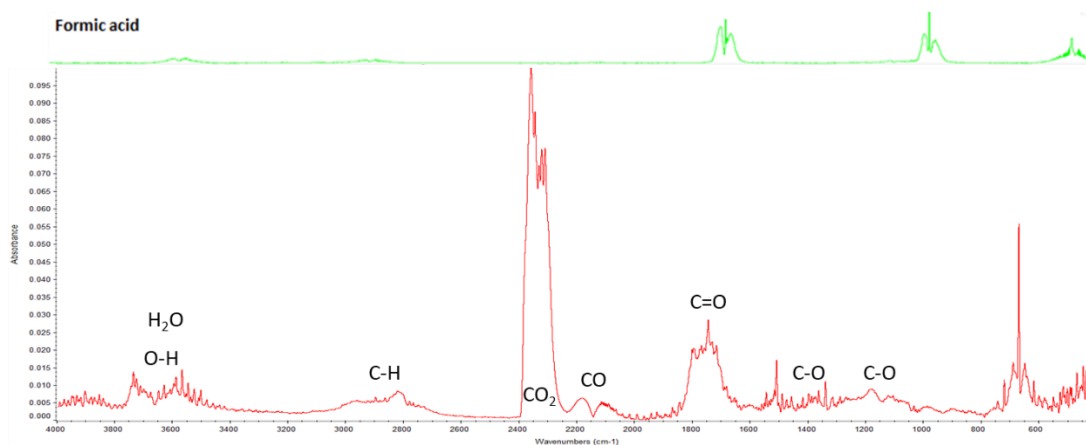


Figure 51: Superposition of the FTIR spectra of CLT at 21 vol-% O₂ at 333°C along with spectra of formic acid

At oxygen levels of 18, 15 and 10%, it appears that the thermal decomposition is still a two-stage process (Figure 49a, Figure 49b and Figure 49c). The start of the thermal decomposition does not seem to be influenced by the oxygen concentration as the temperature at 5% of weight loss are in the same range with a standard deviation of 5°C, which corresponds to 2% of the mean. The first stage of decomposition is also similar for all oxygen levels. However, the second stage differs between 10 vol-% O₂ and the other oxygen levels. Indeed, the decomposition process at 10 vol-% O₂ is delayed in temperature (Figure 49b) and in time (Figure 49c). The onset of oxidation of the residue begins around 410°C for all oxygen levels but the reaction proceeds at a much slower rate (-38% in DTG_{max} from 21 to 10 vol-% O₂) at 10 vol-% O₂. As a result, the end of the second stage is around 512°C (Table 10), which is 60°C more than the mean value at 21, 18 and 15 vol-% O₂. Though the oxidation process is delayed at 10 vol-% O₂, around 91% of weight is lost for all oxygen concentrations (Table 10). It should be noted that no difference was observed in the FTIR spectra whatever the oxygen level (Appendix 3 p220).

1.1.3. Comparison between inert and oxidative atmospheres

The thermal decomposition of CLT under both nitrogen and several oxygen concentrations was studied with TGA-FTIR analysis. The decomposition under nitrogen is a one-stage process while it is a two-stage process under oxygen atmospheres. Oxygen has a low impact on the beginning of thermal decomposition, as the temperatures of 5% of weight loss are close (272°C at 21 vol-% O₂ and 279°C at 10 vol-% O₂) (Table 10). The gas production is also similar (Figure 52) with mainly water and carbon dioxide released before 220°C under nitrogen and before 200°C under oxygen.

Then, oxygen seems to increase the rate of decomposition of CLT, as the slope of the first dTG peak is more important on the oxygen curves than on the nitrogen curve (Figure 46b). Moreover, under nitrogen, a break in slope takes place around 340°C with a shift to the right of the 1150-1200 cm⁻¹ absorption band, indicating a chemical change in the volatile production. This is not observed under oxygen where CO₂, CO, H₂O, aldehydes, ketones, alcohols, acids, and aromatic compounds are released from 200 to 350°C (Figure 52). It should be noted that methane was not detected under oxygen atmospheres compared to nitrogen atmosphere. Indeed, in the presence of oxygen, methane might have been oxidized to CO₂ or CO.

At the end, after an important drop in gas production under nitrogen atmosphere, the thermal decomposition reaches a low production of methane and water from 370 to 680°C (Figure 52). In comparison, under oxygen atmosphere, a second step corresponding to oxidation of the residue is observed between 415 and 460 °C. The gases released are mainly CO₂ and CO (Figure 52). It should be highlighted more residue was obtained under nitrogen experiments, as 76% of the mass is lost while 91% in mean in consumed under oxygen.

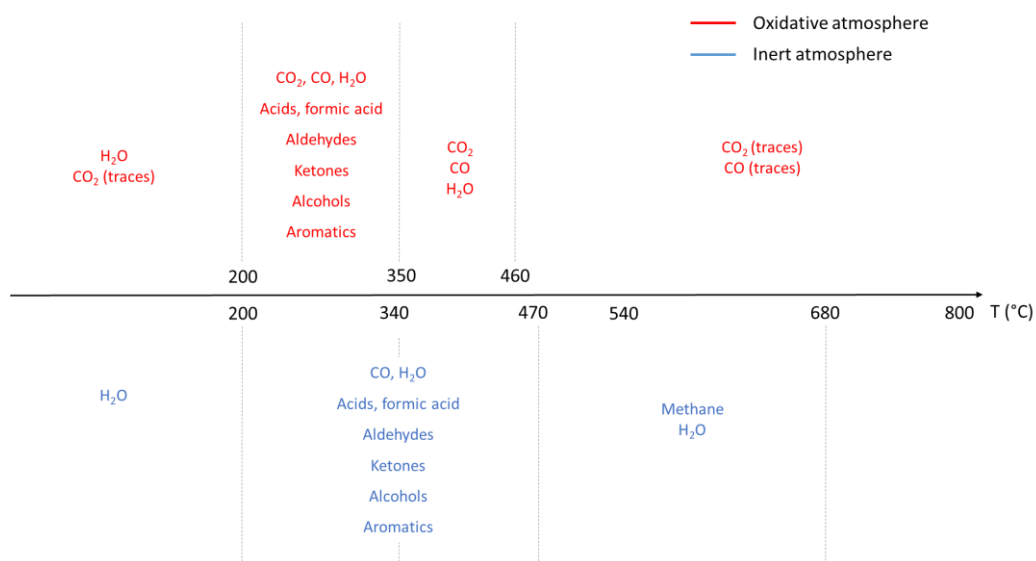
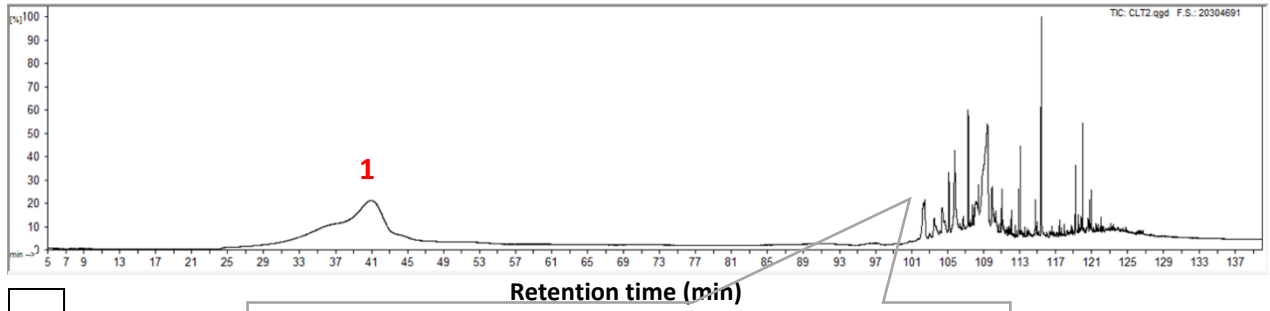


Figure 52: Gases released during the decomposition of CLT under oxidative (red) and inert (blue) atmosphere as a function of temperature

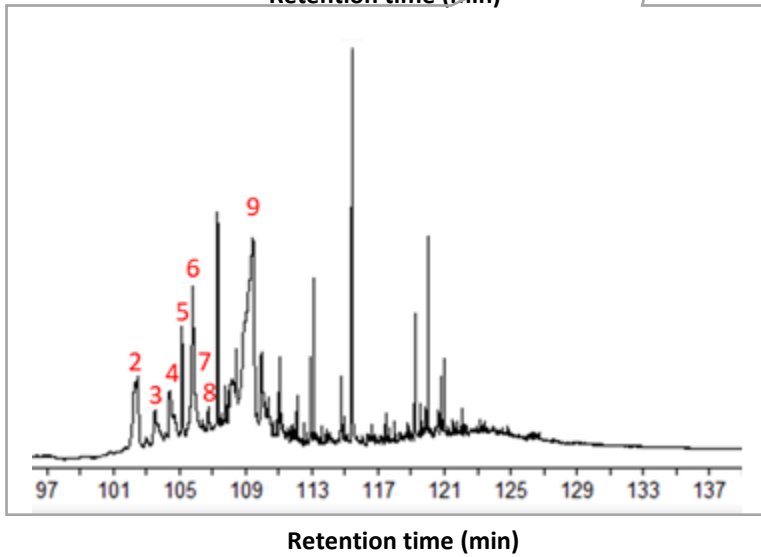
Many organic compounds are released during the thermal decomposition of CLT, which makes it difficult to fully analyze the gas composition. As seen previously, aromatic compounds are probably released but with no more information on the precise structure. Thus, PY-GC/MS analysis was carried out to investigate in more detail the gaseous emissions during pyrolysis.

1.2. Characterization of Cross Laminated Timber by Pyrolysis-Gas Chromatography Mass Spectroscopy

Py-GC/MS was performed on CLT at a rate of 10°C/min from 40 to 800°C. The first products detected are H₂O and CO₂ with a retention time between 25 and 50 min (Figure 53a). Between 100 and 129 min of retention, a tree of peaks is observed. Eight peaks have been potentially identified; they mainly correspond to complex aromatic structures (Table 11). The peaks 2, 5, 7 and 8 are phenolic compounds ascribed to lignin decomposition. According to the literature, 2-methoxy-4-methylphenol and 2-methoxy-4-vinylphenol would be the most probable compounds released and identified previously on the FTIR spectra [96], [98]. The peaks 3 and 9, corresponding to 3,6-dianhydro- α -glucopyranose and levoglucosan, are characteristic compounds of cellulose decomposition [99], [100]. The presence of levoglucosan is in accordance with literature [26], which reports that cellulose first is decomposed into an active compound, known as levoglucosan. Similarly, 3,6-dianhydro- α -glucopyranose is known to be released from levoglucosan decomposition [101]. The peak 4, corresponding to 5-(hydroxymethyl)-2-furfural, is mainly related to hemicellulose decomposition [26].



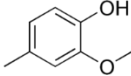
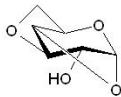
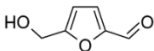
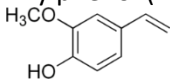
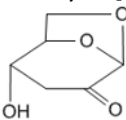
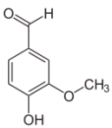
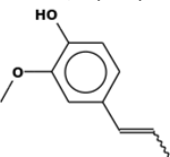
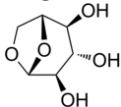
a



b

Figure 53: CLT chromatogram a. full size b. zoom from 97 to 137 min

Table 11: Identification of the main decomposition products of CLT

	Retention time (min)	M (g/mol)	Confidence (%)	Molecule
1	25-50 41.1	18 44	-	H ₂ O CO ₂
2	102.3	138	85	2-Methoxy-4-methylphenol (creosol) 
3	103.5	144	65	3,6-Dianhydro-alpha-glucopyranose 
4	104.4	126	56	5-(Hydroxymethyl)-2-furfural 
5	105.1	150	97	2-Methoxy-4-vinylphenol (4-vinylguaiacol) 
6	105.8	144	73	2-Hydroxy-6,8-dioxabicyclo[3.2.1]octan-4-one 
7	106.8	152	87	Vanillin 
8	107.3	164 164 164 164	95 95 92 90	2-Methoxy-4-1-(1-propenyl)-phenol 
9	108.2-109.5	162	87	Levoglucosan 

The Py-GC/MS study enabled to identify possible aromatic structures found in the previous FTIR spectra. It also confirmed the presence of characteristic products released from wood pyrolysis.

2. Characterization of wood fiber thermal behavior

2.1. Characterization of Wood Fiber by Thermogravimetric Analysis coupled to Fourier Transform Infrared spectroscopy

TGA-FTIR experiments are conducted on wood fiber samples. The studied conditions are 100% N₂, 21, 18, 15 and 10 vol-% O₂. The studied parameters are the initial decomposition temperature ($T_{5wt\%}$) at 5 wt% weight loss, the burnout temperature (T_f) at the end set temperature, the maximum mass loss rate (DTG_{max}) and the total weight loss of wood fiber (Table 12 and Table 13). The Appendix 3 p220 gathers the duplicate curves of each oxygen level tested while the curves below only present the curve that fitted the best the mean one.

2.1.1. Inert atmosphere

When subjected to nitrogen atmosphere, the thermal decomposition of WF follows an apparent single-stage process (Figure 54a) occurring between 200 and 640°C and resulting in a weight loss of 73% (Table 12). The dTG curve (Figure 54b) displays a single peak representing the fastest mass loss at around 367°C, with a rate of 10.2%/min (Table 12). However, a slight change in slope within the dTG peak is observed around 316°C, indicating a more complex decomposition process, which involves additional decomposition reactions. To gain further insights into the phenomena associated with the thermal decomposition of WF, the chemigram of the FTIR analysis is plotted alongside the dTG curve (Figure 54b). The chemigram reveals four temperatures of interest, and the corresponding spectra for each temperature are presented (Figure 55).

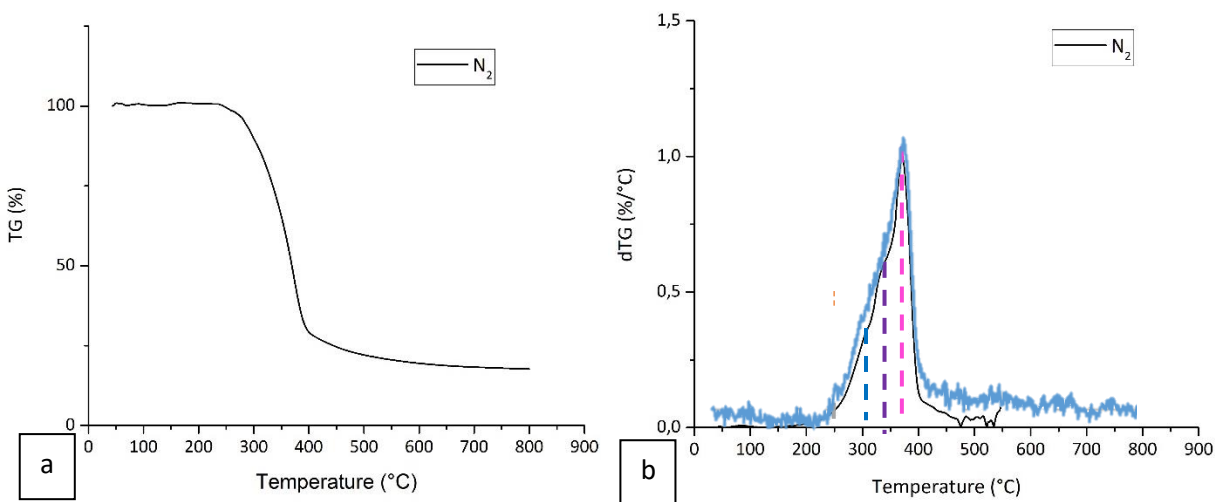


Figure 54: TGA-FTIR of WF under N_2 at $10^\circ\text{C}/\text{min}$. a. TG curve b. dTG curve (black) and chemigram (blue)

Table 12: TGA parameters of WF under nitrogen

Atmosphere	$T_{5\text{wt}\%}$ ($^\circ\text{C}$)	T_f ($^\circ\text{C}$)	DTG_{max} (%/min)	Weight loss (%)
N_2	276	394	10.2	73

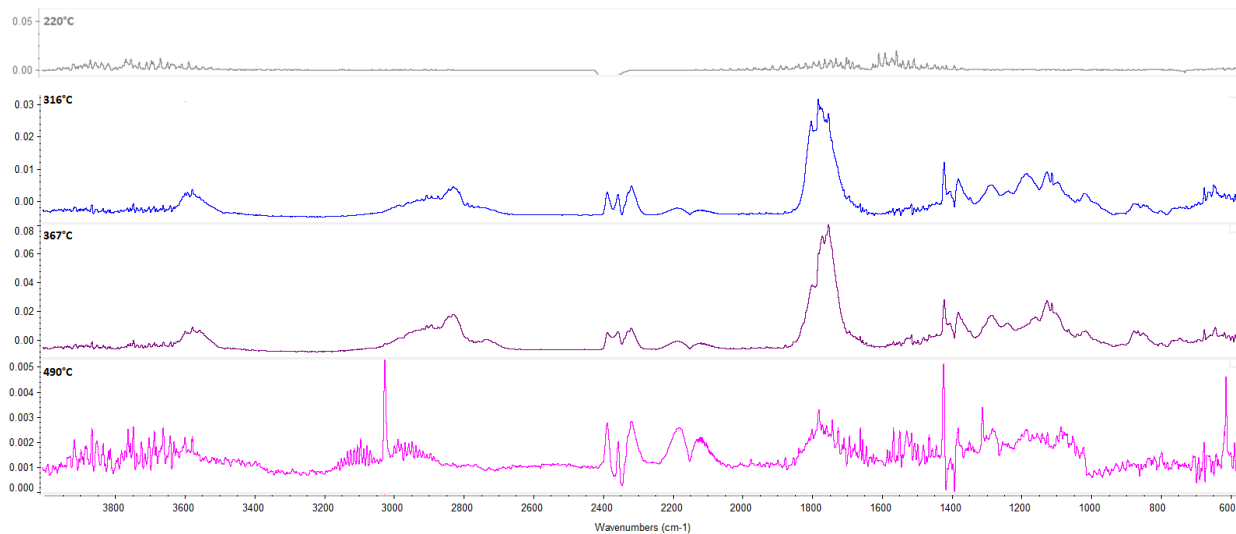


Figure 55: FTIR spectra of WF under nitrogen at 220, 316, 367, and 490°C

The initial stage of WF devolatilization is like the one observed in CLT, namely water devolatilization occurring between ambient temperature and 200°C (Figure 55). Between 200°C and 367°C , there is a significant increase in the decomposition rate of WF, accompanied by the release of volatiles (Figure 54b) and the appearance of new absorption bands in the FTIR spectra (Figure 55). As explained earlier for CLT,

this increase in volatiles can be attributed to the devolatilization of hemicellulose, cellulose and lignin [36], [95] [96], [97]. A small break in slope is observed too around 316°C, followed by a peak at 367°C. The FTIR spectra at 316°C and 367°C are superimposed with reference gases (). In both spectra, strong absorption in the range of 4000-3500 cm⁻¹ indicates the presence of water, phenols, and alcohols. Characteristic absorptions in the range of 2240-2050 cm⁻¹ indicate the presence of CO. As for CLT, CO is mainly formed from the breakage of the C=O bond and of the ether bond. Moreover, between 3000 and 2700 cm⁻¹, the absorptions are attributed to C-H stretching vibrations. The small peak at 3000 cm⁻¹ is attributed to methane, produced the same way as for CTL. Furthermore, the FTIR spectra of WF at 316°C and 367°C exhibit the presence of acids, aldehydes, ketones, or alcohols with absorption bands in the range 1400-1100 cm⁻¹ corresponding to the C-O vibration (). The C=O stretching of aldehydes, ketones and acids is found in the range 1850-1600 cm⁻¹. A notable difference between the spectra at 316°C and 367°C is observed in the region between 1215 and 1240 cm⁻¹. Specifically, at 316°C, the absorption is centered around 1160-1215 cm⁻¹, while at 367°C, it shifts to around 1145-1175 cm⁻¹. As for CLT, accurate analysis of volatiles is complex due to four overlapping chemical groups (alcohols, aldehydes, ketones, and carboxylic acids) in the same region. In addition, peaks in the range of 900 to 800 cm⁻¹ are indicative of aromatic C-C stretching, suggesting the presence of complex aromatic compounds released during lignin decomposition (cresol or guaiacol type compounds) and during cellulose and hemicellulose decomposition (furan) (see Figure 9 p46, Figure 10 p47 and Figure 11 p48).

After reaching the peak at 367°C, the dTG curve and the intensity of gas production start to decrease (Figure 54b). This can be attributed to the end of cellulose and hemicellulose devolatilization lignin [36], [95] [96], [97]. Between 394°C and 800°C, the gas production gradually decreases, indicating the end of lignin volatilization. From the FTIR spectra (Figure 55), it is observed that at a temperature of 490°C, CO, H₂O, and CH₄ are released, while the previously mentioned organic compounds are present only in trace amounts.

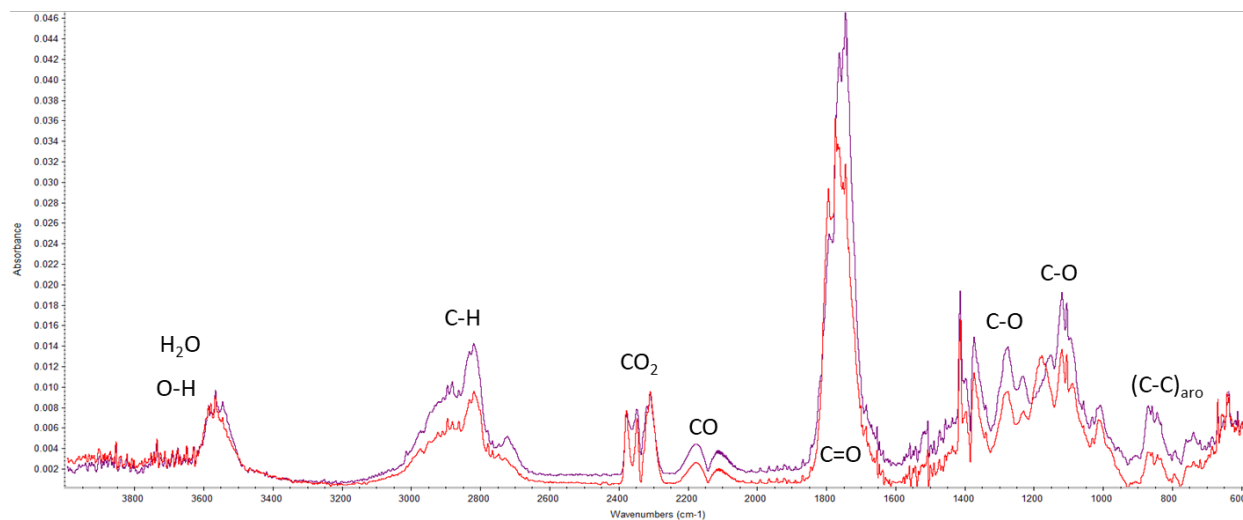


Figure 56: Superposition of the FTIR spectra of WF at 316°C (red) and at 367°C (purple)

2.1.2. Oxidative atmosphere

Under an oxygen concentration of 21%, the thermal decomposition of WF exhibits an apparent two-stage process (Figure 57a). This process occurs between 200 and 394°C, resulting in a weight loss of 89% (Table 13). The dTG curve (Figure 57b) reveals two distinct peaks: one at 340°C with a decomposition rate of 12.2%/min, and another at 480°C with a decomposition rate of 4.2%/min (Table 13). The chemigram analysis highlights four temperatures of interest (150, 340, 400 and 480 °C) and the corresponding spectra are plotted (Figure 58).

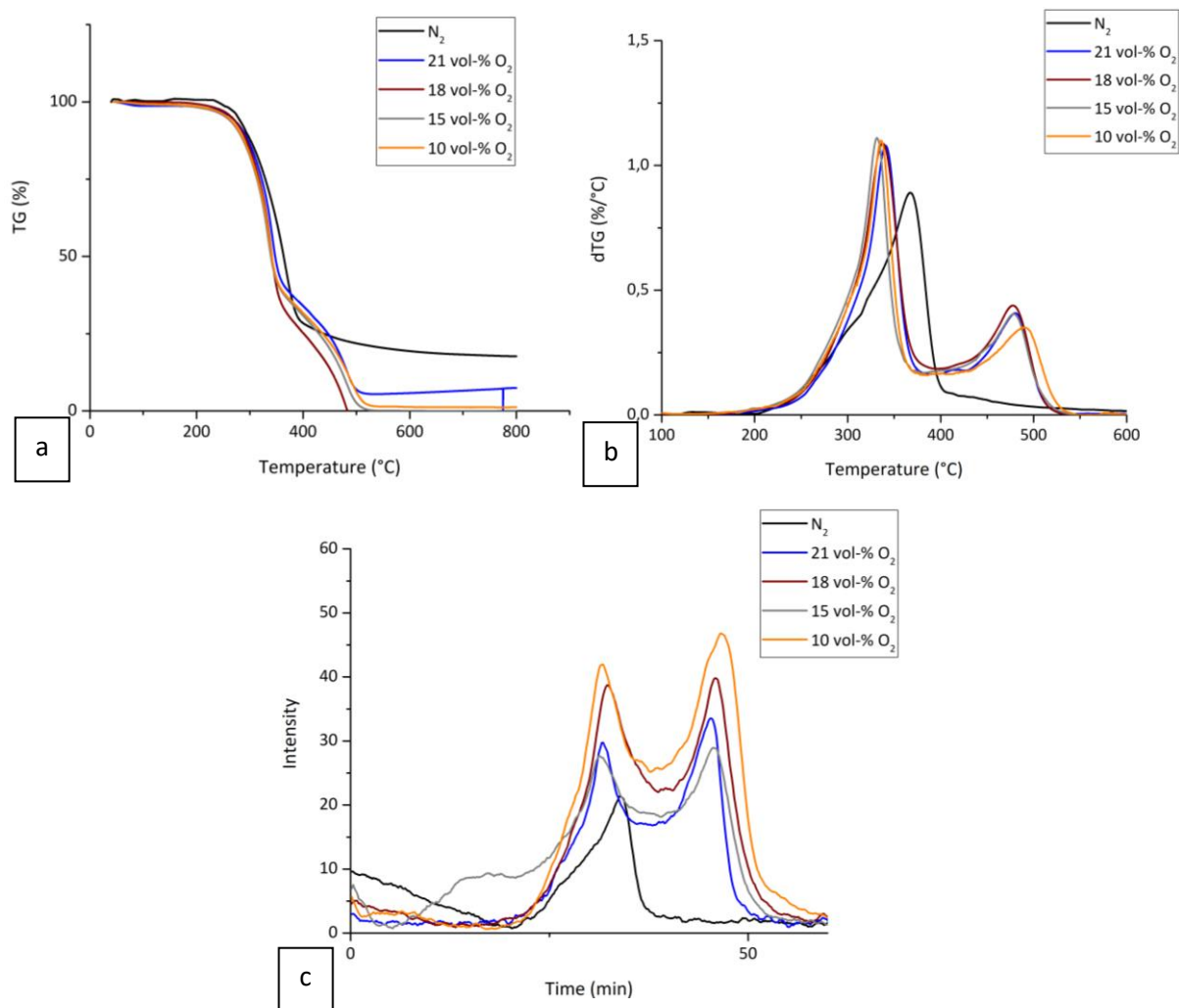


Figure 57: TGA-FTIR of WF under N₂ and different oxygen levels at 10°C/min. a. TG curves b. dTG curves c. chemigrams

Table 13: TGA parameters of WF under different oxygen concentrations

Atmosphere	T _{5wt%} (°C)	T _f (°C)	DTG _{max} (%/min)	Weight loss (%)
N ₂	276	394	10.2	73
21 vol-% O ₂	267	496	12.2	89
18 vol-% O ₂	268	493	12.8	99
15 vol-% O ₂	258	494	11.1	94
10 vol-% O ₂	261	501	11.8	92

Water devolatilization of WF is observed from ambient temperature to 200 °C (Figure 58). Then, from 200°C to 340°C, the decomposition rate rapidly increases (Figure 57b and Figure 57c) with additional

absorption bands on FTIR spectra (Figure 58). At 340°C on the FTIR spectrum, the detection of water, phenols, and alcohols is evident through the O-H vibration within the 4000-3500 cm^{-1} range. Additionally, the presence of acids, aldehydes, or ketones is indicated by the C-O vibration in the range of 1400-1100 cm^{-1} and C=O stretching within the range of 1850-1600 cm^{-1} (). Lastly, the FTIR spectrum reveals the presence of CO and CO₂, identified by absorption bands at 2240-2050 cm^{-1} and 2400-2240 cm^{-1} , respectively. In addition to deacidification reactions and carbonyl breakage, CO₂ is released from the reaction between the carbon of the residue and oxygen. As for CLT, CO also is produced from incomplete reaction between carbon and oxygen, in addition to carbonyl and ether bond breakage [26]. There is again a strong peak at 1510 cm^{-1} attributed to benzene ring skeletons in aromatic compounds [16].

Following the peak at 340°C, which indicates the end of cellulose and hemicellulose devolatilization, there is a significant drop in the dTG curve and gas production intensity. It continues until a plateau reached between 370 and 423°C (Figure 57b and Figure 57c). In this step, the main gases produced are CO, CO₂, and small amounts of water (Figure 58). The decomposition of lignin is completed and the relatively low rate of devolatilization allows oxygen to interact at the wood surface. Heterogeneous oxidation mechanisms occur within the previously formed char. Subsequently, the dTG curve and chemigram exhibit a rapid increase, culminating in a peak at 480°C. This is characterized by a secondary decrease in the TG curve (Figure 57a). The FTIR spectrum at 480°C (Figure 58) indicates the presence of CO and CO₂ suggesting the oxidation of the residual components. Following the peak at 480°C, both chemigram and dTG curve exhibit a gradual decrease (Figure 57b and Figure 57c) until reaching a value of zero between 480 and 800°C. During this stage, there is a minimal production of CO₂, CO, and water (Figure 58).

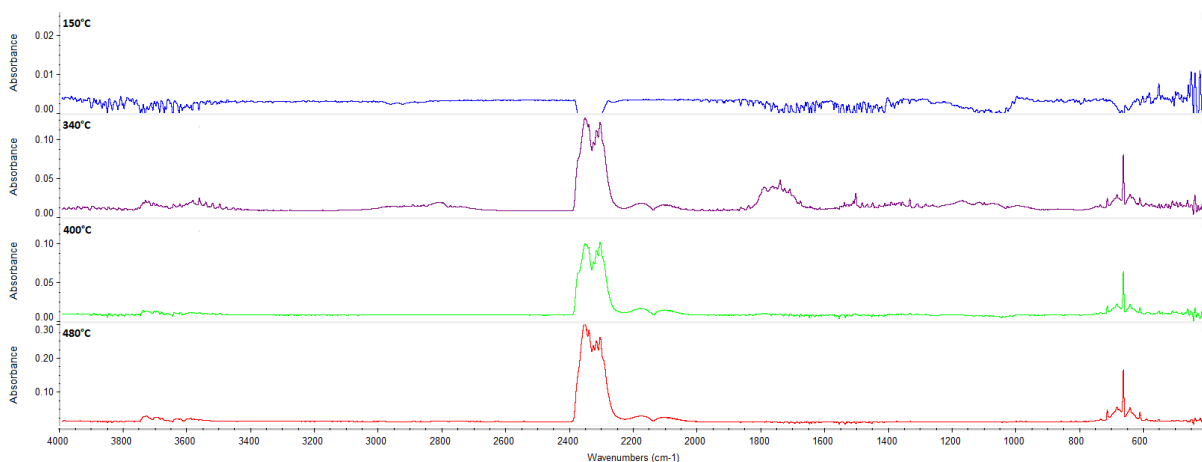


Figure 58: FTIR spectra of WF at 21% O₂ at 150, 340, 400, and 480°C

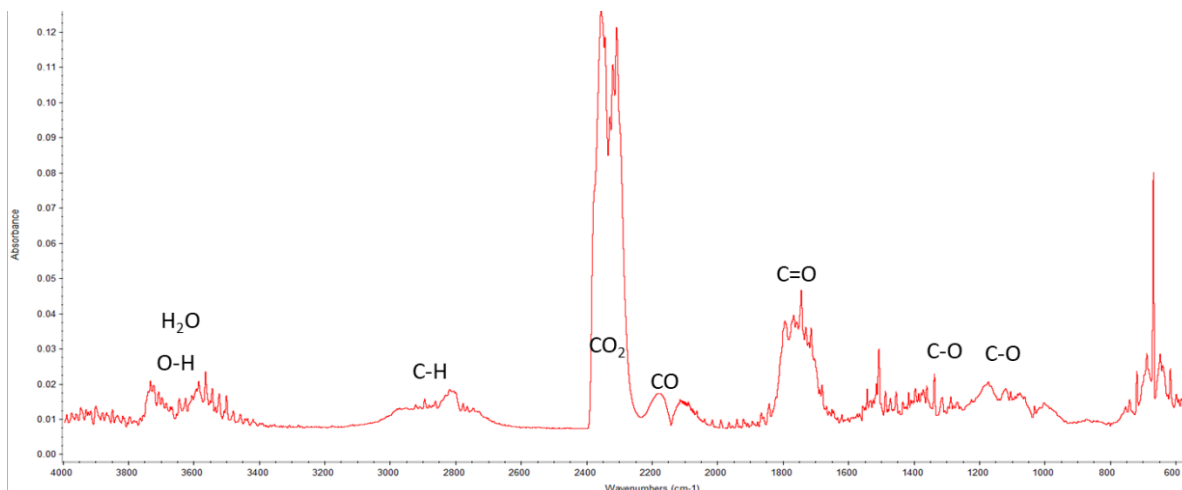


Figure 59: Superposition of the FTIR spectra of WF at 340°C

When the oxygen concentration is lowered to 18, 15, or 10 vol-% O₂, the thermal decomposition of WF still follows an apparent two-stage process (Figure 57a, Figure 57b and Figure 57c). The initial stages of thermal decomposition do not seem to be significantly affected by the oxygen concentration, as the temperatures at 5% weight loss are within the same range for all oxygen levels, with a standard deviation of 5°C (2% of the mean). However, it is worth mentioning that the experiment conducted at 18% O₂ encountered some difficulties in stabilizing the weight, which may have affected the TG curve. The second stage of decomposition exhibits slight variations between 10 vol-% O₂ and the other oxygen levels. Specifically, at 10 vol-% O₂, the decomposition process is delayed both in temperature (Figure 57b) and in time (Figure 57c). The onset of residue oxidation occurs around 423°C for all oxygen levels, but the end of the second stage occurs around 501°C at 10 vol-% O₂, which is 10 degrees higher than the mean value observed for 21, 18, and 15 vol-% O₂ (Table 13). Despite the delayed oxidation process at 10 vol-% O₂, approximately 92% of weight loss is measured for all oxygen concentrations (Table 13). Notably, no significant differences were observed in the FTIR spectra regardless of the oxygen level (Appendix p228).

2.1.3. Comparison between inert and oxidative atmospheres

The TGA-FTIR analysis of WF under nitrogen and oxygen reveals notable differences in the thermal decomposition process. Indeed, the decomposition follows a one-stage process under a nitrogen atmosphere, whereas it becomes a two-stage process under oxygen atmospheres. Moreover, the oxygen has a low influence on the onset of thermal decomposition, as indicated by the similar temperatures of 5% weight loss at the several oxygen concentrations (Table 13).

Furthermore, the gas production, mainly consisting of water, is also similar before 200°C under both nitrogen and oxygen atmospheres (Figure 60). However, the presence of oxygen accelerates the rate of decomposition, highlighted by the steeper and more pronounced slope of the first dTG peak in the oxygen curves (Figure 57b). Furthermore, in the presence of nitrogen, a distinct change in slope occurs at approximately 340°C, accompanied by a rightward shift of the absorption band within the 1150-1200 cm^{-1} range. This shift signifies a chemical change in the volatile production. This is not observed under oxygen where CO_2 , CO, H_2O , aldehydes, ketones, alcohols, acids, and aromatic compounds are released from 200 to 350°C (Figure 60). Particularly, methane is not detected in the oxygen experiments, suggesting a potential oxidation to CO_2 or CO.

Finally, from 394 to 800°C, the thermal decomposition of WF under a nitrogen atmosphere stabilizes after a significant drop in the production of CO, H_2O , CH_4 (Figure 60). In contrast, under an oxygen atmosphere, a second stage characterized by oxidation reactions of the residue occurs between 423 and 508°C, with the main gases released being CO_2 and CO (Figure 60). It is worth noting that the nitrogen experiment on WF leaves a higher residue (73%) while the mean mass loss under oxygen atmospheres is around 92%. This difference indicates that oxygen contributes to more extensive decomposition of the WF material.

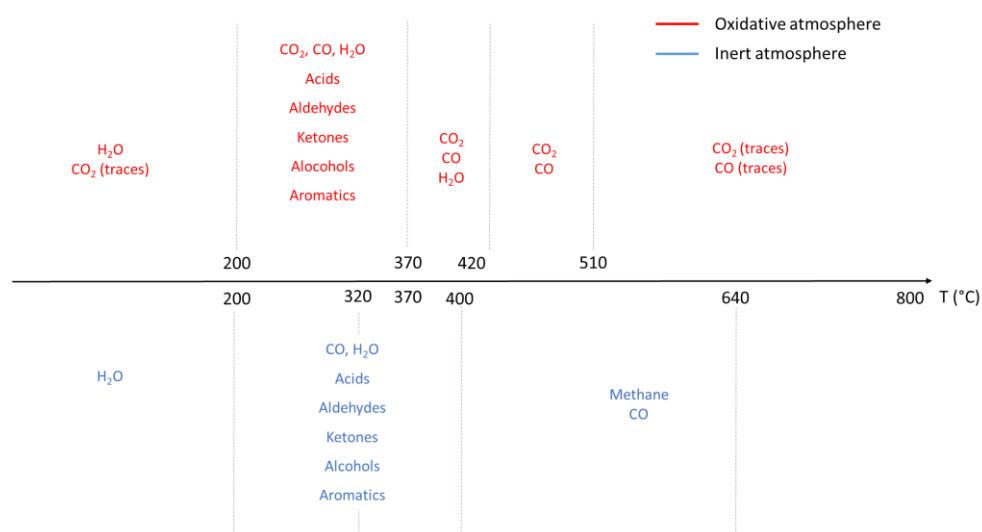


Figure 60: Gases released during the decomposition of WF under oxidative (red) and inert (blue) atmosphere as a function of temperature

Numerous organic compounds are released during the thermal decomposition of WF, which makes it hard to fully analyze the gas composition. As seen previously, aromatic compounds are possibly released but with no more information on the exact structure. Thus, PY-GC/MS analysis was carried out to examine in more detail the gaseous emissions during pyrolysis.

2.2. Characterization of wood fiber by Pyrolysis-Gas Chromatography Mass Spectroscopy

Py-GC/MS was performed on WF at a rate of 10°C/min from 40 to 800°C. The first products detected are H₂O, N₂ and CO₂ with a retention time between 25 and 45 min (Figure 61a). Between 101 and 129 min of residence, a tree of peaks is observed. Nine peaks have been potentially identified; they mainly correspond to complex aromatic structures (Table 14). The peak 2 is ascribed to butylaldehyde, which might be released from the binder of wood fiber consisted of isocyanate-based compounds. The peak 3, corresponding to 5-(Hydroxymethyl)-2-furfural, is related to hemicellulose decomposition. The peaks 4, 6, 8 and 9, are phenolic compounds ascribed to lignin decomposition, with 2-Methyl-3-Methoxyphenol and 2-Methoxy-4-vinylphenol being the most probable compounds released and identified previously on the FTIR spectra [96], [98]. The peaks 5 and 7, corresponding to 3,6-Dianhydro- α -glucopyranose and levoglucosan, are characteristic compounds of cellulose decomposition [101].

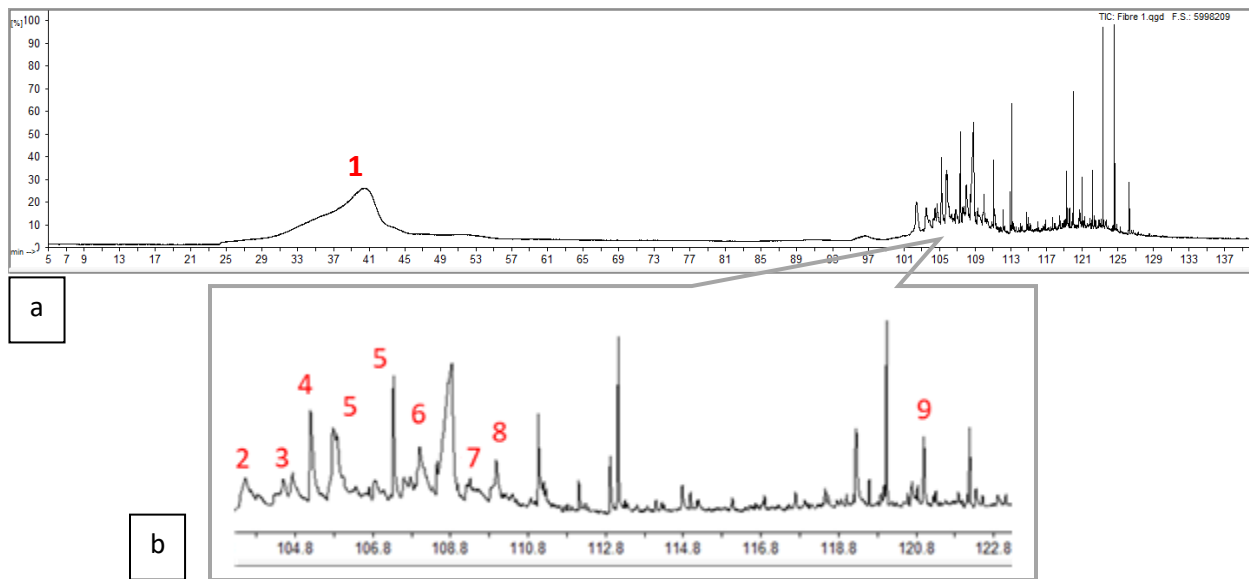

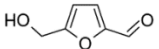
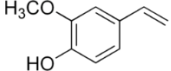
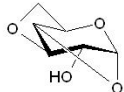
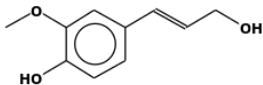
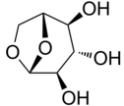
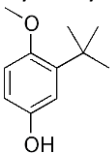
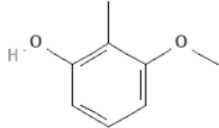


Figure 61: WF chromatogram a. full size b. zoom from 97 to 137 min

Table 14: Identification of the main decomposition products of WF

	Retention time (min)	M (g/mol)	Confidence (%)	Molecule
1	30-45	18 44	-	H ₂ O CO ₂
2	103.5	72	66	Butylaldehyde 
3	104.7	126	65	5-(Hydroxymethyl)-2-furfural 
4	105.2	150	96	2-Methoxy-4-vinylphenol (4-vinylguaiacol) 
5	105.9-107.3	144	52	3,6-Dianhydro-alpha-glucopyranose 
6	108.5	180	56	4-((1E)-3-Hydroxy-1-propenyl)-2-methoxyphenol 
7	108.0 108.8	162	48 94	Levoglucosan 
8	110.0	180	49	Butyl hydroxyanisole 
9	121.0	136	50	2-Methyl-3-Methoxyphenol 

The Py-GC/MS study enabled to identify possible aromatic structures found in the previous FTIR spectra and established the presence of characteristic products of wood pyrolysis.

Conclusion

The thermal decomposition of both Cross Laminated Timber and Wood Fiber was studied at matter scale with TGA-FTIR and Py-GC/MS experiments.

The TGA-FTIR study revealed that these two wood-based materials behave similarly regarding the gas production and the decomposition stages. Under nitrogen, the decomposition is an apparent one-stage process while under oxygen it is an apparent two-stage process with an additional reaction of oxidation of the char. The oxygen concentration does not affect the onset temperature of thermal decomposition. These findings are in agreement with previous published studies [16], [102]. Moreover, the main decomposition products in the first stage of decomposition are H₂O, CO₂, CO, aldehydes, ketones, acids, phenol type compounds and CH₄ (only under nitrogen) while H₂O, CO₂, CO are produced during the char oxidation step.

The Py-GC/MS experiments allowed an exhausting listing of pyrolysis products, especially of phenol-based products. The release of levoglucosan, 3,6-dianhydro- α -glucopyranose, 5-(hydroxymethyl)-2-furfural and 2-methoxy-4-vinylphenol was reported for both CLT and WF, which agrees with literature [26]. Differences in phenol compounds are observed between WF and CLT due to the distinct wood sources used in their production. CLT is derived from spruce while WF is made from a mixture of softwood species.

This study conducted at matter scale gives essential data for the analysis at material scale, especially for the Controlled-Atmosphere Cone Calorimeter experiments. Comparison remains to be made between the gas production at matter scale and material scale.

Chapter 4: Fire behavior, gas, and aerosol emissions of an assembly of Cross-Laminated Timber/Wood Fiber with a Controlled-Atmosphere Cone Calorimeter coupled to a Fourier Transformed Infrared spectroscopy and an Electrical Low Pressure Impactor

1. EFFECT OF OXYGEN AND HEAT FLUX ON THE FIRE BEHAVIOR, GAS AND AEROSOL PRODUCTION OF CROSS-LAMINATED TIMBER	128
1.1. EFFECT OF OXYGEN ON CROSS-LAMINATED TIMBER AT 50 kW/M ²	129
1.1.1. <i>Mass loss and heat release of Cross-Laminated Timber at 50 kW/m².....</i>	129
1.1.2. <i>Gas production of Cross-Laminated Timber at 50 kW/m².....</i>	133
1.1.3. <i>Aerosol production of Cross-Laminated Timber at 50 kW/m².....</i>	137
1.2. EFFECT OF OXYGEN ON CROSS-LAMINATED TIMBER AT 20 kW/M ²	138
1.2.1. <i>Mass loss and heat release of Cross-Laminated Timber at 20 kW/m².....</i>	138
1.2.2. <i>Gas production of Cross-Laminated Timber at 20 kW/m².....</i>	141
1.2.3. <i>Aerosol production of Cross-Laminated Timber at 20 kW/m².....</i>	142
1.3. COMPARATIVE EFFECT OF OXYGEN AND HEAT FLUX OF CROSS-LAMINATED TIMBER.....	143
1.4. CONCLUSION	147
2. EFFECT OF OXYGEN AND HEAT FLUX ON THE FIRE BEHAVIOR, GAS AND AEROSOL PRODUCTION OF WOOD FIBER.....	148
2.1. EFFECT OF OXYGEN ON WOOD FIBER AT 50 kW/M ²	148
2.1.1. <i>Mass loss and heat release of wood fiber at 50 kW/m².....</i>	148
2.1.2. <i>Gas production of wood fiber at 50 kW/m².....</i>	151
2.1.3. <i>Aerosol production of wood fiber at 50 kW/m².....</i>	153
2.2. EFFECT OF OXYGEN ON WOOD FIBER AT 20 kW/M ²	155
2.2.1. <i>Mass loss and heat release of wood fiber at 20 kW/m².....</i>	155
2.2.2. <i>Gas production of wood fiber at 20 kW/m².....</i>	157
2.2.3. <i>Aerosol production of wood fiber at 20 kW/m².....</i>	159
2.3. COMPARATIVE EFFECT OF OXYGEN AND HEAT FLUX OF WOOD FIBER	160
2.4. CONCLUSION	164
3. EFFECT OF OXYGEN ON THE FIRE BEHAVIOR, GAS AND AEROSOL PRODUCTION OF AN ASSEMBLY OF CROSS-LAMINATED TIMBER AND WOOD FIBER.....	164
3.1. EFFECT OF THE ASSEMBLY AND THE OXYGEN LEVEL AT 50 kW/M ²	165
3.1.1. <i>Fire behavior, gas production and aerosol production of the Cross-Laminated Timber/Wood Fiber assembly</i> 165	
3.1.1.1. Ignition and heat release of Cross-Laminated Timber/Wood fiber at 50 kW/m ²	165
3.1.1.2. Gas production of Cross-Laminated Timber/Wood fiber at 50 kW/m ²	168
3.1.1.3. Aerosol production of Cross-Laminated Timber/Wood fiber at 50 kW/m ²	170
3.1.2. <i>Effect of oxygen level on the CLT/WF assembly fire behavior, gas and aerosol production at 50 kW/m²</i> 172	
3.1.2.1. Ignition and heat release of the CLT/WF assembly at 50 kW/m ²	172
3.1.2.2. Gas production of the CLT/WF assembly at 50 kW/m ²	173
3.1.2.3. Aerosol production of the CLT/WF assembly at 50 kW/m ²	175
3.2. EFFECT OF THE ASSEMBLY AND THE OXYGEN LEVEL AT 20 kW/M ²	176
3.2.1. <i>Fire behavior of the assembly, gas production and aerosol production of the Cross-Laminated Timber/Wood Fiber assembly at 20 kW/m².....</i>	176

3.2.1.1.	Ignition and heat release of the CLT/WF assembly at 20 kW/m ²	176
1.1.1.1.	Gas production of the CLT/WF assembly at 20 kW/m ²	179
3.2.1.2.	Aerosol production of the CLT/WF assembly at 20 kW/m ²	182
3.2.2.	<i>Effect of oxygen level on the CLT/WF assembly fire behavior, gas and aerosol production at 20 kW/m²</i> 184	
3.2.2.1.	Ignition and heat release of CLT/WF at 20 kW/m ²	184
3.2.2.2.	Gas production of CLT/WF at 20 kW/m ²	185
3.2.2.3.	Aerosol production	187
3.3.	COMPARATIVE EFFECT OF OXYGEN AND HEAT FLUX	187
3.4.	CONCLUSION	192
4.	CONCLUSION	193

This chapter focuses on the use of the Controlled-Atmosphere Cone Calorimeter (CACC) coupled to a Fourier-Transform Infrared spectroscopy (FTIR) and an Electrical Low Pressure Impactor (ELPI). As previously described in the Chapter 2 (section 4.2 p80), this bench allows for studying the reaction to fire, gas and aerosol emissions of materials under various fire scenarios. Especially, this study is conducted on Cross-Laminated Timber (CLT), Wood Fiber (WF) and the assembly of CLT/WF at two different heat fluxes (50 and 20 kW/m²) and four oxygen concentrations (21, 18, 15 and 10 vol-% O₂) to assess a wide range of fire conditions (ISO 19706 [11]). These various settings will enable having a comprehensive understanding of how CLT, WF and CLT/WF are affected by the oxygen concentration.

First, the effect of oxygen and heat flux on the reaction to fire, gas, and aerosol production of CLT is studied. Then, the same study is done on WF. Finally, before assessing the effect of oxygen on the assembly of CLT/WF, the effect of the combination itself is investigated. For the whole study, the time to ignition is defined as t_i , the time to flameout as t_{out} , the peak of HRR as pHRR and the peak of MLR as pMLR.

1. Effect of oxygen and heat flux on the fire behavior, gas, and aerosol production of Cross-Laminated Timber

The reaction to fire of Cross-Laminated Timber strongly depends on the environment conditions such as the oxygen concentration and the heat flux. Firstly, the impact of oxygen on the fire reaction, gas, and aerosol emissions of CLT is discussed at 50 kW/m², followed by a description of these effects at 20 kW/m². These two heat fluxes are chosen to study the potential differences between a well-ventilated fire and smoldering combustion. Towards the conclusion, a comparative analysis of the influence of both oxygen concentration and heat flux is conducted.

1.1. Effect of oxygen on Cross-Laminated Timber at 50 kW/m²

At 50 kW/m², the investigation of the oxygen's impact begins with a focus on the mass loss and heat release rates. Then, a comprehensive analysis of gas and aerosol emissions is presented. All the replica curves are gathered in the Appendix p222.

1.1.1. Mass loss and heat release of Cross-Laminated Timber at 50 kW/m²

The influence of oxygen level on the mass loss and the mass loss rate (Figure 62) as well as on the heat release rate (Figure 63) at 50 kW/m² is studied. Before studying the effects of oxygen depletion on the fire behavior of CLT, a description of the steps of its thermal decomposition is provided.

First, between 0 and 19s, as the temperature at the surface of CLT increases, the sample starts to degrade. The free water contained in wood (around 11%) evaporates. Simultaneously, the chemical bonds of wood polymer chains (cellulose, hemicellulose and lignin) start to break [28], [33]. Consequently, tars and decomposition gases are produced. As the gases leave the solid, they encounter the oxygen present in the atmosphere. Concurrently, oxygen may diffuse into the solid and oxidize the wood effluents. Triggered by the igniter, the mixture ignites at 19s and the flame spreads onto the whole surface of the sample.

It results, in a second step, in a fast increase in the MLR and the HRR, which reach maxima at 60s (Figure 62a and Figure 63). A carbonaceous layer is formed on top of the wood, which reduces the heat transfers between the wood surface and the pyrolysis front. This carbonaceous layer creates then a thermal insulation [103]. As a result, pyrolysis of wood slows down and the MLR and HRR decrease.

From 200s, a small increase in MLR occurs. To understand this behavior, five thermocouples were embedded in CLT at 2, 10, 20, 30 and 38 mm from the exposed surface. When the MLR increased, the thermocouple inserted at 10 mm from the surface reached a 100 °C plateau (see Appendix p228). This temperature is assigned to water evolution as CLT undergoes dehydration reactions [104].

At longer times ($t > 700$ s), the sample reaches a thermal steady state, which is characterized by quasi-constant MLR and HRR (Figure 62a and Figure 63) and a constant thickness of char layer [54].

In a next step, second peaks of MLR and HRR occur around 2500s. At this peak, the temperature measured at 38 mm from the surface of CLT is 320°C. It means that the pyrolysis front reaches the back of the sample and thus the ceramic holder induces a thermal feedback (accumulation of heat at the bottom) that

accelerates the decomposition [103]. It should be noted that only the samples at 21 vol-% O₂ lasted 3200s because it was not what we focused on for the other oxygen levels.

Finally, flame extinguishes as the fuel contained in the solid phase diminishes, which leads to the decrease in the MLR and the. Smoldering will then take place in the remaining char (visual observation).

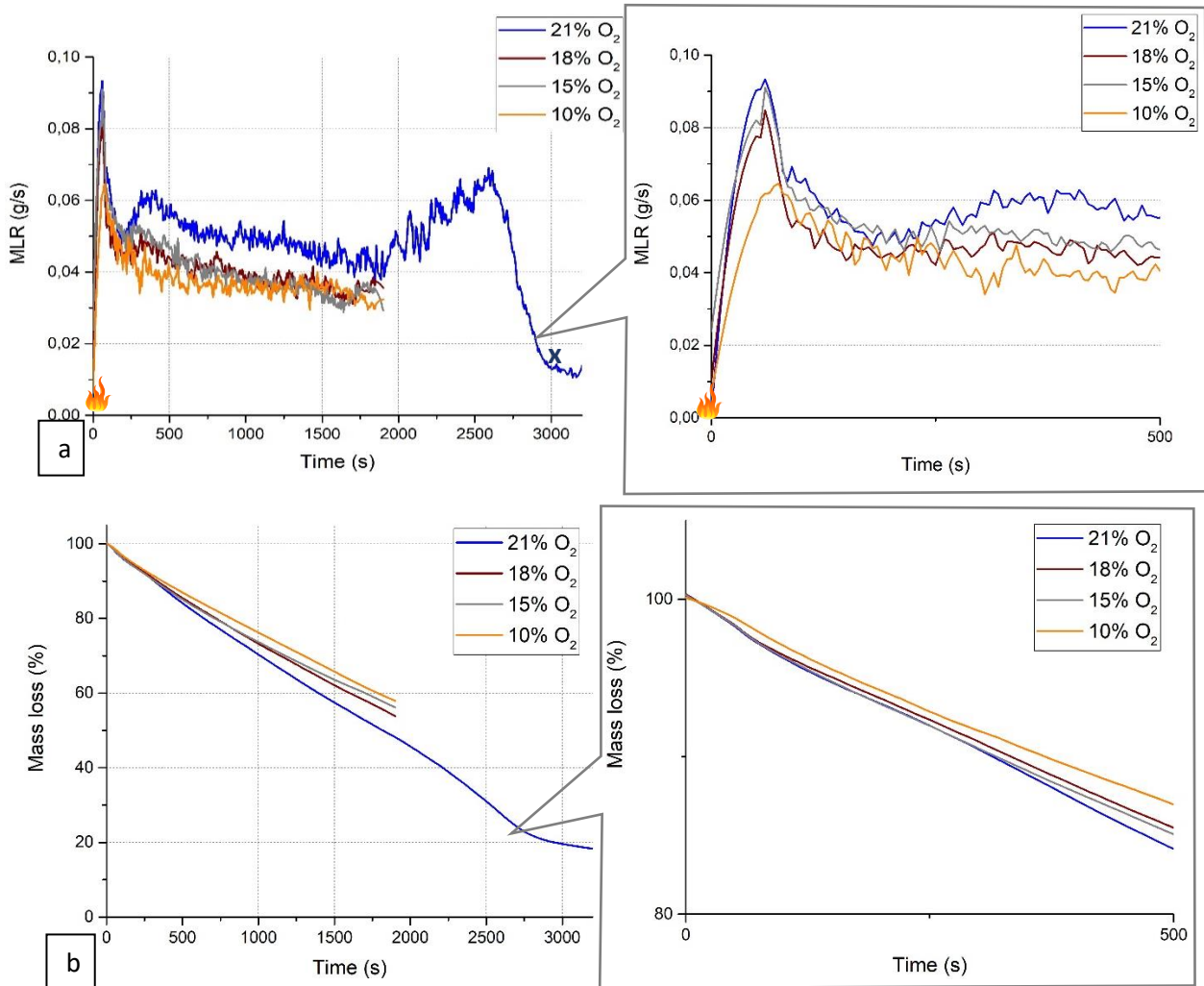


Figure 62: Effect of oxygen concentration on CLT at 50 kW/m²: a. MLR; b. mass loss

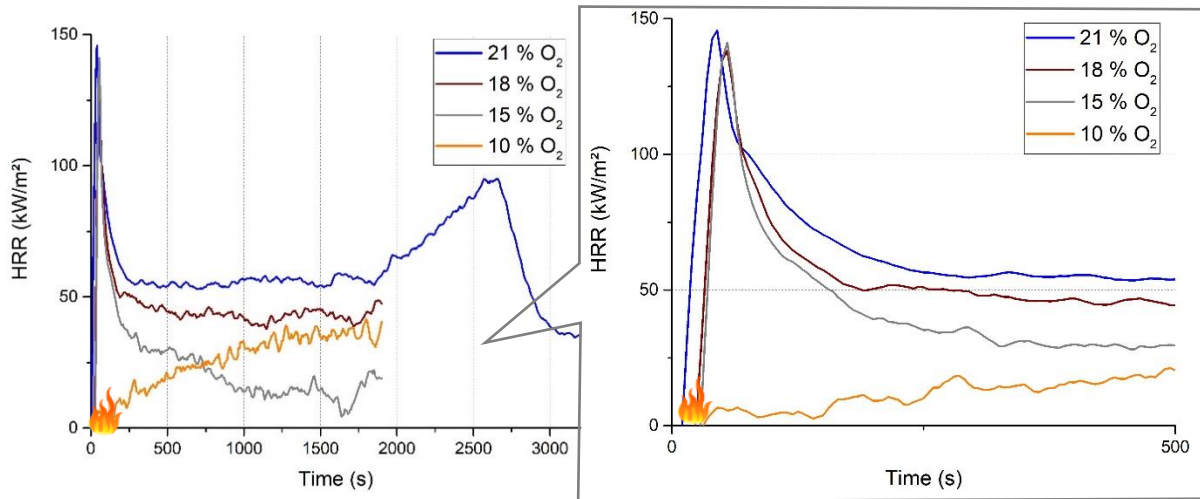


Figure 63: Effect of oxygen concentration on CLT at 50 kW/m² on the HRR

Table 15: Influence of oxygen on the fire parameters of CLT at 50 kW/m²

Oxygen concentration (vol-%)	t _i (s)	Standard deviation (s)	pMLR (g/s)	Standard deviation (g/s)	pHRR (kW/m ²)	Standard deviation (kW/m ²)
21	19	1.5	0.093	0.004	143	12
18	18	1.5	0.085	0.009	138	8
15	21	0.7	0.091	0.010	141	9
10	-	-	0.065	0.019	41	13

However, the oxygen concentration modifies the previous description of the thermal decomposition of CLT. Initially, the decomposition exhibits a flaming behavior at 21, 18 and 15 vol-% O₂ but switches to a non-flaming state at 10 vol-% O₂. To have a reaction of combustion, the mixture fuel/oxidant needs to reach the lean flammability limit. If there is enough energy produced by the reaction to overcome heat losses, the flame will spread on the whole surface of the sample [31]. Thus, at 50 kW/m², the oxygen concentration affects the burning behavior of CLT with a lean flammability limit comprised between 15 and 10 vol-% O₂.

Specifically, for the flaming samples (21, 18 and 15 vol-% O₂), the time to ignition, pMLR and pHRR are all in the same range considering the standard deviations, whatever the oxygen level (Table 15). Thus, at the early stage of the test, the heat received at the surface of CLT mainly governs the decomposition of the sample. In the previous TGA tests (see 0 p108), the temperature at which 5% weight loss was not

influenced by oxygen concentration. This finding agrees with the observation that the times to ignition are not influenced by oxygen decrease.

In the other hand, after 105s, the mass loss of the specimen at 21 vol-% O₂ accelerates while the mass losses at 18 and 15 vol-% O₂ remain close (less than 0.7% of difference) (Figure 62b). After 1100s, the same observations are made at 18 vol-% O₂, whose mass loss becomes slightly faster than at 15 vol-% O₂ (Figure 62b). In fact, oxygen decrease leads to a lower oxygen availability for the reaction of combustion. As a result, less heat is produced, which reduces the flame temperature and thus the flame thermal feedback to the surface of the solid [54]. Consequently, as less heat is transferred to the pyrolysis front with decreasing oxygen, the decomposition rate of wood is slower [33]. This is also evidenced by the amount of CLT residue being lower at 21 vol-% O₂ than at 15 vol-% O₂ after 32 min of test (Figure 62b). Therefore, at 50 kW/m², high oxygen concentrations lead to faster kinetics of decomposition.

Moreover, the HRR values reached after the peak of ignition of CLT are affected by oxygen concentration (Figure 63). Indeed, there is a 27% reduction in the HRR values around 250s between 21 and 15 vol-% O₂. It is worth noting that the steady-state reached after ignition is related to the thickness of the char layer [31]. Or, as explained above, a reduction in oxygen concentration results in the formation of a thicker char layer, which in turn diminishes the heat transfer to the pyrolysis front. To go further at 15 vol-% O₂, from 500s, the HRR drops to 12 kW/m², and small flames are located on the edges of the specimen at the end of the test. This can be attributed to the decrease in flame intensity as oxygen levels decrease. As expected, at 50 kW/m², low oxygen concentrations lead to lower HRR values after ignition.

For the non-flaming sample (10 vol-% O₂), the MLR curve has the same shape as other oxygen levels (Figure 62a) but the pMLR is decreased by 43% compared to the pMLR at 21% of O₂ (Figure 62a). Indeed, while the heat flux is high enough for sample decomposition, the limited oxygen supply prevents flaming combustion, which otherwise would enhance the decomposition rate. As a result, the MLR slows down as char is forming (Table 15). However, as heat increases at the surface of the char, smoldering occurs with a steady HRR at 40 kW/m² from 750s.

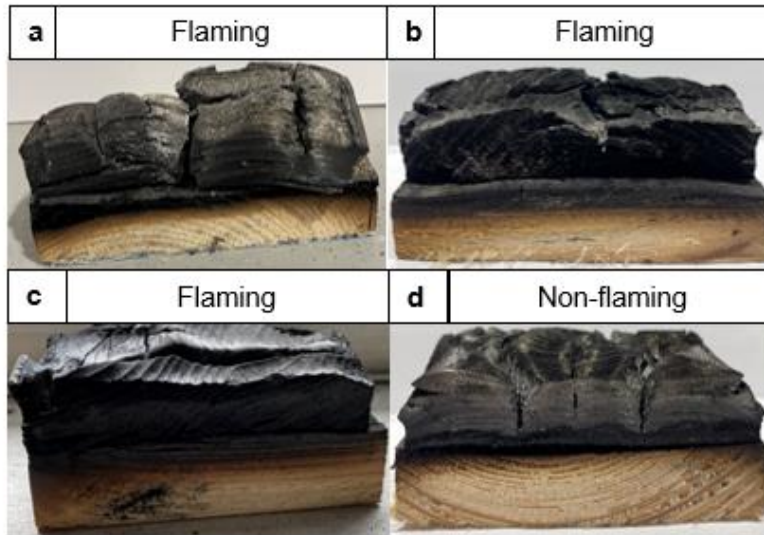


Figure 64: Sliced CLT after 32 min of test at 50 kW/m² at a. 21 vol-% O₂, b. 18 vol-% O₂, c. 15 vol-% O₂ and d. 10 vol-% O₂

Overall, two behaviors are observed at 50 kW/m² according to the oxygen concentration: flaming at 21, 18 and 15 vol-% O₂ and non-flaming at 10 vol-% O₂. For the flaming specimens, the ignition period is not affected by oxygen depletion as the pMLR, time to ignition and pHRR are similar whatever the oxygen level. However, the decrease in oxygen leads to slowest decomposition and heat release rates after char formation. For the non-flaming combustion (10 vol-% O₂), the HRR and MLR are significantly lower than for flaming samples.

1.1.2. Gas production of Cross-Laminated Timber at 50 kW/m²

In addition to its impact on the fire parameters of CLT, the oxygen concentration also plays a significant role in the gas production. The composition and quantity of gaseous products emitted are tied to the oxygen content.

Wood combustion is a multi-component complex process as it is composed of three polymers: cellulose, hemicellulose, and lignin. As described in the Chapter 1 (section 3.2.1 p45), thermal decomposition of wood starts with the evaporation of water by dehydration reactions. Then, different chemical bonds within the polymers are broken following either depolymerization (breaking of the bonds between the monomer units of the wood polymers), fragmentation (linkage of covalent bonds of polymers) and/or char formation. This results in the release of volatile compounds and rearrangement reactions within the wood matrix. Some of the volatiles produced are unstable and may undergo secondary reactions, known as

cracking (breaking of chemical bonds within the volatile compounds) or recombination (combination of volatiles compounds) [26].

More precisely, for the flaming specimens (21, 18 and 15 vol-% O₂), many condensable organic compounds are identifiable on the FTIR spectra in the beginning of thermal exposure. The main compounds released are water, carbon dioxide, carbon monoxide, formaldehyde, methanol, formic acid, and phenol type compounds (Appendix 8 p229). The identification of these gases is in agreement with the literature [26], [104] (Table 16), which generally ascribe their formation to fragmentation and/or breaking of chemical groups of cellulose, hemicellulose and lignin. These gases are also consistent with results of the TGA-FTIR tests carried out under oxidative atmospheres (section 0 p108). More precisely, the phenol type compounds may be ascribed to 2-methoxy-4-methylphenol and 2-methoxy-4-vinylphenol, as observed with Py-GC/MS studies (section 1.2 p113). Quantitatively, a peak in formaldehyde production (up to 88 ppm) (Figure 65a) before ignition attests for the decomposition of wood entities. This peak increases with oxygen decrease, as less oxygen is available to oxidize chemical bonds.

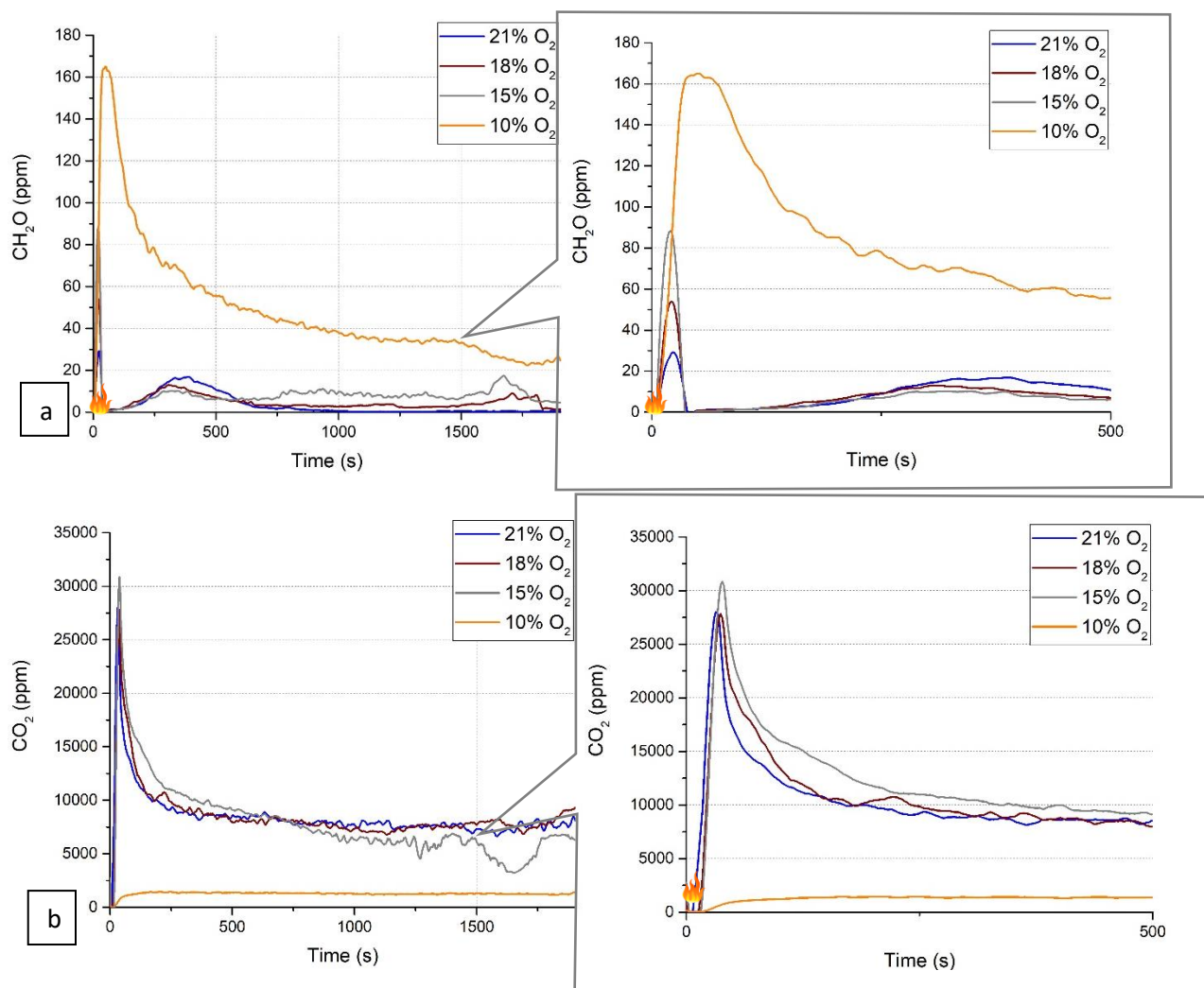
Table 16: Organic compounds detected in FTIR analysis and their possible way of formation

Organic compound	Possible way of formation [26]
Formaldehyde (CH ₂ O)	- Fragmentation of C-C bond linked to hydroxyl groups (lignin)
Methanol (CH ₃ OH)	- Fragmentation of methoxy groups (hemicellulose and lignin)
Formic acid (HCOOH)	- Rupture of carboxylic acid functions (hemicellulose)
Acetic acid (H ₃ CCOOH)	- Fragmentation of acetic substituents (hemicellulose) - Reaction of C-C bonds within and between alkyl chains (lignin) - Breaking of glycosidic linkages (cellulose)
Phenol compounds	- Breaking of ether bonds between monomers units (lignin) - Reaction of C-C bonds within and between alkyl chains (lignin)

Then, the hot gaseous products generated during the thermal exposure of CLT combine with oxygen and undergo oxidation, ultimately resulting in ignition. Consequently, the organic compounds are no longer detectable in the FTIR spectra, while there is a significant increase in the production of CO₂. At ignition, the CO₂ emission peaks around 30000 ppm for the three oxygen levels and then reaches a steady state (Figure 65b). The high quantity of CO₂ released at ignition is due to a rapid depolymerization of wood units that gives unstable intermediaries. These intermediaries contain carboxyl and carbonyl groups that

undergo fragmentation [26], as those observed on the FTIR spectra previously mentioned (formic acid and formaldehyde).

Increases in CO are observed for all flaming specimens at ignition and from 200 to 600s because of decomposition reactions (Figure 65c). However, it is worth noting that the emissions in CO are higher at 15 vol-% O₂, especially as there is a noticeable rise in CO production from 750s. Similarly, from 1700s and at both 18 and 15 vol-% O₂, a peak in CO emission occurs. These observations suggest that the lack of oxygen shifts the reaction of combustion towards incompleteness. This is corroborated by a CO/CO₂ ratio greater than 0.05 and less intense flames located on the edges of the specimen. Additionally, an increase in CH₄ (Figure 65d), which is released from demethylation reactions of the remaining methyl (-CH₃) substituents of the residue, occurs at the same time and thus argue in favor of the combustion reaction being below stoichiometry. Thus, the decrease in oxygen leads to incomplete reactions of combustion with an increase in CO and CH₄.



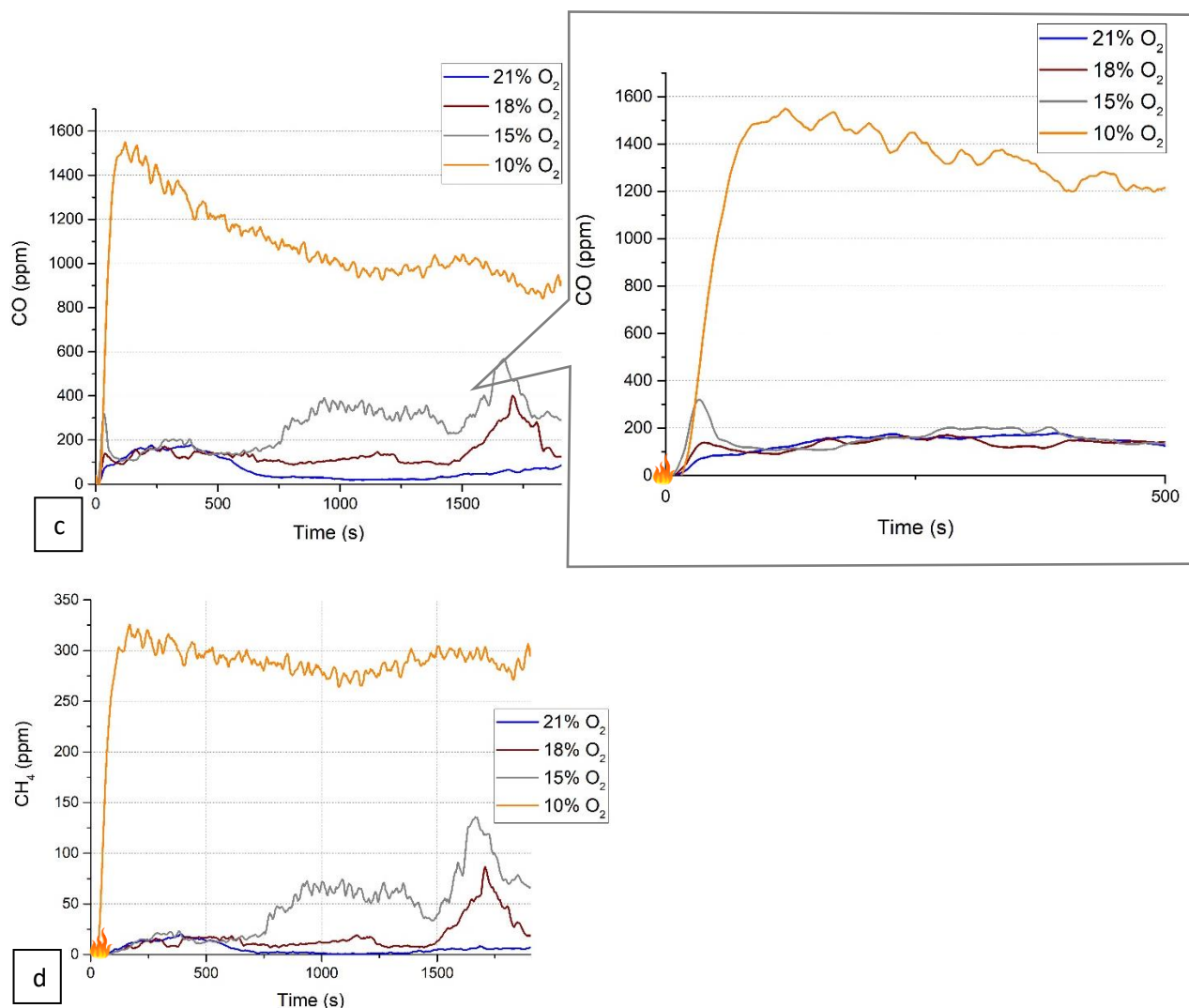


Figure 65: Influence of the oxygen level on the gaseous emissions of CLT at 50 kW/m²: a. CH₂O, b. CO₂; c. CO and d. CH₄

For the non-flaming specimen (10 vol-% O₂), in the beginning of thermal exposure, water, carbon dioxide, carbon monoxide, methane, formaldehyde, methanol, formic acid and phenol type compounds are identifiable on the FTIR spectra (Appendix 8 p229). Moreover, a high and broad peak of formaldehyde is produced (Figure 65a) as wood decomposes.

Then, a strong and broad peak of CO production follows it while the CO₂ production is very low, with a CO/CO₂ ratio of 1.37. Indeed, there is not enough oxygen to oxidize the CO produced into CO₂. Thus, the production of unburnt hydrocarbon species is promoted, with a high production of methane throughout the experiment (Figure 65d) while a peak of ethene (23 ppm) around 120s is detected and is followed by a peak of propene (15 ppm). Thus, non-flaming combustion promotes the emission of aldehydes, carbon monoxide, methane, and alkenes.

For flaming specimens (21, 18 and 15 vol-% O₂), oxygen decrease favors incomplete combustion at the end of the test with an increase in CO and CH₄ production. For non-flaming conditions, smoldering promotes the production of aldehyde and non-oxidized compounds. Therefore, the production of hazardous gases is more pronounced at lower oxygen levels and during non-flaming combustion.

1.1.3. Aerosol production of Cross-Laminated Timber at 50 kW/m²

To provide a comprehensive characterization of the gas phase, the study also investigates the impact of oxygen level on the aerosol size distribution.

At ignition, at 21 and 18 vol-% O₂, the distribution size of aerosols is multimodal and centered on the modes 0.267, 0.173 and 0.407 μm. The distribution at 15 vol-% O₂ is different with a distribution centered on 0.173, 0.267 and 0.109 μm (Figure 66a). These distributions relate to an accumulation mode of aerosols (0.1-1 μm), which corresponds to the agglomeration and growth of particles [105]. The concentration of aerosols in these modes is the highest at 15 vol-% O₂ but the orders of magnitude are close. Then, the multimodal distribution is crushed by a great increase in the mode 0.03 μm (Figure 66b). Consequently, the distribution becomes monomodal and centered on the mode 0.03 μm. This corresponds to a nucleation mode (diameter inferior to 0.1 μm), signifying the formation of fresh aerosols. This may be due to the nucleation of volatiles particles as the effluent mixture cools down after ignition. Indeed, vaporized gases condensed and became particles having very small size [36] [37] [105].

At 10 vol-% O₂ (non-flaming), the distribution is monomodal and centered on the mode 0.03 μm (Figure 66a). A multimodal distribution size of aerosols centered on the modes 0.267 and 0.173 μm is also observed. It might be due to the fast-solid decomposition rate that leads to the formation of various particle sizes. Compared to the flaming specimens, the concentration in the mode 0.03 μm is slightly higher (Figure 66b). In some studies, the lack of oxygen is shown to increase the number of particles. Indeed, with less oxygen available, the number of unburnt particles increases [43], [108].

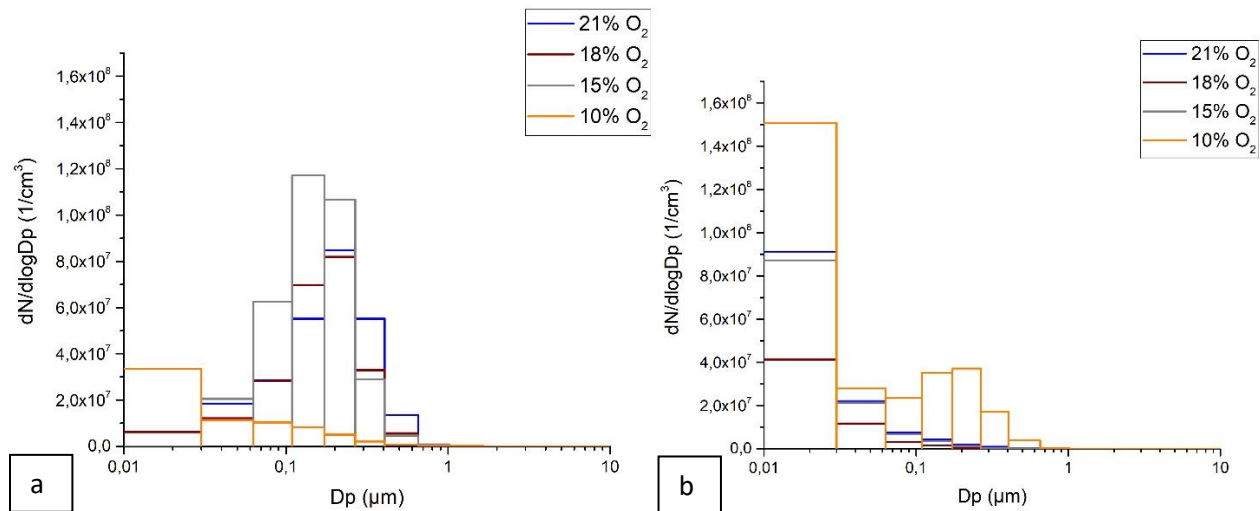


Figure 66: Distribution size of aerosols of CLT at 50 kW/m² at: a. ti, b. 1500s

At 21 and 18 vol-% O₂, a multimodal distribution centered on the modes 0.267, 0.173 and 0.407 µm is observed at ignition while at 15 vol-% O₂ smaller particles (0.173, 0.267 and 0.109 µm) are produced. For all flaming specimens, the multimodal distribution is replaced by a monomodal distribution centered on the mode 0.03 µm. For the non-flaming specimen, the distribution is monomodal centered on the mode 0.03 µm. Globally, the decrease in oxygen seems to produce smaller particles.

The influence of oxygen on the reaction to fire, the gas, and the aerosol production of CLT was fully assessed at 50 kW/m². It is advisable to investigate the influence of oxygen under less severe thermal conditions to determine whether similar behaviors persist.

1.2. Effect of oxygen on Cross-Laminated Timber at 20 kW/m²

At 20 kW/m², the influence of oxygen is first assessed on the mass loss and heat release rates before investigating the gas and aerosol emissions. All the replica curves are gathered in the Appendix p232.

1.2.1. Mass loss and heat release of Cross-Laminated Timber at 20 kW/m²

At the beginning of the thermal exposure, the evolution of the remaining mass as a function of time (Figure 67a) is very slow and similar whatever the oxygen concentration.

However, around 550s at 21 vol-% O₂, and around 1042s at 18 vol-% O₂, the samples ignite leading to a drop in mass fraction. Simultaneously, the MLRs (Figure 67b) and HRRs (Figure 68) reach a peak. More precisely, from 18 to 21 vol-% O₂, the time to ignition more than doubles while the pHRR and pMLR are decreased by 47 and 33% respectively (Table 17). Therefore, as observed in the literature [37] [52], oxygen

decrease leads to a delay in ignition, along with a reduction in the flame's temperature because of the limited availability of oxygen to maintain the combustion [39]. This decrease in flame temperature, in turn, results in reduced thermal feedback to the surface of CLT, affecting mass loss and heat release rates at ignition.

In the end, the samples flame out to reach a steady state around 0.25 g/s in MLR and 20 kW/m² in HRR. Furthermore, it is worth noting that the amount of CLT residue after 32 min of test is 68% at 21 vol-% O₂ whereas it increases to 77% at 18 vol-% O₂ (Figure 69). Higher oxygen content leads to increased carbonization of the CLT thickness. Thus, the pyrolysis front moves more rapidly through the thickness of the wood. This underlines that heat transfer is enhanced due to the presence of a less protective char layer.

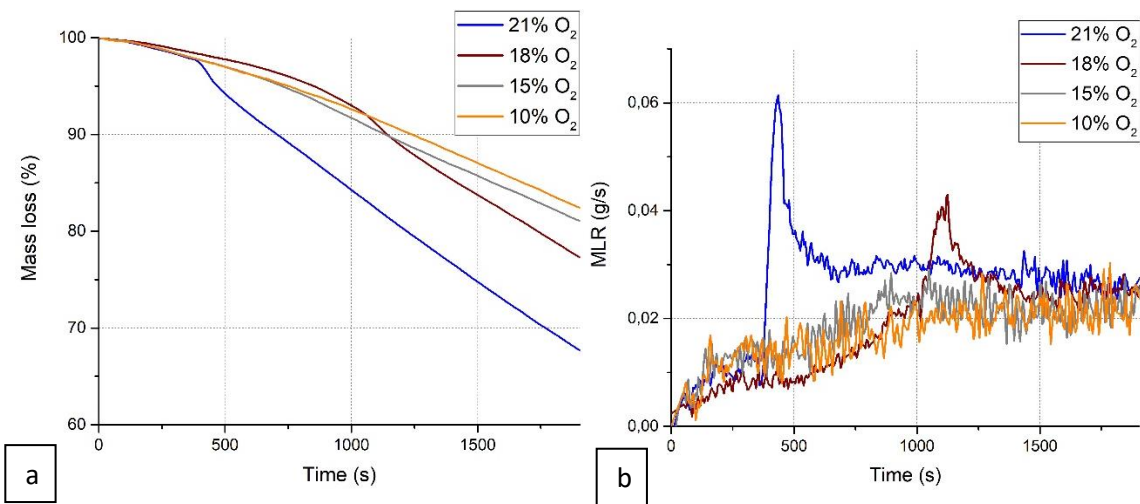


Figure 67: Effect of oxygen concentration on CLT at 20 kW/m²: a. mass loss; b. MLR

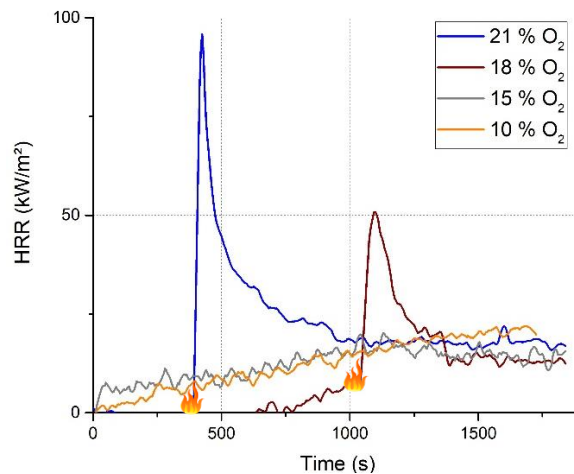


Figure 68: Effect of oxygen concentration on the HRR of CLT at 20kW/m²

Table 17: Influence of oxygen on the fire parameters of CLT at 20kW/m²

Oxygen concentration (%)	t _i (s)	Standard deviation (s)	pMLR (g/s)	Standard deviation (g/s)	pHRR (kW/m ²)	Standard deviation (kW/m ²)
21	400	105	0.061	0.003	96	4
18	1042	257	0.041	0.021	51	7
15	-	-	0.023	0.034	20	4
10	-	-	0.024	0.022	22	13

At 15 and 10 vol-% O₂, the thermal decomposition of CLT occurs without flames. The mass losses (Figure 67a) are similar until 700s where the mass loss at 15 vol-% O₂ slightly increases. The MLR and HRR curves follow a slow increase in the beginning and stabilize at values around 0.2 g/s in MLR (Figure 67b) and 20 kW/m² in HRR (Figure 68). The amount of CLT residue after 32 min is 81% at 15 vol-% O₂ and 82% at 10 vol-% O₂ (Figure 69c and Figure 69d). At these low oxygen concentrations and under 20 kW/m², the concentration of oxygen does not seem to have a significant impact on the decomposition rate of the CLT.

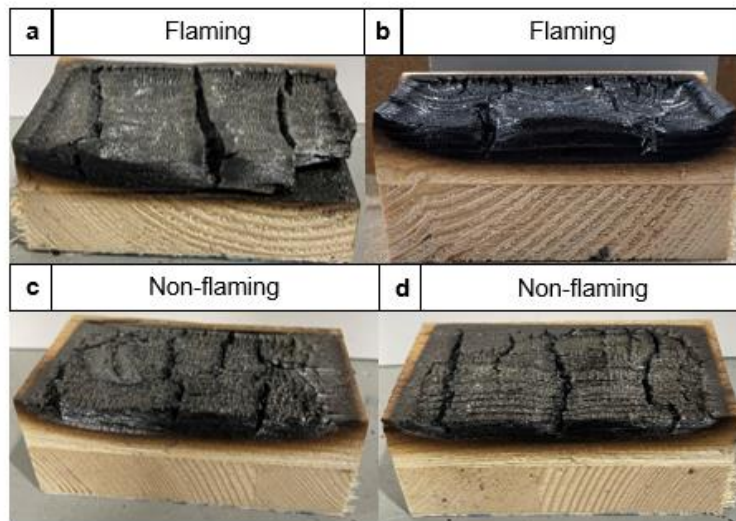


Figure 69: Sliced CLT after 32 min of test at 20 kW/m² at a. 21 vol-% O₂, b. 18 vol-% O₂, c. 15 vol-% O₂ and d. 10 vol-% O₂

In summary, at 20 kW/m², two behaviors are observed according to the oxygen concentration: flaming at 21 and 18 vol-% O₂ and non-flaming at 15 and 10 vol-% O₂. In the case of flaming combustion, a decrease in oxygen concentration leads to a delayed ignition and a reduction in heat release and mass loss rates at

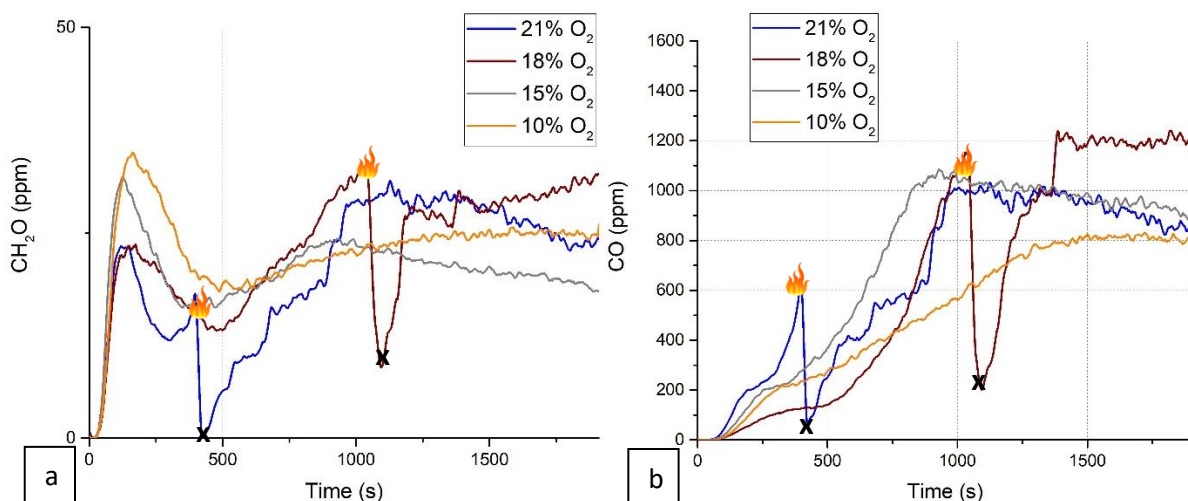
ignition. When the combustion is non-flaming, the mass loss and heat release rates are poorly affected by the oxygen level.

1.2.2. Gas production of Cross-Laminated Timber at 20 kW/m²

For the flaming specimens (21 and 18 vol-% O₂), in the first events of thermal decomposition, the compounds identifiable on the FTIR spectra are water, carbon dioxide, carbon monoxide, formaldehyde, methanol and formic acid (Appendix 10 p237).

Before 200s, a peak of formaldehyde occurs as CLT thermally decomposes at 21 vol-% (Figure 70a). Then, from 300s, another peak of formaldehyde is reached as well as one of CO and CH₄ (Figure 70b and Figure 70c), which may be ascribed to depolymerization reactions. At 400s, the sample ignites and a peak in CO₂ occurs (Figure 70d). The CO₂ concentration rapidly decreases until the sample flames out. As a result, peaks of CH₂O, CO and CH₄ arise at 1050s. Similarly, at 18 vol-% O₂, the second peak of formaldehyde (Figure 70a) as well as these of CO and CH₄ are reached at 1035s (Figure 70b and Figure 70c). CLT ignites at 1042s with a peak of CO₂ emission and then flames out at 1160s with an increase in CH₂O, CO and CH₄. Therefore, the gaseous emissions are similar at 18 vol-% O₂ but oxygen reduction leads to delayed and longer production phases.

In general, for both conditions, the CO/CO₂ ratio is greater than 0.05 during the whole test (incomplete combustion). Moreover, the production of carbon dioxide at ignition is decreased by 41% from 21 to 18 vol-% O₂ while the production of CO doubles, and the production of CH₄ triples from 21 to 18 vol-% O₂. Thus, a slow kinetic of decomposition coupled to a reduced oxygen availability, favors the production of CO and CH₄.



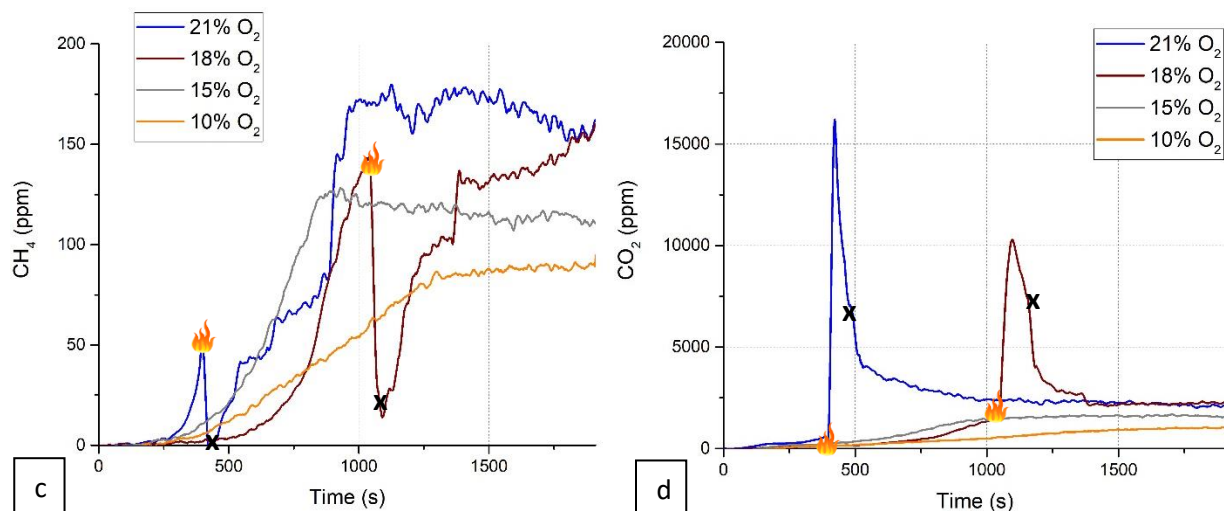


Figure 70: Influence of the oxygen level the gaseous emissions of CLT at 20 kW/m²: a. CH₂O; b. CO; c.CH₄ and d. CO₂. (x is for flameout)

For non-flaming combustion (15 and 10 vol-% O₂), FTIR analysis reveal that the organic compounds produced are the same as for the flaming specimens and that they are produced during the whole test (Appendix 10 p237). At the beginning of the test, before 250s, a peak of formaldehyde arises (Figure 70a) as CLT decomposes and then the production drops. In the meantime, the production of CO (Figure 70b) and CH₄ (Figure 70c) significantly increases as wood is carbonizing. At 15 vol-% O₂, maxima in CO and CH₄ productions are reached at 935s while they are reached at 1500s at 10 vol-% O₂. Therefore, as observed with flaming specimens, the lack of oxygen alters the kinetics of CO and CH₄ production. Moreover, the production in CO and CH₄ are decreased by 20% and 36% respectively from 15 to 10 vol-% O₂. Thus, at 20 kW/m², the production in unburnt gases is promoted with oxygen increase.

For flaming specimens, oxygen decrease favors incomplete combustion with higher production of CO and CH₄. However, for non-flaming conditions, the production of CO and CH₄ is promoted with the increase of oxygen concentration.

1.2.3. Aerosol production of Cross-Laminated Timber at 20 kW/m²

At ignition, the aerosol size distributions are multimodal and centered on the modes 0.267, 0.173 and 0.109 μm (21 vol-% O₂) and 0.267, 0.173 and 0.407 μm (18 vol-% O₂) (Figure 71a). These sizes correspond to the accumulation mode. Then, as observed at 50kW/m², the multimodal distributions are crushed by a great increase in the 0.03 μm mode. Consequently, the distribution becomes monomodal and centered on that 0.03 μm mode (Figure 71b), which corresponds to nucleation. The concentration in aerosols is slightly higher at 21 vol-% O₂ but globally of the same order of magnitude.

For the non-flaming specimens, the distribution is also monomodal centered on the mode 0.03 μm during the whole test (Figure 71a and Figure 71b). The concentration in the mode 0.03 μm is similar between 15 and 10 vol-% O_2 .

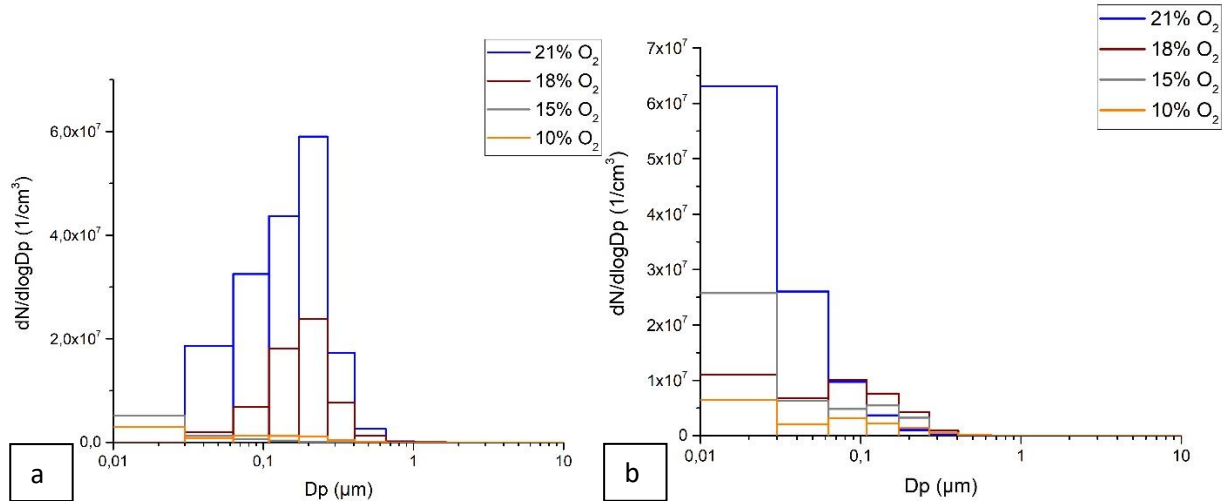


Figure 71: Distribution size of aerosols of CLT at 20 kW/m^2 at: a. t_i , b. 1500s

For the flaming specimen (21 and 18 vol-% O_2), a multimodal distribution centered on the modes 0.267 and 0.173 μm is observed at ignition. Then, it is replaced by a monomodal distribution centered on the mode 0.03 μm . For the non-flaming specimen, the distribution is monomodal centered on the mode 0.03 μm .

1.3. Comparative effect of oxygen and heat flux of Cross-Laminated Timber

The fire behavior as well as the gas and aerosol production of CLT according to the oxygen concentration and the heat flux were investigated. It was observed that oxygen and heat flux are limiting factors to enable combustion as well as altering the kinetics of decomposition. The combination of both highlights different fire behaviors, which are detailed hereafter.

The first decomposition behavior observed with CLT is flaming combustion (Figure 74), which occurs at 50 kW/m^2 at 21, 18 and 15 vol-% O_2 and at 20 kW/m^2 at 21 and 18 vol-% O_2 .

At 50 kW/m^2 and at 21, 18 and 15 vol-% O_2 , the times to ignition (Table 15) and the maxima of MLR are similar (considering standard deviations) (Figure 72). Thus, only the heat flux governs the solid decomposition at ignition, like pyrolysis. It underlines the fact that surface oxidation reactions do not contribute to the degradation of the condensed phase, which is consistent with literature. Indeed, Di Blasi [47] claims that the flame prevents heterogeneous reactions, and that oxygen cannot diffuse through the

flame as it is consumed at its boundaries. Moreover, according to Kashiwagi [48], the region near the flame is poor in oxygen because of the homogenous reactions of combustion. As a result, all oxidative reactions near the surface stop. Furthermore, lowering the heat flux to 20 kW/m² tightens the flammability conditions. Indeed, at 18 vol-% O₂ and 20 kW/m², the ignition of CLT is 53 times delayed in time compared to 50 kW/m². Similarly, at 20 kW/m², the time to ignition at 18 vol-% O₂ is increased by a factor of 2.5 compared to the time to ignition at 21 vol-% O₂. Therefore, the ignition of CLT at 20 kW/m² is not only governed by heat but also by oxygen concentration.

Moreover, the oxygen concentration does affect the phenomena occurring in the gas phase, which have a direct impact on the condensed phase. As explained in the section 1.1.1 p129, the heat release and mass loss rates at 50 kW/m² and 18 and 15 vol-% O₂ decrease as the flame's temperature decreases with oxygen vitiation. These observations not only hold true at low heat flux but also worsen. Indeed, from 50 to 20 kW/m², the pMLRs are reduced by 34% at 21 vol-% O₂ and by 50% at 18 vol-% O₂ (Figure 72).

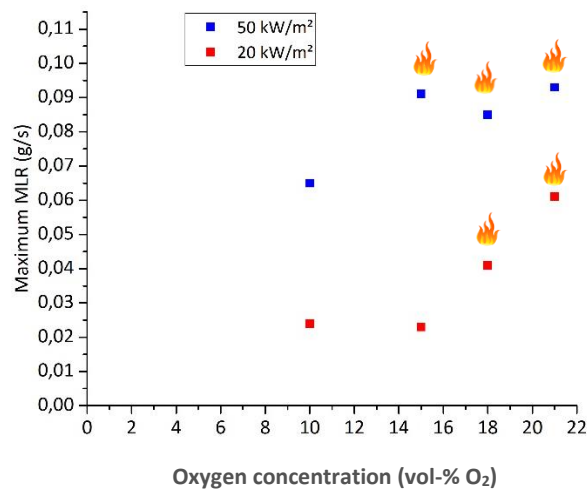


Figure 72: Effect of oxygen and heat flux on the maximum MLR of CLT

As a result, the reaction of combustion shifts in time to incompleteness. At 50 kW/m², the yields in CO and CH₄ double from 21 to 18 vol-O₂ and triple from 21 to 15 vol-% O₂ (Figure 73). Therefore, oxidation reactions of organic compounds into CO₂ end up being disadvantaged against oxidation into CO with oxygen vitiation at 50 kW/m². In the other hand, the yields of CO, CH₄ and CH₂O more than double from 50 to 20 kW/m² at both 21 and 18 vol-% O₂ while those of CO₂ are divided by 2 (Figure 73). As the ignition of CLT at 20 kW/m² is significantly delayed and lasts less time, much of the overall gas production is not burnt and thus oxidized into CO₂ by the flame. Thus, flaming combustion at a low heat flux leads to higher production of unburnt gases.

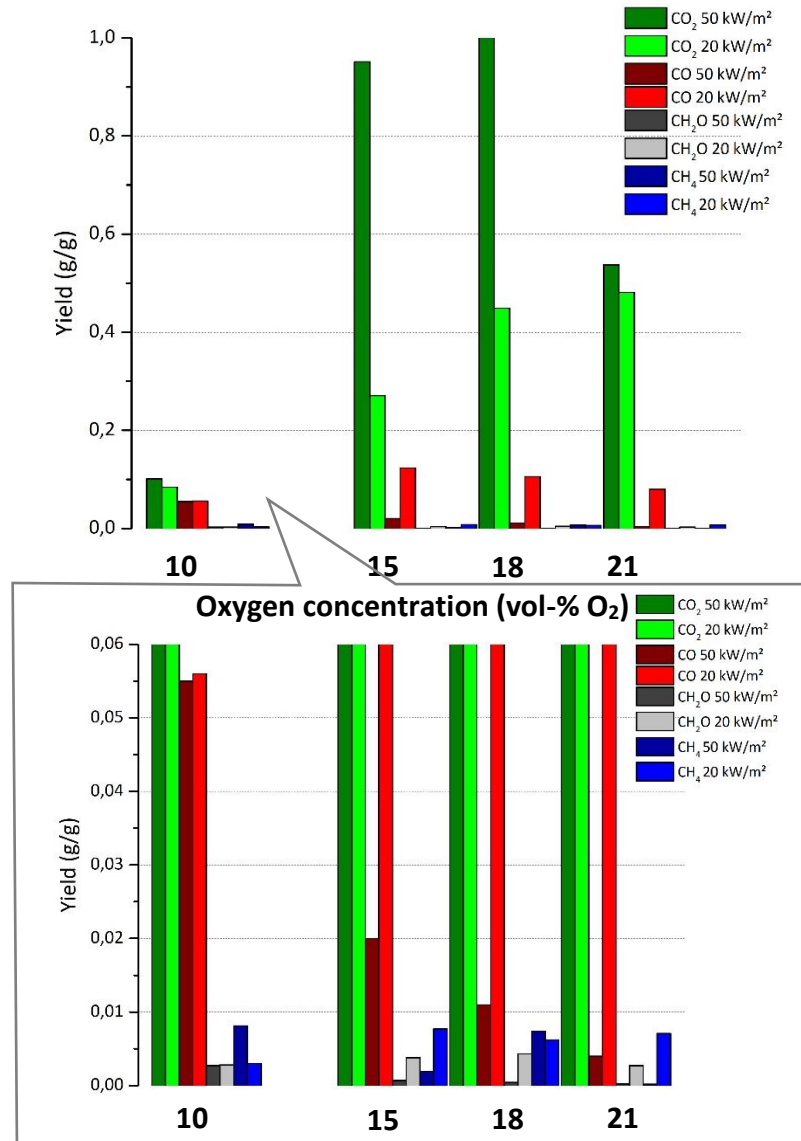


Figure 73: Total yields of CO₂, CO, CH₂O and CH₄ of CLT as a function of oxygen level and heat flux

At 50 and 20 kW/m², the distribution of aerosol particle size is multimodal centered on the modes 0.267 and 0.173 μm at ignition. The third mode fluctuates between 0.407 and 0.109 μm, with a tendency to slightly favor smaller particles in the cases of incomplete combustion. It shifts then to a monomodal distribution centered on the mode 0.03 μm.

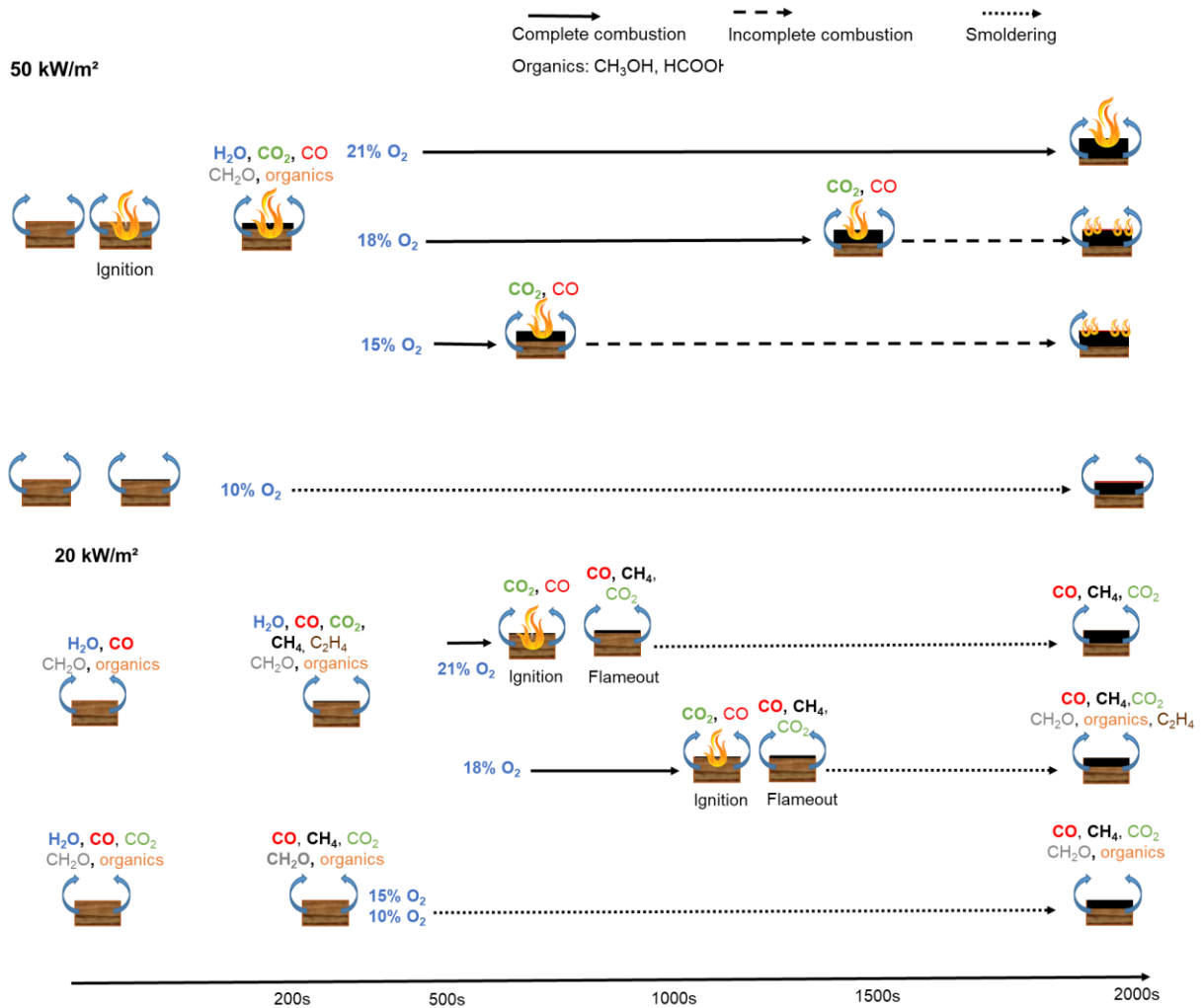


Figure 74: Flaming and non-flaming decomposition of CLT

The second decomposition type of CLT is non-flaming combustion (Figure 74), which occurs at 50 kW/m² at 10 vol-% O₂ and at 20 kW/m² at 15 and 10 vol-% O₂.

At 50 kW/m², though the MLR curve at 10 vol-% exhibits a similar shape to those of the flaming specimen (21, 18 and 15 vol-% O₂) (Figure 62a), there is insufficient oxygen to ignite the released volatiles. Moreover, reducing the heat flux to 20 kW/m² leads to an even higher demand in oxygen to have a flaming combustion. Indeed, the combustion is not flaming at 15 vol-% O₂ whereas it was flaming at 50 kW/m².

Moreover, it should be highlighted that the MLR curves of flaming (21 vol-% O₂ non-included) and non-flaming specimens at 50 kW/m² are close in value (around 0.4 g/s) during the steady state reached after the peak (Figure 62a). As the sample at 10 vol-% O₂ undergoes oxidation at the char's surface, it suggests that smoldering governs the solid decomposition rate during the steady-state at 18, 15 and 10 vol-% O₂. Moreover, lowering the heat flux to 20 kW/m² results in lower solid decomposition rates as the pMLR is

reduced by 63% between the 10 vol-% O₂ cases (Figure 72). It should be underlined that at 20 kW/m², the pMLR at 15 and 10 vol-% O₂ are similar (Figure 72). Thus, the oxygen has no significant impact on the decomposition of the condensed phase 20 kW/m².

Moreover, at 50 kW/m², the lack of oxygen significantly increases the yields of CH₄ and CO (110 times higher from 21 to 10 vol-% O₂) as there is not enough oxygen to oxidize organic volatiles into CO₂ (

Figure 73). Surprisingly, the yields of CO₂ and CO are similar at 10 vol-% O₂ between 50 and 20 kW/m² while those of CH₄ are slightly higher at 50 kW/m². The higher heat flux enables the thermal breakdown of bonds, leading to increased emissions of CH₄.

Finally, both at 50 and 20 kW/m², the distribution of particle size is centered on the mode 0.03 μm. In general, the concentration in aerosols is slightly higher at 50 kW/m² than at 20 kW/m². Indeed, more volatile compounds are released from the wood at high heat flux, which can then condense and form aerosols as they cool down and mix with oxygen.

1.4. Conclusion

The assessment of the fire behavior, the gas production, and the aerosol size distribution of CLT was carried out with a CACC coupled with a FTIR and an ELPI. Both heat flux and oxygen revealed to be limiting factors on the combustion process, which enables the classification of fire behaviors of CLT (Figure 75). At 50 kW/m², the critical oxygen concentration for flaming combustion to occur is between 15 and 10 vol-% O₂ while at 20 kW/m² it is between 18 and 15 vol-% O₂.

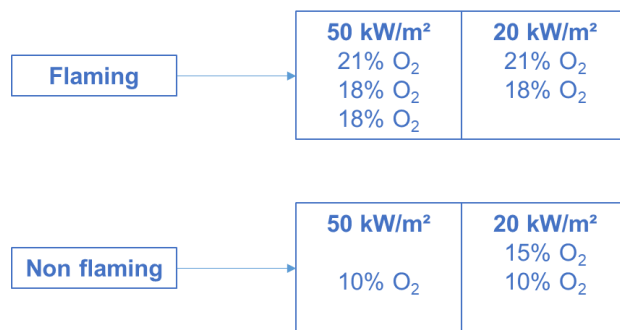


Figure 75: Classification of fire behavior of CLT according to oxygen level and heat flux

In general, oxygen vitiation shifted the reaction of combustion towards incompleteness or even prevented it in some cases. The greatest decomposition and heat release rates were observed at high heat flux (50 kW/m²) and high oxygen level (above 15 vol-% O₂) while the emission of unburnt gases (CO and CH₄) was promoted at reduced heat flux (20 kW/m²). For all flaming specimens, the aerosol size distribution is

mainly centered on the modes 0.267 μm and 0.173 μm at ignition and then shifts to the mode 0.03 μm , while for non-flaming specimens the distribution size of aerosols is centered on the mode 0.03 μm .

2. Effect of oxygen and heat flux on the fire behavior, gas, and aerosol production of Wood Fiber

As for CLT, the reaction to fire of wood fiber highly depends on the environment conditions such as the oxygen level and the heat flux. The effect of oxygen is investigated at 50 kW/m^2 and then at 20 kW/m^2 . In a last part, a comparative study is done to study both of their effects on the fire reaction, gas, and aerosol production of wood fiber.

2.1. Effect of oxygen on Wood Fiber at 50 kW/m^2

First, the impact of oxygen content is examined regarding mass loss and heat release before investigating its effects on gas and aerosol production. All the replica curves are gathered in the Appendix 11 p240.

2.1.1. Mass loss and heat release of wood fiber at 50 kW/m^2

Initially, between 0 and 6 seconds, rising surface temperature initiates wood fiber decomposition. This leads to water evaporation and then to the production of decomposition gases. The mixture of gases and oxygen, triggered by the igniter, ignites around 6s.

As the flame rapidly spreads across the surface wood fiber, there is a significant increase in MLR (Figure 76a) and HRR (Figure 77), reaching their peaks at around 10 seconds. On top of the sample, char forms and diminishes the heat transfer between the surface and the pyrolysis front. This thermal insulation results in a reduction in the pyrolysis process of wood fiber, leading to a decrease in MLR and HRR (Figure 76a and Figure 77).

Then, the MLR and the HRR increase around 600s, accompanied with more vivid flames. The MLR reaches a peak at 0.04 g/s and then decreases to reach an almost zero mass loss rate. In the other hand, the HRR reaches peak at 70 kW/m^2 before decreasing to 30 kW/m^2 . This step corresponds to the thermal return [103], as previously observed with CLT. Shortly thereafter, at around 940 seconds, the sample extinguishes.

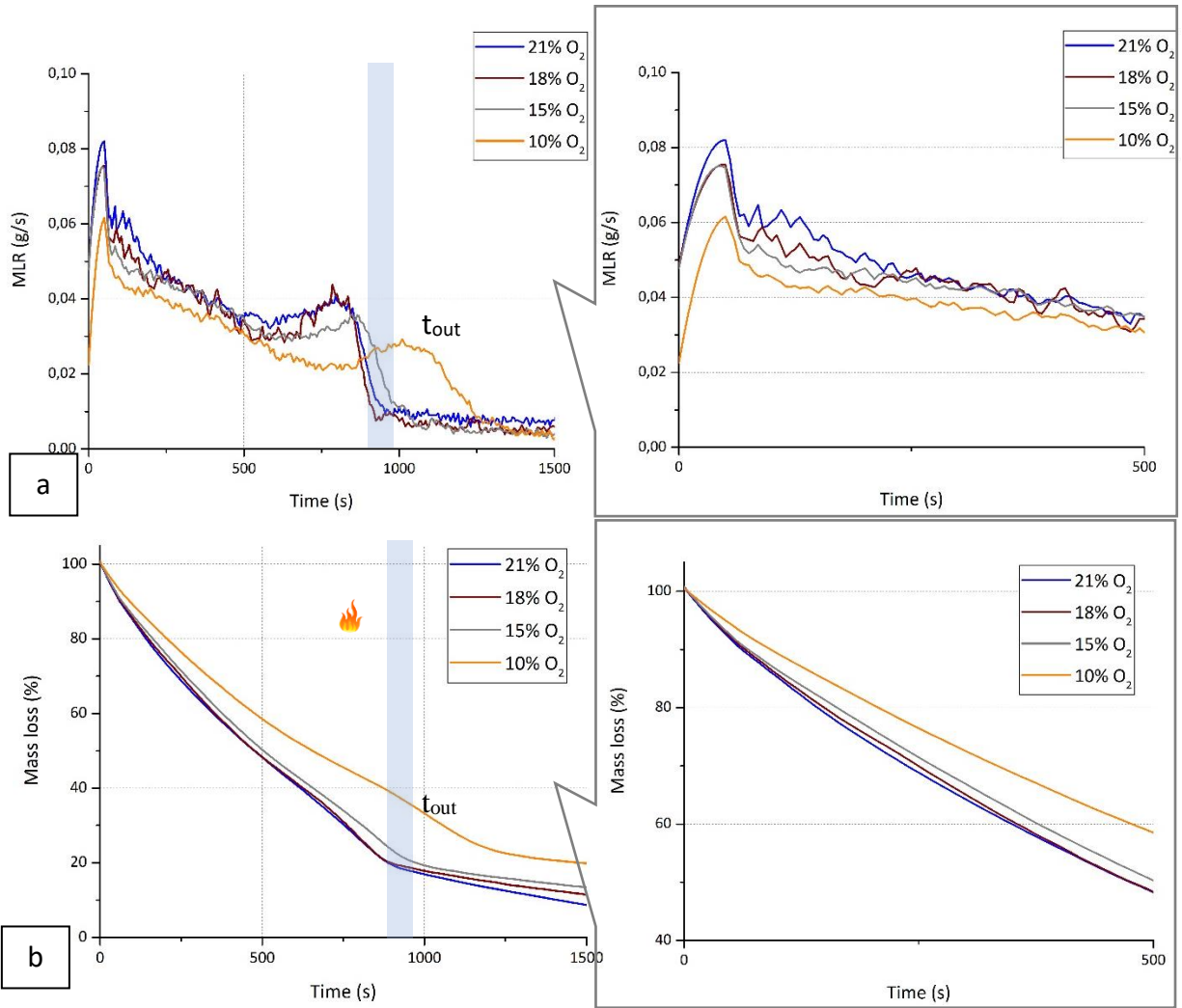


Figure 76: Effect of oxygen concentration on WF at 50 kW/m²: a. MLR, b. mass loss

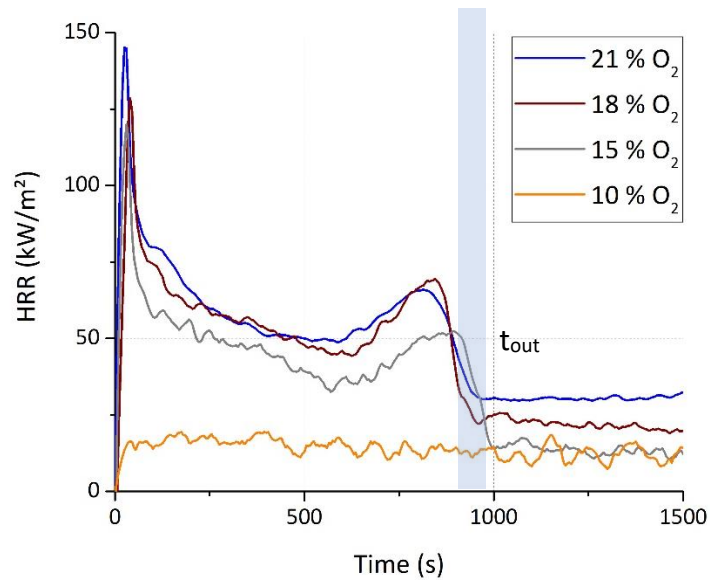


Figure 77: Effect of oxygen concentration on the HRR of WF at 50 kW/m²

As observed with CLT, the fire behavior of WF is affected by the concentration of oxygen. Indeed, the thermal decomposition occurs with flames at 21, 18 and 15 vol-% O₂ but without flames at 10 vol-% O₂. Thus, the lean flammability limit of wood fiber at 50 kW/m² is comprised between 15 and 10 vol-% O₂.

More precisely, for the burning specimens (21, 18 and 15 vol-% O₂), the time to ignition is not affected by the oxygen concentration as they are in the same range (Table 18). This result is consistent with the findings of the TGA analyses on wood fiber wherein it was observed that the oxygen concentration had no influence on the temperature at which 5% of the weight was lost (Chapter 3 section 0 p119). On the other hand, between 21 and 15 vol-% O₂, the pHRR and the MLR are reduced by 17% and 11% (Table 18). The reduction in oxygen availability reduces the efficiency of the reaction of combustion. Thus, in addition to the heat received at the surface of WF, the oxygen concentration has a slight impact on the fire behavior at ignition.

Moreover, around 50s, the mass loss becomes slightly faster at 21 and 18 vol-% O₂ than at 15 vol-% O₂ (Figure 76b). In addition, there is a 17% of difference between the HRR at 21 and 15 vol-% O₂. At 15 vol-% O₂, the limited oxygen content leads to a diminished flame intensity due to an insufficient number of oxidation reactions to maintain the flame. Consequently, there is an increase in the amounts of wood fiber residue after 30 min of test: 5% at 21 vol-% O₂, 8% at 18 vol-% O₂ and 11% at 15 vol-% O₂ (Figure 76b). Thus, oxygen decrease leads to slower kinetics of decomposition and heat release below 18 vol-% O₂.

Table 18: Influence of oxygen on the fire parameters of WF at 50 kW/m²

Oxygen concentration (%)	t _i (s)	Standard deviation (s)	t _{out} (s)	Standard deviation (s)	pMLR (g/s)	Standard deviation (g/s)	pHRR (kW/m ²)	Standard deviation (kW/m ²)
21	6	0	940	3	0.110	0.010	144	1
18	9	1	945	2	0.102	0.008	128	10
15	6	1	974	2	0.098	0.003	120	0
10	-	-	-	-	0.072	0.002	19	6

Furthermore, at 10 vol-% O₂, the MLR curve has a similar shape as the curves for other oxygen levels (Figure 76a) but the decomposition occurs without flames because of limited oxygen concentration in the environment. As a result, the HRR exhibits a gradual increase during the initial stages of the test (Figure 77). It is worth noting that the pMLR and pHRR are reduced by 35 and 86% compared to the ones at 21 vol-% O₂ (Table 18). Notably, the peak of thermal return occurs around 1100 seconds, which represents

an increase of 47% compared to the flaming specimen at 21 vol-% O₂. Thus, the kinetics of decomposition are significantly decreased compared to a flaming combustion.

In summary, at 50 kW/m², two behaviors are observed according to the oxygen concentration: flaming at 21 and 18 vol-% O₂ and non-flaming at 15 and 10 vol-% O₂. The time to ignition remains unaffected by the oxygen concentration, but the oxygen level does have an impact on the pHRR, pMLR, as well as the HRR and MLR after ignition. For the non-flaming combustion (10 vol-% O₂), the HRR and MLR are significantly lower than for flaming samples.

2.1.2. Gas production of wood fiber at 50 kW/m²

In the case of the flaming specimens (21, 18, and 15 vol-% O₂), the analysis of FTIR spectra indicates the presence of several condensable organic compounds before ignition: water, carbon dioxide, carbon monoxide, formaldehyde, methanol, formic acid and phenol type compounds (Appendix 1 p275). These compounds are in accordance with those observed during the initial stage of decomposition of wood fiber in oxidative atmospheres with TGA-FTIR analyses (Chapter 3 section 0 p119). Specifically, the phenol type compounds may be ascribed to 2-methyl-3-methoxyphenol and 2-methoxy-4-vinylphenol as observed with Py-GC/MS studies. For information regarding the potential pathways for the formation of these compounds, the reader can refer to the Table 16 p.134. There are few differences between the several oxygen concentrations, so the description of gas production is done first at 21 vol-% O₂.

At ignition, the previously mentioned organic compounds undergo combustion and no longer appear on FTIR spectra while the production of CO₂ significantly increases, reaching a peak of 28650 ppm at 21 vol-% O₂ (Figure 78a). The substantial release of CO₂ during ignition is attributed to the rapid depolymerization of cellulose, hemicellulose, and lignin.

Following the ignition phase, the CO₂ production remains constant, but peaks in CO (Figure 78b) and CH₄ (Figure 78d) concentrations, at around 450 ppm and 50 ppm respectively, are attributed to the carbonization process of WF. The production in CO and CH₄ increase again between 250 and 750 seconds can be attributed to the diminishing flame intensity during that period. Indeed, flames are much smaller than at ignition and located on the edges of the sample (visual observation). Consequently, there might be zones of incomplete combustion, producing CO and CH₄.

From 600s onward, an increase in CO₂ is observed due to faster decomposition rates induced by thermal return. A significant peak in CO (900 ppm) and CH₄ (250 ppm) follows this, as well as smaller peaks in

ethene (Figure 78e). The release of these hydrocarbon products highlights that the combustion becomes increasingly incomplete, which is confirmed by the CO/CO₂ ratio exceeding 0.05. Flameout occurs right after and leads to a decrease in the gas production.

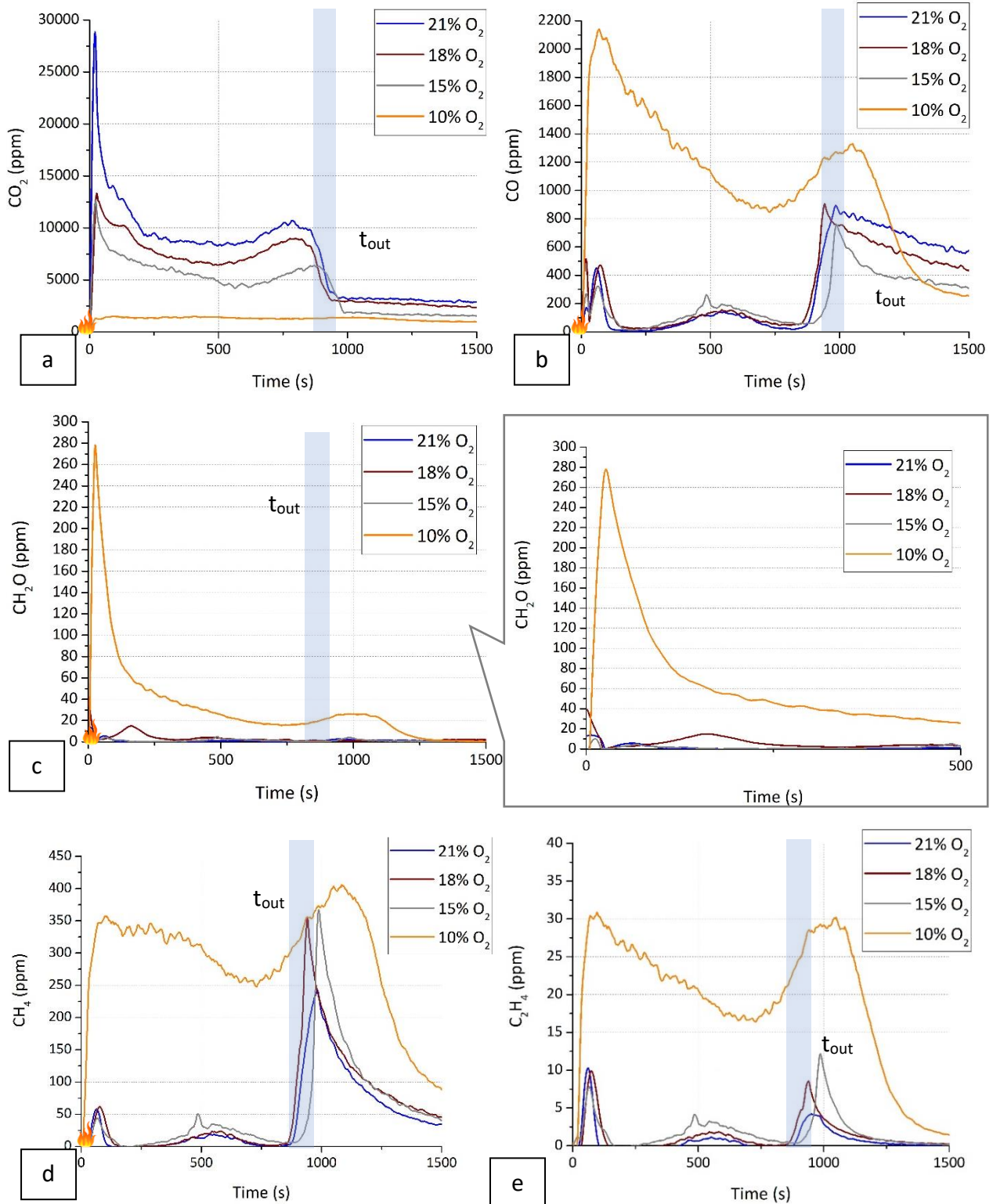


Figure 78: Influence of the oxygen level the gaseous emissions of WF at 50 kW/m²: a. CO₂; b. CO; c. CH₂O; d. CH₄; and e. C₂H₄

Moreover, the oxygen concentration affects the gaseous emissions. First, the peak of CO₂ production at ignition doubles from 15 to 21 vol-% O₂. It should be underlined that there is a significant increase in CO production at ignition as well, with nearly a threefold production increase at 18 vol-% O₂ compared to 21 vol-% O₂. With reduced oxygen availability, the reaction of combustion at ignition favors CO production over CO₂. This is further confirmed by the pHRR at ignition, which decreases with decreasing oxygen concentration (see section 0 p148). Indeed, the formation of CO is less exothermic compared to that of CO₂, resulting in the release of less heat. Additionally, during the thermal return phase leading to flameout, the production of CH₄ is nearly 1.4 times higher at 18 and 15 vol-% O₂ than at 21 vol-% O₂. This demonstrates that the availability of oxygen directly impacts the conversion of fuel into carbon dioxide during the combustion process, and its reduction leads to a preference to produce CO and CH₄.

In the case of the non-flaming specimen (10 vol-% O₂), the FTIR spectra displays the presence of water, carbon dioxide, carbon monoxide, methane, formaldehyde, methanol, formic acid and phenol type compounds in the beginning of the thermal exposure (Appendix 1 p275). Due to the low oxygen concentration, which slows down decomposition rates and limits oxidation, prominent and broad peaks are observed in the early stages of the test including CH₂O (275 ppm) (Figure 78c), CO (2100 ppm) (Figure 78b), CH₄ (350 ppm) (Figure 78d), as well as C₂H₄ (30 ppm) (Figure 78e). These compounds represent the production of partially oxidized and unburnt hydrocarbon species due to the insufficient oxygen for a complete oxidation. In parallel, the production of CO₂ remains very low (Figure 78a), with a CO/CO₂ ratio of 1.7. The limited oxygen availability hinders the oxidation of CO into CO₂.

For flaming specimens (21, 18 and 15 vol-% O₂), oxygen reduction does not much affect the production of thermal decomposition gases. However, non-flaming combustion promotes the production of aldehydes and unburnt gases (methane and ethene).

2.1.3. Aerosol production of wood fiber at 50 kW/m²

At ignition, at 21 and 18 vol-% O₂, the distribution size of aerosols is multimodal and centered on the modes 0.267, 0.173 and 0.407 μm. The distribution at 15 vol-% O₂ is slightly different with a distribution centered on the modes 0.173, 0.267 and 0.109 μm (Figure 79a). These sizes indicate the presence of an accumulation mode of aerosols within the range of 0.1-1 μm, corresponding to particle agglomeration and growth [17]. The concentrations of aerosols in these modes are similar and of the same order of

magnitude. Following ignition, the aerosol size distribution changes to a monomodal pattern centered on the mode 0.03 μm (Figure 79b). This mode corresponds to a nucleation mode, characterized by particles with diameters smaller than 0.1 μm , indicating the formation of fresh aerosols. As for CLT, this phenomenon may be attributed to the nucleation of volatile particles as the effluent mixture cools down after ignition. The vaporized gases condense and form particles with very small sizes [105], [106], [107].

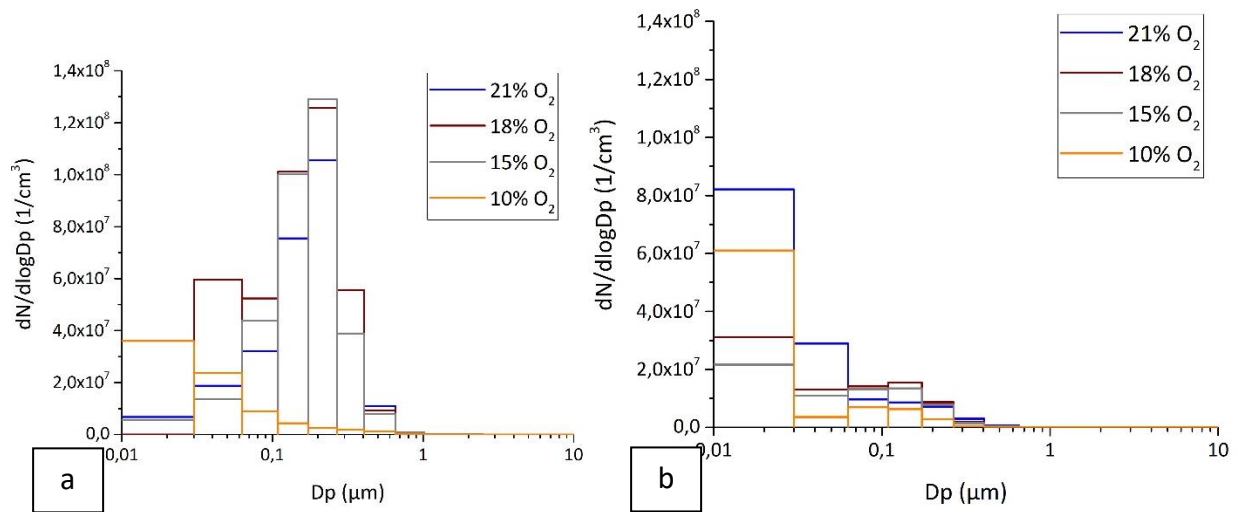


Figure 79: Distribution size of aerosols of WF at 50 kW/m² at: a. ti, b. 800s

In the case of 10 vol-% O₂ (non-flaming), the aerosol size distribution is monomodal and centered on the mode of 0.03 μm (Figure 79a). Contrasting with the flaming specimens at 18 and 15 vol-% O₂, the concentration in the mode 0.03 μm at 10 vol-% O₂ is slightly higher (Figure 79b). This difference can potentially be attributed to vitiation, which refers to the increase in the number of particles resulting from incomplete combustion [42] [106]. The lower oxygen concentration in the environment during non-flaming combustion might contribute to the accumulation of particulate matter, leading to a slightly higher concentration in the 0.03 μm mode.

To fully assess the influence of oxygen on the reaction to fire, gas production and aerosol production of wood fiber, it would be beneficial to study the effects of oxygen under less aggressive thermal attack conditions. It would help to determine if the observed effects of oxygen concentration on combustion, gas production, and aerosol formation persist across a range of fire conditions.

2.2. Effect of oxygen on Wood Fiber at 20 kW/m²

The reaction to fire of wood fiber depends on the thermal attack; hence, the effect of oxygen was assessed at 20 kW/m². This heat flux allows the study of less aggressive fire scenarios. All the replica curves are gathered in the Appendix 13 p250.

2.2.1. Mass loss and heat release of wood fiber at 20 kW/m²

The evolution of the remaining mass of wood fiber as a function of time (Figure 80a) exhibits a slow increase at the beginning of the test for all oxygen concentrations. However, at 21, 18 and 15 vol-% O₂, a drop in the remaining mass occurs around 45s due to wood decomposition. Ignition quickly follows at an average of 62s, leading to peaks in MLR (Figure 80b) and HRR (Figure 81). Notably, the time to ignition is not affected by the oxygen concentration considering the standard deviations (Table 19). As at 50 kW/m², this observation agrees with the findings of TGA tests, where it was noted that the temperature at which 5% weight loss occurred remained consistent regardless of variations in oxygen concentration. However, there is a decrease of 24% and 12% in pMLR and pHRR respectively from 21 to 15 vol-% O₂ (Table 19). As previously explained, oxygen is crucial for sustaining a flame; therefore, reduced availability leads to a slower and less intense development and propagation of the flame within the wood. Consequently, oxygen reduction from 15 vol-% O₂ affects both the mass loss and the heat release at ignition.

After the ignition phase, the wood fiber carbonizes leading to decreases in MLR and HRR (Figure 80b and Figure 81). However, at around 120s, the remaining mass curve at 21 vol-% O₂ decreases faster than the 18 and 15 vol-% O₂ (Figure 80a). Moreover, the decline in HRR is significantly increased with oxygen reduction (Figure 81). In fact, the limited availability of oxygen leads the samples to flame out at 109 and 340s at 15 and 18 vol-% O₂ respectively. In comparison to 18 vol-% O₂, wood fiber extinguishes 340s later at 21 vol-% O₂. This illustrates that a lack of oxygen accelerates flameout, as there is insufficient oxygen to sustain the flame.

After 25 minutes of testing, the remaining amount of wood fiber is 21% at 21 vol-% O₂, 31% at 18 vol-% O₂, and 36% at 15 vol-% O₂ (Figure 80a). This is consistent with the previous observations, where a decrease in oxygen concentration leads to an earlier shift towards flaming out, resulting in less degradation of the sample at lower oxygen concentrations.

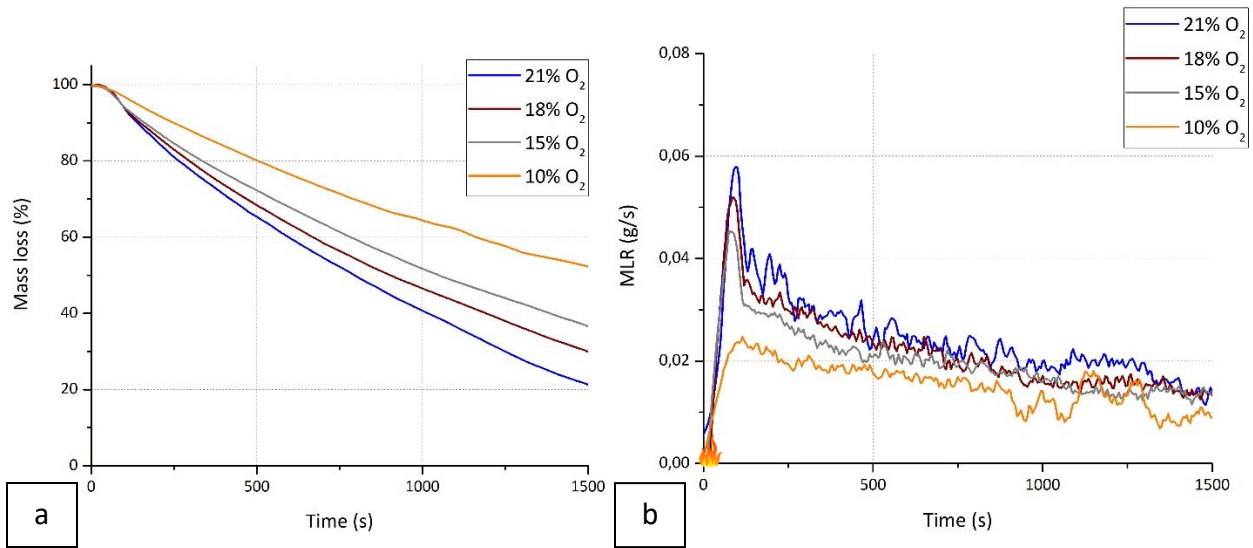


Figure 80: Effect of oxygen concentration on WF at 20 kW/m²: a. mass loss; b. MLR

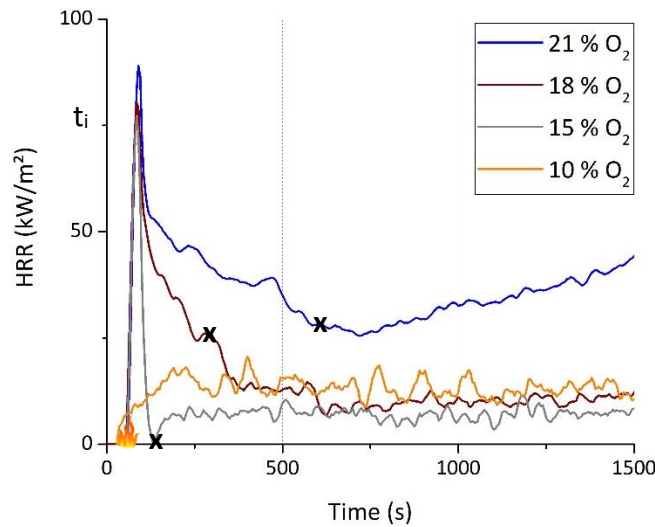


Figure 81: Effect of oxygen concentration on the HRR of WF at 20 kW/m², x is for flameout

Table 19: Influence of oxygen on the fire parameters of WF at 20 kW/m²

Oxygen concentration (%)	t _i (s)	Standard deviation (s)	t _{out} (s)	Standard deviation (s)	pMLR (g/s)	Standard deviation (g/s)	pHRR (kW/m ²)	Standard deviation (kW/m ²)
21	69	3	650	6	0.058	0.02	87	3
18	62	7	310	4	0.052	0.002	78	6
15	56	5	109	2	0.044	0.002	77	2
10	-	-	-	-	0.027	0.02	21	3

At 10 vol-% O₂, the thermal decomposition of wood fiber occurs without flames. The mass loss (Figure 80a) shows a slow decrease once the sample is exposed to the heat flux. Consequently, the MLR (Figure 80b) and the HRR (Figure 81) exhibit a gradual increase in the beginning, reaching a peak value of 0.027 g/s and 20 kW/m² (Table 19) at around 80s. Afterward, the MLR and HRR reach a steady-state for the rest of the test. In the absence of flames and with a relatively low heat flux, the combustion proceeds at a slower rate, resulting in a relatively constant heat release rate. The amount of wood fiber residue remaining after 25 minutes of testing is 52% (Figure 80a). This observation is consistent with the rates of mass loss and heat release discussed above, indicating that a significant portion of the sample remains unburnt.

In summary, at 20 kW/m², the combustion is flaming at 21, 18 and 15 vol-% O₂ and non-flaming 10 vol-% O₂. For the flaming specimens, the ignition time is not affected by oxygen content while the peaks of mass loss rate and heat release rate are slightly affected. For the non-flaming specimen, the rates of solid decomposition and heat release are greatly reduced due to the low heat flux coupled to low oxygen content.

2.2.2. Gas production of wood fiber at 20 kW/m²

For the flaming specimens (21, 18, and 15 vol-% O₂), during the initial stages of thermal decomposition, wood fiber releases a combination of water, carbon dioxide, carbon monoxide, formaldehyde, methanol, formic acid and phenol type compounds (Appendix 14 p256). Quantitatively, a peak in formaldehyde production (Figure 82c) attests for wood decomposition for all oxygen levels.

At ignition, the production in formaldehyde drops while there is a significant increase in CO₂ and CO productions (Figure 82a) at all oxygen concentrations. However, wood fiber produces 43% more CO₂ at 21 than at 15 vol-% O₂, which is consistent with the difference observe in HRR at ignition. This indicates that the combustion reaction is less efficient at lower oxygen concentrations, resulting in less fuel being converted into CO₂ due to the limited availability of oxygen and thus a less exothermic reaction.

Following these increases, the concentration of CO₂ gradually decreases until the samples flame out. At this point, peaks in CH₂O (Figure 82c), CO (Figure 82b), and CH₄ (Figure 82d) arise, indicating the presence of unburnt gases as they are no longer consumed in the flame. Notably, after flaming out, the production of CO and CH₄ reaches a steady state, with higher values observed at higher oxygen levels. Indeed, CO production at 21 vol-% O₂ is on average 23% and 85% higher than at 18 and 15 vol-% O₂ respectively. Similarly, the production in CH₄ doubles from 15 to 21 vol-% O₂. These increases can be attributed to the

increased production of unburnt gases resulting from thermo-oxidative reactions in the presence of higher oxygen concentrations.

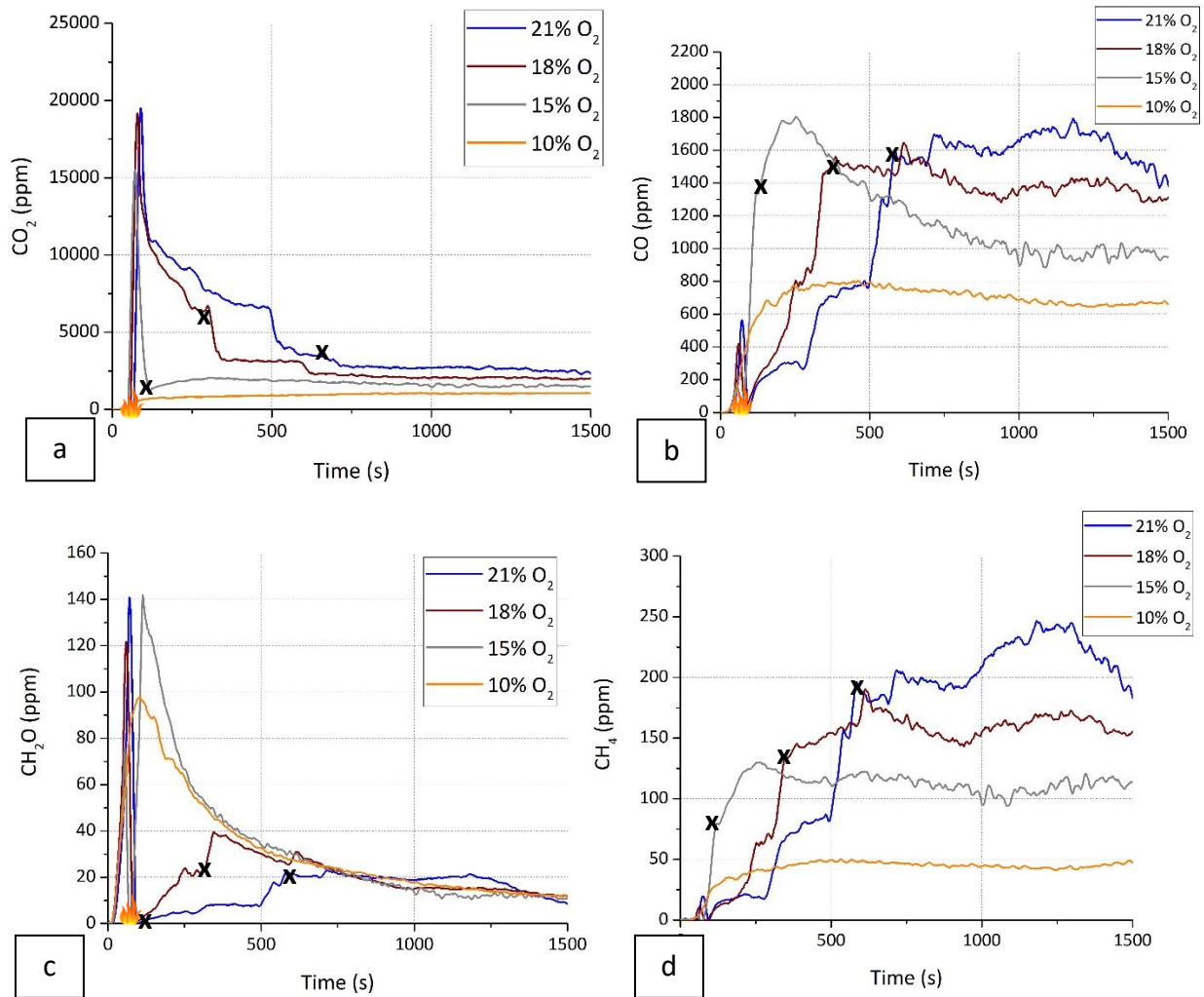


Figure 82: Influence of the oxygen level the gaseous emissions of WF at 20 kW/m²: a. CO₂; b. CO; c. CH₂O and d. CH₄

In the case of non-flaming combustion (10 vol-% O₂), water, carbon dioxide, carbon monoxide, methane, methanol, formic acid and phenol type compounds are identified on FTIR spectra (Appendix 14 p256), but unlike for the flaming specimens, they are released throughout the entire test. Additionally, the CO/CO₂ ratio remains above 0.05 for the entire duration of the test, indicating incomplete combustion, as the production of CO₂ remains very low (around 1000 ppm) (Figure 82a). At around 110s, there is a peak of formaldehyde production (100 ppm) (Figure 82c) as the wood fiber decomposes. Simultaneously, there is a significant increase in the production of CO and CH₄, corresponding to the carbonization of the wood fiber (Figure 82b and Figure 82c). Both compounds reach a steady state (~750 ppm for CO and ~50 ppm

for CH₄) for the rest of the test as the wood fiber gradually undergoes carbonization. Due to the low solid decomposition rate at low oxygen concentration, the gas production remains relatively low and steady.

For the flaming specimens (21, 18 and 15 vol-% O₂), CO₂ and CO are produced in great quantities, which increase with oxygen concentration. For non-flaming conditions (10 vol-% O₂), wood fiber produces mainly CO and CH₄ throughout the test.

2.2.3. Aerosol production of wood fiber at 20 kW/m²

At ignition, the size distribution is monomodal centered on the mode 0.03 μm for all flaming specimen (Figure 83a). This underlines that the ignition of wood fibers at a lower heat flux generates significantly fewer smaller aerosols compared to ignition at a high heat flux. In fact, at lower heat flux, there is less energy available to break down and agitate the aerosol particles, leading to the formation of finer aerosols. Higher heat flux levels, on the other hand, can result in more turbulent conditions, which may cause larger aerosol particles to form due to coagulation and collision processes. In addition, at 20 kW/m², there may be better oxygen diffusion into wood fiber porous structure, promoting the formation of smaller aerosols. Finally, the size distribution is still monomodal centered on the mode 0.03 μm (Figure 83b) at the end of the test. The concentration in aerosols globally of the same magnitude.

At 10 vol-% O₂, the distribution is also monomodal centered on the mode 0.03 μm during the whole test (Figure 83a and Figure 83b). The concentration in aerosols at the mode 0.03 μm is quite low compared to the flaming specimens and indicates the decomposition at low heat flux and low oxygen level does not produce many aerosols.

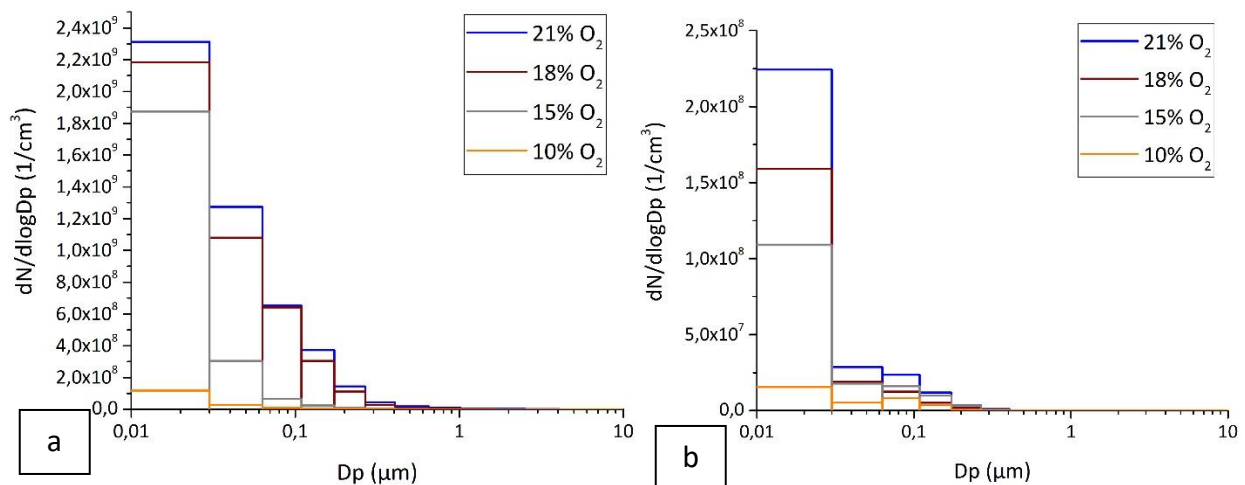


Figure 83: Distribution size of aerosols of WF at 20 kW/m² at: a. ti, b. 800s

For all specimens, flaming or non-flaming, a monomodal distribution centered on the mode 0.03 μm is observed, with a higher concentration in aerosols for the flaming specimen.

2.3. Comparative effect of oxygen and heat flux of wood fiber

The fire behavior of wood fiber was thoroughly investigated by considering the influence of both oxygen level and heat flux. These parameters play crucial roles in determining the fire reaction of wood fiber, which results in various fire scenarios, each with its own characteristics.

Flaming combustion is observed at oxygen levels of 21, 18, and 15 vol-% O_2 (Figure 86) at both 50 and 20 kW/m^2 , indicating that the lean flammability limit of WF at 50 and 20 kW/m^2 is comprised between 15 and 10 vol-% O_2 . Notably, neither the times to ignition at 50 nor 20 kW/m^2 are affected by oxygen concentration considering the standard deviations (Table 18 and Table 19). However, the times to ignition are affected by the heat flux. Indeed, at 21 vol-% O_2 , the ignition of wood fiber is delayed by a factor of 12 from 50 kW/m^2 to 20 kW/m^2 . This trend is consistently observed across various oxygen concentrations. Thus, lowering the oxygen concentration does not impact the time to ignition of wood fiber, whereas reducing the heat flux does. It is worth noting that WF ignites very rapidly compared to CLT. Indeed, at 21 vol-% O_2 , the time to ignition decreases by 68% at 50 kW/m^2 and 82% at 20 kW/m^2 . The fast time to ignition of wood fiber, whatever the oxygen content, can be attributed to its unique structure consisting of fibers. This structure results in a high specific surface area and voids that facilitate fluid and heat transfer as well as oxygen access.

Moreover, the pMLR at ignition decreases when lowering the heat flux (Figure 84). Indeed, from 50 to 20 kW/m^2 , the pMLRs are reduced by 36% at 21 vol-% O_2 . This trend applies for all oxygen concentrations. In addition to the effect of heat flux, the oxygen concentration influences the pMLR at ignition at 20 kW/m^2 while it does not at 50 kW/m^2 considering the standard deviations (Table 18 and Table 19). It appears that the heat flux governs the solid decomposition at ignition at 50 kW/m^2 , while the oxygen concentration becomes a significant factor at 20 kW/m^2 (Figure 84). With reduced heat available to facilitate flame establishment, the role of oxygen becomes more pronounced in sustaining the flame. As expected, higher oxygen levels result in a more intense flame, leading to increased thermal feedback and a higher rate of solid decomposition.

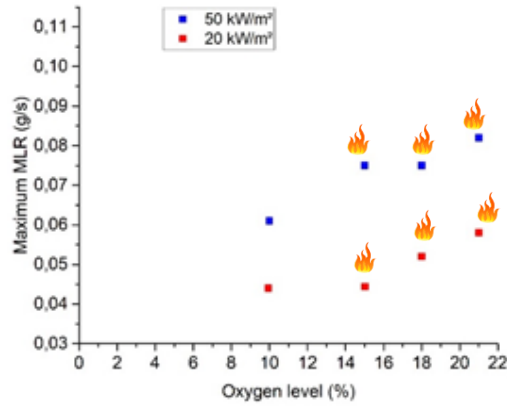


Figure 84: Effect of oxygen and heat flux on the maximum MLR of WF

Furthermore, it is noteworthy that the overall gas yields of wood fiber at 20 kW/m² are significantly higher than those at 50 kW/m². Indeed, at 21 vol-% O₂ and from 50 to 20 kW/m², the yields of CO₂ triples while those of CO are multiplied by 8 (Figure 85). In fact, when subjected to low heat fluxes, wood fiber extinguishes quickly and results in higher CO and CO₂ emissions compared to high heat fluxes where WF ignites later. Additionally, the low heat flux conditions may lead to incomplete combustion, further contributing to increased CO yields. Furthermore, with oxygen vitiation, this difference in yields between heat fluxes decrease for CO₂ and CO (Figure 85). Indeed, at 20 kW/m², oxygen vitiation leads sooner to flame out, which induces higher CO and CH₄ emissions. Thus, the yields in CO increase while those in CO₂ decrease due to incomplete combustion. At 50 kW/m², oxygen vitiation appears to have poor influence on the yields of CO and CO₂ as the fire behaviors are similar.

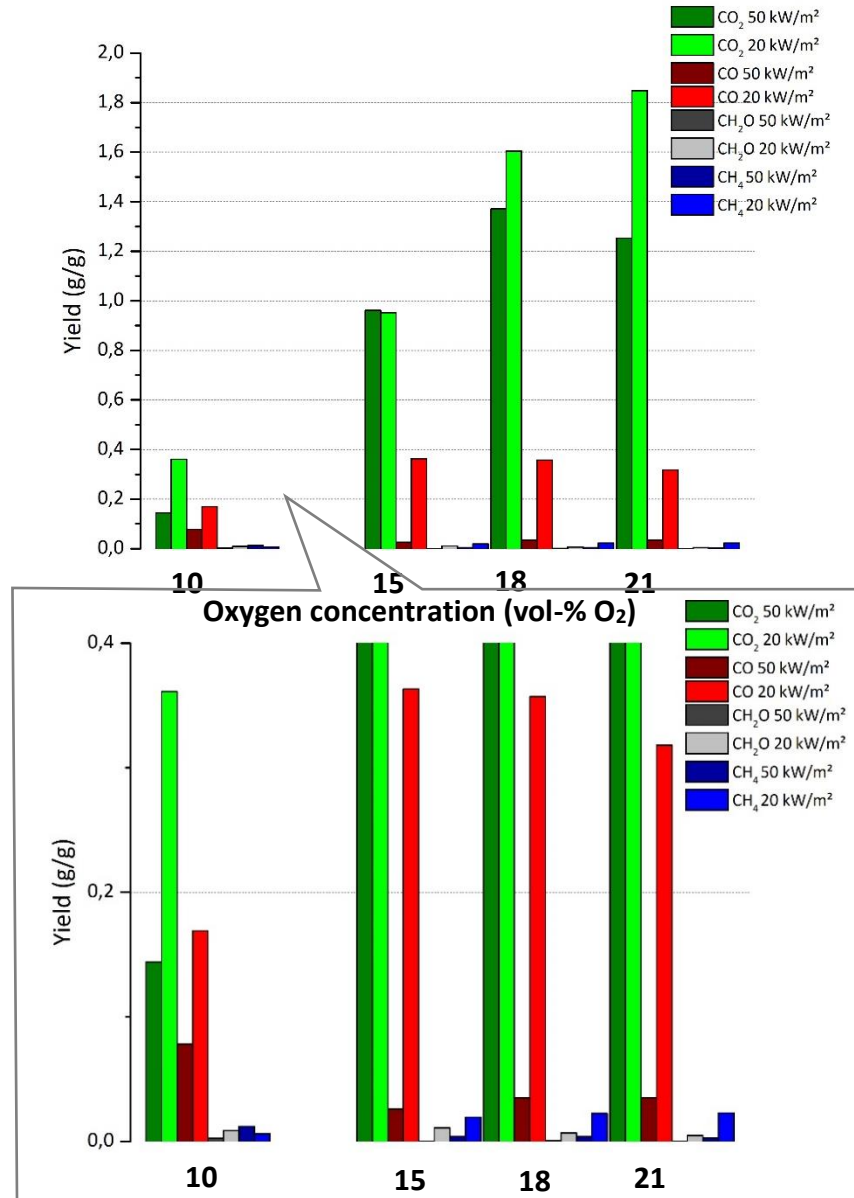


Figure 85: Total yield of CO₂, CO, CH₂O and CH₄ of WF as a function of oxygen level and heat flux

Regarding the distribution of aerosol particle sizes, for the flaming samples at 50 kW/m², the particle size distribution is initially centered on modes at 0.267 and 0.173 μm at ignition, and then it shifts to a mode centered on 0.03 μm . At 20 kW/m², a monomodal distribution centered on the mode 0.03 μm is observed throughout the entire test duration. As explained before, low heat fluxes lead to reduced thermal turbulence and better oxygen diffusion. Thermal turbulence promotes the collision and agglomeration phenomenon, leading to the formation of larger aerosols, while oxygen diffusion facilitates the oxidation of aerosols into finer particles.

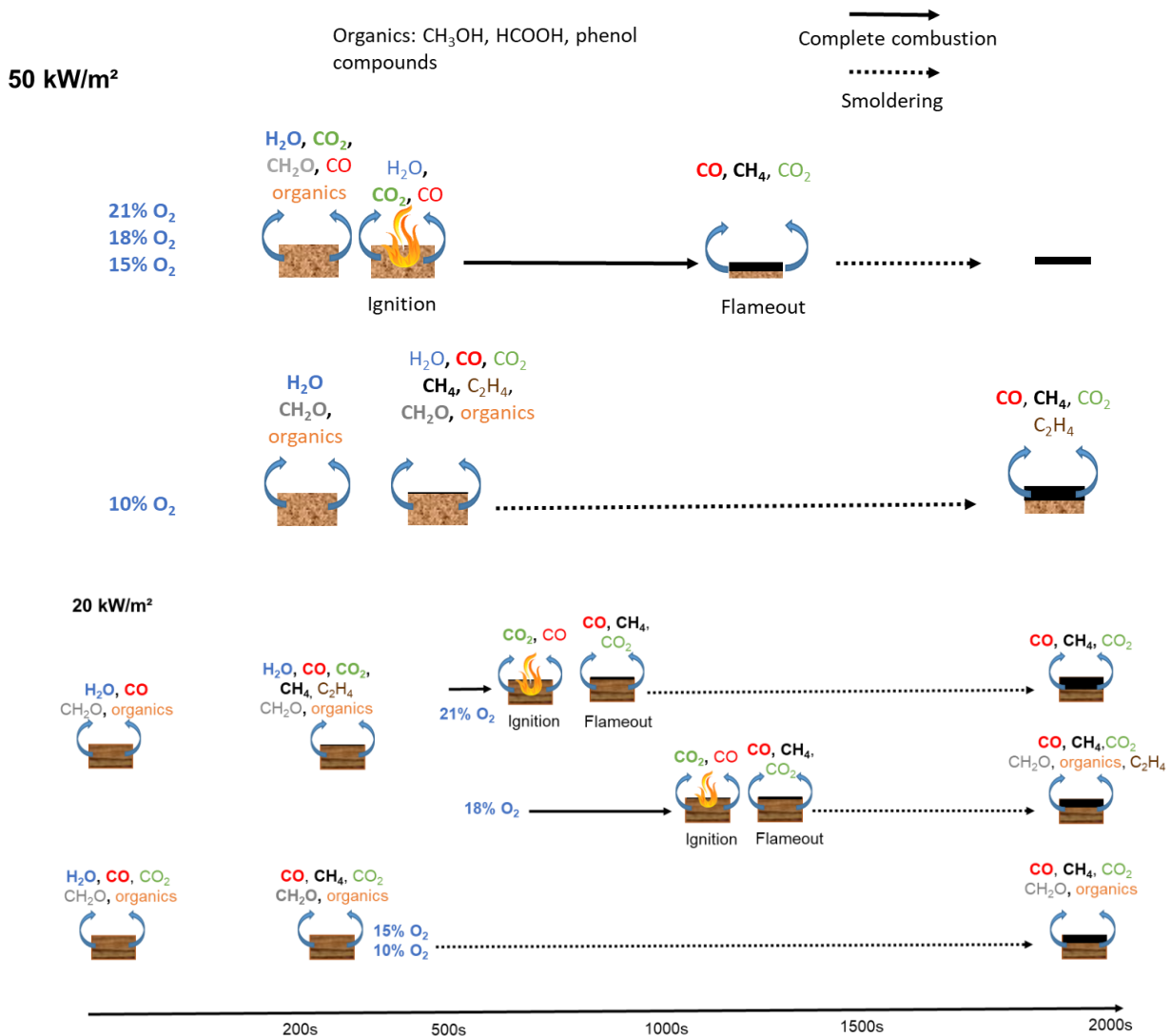


Figure 86: Flaming and non-flaming decomposition of WF

In the case of non-flaming combustion (10 vol-% O₂), observed at both 50 and 20 kW/m² (Figure 86), reducing the heat flux leads to a reduction of 63% of the maximum mass loss rate (Figure 84). This indicates that the heat flux has a significant impact on the solid decomposition rate despite the low oxygen concentration.

Furthermore, from 50 to 20 kW/m², the yields of CO₂ and CO are multiplied respectively by 3.5 and 2. In fact, additional gases are produced at 50 kW/m², such as CH₄, C₂H₄ and aldehydes, which reduces the overall production of CO₂ and CO. Indeed, at high heat flux the bonds are broken more easily than at low heat flux, which allows for more gases to be produced. Besides, it should be highlighted that the CO and CO₂ yields are decreased compared to flaming specimens at 20 kW/m² while the yields of CO and CH₄

increase at 50 kW/m². Thus, at 20 kW/m² the yields are mainly affected by the lower rate of decomposition while at 50 kW/m² the yields of CO and CH₄ are affected by oxygen concentration.

Finally, in the case of non-flaming combustion, the distribution of particle sizes is centered on the mode 0.03 μm at both 20 and 50 kW/m². It should be underlined that the concentration in aerosols significantly increases from 50 to 20 kW/m². High heat fluxes might lead to the decomposition of soot precursors and thus reduces the number of aerosols.

2.4. Conclusion

The assessment of the fire behavior, gas production and aerosol size distribution of wood fiber (WF) was conducted using a Cone Calorimeter (CACC) coupled with a Fourier Transform Infrared Spectroscopy (FTIR) and an Electrical Low Pressure Impactor (ELPI). The findings have illustrated that both heat flux and oxygen concentration are essential factors in determining the combustion characteristics of wood fiber (Figure 87). At both heat flux levels of 50 kW/m² and 20 kW/m², the critical oxygen concentrations required for flaming combustion to take place were found to be between 15 and 10 vol-% O₂.

Overall, when the oxygen concentration is reduced, it hinders the complete combustion of wood fiber and can even prevent combustion in certain cases. This incomplete combustion is characterized by the increased emission of unburnt species such as carbon monoxide and methane. These effects are more pronounced at lower heat flux levels.

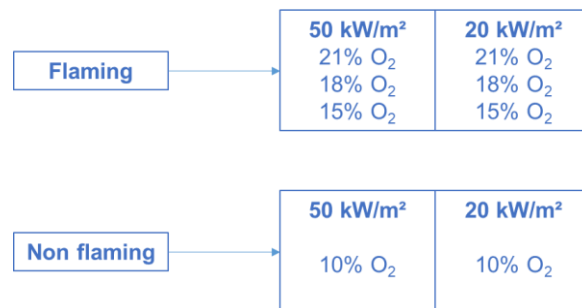


Figure 87: Classification of fire behavior of WF according to oxygen level and heat flux

3. Effect of oxygen on the fire behavior, gas, and aerosol production of an assembly of Cross-Laminated Timber and Wood Fiber

The objective of this section is to evaluate the fire behavior, gas production and aerosol production of an assembly of Cross-Laminated Timber and wood fiber, while also exploring the impact of different oxygen

concentrations on this combination. To have a comprehensive analysis of the effect of combining 50x100 mm CLT to 50x100 mm WF, the 50x100 single samples were first tested separately. As the samples are separated by ceramic fiber, this section focuses on the gas phase phenomena rather than solid interactions.

3.1. Effect of the assembly and the oxygen level at 50 kW/m²

Before examining the effect of oxygen on the CLT/WF assembly, it is essential to investigate the influence of the combination itself. To achieve this, a comparative analysis of the fire behavior, gas production and aerosol production is conducted between half specimens, entire specimens and the CLT/WF assembly at 50 kW/m² and 20 kW/m². All the replica curves are gathered in the Appendix 15 p260.

3.1.1. Fire behavior, gas production and aerosol production of the Cross-Laminated Timber/Wood Fiber assembly

3.1.1.1. *Ignition and heat release of Cross-Laminated Timber/Wood fiber at 50 kW/m²*

At 50 kW/m², the samples ignite at 21, 18, 15 vol-% O₂ while the combustion is not flaming at 10 vol-% O₂. More precisely, at 21 vol-% O₂, the CLT/WF combination ignites at 7s, which corresponds to the time to ignition of single WF whereas single CLT ignites at least 12s later (Table 20). Visually, it is observed that the wood fiber ignites first, followed by near-instantaneous flame spread on the CLT. At 18 vol-% O₂, the WF ignites first at 7s, followed by the CLT at 9s. In this case, the ignition of CLT is visually not instantaneous. However, it is still at least 9s sooner than single specimens of CLT (Table 20). At 15 vol-% O₂, WF ignites first at 9s, followed 10s later by CLT. Under this condition, the ignition of CLT corresponds to the ignition of single CLT, which suggests that the effect of WF on CLT is negligible in these conditions. Excluding the effect of oxygen, which will be discussed in the next section, the combination of WF and CLT at 21 and 18 vol-% O₂ has the effect of hastening the ignition of CLT.

Table 20: Fire parameters of CLT/WF at 50 kW/m²

	t_i (s)	Standard deviation (s)	t_{out} (s)	Standard deviation (s)	pHRR (kW/m²)	Standard deviation (kW/m²)
21% O₂						
CLT: 1	19	2	-	-	143	12
CLT: ½	26	8	-	-	77	7
WF: 1	6	0	970	2	144	1
WF: ½	6	0	900	1	80	6
CLT/WF	7	1.5	900	100	122	2
18% O₂						
CLT: 1	18	2	-	-	138	8
CLT: ½	24	3	-	-	73	4
WF: 1	9	1	930	5	128	10
WF: ½	4	1	915	3	40	5
CLT/WF	7 (WF) – 9 (CLT)	1 - 8	950	50	101	6
15% O₂						
CLT: 1	21	1	-	-	141	9
CLT: ½	17	3	-	-	68	7
WF: 1	6	1	1000	7	120	0
WF: ½	9	1	950	14	42	9
CLT/WF	9 (WF) – 19 (CLT)	1.4 – 2.8	900	15	106	4
10% O₂						
CLT: 1	-	-	-	-	41	13
CLT: ½	-	-	-	-	50	4
WF: 1	-	-	-	-	19	6
WF: ½	-	-	-	-	30	3
CLT/WF	-	-	-	-	10	1

Moreover, it is noteworthy that the HRR curves of the CLT/WF flaming assembly (21, 18 and 15 vol-% O₂) follow both the trends of half CLT and half WF. Indeed, a peak of HRR is reached at ignition (Figure 88a, Figure 88b and Figure 88c) before decreasing as char is forming on both CLT and WF. As CLT and WF ignite in the same range of time, a single peak is observed for both ignitions. More precisely, the pHRRs of flaming assemblies are slightly lower, ranging from 12 to 27%, compared to the pHRR of an entire sample of CLT or WF (Table 20) and that at all oxygen concentrations. This suggests that the heat released at ignition might be slightly influenced by the combination. However, it is complex to determine whether this effect is indeed real or attributed to the sample configuration influencing the flame. Since the samples are separated by ceramic fiber and alumina, this introduces different boundary conditions. It would be interesting to investigate whether the pHRR of the assembly is equivalent to the sum of the pHRRs of the

two half samples of CLT and WF. However, for the same reasons as previously, this aspect will not be addressed in the discussion.

After ignition, the HRR curves of the CLT/WF assembly are steady at similar values as entire CLT and WF samples (60 kW/m² at 21 vol-% O₂ and 50 kW/m² at 18 and 15 vol-%O₂). Around 600s, the HRR curves of CLT/WF depict a 2nd peak of HRR, which corresponds to the thermal return of wood fiber, observed for both half and entire samples of WF (green curves of Figure 88a, Figure 88b and Figure 88c). The WF part of the assembly flames out after this step, which would induce a decrease in HRR for single WF. However, for the CLT/WF assembly, the HRR remains steady at levels close to the CLT sample as it is still burning.

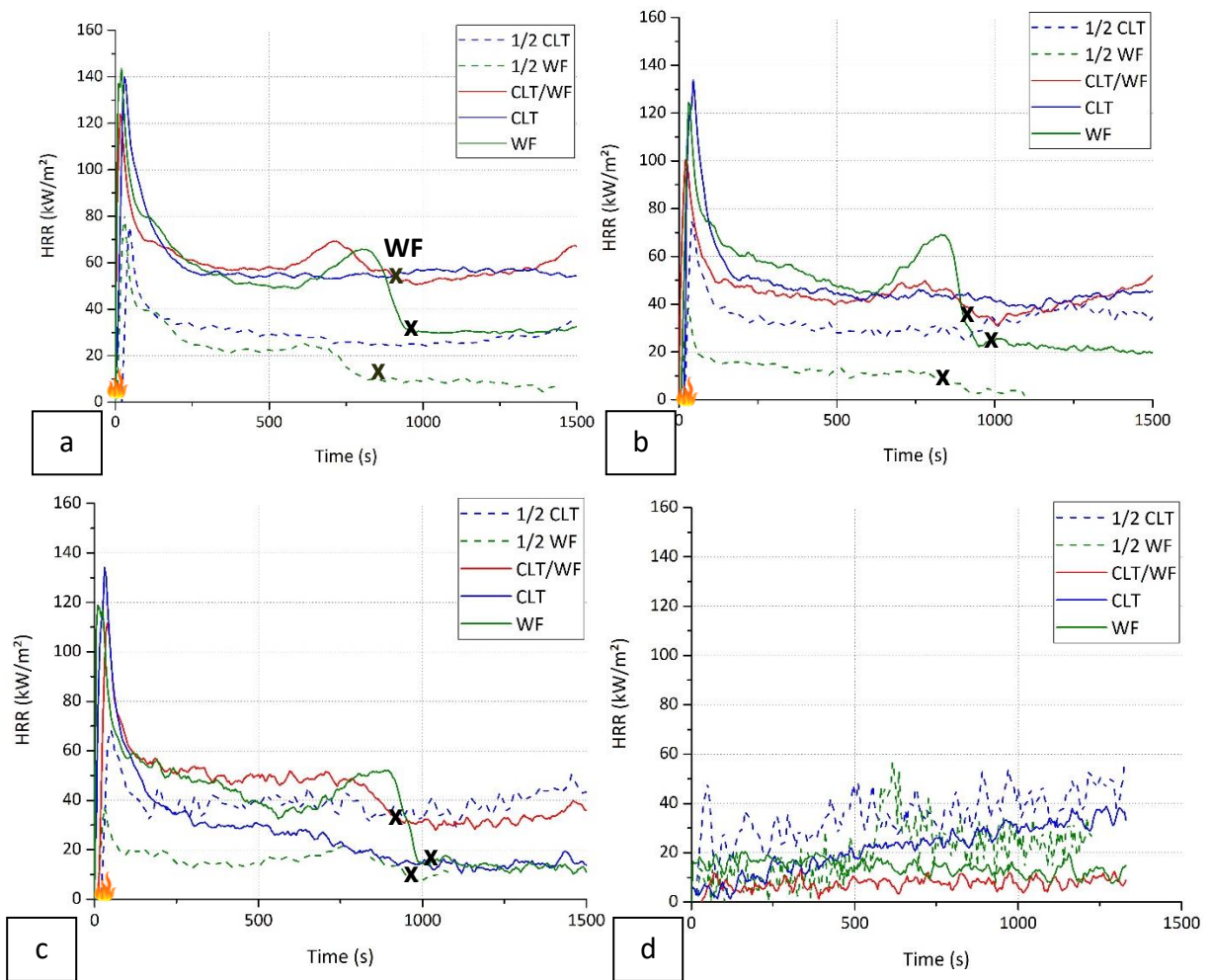


Figure 88: Effect of the combination on the HRR at 50 kW/m² at a. 21 vol-% O₂, b. 18 vol-% O₂, c. 15 vol-% O₂ and d. 10 vol-% O₂, x is for flameout

Furthermore, at 10 vol-% O₂, the CLT/WF combination decomposes without flames. Low values of HRR are obtained because the oxygen consumption is at the limit range of the measuring device, thus the measurement is noisy. However, in trends, the HRR slowly increases in the early stage of the test and

remains steady until the end of the test (Figure 88d). This behavior is consistent with those of single CLT and WF.

These results point out that combining WF and CLT influences the ignition of CLT at 21 and 18 vol-% O₂ but not at 15 vol-% O₂. Moreover, the HRR curves of the assembly are the succession of both single behaviors of CLT and WF. To better understand the HRR results and possible interactions in the gas phase, the gas production of the CLT/WF combination is assessed.

3.1.1.2. Gas production of Cross-Laminated Timber/Wood fiber at 50 kW/m²

In this section, the gas production of the CLT/WF assembly is compared to the ones of half and entire samples of CLT and WF.

At the beginning of the thermal exposure, water, carbon dioxide, carbon monoxide, formaldehyde, methanol, formic acid, and phenol type compounds are identifiable on FTIR spectra (Appendix 16 p265). As for the HRRs, the curves of CO₂, CO, CH₂O and CH₄ production at 21 vol-% O₂ follow the trends of both half CLT and half WF. More precisely, the production of CH₂O peaks as the half samples of CLT and WF undergo decomposition before ignition (Figure 89a). Then, a peak of CO₂ occurs at ignition (Figure 89b), swiftly followed by peaks in CO and CH₄ due to the carbonization of CLT and WF (Figure 89c and Figure 89d).

Upon thermal return, there are increases in CO₂, CO and CH₄, as the behavior of a single WF specimen. Notably, there is nearly twice the amount of CO and CH₄ emitted by a half WF specimen (green curve) compared to the WF in the assembly (red curve). In fact, the thermal return of half WF occurs approximately 150 seconds earlier than that of WF in the assembly. Furthermore, the remaining mass of half WF before the thermal return is 32%, while at 18 vol-% O₂, it is 21%. It is interesting because the thermal return at 18 vol-% O₂ takes place around 800s like the CLT/WF assembly. As the thermal gradient leading to thermal return is faster in the half WF, there is more sample to decompose, and thus more CO produced.

At the end of the test, excluding CO₂ as CLT is still burning, all gaseous emissions decrease. Except for small increases in CO and CH₄ production (related to CLT incomplete combustion and discussed in the next section), the same trends are observed at 18 and 15 vol-% O₂ (see Appendix 17 p268).

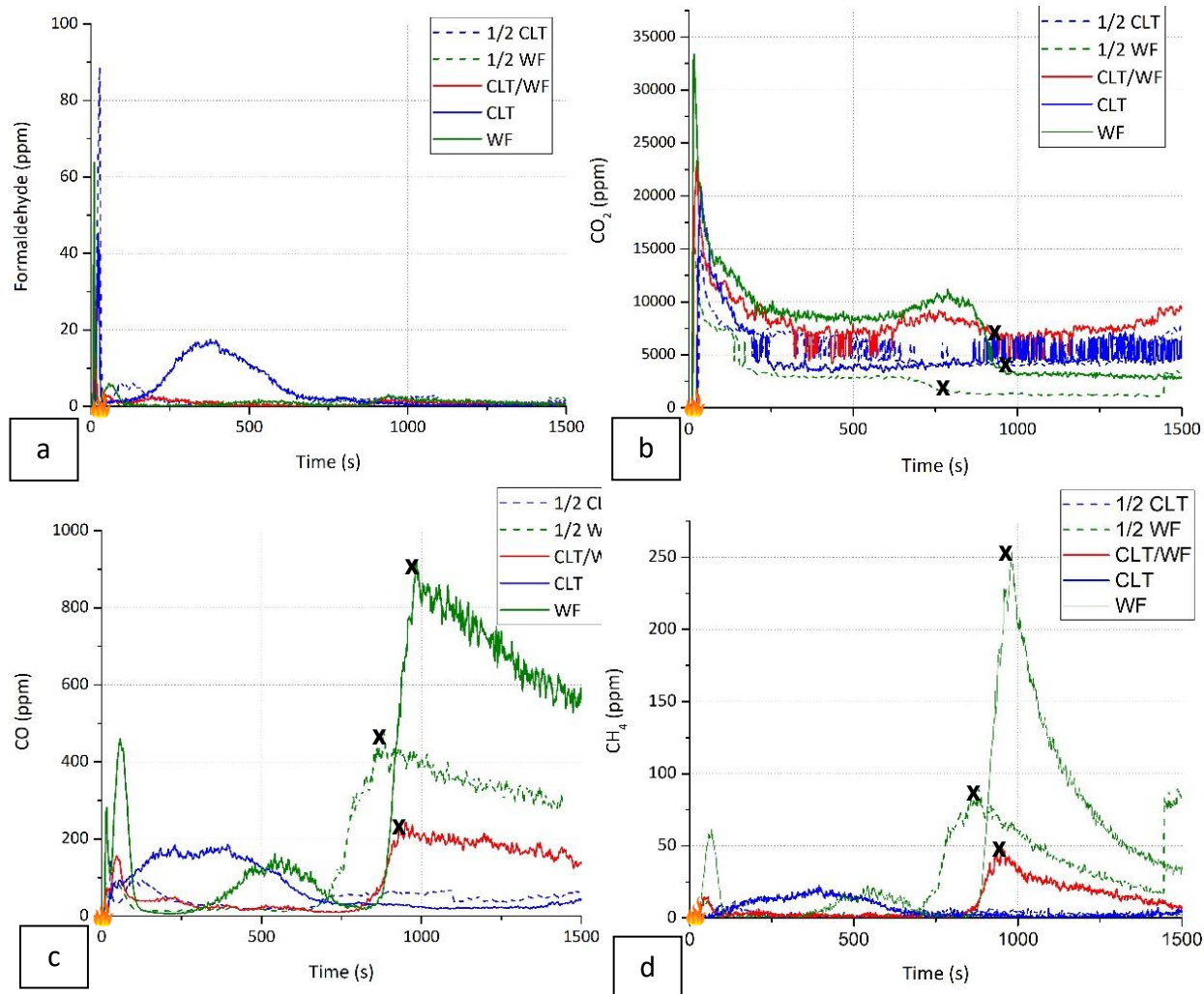


Figure 89: Gas production of the CLT/WF combination, half samples, and entire samples of CLT and WF at 21 vol-% O₂. a. CH₂O, b. CO₂, c. CO, d. CH₄

At 10 vol-% O₂ (non-flaming combustion), there are noticeable increases of CH₂O (Figure 90a), CO₂ (Figure 90b), CO (Figure 90c), and CH₄ (Figure 90d) at the start of the decomposition. These increases are observed for all samples (CLT and WF) and are of similar magnitude than the entire samples of CLT or WF.

Then, the production of CH₂O, CO and CH₄ decrease to reach a steady state, while that of CO₂ remains relatively stable. It should be underlined that the thermal return leading to increases in the overall gas production of half WF (green curves) does not clearly appear in the assembly gas production curves. Yet, slight increases in CO, CH₄ and CO₂ productions are observed around 700s, which could potentially be ascribed to thermal return of WF.

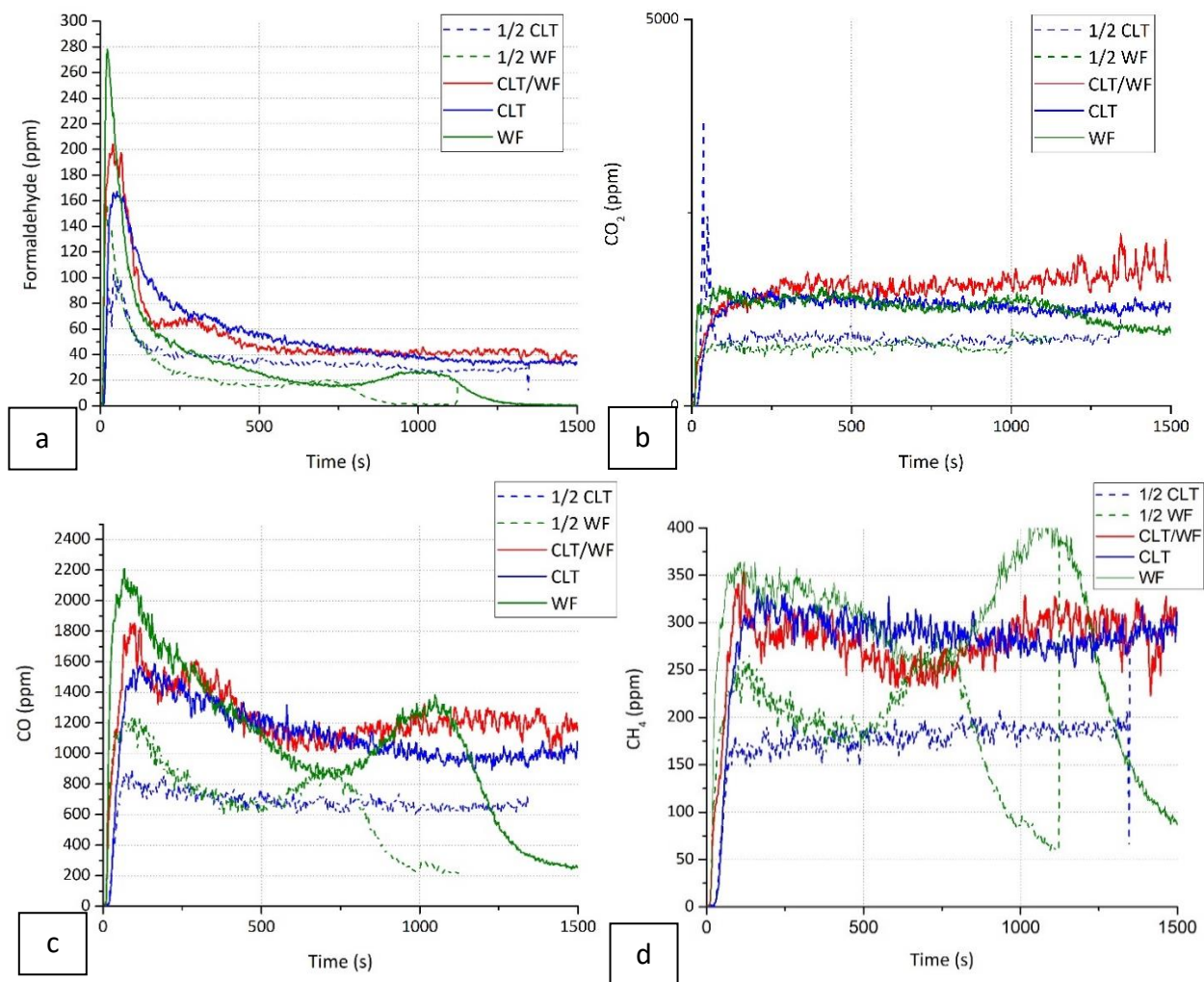


Figure 90: Gas production of the CLT/WF combination, half samples, and entire samples of CLT and WF at 10 vol-% O₂. a. CH₂O, b. CO₂, c. CO, d. CH₄

In this section, the effect of the CLT/WF assembly on the gas production was assessed at 21, 18, 15 and 10 vol-% O₂. The shapes of the gas production curves of the assembly are the result of successive gas production of CLT and WF, which suggest no significant interactions between the two materials.

3.1.1.3. Aerosol production of Cross-Laminated Timber/Wood fiber at 50 kW/m²

In this section, the effect of the assembly of CLT/WF at ignition or at the beginning of thermal exposure on the aerosol production is investigated.

At 21 vol-% O₂, the distribution size of aerosols of the assembly is multimodal centered on the modes 0.267, 0.173 and 0.407 μm (Figure 91a). This distribution is similar as the ones of CLT and WF, both entire and half samples. Moreover, at 18 and 15 vol-% O₂ (Figure 91b and Figure 91c), the distributions size in

aerosols are multimodal centered on the modes 0.173, 0.267 and 0.109 μm , which is alike as single half CLT and WF.

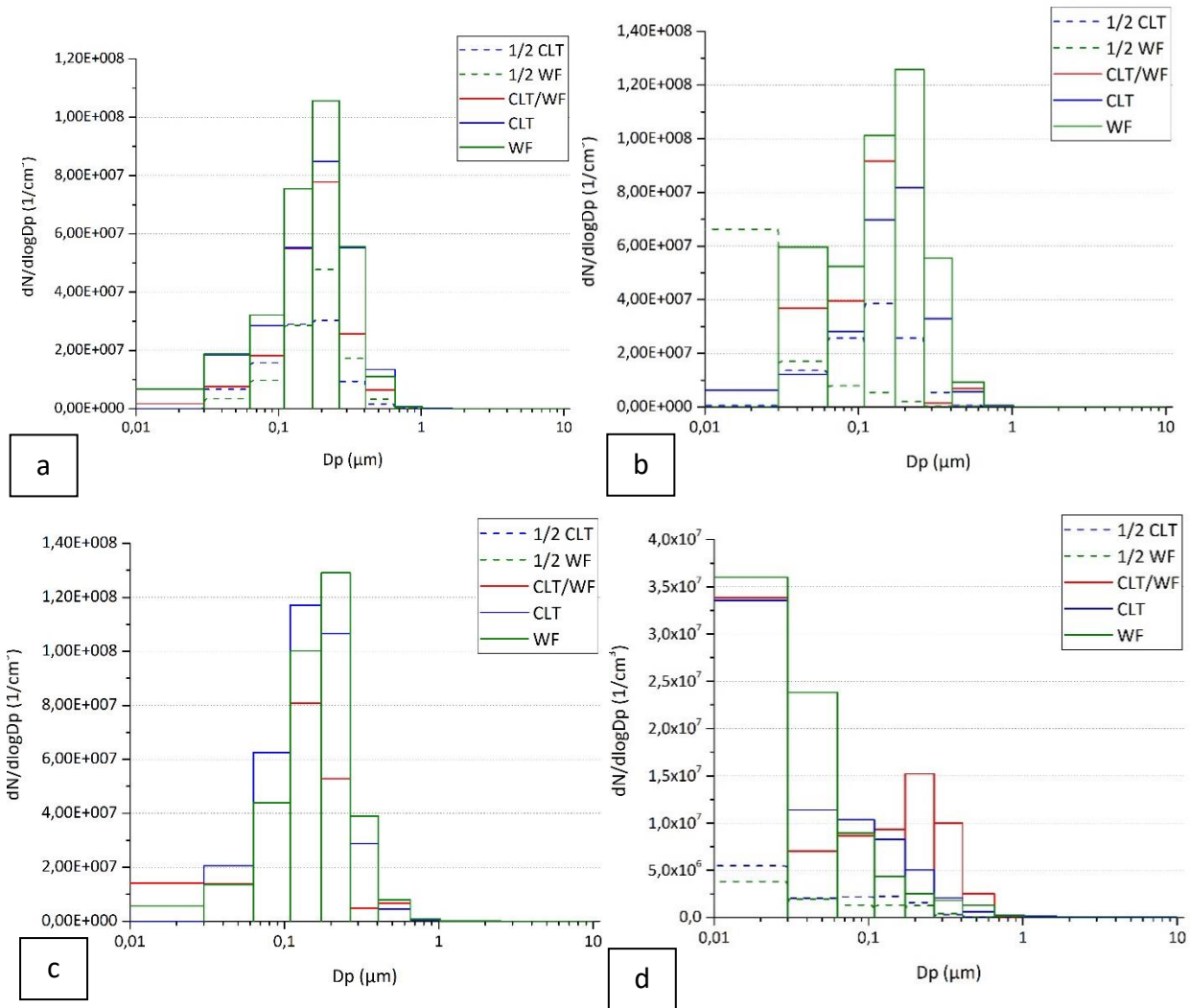


Figure 91: Distribution size of aerosols at 50 kW/m²: a. 21 vol-% O₂, b. 18 vol-% O₂, c. 15 vol-% O₂ and d. 10 vol-% O₂

At 10 vol-% O₂ (Figure 91d), all the distributions are centered on the modes 0.03 μm . As for single CLT (see section 1.1.3 p137 for better scale), a multimodal distribution centered on the modes 0.267, 0.407, 0.173 and 0.109 is observed for the CLT/WF assembly.

To summarize, it can be concluded that the ignition of the easier-to-ignite material, in this case WF, can trigger the ignition of the other material (CLT). For both flaming and non-flaming samples, the CLT/WF assembly's curves of HRR and gas production follow the trends observed in single materials. Moreover, the aerosol size distribution is like that of single CLT and WF for both flaming and non-flaming samples. All

these observations suggest that CLT and WF do not interact during thermal decomposition, except at ignition. The assembly behave like a single material whose behavior is the succession of those of CLT and WF. It should be verified whether the oxygen has the same effect on the CLT/WF assembly than on single materials.

3.1.2. Effect of oxygen level on the CLT/WF assembly fire behavior, gas, and aerosol production at 50 kW/m²

As the reaction to fire, gas, and aerosol production of CLT and WF depend on the oxygen level, it is essential to study whether the assembly of the CLT/WF responds the same way. In this section, only the data on ignition, HRR, gas and aerosol of the assembly at 50 kW/m² and 21, 18, 15 and 10 vol-% O₂ are presented.

3.1.2.1. Ignition and heat release of the CLT/WF assembly at 50 kW/m²

The effect of oxygen concentration on ignition (Table 20) and the heat release rate at 50 kW/m² (Figure 92) is studied.

As a recall, at 21, 18 and 15 vol-% O₂, WF ignites first at times to ignition like those of single WF (Table 20). The oxygen level, which had no influence on the time to ignition of CLT (Table 15 p131) and WF (Table 18 p150), neither influences the time to ignition of WF in the assembly considering the standard deviations. However, it does influence the ignition of CLT; while the ignition of CLT by WF is instantaneous at 21 vol-% O₂, it takes a few more seconds at 18 vol-% O₂. The oxygen effect is even greater at 15 vol-% O₂ where the time to ignition of CLT increases of 10s compared to 18 vol-% O₂ (Table 20). It suggests that at 21 and 18 vol-% O₂ the heat induced on the surface of CLT by the WF is high enough to accelerate the decomposition of CLT. However, at 15 vol-% O₂, the additional temperature is too low to lead to a sooner ignition of CLT. Consequently, it confirms that the flux radiated by the flame of WF decreases with oxygen concentration and that oxygen affects the ignition of the assembly of CLT/WF.

Moreover, the oxygen level has a slight influence on the HRR at ignition. Indeed, there is an 11% of decrease between the pHRR from 21 to 15 vol-% O₂ (Table 20). In fact, this effect was observed with the WF (0 p148) but not with the CLT (1.1.1129). As explained, the lack of oxygen leads to a less intense flame as there is less oxygen to complete the reaction of combustion. Moreover, the steady state (Figure 92), reached after ignition also exhibits higher HRR values at higher oxygen levels, as experienced with CLT (Figure 63 p131). These differences are related to the char layer of CLT, which are thicker with oxygen decrease.

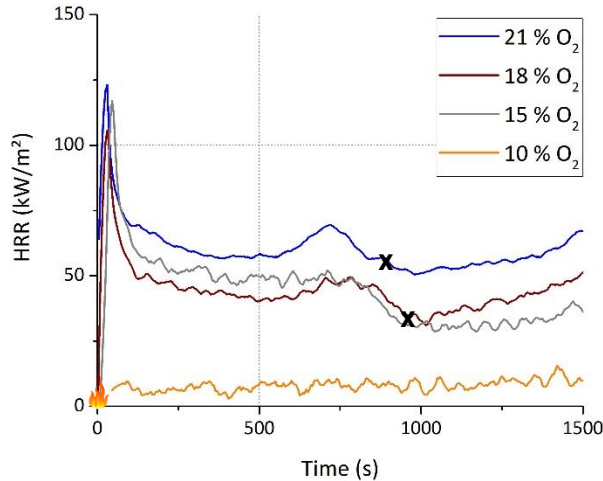


Figure 92: Effect of oxygen on the HRR of the CLT/WF assembly at 50 kW/m², x is for flameout

Between 15 and 10 vol-% O₂, the combustion behavior switches from flaming to non-flaming (Figure 92). At 10 vol-% O₂, the fuel/oxidant mixture falls below the limiting oxygen concentration. Initially, a gradual increase occurs during the early stages of the test before stabilizing.

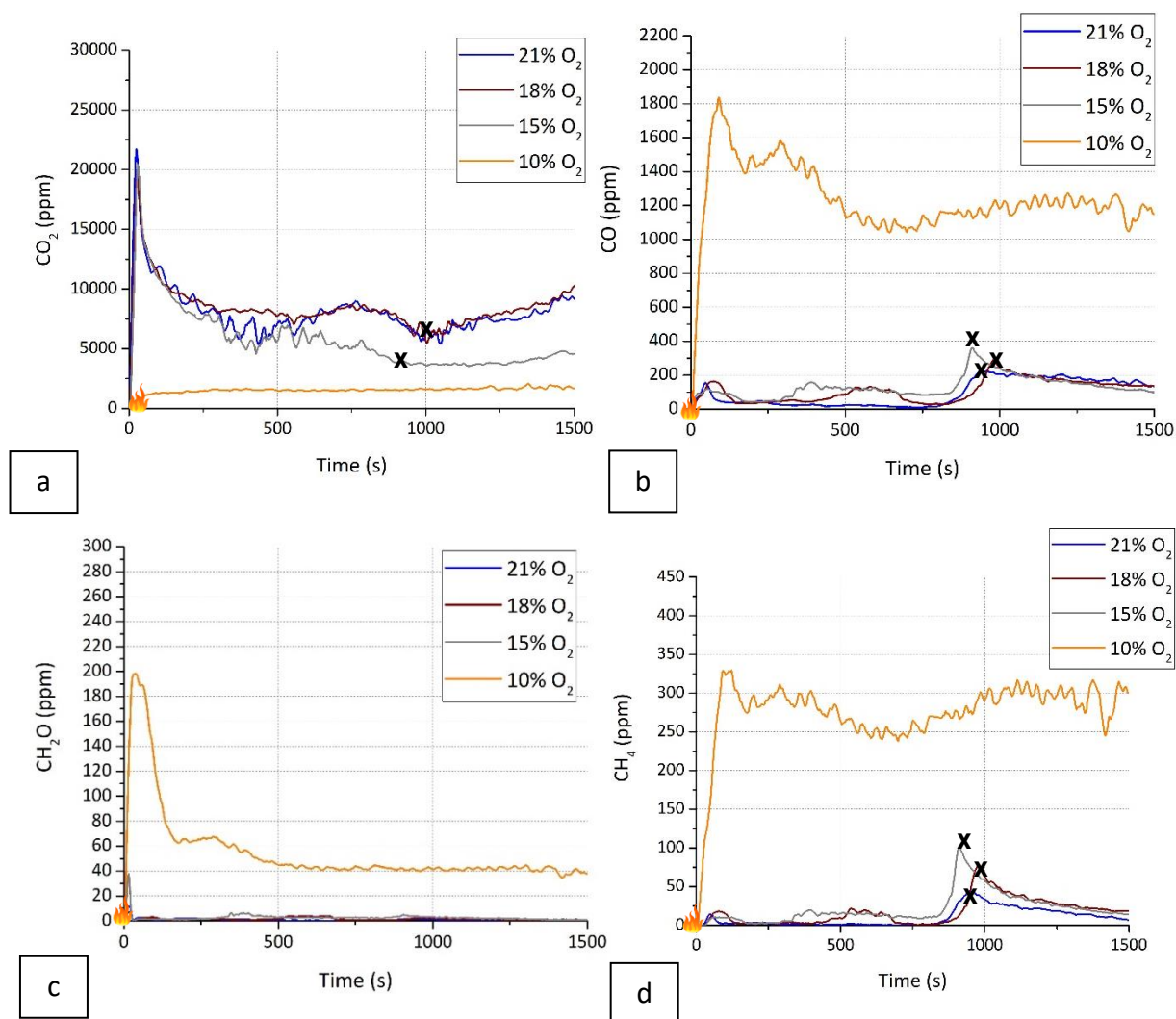
At 50 kW/m², the decrease in oxygen leads to a delay in the ignition of CLT while the ignition of WF is not affected. It also slightly affects the pHRR at ignition and the steady state. At 10 vol-% O₂, the combustion switches to non-flaming. It is interesting to note that the HRR of the assembly of CLT/WF undergoes the same effect of oxygen as single CLT or WF.

3.1.2.2. Gas production of the CLT/WF assembly at 50 kW/m²

For flaming specimens (21, 18 and 15 vol-% O₂), the FTIR spectra display the presence of water, carbon dioxide, carbon monoxide, formaldehyde, methanol, formic acid and phenol type compounds (Appendix 16 p265). For further details on the potential formation pathways of these compounds, the reader can refer to the Table 16 p134.

In general, for each curve of gas production, the same shape is found whatever the flaming sample. Nevertheless, the production of CO (Figure 93b) increases from 300s at 15 vol-% O₂ and from 400s at 18 vol-% O₂. These increases are due to zones of incomplete combustion within the samples, which are caused by a lower oxygen availability. Moreover, during the thermal return of WF, the concentration in CO and CH₄ doubles from 21 to 15 vol-% O₂ (Figure 93b and Figure 93d). The limited oxygen supply directly impacts the conversion of fuel into carbon dioxide (Figure 93a) during the combustion process. Similar observations were made for single CLT (1.1.2 p.133) and WF (0 p.151).

At 10 vol-% O₂, the gas production is altered by the absence of flaming combustion. On the FTIR spectra, water, carbon dioxide, carbon monoxide, methane, ethene, formaldehyde, methanol, acid formic and phenol type compounds are identifiable at the beginning of the thermal decomposition (Appendix 16 p265). Quantitatively, the production of CO, CH₄ and CH₂O are respectively 9, 18 and 7 times higher than at 21 vol-% O₂ at the peak of thermal decomposition (Figure 93b, Figure 93c and Figure 93d). Moreover, peaks in ethene (20 ppm) (Figure 93e) occur during the decomposition, which were not observed for flaming samples. Thus, oxygen vitiation favors the production of unburnt species at the expense of carbon dioxide (Figure 93a).



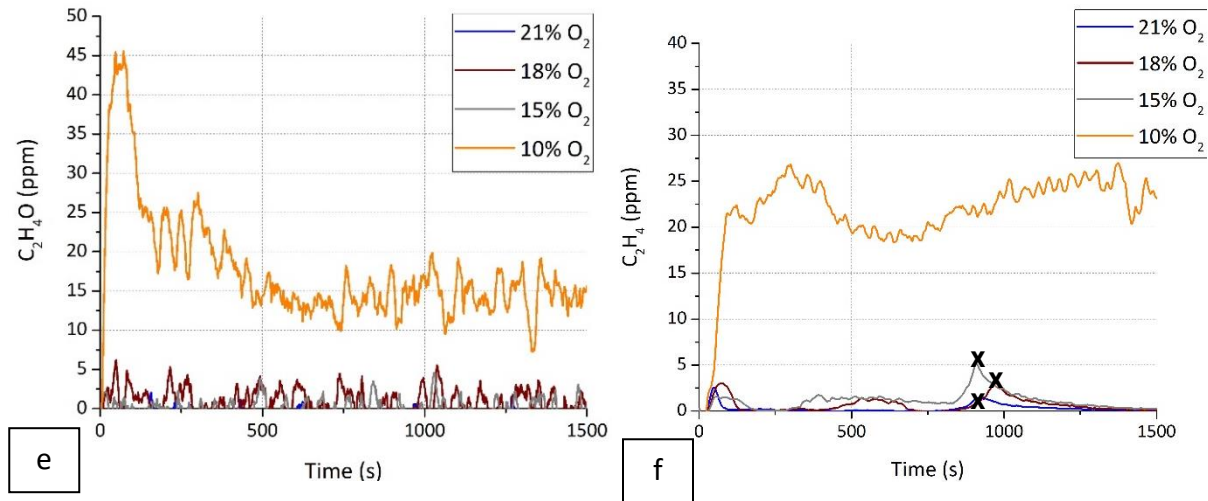


Figure 93: Influence of the oxygen level the gaseous emissions of the CLT/WF assembly at 50 kW/m²: a. CO₂; b. CO; c. CH₂O d. CH₄; and e. C₂H₄, x is for flameout

At 50 kW/m², oxygen decrease favors incomplete combustion and thus the production of unburnt gases such as CO and CH₄. When the combustion is non-flaming, the production in unburnt is promoted.

3.1.2.3. Aerosol production of the CLT/WF assembly at 50 kW/m²

To conclude this characterization, the effect of oxygen on the aerosol size distribution is assessed.

At 21 vol-% O₂, the aerosol size distribution at ignition is multimodal centered on the modes 0.267, 0.173 and 0.407 μm (Figure 94a). Oxygen decrease slightly modifies this distribution at 18 and 15 vol-% O₂ as the distribution is also multimodal but centered on the modes 0.173, 0.267 and 0.109 μm. It suggests that aerosols of smaller size are promoted with oxygen decrease for the assembly of CLT/WF. This was also observed for CLT and WF. Overall, the concentration of aerosols in these modes are of the same order of magnitude. Following ignition, the aerosol size distribution switches to a monomodal pattern centered on the mode 0.03 μm (Figure 94b), as observed for single CLT and WF.

For non-flaming specimen (10 vol-% O₂), during the whole test the distribution is centered on the mode 0.03 μm but it also exhibits a multimodal distribution on the modes 0.173, 0.109 and 0.267 μm, which was observed with CLT too.

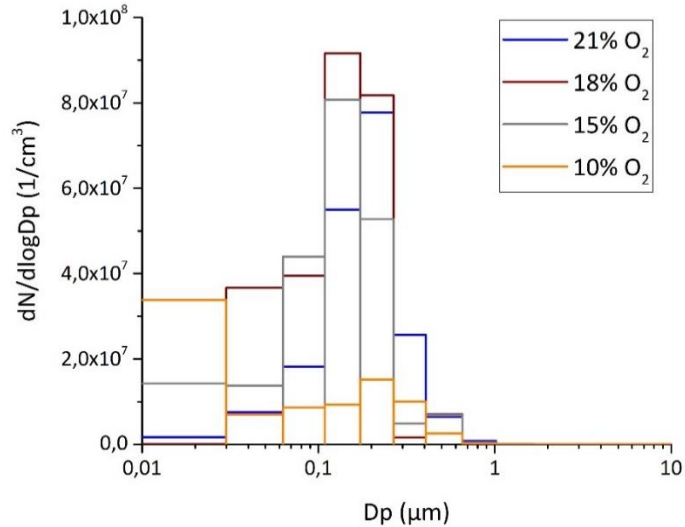


Figure 94: Distribution size of aerosols of the CLT/WF assembly at 50 kW/m² at: a. ti or the beginning of the thermal exposure

After conducting a complete assessment of the influence of oxygen on the fire behavior, gas production, and aerosol production of the CLT/WF assembly at 50 kW/m², it is crucial to replicate this study at a lower heat flux. The temperature variations may significantly affect the previously established understanding of the impact of oxygen level.

3.2. Effect of the assembly and the oxygen level at 20 kW/m²

As the reaction to fire of CLT and WF depends on the thermal attack, the behavior of the CLT/WF assembly under reduced oxygen was assessed at 20 kW/m². The effect of combining CLT to WF is studied first before investigating the influence of oxygen of the fire behavior, gas, and aerosol emissions of the CLT/WF assembly. All the replica curves are gathered in the Appendix 1 p270.

3.2.1. Fire behavior of the assembly, gas production and aerosol production of the Cross-Laminated Timber/Wood Fiber assembly at 20 kW/m²

3.2.1.1. Ignition and heat release of the CLT/WF assembly at 20 kW/m²

At 20 kW/m², the samples at 21, 18 and 15 vol-% O₂ ignite while the decomposition is non-flaming at 10 vol-% O₂.

More precisely, at 21 vol-% O₂, the WF part of the assembly ignites at 81s, which is like the time to ignition of single WF considering the standard deviations. The CLT of the assembly ignites at 202s whereas a single CLT ignites at least around 400s (Table 21). It is also interesting to note that WF flames out just before the ignition of CLT, while a single WF would burn until at least 450s. Consequently, the ignition of WF triggers an earlier ignition of CLT, and conversely, the ignition of CLT may lead to a quicker flaming-out of WF.

Moreover, at 18 and 15 vol-% O₂, the times to ignition of WF are also close to single WF considering the standard deviations (Table 21). However, the CLT part of the assembly does not ignite. In the case of 18 vol-% O₂, there are enough volatiles produced (see the section 1.1.1.1 p.179), which would typically lead to the ignition of single CLT. However, the removal of the igniter after WF ignition prevents the ignition of CLT. As a result, a heat flux of 20 kW/m² is insufficient for CLT to self-ignite at 18% vol-% O₂. In the case of 15 vol-% O₂, both single CLT and CLT of the CLT/WF assembly decompose without igniting, which is due to oxygen lacking. This will be discussed in the next sections.

Table 21: Fire parameters of CLT/WF at 20 kW/m²

	t _i (s)	Standard deviation (s)	t _{out} (s)	Standard deviation (s)	pHRR (kW/m ²)	Standard deviation (kW/m ²)
21% O₂						
CLT: 1	400		-	-	96	4
CLT: ½	700	105	1320	33	34	
WF: 1	69	3	600	42	87	3
WF: ½	48	1	450	59	75	9
CLT/WF	81 (WF) - 202 (CLT)	14 - 47	200 (WF)	28	30 (WF) -74 (CLT)	5-6
18% O₂						
CLT: 1	1000		1400	22	51	7
CLT: ½	770	257	950	41	21	4
WF: 1	62	7	760	45	78	6
WF: ½	45	3	315	33	25	2
CLT/WF	91 (WF)	25	280	35	38	5
15% O₂						
CLT: 1	-	-	-	-	10	4
CLT: ½	-	-	-	-	12	2
WF: 1	56	5	125	4	78	2
WF: ½	47	1	90	4	18	4
CLT/WF	110 (WF)	8	115	49	45	11

The HRR curves of the CLT/WF assembly follow the trends of half CLT and half WF. Indeed, at 21 vol-% O₂, two peaks of heat release occur (Figure 95a), corresponding to the WF and CLT ignitions. The pHRR of WF is slightly lower than the pHRR of half WF while the pHRR of CLT is more than two times the one of half CLT. At the end of the test, as half and entire single CLT, the HRR of the CLT/WF assembly remains around 20 kW/m² as CLT is still burning.

Moreover, at 18 and 15 vol-% O₂, the HRR curves (Figure 95b and Figure 95ac) follow the trend of WF at the beginning, with pHRR similar as half specimens of WF. The HRR drops as WF flames out but slightly

increases again around 600 and 800s at 15 and 18 vol-% O₂ respectively as CLT starts to decompose. At the end of test, the HRR remain steady around 20 kW/m².

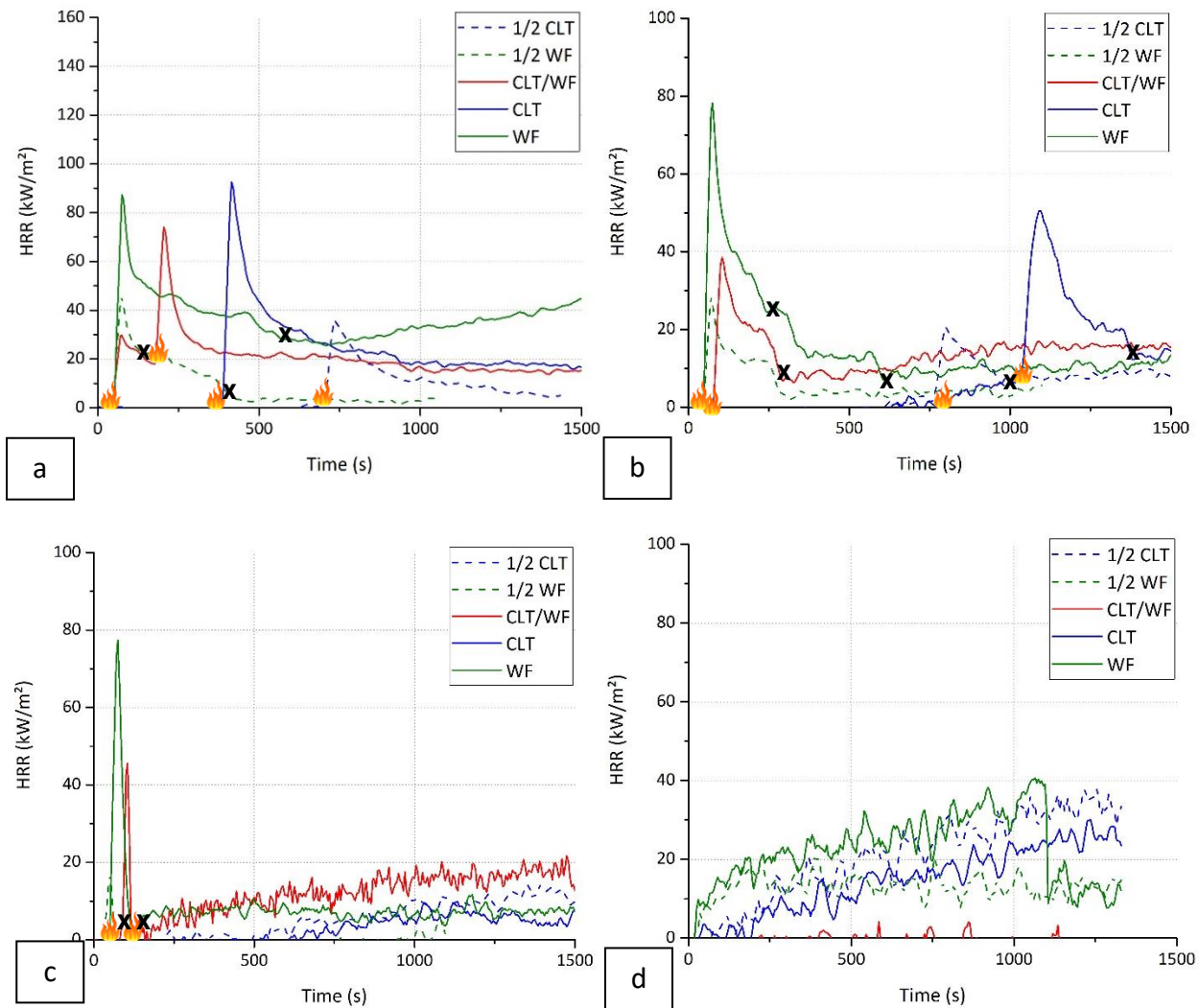


Figure 95: Effect of the combination on the HRR at 20 kW/m² at a. 21 vol-% O₂, b. 18 vol-% O₂, c. 15 vol-% O₂ and d. 10 vol-% O₂, x is for flameout

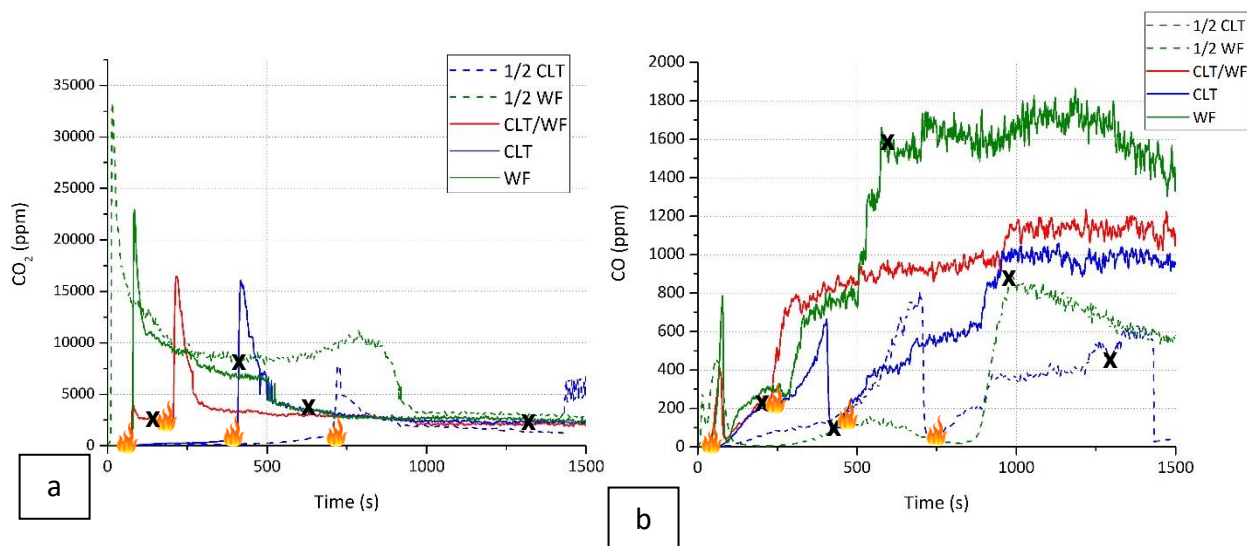
At 10 vol-% O₂, the CLT/WF assembly decomposes without flames. Low values of HRR are obtained because the oxygen consumption is at the limit range of the measuring device, thus the measurement is noisy. However, in trends, the HRR is expected to increase in the early stage of the test and remain steady for the rest of the test (Figure 95d). This behavior would be consistent with the ones of single CLT and WF.

These results point out that combining WF and CLT influences ignition. However, from the HRR data, no interaction seems to occur between CLT and WF. To better assess the phenomenon and possible interactions in the gas phase, the gas production of the CLT/WF combination is investigated.

1.1.1.1. Gas production of the CLT/WF assembly at 20 kW/m²

In this section, the gaseous emissions of the CLT/WF assembly are compared to the ones of half and entire samples of CLT and WF.

At the beginning of the thermal exposure, water, carbon dioxide, carbon monoxide, formaldehyde, methanol, formic acid and phenol type compounds are identifiable on FTIR spectra at 21, 18 and 15 vol-% O₂ (Appendix 19 p275). More precisely, at 21 vol-% O₂, the curves of CO₂, CO, CH₂O and CH₄ productions follow the trends of both half CLT and half WF but earlier in time. Formaldehyde is first emitted (Figure 96c) as the sample thermally decomposes. Then, the production of CO₂ (Figure 96a) peaks at the WF ignition while peaks of CO (Figure 38b) and CH₄ (Figure 38d) occur right after ignition as the sample carbonizes. The production of CO₂ peaks again as CLT ignites around 200s before reaching a steady state, which is consistent with the CO₂ production curve of single CLT. As WF flames out, a dramatic increase in CO and CH₄ occur until reaching a steady state, as for single WF. Consequently, the overall gas production of the CLT/WF assembly at 21 vol-% O₂ is the succession of single gas production of CLT and WF but with different kinetics.



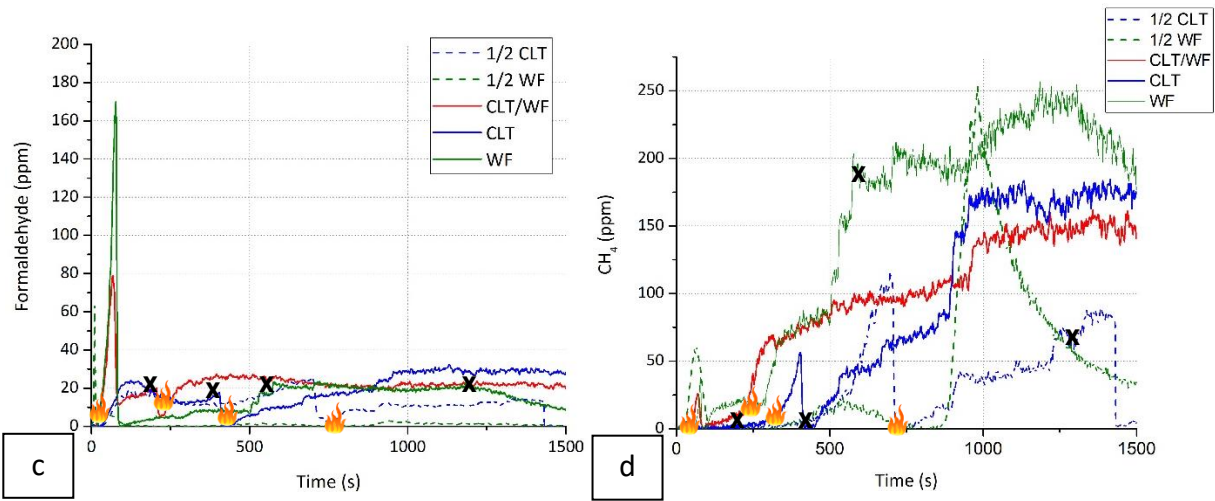
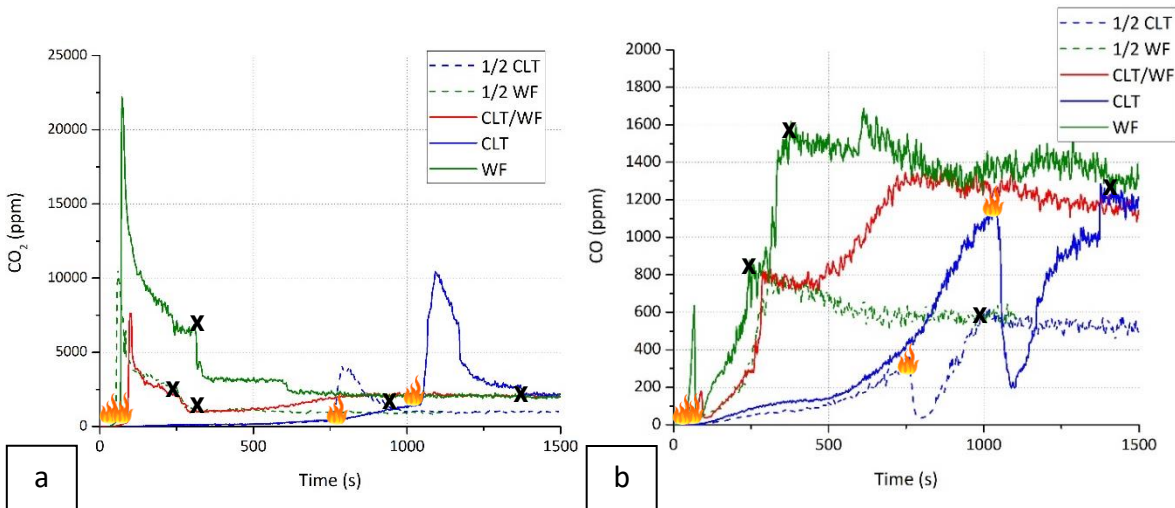


Figure 96: Gas production of the CLT/WF combination, half samples, and entire samples of CLT and WF at 20 kW/m² and 21 vol-% O₂. a. CH₂O, b. CO₂, c. CO, d. CH₄

At 18 and 15 vol-% O₂, the trends in gaseous emissions are similar and can be identified as the succession of WF and CLT single's behavior too. Indeed, before the ignition of WF, a peak in CH₂O emission (Figure 97c) arises as the sample decomposes. It is followed at WF ignition by a peak of CO₂ (Figure 97a), which production last until WF flames out. Moreover, increases in CO (Figure 97b) and CH₄ (Figure 97d) follow as the WF flames out and they reach maxima at 300s. Simultaneously the production of CH₂O arises again to reach a peak, corresponding to the decomposition of CLT (blue curves). However, as there is no sparkle to ignite the mixture, the production of CO and CH₄ dramatically increases. Consequently, the production in CO₂ displays a slight increase but remain low as the oxidation reaction favors the production of CO (ratio CO/CO₂ ~ 0.65). At the end of the test, all gaseous emissions reach a steady state. The curves at 15 vol-% O₂ can be found in the Appendix 1 p275.



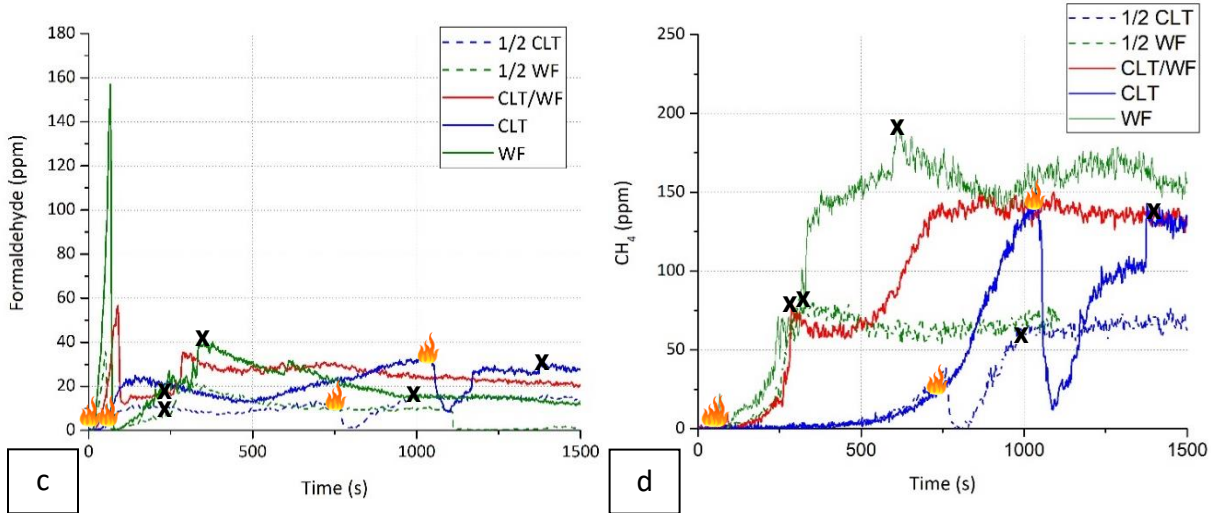
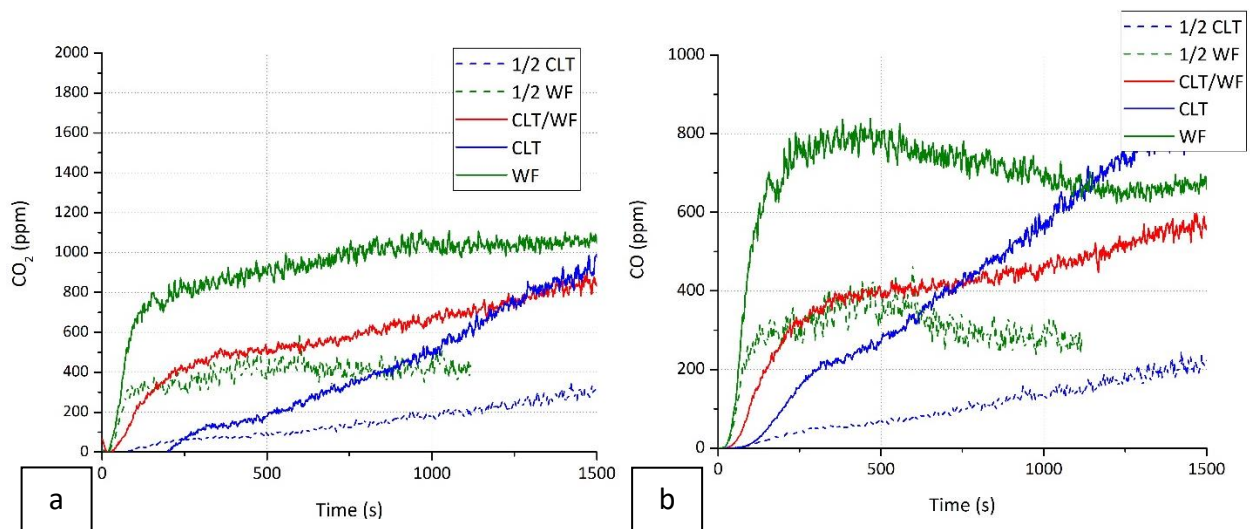


Figure 97: Gas production of the CLT/WF combination, half samples, and entire samples of CLT and WF at 20 kW/m² and 18 vol-% O₂. a. CH₂O, b. CO₂, c. CO, d. CH₄

At 10 vol-% O₂, the gas production of the CLT/WF is the succession of WF and CLT trends. The thermal decomposition starts with the release of CH₂O (Figure 98c) and CO₂ (Figure 98a), which are quickly followed with increases of CO (Figure 98b) and CH₄ (Figure 98d). These gas productions mainly correspond to the WF decomposition (green curves). It is interesting to note that from 400s the increases of gas production, apart from CH₂O, are ascribed to the decomposition of CLT (blue curves).



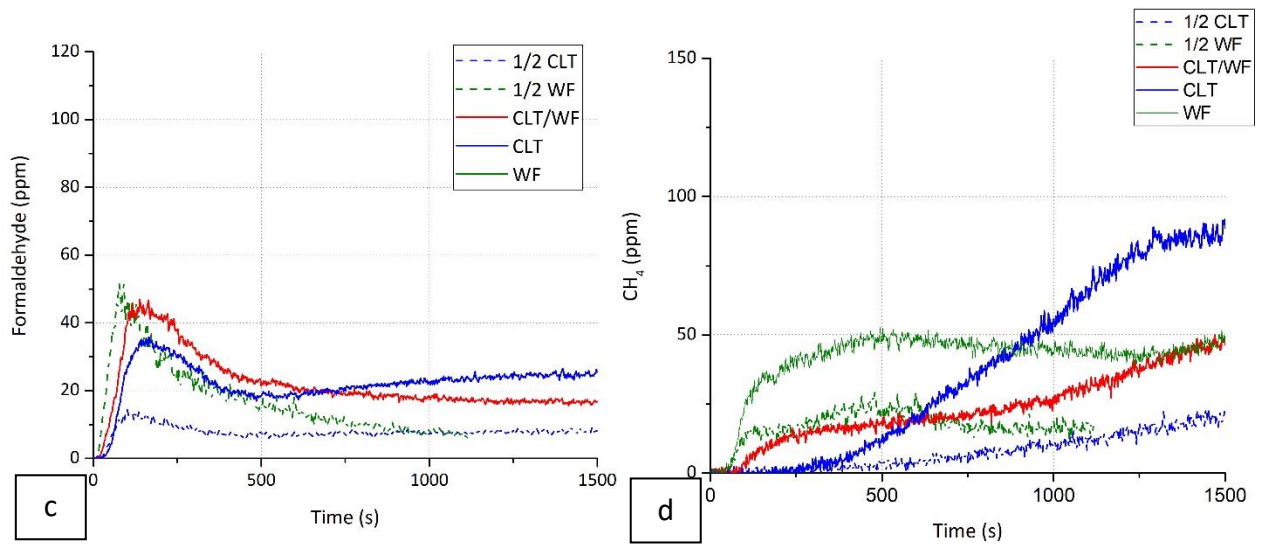


Figure 98: Gas production of the CLT/WF combination, half samples, and entire samples of CLT and WF at 20 kW/m² and 10 vol-% O₂. a. CH₂O, b. CO₂, c. CO, d. CH₄

In this section, the effect of the CLT/WF assembly on the gas production was assessed at 21, 18, 15 and 10 vol-% O₂. The shapes of the gas production curves of the CLT/WF assembly are the result of successive gas production of single CLT and WF, which suggests no interactions between the CLT and WF.

3.2.1.2. Aerosol production of the CLT/WF assembly at 20 kW/m²

In this section, the effect of the assembly of CLT/WF the aerosol production is studied, at ignition or at the beginning of thermal exposure on.

At 21 vol-% O₂, the distribution size of aerosols of the CLT/WF assembly at ignition is multimodal centered on the modes 0.109, 0.173 and 0.267 μm (Figure 99a). The aerosol size distribution is similar to that of CLT, even though CLT's distribution was primarily centered on 0.267 and 0.173 μm (see section 1.2.3 p.142). Moreover, the concentration in aerosols of the CLT/WF assembly is very low compared to single samples of CLT and WF, which can be surprising. This might be due to a technical issue; thus, the value of concentration should not be considered. At 18 and 15 vol-% O₂ (Figure 99b and Figure 99c), the distribution size of aerosols is monomodal centered on the mode 0.03 μm, which is similar to the WF aerosol size distributions (see section 2.2.3 p159).

Moreover, at 10 vol-% O₂ (non-flaming), the distribution size of aerosol is monomodal centered on the mode 0.03 μm, which is consistent with single CLT and WF.

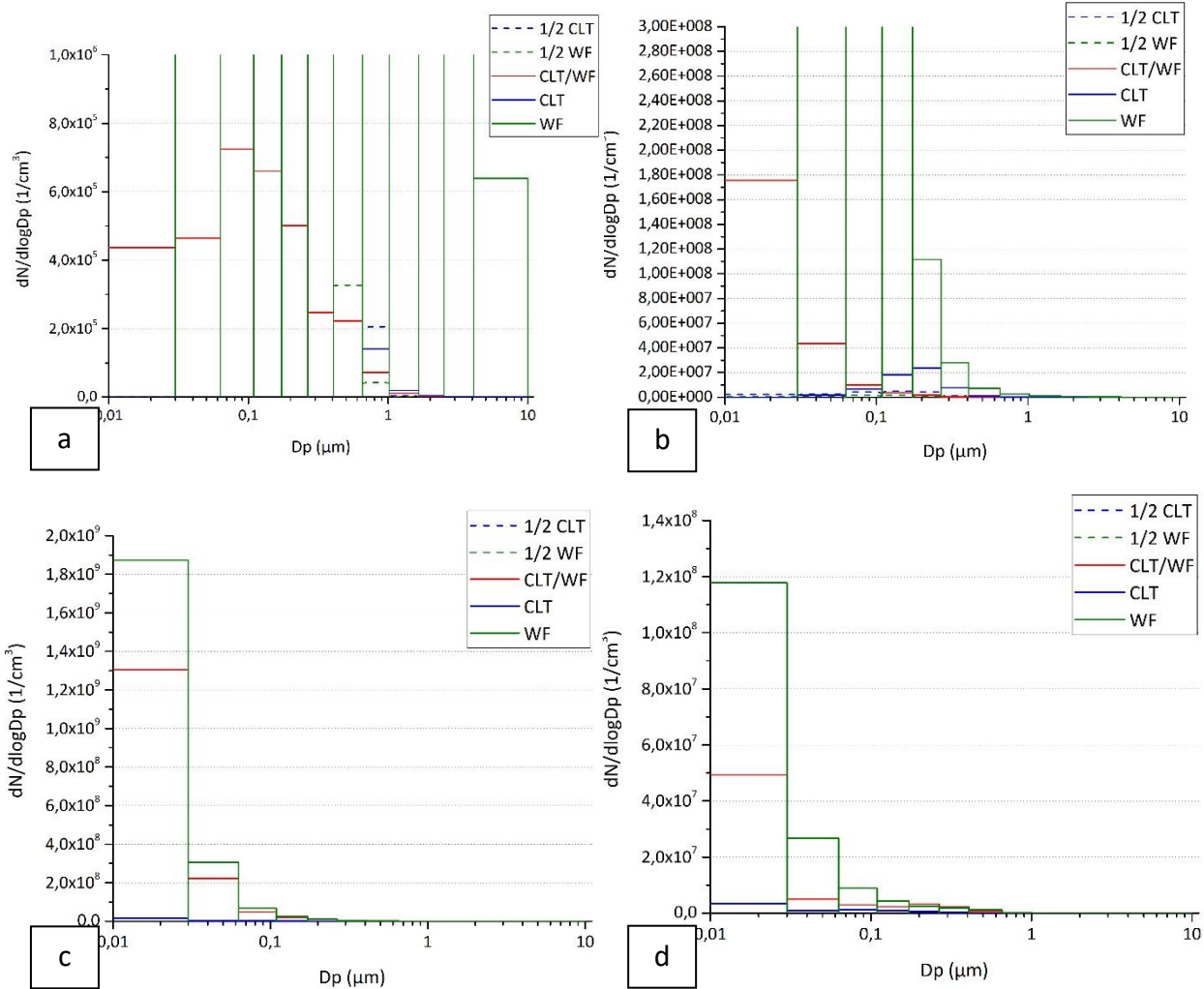


Figure 99: Distribution size of aerosols of WF at 20 kW/m² at ti: a. 21 vol-% O₂, b. 18 vol-% O₂, c. 15 vol-% O₂ and at the beginning of thermal exposure: d. 10 vol-% O₂

To conclude, the ignition of the easiest material, here WF, accelerates the ignition of the other material at 21 vol-% O₂. Regarding the HRR, the curves of the CLT/WF assembly follow the same trend as single materials whatever the oxygen concentration. The same observations are made regarding the gas production. All these observations suggest that CLT and WF do not interact during thermal decomposition, except at ignition. The assembly behaves like a single material whose behavior is the succession of those of CLT and WF. Finally, it is important to verify whether oxygen has a similar effect on the CLT/WF assembly as it does on single materials.

3.2.2. Effect of oxygen level on the CLT/WF assembly fire behavior, gas, and aerosol production at 20 kW/m²

As the reaction to fire, gas, and aerosol production of CLT and WF depend on the oxygen level and the heat flux, it is paramount to study whether the assembly of both materials respond the same way. In this section, only the data on ignition, HRR, gas and aerosol of the assembly at 20 kW/m² and 21, 18, 15 and 10 vol-% O₂ are presented.

3.2.2.1. *Ignition and heat release of CLT/WF at 20 kW/m²*

At 20 kW/m², the samples at 21, 18 and 15 vol-% O₂ decompose with flames. More specifically, CLT ignites in addition to WF only at 21 vol-% O₂. Indeed, at 18 and 15 vol-% the oxygen content is not high enough for its ignition. Nevertheless, single CLT ignited at 18 vol-% O₂, but as explained in the previous section, the igniter is removed once the WF ignites for the CLT/WF experiments. Thus, the lack of spark in addition to the lack of oxygen prevents the ignition of CLT. Moreover, regarding the ignition of the WF, the decrease in oxygen does not seem to affect ignition times if standard deviations are considered (Table 21). The same conclusions were drawn with single WF (0 p155).

Furthermore, oxygen decrease has negligible impact on the pHRR of WF (regarding standard deviations). It is noteworthy that around 1000s, the curves of HRR at 21, 18 and 15 vol-% O₂ merge around a 17 kW/m² steady state (Figure 100). Indeed, at 21 vol-% O₂, the CLT is essentially extinguished (with only small flames visible at the edges) while it undergoes decomposition without flames at 18 and 15 vol-% O₂. Thus, the samples are all governed by smoldering in the end of the test.

At 10 vol-% O₂, neither WF nor CLT ignite, thus the decomposition occurs without flames. There is a slow increase in the beginning, but the HRR remains steady at 5 kW/m² for the rest of the test.

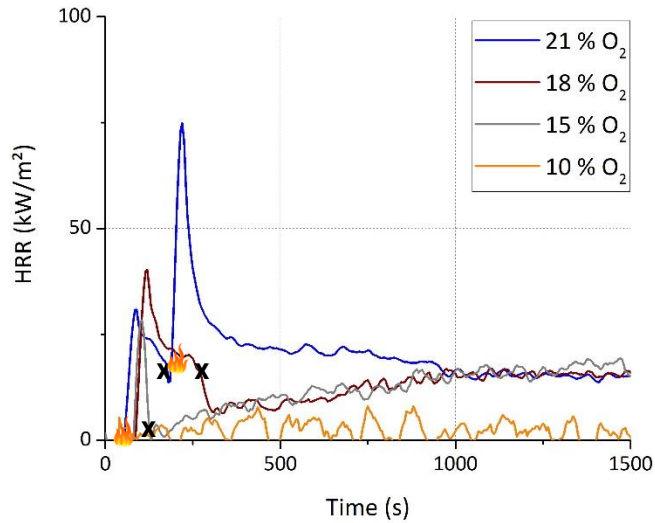


Figure 100: Effect of oxygen of CLT/WF on HRR at 20 kW/m²

At 20 kW/m², the decrease in oxygen has negligible impact on the times to ignition and peaks of HRR of WF. However, it does prevent the ignition of CLT at 15 vol-% O₂. At 10 vol-% O₂, the thermal decomposition occurs without flames.

3.2.2.2. Gas production of CLT/WF at 20 kW/m²

For flaming specimens, the FTIR spectra display before the ignition of WF the presence of water, carbon dioxide, carbon monoxide, formaldehyde, methanol, formic acid and phenol type compounds (Appendix 16 p265). A peak in formaldehyde before ignition also attests for wood decomposition (Figure 101c).

At 21 vol-% O₂, peaks of CO₂ (Figure 101a), CO (Figure 101b) and CH₄ (Figure 101d) arise at ignition of WF. It should be highlighted that the CO/CO₂ ratio is of 0.1, which indicates that the combustion is incomplete at ignition. This would explain the sudden extinction of WF at 21 vol-% O₂. Moreover, right after WF extinguishment, maxima in CO₂ and CO are reached again with CLT ignition. However, the CO/CO₂ is of 0.04, which corresponds to a complete combustion. Thus, it seems that the CLT hindered the combustion of WF. In the end of the test, the production of CO₂ slowly decreases while the one of CO and CH₄ increases as the combustion becomes incomplete. The low heat flux does not maintain the reaction of combustion despite the high oxygen level.

Furthermore, at 18 and 15 vol-% O₂, peaks in CO₂ (Figure 101a) and CO (Figure 101b) also arise at ignition. However, the CO/CO₂ ratio is higher at 18 vol-% O₂ than at 15 vol-% O₂ (0.025 vs. 0.0375), which allows for a longer flaming combustion before flameout. Increases in CO and CH₄ (Figure 101c) quickly follow

extinguishment of wood fiber. In comparison, from 15 to 18 vol-% O₂, the production of CO and CH₄ doubles at flame out.

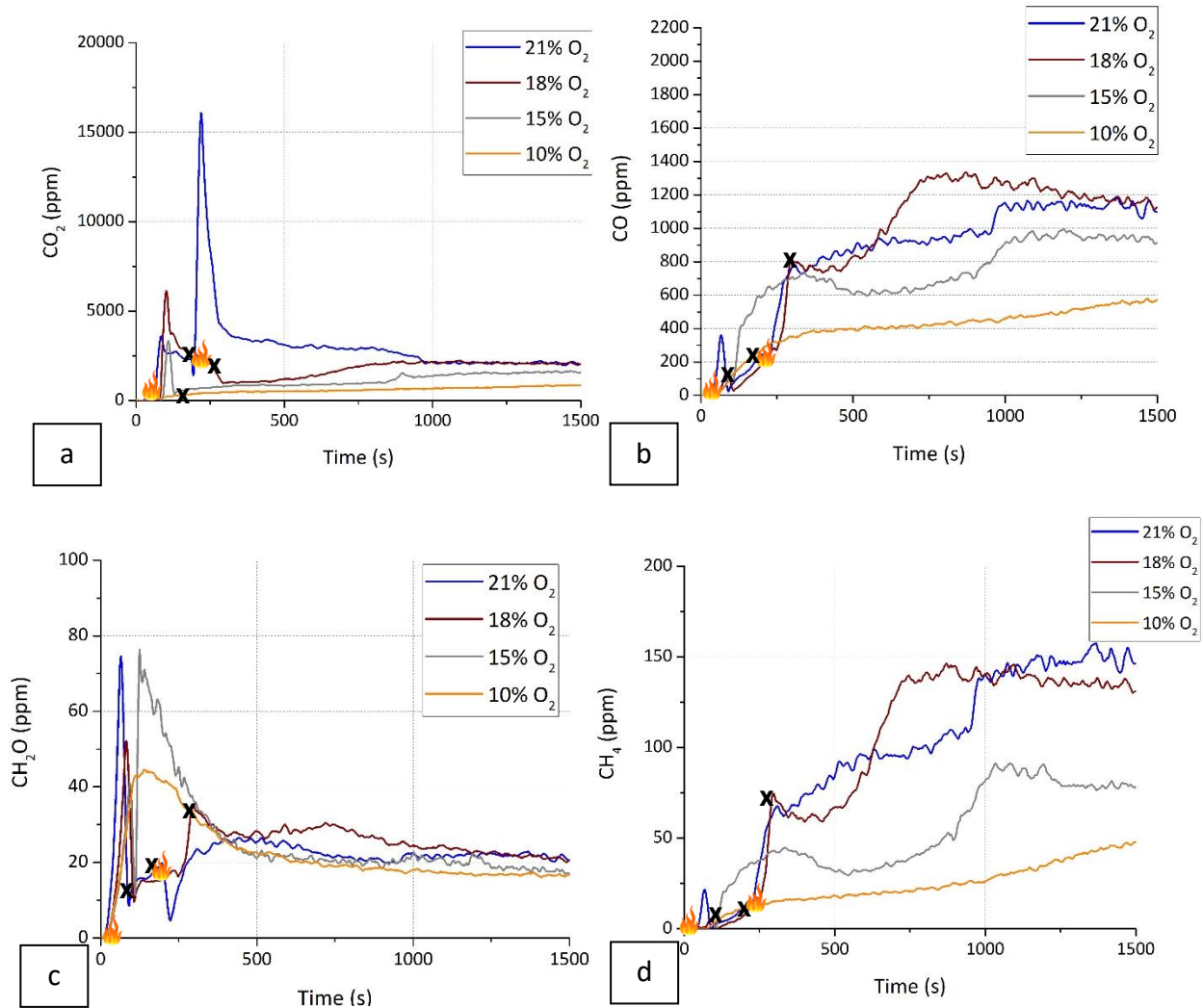


Figure 101: Influence of the oxygen level on the gaseous emissions of CLT/WF assembly at 20 kW/m²: a. CO₂; b. CO; c. CH₂O d. C₂H₄O; and e. CH₄

At 10 vol-% O₂, the FTIR spectra reveal the presence of water, carbon dioxide, carbon monoxide, formaldehyde, methanol and formic acid in the beginning of the thermal decomposition (Appendix 19 p275). As the decomposition rates are low, the gas production is low too. Only few formaldehydes (44 ppm) along with CO (200 ppm) are released in the beginning. As the emission of CH₂O decreases, the emissions of CO and CH₄ gradually increase during the rest of the test, while the concentration of CO₂ remains at around 700 ppm (Figure 101a).

At 20 kW/m², the production of unburned gases is enhanced during the flaming out of WF and when CLT undergoes decomposition without flames, particularly at high oxygen levels.

3.2.2.3. Aerosol production

To conclude this characterization, the effect of oxygen on the aerosol size distribution is assessed.

It appears that the aerosol distribution size is only multimodal centered on the modes 0.109, 0.173 and 0.267 at 21 vol-% O₂, which is not seeable on the curve because of the concentration, as explained before. The decrease in oxygen shifts then the aerosol size distributions towards monomodal distributions centered on the mode 0.03 μm (Figure 102).

At 10 vol-% O₂, the distribution size of aerosols is monomodal centered on the mode 0.03 μm.

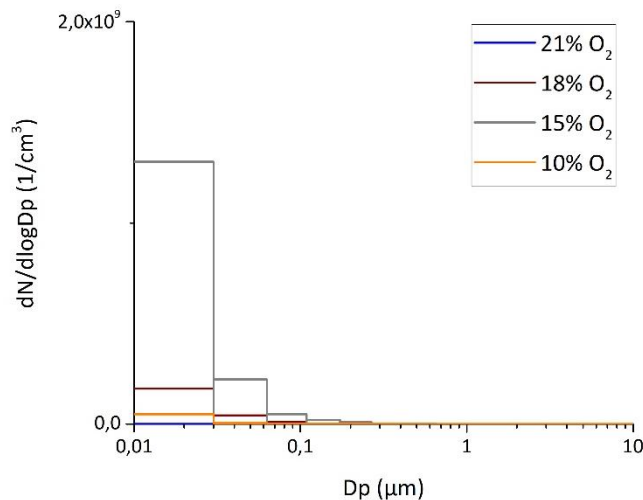


Figure 102: Effect of oxygen on the distribution size of aerosols of CLT/WF at 20 kW/m² at ti or the beginning of thermal exposure

To conclude, oxygen decrease leads to the production of smaller sizes of aerosols at 20 kW/m².

3.3. Comparative effect of oxygen and heat flux

The reaction to fire, gas, and aerosol production of an assembly of CLT and WF was fully assessed in the previous sections by considering the effect of the assembly, the oxygen, and the heat flux. These two later parameters are essential when investigating the response of a material in a fire scenario. This section focuses on classifying the behaviors of the CLT/WF assembly according to oxygen and heat flux. In general, two main behaviors were highlighted: flaming and non-flaming.

Flaming combustion occurs at both 50 and 20 kW/m² at 21, 18 and 15 vol-% O₂ (Figure 106). However, ignitability risks are higher at 50 kW/m². Indeed, at 21 vol-% O₂, the time to ignition of WF is nearly 12 times faster at 50 kW/m² than at 20 kW/m² (Figure 103). Moreover, CLT ignites at 21, 18 and 15 vol-% O₂ at 50 kW/m² while it only occurs at 21 vol-% O₂ at 20 kW/m² and at least 10 times later.

Moreover, it is noteworthy that the ignition of CLT (50 kW/m², 21 and 18 vol-% O₂ and at 20 kW/m², 21 vol-% O₂) occur earlier than single samples of CLT. It is due to the flaming WF radiates an additional heat flux on the surface of CLT, thus increasing its temperature and mass loss rate. The radiation back from a flame to the surface of burning wood has been found to be under 10 kW/m² at 50 kW/m² [109]. However, as the surface of CLT is close to the flame and not directly above the flame, it is difficult to determine the amount of radiation received. It was also observed by Vincent that the easiest flammable material ignited the sample next to it [21]. Overall, the times to ignition of the CLT/WF assembly are mainly affected by the heat flux, though oxygen have a slight influence at 20 kW/m² and on CLT at 50 kW/m².

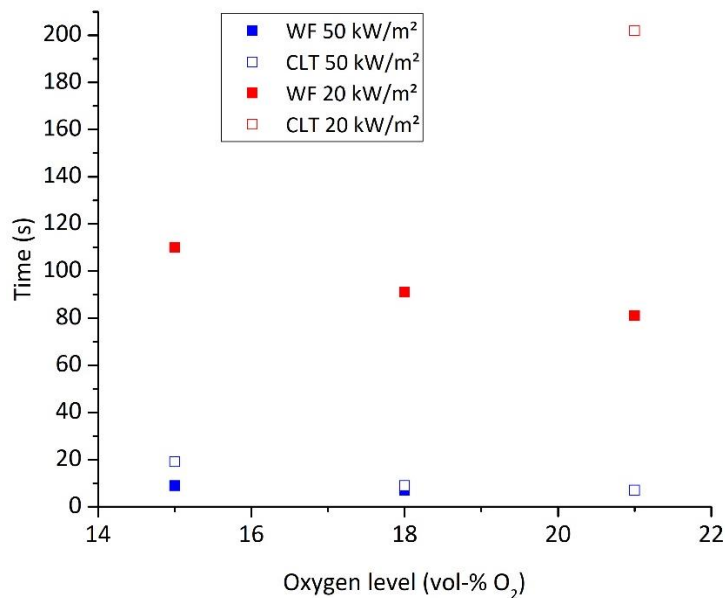


Figure 103: Effect of oxygen level on the times to ignition of the CLT/WF assembly at 50 and 20 kW/m²

Moreover, the assemblies of CLT/WF at 50 kW/m² release much more energy during the first 600s of test than specimens at 20 kW/m² (Figure 104). Indeed, the total heat release at 600s (THR_{600s}) at 50 kW/m² and 21 vol-% O₂ (38 MJ/m²) is 2.5 times higher than at 20 kW/m² and 21 vol-% O₂ (15 MJ/m²). At 15 vol-% O₂, the factor between the THR_{600s} at 50 and 20 kW/m² rise to 8. In general, the THR_{600s} is mainly impacted by the heat flux but also by the oxygen level at 20 kW/m².

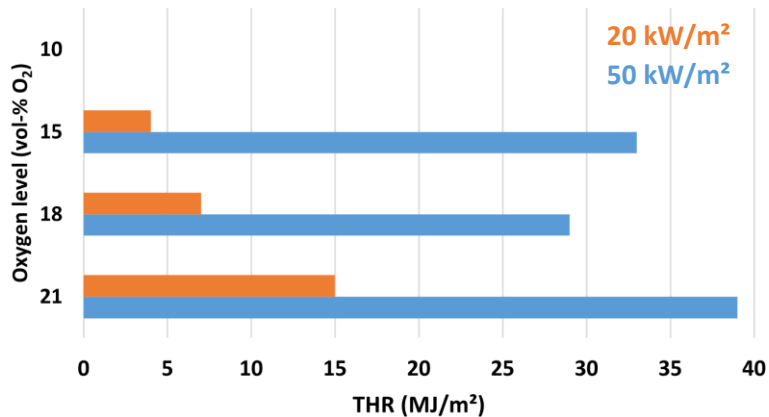


Figure 104: Effect of oxygen on the THR_{600s} of the CLT/WF assembly at 50 and 20 kW/m^2

However, the overall gas production over 600s of test at 20 kW/m^2 is more significant than at 20 kW/m^2 . Indeed, for the flaming specimens, the yields of unburnt gases, including CO and CH_4 , are much higher whatever the oxygen level at 20 kW/m^2 . More precisely, from 50 to 20 kW/m^2 , the yields of CO and CH_4 at 21 vol-% O_2 are multiplied by 20 and 3 respectively (Figure 105). Moreover, from 50 to 20 kW/m^2 , the yields of CO_2 decrease by 60% at 18 and 15 vol-% O_2 . This underlines that the reaction of combustion is much efficient at higher heat flux, which is consistent with the previous values of THR_{600s} .

In addition to the heat flux, the oxygen decrease affects the CO yields at 50 kW/m^2 and the yields of CO_2 and CO at 20 kW/m^2 . Indeed, the yields in CO are multiplied by 3 from 21 to 15 vol-% O_2 , which is consistent with the reaction of combustion becoming more incomplete with time and oxygen decrease. Moreover, at 20 kW/m^2 , there is a 64% reduction in the yields of CO_2 from 21 to 15 vol-% O_2 while the yields of CO increase by 70%. This reduction is mainly due the CLT part of the assembly not igniting at 18 and 15 vol-% O_2 , which increases the unburnt gases yields.

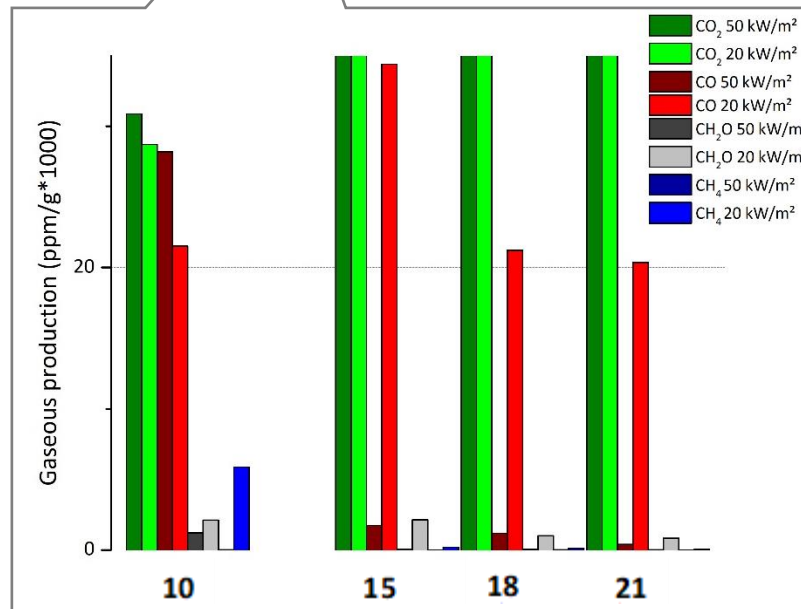
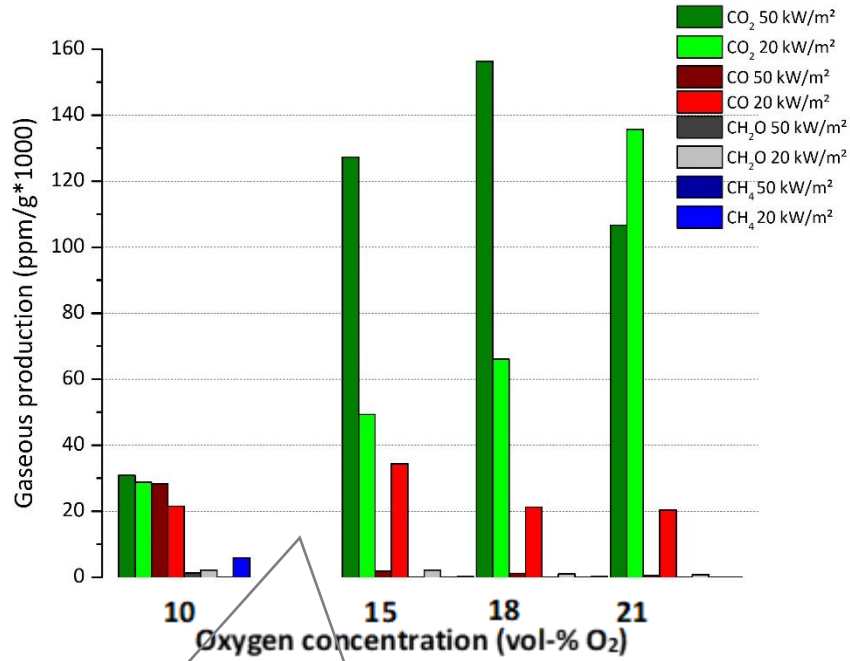


Figure 105: Effect of oxygen on the gaseous emissions of the CLT/WF assembly at 50 and 20 kW/m² for 600s of test

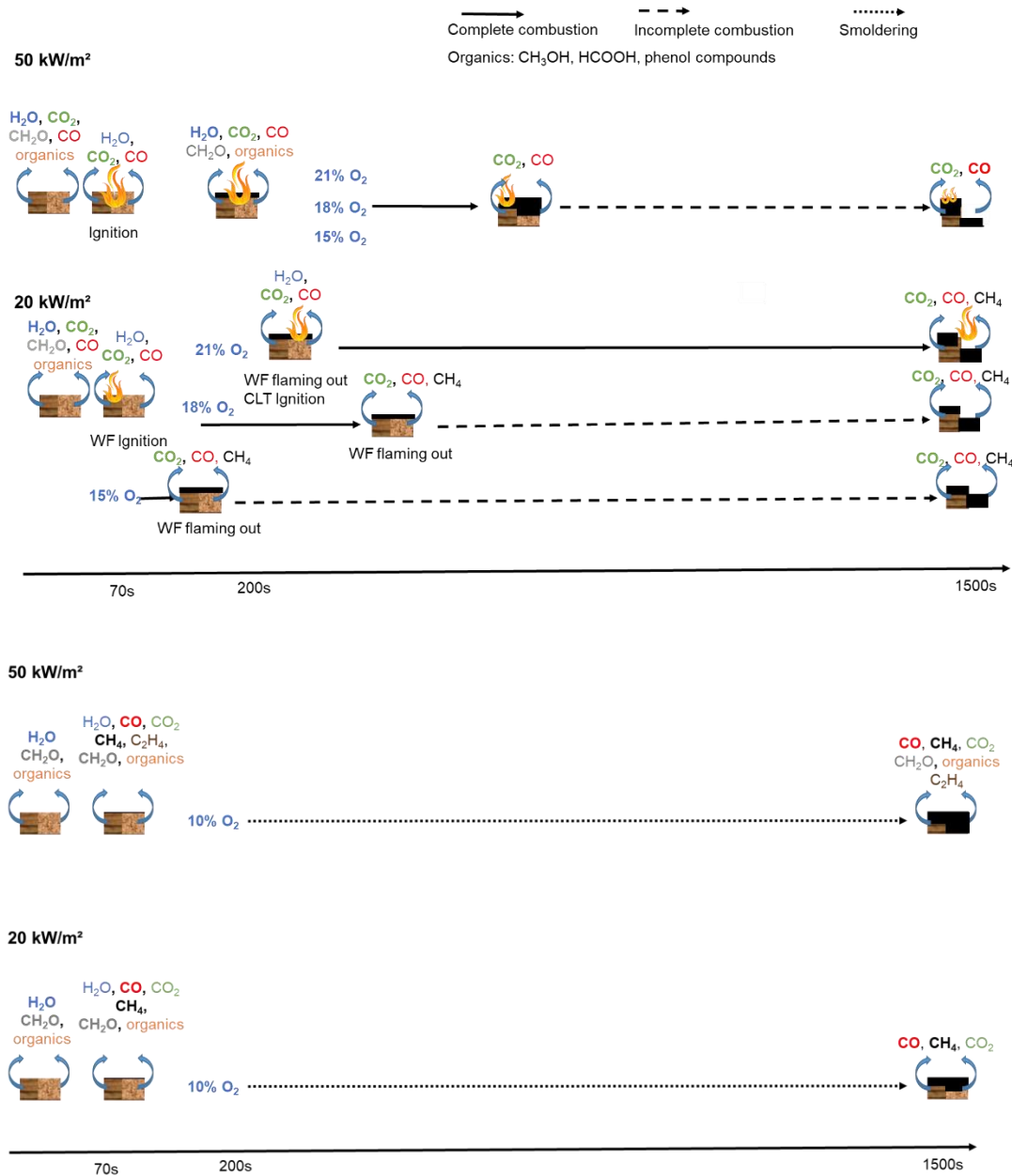


Figure 106: Flaming and non-flaming decomposition of the assembly of CLT/WF

Finally, the last condition investigated is non-flaming combustion at 10 vol-% O₂ at both 50 and 20 kW/m² (Figure 106). In both cases, low values of HRR are observed; however, from 20 to 50 kW/m², the HRR values double. Higher heat flux results in increased sample decomposition and consequently, a higher release of energy.

Moreover, in contrary to the flaming cases, the yield of unburnt species (CO and CH₄) is promoted at 50 kW/m². Indeed, the yields of CO and CH₄ at 50 kW/m² are respectively reduced by 21% and 83% from 20

to 50 kW/m². The combination of higher heat flux with low oxygen concentration enables the production of additional gases, like methane, which do not undergo complete oxidation.

Finally, both heat flux gives a monomodal aerosol size distribution centered on the mode 0.03 μm with concentration in the same range (10⁷ #/cm³).

3.4. Conclusion

The assessment of the fire behavior, gas production, and aerosol size distribution of an assembly of CLT/WF was conducted using a Cone Calorimeter (CACC) coupled with a Fourier Transform Infrared Spectroscopy (FTIR) and an Electrical Low Pressure Impactor (ELPI). The results highlighted that the assembly itself, the heat flux and the oxygen concentration play key roles in determining the combustion behavior of the assembly of CLT/WF. At both heat flux of 50 kW/m² and 20 kW/m², the critical oxygen levels necessary for flaming combustion to occur were found to be between 15 and 10 vol-% O₂ (Figure 107).

In summary, the combination of WF with CLT generally does not have a significant effect on the time to ignition of WF, but it does impact the time to ignition of CLT, with WF accelerating the ignition of CLT. Additionally, the HRR and gas production curves appear to be a succession of the individual behaviors of WF and CLT, suggesting that the two materials do not significantly interact during combustion. The aerosol size distributions are also close to single CLT and WF. These observations apply to both 50 and 20 kW/m².

Reduced oxygen content has no effect on WF ignition times, but it delays (50 kW/m², 15 vol-%O₂) or even prevent ignition of CLT (20 kW/m², 18 and 15 vol-% O₂). Furthermore, the production of unburnt gases, including CO and CH₄, increases significantly with reduced oxygen levels at both 50 and 20 kW/m². For the flaming specimens, the overall gaseous yields were higher at 20 kW/m² than at 50 kW/m².

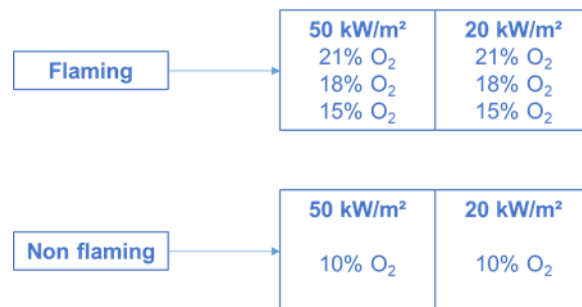


Figure 107: Classification of fire behavior of the CLT/WF assembly according to oxygen level and heat flux

4. Conclusion

The first objective was to study the effect of oxygen on the fire behavior, the gas and aerosol emissions of Cross-Laminated Timber and wood fiber. The next challenge was to assess the effect of combining both CLT with WF on the previous parameters. Finally, the goal was to investigate whether the effects of oxygen on the assembly of CLT/WF were like those on CLT and WF. To carry out this work, the Controlled-Atmosphere Cone Calorimeter (CACC) coupled to Fourier-Transform Infrared spectroscopy (FTIR) and an Electrical Low Pressure Impactor (ELPI) was used and revealed to be properly suited. The experiments were conducted at two different heat fluxes (50 and 20 kW/m²) to assess a wide range of fire conditions, from well-ventilated fires to smoldering.

At 50 kW/m², the start of the thermal decomposition of flaming samples is mainly governed by the heat flux for both CLT and WF. Indeed, oxygen concentration has a low impact on the times to ignition and mass loss rates. However, post-ignition, the decomposition rate of the condensed phase and the heat release in the gas phase slow down significantly with decreasing oxygen levels. Additionally, the production of unburnt gases, such as carbon monoxide and methane, is greatly increased, and smaller aerosol particles were produced. Decreasing the oxygen level to 10 vol-% O₂ results in lower mass loss and energy release but a substantial increase in unburnt emissions, especially hydrocarbons and aldehydes.

Moreover, at 20 kW/m², decreasing the oxygen concentration delays the ignition of CLT but not of WF due to its higher ignitability. Unlike high heat flux conditions, oxygen vitiation results in a decrease in both mass loss and heat release during ignition. Overall, low heat flux conditions with reduced oxygen led to notable increases in CO and CH₄ while decreasing CO₂ yields.

Finally, combining CLT to WF results in the superposition of the two behaviors previously described. However, the ignition of CLT is affected by that of WF. It is worth noting that oxygen has a similar effect on the CLT/WF assembly as it does on single materials.

This research provides exhaustive results on the fire behaviors, gas, and aerosol productions of CLT, WF and CLT/WF in various fire conditions. Expanding this research to a larger scale would be valuable, as phenomena observed at bench-scale may differ from those at a real scale. This supplementary dataset could support in establishing links between results obtained at different scales.

Chapter 5: Fire behavior, gas, and aerosol emissions of an assembly of Cross-Laminated Timber/Wood Fiber with an intermediate scale enclosure coupled to a Fourier Transformed Infrared spectroscopy and an Electrical Low Pressure Impactor

1. FIRE BEHAVIOR, GAS AND AEROSOL PRODUCTION OF THE CROSS-LAMINATED TIMBER/WOOD FIBER ASSEMBLY AT 40 kW 194
2. FIRE BEHAVIOR, GAS AND AEROSOL PRODUCTION OF THE CROSS-LAMINATED TIMBER/WOOD FIBER ASSEMBLY AT 90 kW 197
3. CONCLUSION..... 200

To complete the results obtained with the CACC, this chapter focuses on the use of an intermediate scale enclosure coupled to a Fourier-Transform Infrared spectroscopy (FTIR) and an Electrical Low Pressure Impactor (ELPI). As previously described in the Chapter 2 (section 5 p95), this bench allows for studying the reaction to fire, gas and aerosol emissions of meter sized panels exposed to the flame of a propane burner. These experiments are conducted on Cross-Laminated Timber (CLT), Wood Fiber (WF) and the assembly of CLT/WF at two different heat powers (40 and 90 kW).

Preliminary results have been obtained but few calibrations tests remain to be done to calculate the HRR properly. Nevertheless, data on oxygen consumption, gas, and aerosol production of CLT, WF and CLT/WF at both 40 and 90 kW are presented hereafter. The curves of single materials can be found in the Appendix p279.

1. Fire behavior, gas, and aerosol production of the Cross-Laminated Timber/Wood fiber assembly at 40 kW

At 40 kW, the fire behaviors of CLT and WF greatly differ. Indeed, for CLT, after 2 min of exposure and for 8 min, the flame slightly adheres on the edges of its carbonization front. Then, the carbonization front stays still, with 1/3 of CLT carbonized (Figure 108a). However, for WF, the flame adheres widely from 30s of test and with a lot of smoke released. Then, flame adherence slows down and is located only on the edges of the carbonization front and that for 8 min. In the end of the test, $\frac{3}{4}$ of the WF is degraded, with the middle totally consumed (Figure 108b).

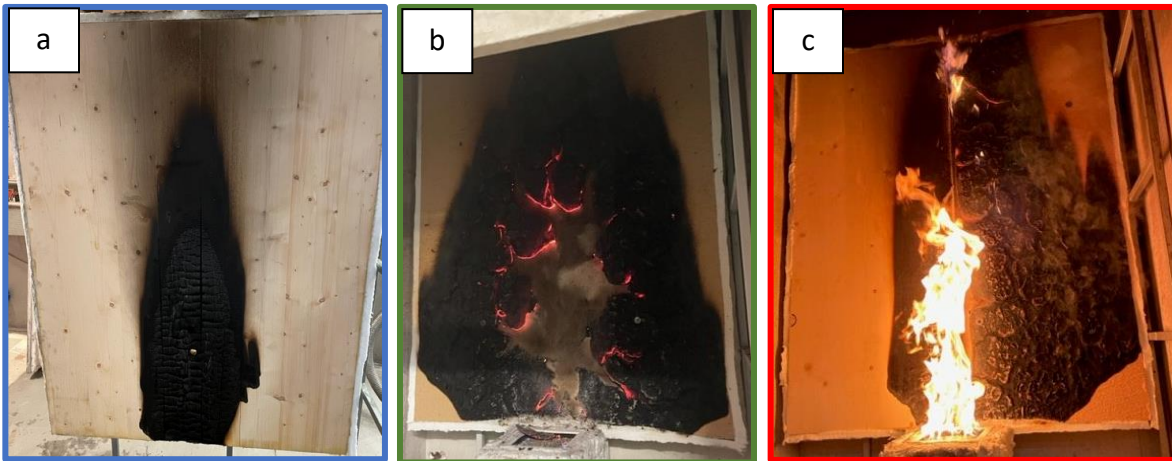


Figure 108: Photos taken after 30 min of test at 40 kW. a. CLT, b. WF and c. CLT/WF

Moreover, when exposed to the flame burner, CLT slowly carbonizes with a low consumption of oxygen (Figure 109) and thus few release of CO_2 (<1000 ppm) (Figure 110a). However, WF consummates more than twice the amount of oxygen consumed by CLT (Figure 109), which results in twice the amount of CO_2 produced (Figure 110a). It should be noted that the decomposition of WF is highly incomplete with a CO/CO_2 ratio of 0.54 from 600 to 1400s. This results in high production of CO (1400 ppm) (Figure 110b) and CH_4 (100 ppm) (Figure 110c) as they are not fully oxidized. This is due to WF shrinking, creating limiting access to oxygen.

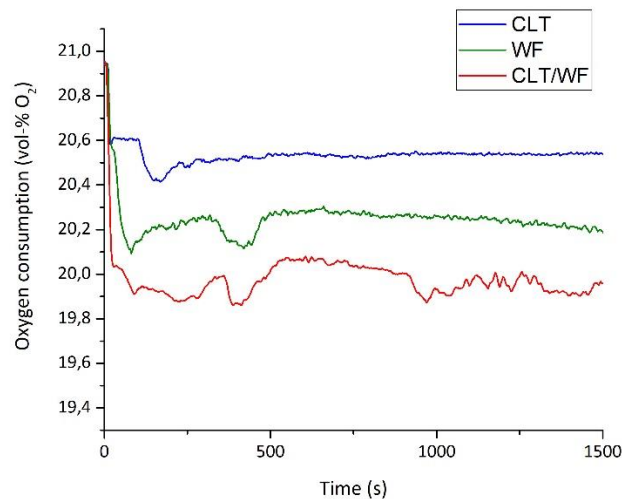


Figure 109: Oxygen consumption of CLT, WF and CLT/WF at 40 kW

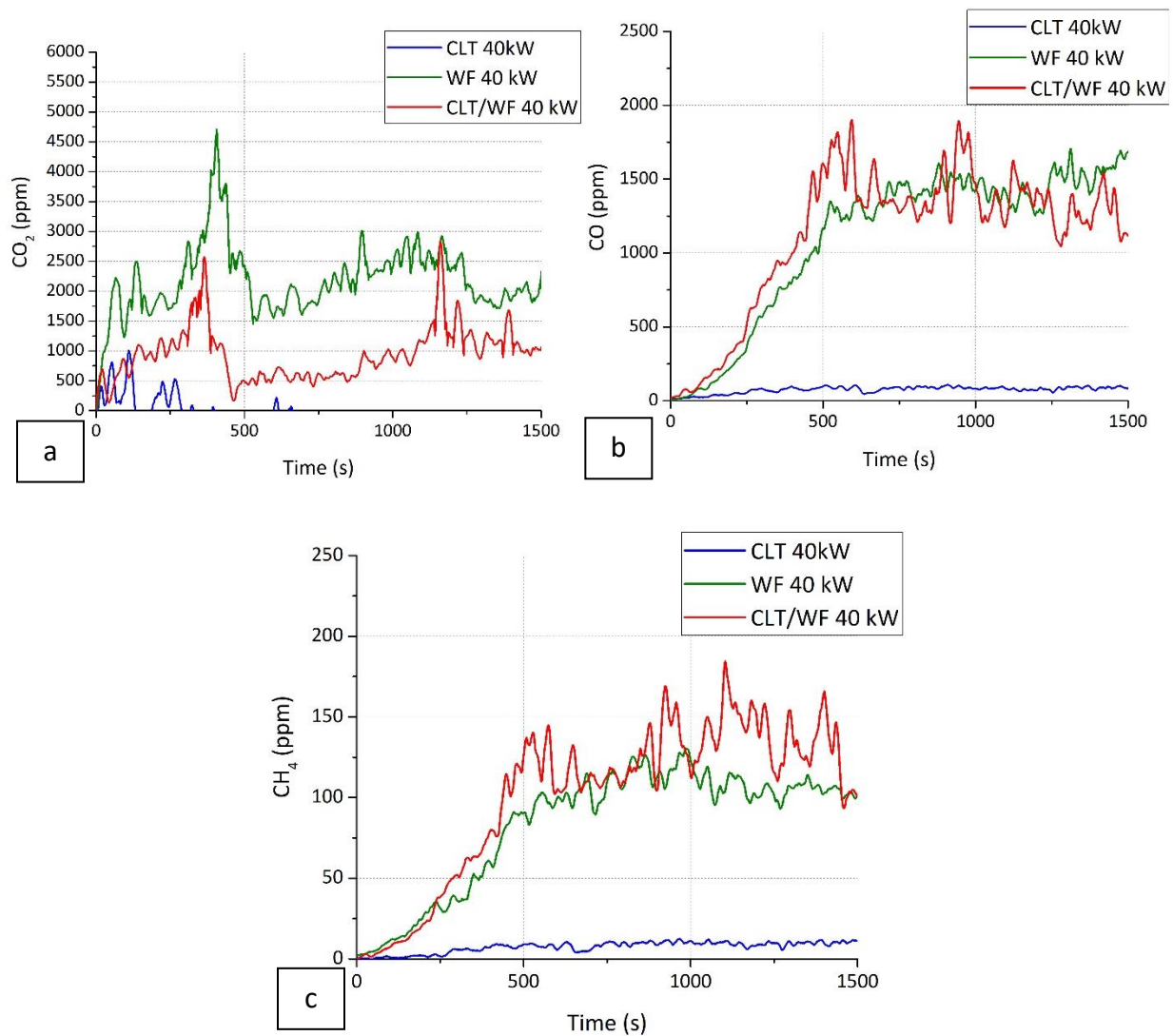


Figure 110: Gas production of CLT, WF and CLT/WF at 40 kW. a. CO₂, b. CO and c. CH₄

Furthermore, the global aerosol size distributions of CLT and WF over the test are multimodal centered on 0.173, 0.109 and 0.267 μm and with a high participation of the mode 0.03 μm for CLT and 0.063 μm for WF (Figure 111).

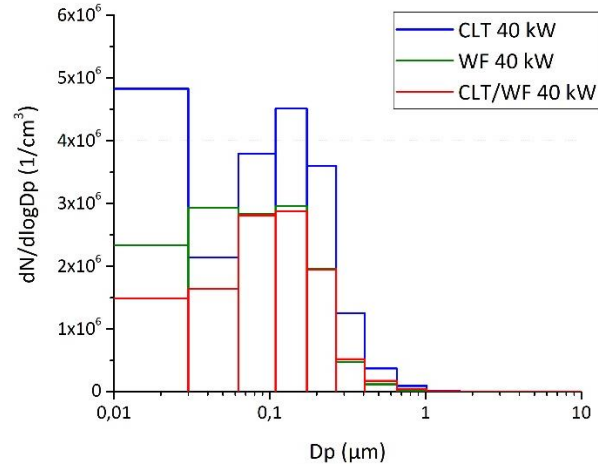


Figure 111: Global aerosol size distribution of CLT, WF and CLT/WF at 40 kW

Finally, when combining CLT to WF, the flame adheres on WF from 1 min of test while CLT remains untouched. After 4 min, WF starts to shrink and crack while CLT starts to carbonize only 3 min later. After 30 min of test, 1/3 of CLT is consumed while ¾ of WF is consumed (Figure 108c). Moreover, the assembly of CLT/WF consummate 14% more oxygen than the entire wood fiber (Figure 109). In fact, the production of CO₂ is divided by 2 compared to that of entire WF (Figure 110a) while the production of CO (Figure 110b) and CH₄ (Figure 110c) are similar to the entire sample of WF. It appears that the oxygen consumed favors the production of CO whether than in CO₂. The combustion is thus incomplete, which explains the high production of CH₄ (150 ppm). Besides, the aerosol size distribution is centered multimodal centered on the modes 0.173, 0.109 and 0.267 μm with a great participation of the modes 0.063 and 0.03 μm, just as CLT and WF.

To conclude, at 40 kW, the reaction to fire and gas production of the CLT/WF assembly is due to the decomposition of WF. WF decomposes and shrinks rapidly, which leads to incomplete combustion with high CO and CH₄ production, while CLT slowly carbonizes.

2. Fire behavior, gas, and aerosol production of the Cross-Laminated Timber/Wood fiber assembly at 90 kW

Furthermore, at 90 kW, the same trends as at 40 kW are observed but with higher kinetics. Indeed, for CLT, flame adherence on the edges of the carbonization front starts 1 min sooner. It lasts 15 min, which is 7 min more than at 40 kW, and then the front of carbonization stays still. After 30 min, half of CLT is degraded (Figure 112a). Moreover, for WF, flame adherence starts from the beginning of the thermal exposure, slows down after 3 min, and stops after 4 min. After 6 min, all the WF is consumed, which results after 30 min of test of the complete fall out of WF in the middle (Figure 112b).

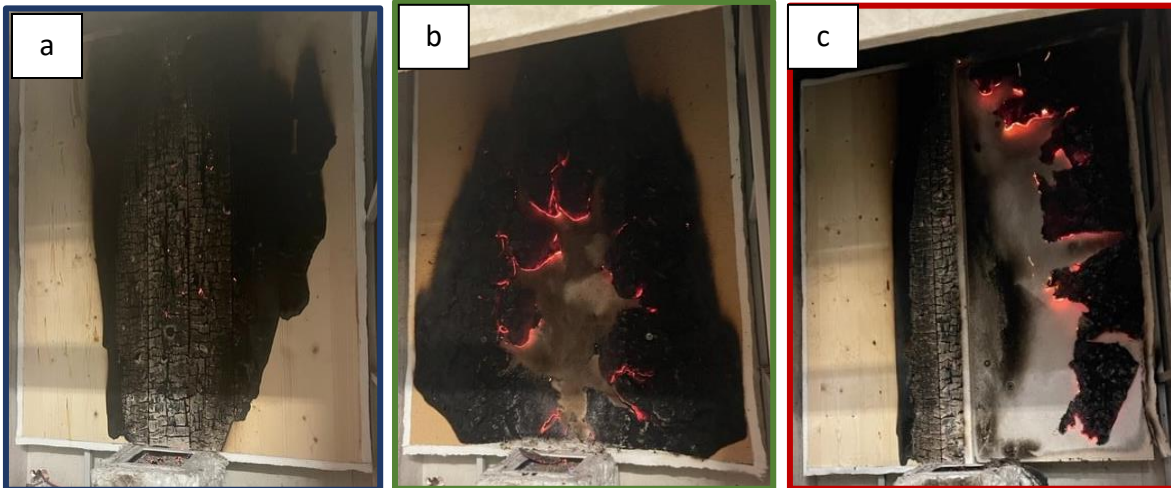


Figure 112: Photos taken after 30 min of test at 90 kW. a. CLT, b. WF and c. CLT/WF

As experienced at 40 kW, CLT slowly carbonizes with a low consumption of oxygen (Figure 113) and thus low amounts of CO_2 produced (<2000 ppm) (Figure 114a). In the contrary, WF consummates 77% more of oxygen than CLT (Figure 113), resulting in 3 times more CO_2 produced (Figure 114a). The decomposition of WF is even more incomplete with a CO/CO_2 ratio of 2.4 from 400 to 1400s. Compared to 40 kW where the combustion was already incomplete, the production of CO (2500 ppm) (Figure 110b) and CH_4 (200 ppm) dramatically increase (Figure 110c) at higher heat power.

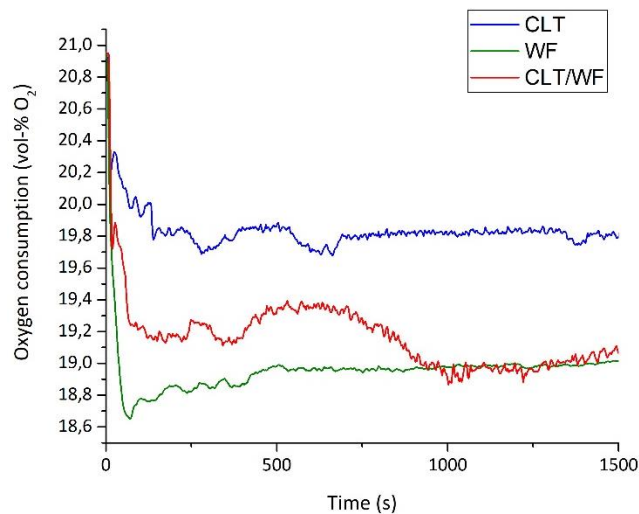


Figure 113: Oxygen consumption of CLT, WF and CLT/WF at 90 kW

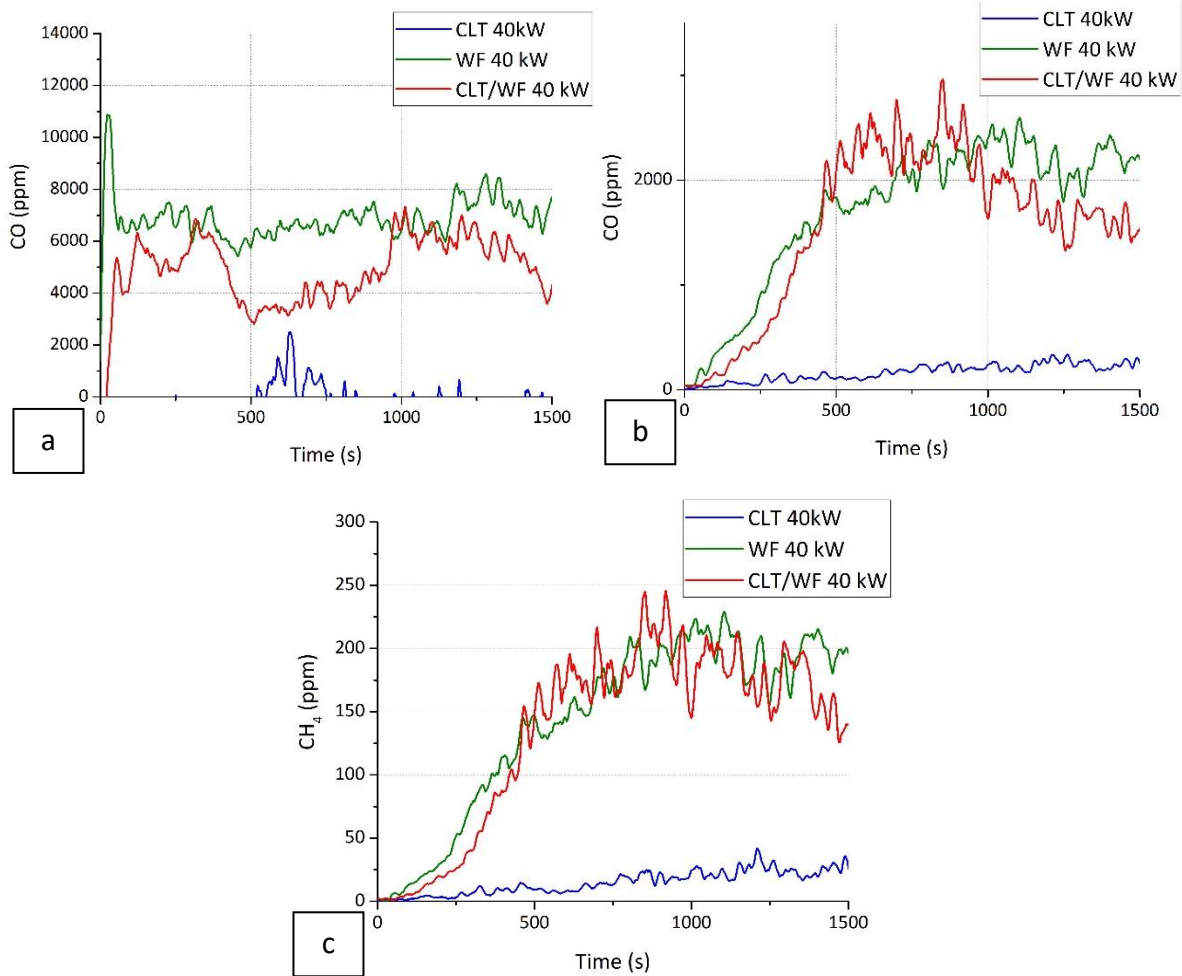


Figure 114: Gas production of CLT, WF and CLT/WF at 90 kW. a. CO₂, b. CO and c. CH₄

Furthermore, the global aerosol size distributions of CLT and WF over the test are multimodal centered on 0.109, 0.173 and 0.267 μm and with a high participation of the mode 0.03 μm for CLT and 0.063 μm for WF (Figure 115). In comparison to 40 kW, the concentration in aerosols is slightly higher and centered preferably on smaller particles (0.109 μm).

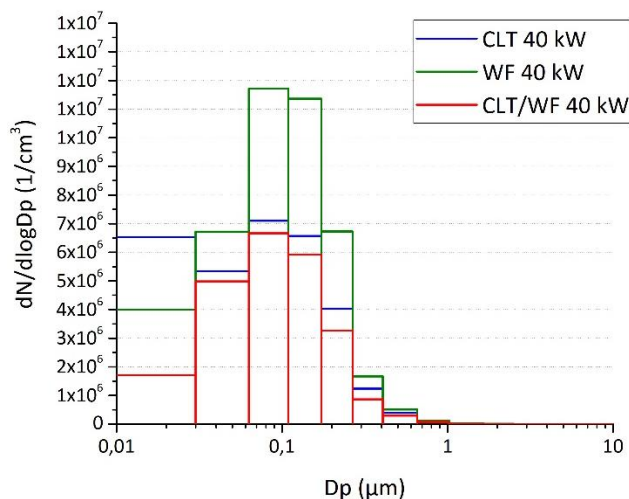


Figure 115: Global aerosol size distribution of CLT, WF and CLT/WF at 90 kW

Finally, when combining CLT to WF, the flame adheres from the start of the test while CLT remains untouched. After 2 min, WF starts to shrink and crack while CLT starts to carbonize only 2 min later. After 30 min of test, more than 1/3 of CLT is consumed while nearly all WF is consumed (Figure 108c). Moreover, at 90 kW, a decrease of 21% in oxygen consumption is observed compared to single WF (Figure 113). As the half part of WF decomposes and shrinks rapidly, there is less fuel to consume oxygen. As a result, the CO₂ production of CLT/WF and WF are similar in the first 600s but as half WF shrinks, it slowly decreases (Figure 114a). Due to incomplete combustion zones, the production of CO (2500 ppm) (Figure 114b) and CH₄ (200 ppm) (Figure 114c) remains high. Besides, the aerosol size distribution is centered multimodal centered on the modes 0.173, 0.109 and 0.267 μm with a great participation of the modes 0.063, like WF and CLT.

In conclusion, at 90 kW, the reaction to fire and gas production of the CLT/WF assembly are mostly attributed to the decomposition of WF. WF decomposes and shrinks even more rapidly than at 40 kW, which leads to higher CO and CH₄ production, while CLT slowly carbonizes.

3. Conclusion

To conclude, this study has revealed that on a larger scale, CLT exhibits minimal flame adherence and carbonizes slowly, resulting in limited gas emissions (CO₂). Conversely, wood fiber degrades rapidly and emits a substantial amount of gas (CO₂, CO, CH₄). When CLT and wood fiber are combined, the first results do not indicate any significant interaction between the two materials. While in the CACC tests, the wood fiber had an impact on the inflammation of CLT, here, it has no such effect. Instead, each material degrades independently, with wood fiber being primarily responsible for most gas emissions. These findings align

with those obtained from the CACC results, where the gas production was the result of both single behaviors. To further assess the results obtained, it would be beneficial to conduct continuous or pre-and-post weighing of samples, enabling a more detailed comparison of gas yields. Additionally, ongoing calibration tests involving the burner and the ventilation system aim to achieve accurate HRR calculations. Lastly, the use of an alternative FTIR probe could potentially capture a wider range of gases, offering a more comprehensive analysis.

Conclusion

In conclusion, this research involved an extensive and systematic investigation into the fire behavior, gas, and aerosol emissions of Cross-Laminated Timber (CLT), wood fiber (WF) and their assembly within varying oxygen-reduced environments. This study was conducted with experimental methodologies developed across different scales and under diverse fire conditions.

Essential to this study was the development of two benches: an adapted Controlled-Atmosphere Cone Calorimeter and a meter sized enclosure. For both benches, the setting of raw smoke sampling with Fourier-Transform Infrared Spectroscopy (FTIR) and Electrical Low-Pressure Impactor (ELPI) allowed for a comprehensive characterization of gases and aerosols emitted during a fire.

Initial experiments conducted at matter scale using TGA-FTIR displayed insights into the influence of oxygen concentration on the thermal decomposition and gaseous emissions of CLT and WF. These experiments outlined the shift from an apparent one-stage thermal decomposition under nitrogen to an apparent two-stage process induced by the presence of oxygen. Furthermore, while reducing the oxygen concentration had no impact on the start of decomposition, it did, however, result in a reduction in the decomposition rate. For both atmospheres, diverse decomposition products including H₂O, CO, aldehydes, carboxylic acids, and phenol compounds were observed during the first stage of decomposition while only CO₂, H₂O and CO were emitted during char oxidation under oxygen. Finally, using Py-GC/MS analysis provided additional information into the organic volatiles released throughout the process of wood decomposition.

Moreover, the study assessed the fire behavior, gas, and aerosol emissions of CLT, WF and the CLT/WF assembly at bench-scale using the CACC-FTIR-ELPI apparatus under varying oxygen concentrations (21, 18, 15, and 10 vol-% O₂) and two heat fluxes (50 and 20 kW/m²). These results have led to a better understanding of the effect of oxygen in various fire conditions. Indeed, they revealed different fire behaviors, decomposition rates and gas and aerosol emissions according to oxygen levels and heat fluxes. As the oxygen concentration decreased, there was a significant reduction in the decomposition rate, often accompanied by a transition from flaming to non-flaming combustion. Simultaneously, an important increase in unburnt species (CO, CH₄ and organics), along with an increase in submicronic-sized aerosols, was observed for both CLT and WF. Especially, these trends persisted when combining CLT with WF,

highlighting the absence of significant interactions. However, it is worth noting that the radiative effect of WF's flame accelerated the ignition of CLT at both high and low heat flux levels.

At a larger scale, experiments were conducted using a meter sized enclosure fitted with a propane burner and FTIR and ELPI analyses. CLT exhibited negligible flame adherence and slow carbonization, resulting in limited gas emissions, mainly carbon dioxide. Conversely, the rapid degradation of wood fiber contributed to significant gas emissions, including carbon dioxide, carbon monoxide and methane. When CLT and WF were combined, preliminary results did not indicate any significant interaction between the two materials. In contrast to the findings with the CACC, where WF impacted CLT ignition, no such effect was observed here. The materials instead degraded independently, with WF appearing as the main contributor to most gas emissions. These findings agree with the observations from CACC results, where gas production resulted from the distinct behaviors of each material. This highlights the importance of considering both individual and combined behaviors for a comprehensive fire safety assessment.

Additionally, the CO/CO₂ ratio appeared as a key parameter in fire safety engineering, acting as a valuable indicator of combustion efficiency and potential hazards. Particularly, the observed increases in CO yields under reduced oxygen levels and heat flux highlighted the hazards regarding smoldering fires.

This research not only improved the understanding of the effect of oxygen level on the fire behavior and emissions of wooden materials but also developed original experimental methodologies to study potential interactions into two assembled materials during fire incidents. Specifically, it highlighted scale limitations, as the detrimental effects of WF on CLT ignition were apparent at bench scale but not observed at intermediate scale. It underlined the critical need for diverse testing methods to facilitate the interpretation of results to real scenarios, ensuring the applicability and reliability of fire safety assessments. The study demonstrated, as wondered in the introduction, that variations in fire conditions, including oxygen content and thermal attack, significantly influenced the fire behavior, as well as gas and aerosol emissions of Cross-Laminated Timber, wood fiber and their assembly within a building system.

To finish, existing limitations within current fire toxicity regulations must be considered. The growing understanding of fire behaviors, as demonstrated in this research, necessitates a more comprehensive approach to toxicity assessments, considering a broader spectrum of emissions and their potential health impacts.

Perspectives

The homemade bench controlled-atmosphere cone calorimeter coupled to Fourier-transform Infrared Spectroscopy (FTIR) and Electrical Low Pressure Impactor (ELPI) will allow to assess the fire behavior, gas and aerosol emissions of several materials used in the building field and thus to have first insights on the smoke related risks.

To improve this setup, it could be interested to couple the ELPI to a Scanning Mobility Particle Sizer (SMPS) to obtain a wider range of particles sizes, especially smaller sizes ($<0.03 \mu\text{m}$). Additionally, conducting further analysis of aerosol morphology, such as employing Scanning Electron Microscopy (SEM), could complement and/or validate the data already obtained with ELPI. Since the two techniques employ different sampling methods, they provide an opportunity to cross-reference and validate the data. Implementing a methodology for measurement of Volatile Organic Compounds (VOCs) is essential for a more accurate analysis of emissions, especially in scenarios involving thermal decomposition without a flame (such as the smoldering fire phenomenon). This could involve strategically placing sampling chambers connected to appropriate sensors, like Tenax tubes, at different times during the test.

At a larger scale, the enclosure coupled to Fourier-transform Infrared Spectroscopy (FTIR) and Electrical Low Pressure Impactor (ELPI) provides first results on the effect of assembling CLT to WF on the fire behavior, gas, and aerosol emissions. To further assess the results obtained, it would be beneficial to conduct continuous or pre-and-post weighing of samples, enabling a more detailed comparison of gas yields. Additionally, ongoing calibration tests involving the burner and the ventilation system aim to achieve accurate HRR calculations. Lastly, the use of an alternative FTIR probe could potentially capture a wider range of gases, offering a more comprehensive analysis.

To take this project a step further, it is advisable to enhance the intermediate-scale test bench, allowing for the examination of vitiated conditions. As demonstrated in this research, significant gases and aerosols are generated in these conditions. This adaptation would facilitate the link of data obtained with the CACC in vitiated atmosphere to potential intermediate-scale data. Furthermore, in addition to conducting this study on wood materials, it would be pertinent to extend this research to include other building materials, such as polyurethane (PU) or expanded polystyrene (PSE) insulating foams. Following this, the data relating to gas and aerosol emissions resulting from various combinations of materials representing building systems, such as CLT/biosourced, CLT/PU, or CLT/PSE, etc., could be systematically compiled into a

database. This database could serve as a valuable resource for conducting studies in the field of fire safety engineering.

Bibliography

- [1] J. J. Hall et B. Harwood, Smoke or Burns - Which is Deadlier ?, *NFPA Journal*, vol.89(1), p. 38-43, 1995, issn: 1054-8793.
- [2] E. Guillaume, Effets du feu sur les personnes, p. 163, 2006.
- [3] ISO 13571. Life-threatening components of fire — Guidelines for the estimation of time to compromised tenability in fires. 2012.
- [4] A. A. Stec et R. Hull, *Fire Toxicity*. Woodhead Publishing, 2010, isbn: 9780081014875.
- [5] A. A. Stec, Fire toxicity – The elephant in the room?, *Fire Safety Journal*, vol. 91, p. 79-90, juill. 2017, doi: 10.1016/j.firesaf.2017.05.003.
- [6] NF EN ISO 13943:2018 :Fire Safety - Vocabulary. 2018.
- [7] C. Diblasi, Modeling chemical and physical processes of wood and biomass pyrolysis, *Progress in Energy and Combustion Science*, vol. 34, n° 1, p. 47-90, févr. 2008, doi: 10.1016/j.pecs.2006.12.001.
- [8] F.-X. Ouf, Caractérisation des aérosols émis lors d'un incendie, Université de Rouen, 2006.
- [9] A. Canals, M. A. Aguirre, et A. Mazaher, Aerosol characterization, in *Analytical Nebulizers: Fundamentals and Applications*, Elsevier., 2023, p. 35-53.
- [10] B. G. Mustafa, Toxic species and particulate emissions from wood and pool fires, p. 342, 2019
- [11] ISO 19706:2011. Guidelines for assessing the fire threat to people. 2011.
- [12] C. Vagner, M. Cohez, H. Vahabi, et M. Ferriol, Chimie de la combustion des polymères et ignifugation, *Techniques de l'Ingénieur*, 2016.
- [13] E. Guillaume, Essais normalisés de comportement au feu, *Techniques de l'Ingénieur*, 2018.
- [14] M. G. Grønli, G. Várhegyi, et C. Di Blasi, Thermogravimetric Analysis and Devolatilization Kinetics of Wood, *Ind. Eng. Chem. Res.*, vol. 41, n° 17, p. 4201-4208, août 2002, doi: 10.1021/ie0201157.
- [15] T. Sebio-Puñal, S. Naya, J. López-Beceiro, J. Tarrío-Saavedra, et R. Artiaga, Thermogravimetric analysis of wood, holocellulose, and lignin from five wood species, *J Therm Anal Calorim*, vol. 109, n° 3, p. 1163-1167, sept. 2012, doi: 10.1007/s10973-011-2133-1.
- [16] Y. Yang, T. Fu, F. Song, X. Song, X.-L. Wang, et Y.-Z. Wang, Wood-burning processes in variable oxygen atmospheres: thermolysis, fire, and smoke release behavior, *Polymer Degradation and Stability*, vol. 205, 2022, doi: <https://doi.org/10.1016/j.polymdegradstab.2022.110158>.
- [17] R. E. Lyon et R. N. Walters, Pyrolysis combustion flow calorimetry, *Journal of Analytical and Applied Pyrolysis*, vol. 71, n° 1, p. 27-46, mars 2004, doi: 10.1016/S0165-2370(03)00096-2.

- [18] L. Bustamente Valencia, Etude expérimentale et numérique de la décomposition thermique des matériaux à trois échelles : application à une mousse polyéther polyuréthane utilisée dans les meubles rembourrés, Engineering Sciences [physics]. ISAE-ENSMA Ecole Nationale Supérieure de Mécanique et d'Aérotechnique - Poitiers, 2009. English. NNT : . tel-00444898.
- [19] D. Marquis, Caractérisation et modélisation multi échelle du comportement au feu d'un composite pour son utilisation en construction navale, 2010, Corpus ID: 190661913.
- [20] A. Camillo, Multi-scale investigation of fire behavior of a seat and a wall panel from European railway transport system, ISAE-ENSMA Ecole Nationale Supérieure de Mécanique et d'Aérotechnique - Poitiers, 2013. English. (NNT : 2013ESMA0014). (tel-00924616).
- [21] C. Vincent, Caractérisation du comportement au feu des matériaux de l'habitat : Influence de l'effet d'échelle, 2016, CorpusID:133923914.
- [22] T. Fateh, Etude expérimentale et numérique de la cinétique de décomposition thermique de contreplaqués en bois, ISAE-ENSMA Ecole Nationale Supérieure de Mécanique et d'Aérotechnique - Poitiers, 2011. Français. (NNT :). (tel-00667332).
- [23] C. Sarah, An instrumented controlled-atmosphere cone calorimeter to characterize electrical cable behavior in depleted fires, p. 249, Université de Lille, 2019. English. (NNT :). (tel-02521972).
- [24] X. Deglise et A. Donnot, Bois et énergie, *Techniques de l'Ingénieur*, 2004, doi: <https://doi.org/10.51257/a-v2-be8535>.
- [25] A. I. Bartlett, R. M. Hadden, et L. A. Bisby, A Review of Factors Affecting the Burning Behavior of Wood for Application to Tall Timber Construction, *Fire Technology*, vol 55, p.1-55, 2018, doi: 10.1007/s10694-018-0787-y.
- [26] F.-X. Collard et J. Blin, A review on pyrolysis of biomass constituents: Mechanisms and composition of the products obtained from the conversion of cellulose, hemicelluloses and lignin, *Renewable and Sustainable Energy Reviews*, vol. 38, p. 594-608, oct. 2014, doi: 10.1016/j.rser.2014.06.013.
- [27] M. Zhang *et al.*, A review of bio-oil upgrading by catalytic hydrotreatment: Advances, challenges, and prospects, *Molecular Catalysis*, vol. 504, p. 111438, mars 2021, doi: 10.1016/j.mcat.2021.111438.
- [28] K. L. Friquin, Material properties and external factors influencing the charring rate of solid wood and glue-laminated timber, *Fire Mater.*, vol. 35, n° 5, p. 303-327, août 2011, doi: 10.1002/fam.1055.

- [29] L. Yang, X. Chen, X. Zhou, et W. Fan, The pyrolysis and ignition of charring materials under an external heat flux, *Combustion and Flame*, vol. 133, n° 4, p. 407-413, juin 2003, doi: 10.1016/S0010-2180(03)00026-9.
- [30] A. Inghelbrecht, Evaluation of the burning behaviour of wood products in the context of structural fire design, 2014, CorpusID:204770082.
- [31] E. Mikkola, Charring Of Wood Based Materials, *Fire Saf. Sci.*, vol. 3, p. 547-556, 1991, doi: 10.3801/IAFSS.FSS.3-547.
- [32] A. Buchanan, A. K. Abu, Structural design for fire safety, 2016, doi: 10.1002/9781118700402.index.
- [33] C. Di Blasi, H. G. Hernandez, et A. Santoro, Radiative Pyrolysis of Single Moist Wood Particles, *American Chemical Society*, vol. 39, 2000, doi: <https://doi.org/10.1021/ie990720i>.
- [34] R. White et M. Diertenberger, *Wood products: thermal degradation and fire*. Encyclopedia of materials : science and technology. Elsevier Science Ltd, p.9712-9716, 2001.
- [35] H. Yang, R. Yan, H. Chen, D. H. Lee, et C. Zheng, Characteristics of hemicellulose, cellulose and lignin pyrolysis, *Fuel*, vol. 86, n° 12-13, p. 1781-1788, août 2007, doi: 10.1016/j.fuel.2006.12.013.
- [36] C. Diblasi, Modeling chemical and physical processes of wood and biomass pyrolysis, *Progress in Energy and Combustion Science*, vol. 34, n° 1, p. 47-90, févr. 2008, doi: 10.1016/j.pecs.2006.12.001.
- [37] F. Shafizadeh, Pyrolysis and Combustion of Cellulosic Materials, in *Advances in Carbohydrate Chemistry*, vol. 23, p.419-474, 1968, doi: [https://doi.org/10.1016/S0096-5332\(08\)60173-3](https://doi.org/10.1016/S0096-5332(08)60173-3).
- [38] D. Shen et S. Gu, The mechanism for thermal decomposition of cellulose and its main products, 2009, *Bioresource Technology*, vol.100, p.6496-6504, 2009, doi: <https://doi.org/10.1016/j.biortech.2009.06.095>.
- [39] T. J. Ohlemiller, T. Kashiwagi, et K. Werner, Wood gasification at fire level heat fluxes, *Combustion and Flame*, vol. 69, n° 2, p. 155-170, août 1987, doi: 10.1016/0010-2180(87)90028-9.
- [40] F. Shafizadeh, Industrial pyrolysis of cellulosic materials, *Applied polymer symposium*, vol.28, p.153-174, 1975.
- [41] U. K. Shivadev et H. W. Emmons, Thermal degradation and spontaneous ignition of paper sheets in air by irradiation, *Combustion and Flame*, vol.22(2), p.223-236, 1974.
- [42] A. Broido et M. A. Nelson, Char yield on pyrolysis of cellulose, *Combustion and Flame*, vol.24, p.263-268, 1975.
- [43] T. Hertzberg et P. Blomqvist, Particles from fires? a screening of common materials found in buildings, *Fire Mater.*, vol. 27, n° 6, p. 295-314, nov. 2003, doi: 10.1002/fam.837.

- [44] A. Frangi et M. Fontana, « Charring rates and temperature profiles of wood sections », *Fire Materials*, 2003.
- [45] M. Cedering, Effect on the charring rate of wood in fire due to oxygen content, moisture content and wood density, *Proceedings of the fourth international conference structures in fire*, Universidade de Aveiro , 2006.
- [46] V. D. Thi, Modélisation du comportement au feu des structures en bois, Mécanique des structures, Université de Lorraine, 2017.
- [47] F. W. Mowrer et R. B. Williamson, Methods to characterize heat release rate data, *Fire Safety Journal*, vol. 16, n° 5, p. 367-387, janv. 1990, doi: 10.1016/0379-7112(90)90009-4.
- [48] W. K. Chow, Assessment on Heat release Rate of Furniture Foam Arrangement by a Cone Calorimeter, *Journal of Fire Sciences*, vol.20(4), p.319-328, 2002, doi: <https://doi.org/10.1177/073490402762574758>
- [49] W. K. Chow et H. W. Au Yeung, On the superposition of heat release rate for polymeric materials, *Architectural Science Review*, vol.46(2), p.145-150, 2003, doi: <https://doi.org/10.1080/00038628.2003.9696977>.
- [50] W. K. Chow et S. S. Han, Superposition of heat release rates curves for combustibles with bench-scale tests, *Polymer Testing*, vol25(1), p.75-82, 2006, doi: <https://doi.org/10.1016/j.polymertesting.2005.09.016>.
- [51] P. Blomqvist, M. S. McNamee, A. A. Stec, D. Gylestam, et D. Karlsson, Detailed study of distribution patterns of polycyclic aromatic hydrocarbons and isocyanates under different fire conditions, *Fire and Materials*, vol.38(1), p.125-144, 2014, doi: 10.1002/fam.2173.
- [52] V. Babrauskas, Charring rate of wood as a tool for fire investigations, *Fire Safety Journal*, vol.40(6), p.528-554, 2005, doi: <https://doi.org/10.1016/j.firesaf.2005.05.006>.
- [53] M. A. Delichatsios, Piloted ignition times, critical heat fluxes and mass loss rates at reduced oxygen atmospheres, *Fire Safety Journal*, vol. 40, n° 3, p. 197-212, avr. 2005, doi: 10.1016/j.firesaf.2004.11.005.
- [54] J. Cuevas, J. L. Torero, et C. Maluk, Flame extinction and burning behaviour of timber under varied oxygen concentrations, *Fire Safety Journal*, vol. 120, p. 103087, mars 2021, doi: 10.1016/j.firesaf.2020.103087.
- [55] F. Richter, F. X. Jervis, X. Huang, et G. Rein, Effect of oxygen on the burning rate of wood, *Combustion and Flame*, vol. 234, p. 111591, déc. 2021, doi: 10.1016/j.combustflame.2021.111591.

- [56] NF EN 15425. Adhesives - One component polyurethane (PUR) for load-bearing timber structures - Classification and performance requirements. 2023.
- [57] EN 13238:2010. Reaction to fire tests for building products - Conditioning procedures and general rules for selection of substrates. 2010.
- [58] F. R. Quant, R. C. Flagan, et K. D. Horton, Implementation of a Scanning Mobility Particles Sizer (SMPS), *Journal of Aerosol Science*, vol.24(1), p.83-84.
- [59] E. Gustafsson, M. Strand, et M. Sanati, Physical and Chemical Characterization of Aerosol Particles Formed during the Thermochemical Conversion of Wood Pellets Using a Bubbling Fluidized Bed Gasifier, *Energy Fuels*, vol. 21, n° 6, p. 3660-3667, nov. 2007, doi: 10.1021/ef7002552.
- [60] J. Rhodes, C. Smith, et A. A. Stec, Characterisation of soot particulates from fire retarded and nanocomposite materials, and their toxicological impact, *Polymer Degradation and Stability*, vol. 96, n° 3, p. 277-284, mars 2011, doi: 10.1016/j.polymdegradstab.2010.07.002.
- [61] J. Keskinen, K. Pietarinen, et M. Lehtimäki, Electrical low pressure impactor, *Journal of Aerosol Science*, vol. 23, n° 4, p. 353-360, juin 1992, doi: 10.1016/0021-8502(92)90004-F.
- [62] F. E. Ngohang, Combination of mass loss cone, Fourier transform infrared spectroscopy and electrical low pressure impactor to extend fire behavior characterization of materials, Lille, 2014.
- [63] ISO 5660-1:2015. Reaction-to-fire tests — Heat release, smoke production and mass loss rate — Part 1: Heat release rate (cone calorimeter method) and smoke production rate (dynamic measurement). 2015.
- [64] C. Huggett, Estimation of rate of heat release by means of oxygen consumption measurements, *Fire and Materials*, vol.4(2), p.61-65, 1980, doi: <https://doi.org/10.1002/fam.810040202>.
- [65] M. J. Hurley *et al.*, Éd., *SFPE Handbook of Fire Protection Engineering*. New York, NY: Springer New York, 2016. doi: 10.1007/978-1-4939-2565-0.
- [66] V. Babrauskas, Development of the Cone Calorimeter-A Bench-scale Heat Release Rate Apparatus Based on Oxygen Consumption, *Fire and Materials*, vol.8(2), p.81-95, 1984, doi: <https://doi.org/10.1002/fam.810080206>.
- [67] ISO 5659-2:2017. Plastics – Smoke generation – Part 2: Determination of optical density by a single chamber test. 2017.
- [68] XP ISO/TS 19700. Controlled equivalence ratio method for the determination of hazardous components of fire effluents - Steady-state tube furnace. 2017.
- [69] A. A. Stec et T. R. Hull, Assessment of the fire toxicity of building insulation materials, *Energy and Buildings*, vol. 43, n° 2-3, p. 498-506, févr. 2011, doi: 10.1016/j.enbuild.2010.10.015.

- [70] ISO 12136. Reaction to fire tests — Measurement of material properties using a fire propagation apparatus. 2011.
- [71] M. Werrel, J. H. Deubel, S. Krüger, A. Hofmann, et U. Krause, The calculation of the heat release rate by oxygen consumption in a controlled-atmosphere cone calorimeter: Heat release rate in a controlled-atmosphere cone calorimeter, *Fire Mater.*, vol. 38, n° 2, p. 204-226, mars 2014, doi: 10.1002/fam.2175.
- [72] G. Mulholland, M. Janssens, S. Yusa, W. Twilley, et V. Babrauskas, The Effect Of Oxygen Concentration On Co And Smoke Produced By Flames, *Fire Saf. Sci.*, vol. 3, p. 585-594, 1991, doi: 10.3801/IAFSS.FSS.3-585.
- [73] V. Babrauskas, W. H. Twilley, M. Janssens, et S. Yusa, A cone calorimeter for controlled-atmosphere studies, *Fire Mater.*, vol. 16, n° 1, p. 37-43, janv. 1992, doi: 10.1002/fam.810160106.
- [74] R. Petrella et N. Bartho, The controlled-atmosphere cone calorimeter – an improved tool for fire testing of materials, *Fire and Materials*, Proceeding of the 1st International Conference Fire and Materials, p.311-321, 1992.
- [75] R. Christy et R. Petrella, Controlled-atmosphere cone calorimeter, *Fire Polymers*, Fire Polymers II, vol.31, p.498-517, 1995, doi: 10.1021/bk-1995-0599.ch031.
- [76] J. E. Leonard, P. A. Bowditch, et V. P. Dowling, Development of a controlled-atmosphere cone calorimeter, *Fire Mater.*, vol. 24, n° 3, p. 143-150, mai 2000, doi: 10.1002/1099-1018(200005/06)24:3<143::AID-FAM728>3.0.CO;2-L.
- [77] E. Mikkola, Effects of oxygen concentration on cone calorimeter results, in *6th. International Fire Conference (Interflam '93)*, p.49-57, 1993.
- [78] J. Hietaniemi, R. Kallonen, et E. Mikkola, Burning characteristics of selected substances: production of heat, smoke and chemical species, *Fire Mater.*, vol. 23, n° 4, p. 171-185, juill. 1999, doi: 10.1002/(SICI)1099-1018(199907/08)23:4<171::AID-FAM680>3.0.CO;2-C.
- [79] J. Hietaniemi, R. Kallonen, et E. Mikkola, Fires at chemical warehouses, *VTT*, Technical Research Centre of Finland, 1997, issn: 1235-0605.
- [80] C. Gomez, M. Janssens, et A. Zalkin, « Measuring yields of toxic gases from materials during different stages of fire development », *Fire and Materials*, 2011.
- [81] D. M. Marquis, E. Guillaume, A. Camillo, et T. Rogaume, Usage of controlled-atmosphere cone calorimeter to provide input data for toxicity modelling, Proceedings of the 12th International Conference on Fire and Materials, Interscience Communications, p.121-134, 2011.

- [82] D. M. Marquis, E. Guillaume, A. Camillo, et T. Rogaume, Usage of controlled-atmosphere cone calorimeter to provide input data for toxicity modelling, Proceedings of the 12th International Conference on Fire and Materials, Interscience Communications, p.121-134, 2011.
- [83] D. Marquis, E. Guillaume, et D. Lesenechal, Accuracy (Trueness and Precision) of Cone Calorimeter Tests with and Without a Vitiated Air Enclosure, *Procedia Engineering*, vol. 62, p. 103-119, 2013, doi: 10.1016/j.proeng.2013.08.048.
- [84] D. Marquis, E. Guillaume, et A. Camillo, Effects of oxygen availability on the combustion behaviour of materials in a controlled atmosphere cone calorimeter, *Fire Saf. Sci.*, vol. 11, p. 138-151, 2014, doi: 10.3801/IAFSS.FSS.11-138.
- [85] A. Alarifi, G. Andrews, L. Witty, et H. Phylaktou, Ignition and toxicity of selected aircraft interior materials using the cone calorimeter and FTIR analysis, Proceedings of the InterFlam 2013. InterScience Communications, vol. 1, p.37-48, ISBN: 978-0-9556548-9-3.
- [86] Irshad, A., Andrews, G., Phylaktou, H., Gibbs, B., et International Seminar On Fire And Explosion Hazards (9; 2019; Saint Petersburg, Russia), Development of the Controlled Atmosphere Cone Calorimeter to Simulate Compartment Fires, 2019, doi: 10.18720/SPBPU/2/K19-90.
- [87] D. M. Marquis et É. Guillaume, Effects of under-ventilated conditions on the reaction-to-fire of a polyisocyanurate foam, Proceedings of the 13th International Conference on Fire and Materials, Interscience Communications, 2013.
- [88] ISO/TS 5660-5:2020. Reaction-to-fire tests — Heat release, smoke production and mass loss rate — Part 5: Heat release rate (cone calorimeter method) and smoke production rate (dynamic measurement) under reduced oxygen atmospheres. 2020.
- [89] W. Thornton, The Relation of Oxygen to the Heat of Combustion of Organic Compounds, *Philosophical Magazine and Journal of Science*, The London, Edinburgh, and Dublin Philosophical Magazine and Journal of Science, vol.33(194), p.196-203, 1917, doi : <https://doi.org/10.1080/14786440208635627>.
- [90] M. Janssens, Measuring rate of heat release by oxygen consumption, *Fire Technology*, vol.27, p.234-249, 1991, doi: <https://doi.org/10.1007/BF01038449>.
- [91] D. T. Gottuk, R. J. Roby, et C. L. Beyler, The role of temperature on carbon monoxide production in compartment fires, *Fire Safety Journal*, vol. 24, n° 4, p. 315-331, janv. 1995, doi: 10.1016/0379-7112(95)00027-5.

- [92] W. M. Pitts, Application of Thermodynamic and Detailed Chemical Kinetic Modeling to Understanding Combustion Product Generation in Enclosure Fires, *Fire Safety Journal*, vol.23(3), p.271-303, 1994, doi: [https://doi.org/10.1016/0379-7112\(94\)90032-9](https://doi.org/10.1016/0379-7112(94)90032-9).
- [93] BS EN 13823:2020. Reaction to fire tests for building products — Building products excluding floorings exposed to the thermal attack by a single burning item. 2020.
- [94] B. Lafdal, Étude expérimentale et numérique des feux sous-ventilés, Sciences de l'ingénieur [physics]. Université de Lorraine, 2022. Français.
- [95] Y. Peng et S. Wu, The structural and thermal characteristics of wheat straw hemicellulose, *Journal of Analytical and Applied Pyrolysis*, vol. 88, n° 2, p. 134-139, juill. 2010, doi: 10.1016/j.jaap.2010.03.006.
- [96] S. Wang *et al.*, Comparison of the pyrolysis behavior of lignins from different tree species, *Biotechnology Advances*, vol. 27, n° 5, p. 562-567, sept. 2009, doi: 10.1016/j.biotechadv.2009.04.010.
- [97] G. Lv et S. Wu, Analytical pyrolysis studies of corn stalk and its three main components by TG-MS and Py-GC/MS, *Journal of Analytical and Applied Pyrolysis*, vol. 97, p. 11-18, sept. 2012, doi: 10.1016/j.jaap.2012.04.010.
- [98] R. Alén, E. Kuoppala, et P. Oesch, Formation of the main degradation compound groups from wood and its components during pyrolysis, *Journal of Analytical and Applied Pyrolysis*, vol. 36, n° 2, p. 137-148, juin 1996, doi: 10.1016/0165-2370(96)00932-1.
- [99] P. R. Patwardhan, D. L. Dalluge, B. H. Shanks, et R. C. Brown, Distinguishing primary and secondary reactions of cellulose pyrolysis, *Bioresource Technology*, vol. 102, n° 8, p. 5265-5269, avr. 2011, doi: 10.1016/j.biortech.2011.02.018.
- [100] Q. Lu, X. Yang, C. Dong, Z. Zhang, X. Zhang, et X. Zhu, Influence of pyrolysis temperature and time on the cellulose fast pyrolysis products: Analytical Py-GC/MS study, *Journal of Analytical and Applied Pyrolysis*, vol. 92, n° 2, p. 430-438, nov. 2011, doi: 10.1016/j.jaap.2011.08.006.
- [101] I. Itabaiana Junior, M. Avelar Do Nascimento, R. O. M. A. De Souza, A. Dufour, et R. Wojcieszak, Levoglucosan: a promising platform molecule?, *Green Chem.*, vol. 22, n° 18, p. 5859-5880, 2020, doi: 10.1039/D0GC01490G.
- [102] M. X. Fang, D. K. Shen, Y. X. Li, C. J. Yu, Z. Y. Luo, et K. F. Cen, Kinetic study on pyrolysis and combustion of wood under different oxygen concentrations by using TG-FTIR analysis, *Journal of Analytical and Applied Pyrolysis*, vol. 77, n° 1, p. 22-27, août 2006, doi: 10.1016/j.jaap.2005.12.010.

- [103] JG Quintiere et B. Rhodes, Fire growth models for materials, *National Institute of Standards and Technology*, 1994.
- [104] A. L. Sullivan et R. Ball, Thermal decomposition and combustion chemistry of cellulosic biomass, *Atmospheric Environment*, vol. 47, p. 133-141, févr. 2012, doi: 10.1016/j.atmosenv.2011.11.022.
- [105] S. Laaongnaun et S. Patumsawad, Particulate matter characterization of the combustion emissions from agricultural waste products, *Heliyon*, vol. 8, n° 8, p. e10392, août 2022, doi: 10.1016/j.heliyon.2022.e10392.
- [106] S. Hosseini *et al.*, Particle size distributions from laboratory-scale biomass fires using fast response instruments, *Atmos. Chem. Phys.*, vol. 10, n° 16, p. 8065-8076, août 2010, doi: 10.5194/acp-10-8065-2010.
- [107] J. S. Lighty, J. M. Veranth, et A. F. Sarofim, Combustion Aerosols: Factors Governing Their Size and Composition and Implications to Human Health, *Journal of the Air & Waste Management Association*, vol. 50, n° 9, p. 1565-1618, sept. 2000, doi: 10.1080/10473289.2000.10464197.
- [108] T. Nussbaumer, C. Czasch, N. Klippel, L. Johansson, et C. Tullin, Particulate Emissions from Biomass Combustion in IEA Countries, International Energy Agency (IEA) Bioenergy Task 32 and Swiss Federal Office of Energy, 2008, ISBN: 3-908705-18-5.
- [109] K. Li, D. S. W. Pau, J. Wang, et J. Ji, Modelling pyrolysis of charring materials: determining flame heat flux using bench-scale experiments of medium density fibreboard (MDF), *Chemical Engineering Science*, vol. 123, p. 39-48, févr. 2015, doi: 10.1016/j.ces.2014.10.043.

Appendix

Appendix 1

Replica curves of the fire behavior of PMMA in the CACC at 50 kW/m²

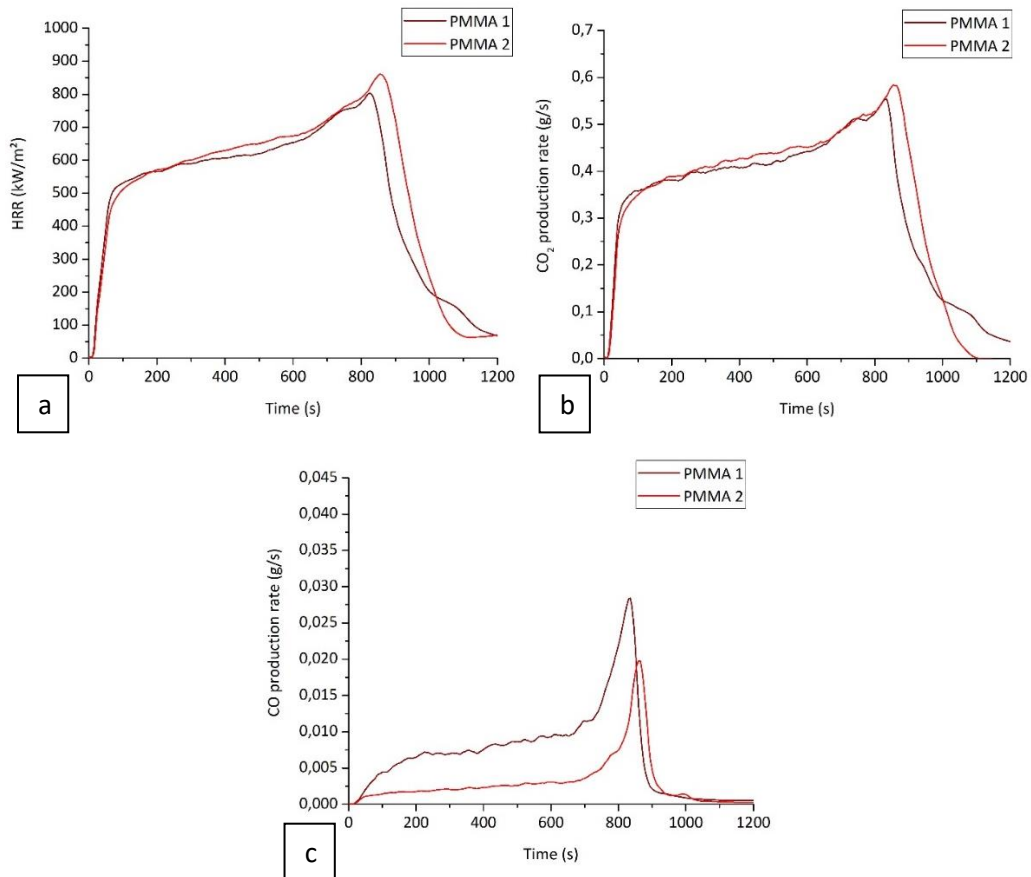


Figure 116: Fire behavior of PMMA at 50 kW/m² and 21 vol-% O₂: a. HRR, b. CO₂ production rate and c. CO production rate

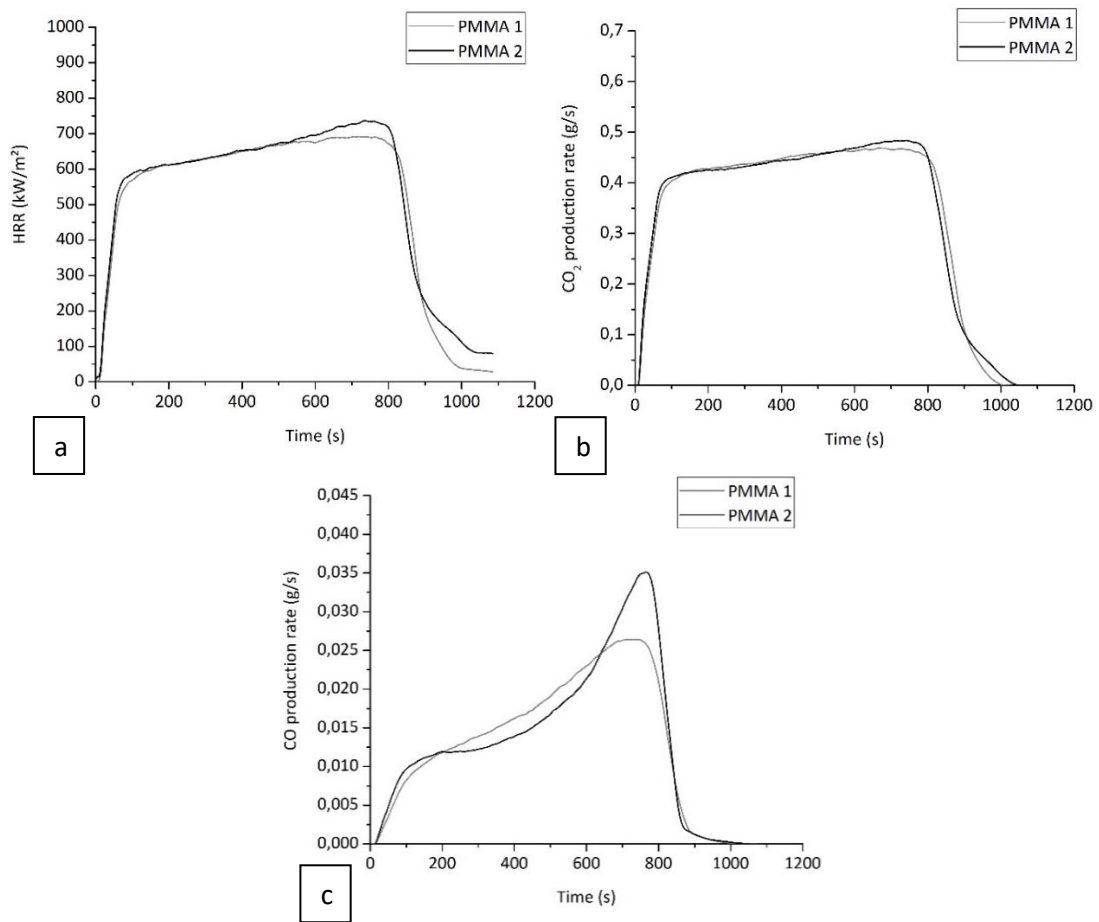


Figure 117: Fire behavior of PMMA at 50 kW/m² and 18 vol-% O₂: a. HRR, b. CO₂ production rate and c. CO production rate

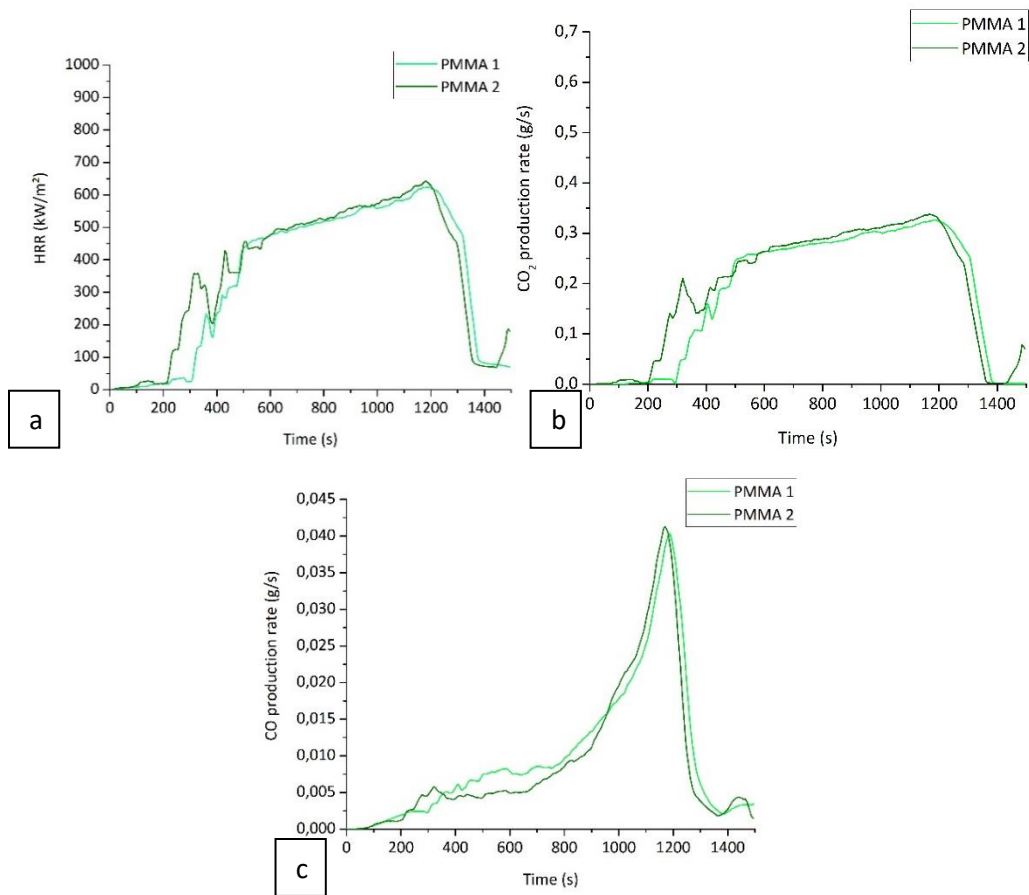


Figure 118: Fire behavior of PMMA at 50 kW/m² and 15 vol-% O₂: a. HRR, b. CO₂ production rate and c. CO production rate

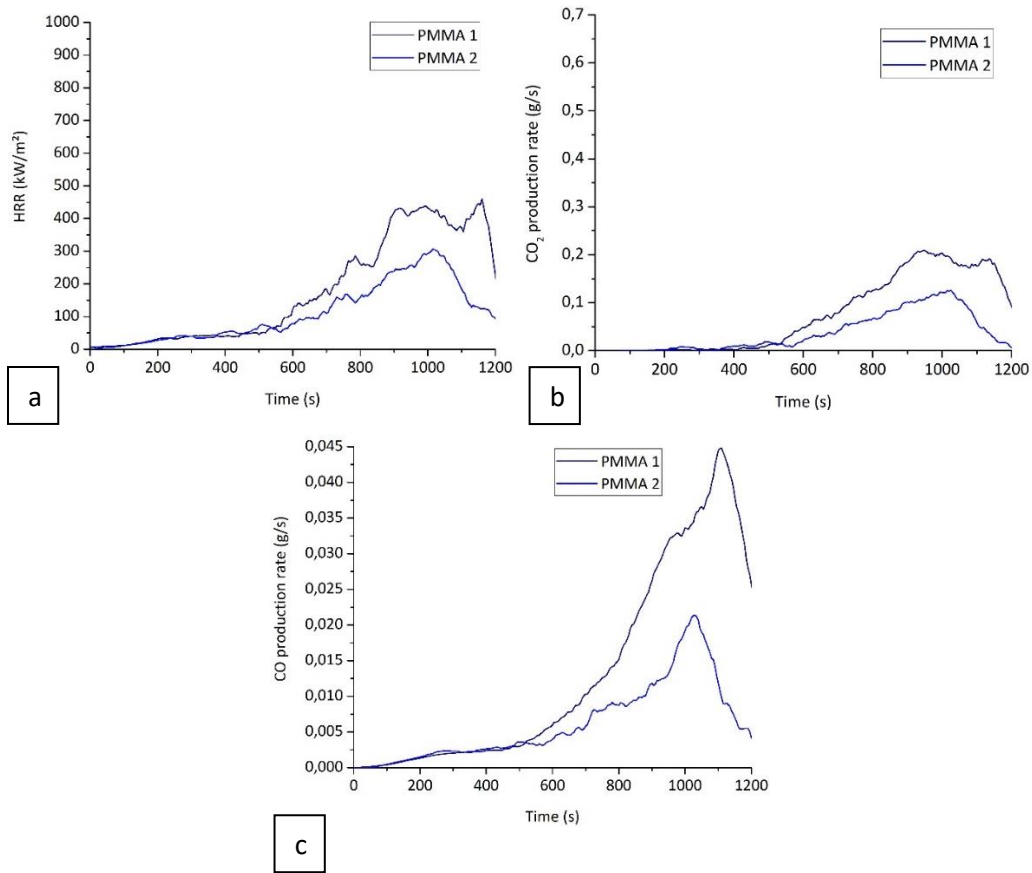


Figure 119: Fire behavior of PMMA at 50 kW/m² and 10 vol-% O₂: a. HRR, b. CO₂ production rate and c. CO production rate

Appendix 2

TG and dTG replica curves of CLT

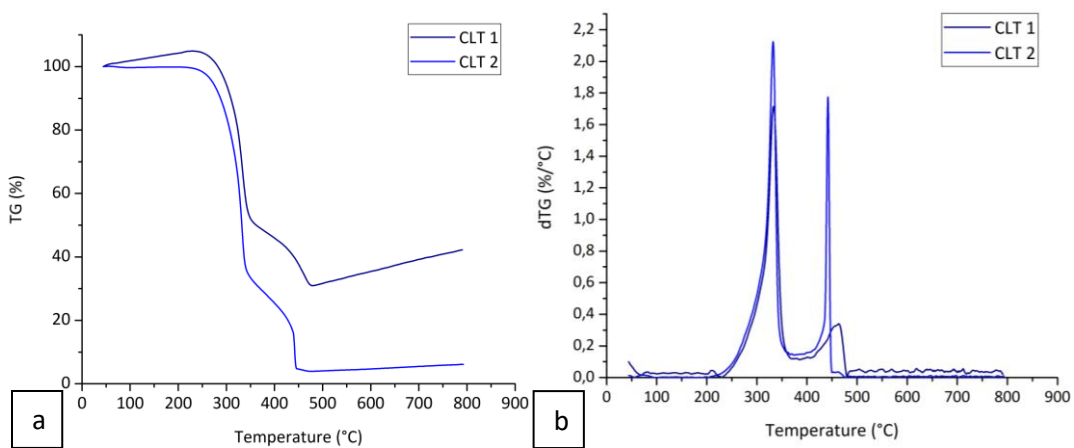


Figure 120: TGA-FTIR test of CLT at 21 vol-% O₂: a. TG and b. dTG

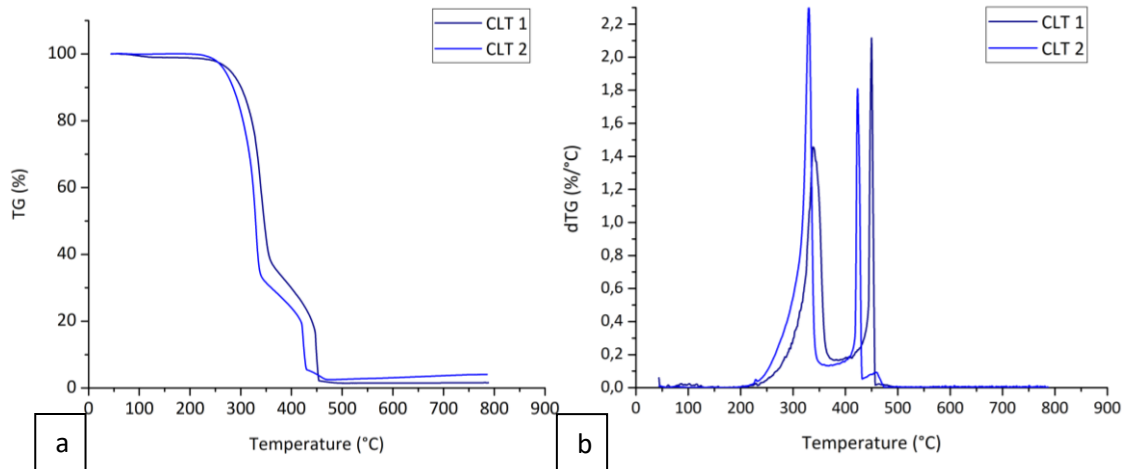


Figure 121: TGA-FTIR test of CLT at 18 vol-% O₂: a. TG and b. dTG

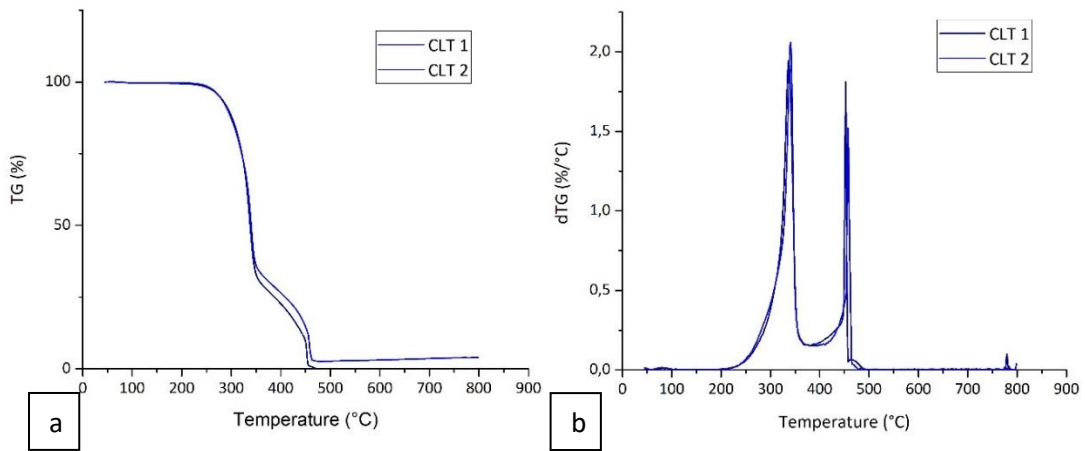


Figure 122: TGA-FTIR test of CLT at 15 vol-% O₂: a. TG and b. dTG

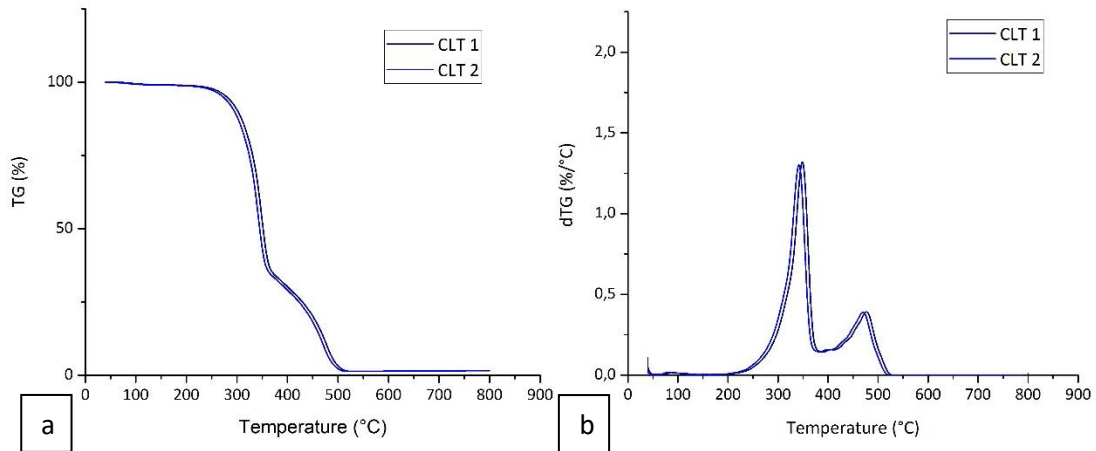


Figure 123: TGA-FTIR test of CLT at 10 vol-% O₂: a. TG and b. dTG

Appendix 3

FTIR spectra of CLT

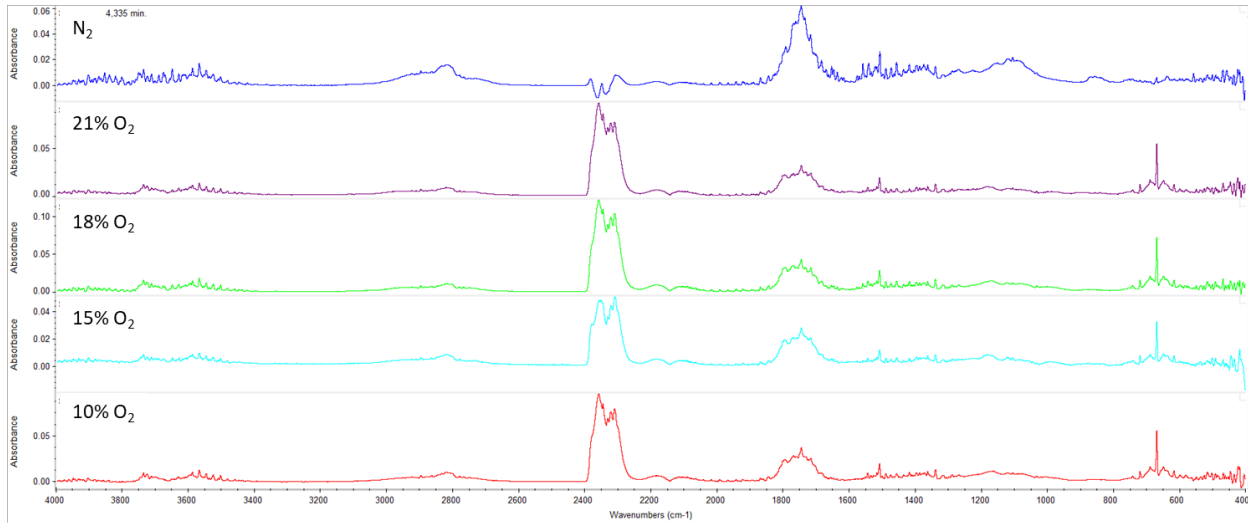


Figure 124: FTIR spectra of CLT under N₂, 21, 18, 15 and 15 vol-% O₂ at the first peak of decomposition

Appendix 4

TG and dTG replica curves of WF

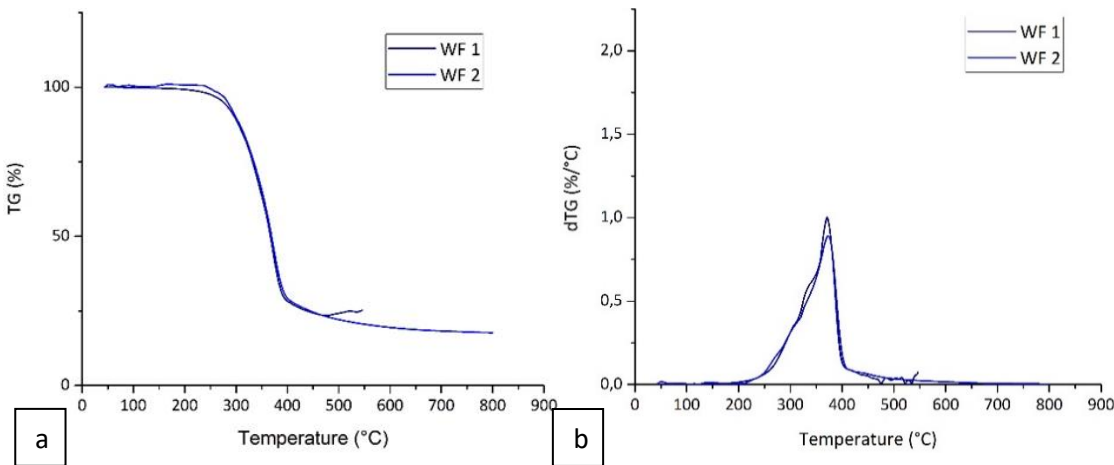


Figure 125: TGA-FTIR test of WF under N₂: a. TG and b. dTG

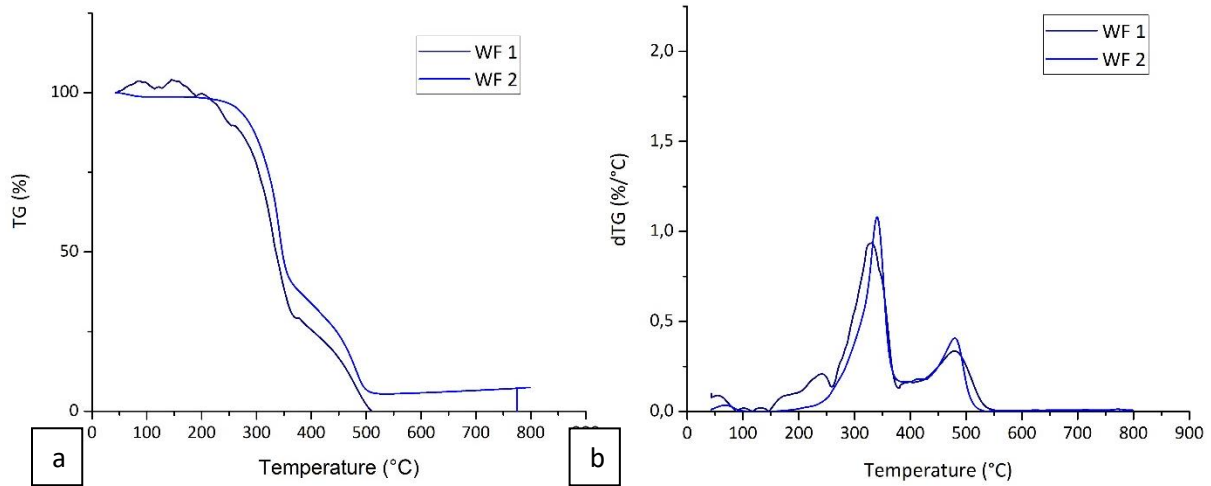


Figure 126: TGA-FTIR test of WF at 21 vol-% O₂: a. TG and b. dTG

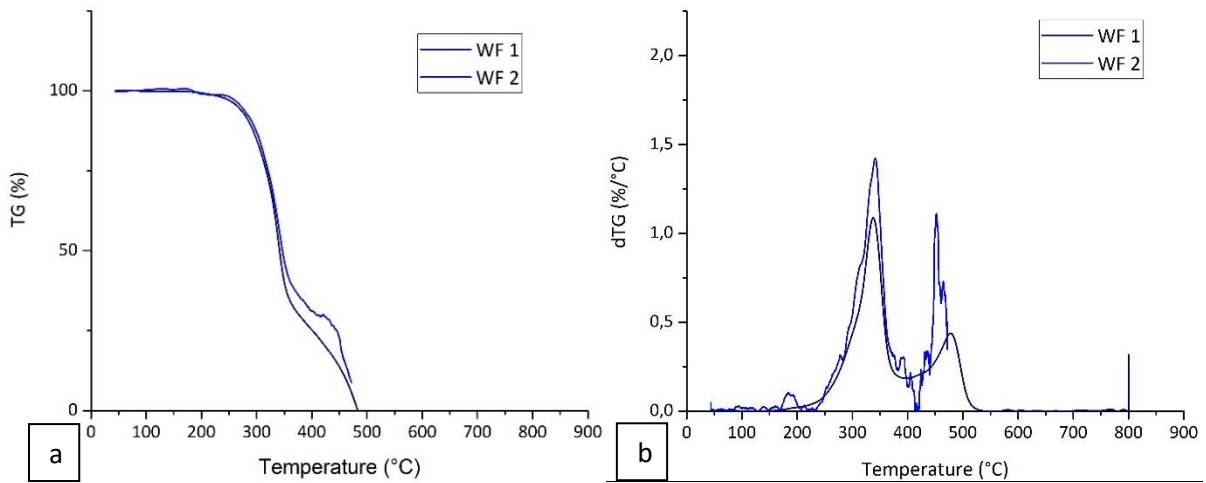


Figure 127: TGA-FTIR test of WF at 18 vol-% O₂: a. TG and b. Dtg

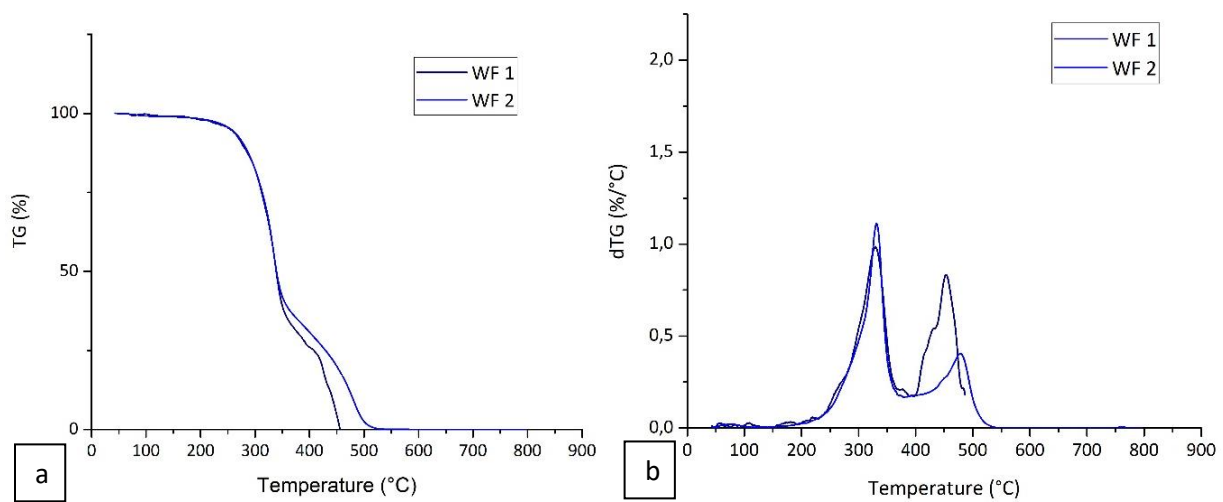


Figure 128: TGA-FTIR test of WF at 15 vol-% O₂: a. TG and b. dTG

Appendix 5

FTIR spectra of WF

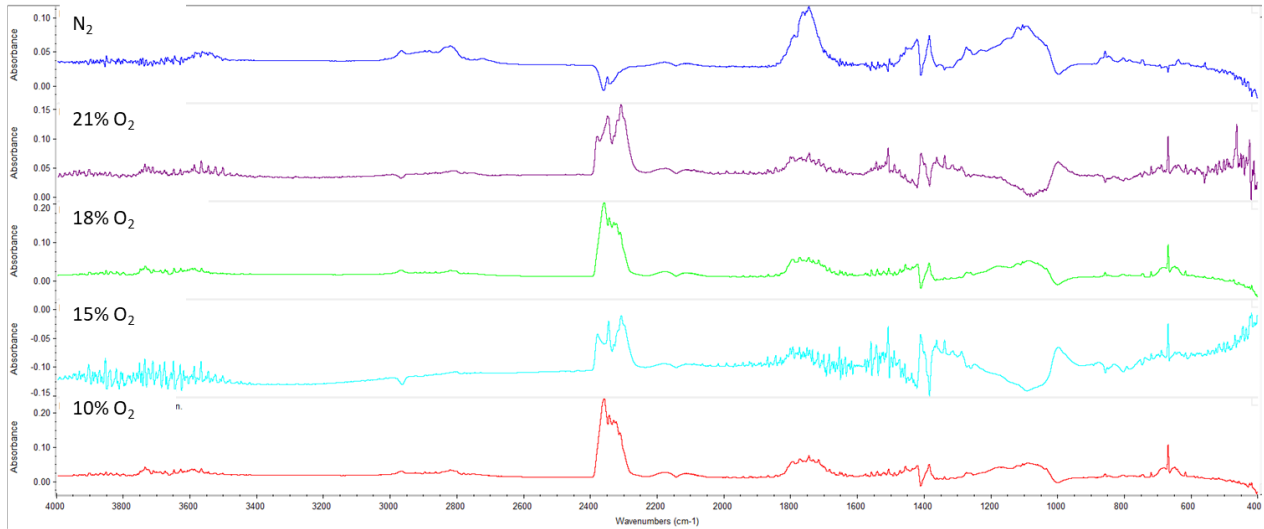
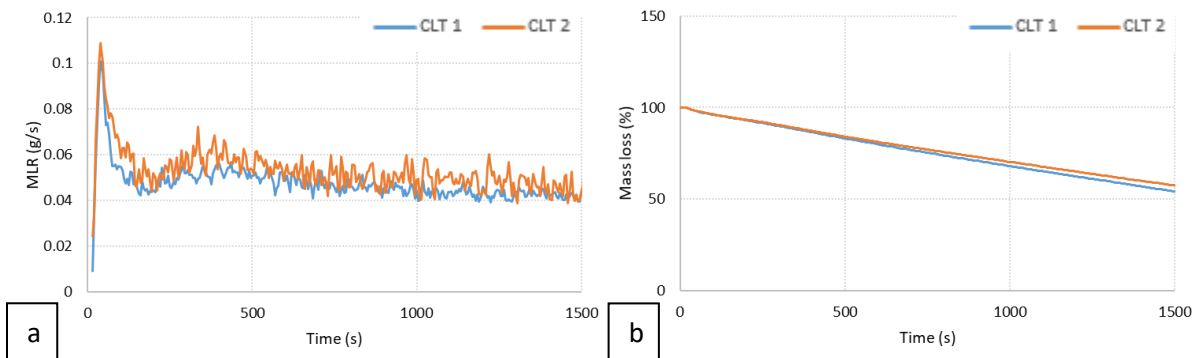


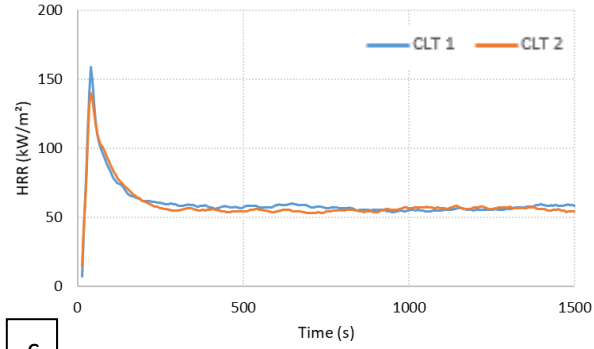
Figure 129: FTIR spectra of WF under N₂, 21, 18, 15 and 10 vol-% O₂ at the first peak of decomposition

Appendix 6

Replica curves of the fire behavior, gas, and aerosol production of CLT in the CACC at 50 kW/m²

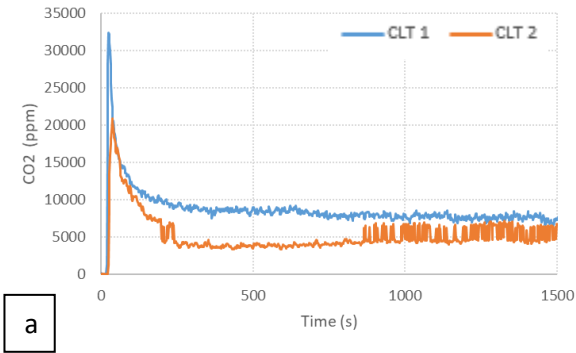
- 21 vol-% O₂



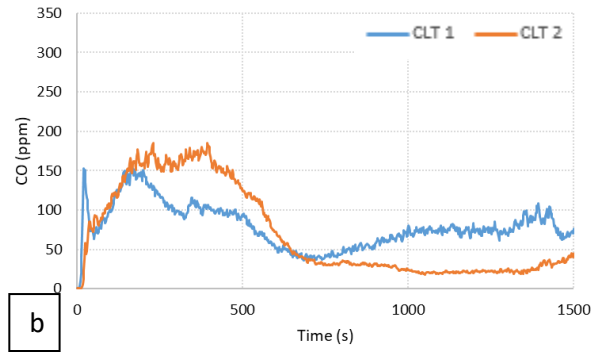


c

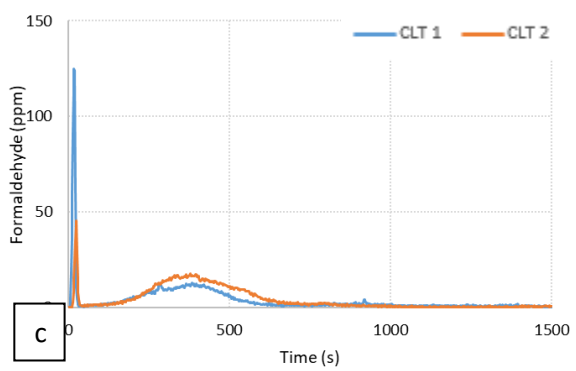
Figure 130: Fire behavior of CLT at 50 kW/m² and 21 vol-% O₂: a. MLR, b. mass loss and c. HHR



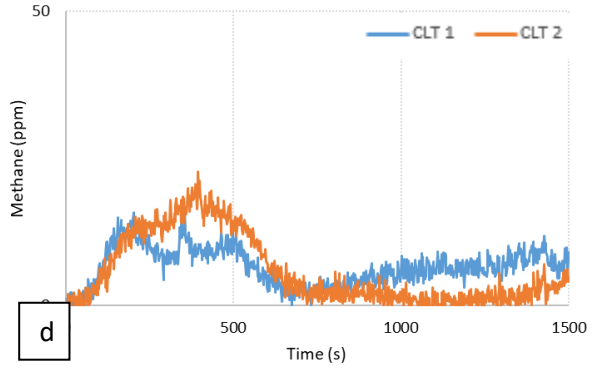
a



b

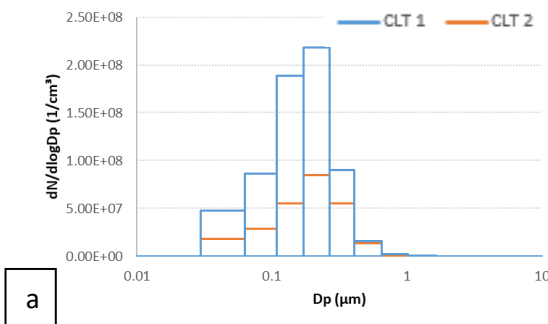


c

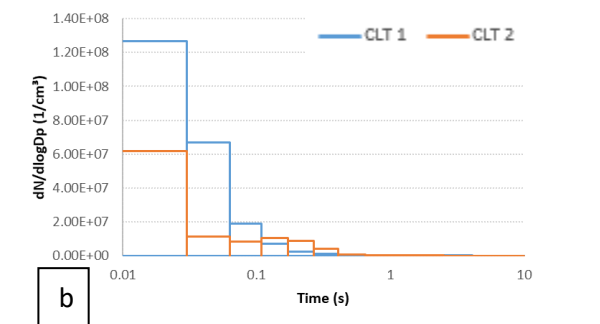


d

Figure 131: Gas production of CLT at 50 kW/m² and 21 vol-% O₂: a. CO₂, b. CO, c. Formaldehyde and c. Methane



a



b

Figure 132: Aerosol size distribution of CLT at 50 kW/m² and 21 vol-% O₂: a. *t_i*, b. 1500s

- 18 vol-% O₂

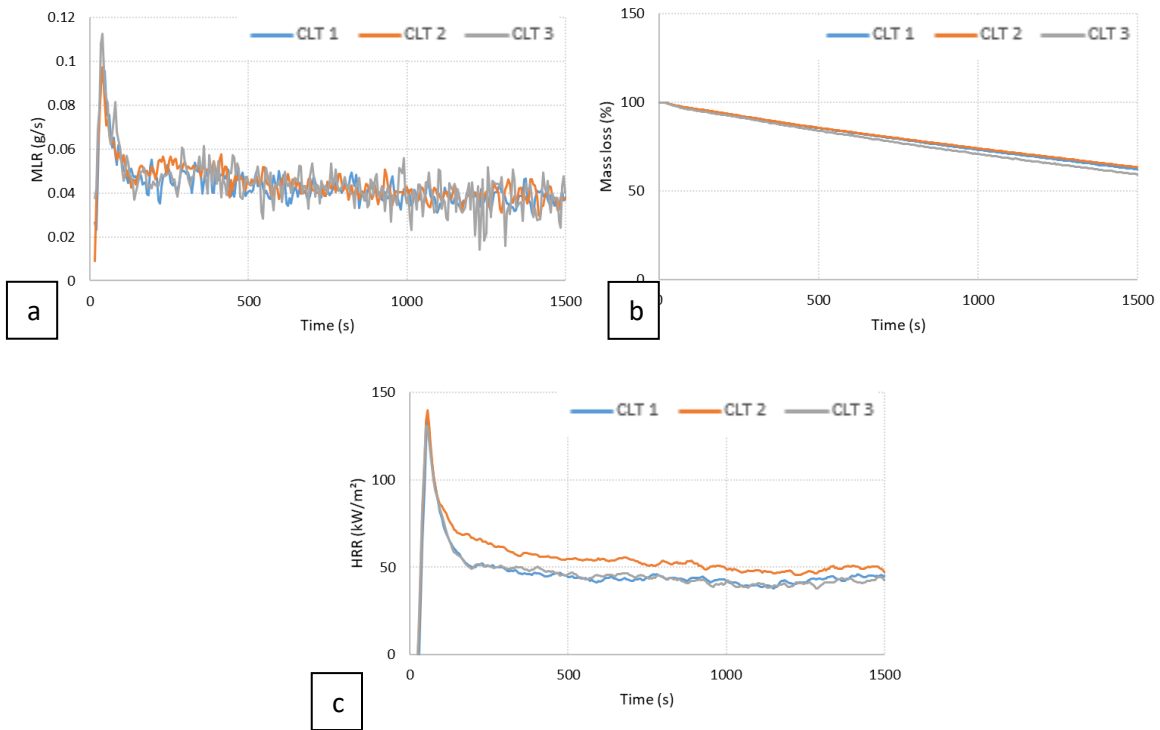
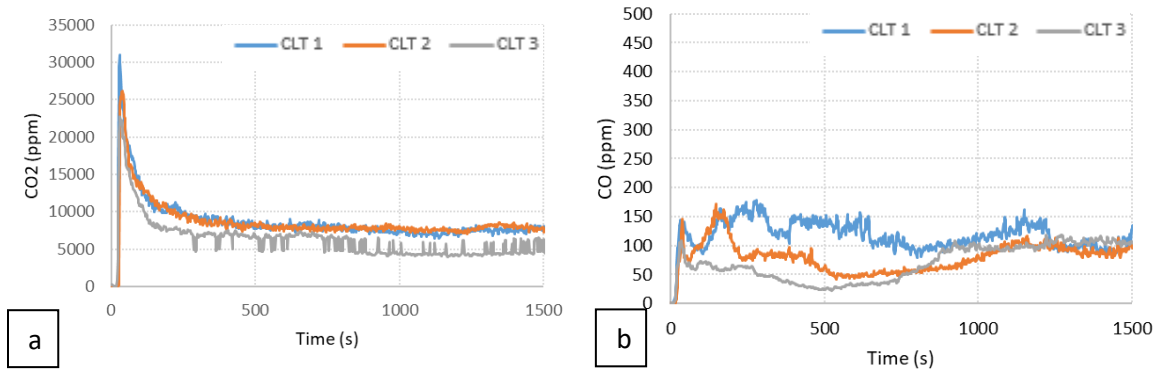


Figure 133: Fire behavior of CLT at 50 kW/m² and 18 vol-% O₂: a. MLR, b. mass loss and c. HHR



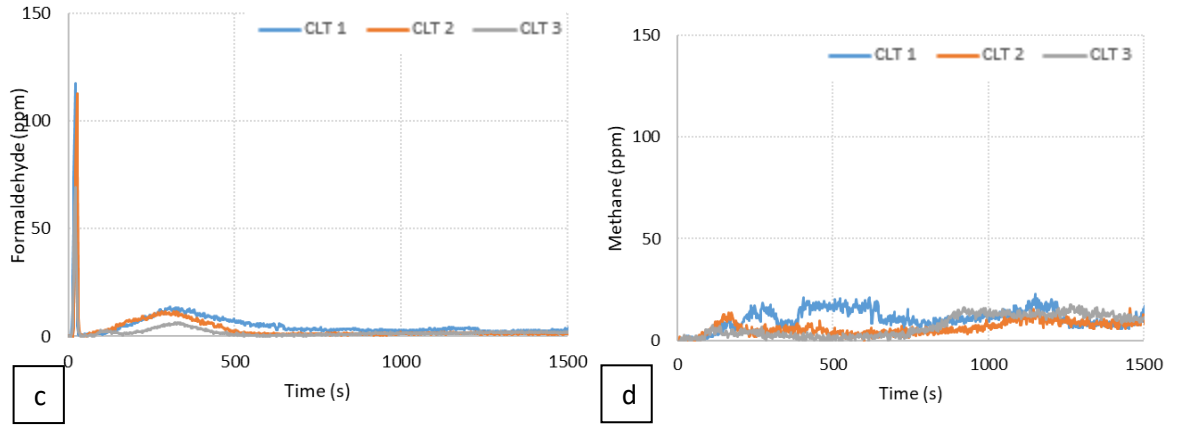


Figure 134: Gas production of CLT at 50 kW/m² and 18 vol-% O₂: a. CO₂, b. CO, c. Formaldehyde and c. Methane

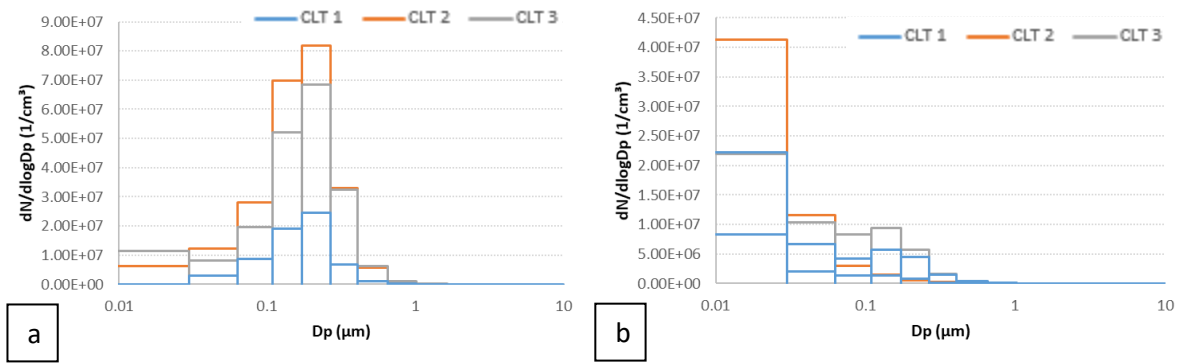
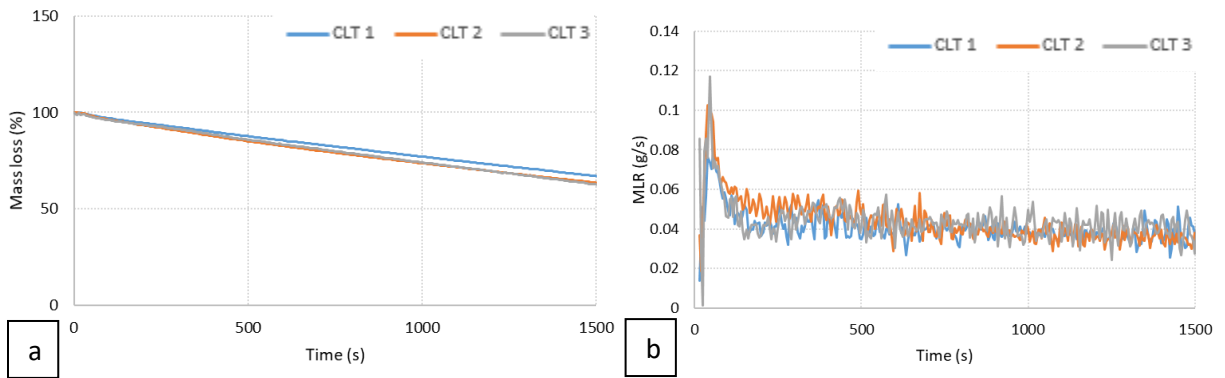


Figure 135: Aerosol size distribution of CLT at 50 kW/m² and 18 vol-% O₂: a. *t_i*, b. 1500s

- 15 vol-% O₂



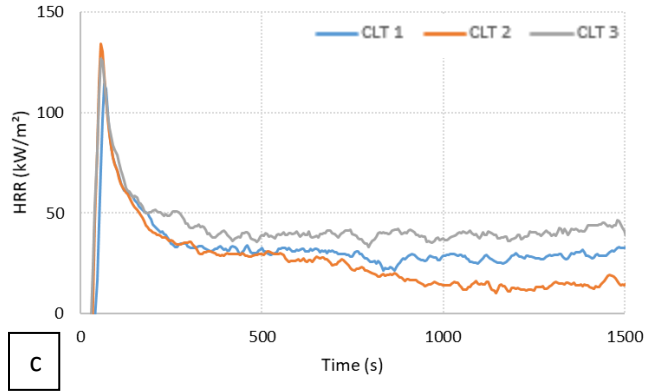


Figure 136: Fire behavior of CLT at 50 kW/m² and 15 vol-% O₂: a. MLR, b. mass loss and c. HRR

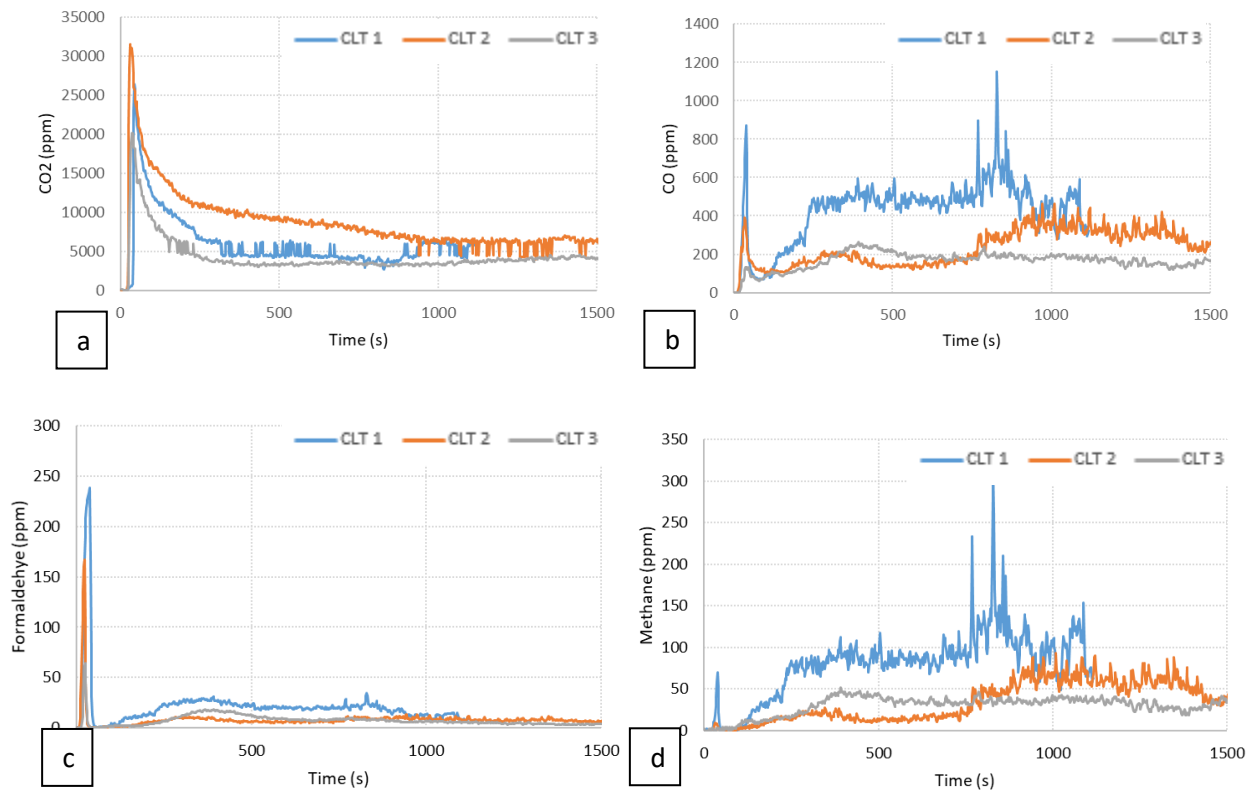


Figure 137: Gas production of CLT at 50 kW/m² and 15 vol-% O₂: a. CO₂, b. CO, c. Formaldehyde and d. Methane

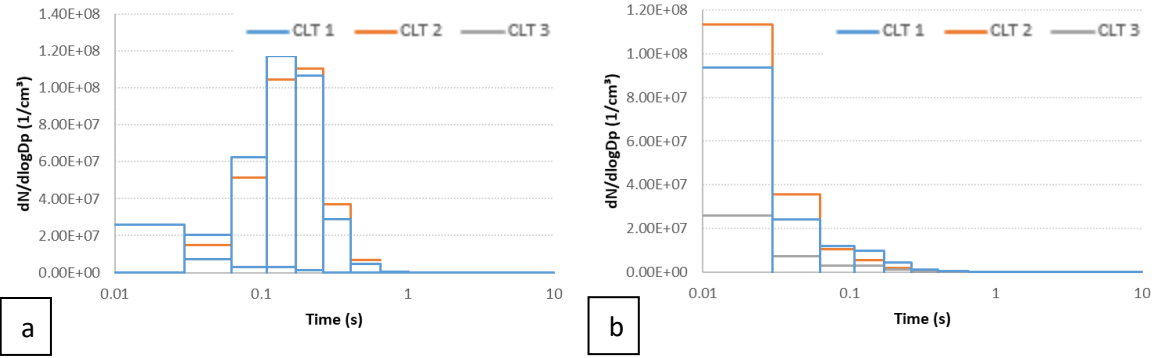


Figure 138: Aerosol size distribution of CLT at 50 kW/m² and 15 vol-% O₂: a. *t*, b. 1500s

- 10 vol-% O₂

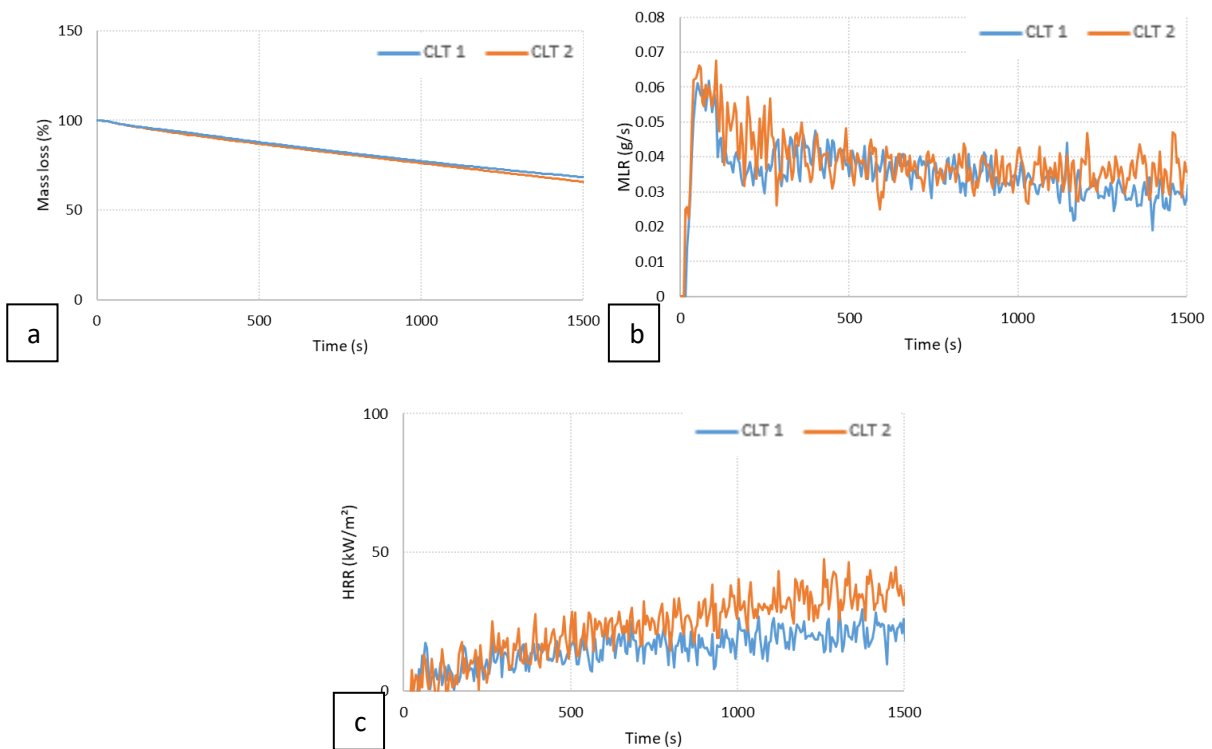
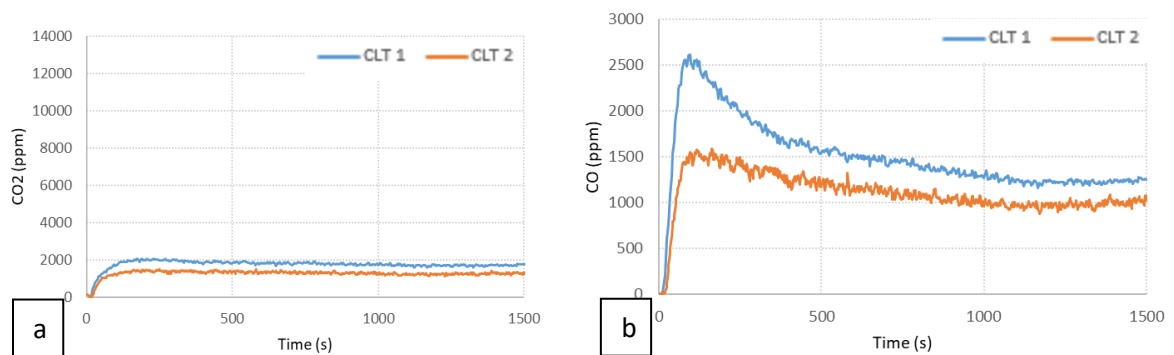


Figure 139: Fire behavior of CLT at 50 kW/m² and 10 vol-% O₂: a. MLR, b. mass loss and c. HRR



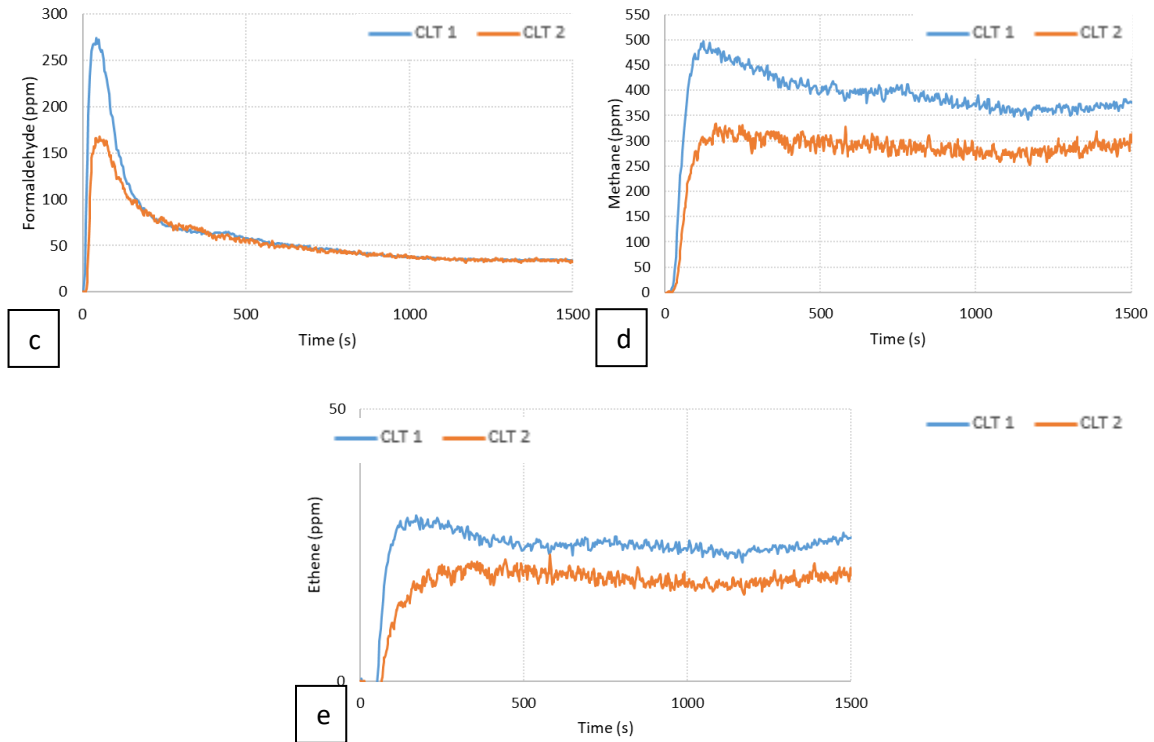


Figure 140: Gas production of CLT at 50 kW/m² and 10 vol-% O₂: a. CO₂, b. CO, c. Formaldehyde, d. Methane and e. Ethene

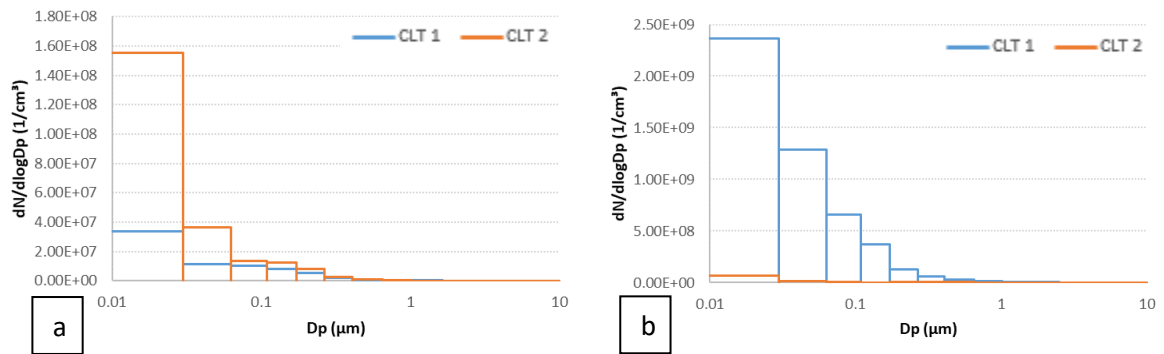


Figure 141: Aerosol size distribution of CLT at 50 kW/m² and 10 vol-% O₂: a. 25s, b. 1500s

Appendix 7

Temperature rise of CLT at 50 kW/m² and 21 vol-% O₂ in the CACC

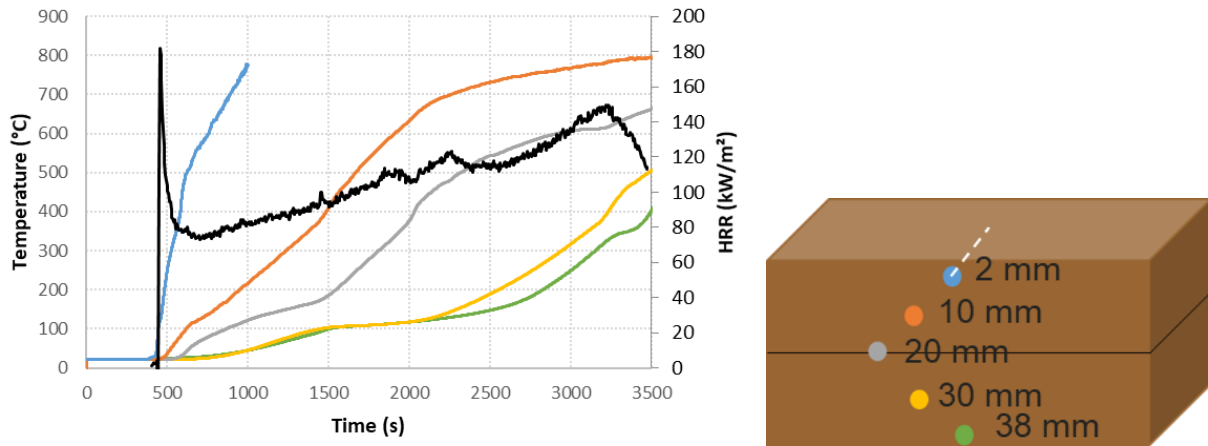


Figure 142: a. Temperature rise and HRR of CLT at 50 kW/m² and 21 vol-% O₂ and b. location of thermocouples

Appendix 8

FTIR spectra of CLT at 50 kW/m²

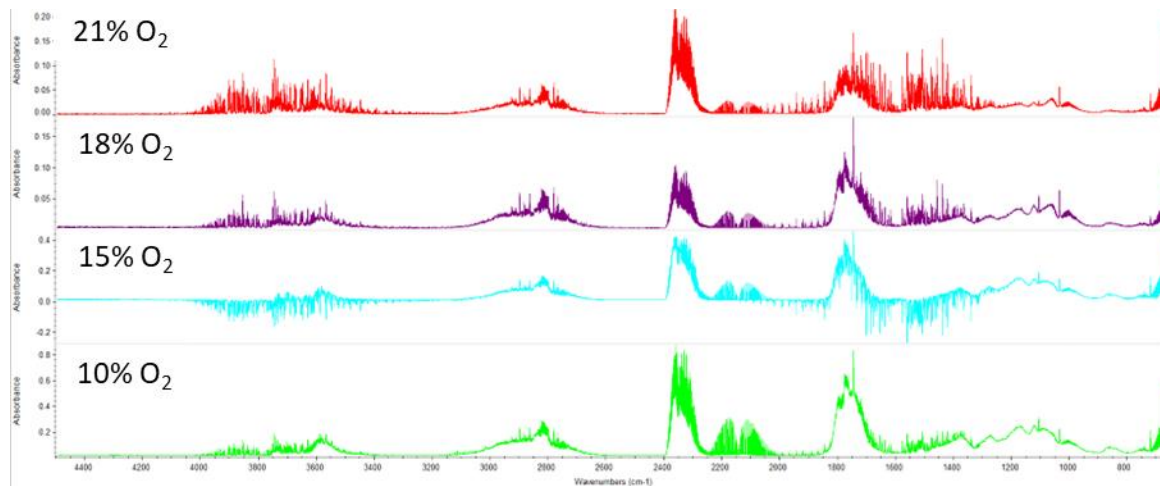


Figure 143: FTIR spectra of CLT at 50 kW/m² at 21, 18, 15 and 10 vol-% O₂ at the start of thermal exposure

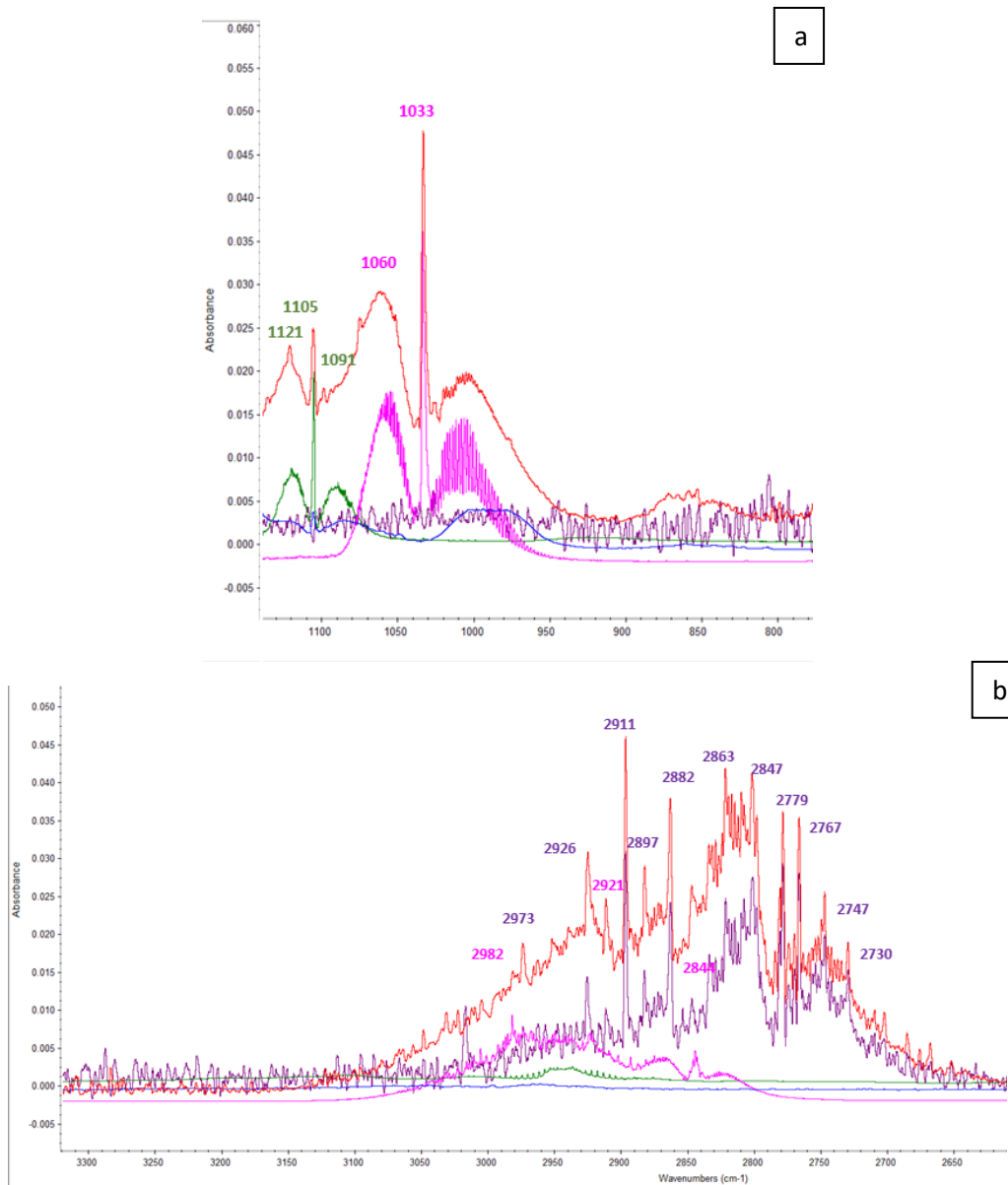
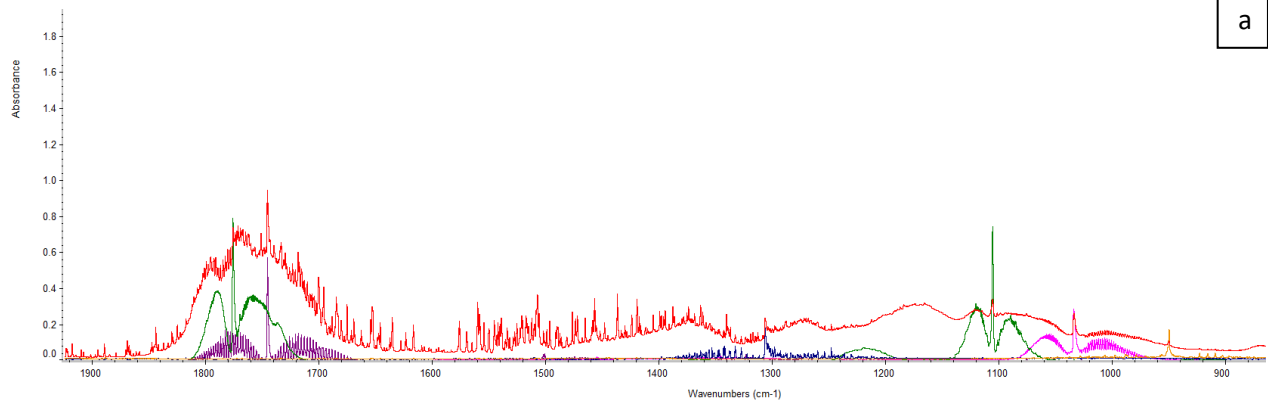
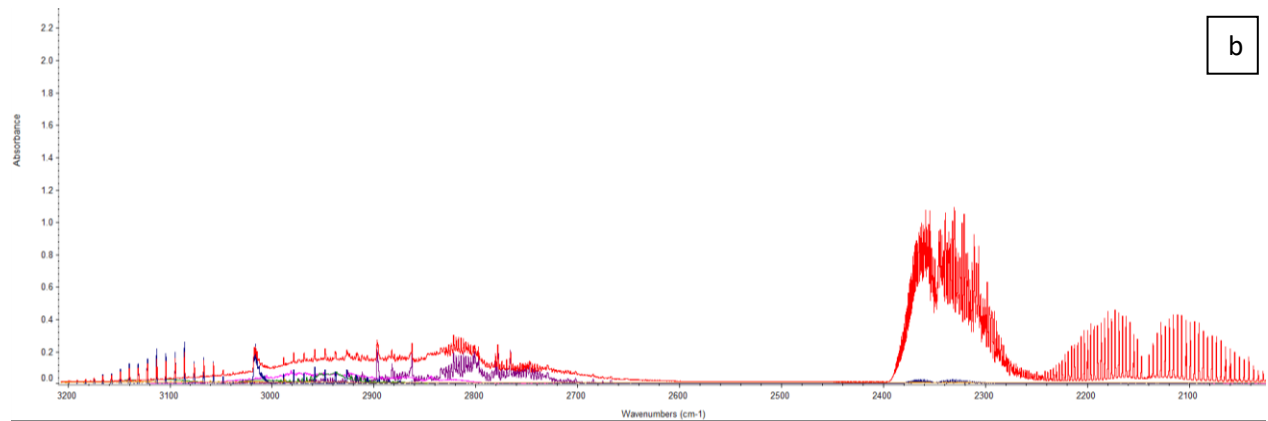


Figure 144: Zoom on the FTIR spectra of CLT at 50 kW/m², 21 vol-% O₂ at the start of thermal exposure (red) along with spectra of formaldehyde (purple), methanol (pink) and formic acid (green) between 1150 and 750 cm⁻¹ (a) and between 3300 and 2500 cm⁻¹ (b)



a



b

Figure 145: Zoom on the FTIR spectra of CLT at 50 kW/m², 10 vol-% O₂ at the start of thermal exposure (red) along with spectra of formaldehyde (purple), methanol (pink), formic acid (green), methane (blue) and ethene (orange) between 1900 and 900 cm⁻¹ (a) and between 3200 and 2000 cm⁻¹ (b)

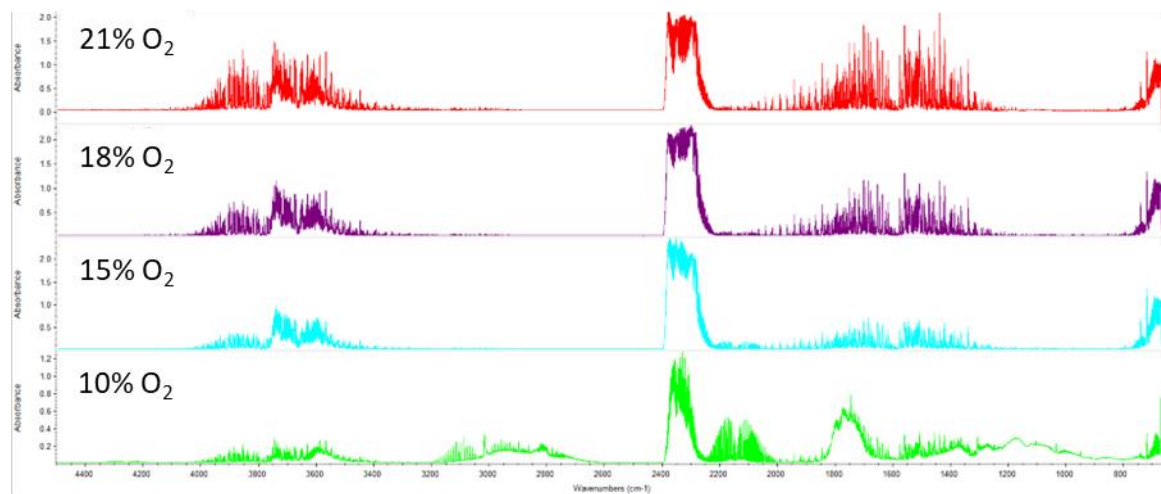


Figure 146: FTIR spectra of CLT at 50 kW/m² at 21, 18, 15 and 10 vol-% O₂ at ignition

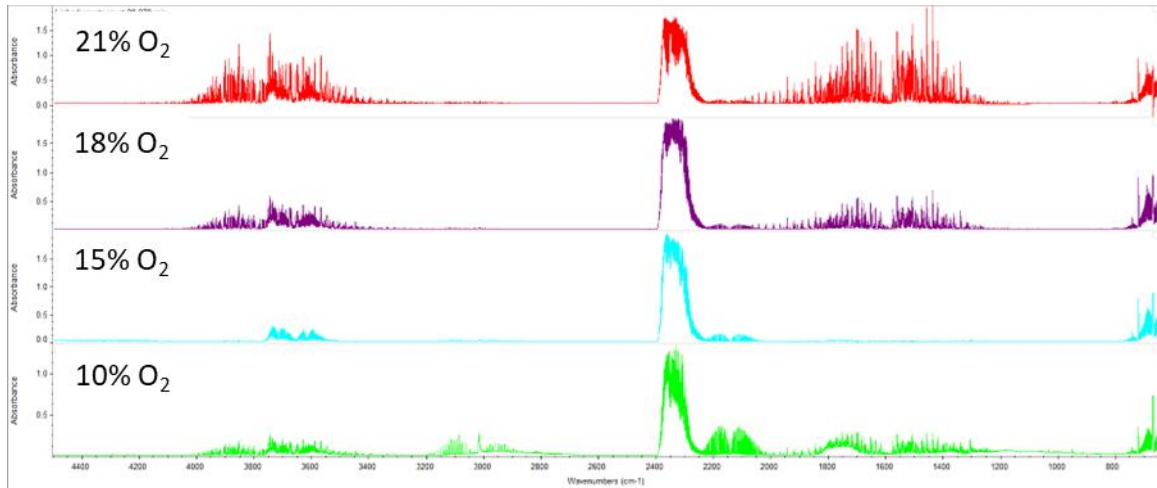
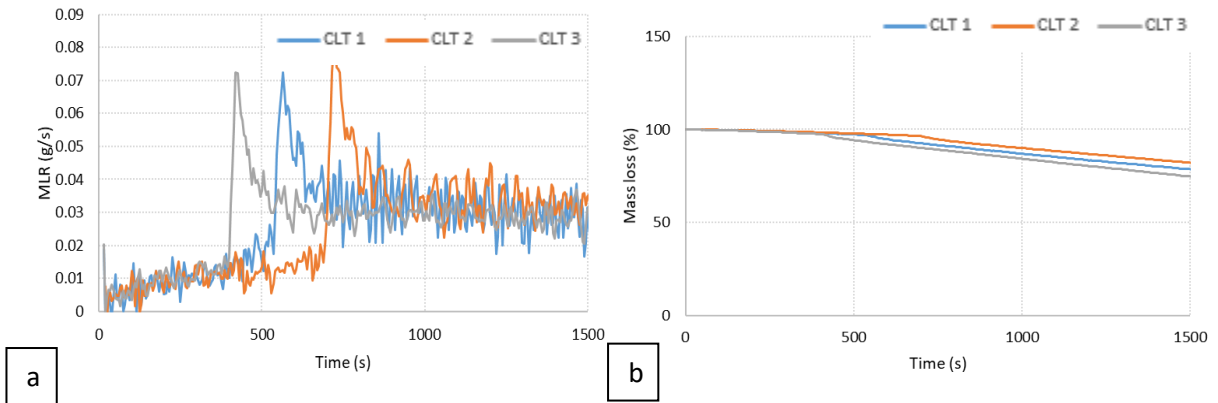


Figure 147: FTIR spectra of CLT at 50 kW/m² at 21, 18, 15 and 10 vol-% O₂ at 20 min of test

Appendix 9

Replica curves of the fire behavior, gas, and aerosol production of CLT in the CACC at 20 kW/m²

- 21 vol-% O₂



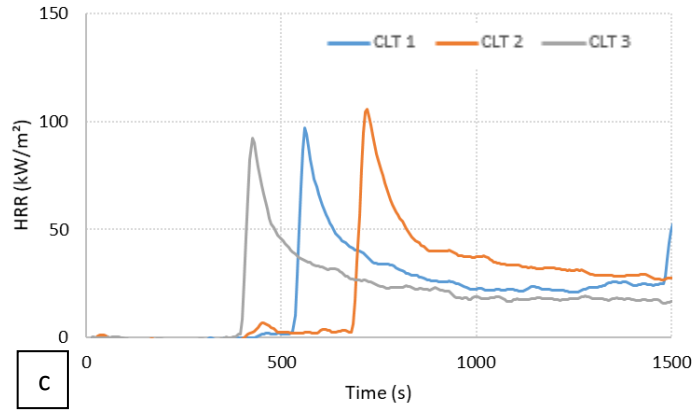


Figure 148: Fire behavior of CLT at 20 kW/m² and 21 vol-% O₂: a. MLR, b. mass loss and c. HHR

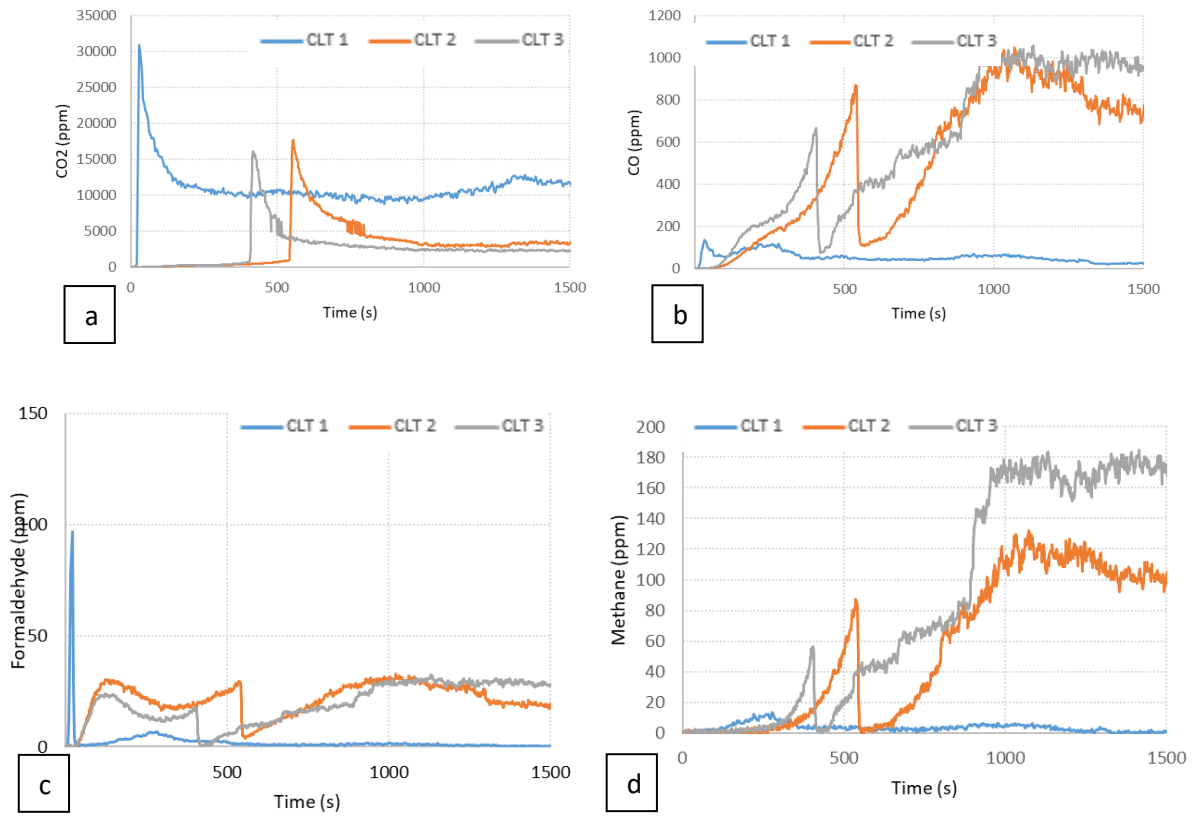


Figure 149: Gas production of CLT at 20 kW/m² and 21 vol-% O₂: a. CO₂, b. CO, c. Formaldehyde, c. Methane

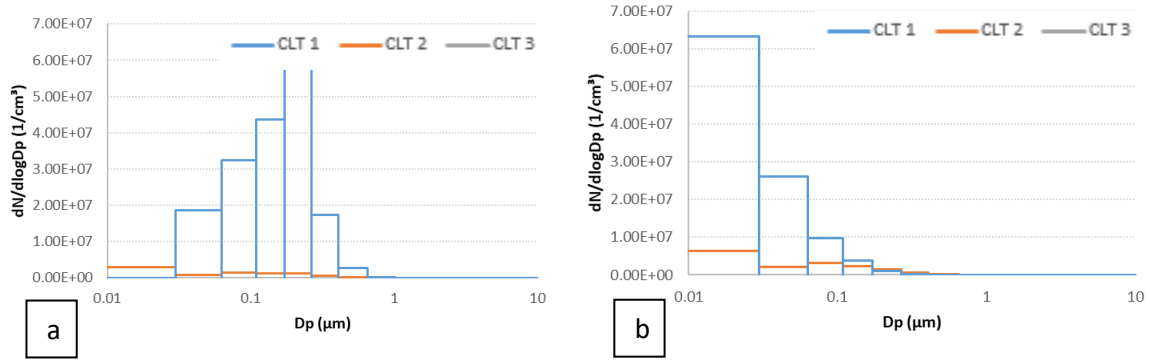


Figure 150: Aerosol size distribution of CLT at 20 kW/m² and 21 vol-% O₂: a. t_i, b. 1500s

- 18 vol-% O₂

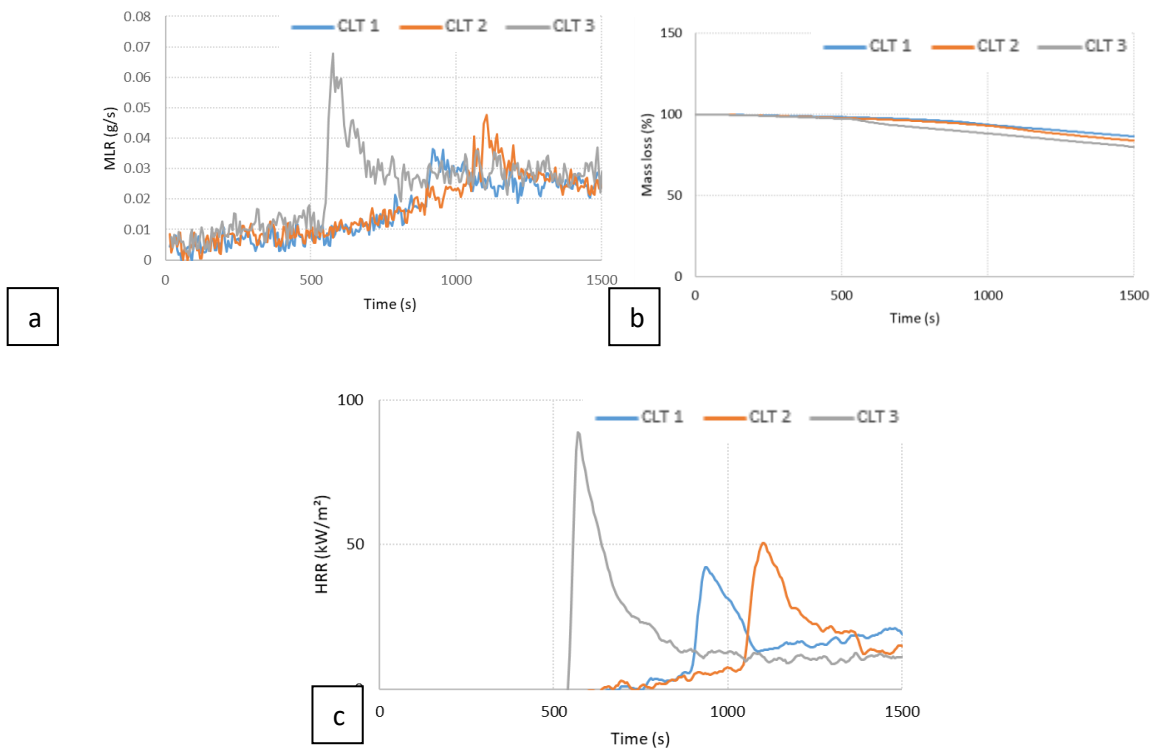


Figure 151: Fire behavior of CLT at 20 kW/m² and 18 vol-% O₂: a. MLR, b. mass loss and c. HRR

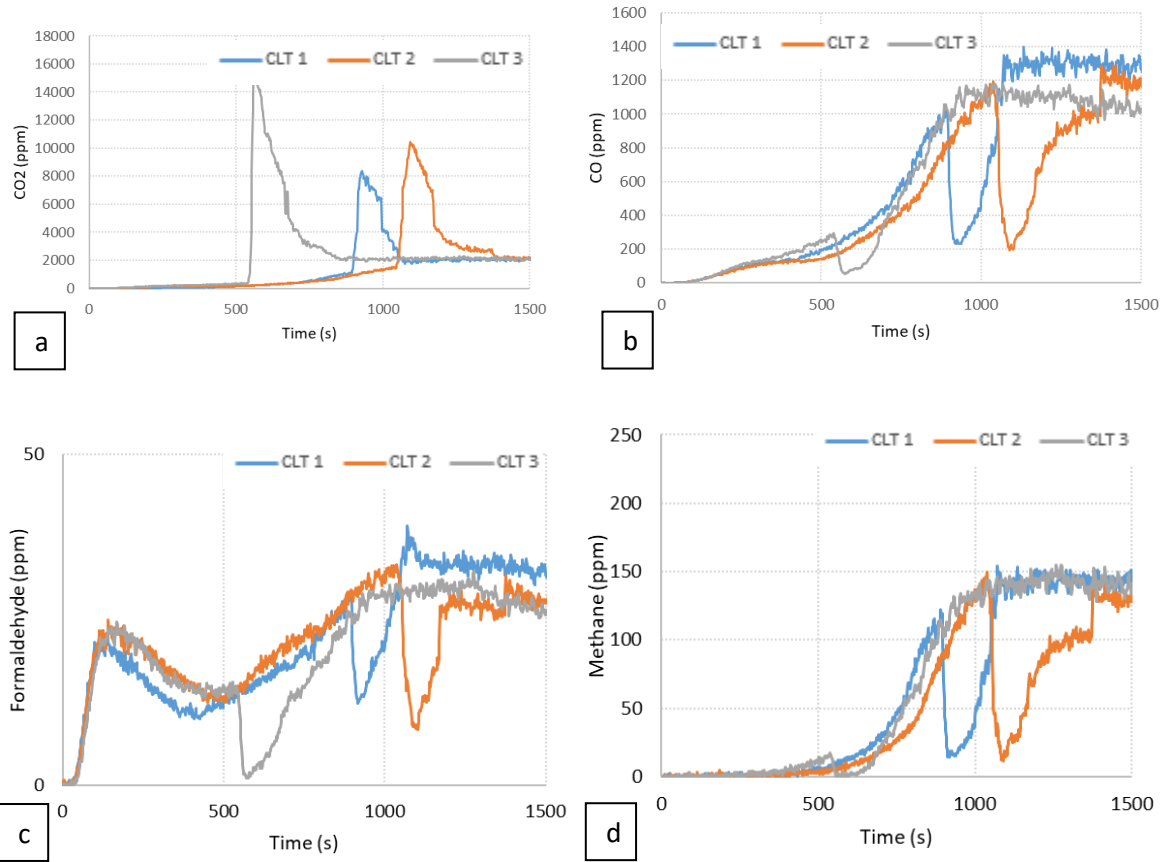


Figure 152: Gas production of CLT at 20 kW/m² and 18 vol-% O₂: a. CO₂, b. CO, c. Formaldehyde, c. Methane

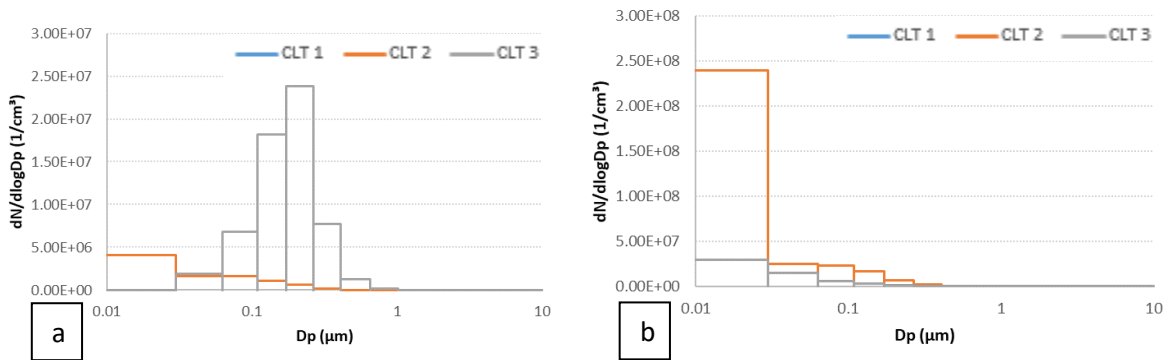


Figure 153: Aerosol size distribution of CLT at 20 kW/m² and 18 vol-% O₂: a. ti, b. 1500s

- 15 vol-% O₂

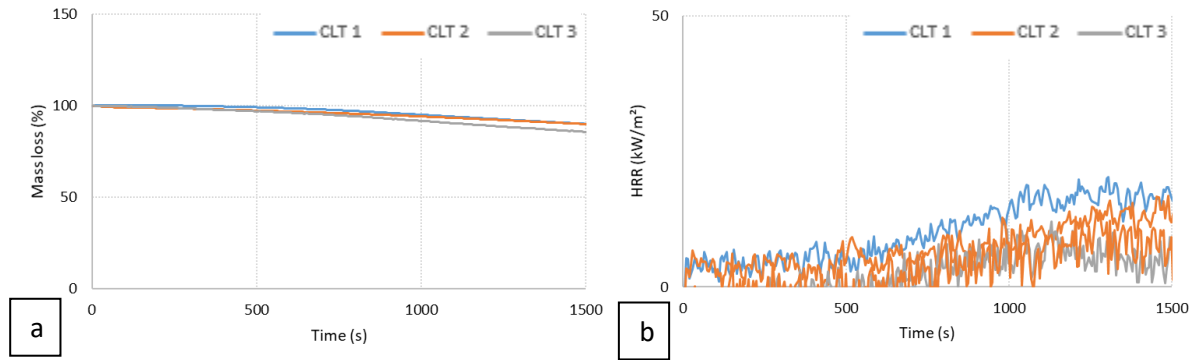


Figure 154: Fire behavior of CLT at 20 kW/m² and 15 vol-% O₂: a. mass loss and b. HHR

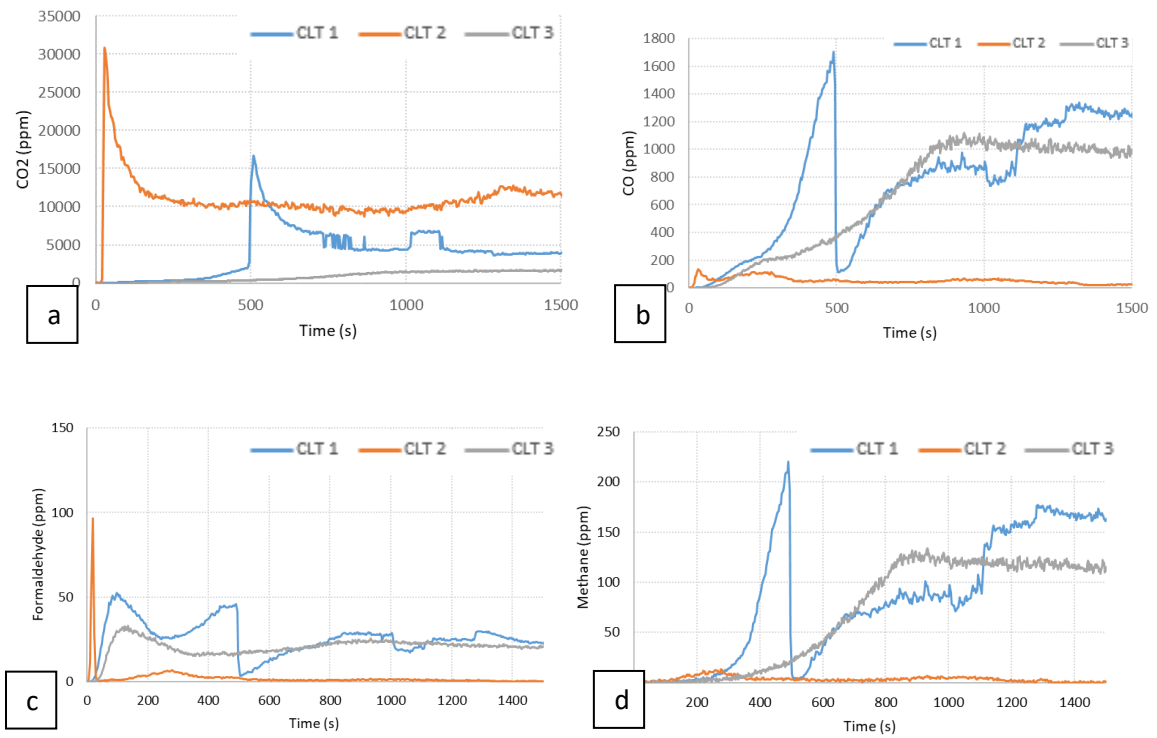


Figure 155: Gas production of CLT at 20 kW/m² and 15 vol-% O₂: a. CO₂, b. CO, c. Formaldehyde, c. Methane

- 10 vol-% O₂

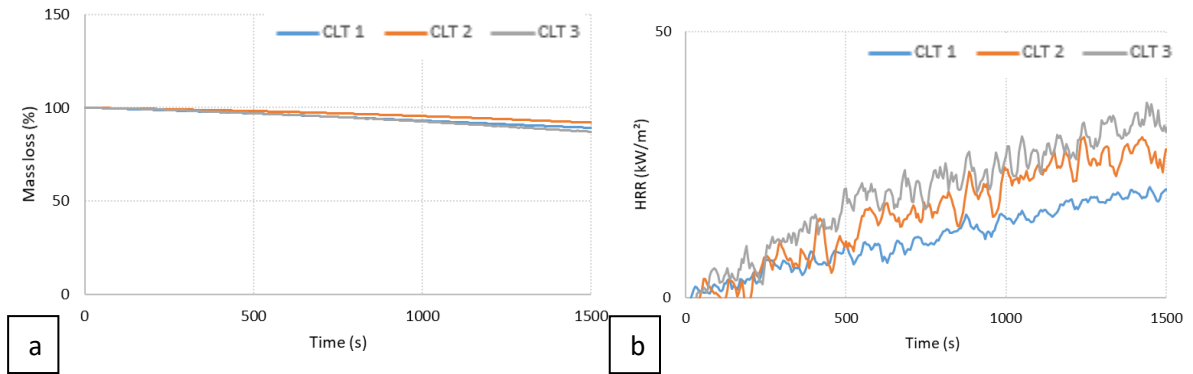


Figure 156: Fire behavior of CLT at 20 kW/m² and 10 vol-% O₂: a. mass loss and b. HHR

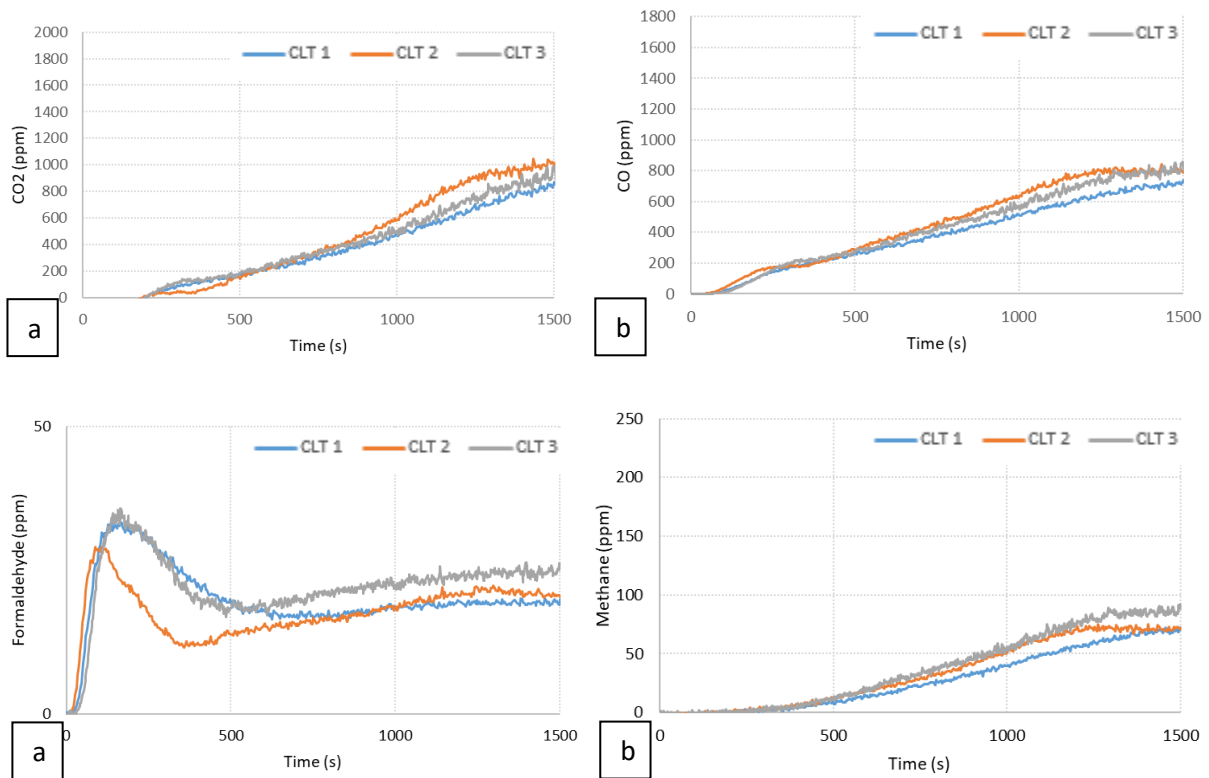


Figure 157: Gas production of CLT at 20 kW/m² and 10 vol-% O₂: a. CO₂, b. CO, c. Formaldehyde, d. Methane

Appendix 10

FTIR spectra of CLT at 20 kW/m²

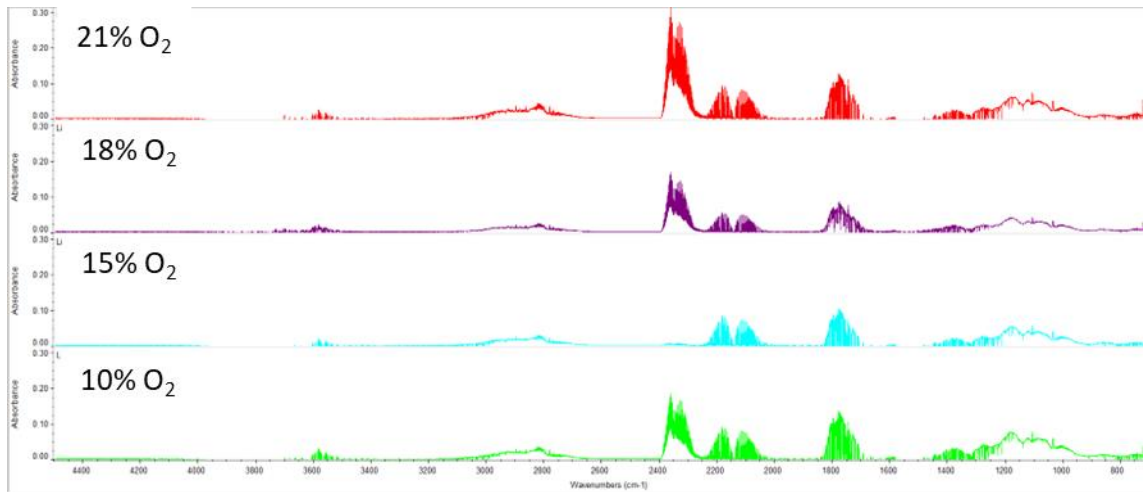


Figure 158: FTIR spectra of CLT at 20 kW/m² at 21, 18, 15 and 10 vol-% O₂ at the start of thermal exposure

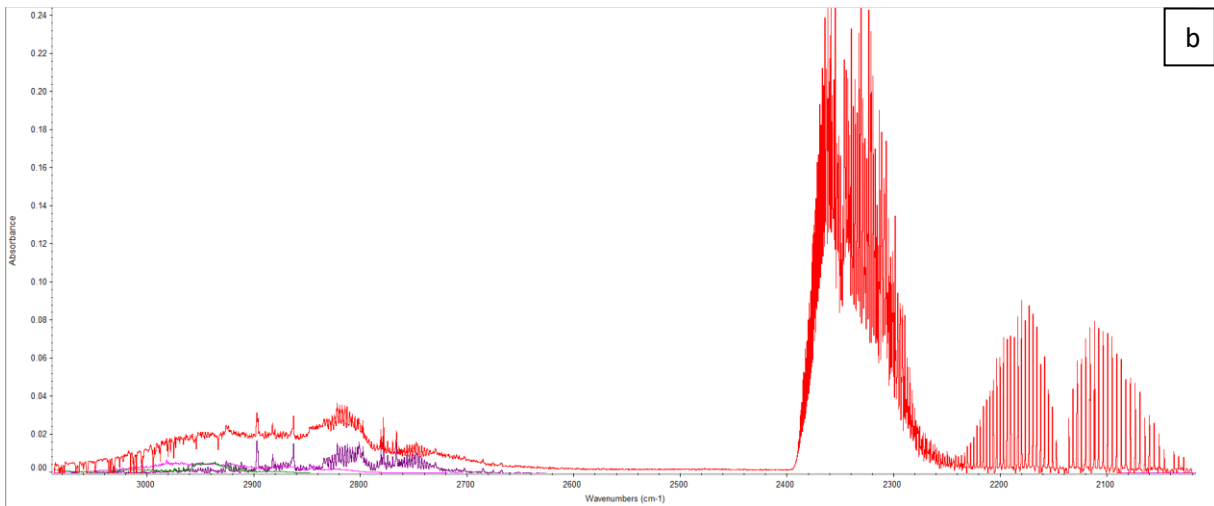
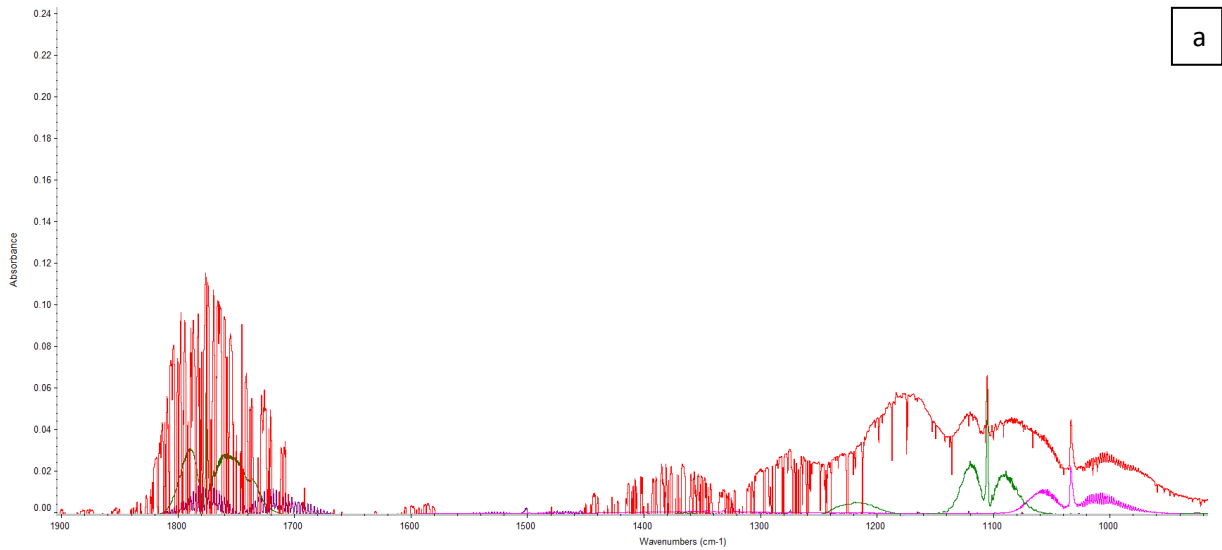


Figure 159: Zoom on the FTIR spectra of CLT at 20 kW/m², 21 vol-% O₂ at the start of thermal exposure (red) along with spectra of formaldehyde (purple), methanol (pink) and formic acid (green) between 1500 and 900 cm⁻¹ (a) and between 3500 and 2000 cm⁻¹ (b)

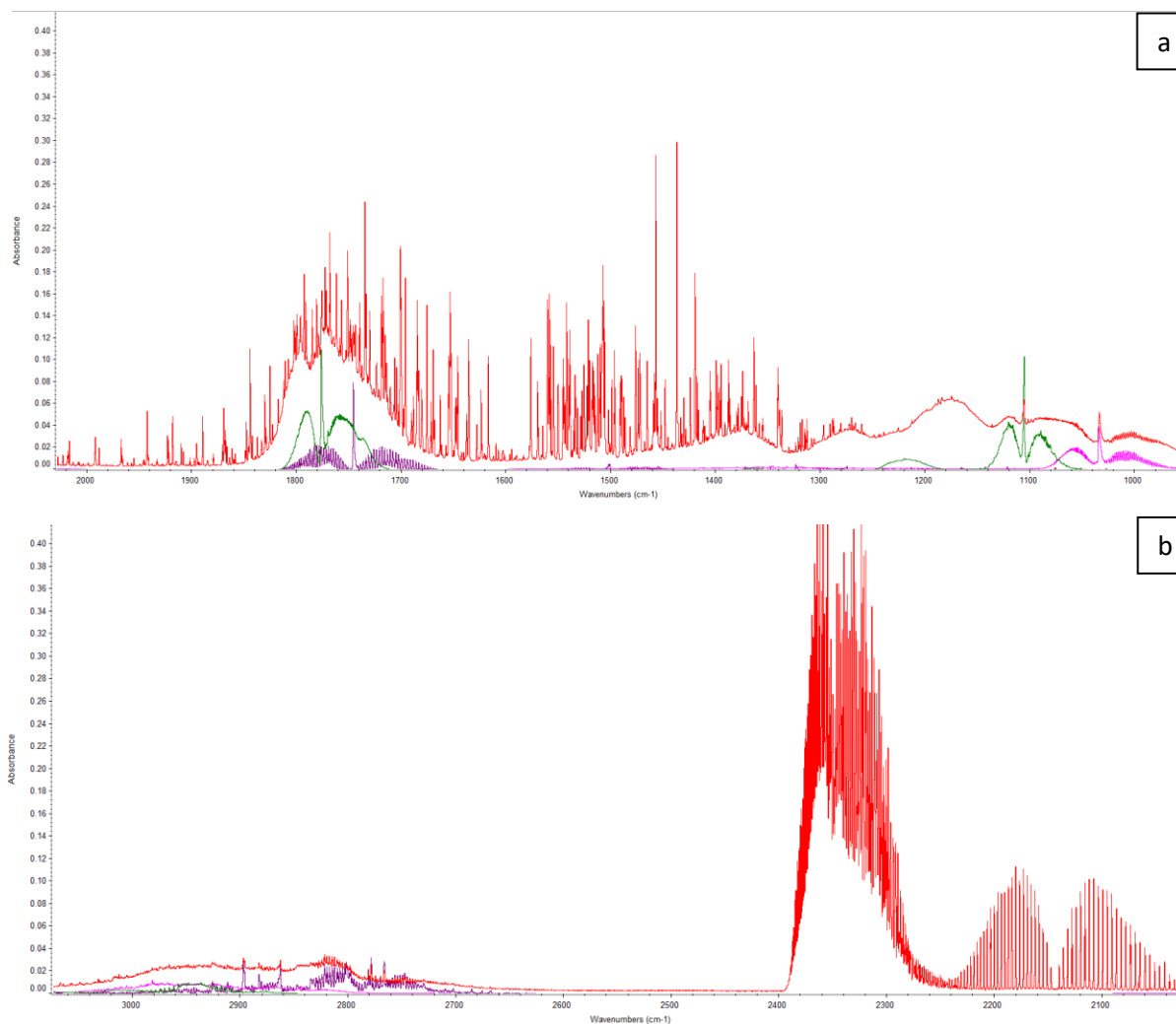


Figure 160: Zoom on the FTIR spectra of CLT at 20 kW/m², 10 vol-% O₂ at the start of thermal exposure (red) along with spectra of formaldehyde (purple), methanol (pink) and formic acid (green) between 2000 and 900 cm⁻¹ (a) and between 3500 and 2000 cm⁻¹ (b)

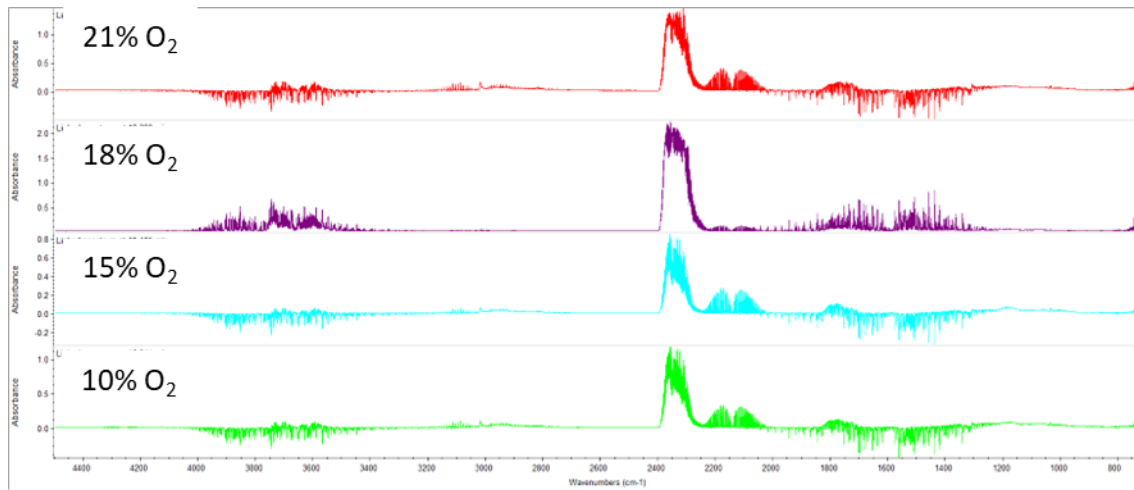


Figure 161: FTIR spectra of CLT at 20 kW/m² at 21, 18, 15 and 10 vol-% O₂ at ignition

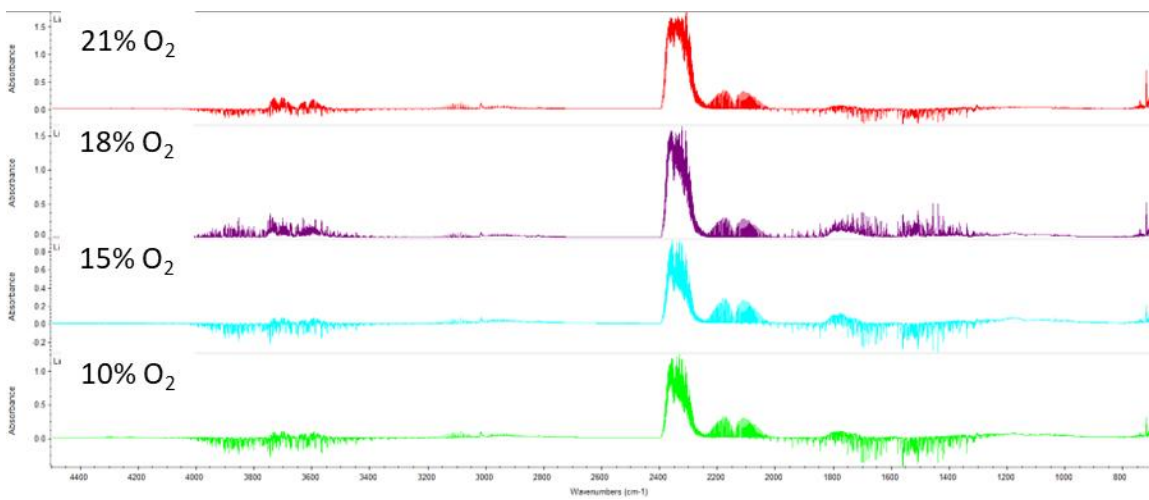


Figure 162: FTIR spectra of CLT at 20 kW/m² at 21, 18, 15 and 10 vol-% O₂ at 20 min

Appendix 11

Replica curves of the fire behavior, gas, and aerosol production of WF in the CACC at 50 kW/m²

- 21 vol-% O₂

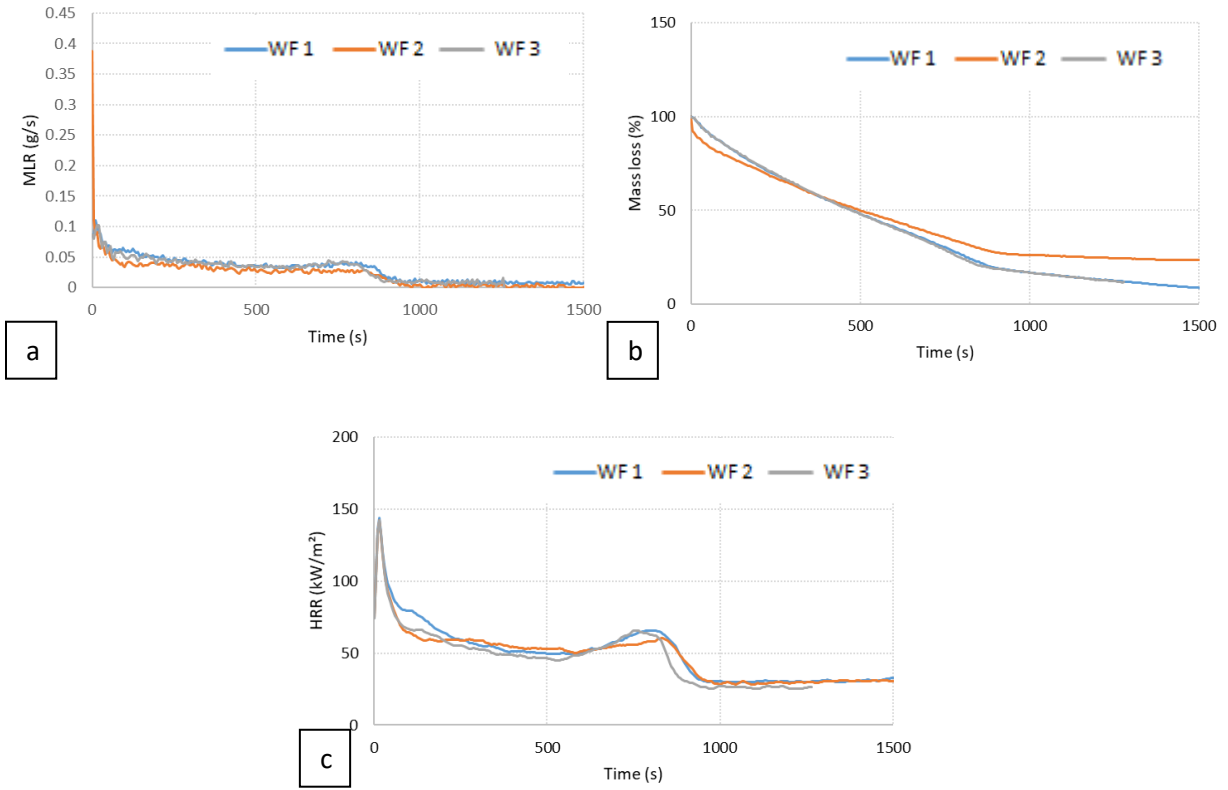
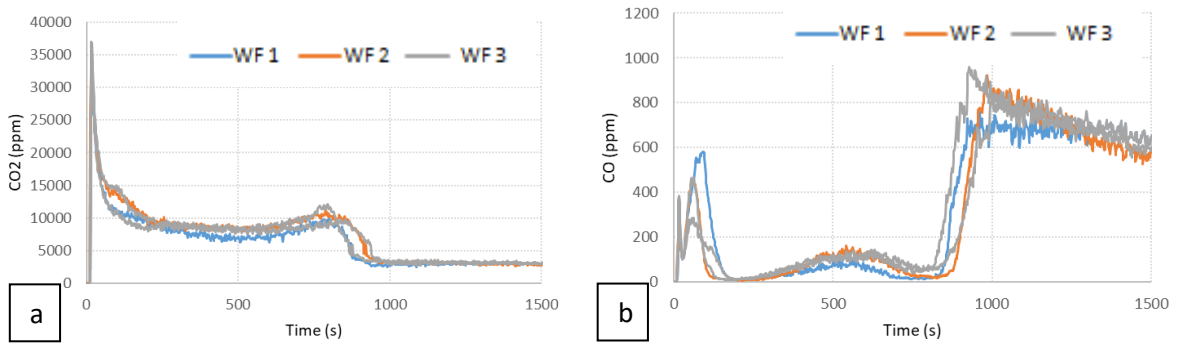


Figure 163: Fire behavior of WF at 50 kW/m² and 21 vol-% O₂: a. MLR, b. mass loss and c. HHR



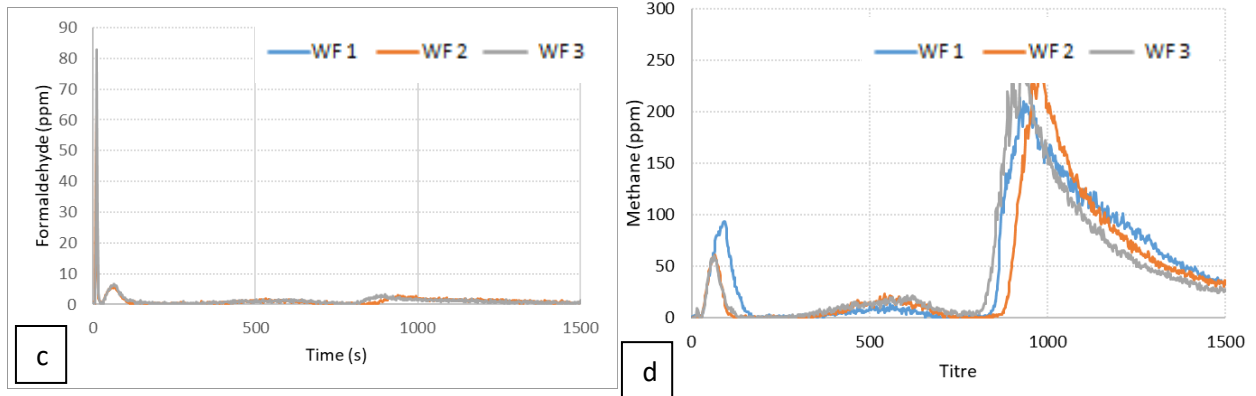


Figure 164: Gas production of WF at 50 kW/m² and 21 vol-% O₂: a. CO₂, b. CO, c. Formaldehyde, c. Methane

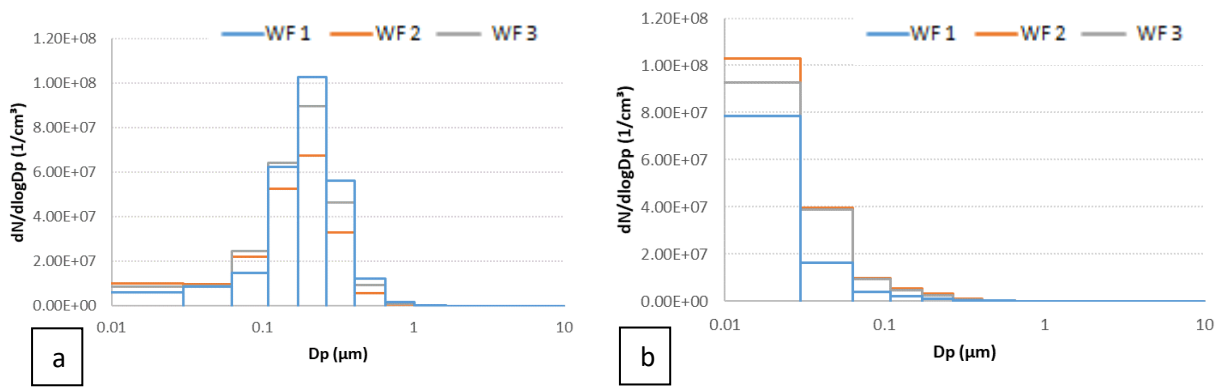
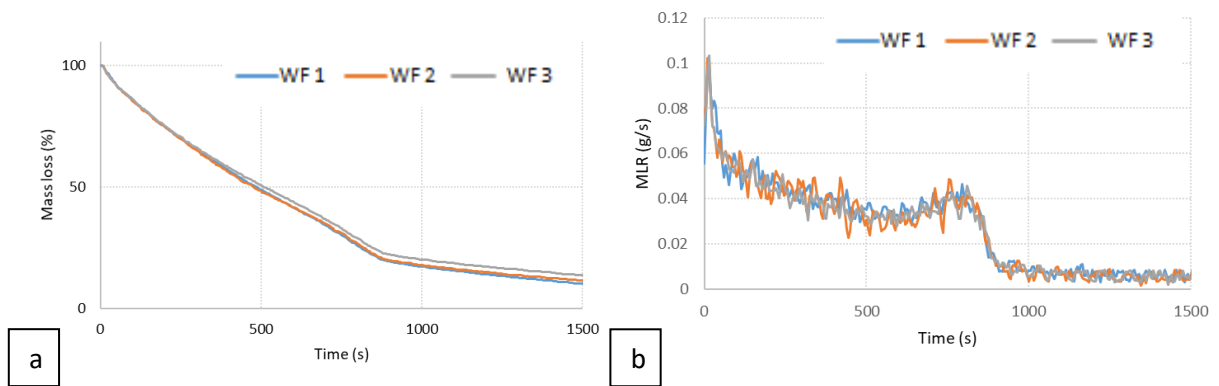


Figure 165: Aerosol size distribution of WF at 50 kW/m² and 21 vol-% O₂: a. ti, b. 800s

- 18 vol-% O₂



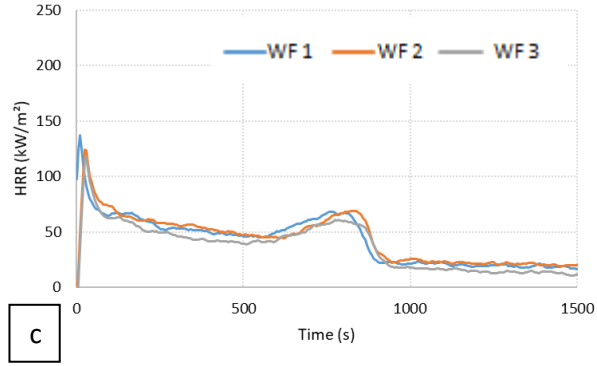


Figure 166: Fire behavior of WF at 50 kW/m² and 18 vol-% O₂: a. MLR, b. mass loss and c. HHR

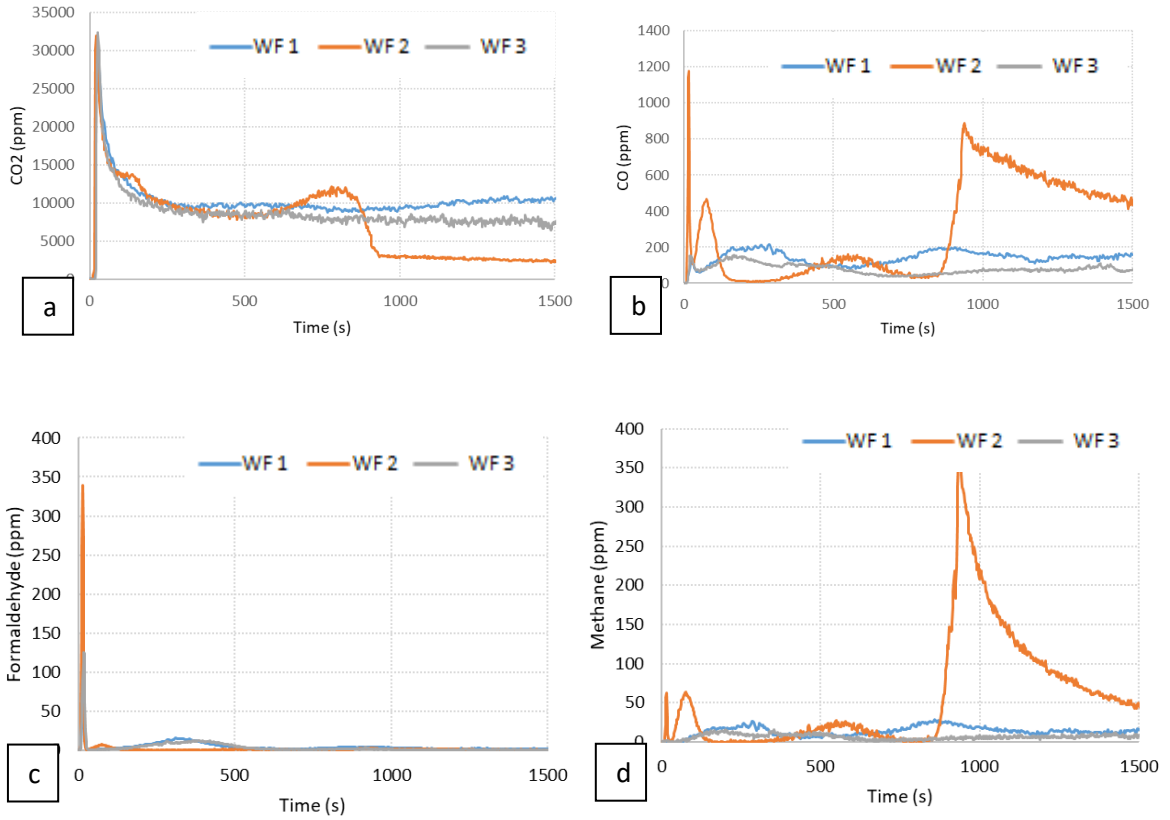


Figure 167: Gas production of WF at 50 kW/m² and 18 vol-% O₂: a. CO₂, b. CO, c. Formaldehyde, d. Methane

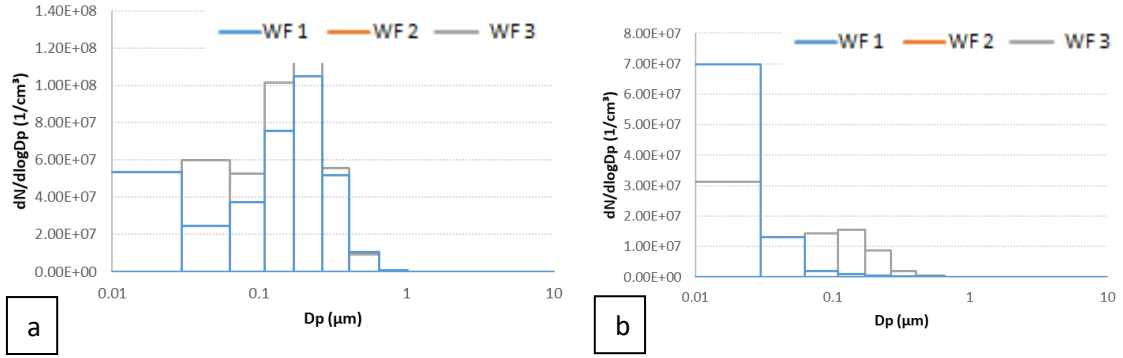


Figure 168: Aerosol size distribution of WF at 50 kW/m² and 21 vol-% O₂: a. ti, b. 800s

- 15 vol-% O₂

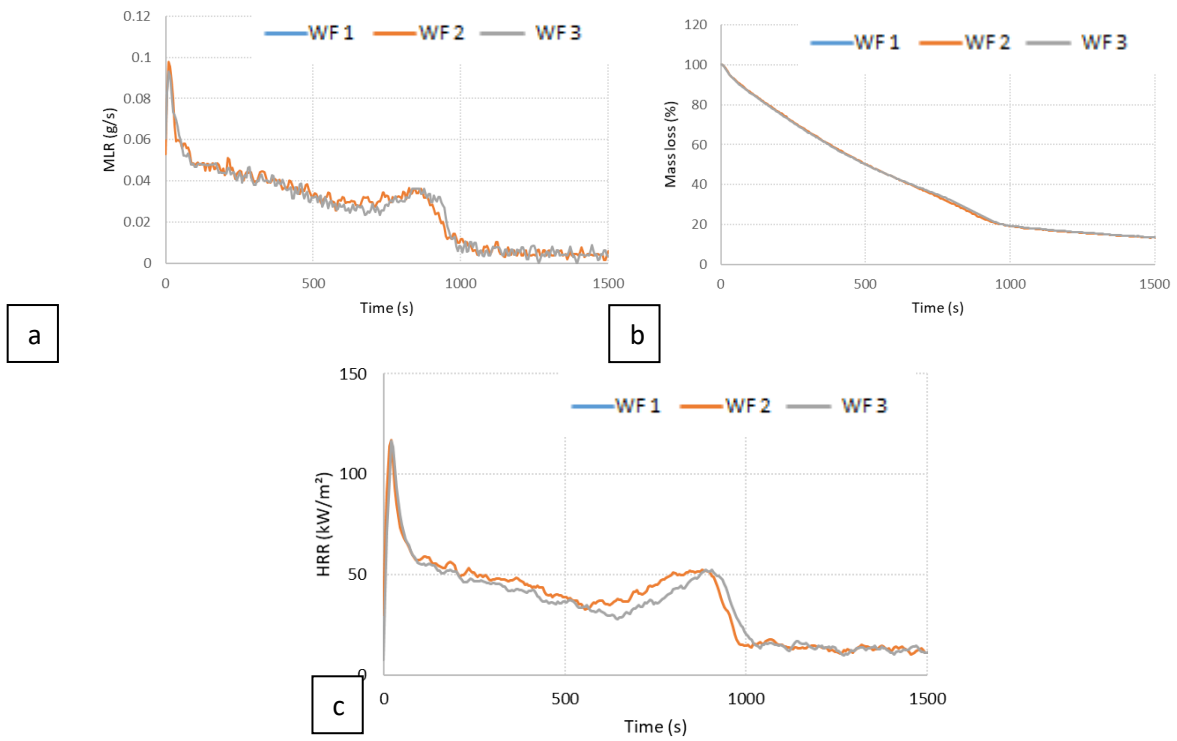
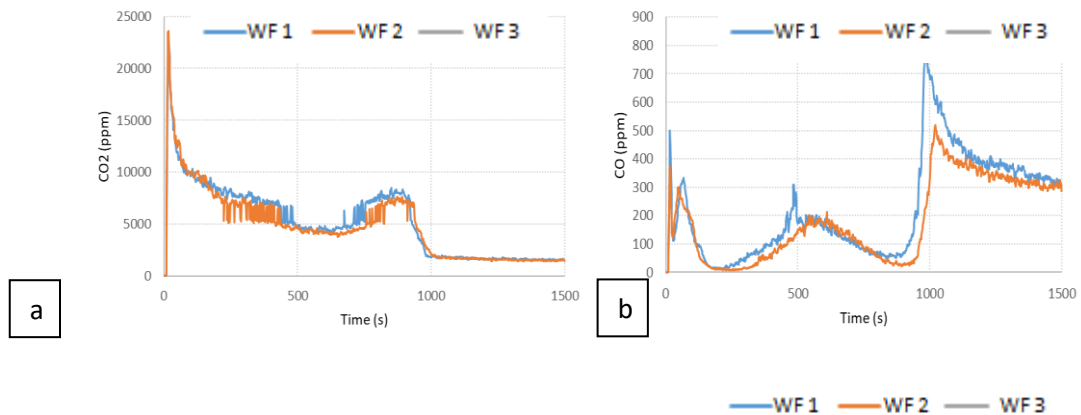


Figure 169: Fire behavior of WF at 50 kW/m² and 15 vol-% O₂: a. MLR, b. mass loss and c. HRR



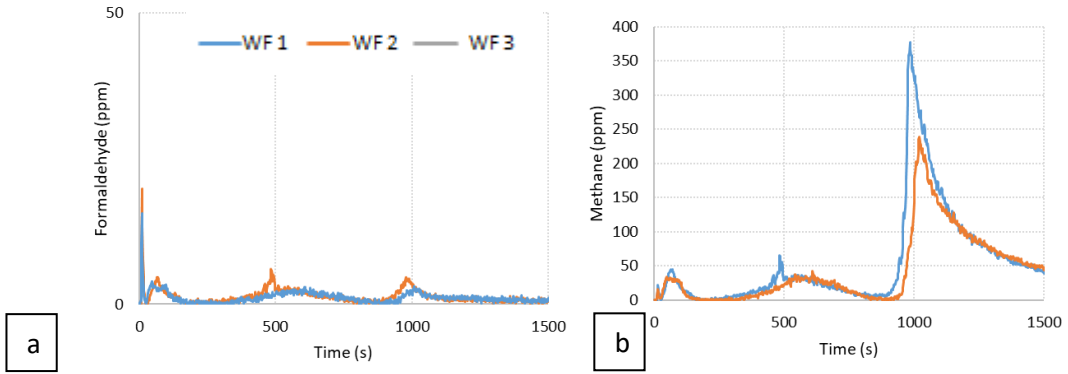


Figure 170: Gas production of WF at 50 kW/m² and 15 vol-% O₂: a. CO₂, b. CO, c. Formaldehde, c. Methane

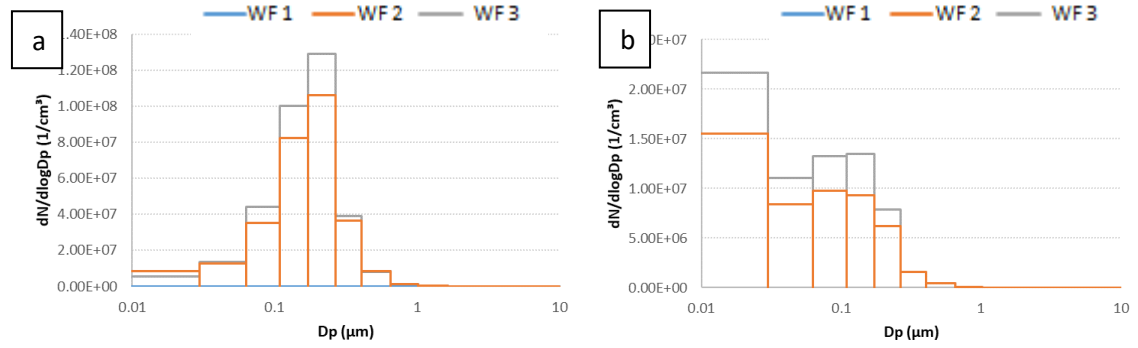


Figure 171: Aerosol size distribution of WF at 50 kW/m² and 15 vol-% O₂: a. ti, b. 800s

- 10 vol-% O₂

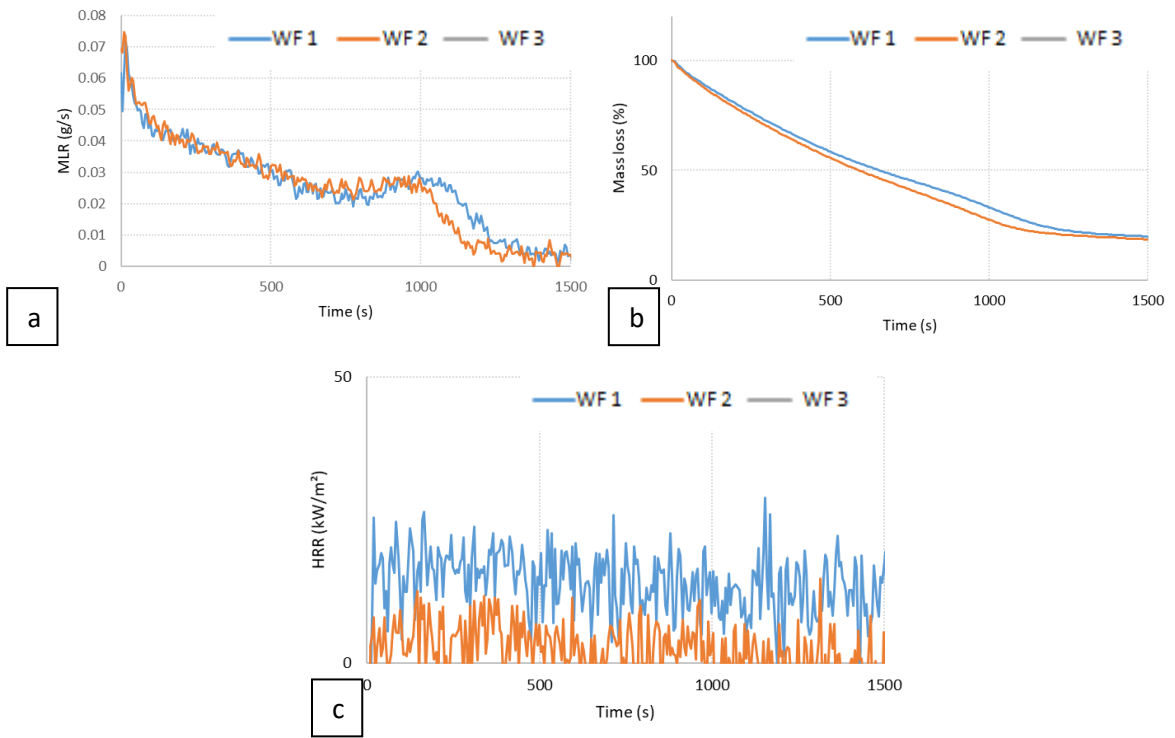
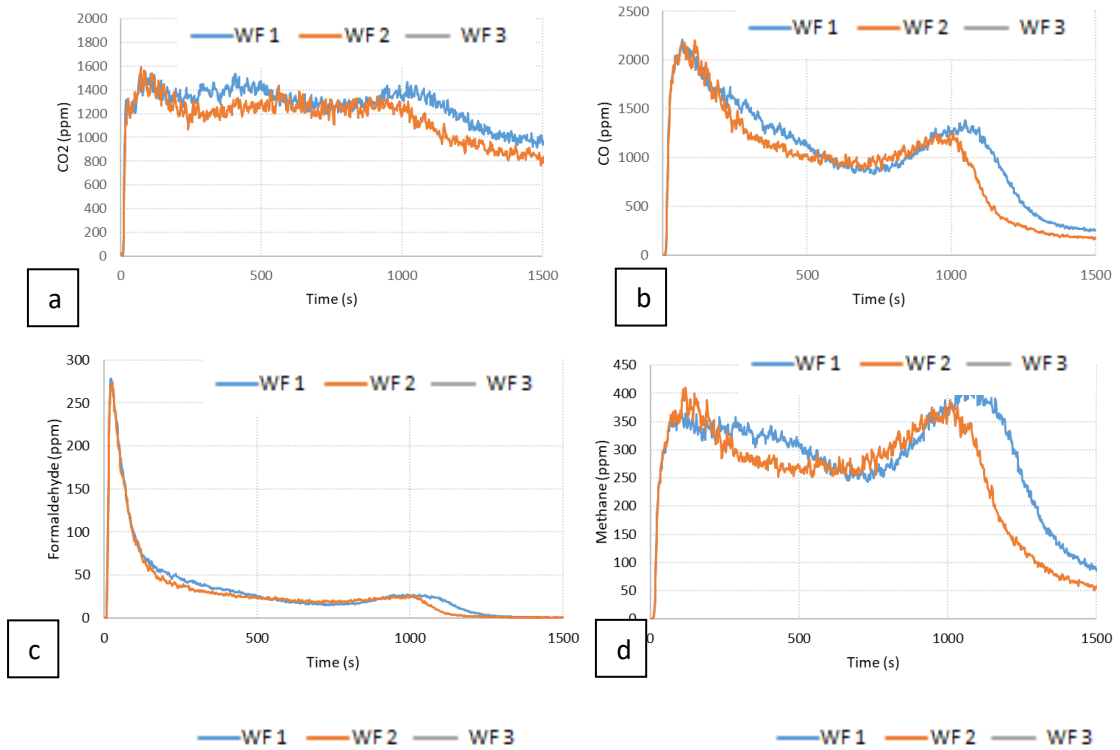
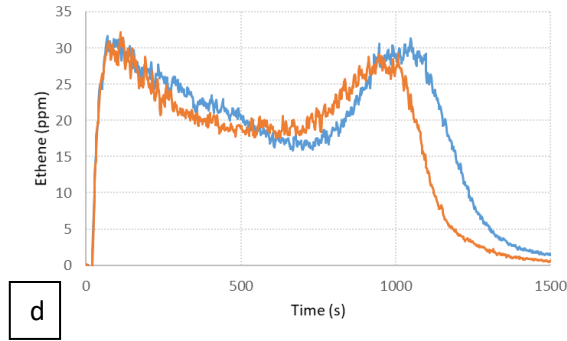


Figure 172: Fire behavior of WF at 50 kW/m² and 10 vol-% O₂: a. MLR, b. mass loss and c. HRR





d

Figure 173: Gas production of WF at 50 kW/m² and 15 vol-% O₂: a. CO₂, b. CO, c. Formaldehyde, c. Methane, d. Ethene

Appendix 12

FTIR spectra of WF at 50 kW/m²

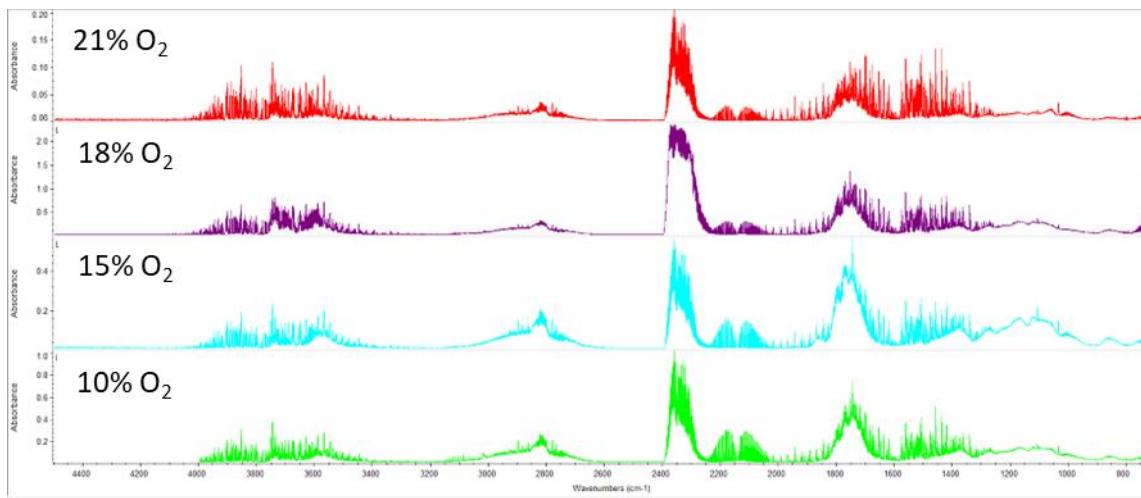
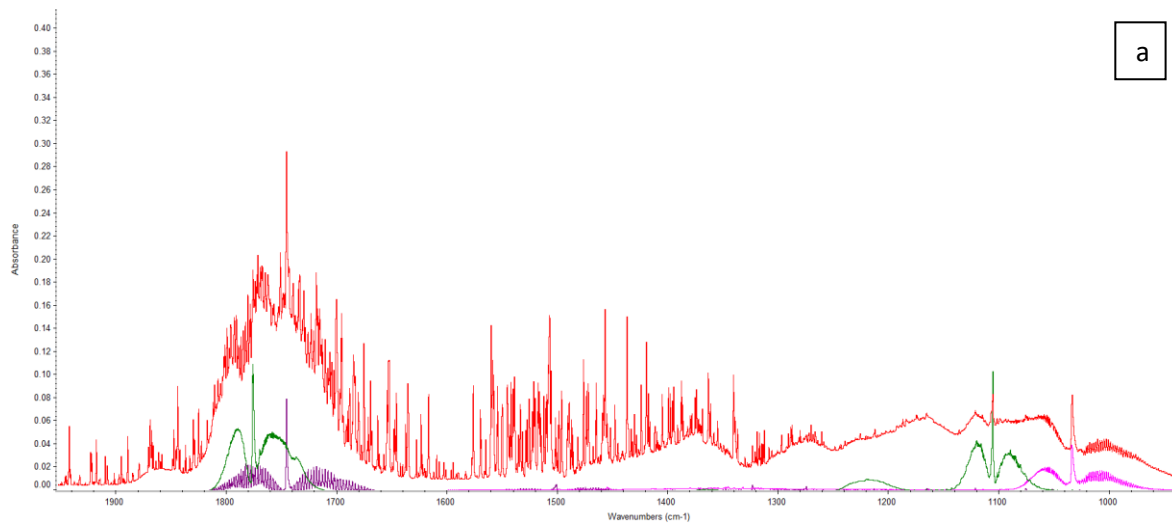
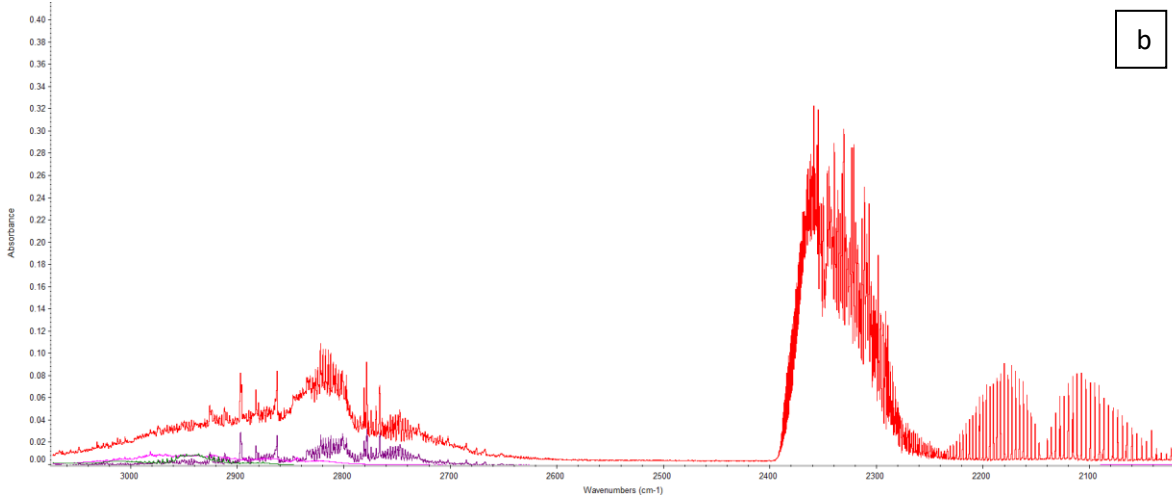


Figure 174: FTIR spectra of WF at 50 kW/m² at 21, 18, 15 and 10 vol-% O₂ at the start of thermal exposure

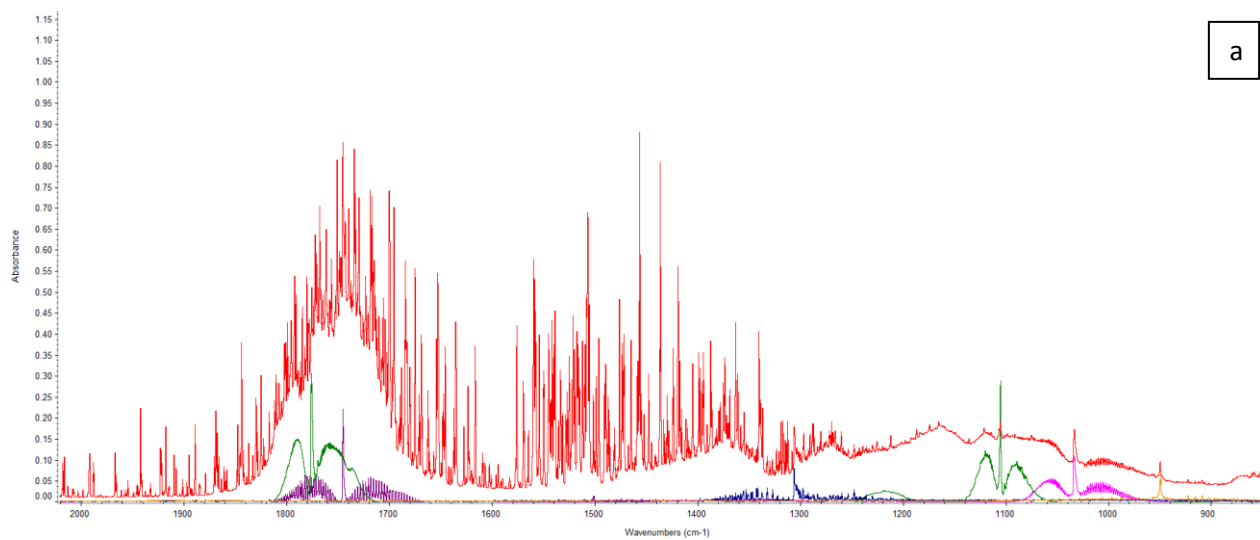


a

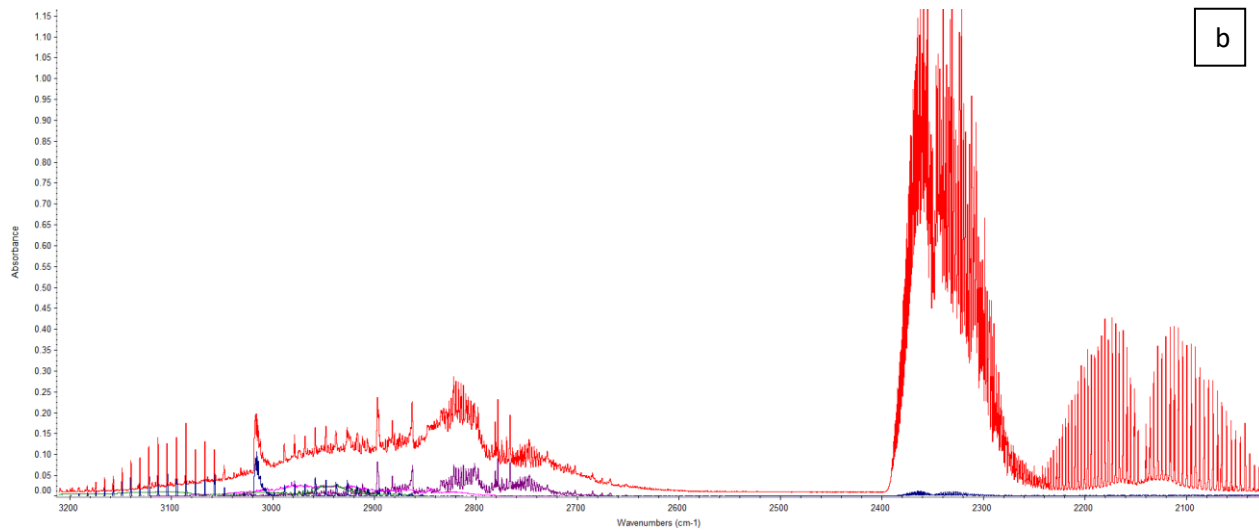


b

Figure 175: Zoom on the FTIR spectra of WF at 50 kW/m², 21 vol-% O₂ at the start of thermal exposure (red) along with spectra of formaldehyde (purple), methanol (pink) and formic acid (green) between 2000 and 900 cm⁻¹ (a) and between 3500 and 2000 cm⁻¹ (b)



a



b

Figure 176: Zoom on the FTIR spectra of WF at 50 kW/m², 10 vol-% O₂ at the start of thermal exposure (red) along with spectra of formaldehyde (purple), methanol (pink), formic acid (green), methane (blue) and ethene (orange) between 2000 and 850 cm⁻¹ (a) and between 3200 and 2000 cm⁻¹ (b)

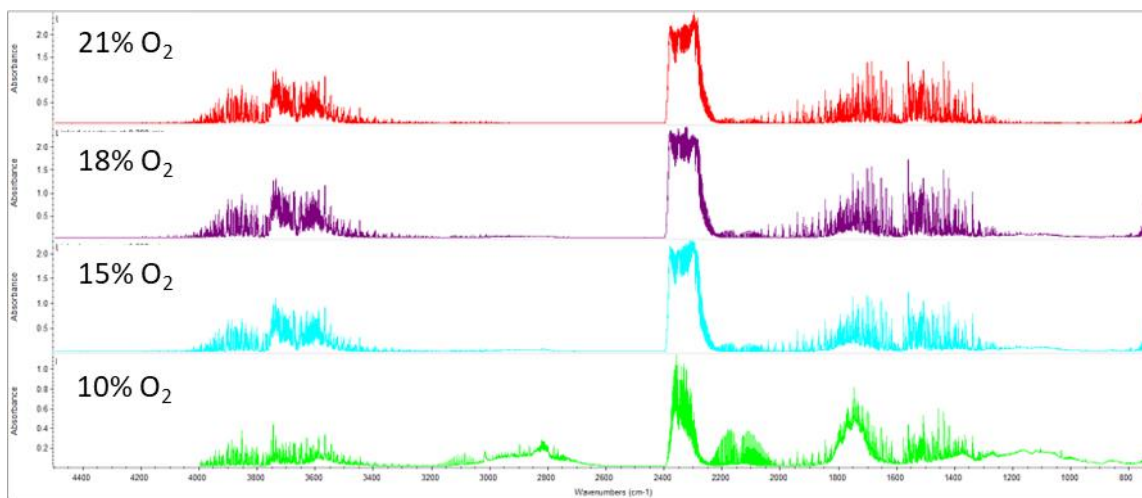


Figure 177: FTIR spectra of WF at 50 kW/m² at 21, 18, 15 and 10 vol-% O₂ at ignition

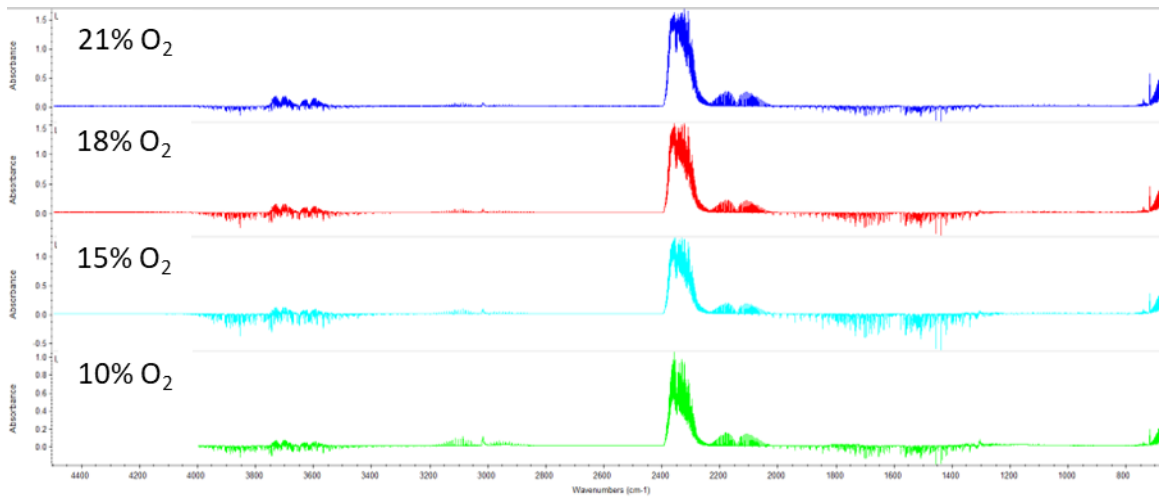


Figure 178: FTIR spectra of WF at 50 kW/m² at 21, 18, 15 and 10 vol-% O₂ at 20 min

Appendix 13

Replica curves of the fire behavior, gas, and aerosol production of WF in the CACC at 20 kW/m²

- 21 vol-% O₂

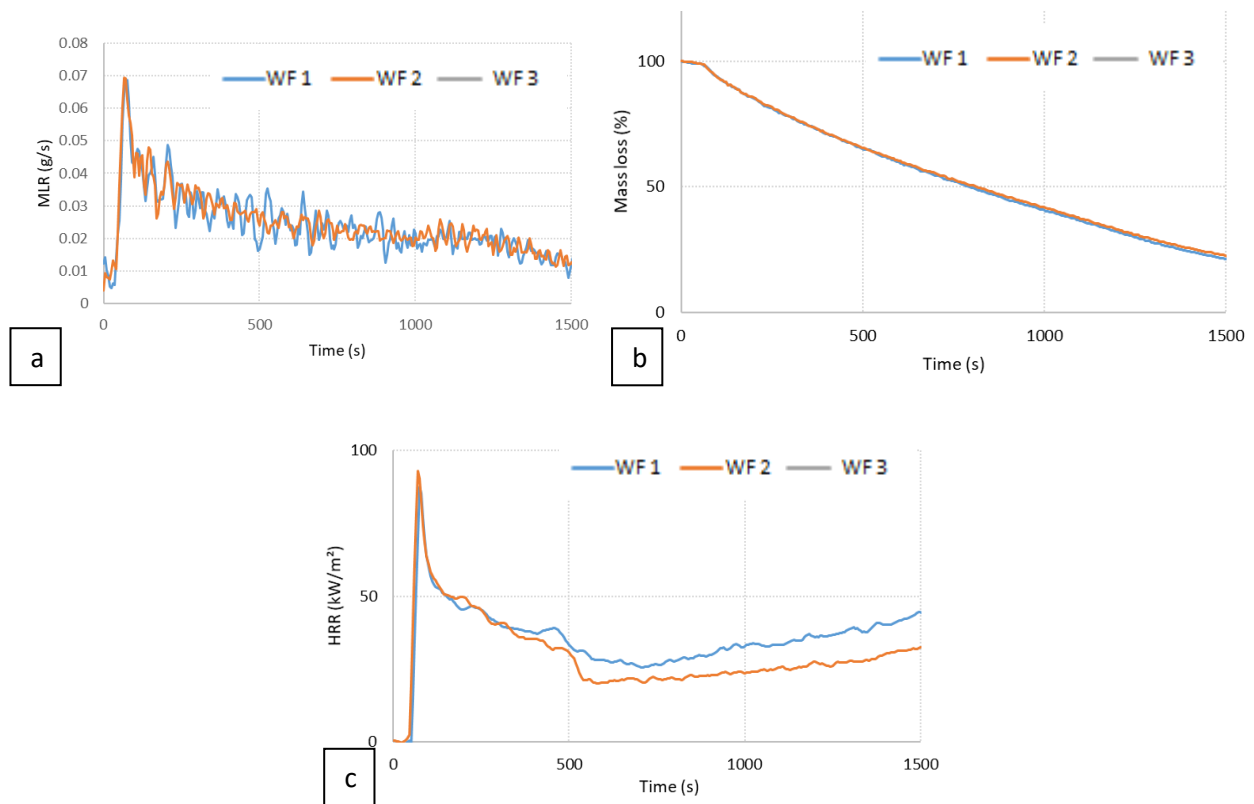


Figure 179: Fire behavior of WF at 20 kW/m² and 21 vol-% O₂: a. MLR, b. mass loss and c. HRR

— WF 1 — WF 2 — WF 3

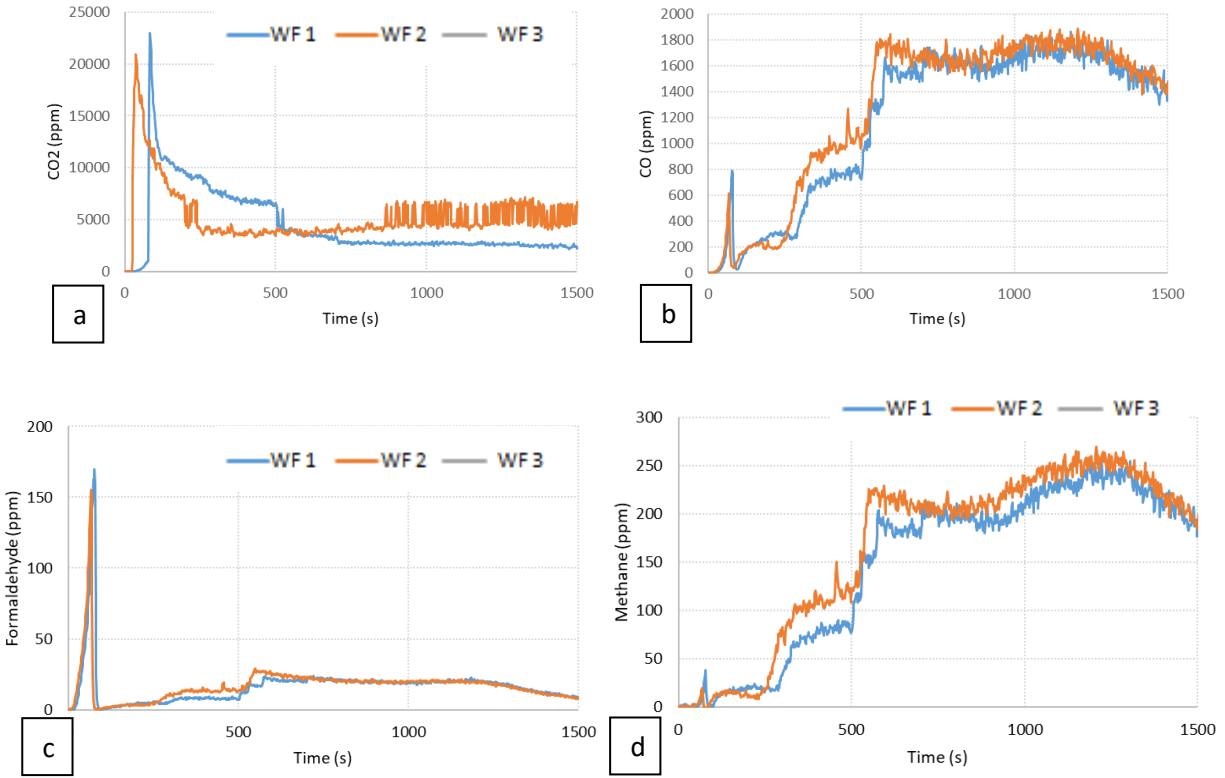


Figure 180: Gas production of WF at 20 kW/m² and 21 vol-% O₂: a. CO₂, b. CO, c. Formaldehyde, c. Methane

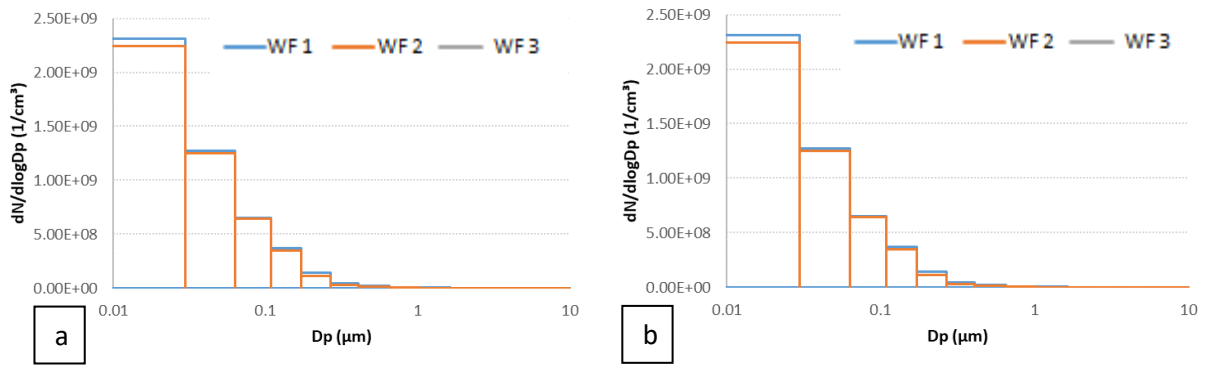


Figure 181: Aerosol size distribution of WF at 20 kW/m² and 21 vol-% O₂: a. ti, b. 800s

- 18 vol-% O₂

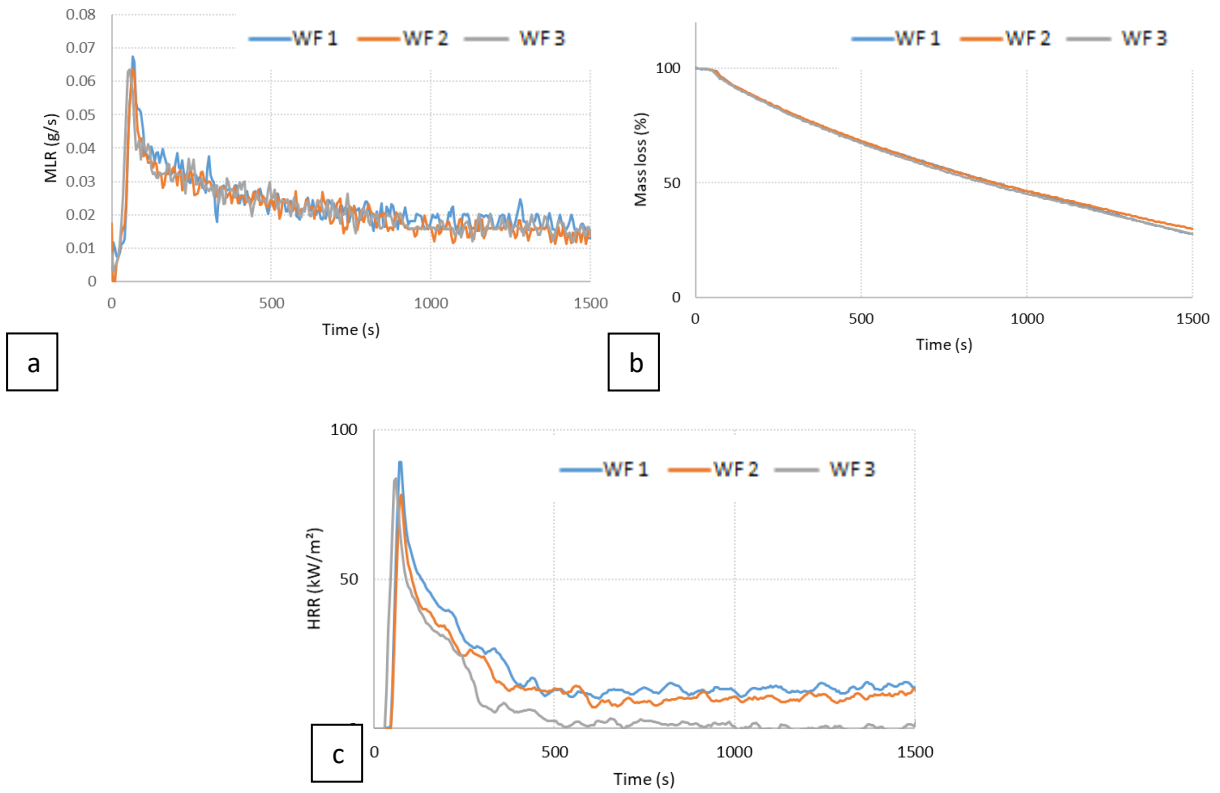
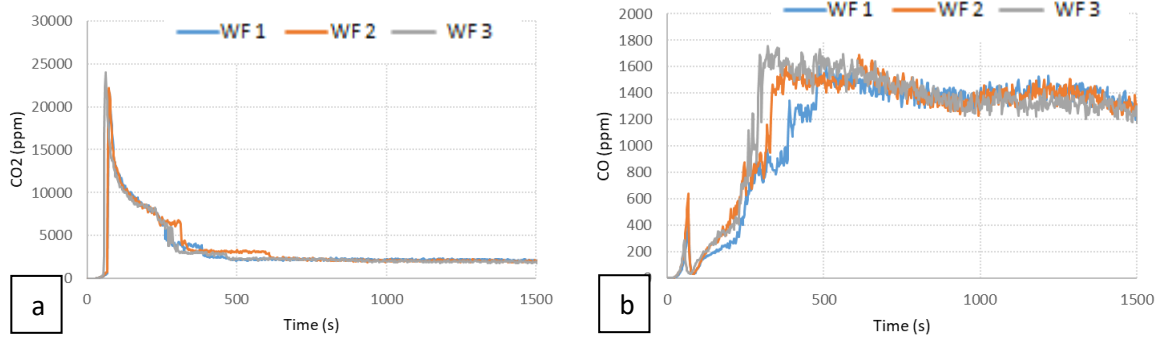


Figure 182: Fire behavior of WF at 20 kW/m² and 18 vol-% O₂: a. MLR, b. mass loss and c. HHR



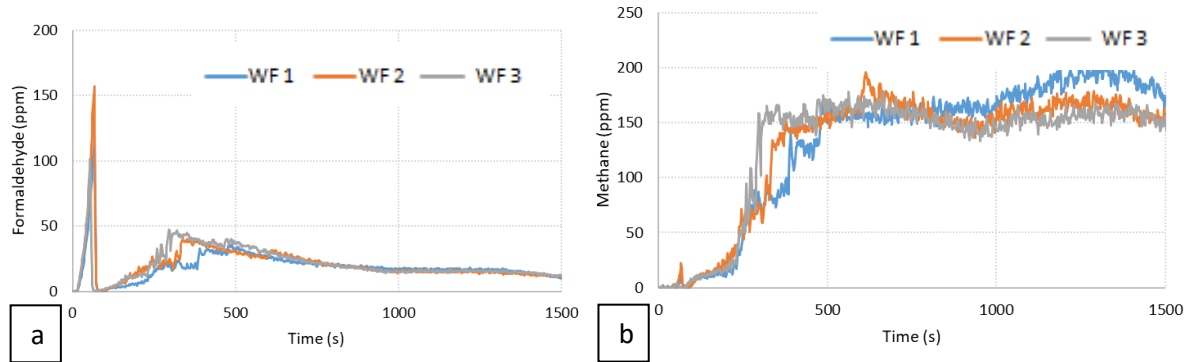


Figure 183: Gas production of WF at 20 kW/m² and 18 vol-% O₂: a. CO₂, b. CO, c. Formaldehyde, c. Methane

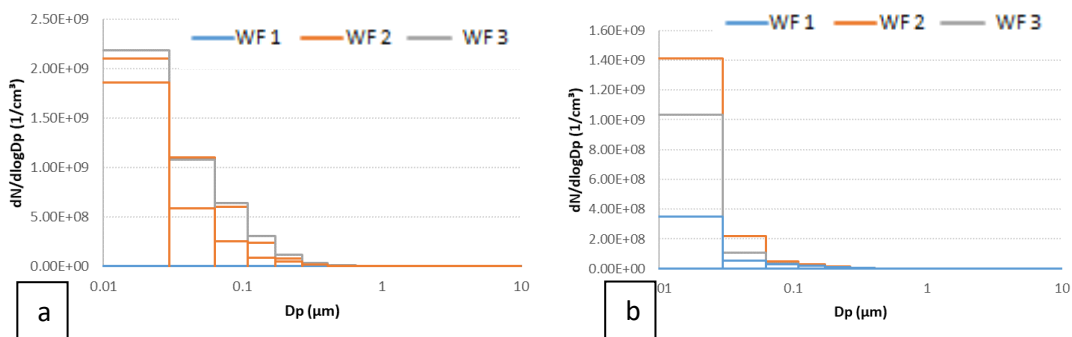
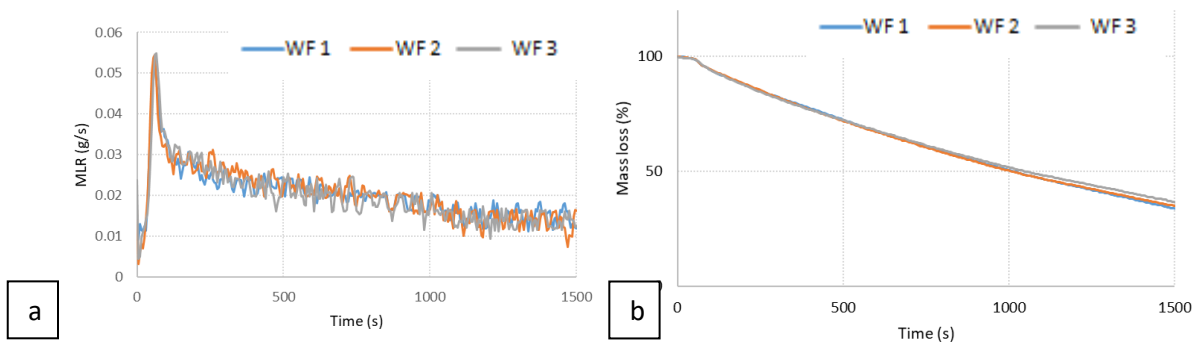


Figure 184: Aerosol size distribution of WF at 20 kW/m² and 18 vol-% O₂: a. ti, b. 800s

- 15 vol-% O₂



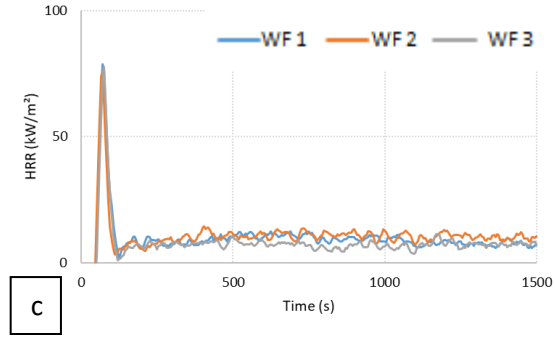


Figure 185: Fire behavior of WF at 20 kW/m² and 15 vol-% O₂: a. MLR, b. mass loss and c. HHR

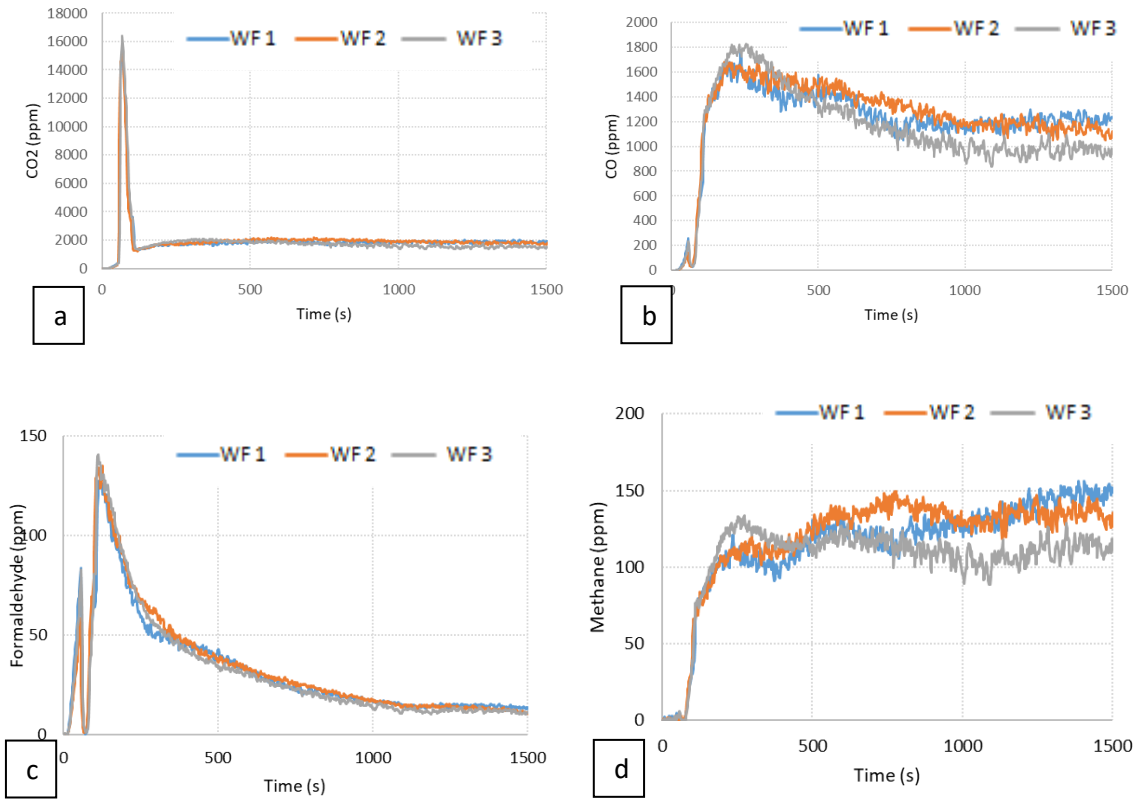


Figure 186: Gas production of WF at 20 kW/m² and 15 vol-% O₂: a. CO₂, b. CO, c. Formaldehyde, c. Methane

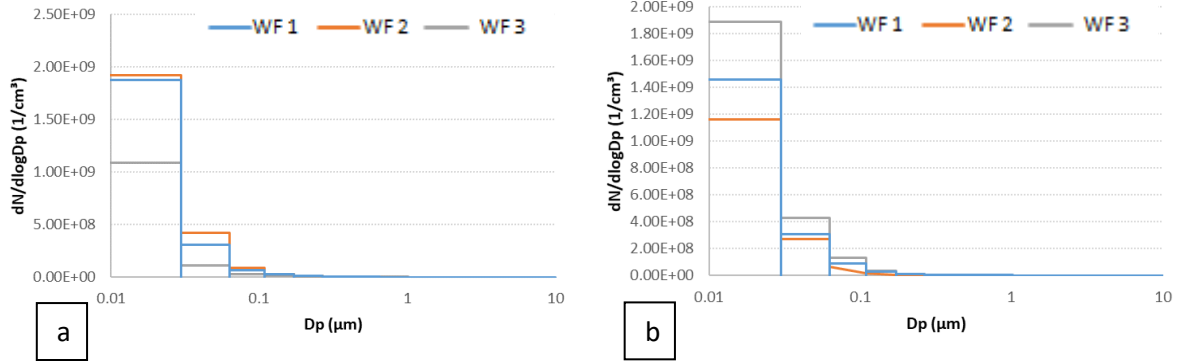


Figure 187: Aerosol size distribution of WF at 20 kW/m² and 15 vol-% O₂: a. ti, b. 800s

- 10 vol-% O₂

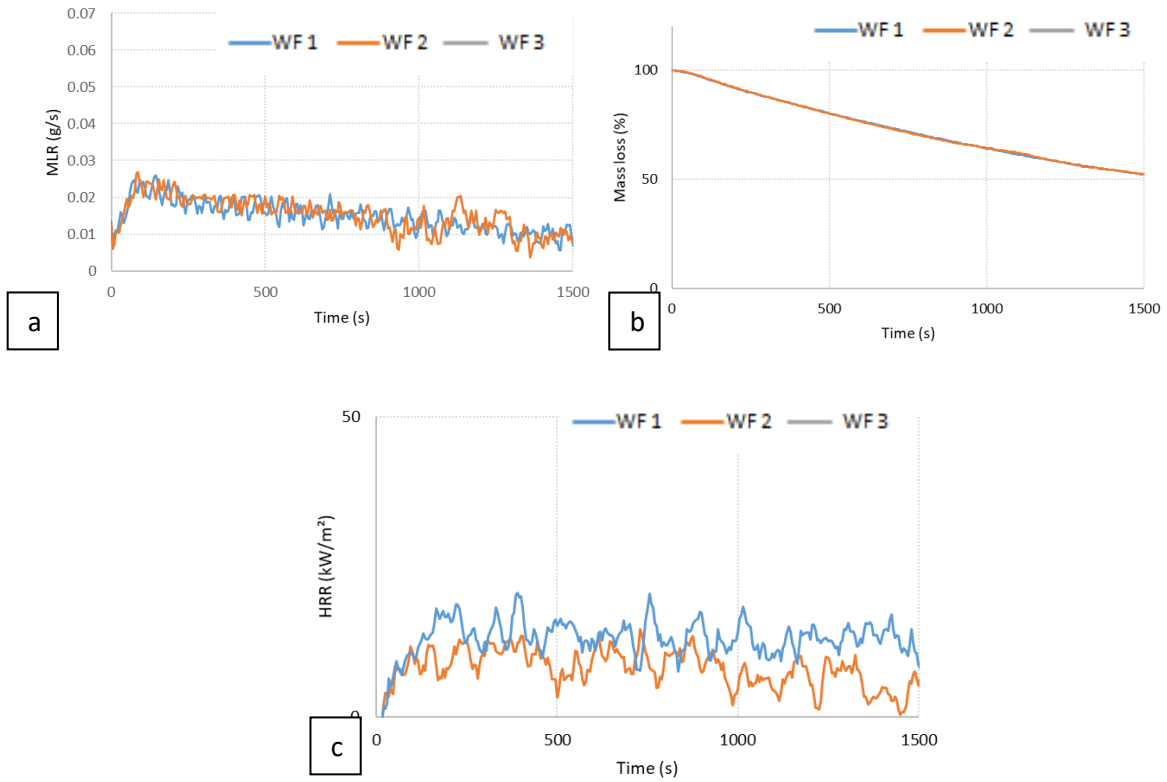


Figure 188: Fire behavior of WF at 20 kW/m² and 10 vol-% O₂: a. MLR, b. Mass loss, c. HRR

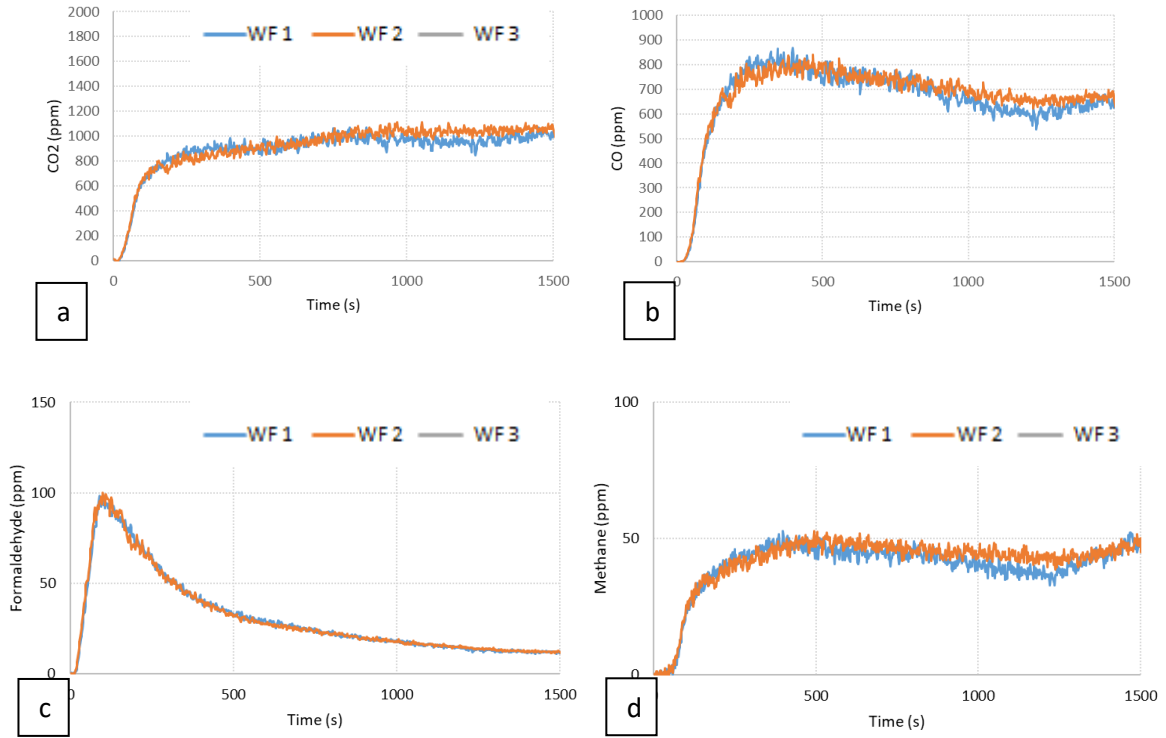


Figure 189: Gas production of WF at 20 kW/m² and 10 vol-% O₂: a. CO₂, b. CO, c. Formaldehyde, c. Methane

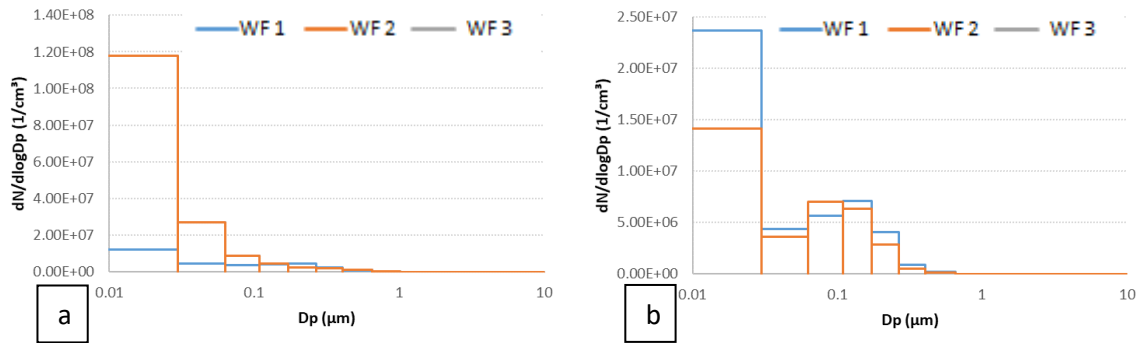


Figure 190: Aerosol size distribution of WF at 20 kW/m² and 10 vol-% O₂: a. ti, b. 800s

Appendix 14

FTIR spectra of WF at 20 kW/m²

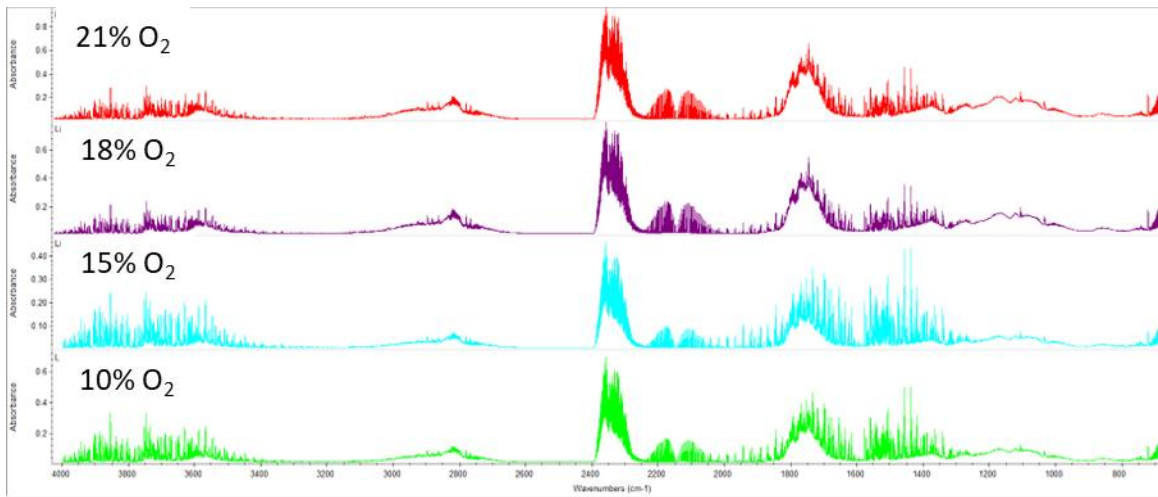
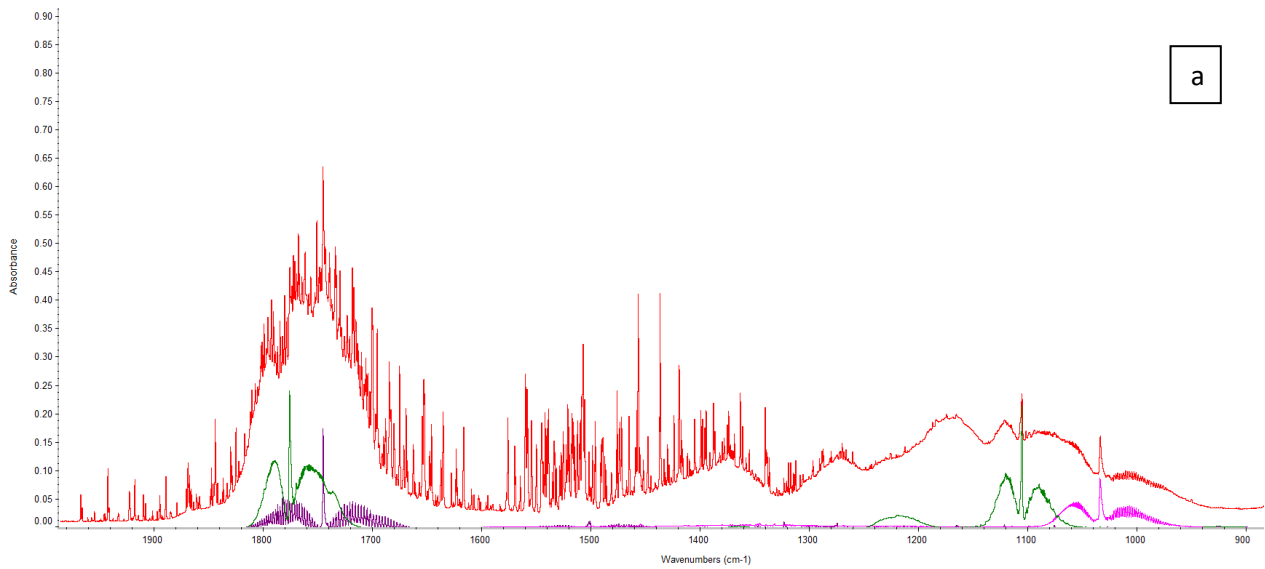


Figure 191: FTIR spectra of WF at 20 kW/m² at 21, 18, 15 and 10 vol-% O₂ at the start of thermal exposure



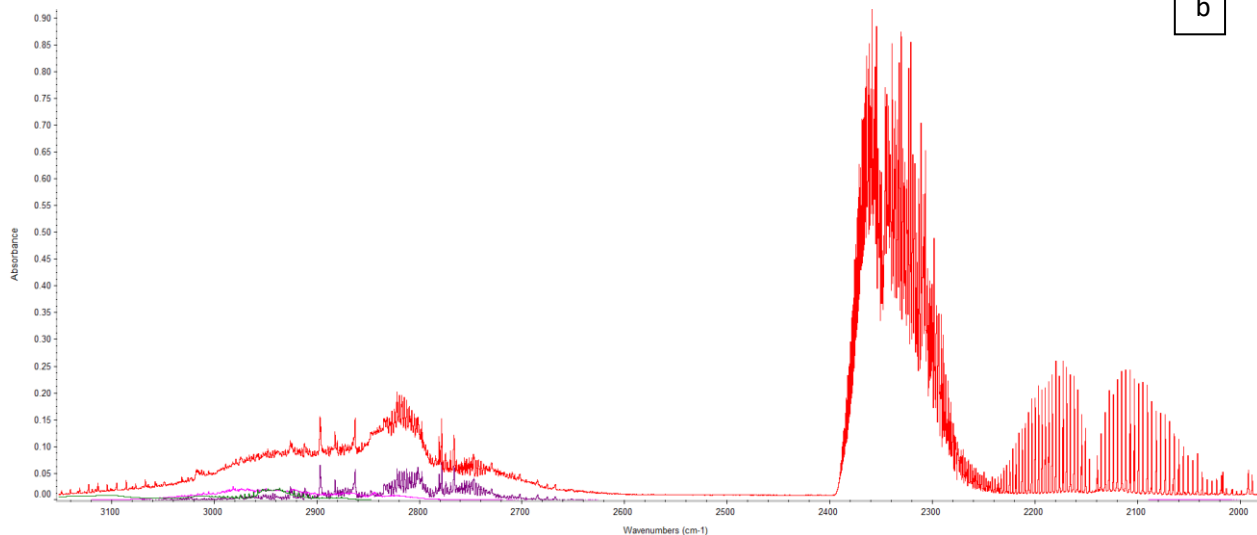
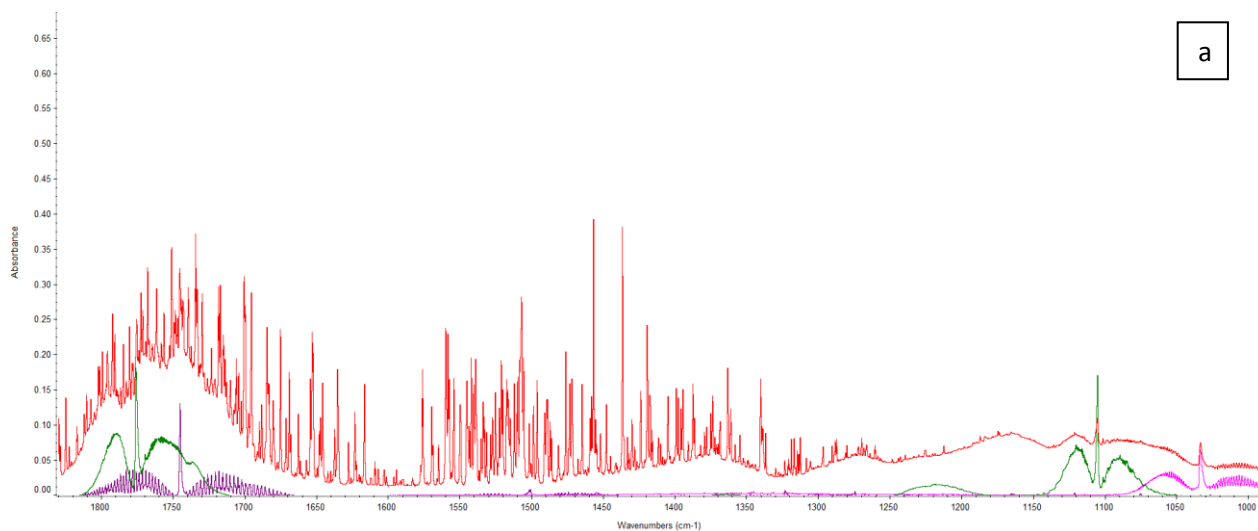
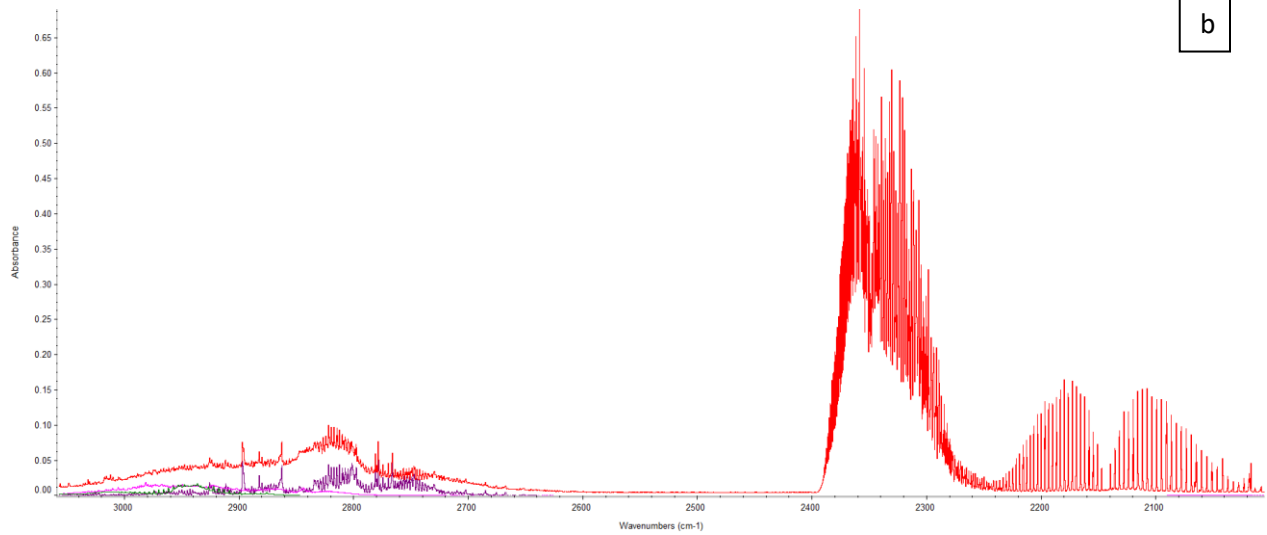


Figure 192: Zoom on the FTIR spectra of WF at 20 kW/m², 21 vol-% O₂ at the start of thermal exposure (red) along with spectra of formaldehyde (purple), methanol (pink) and formic acid (green) between 2000 and 900 cm⁻¹ (a) and between 3200 and 2000 cm⁻¹ (b)





b

Figure 193: Zoom on the FTIR spectra of WF at 20 kW/m², 10 vol-% O₂ at the start of thermal exposure (red) along with spectra of formaldehyde (purple), methanol (pink) and formic acid (green) between 1900 and 1000 cm⁻¹ (a) and between 3100 and 2000 cm⁻¹ (b)

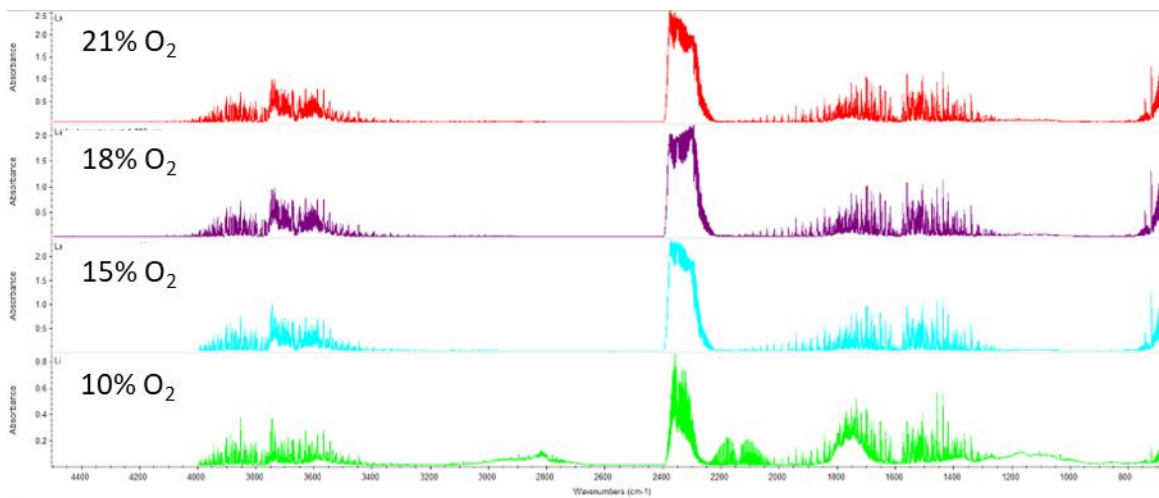


Figure 194: FTIR spectra of CLT at 20 kW/m² at 21, 18, 15 and 10 vol-% O₂ at ignition

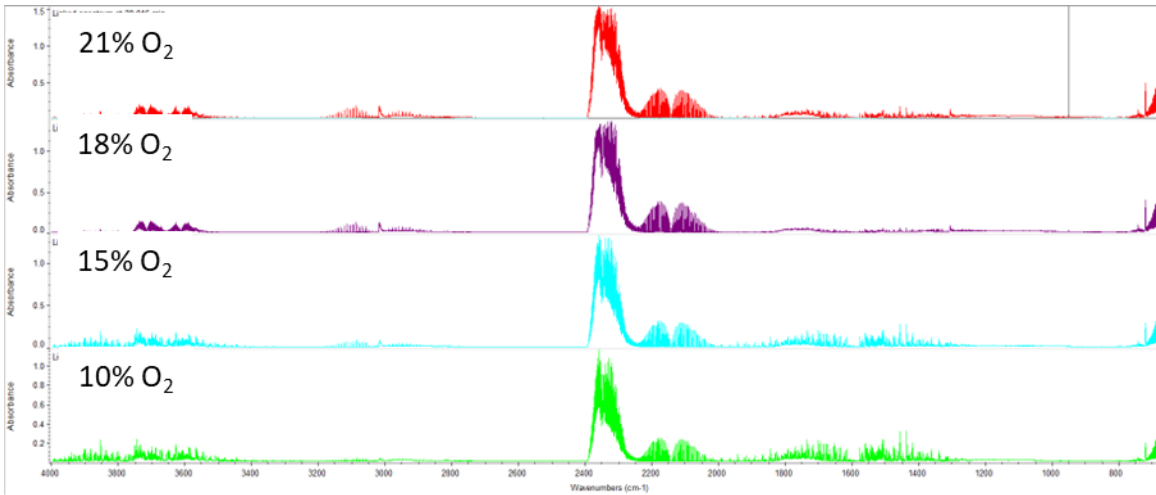


Figure 195: FTIR spectra of CLT at 20 kW/m² at 21, 18, 15 and 10 vol-% O₂ at 20 min

Appendix 15

Replica curves of the fire behavior, gas, and aerosol production of CLT/WF in the CACC at 50 kW/m²

- 21 vol-% O₂

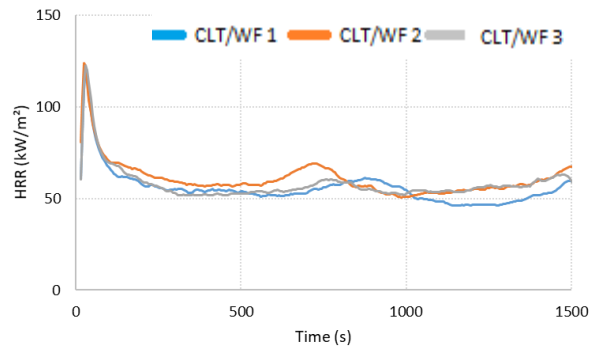
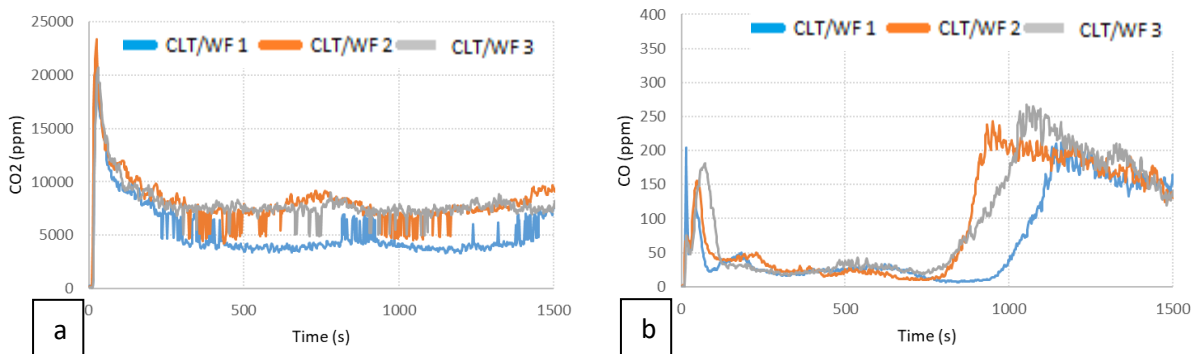


Figure 196: HRR of CLT/ WF at 50 kW/m² and 21 vol-% O₂



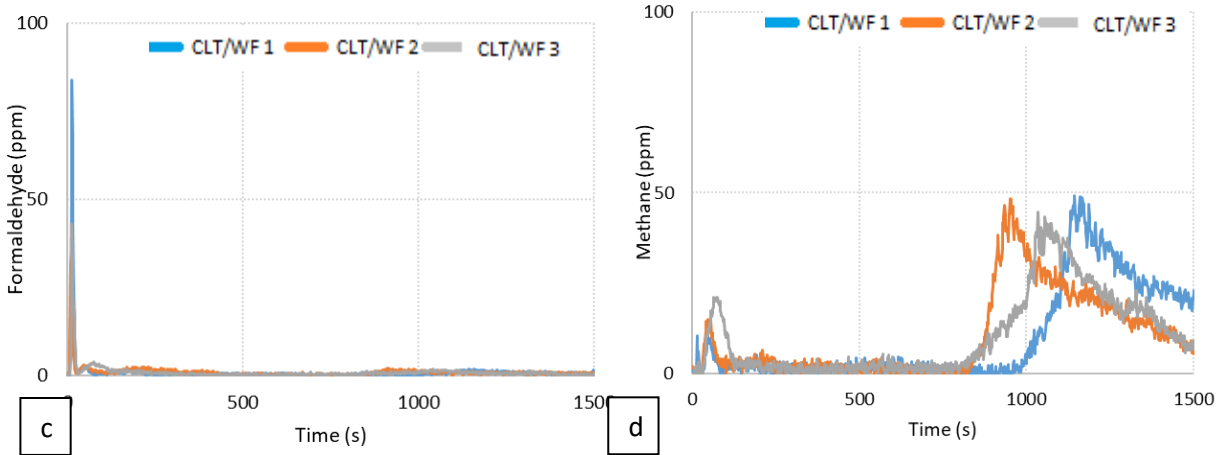


Figure 197: Gas production of CLT/WF at 50 kW/m² and 21 vol-% O₂: a. CO₂, b. CO, c. Formaldehyde, c. Methane

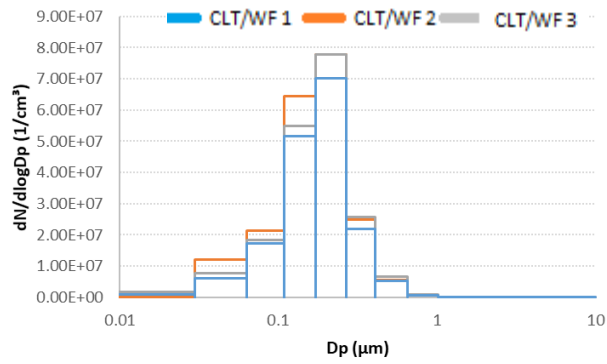


Figure 198: Aerosol size distribution of CLT/WF at 50 kW/m² and 21 vol-% O₂ at ti

- 18 vol-% O₂

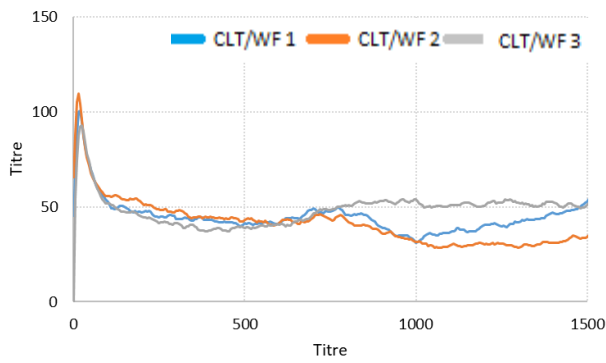


Figure 199: HRR of CLT/ WF at 50 kW/m² and 18 vol-% O₂

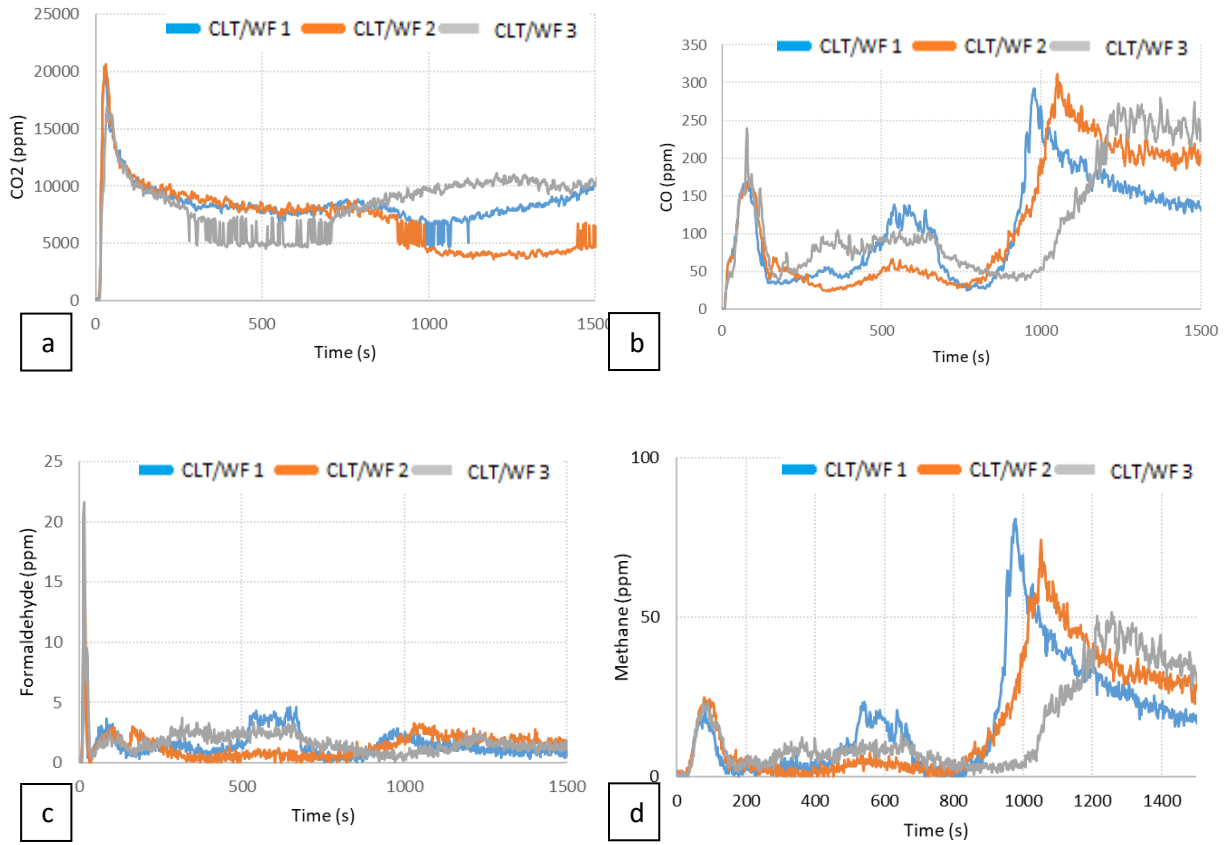


Figure 200: Gas production of CLT/WF at 50 kW/m² and 18 vol-% O₂: a. CO₂, b. CO, c. Formaldehyde, c. Methane

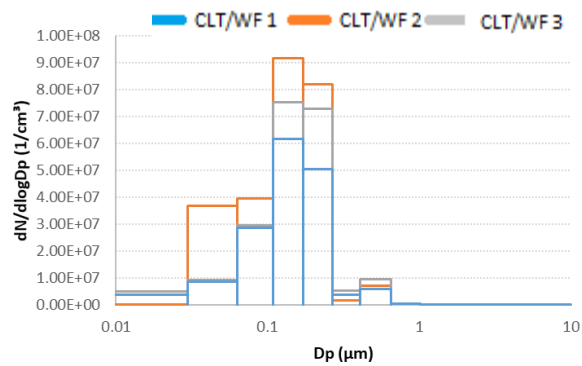


Figure 201: Aerosol size distribution of CLT/WF at 50 kW/m² and 18 vol-% O₂ at *t_i*

- 15 vol-% O₂

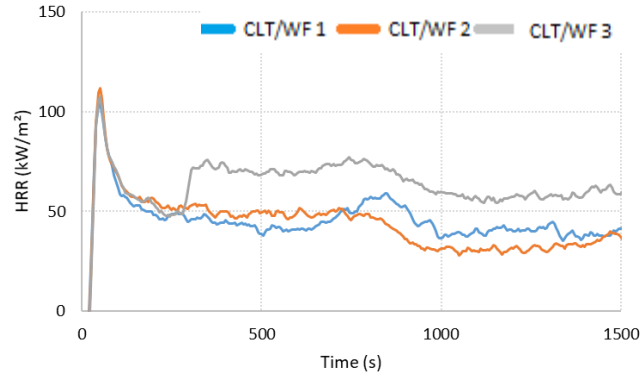


Figure 202: HRR of CLT/ WF at 50 kW/m² and 15 vol-% O₂

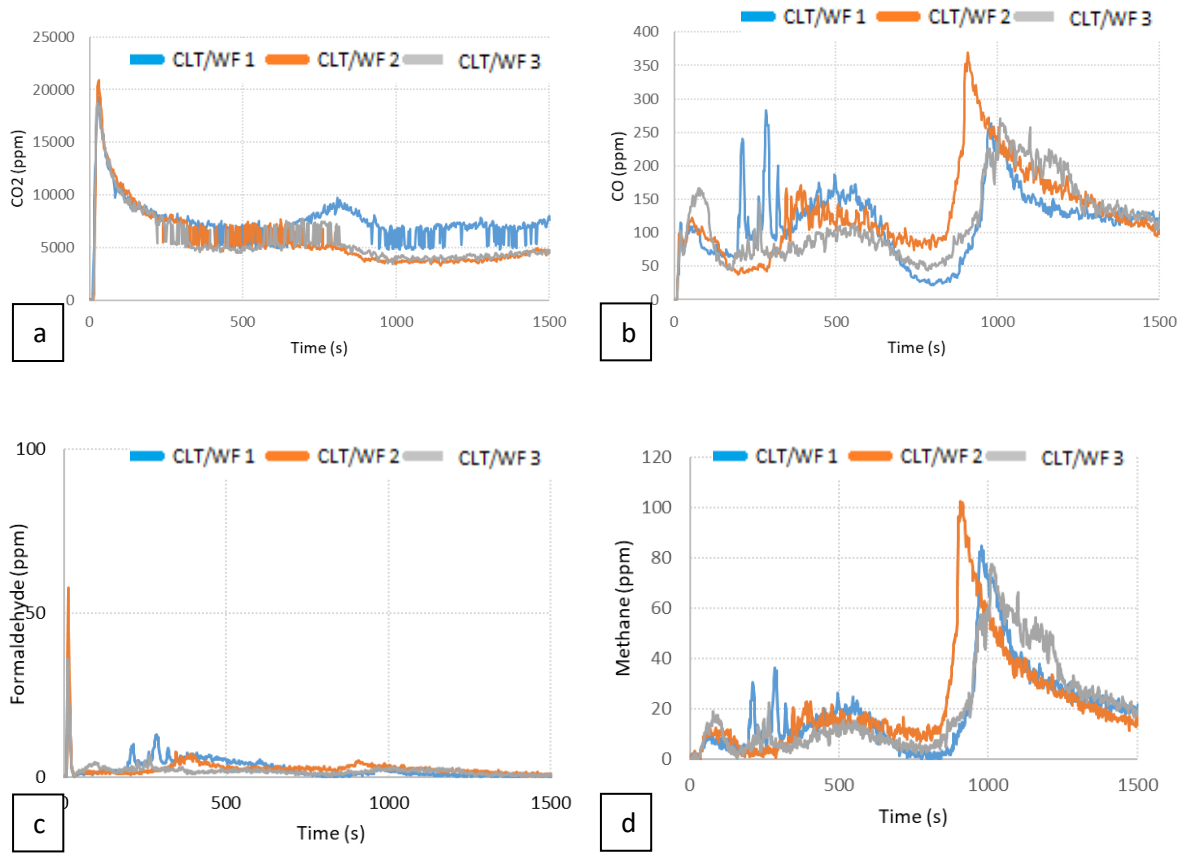


Figure 203: Gas production of CLT/WF at 50 kW/m² and 15 vol-% O₂: a. CO₂, b. CO, c. Formaldehyde, c. Methane

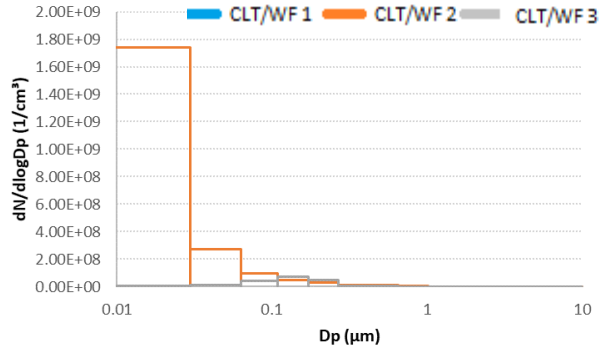


Figure 204: Aerosol size distribution of CLT/WF at 50 kW/m² and 15 vol-% O₂ at ti

- 10 vol-% O₂

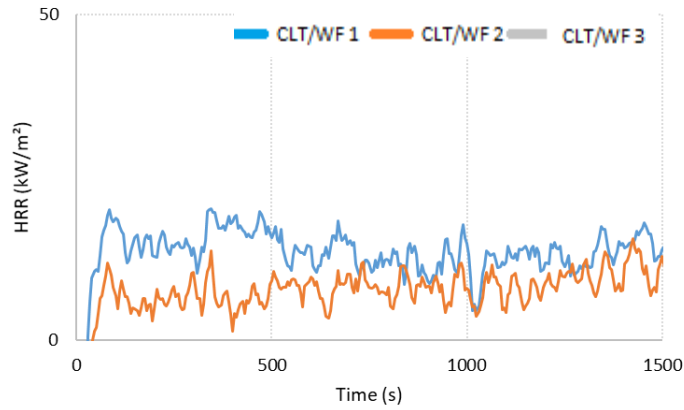
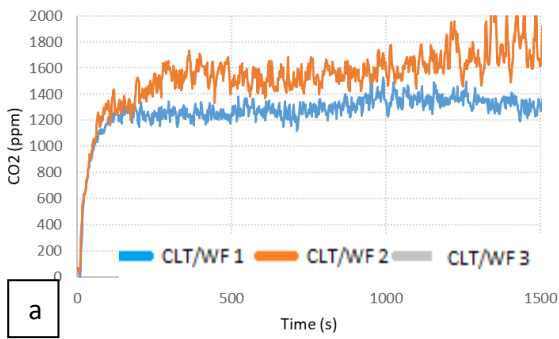
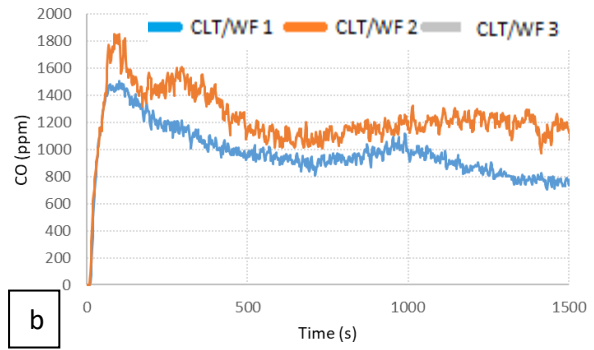


Figure 205: HRR of CLT/WF at 50 kW/m² and 10 vol-% O₂



a



b

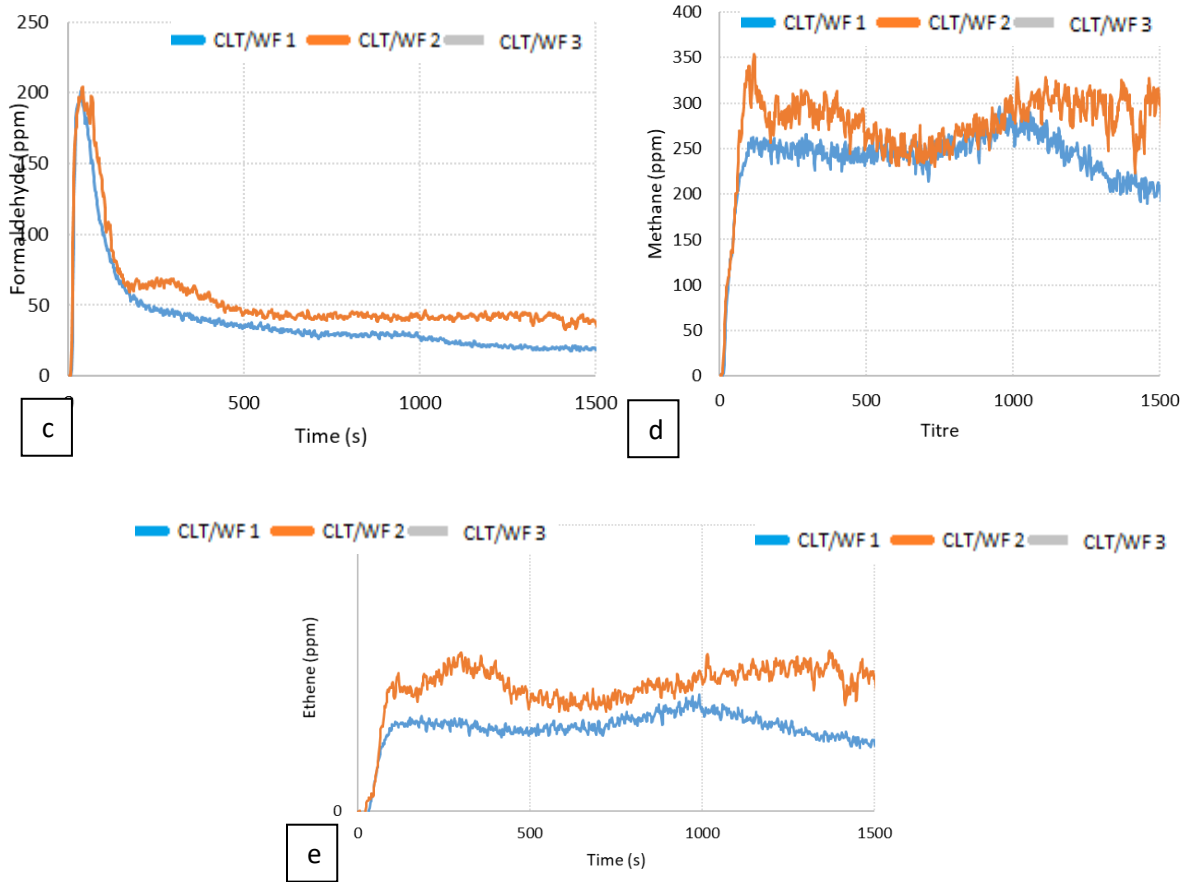


Figure 206: Gas production of CLT/WF at 50 kW/m² and 10 vol-% O₂: a. CO₂, b. CO, c. Formaldehyde, d. Methane and e. Ethene

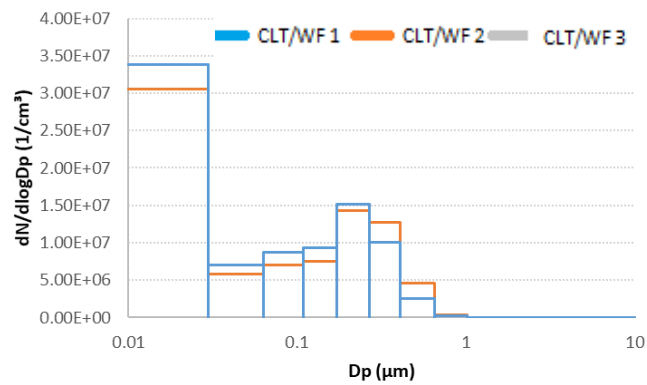


Figure 207: Aerosol size distribution of CLT/WF at 50 kW/m² and 10 vol-% O₂ at 25s

Appendix 16

FTIR spectra of CLT/WF at 50 kW/m²

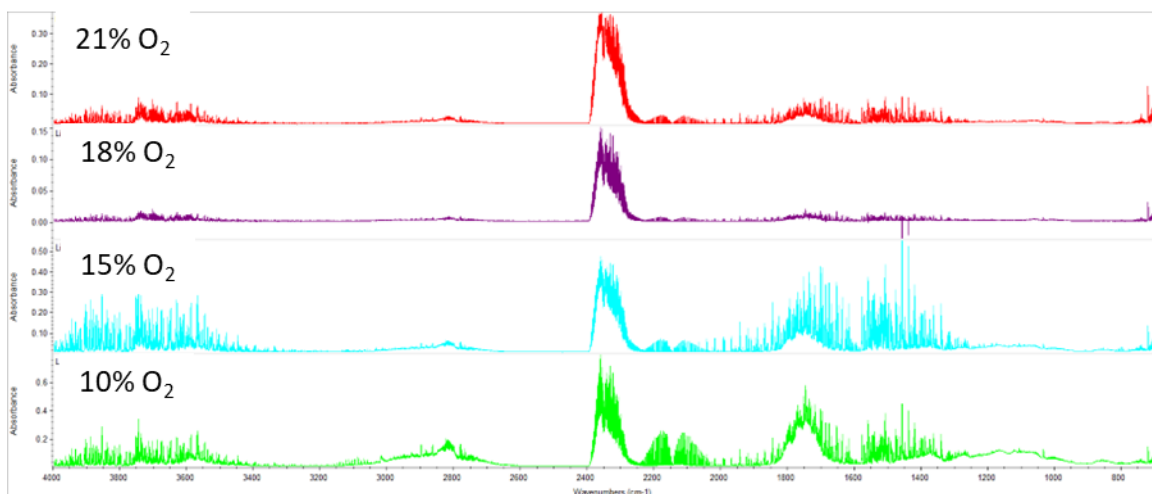


Figure 208: FTIR spectra of CLT/WF at 50 kW/m² at 21, 18, 15 and 10 vol-% O₂ at the start of thermal exposure

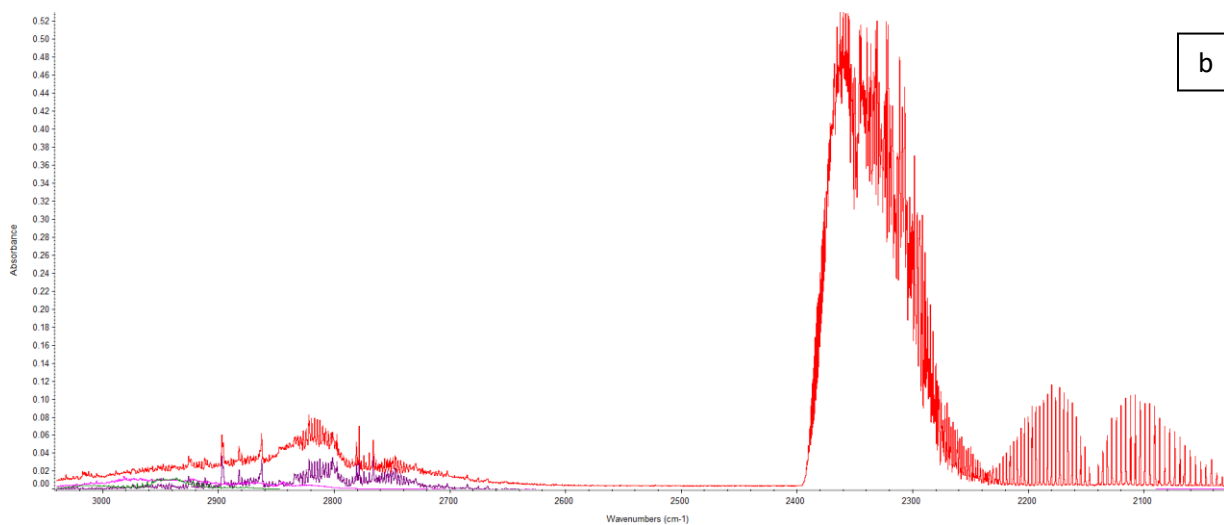
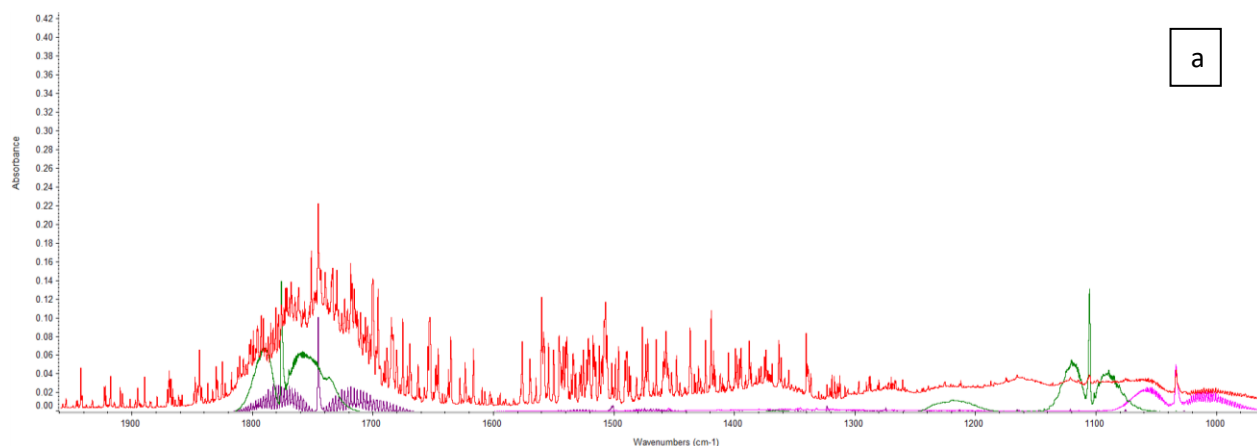
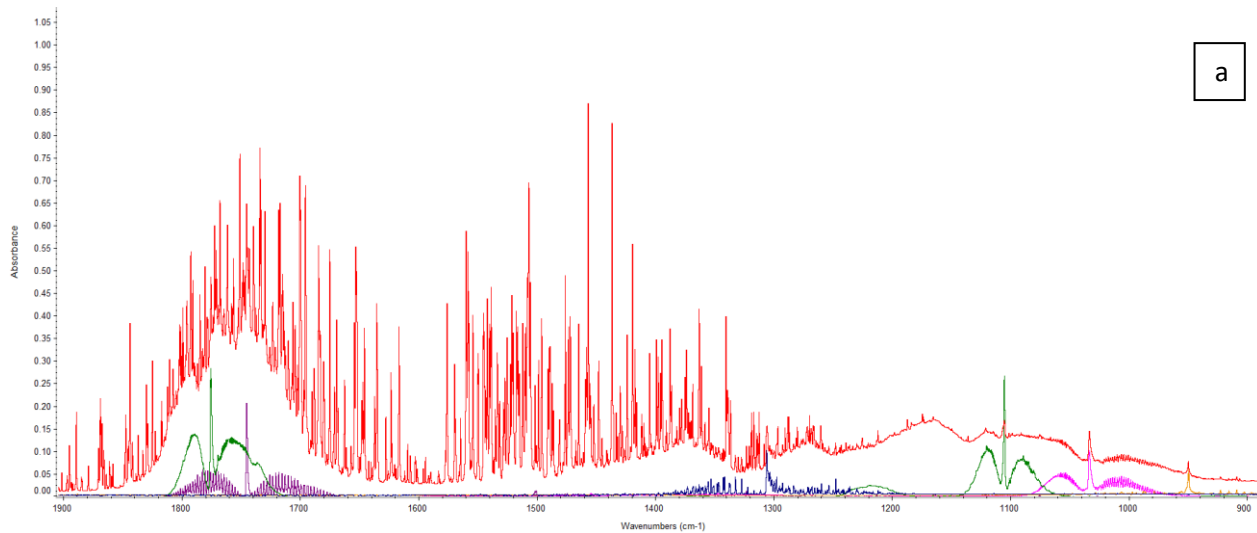
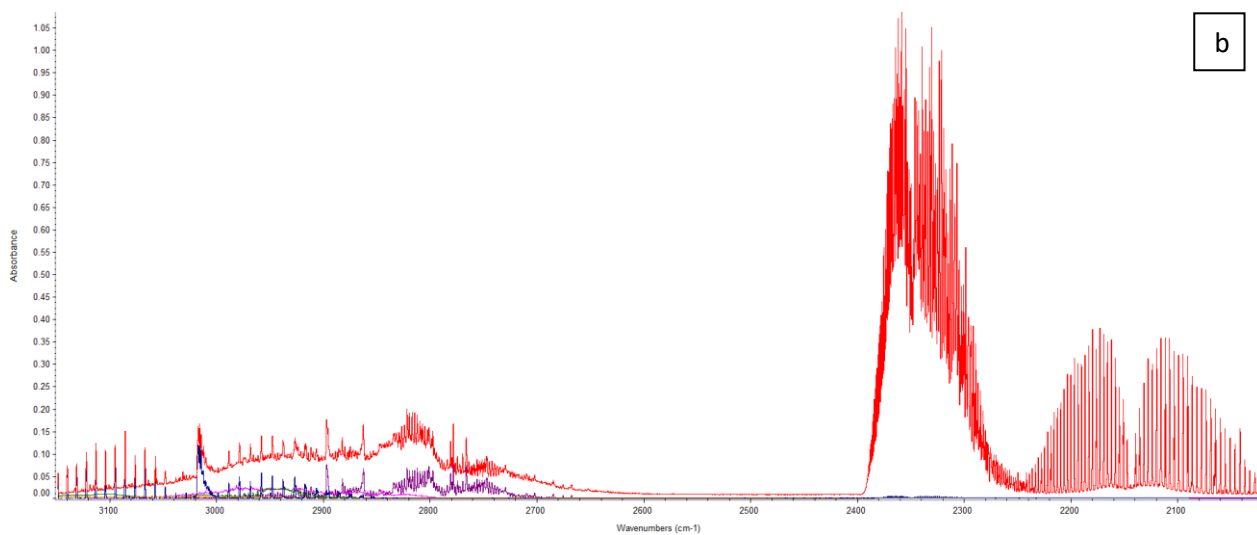


Figure 209: Zoom on the FTIR spectra of CLT/WF at 50 kW/m², 21 vol-% O₂ at the start of thermal exposure (red) along with spectra of formaldehyde (purple), methanol (pink) and formic acid (green) between 2000 and 900 cm⁻¹ (a) and between 3100 and 2000 cm⁻¹ (b)



a



b

Figure 210: Zoom on the FTIR spectra of CLT/WF at 50 kW/m², 10 vol-% O₂ at the start of thermal exposure (red) along with spectra of formaldehyde (purple), methanol (pink), formic acid (green), methane (blue) and ethene (orange) between 1900 and 900 cm⁻¹ (a) and between 3150 and 2000 cm⁻¹ (b)

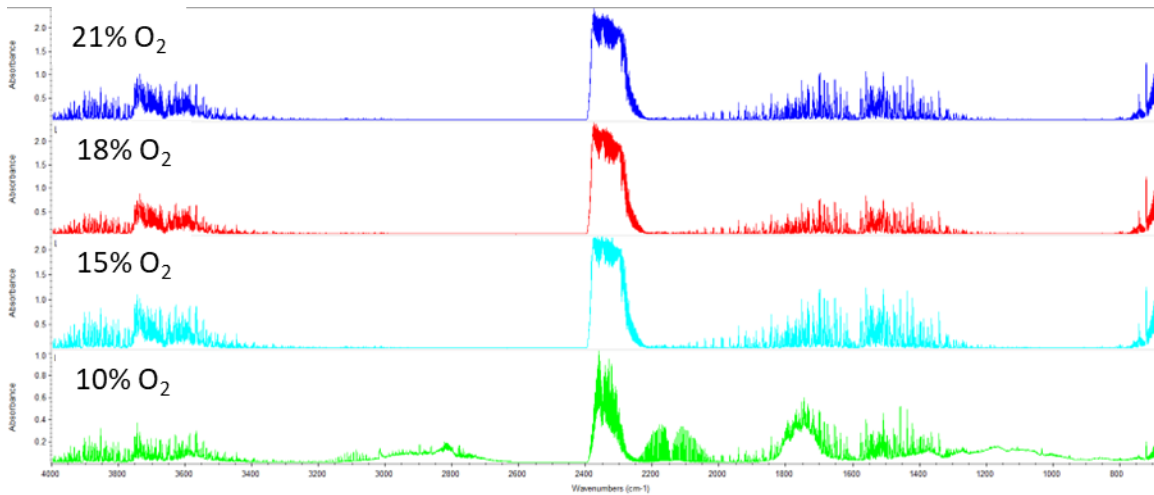


Figure 211: FTIR spectra of CLT/WF at 50 kW/m² at 21, 18, 15 and 10 vol-% O₂ at ignition

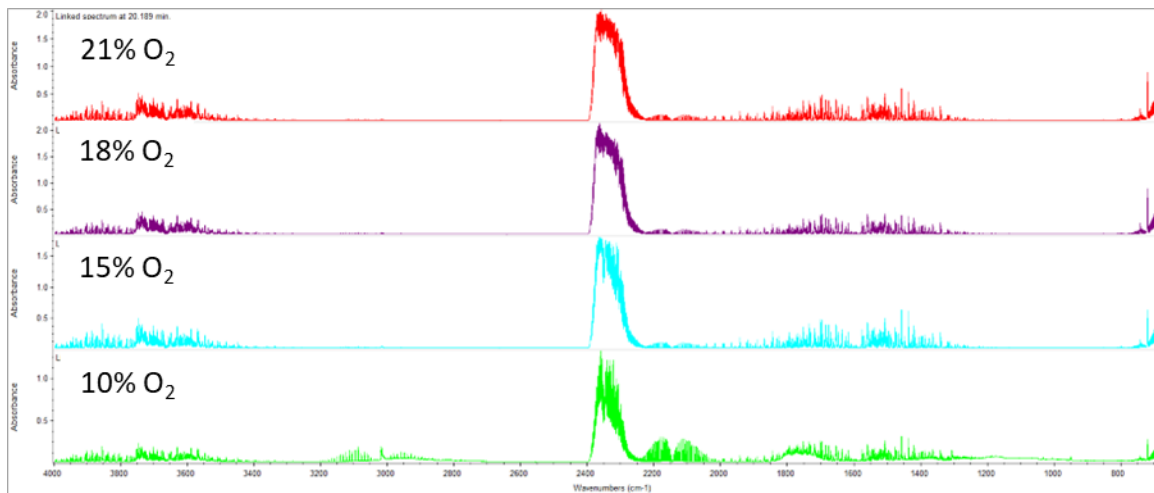


Figure 212: FTIR spectra of CLT/WF at 50 kW/m² at 21, 18, 15 and 10 vol-% O₂ at 20 min

Appendix 17

Superposition of the gas production curves of CLT, WF and CLT/WF at 50 kW/m²

- 18 vol-% O

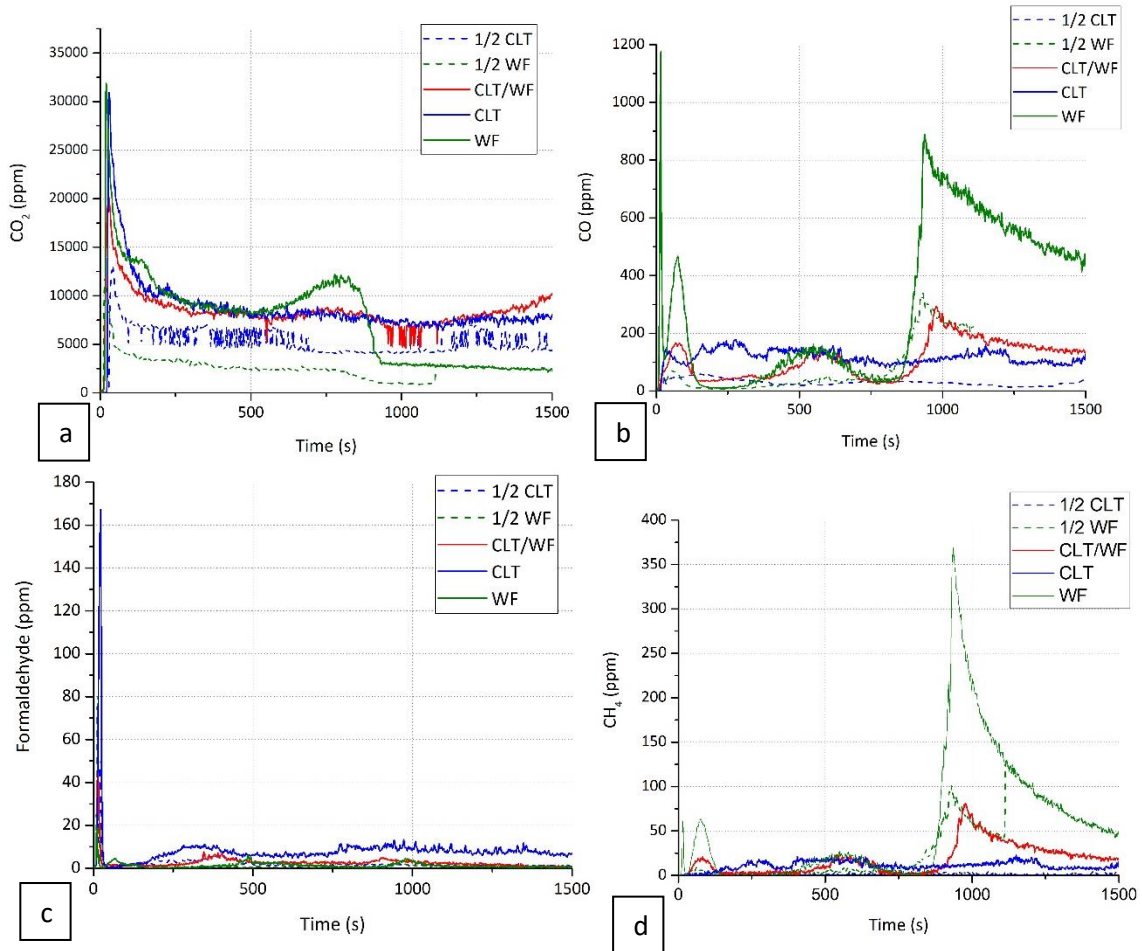
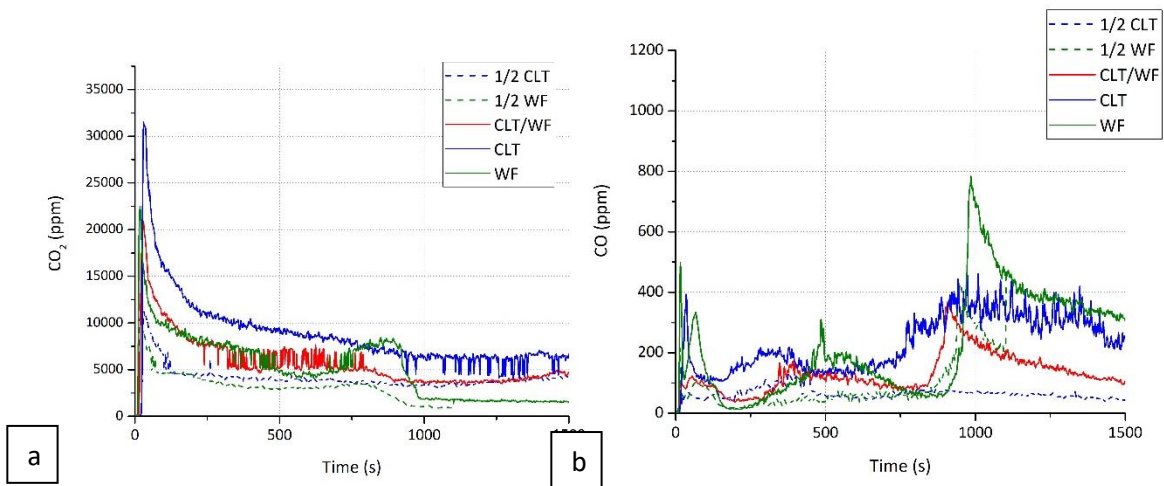


Figure 213: Gas production of the CLT/WF combination, half samples, and entire samples of CLT and WF at 20 kW/m² and 18 vol-% O₂. (a) Carbon dioxide (b) Carbon monoxide (c) Formaldehyde (d) Methane

- 15 vol-% O₂



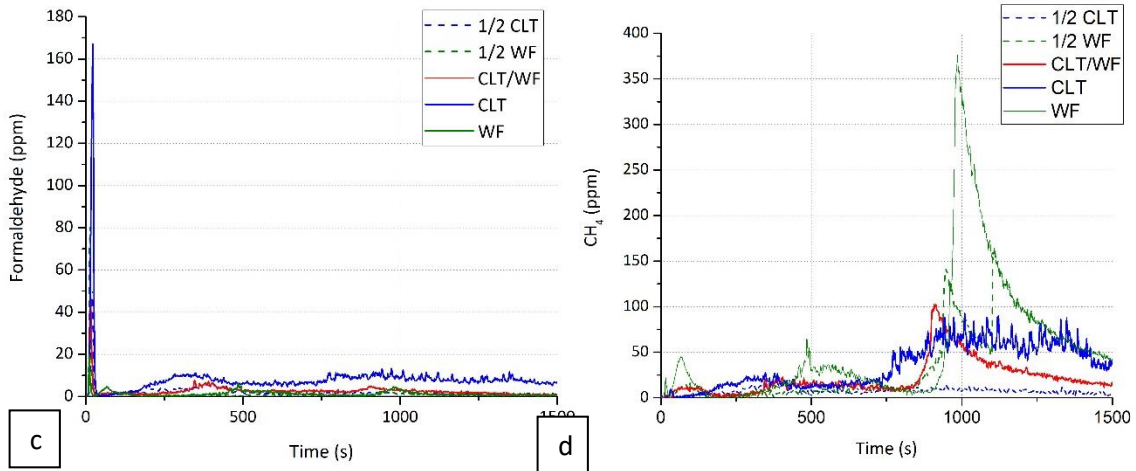


Figure 214: Gas production of the CLT/WF combination, half samples, and entire samples of CLT and WF at 20 kW/m² and 15 vol-% O₂. (a) Carbon dioxide (b) Carbon monoxide (c) Formaldehyde (d) Methane

Appendix 18

Replica curves of the fire behavior, gas, and aerosol production of CLT/WF in the CACC at 20 kW/m²

- 21 vol-% O₂

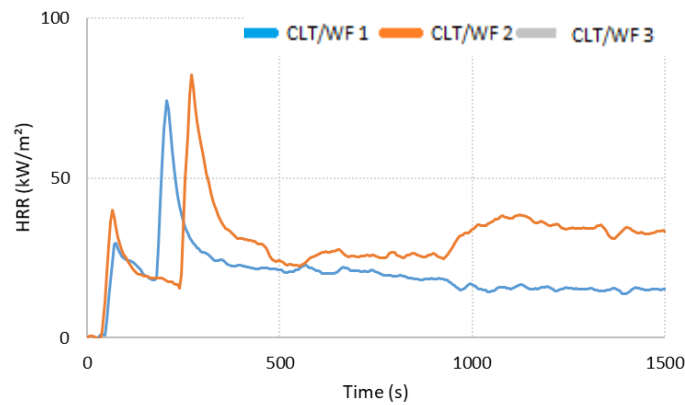
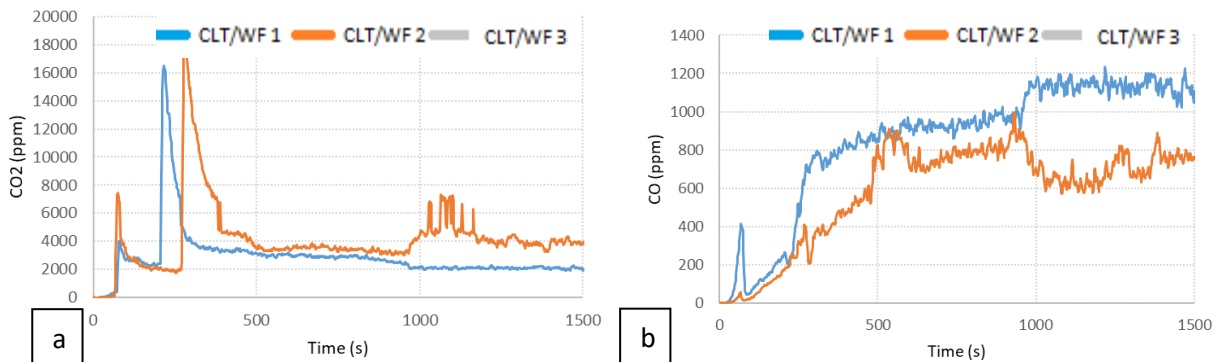


Figure 215: HRR of CLT/ WF at 20 kW/m² and 21 vol-% O₂



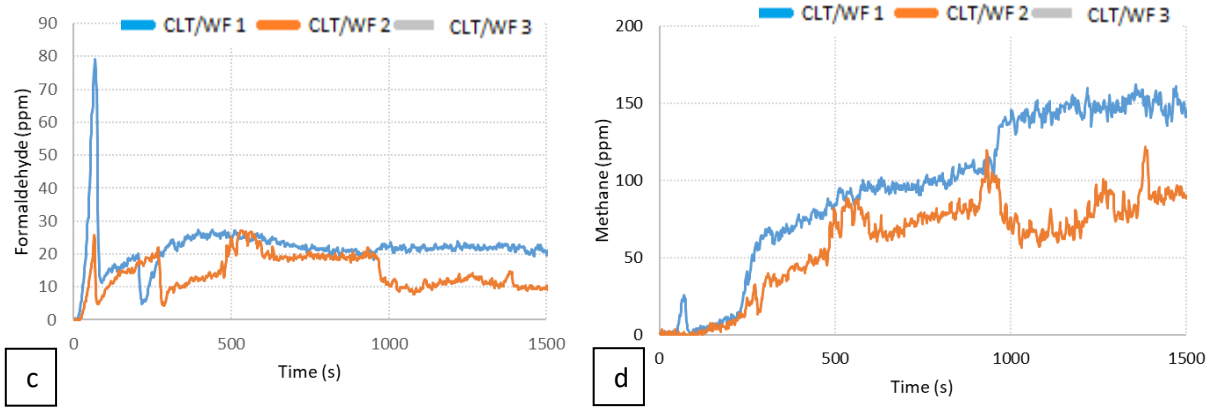


Figure 216: Gas production of CLT/WF at 20 kW/m² and 21 vol-% O₂: a. CO₂, b. CO, c. Formaldehyde, c. Methane

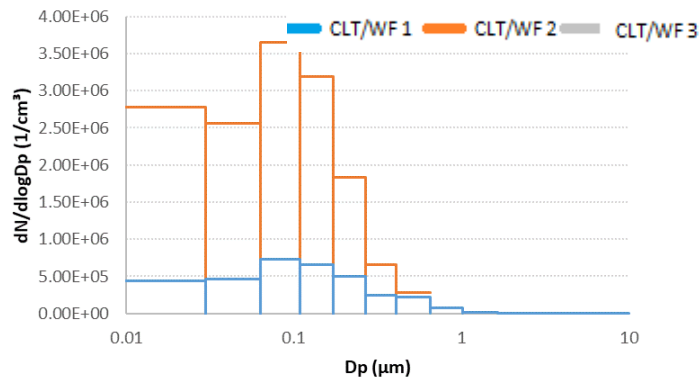


Figure 217: Aerosol size distribution of CLT/WF at 20 kW/m² and 21 vol-% O₂ at t_i

- 18 vol-% O₂

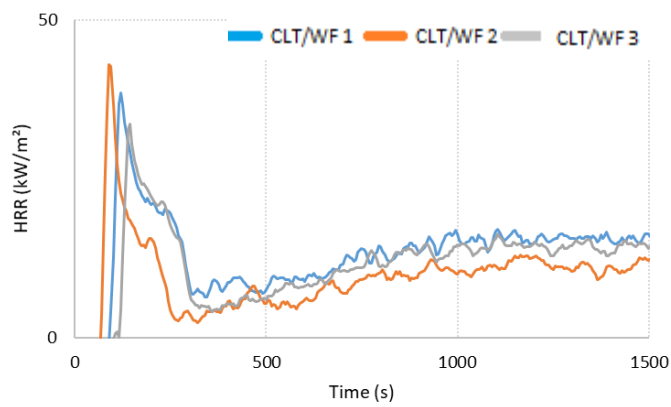


Figure 218: HRR of CLT/WF at 20 kW/m² and 18 vol-% O₂

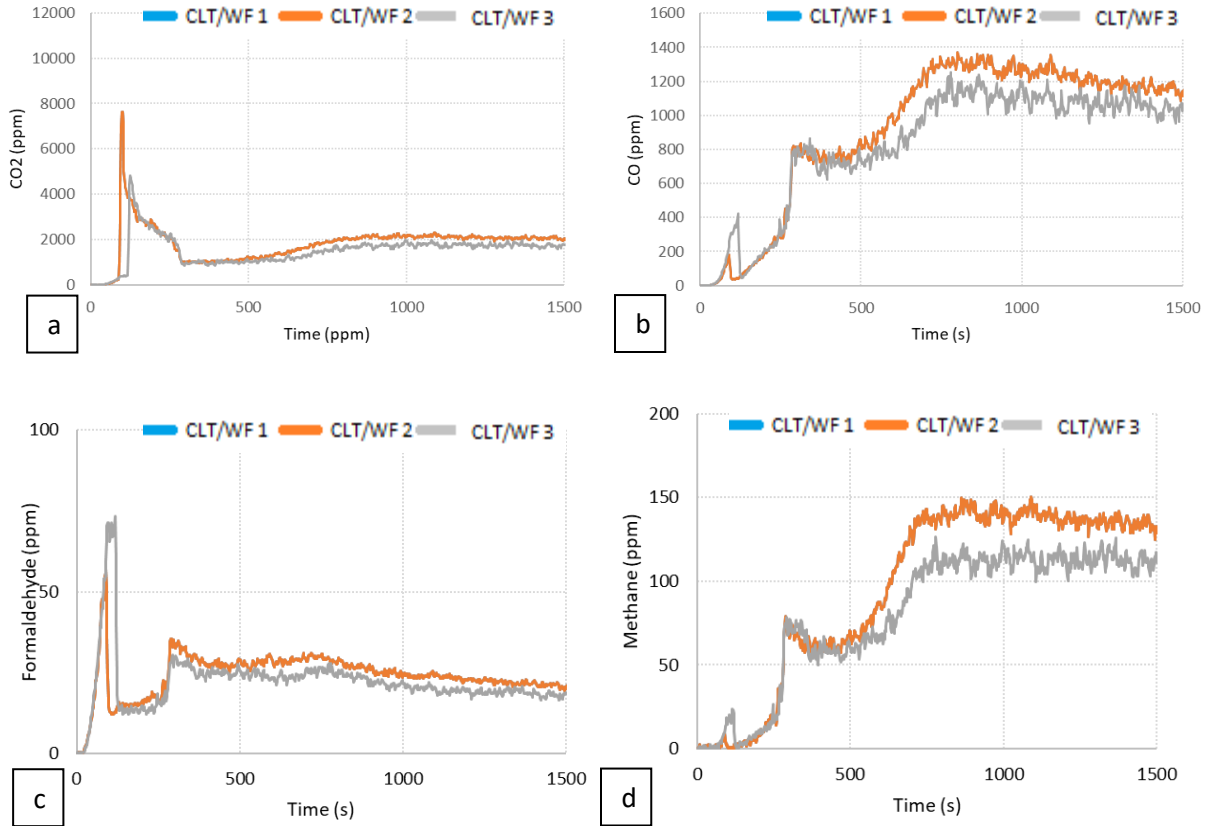


Figure 219: Gas production of CLT/WF at 20 kW/m² and 18 vol-% O₂: a. CO₂, b. CO, c. Formaldehyde, c. Methane

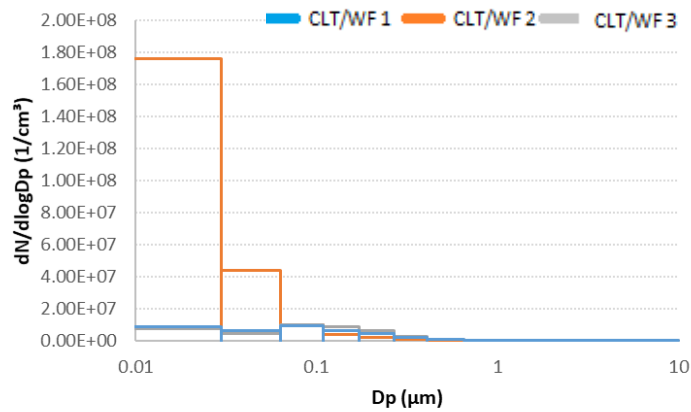


Figure 220: Aerosol size distribution of CLT/WF at 20 kW/m² and 18 vol-% O₂ at ti

- 15 vol-% O₂

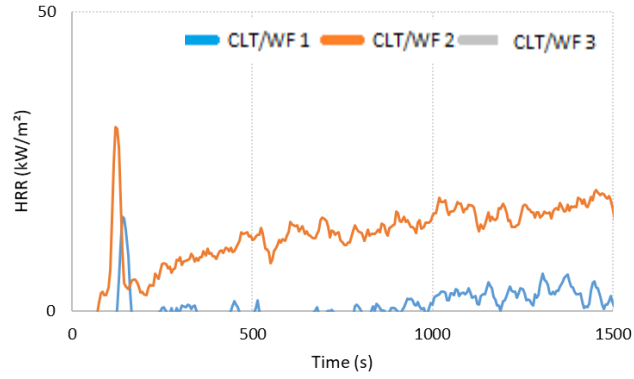


Figure 221: HRR of CLT/WF at 20 kW/m² and 15 vol-% O₂

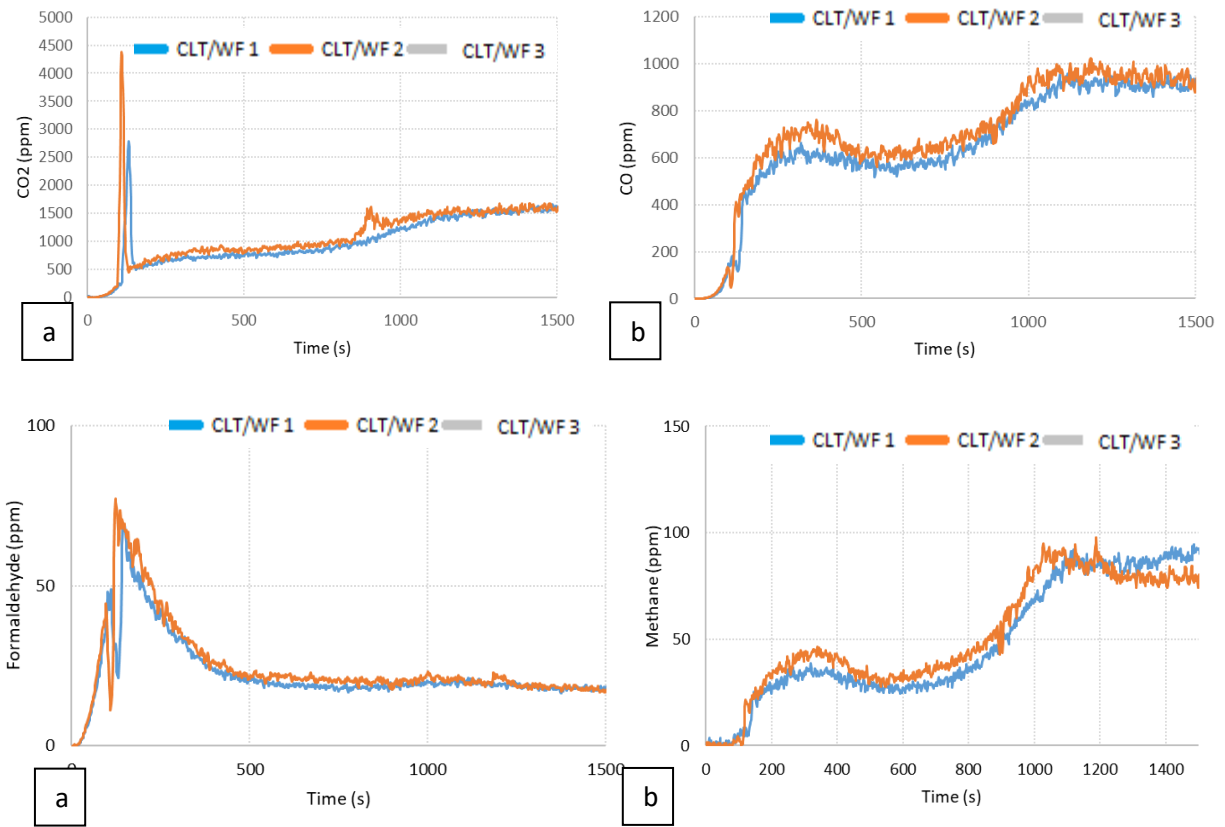


Figure 222: Gas production of CLT/WF at 20 kW/m² and 15 vol-% O₂: a. CO₂, b. CO, c. Formaldehyde, c. Methane

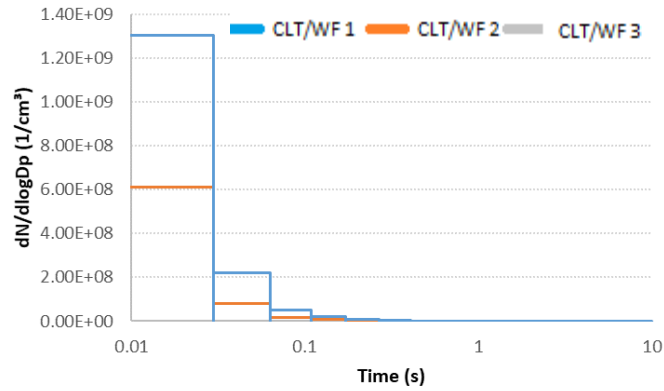


Figure 223: Aerosol size distribution of CLT/WF at 20 kW/m² and 15 vol-% O₂ at t_i

- 10 vol-% O₂

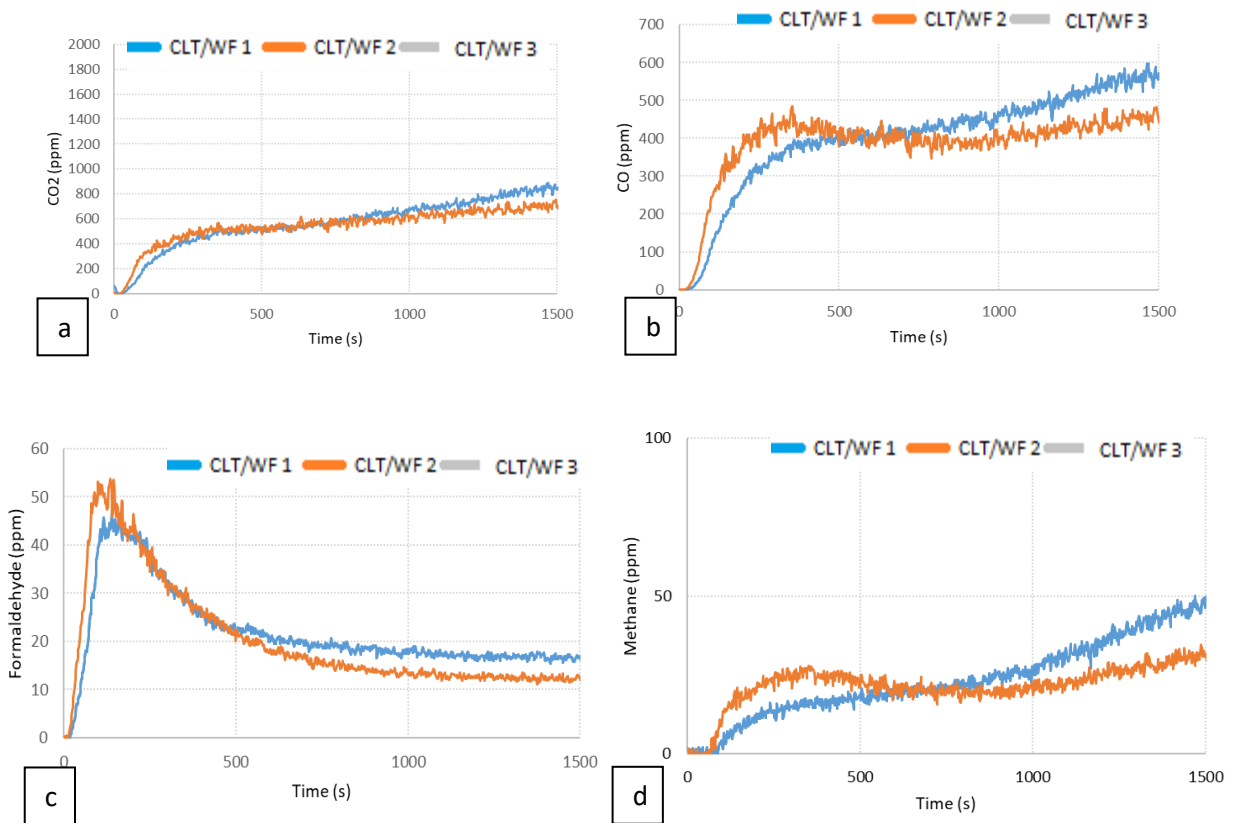


Figure 224: Gas production of CLT/WF at 20 kW/m² and 10 vol-% O₂: a. CO₂, b. CO, c. Formaldehyde, c. Methane

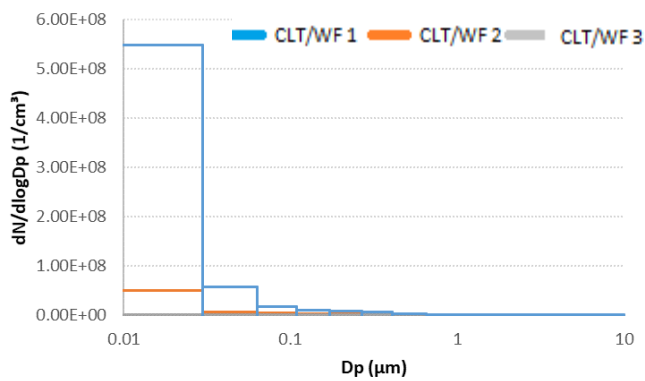


Figure 225: Aerosol size distribution of CLT/WF at 20 kW/m² and 10 vol-% O₂ at 25s

Appendix 19

FTIR spectra of CLT/WF at 20 kW/m²

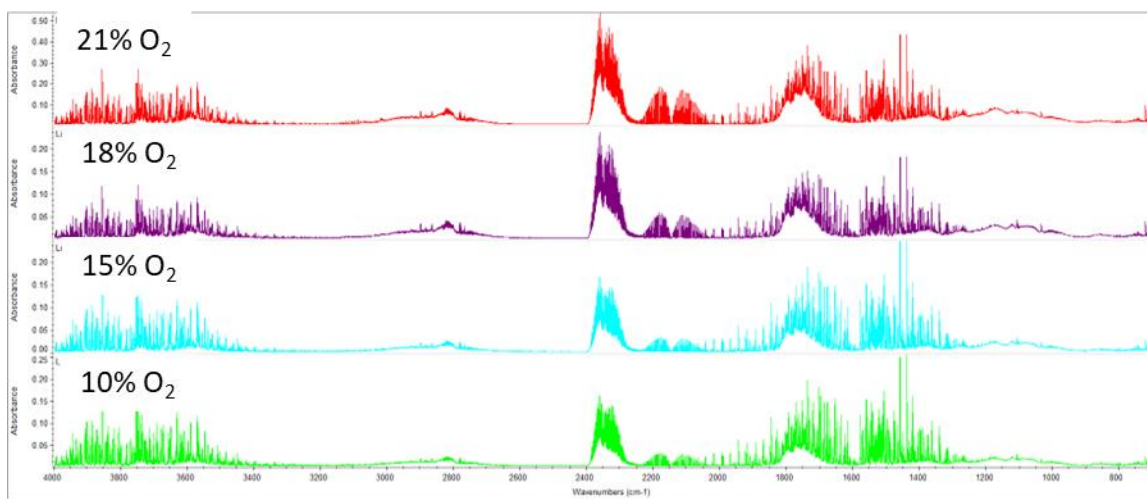
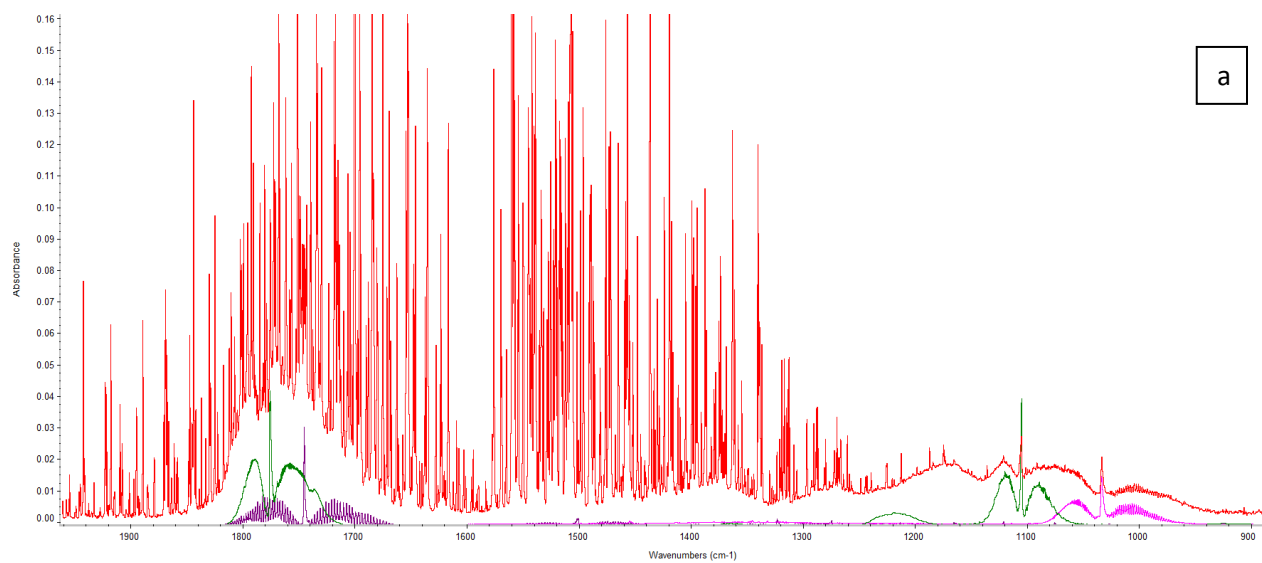
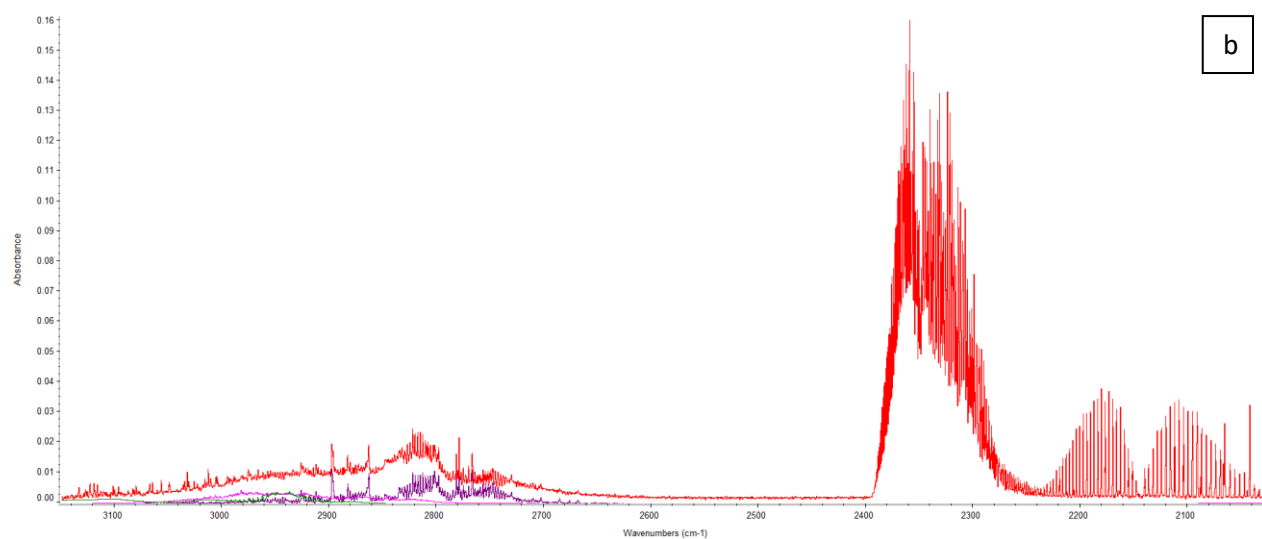


Figure 226: FTIR spectra of CLT/WF at 20 kW/m² at 21, 18, 15 and 10 vol-% O₂ at the start of thermal exposure

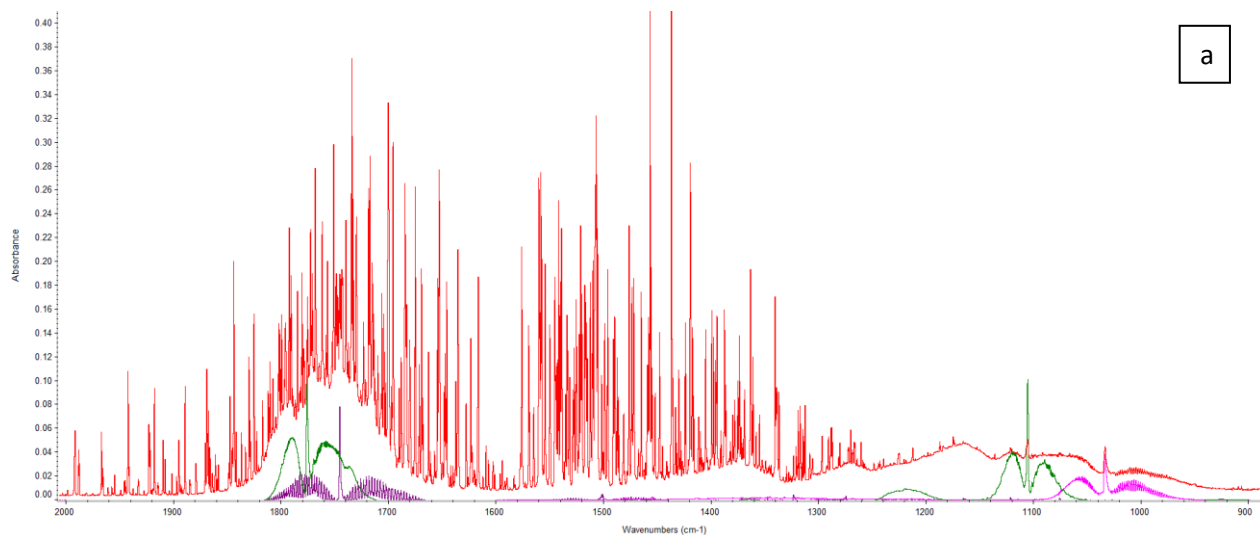


a

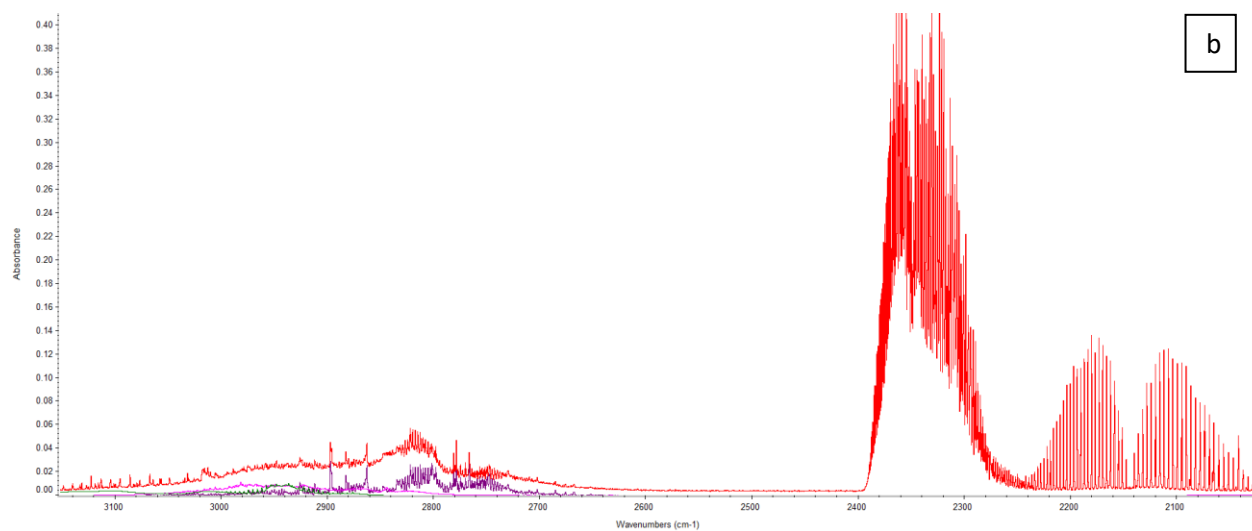


b

Figure 227: Zoom on the FTIR spectra of CLT/WF at 20 kW/m², 21 vol-% O₂ at the start of thermal exposure (red) along with spectra of formaldehyde (purple), methanol (pink) and formic acid (green) between 2000 and 850 cm⁻¹ (a) and between 3150 and 2000 cm⁻¹ (b)



a



b

Figure 228: Zoom on the FTIR spectra of CLT/WF at 20 kW/m², 10 vol-% O₂ at the start of thermal exposure (red) along with spectra of formaldehyde (purple), methanol (pink) and formic acid (green) between 2000 and 900 cm⁻¹ (a) and between 3150 and 2000 cm⁻¹ (b)

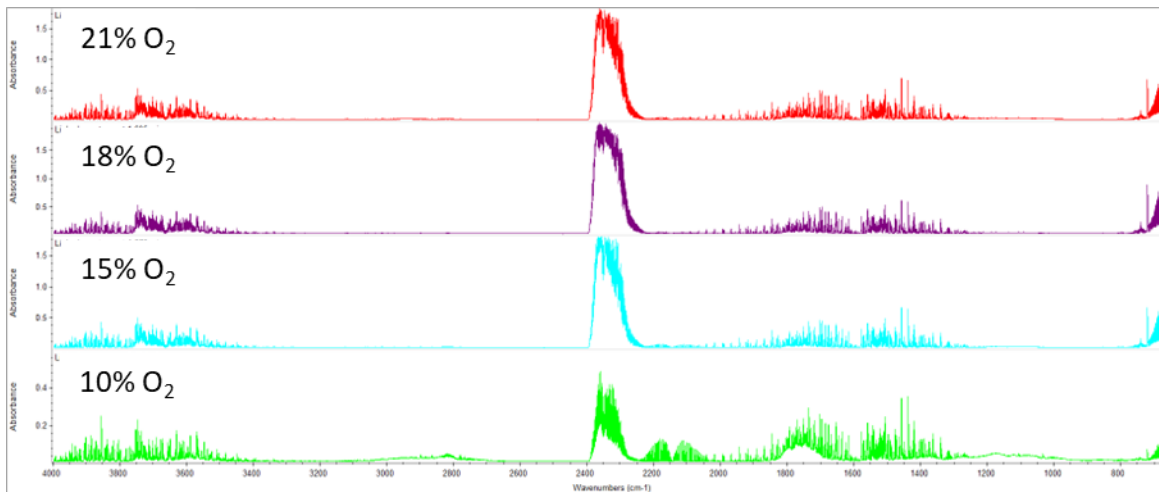


Figure 229: FTIR spectra of CLT/WF at 20 kW/m² at 21, 18, 15 and 10 vol-% O₂ at ignition

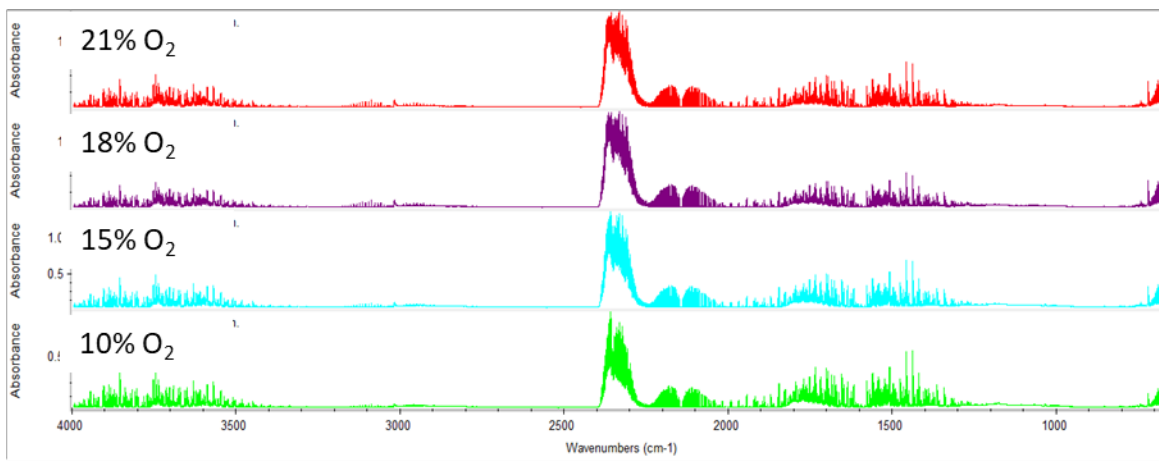


Figure 230: FTIR spectra of CLT/WF at 20 kW/m² at 21, 18, 15 and 10 vol-% O₂ at 20 min

Appendix 20

Superposition of the gas production curves of CLT, WF and CLT/WF at 20 kW/m²

- 15 vol-% O₂

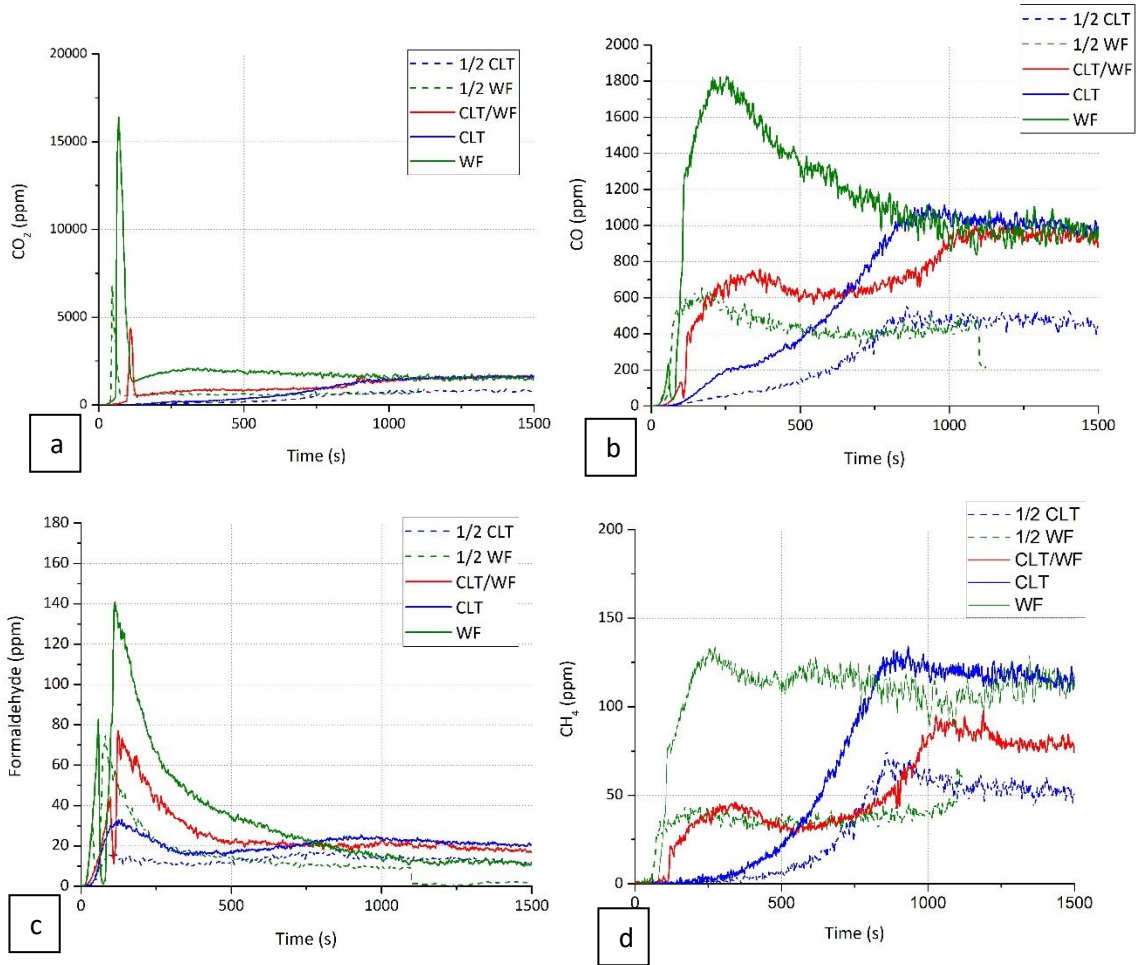


Figure 231: Gas production of the CLT/WF combination, half samples, and entire samples of CLT and WF at 20 kW/m² and 15 vol-% O₂. (a) Carbon dioxide (b) Carbon monoxide (c) Formaldehyde (d) Methane

Appendix 21

Fire behavior, gas, and aerosol production of CLT, WF and CLT/WF in the intermediate scale test

- CLT 40 and 90 kW

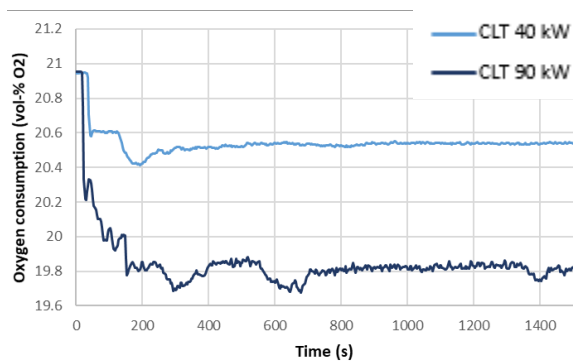


Figure 232: Oxygen consumption of CLT at 40 and 90 kW

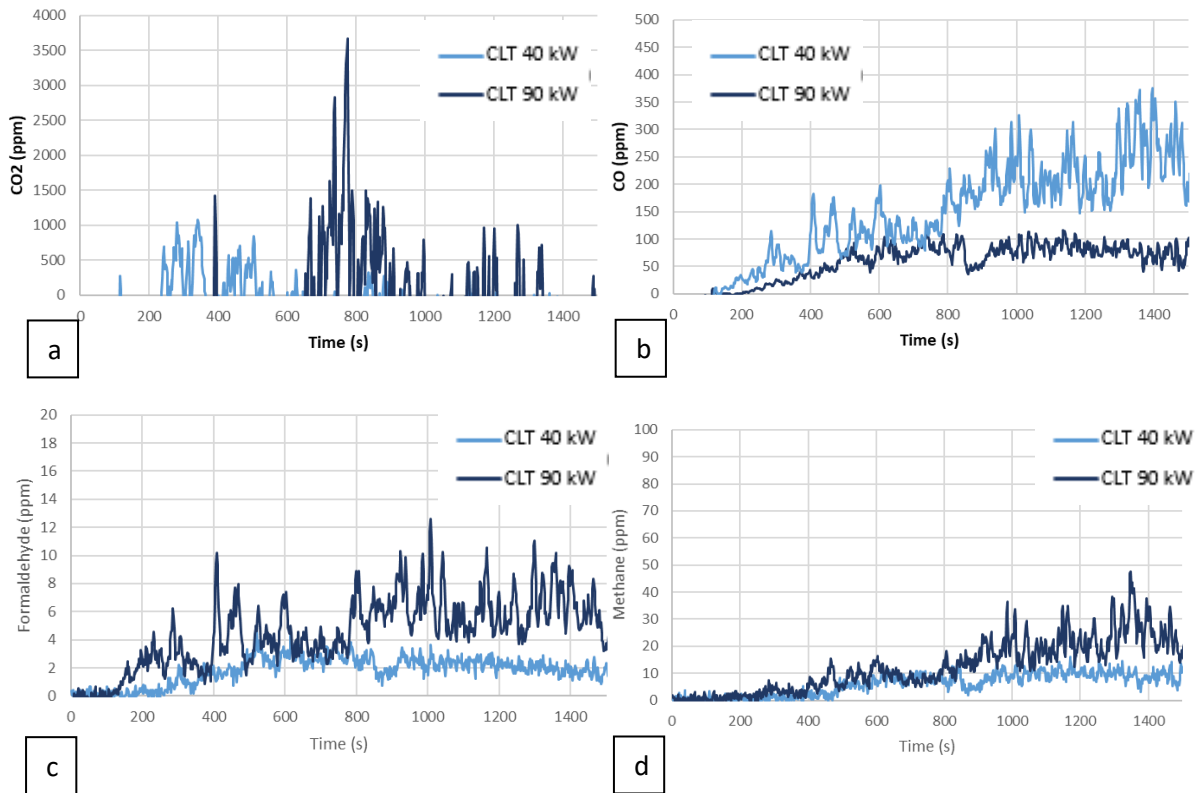


Figure 233: Gas production of CLT at 40 and 90 kW. a. CO₂, b.CO, c. Formaldehyde, d. Methane

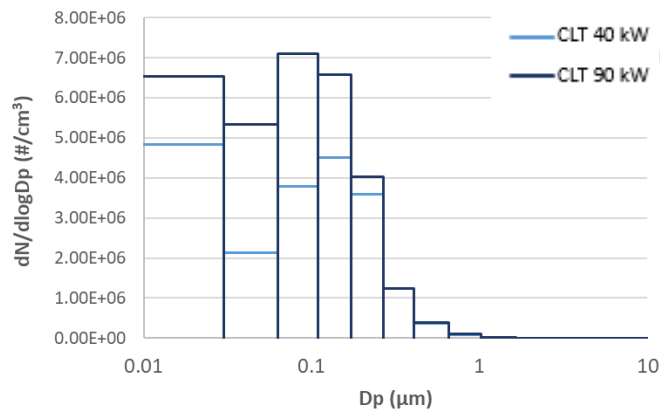


Figure 234: Global aerosol size distribution of CLT at 40 and 90 kW

- WF 40 and 90 kW

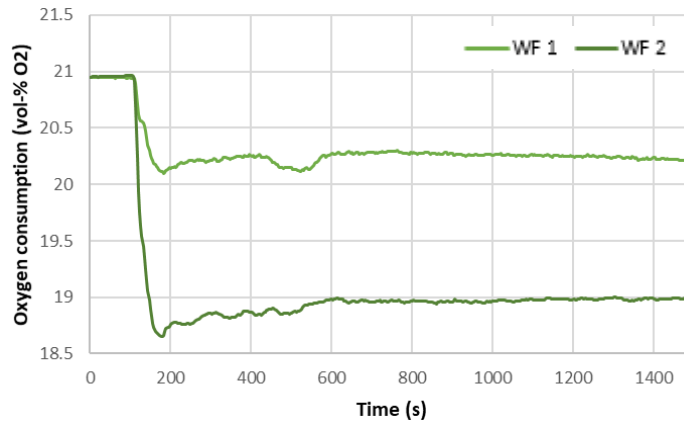


Figure 235: Oxygen consumption of WF at 40 and 90 kW

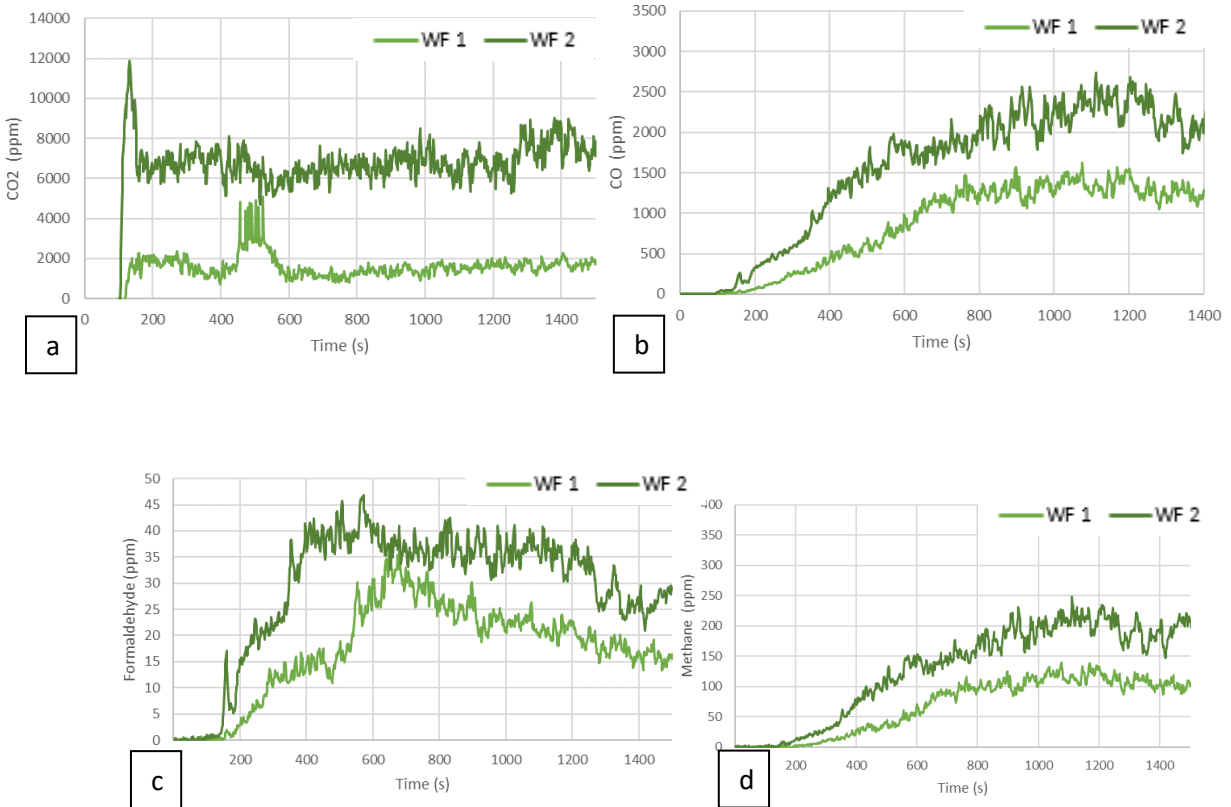


Figure 236: Gas production of WF at 40 and 90 kW. a. CO₂, b.CO, c. Formaldehyde, d. Methane

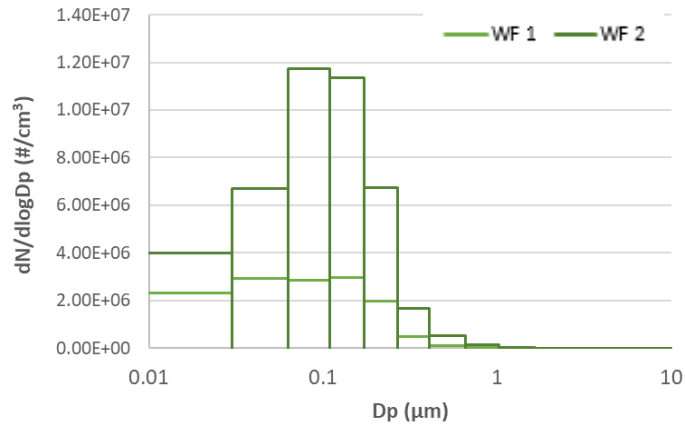


Figure 237: Global aerosol size distribution of WF at 40 and 90 kW

- CLT/WF at 40 and 90 kW

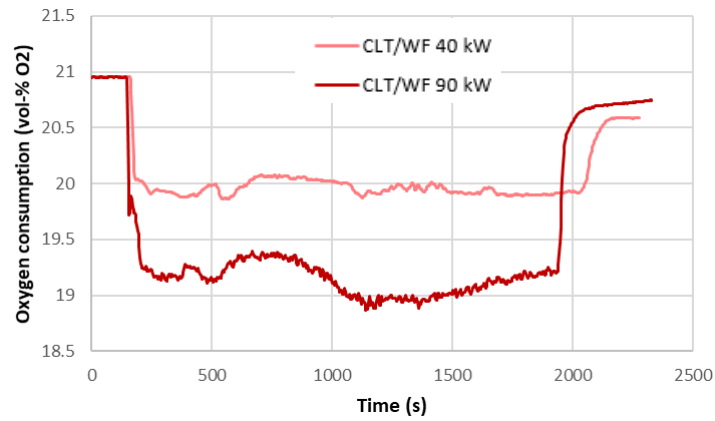
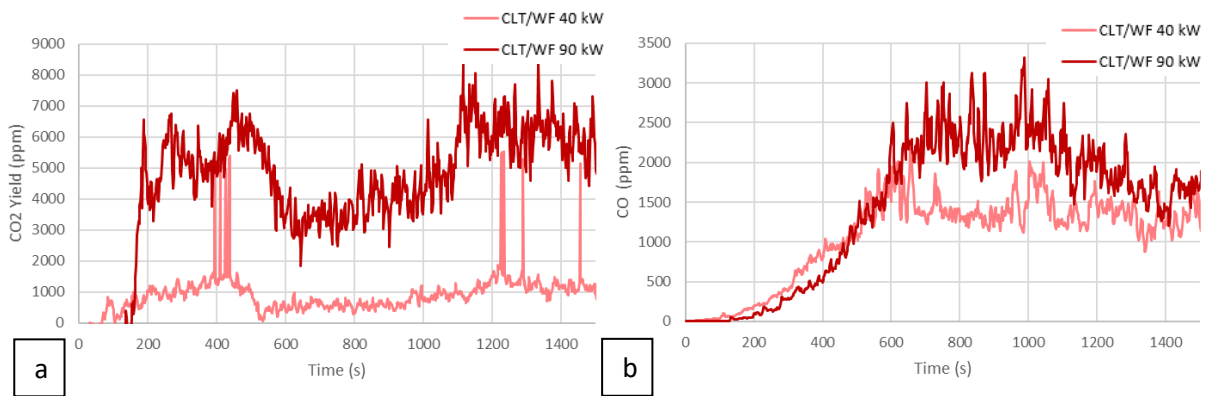


Figure 238: Oxygen consumption of CLT/WF at 40 and 90 kW



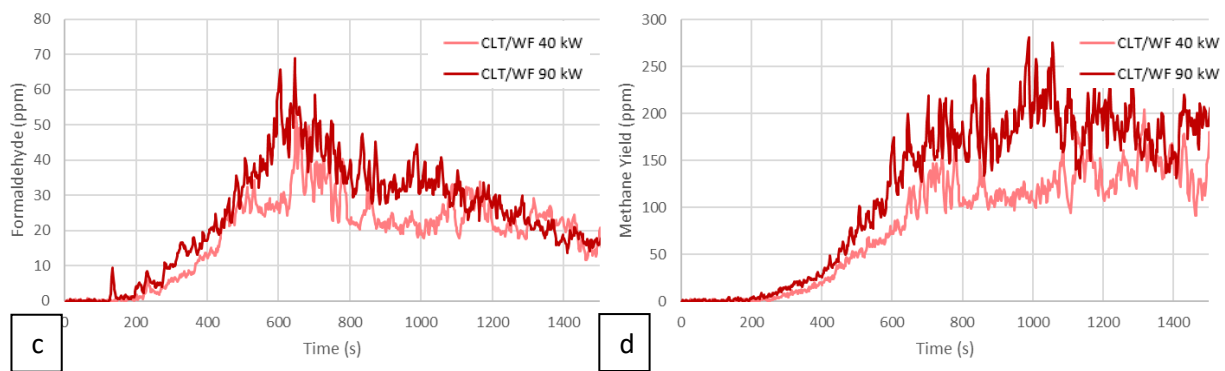


Figure 239: Gas production of WF at 40 and 90 kW. a. CO₂, b.CO, c. Formaldehyde, d. Methane

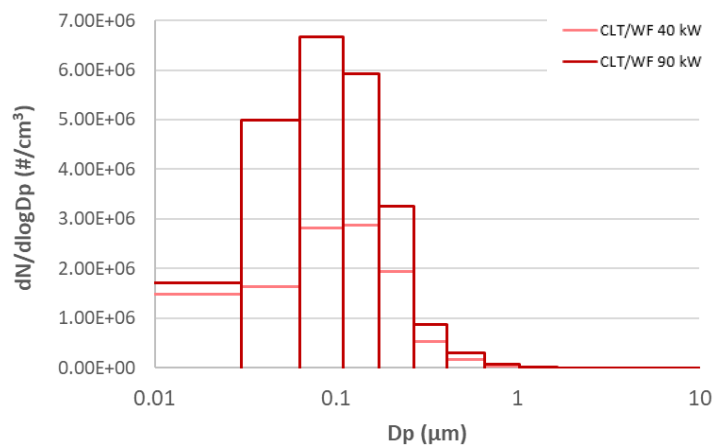


Figure 240: Global aerosol size distribution of CLT/WF at 40 and 90 kW

Résumé en français

Les matériaux en bois sont des matériaux clés dans la lutte contre le changement climatique par le biais de la construction durable. En cas d'incendie, ces matériaux, comme la plupart des matériaux organiques, participent au développement du feu, challengeant leur utilisation. Lors de l'évaluation des risques d'incendie, deux paramètres sont pris en compte : la chaleur dégagée, qui peut entraîner la propagation du feu, et la fumée produite, composée de gaz et d'aérosols, qui peut être toxique. Ces paramètres dépendent de la composition du matériau et des conditions environnementales, telles que la température et la concentration en oxygène. Les incendies sous-ventilés ou viciés, dans lesquels la majeure partie de l'oxygène est consommée par le feu, présentent des risques d'incendie accrus. Pour améliorer la protection contre les incendies, il est essentiel de quantifier la chaleur dégagée, les gaz et les aérosols produits lorsque des matériaux en bois sont brûlés dans des conditions d'appauvrissement en oxygène. Il est également intéressant d'étudier les interactions potentielles entre un assemblage de matériaux en bois, simulant une configuration mur/isolant dans un bâtiment, car elles peuvent modifier les paramètres susmentionnés.

Les généralités sur les risques d'incendie dans les bâtiments ont été passées en revue, en mettant l'accent sur la génération et les étapes de l'incendie. L'inhalation de fumée étant responsable de la plupart des décès dans un incendie, une attention particulière a été accordée à la fumée d'incendie et à la production de gaz et d'aérosols. Ces études ont révélé que les incendies sous-ventilés et viciés sont des scénarios d'incendie dangereux, car ils favorisent la production de gaz asphyxiants et irritants et d'aérosols submicroniques. Lors de l'étude du comportement au feu d'un matériau, il est important de prendre en compte les effets d'échelle. Les comportements à l'échelle de la matière et du matériau doivent être évalués pour comprendre correctement la décomposition thermique. Pour ce faire, les tests pertinents ont été présentés depuis l'échelle de la matière (TGA-FTIR, pyrolyse-GC/MS) jusqu'à l'échelle du matériau (calorimètre à cône, SBI). Chaque test fournit des données nécessaires et complémentaires pour comprendre le comportement au feu d'un matériau. L'approche multi-échelle est l'une des approches actuelles permettant de faire le lien entre les échelles de laboratoire et le feu réel.

Après un état de l'art complet sur les dispositifs existants à l'échelle du banc capables d'évaluer la réaction au feu ainsi que les émissions de gaz et d'aérosols des matériaux, les dispositifs appropriés

pour mener à bien l'investigation expérimentale ont été choisis. À l'échelle de la matière, la décomposition thermique des matériaux en bois est étudiée par Py-GC/MS et par TGA/FTIR. Les deux techniques se complètent en ce qui concerne le processus de décomposition thermique et la production de gaz. À l'échelle du matériau, un calorimètre à cône à atmosphère contrôlée (CACC), couplé à la spectroscopie infrarouge à transformée de Fourier (FTIR) et à un impacteur électrique à basse pression (ELPI), a été développé. Cet équipement est polyvalent et permet d'étudier la réaction au feu des matériaux dans des environnements appauvris en oxygène (1 à 21 vol-% O₂). Plus important encore, la mise en place d'une cheminée a permis l'échantillonnage direct des fumées, suivi de la FTIR et de l'ELPI pour une analyse complète des gaz et des aérosols. La précision du CACC a été comparée aux résultats de la littérature sur le PMMA. À l'échelle intermédiaire, une enceinte ouverte avec un brûleur au propane a été conçue et implémentée avec des mesures FTIR et ELPI. La propagation du feu, la production de gaz et la distribution de la taille des aérosols peuvent être évaluées. La cartographie du flux thermique perçu à 40 et 90 kW a été réalisée et a permis de vérifier qu'un matériau incombustible recevait respectivement 20 et 50 kW/m² en surface.

Les expériences ont d'abord été réalisées à l'échelle de la matière en utilisant l'analyse thermogravimétrique (TGA)-FTIR avec plusieurs concentrations d'oxygène (21, 18, 15 et 10 vol-% O₂). Cette technique a permis d'obtenir des informations préliminaires sur les effets de l'oxygène sur la décomposition thermique et les émissions gazeuses du CLT et du WF. Sous azote, les décompositions thermiques du CLT et du WF sont un processus en une seule étape apparente. Cependant, sous oxygène, une réaction supplémentaire d'oxydation du char se produit et transforme les décompositions thermiques en un processus en deux étapes apparentes. Les principaux produits de décomposition du CLT et du WF au cours de la première étape de décomposition sont de l'eau, du dioxyde de carbone, du monoxyde de carbone, des aldéhydes, des acides carboxyliques et des composés de type phénol, tandis que l'eau, le dioxyde de carbone et le monoxyde de carbone sont produits au cours de l'étape d'oxydation du char. Afin d'obtenir une composition détaillée des composés de type phénol, la pyrolyse-chromatographie gazeuse/spectrométrie de masse (Py-GC/MS) a été effectuée sur le CLT et le WF. Le CLT et le WF ont tous deux libérés du lévoglucosan, du 3,6-Dianhydro- α -glucopyranose, du 5-(Hydroxyméthyl)-2-furfural et du 2-Méthoxy-4-vinylphénol.

Ensuite, l'effet de l'oxygène sur le comportement au feu, les émissions de gaz et d'aérosols du CLT, du WF et du CLT/WF a été étudié à l'échelle du banc avec l'appareil CACC-FTIR-ELPI. Les conditions

variaient entre quatre concentrations d'oxygène (21, 18, 15 et 10 vol-% O₂) et deux flux de chaleur (50 et 20 kW/m²). À 50 kW/m², le CLT et le WF s'enflamment tous deux à 21, 18 et 15 % d'O₂. La diminution de l'oxygène n'a pas d'effet sur le délai d'inflammation ni sur le pMLR, mais elle augmente la production d'imbrûlés (rendement en monoxyde de carbone (Y_{CO}) x3 de 21 à 15 vol-% O₂ pour le CLT). À 20 kW/m², le WF s'enflamme toujours à 21, 18 et 15 vol-% O₂, tandis que le CLT ne s'enflamme qu'à 21 et 18 vol-% O₂. L'abaissement du flux thermique à 20 kW/m² se traduit par des taux de perte de masse plus faibles (-34 % de pMLR à 21 % d'O₂ pour le CLT et -36 % de pMLR à 21 % d'O₂ pour le WF). Elle conduit également à des rendements plus élevés en gaz imbrûlés, les rendements en CO étant multipliés par 2 pour le CLT et par 8 pour le WF à 21 vol-% d'O₂. En outre, l'atténuation de l'oxygène à 20 kW/m² entraîne une diminution supplémentaire du pMLR (-33 % pour le CLT et 9 % pour le WF de 21 à 18 % d'O₂) et une augmentation des rendements en CO (Y_{CO} x3 de 21 à 15 % d'O₂ pour le WF). Enfin, la combinaison du CLT et du WF a entraîné la superposition des comportements au feu et des productions de gaz du CLT et du WF. Cependant, en raison de son effet radiatif, la flamme du WF a conduit à une inflammation plus rapide du CLT à 50 et 20 kW/m². De plus, l'oxygène a eu les mêmes effets sur la réaction au feu, la production de gaz et d'aérosols que sur le WF et le CLT.

De plus, pour compléter les résultats obtenus avec le CACC, un banc à plus grande échelle a été développé. Il s'agit d'une enceinte bien ventilée dans laquelle des panneaux d'un mètre sont exposés à la flamme d'un brûleur tandis que les gaz et les aérosols sont recueillis à l'aide du FTIR et de l'ELPI. Cela permet d'évaluer les réactions au feu (HRR, propagation de la flamme), la concentration de gaz et les caractéristiques des aérosols (distribution et concentration de la taille) des matériaux à plus grande échelle, en fournissant une attaque thermique similaire à l'allumage d'un objet isolé. Des résultats préliminaires ont été obtenus, mais il reste quelques tests d'étalonnage à effectuer pour calculer correctement le HRR. Le CLT présente une adhérence minimale aux flammes et se carbonise lentement, ce qui limite les émissions de gaz (CO₂). Inversement, la fibre de bois se dégrade rapidement et émet une quantité substantielle de gaz (CO₂, CO, CH₄). Lorsque le CLT et la fibre de bois sont combinés, les premiers résultats n'indiquent pas d'interaction significative entre les deux matériaux. Alors que dans les tests CACC, la fibre de bois avait un impact sur l'inflammation du CLT, ici, elle semble n'avoir aucun effet. Au contraire, chaque matériau se dégrade indépendamment, la fibre de bois étant responsable de la majorité des émissions de gaz. Ces résultats sont conformes à ceux obtenus dans le cadre de l'étude CACC, où la production de gaz était le résultat des deux

comportements individuels. Pour mieux évaluer les résultats obtenus, il serait utile de procéder à une pesée continue ou à une pesée avant et après des échantillons, ce qui permettrait une comparaison plus détaillée des rendements en gaz. En outre, les tests d'étalonnage en cours impliquant le brûleur et le système de ventilation visent à obtenir des calculs précis du HRR. Enfin, l'utilisation d'une autre sonde FTIR pourrait potentiellement capturer une plus large gamme de gaz, offrant ainsi une analyse plus complète.

Finalement, une étude complète des effets de l'oxygène sur le comportement au feu, la production de gaz et d'aérosols du CLT, du WF et d'un assemblage de CLT/WF a été réalisée à plusieurs échelles. Il a été démontré, grâce à un calorimètre à cône à atmosphère contrôlée innovant, que la diminution de l'oxygène a un effet considérable sur le processus de combustion et sur la production de gaz et d'aérosols du CLT, de la WF et du CLT/WF. En outre, cette recherche a présenté une nouvelle méthode expérimentale pour évaluer les interactions potentielles entre le CLT et le WF au cours d'un incendie. Les premiers résultats ont montré que le comportement de l'assemblage CLT/WF est la succession de ceux du CLT et du WF, sans interactions.

Assemblage de matériaux bois : effet de l'oxygène sur le développement du feu et l'émission de gaz et d'aérosol.

Les matériaux bois jouent un rôle clé dans la construction durable pour lutter contre le changement climatique. Cependant, en cas d'incendie, ils peuvent contribuer au développement du feu, challengeant leur utilisation. Afin d'améliorer la compréhension des risques d'incendie, des études expérimentales ont été menées pour examiner le comportement du Cross-Laminated Timber (CLT) et de la fibre de bois (WF) à diverses échelles, allant du banc d'essai à l'échelle intermédiaire. Ces études ont pris en compte des variations de température et de concentration en oxygène. Ces recherches se sont concentrées sur l'interaction potentielle entre le CLT et la WF, notamment dans une configuration mur/isolation. Les résultats indiquent que la diminution en oxygène a un impact significatif sur le comportement au feu, les émissions de gaz et d'aérosols du CLT, de la WF et du CLT/WF. De plus, la fibre de bois peut influencer négativement l'allumage du CLT dans certaines conditions. À une échelle plus large, le comportement au feu et la production de gaz de l'assemblage CLT/WF sont similaires à ceux de la WF, sans interactions observées entre les deux matériaux.

Mots-clefs : effluents, aérosols, réaction au feu, viciation, bois, cône calorimètre à atmosphère contrôlée

Wooden materials assembly: effect of oxygen on the development of fire and the emission of gases and aerosols.

Wood materials play a key role in sustainable construction to tackle climate change. However, in the event of fire, they can contribute to fire growth, challenging their use. To improve understanding of fire risk, experimental studies have been carried out to examine the behavior of Cross-Laminated Timber (CLT) and wood fiber (WF) at various scales, from test bench to intermediate scale. These studies considered variations in temperature and oxygen concentration. The research focused on the potential interaction between CLT and WF, particularly in a wall/insulation configuration. The results indicated that oxygen depletion had a significant impact on the fire behavior, gas, and aerosol emissions of CLT, WF and CLT/WF. In addition, wood fiber negatively influenced the ignition of CLT under certain conditions. On a larger scale, the fire behavior and gas production of the CLT/WF assembly are like those of WF, with no interactions observed between the two materials.

Key words: effluents, aerosols, fire reaction, viciation, wood, controlled-atmosphere cone calorimeter